



Universidade do Minho
Escola de Engenharia

Francisco Carrusca Pimenta de Brito

**Thermohydrodynamic Performance of
Twin Groove Journal Bearings Considering
Realistic Lubricant Supply Conditions:
A Theoretical and Experimental Study**



Universidade do Minho
Escola de Engenharia

Francisco Carrusca Pimenta de Brito

**Thermohydrodynamic Performance of
Twin Groove Journal Bearings Considering
Realistic Lubricant Supply Conditions:
A Theoretical and Experimental Study**

Tese de Doutoramento (PhD Thesis)
Área: Engenharia Mecânica, Sector: Tribologia

Trabalho efectuado sob a orientação do
Professor Doutor António A. Sousa Miranda

DECLARAÇÃO

Nome: FRANCISCO CARRUSCA PIMENTA DE BRITO

Endereço Electrónico: francisco@dem.uminho.pt **Telefone:** 967 381 071

N.º do Bilhete de Identidade: 10377388

Título da Tese de Doutoramento:

Thermohydrodynamic Performance of Twin Groove Journal Bearings Considering Realistic Lubricant Supply Conditions: A Theoretical and Experimental Study

Orientador:

Professor Doutor António A. Sousa Miranda

Ano de conclusão: 2009

Ramo de Conhecimento do Doutoramento:

Engenharia Mecânica, Sector: Tribologia

É AUTORIZADA A REPRODUÇÃO INTEGRAL DESTA TESE, APENAS PARA EFEITOS DE INVESTIGAÇÃO, MEDIANTE DECLARAÇÃO ESCRITA DO INTERESSADO, QUE A TAL SE COMPROMETE.

Universidade do Minho, / /

Assinatura: _____

Thermohydrodynamic Performance of Twin Groove Journal Bearings Considering Realistic Lubricant Supply Conditions: An Experimental and Theoretical Study

ABSTRACT

The smooth operation of the power transmission systems found in many transport vehicles and energy production systems is often limited by the reliability of the bearings which support their rotating shafts. Under high shaft speeds and applied loads, hydrodynamic journal bearings may constitute the only acceptable option for the designer.

When predicting the performance of journal bearings submitted to severe operating conditions it is crucial to account for the local variation of the temperature and the viscosity field. Furthermore, the lubricant supply conditions such as lubricant feeding pressure and temperature and the actual groove geometry should be treated realistically in the theoretical analysis.

The present report describes the work carried out by the author, focused on the theoretical and experimental study of the performance of twin groove journal bearings operating under steady state. A particular emphasis was put on the analysis of the influence of lubricant supply conditions.

The work included the development of a Thermohydrodynamic (THD) model for the analysis of the performance of twin groove journal bearings. The model has been based on the simultaneous numerical solution of the generalized Reynolds and Energy equations within the lubricant film and the heat transfer within the bush body. Special care was taken in the treatment of the phenomena taking place in the vicinity of feeding grooves and the modeling of the ruptured film region.

Test programs were carried out at the Laboratory of Tribology and Machine Elements of the University of Minho (LOMT) and at the Laboratory of Solid Mechanics of the University of Poitiers (LMS). The scope of these tests was, on one hand, to provide the scientific community with a wealth of experimental results spanning a wide range of supply conditions and providing an extensive discussion of the phenomena involved. On the other hand, the test programs would allow the validation and refinement of the theoretical model.

RESUMO

O bom funcionamento de muitos sistemas de transmissão de potência em veículos de transporte e em sistemas de produção de energia está frequentemente condicionado pela fiabilidade das chumaceiras que suportam os seus veios rotativos. Em situações onde estão envolvidas velocidades de rotação e cargas elevadas, as chumaceiras radiais hidrodinâmicas podem constituir a única alternativa aceitável para o projectista.

Na previsão do desempenho de chumaceiras submetidas a condições de funcionamento severas, torna-se necessário entrar em linha de conta com a variação local dos campos de temperatura e viscosidade. As condições de alimentação (pressão e temperatura de alimentação, geometria dos sulcos) devem também ser tidas em consideração na formulação do modelo teórico.

A presente dissertação descreve o programa de trabalhos levado a cabo pelo autor no âmbito de um projecto FCT que se dirigiu ao estudo teórico-experimental do desempenho de chumaceiras com dois sulcos de alimentação axiais funcionando em regime estacionário, tendo sido posto um ênfase particular no estudo da influência das condições de alimentação.

Os trabalhos incluíram o desenvolvimento de um modelo termohidrodinâmico (THD) para a previsão do desempenho deste tipo de chumaceiras. Este modelo foi baseado na solução numérica simultânea da equação de Reynolds generalizada, da equação da energia no filme lubrificante e da equação de transmissão de calor através do casquilho. Foi posto um particular cuidado na modelação dos fenómenos que ocorrem na região dos sulcos de alimentação e do fenómeno de ruptura de película.

Foi levado a cabo um programa de testes laboratoriais realizado no Laboratório de Órgãos de Máquinas e Tribologia da Universidade do Minho (LOMT) e no Laboratório de Mecânica dos Sólidos da Universidade de Poitiers (LMS). A realização deste programa de testes teve como objectivo, por um lado, a disponibilização de um conjunto de resultados experimentais com uma ampla gama de variação das condições de alimentação e o respectivo estudo dos fenómenos envolvidos. Por outro lado, a realização do programa de testes teve também em vista a validação e o refinamento modelo teórico desenvolvido.

ACKNOWLEDGEMENTS

The present work was only possible due to the invaluable support of many people and institutions.

I am profoundly grateful to my supervisor Prof. António Sousa Miranda for his unconditional support to my work during these years. He was always there when I needed the help of his knowledge and experience. His thorough revisions helped me to improve enormously the content of the publications we submitted.

I am deeply in debt to Prof. Michel Fillon, who not only provided me a fruitful permanence in his Laboratory, with great work being done together, but he was always present whenever I needed his advice, even being far away. I am also grateful to Prof. Pimenta Claro for his role in the experimental part of the work, and also for his strong commitment to the revision of the papers we submitted together. Lucrécio Costa has also provided an invaluable help to my theoretical work not only with his advice but also because I was able to start on the basis of his previous work. I am equally grateful to Prof. José Carlos Teixeira for his help on the development of the thermal model and to Eurico Seabra's invaluable practical sense and experience with the subtleties and intricacies of sensors and data acquisition systems.

I would like to thank also Senhorinha Teixeira, Paulo Flores, Gaspar Machado, Jorge André, Pedro Lobarinhas, Luís Alves, António Amaral Nunes and many other colleagues of the Mechanical Engineering Department for their advice on theoretical and computational issues. I want to thank Ricardo Ribeiro for Physics department for being able to use the computer cluster *Dirac*. I want to remember also Mr. Leite and Vítor of the workshop of the department, Júlio Caldas, Fernando Araújo and Sérgio Carvalho for their help on the experimental component of the work, and Maria Luísa and Sandra.

All this work was only possible with the financial and logistic support of several institutions which are therefore acknowledged:

-The Tribology and Machine Elements Laboratory (LOMT) where part of the work was undertaken, the CT2M Research Center under which I was integrated, the Mechanical Engineering Department, and the School of Engineering of the University of Minho for all the support given to the work.

-The Laboratory of Solid Mechanics (LMS) of the University of Poitiers, France (URM CNRS

6610) where another part of the experimental work was carried out, along with all those who helped me in the task, in particular Jean Bouyer for his help on the experimental task.

-The FCT - Fundação para a Ciência e a Tecnologia, for funding the project POCTI/39202/EME/2001 (in conjunction with the European Union fund FEDER) and later the PhD grant SFRH / BD / 22278 / 2005.

-The FLAD – Fundação Luso-Americana para o Desenvolvimento – for financing the trip for the presentation of a communication in the International Joint Tribology Conference 2005 in Texas, USA.

- GALP Energia for supplying the lubricant that was used in the LOMT tests.

I cannot end these paragraphs without declaring that I am in sheer debt with God, my family, in particular my parents, and so many good friends who have helped me to accomplish this task with their unfading care, counsel and support. To all the individuals and institutions that were mentioned, as well as to those that were not mentioned but have somehow contributed to the fulfillment of the present work, my deep and sincere THANK YOU!

*A good scientist is a person with original ideas.
A good engineer is a person who makes a design that
works with as few original ideas as possible.*
- Freeman Dyson

CONTENTS

ABSTRACT	iii
RESUMO	v
ACKNOWLEDGEMENTS	vii
CONTENTS	ix
NOMENCLATURE	xv
Latin Symbols	xv
Greek Symbols	xvii
Subscripts	xviii
Abbreviations	xix
NON-DIMENSIONAL VARIABLES AND GROUPS	xxi
CHAPTER I Introduction	1
I.1 Principles of operation	1
I.2 The lubricant supply conditions	3
I.3 The performance prediction of hydrodynamic journal bearings	3
I.4 Outline of the present work	4
CHAPTER II State of the art	5
II.1 Historical background	5
II.2 Pressure and flow calculations	6
II.2.1 The early models	6
II.2.2 The short bearing approximation	6
II.2.3 The advent of numerical methods and computer-based calculations	7
II.2.4 The Reynolds Model	7
II.2.5 The Jacobson-Floberg-Olson (JFO) mass-conserving algorithm	8
II.2.6 Elrod's algorithm and its variants	9
II.2.7 The models of Vijayaraghavan and Keith	12

II.2.8	Other models inspired in Elrod's theory	13
II.2.9	Recent approaches to the pressure-flow problem in journal bearings	13
II.3	Thermal effects	17
II.3.1	The Global Thermal Model	17
II.3.2	The first approaches to the local thermal problem	18
II.3.3	The Generalized Reynolds Equation of Dowson	18
II.3.4	Subsequent approaches to the THD problem	18
II.3.5	The adiabatic condition at the bush-film interface	19
II.3.6	The continuity at the interface and the heat conduction in the bush	19
II.3.7	The axial temperature gradient	21
II.3.8	Shaft temperature calculations	21
II.3.9	The Couette approximation	22
II.3.10	Treatment of cross-film phenomena	22
II.3.11	Thermal mixing in the grooves	23
II.3.12	The CFD approach	25
II.3.13	The treatment of reverse flow	28
II.3.14	The thermal model of the ruptured film zone	29
II.3.15	The consideration of thermal and elastic deformations	38
II.3.16	The Influence of lubricant supply conditions on thermal behavior	40
II.4	Numerical methods and Programming tools	44
II.4.1	Numerical methods	44
II.4.2	Programming tools	45
II.5	Current trends in journal bearing analysis	46
II.5.1	Non-Newtonian effects, namely due to lubricant additives	46
II.5.2	Roughness and micro-texture effects	47
II.5.3	The analysis of Inertia effects	50
II.5.4	Thermal analysis of dynamically loaded journal bearings	51
II.5.5	Optimization techniques in bearing design	51
II.5.6	Influence of form defects and wear	53
II.5.7	Innovative journal bearing solutions	54
II.6	Conclusions	55
CHAPTER III	<i>Theoretical Model</i>	57
III.1	Introduction	57
III.2	Basic Assumptions	58
III.3	Lubricant properties	59
III.4	Journal bearing geometry	60
III.4.1	Basic geometry	60
III.4.2	The unwrapped bearing and the fluid domain	61
III.4.3	Non-dimensional analysis and coordinate transformation	62

III.5	Pressure and velocity field	64
III.5.1	Hydrodynamic lift	64
III.5.2	Film rupture and reformation	65
III.5.3	The Generalized Reynolds Equation	67
III.5.4	The Elrod-Adams algorithm	68
III.5.5	The Elrod algorithm	71
III.5.6	Velocity field	77
III.5.7	Flow rate calculations	80
III.6	Introduction to the thermal problem	82
III.7	The energy equation	84
III.8	The Laplace equation	86
III.9	Thermal boundary conditions	87
III.9.1	Bush – film interface	88
III.9.2	Groove inner walls	88
III.9.3	Bush – ambient interface	89
III.9.4	Shaft - film interface	89
III.10	Thermal modeling of the ruptured film region	90
III.10.1	Effective Length (EL) model	91
III.10.2	Modified effective length (EL_m) model	92
III.11	Thermal modeling of the groove region	96
III.11.1	Global thermal balance	97
III.11.2	Mixing coefficient and inner groove temperature	99
III.11.3	The occurrence of negative flow rate at one of the grooves	101
III.11.4	Incorporating the influence of the groove length into the 2D approach	103
III.11.5	Temperature profiles at the inlet section	104
III.12	Differential thermal expansion compensation	108
III.13	Main performance parameters	109
III.14	Numerical procedure	111
III.14.1	Algorithm description	112
III.14.2	Mesh selection	115
III.14.3	Convergence criteria	119
III.14.4	Elrod Algorithm constant (β)	120
III.15	Conclusions	121
CHAPTER IV	<i>Experimental work at the University of Poitiers (LMS)</i>	123
IV.1	Introduction	123
IV.2	Bearing Test Rig and experimental procedure	124
IV.3	Results and Discussion	130

IV.3.1	Effect of changes in feeding pressure	130
IV.3.2	Influence of changes in feeding temperature.	135
IV.4	Conclusions	139
CHAPTER V Experimental work at the University of Minho		141
V.1	Introduction	141
V.2	Bearing test rig	142
V.2.1	Overview of the rig	142
V.2.2	Bushes and shafts	144
V.2.3	Shaft motion control	145
V.2.4	Loading system	146
V.2.5	Lubricant feeding system and feeding pressure regulation	146
V.2.6	Feeding temperature regulation system	147
V.2.7	Data acquisition system	148
V.2.8	Temperature measurement	150
V.2.9	Lubricant flow rate measurement	153
V.2.10	Shaft locus measurement	156
V.3	Detailed procedure followed during test sessions	161
V.4	Results and discussion	163
V.4.1	Test program	163
V.4.2	Influence of shaft speed and applied load	164
V.4.3	Influence of feeding pressure	172
V.4.4	Influence of feeding temperature	177
V.4.5	Influence of bearing clearance	183
V.4.6	Influence of the number of grooves	185
V.5	Conclusions	192
CHAPTER VI Model validation		195
VI.1	Introduction	195
VI.2	Tuning of parameters	195
VI.2.1	Mixing factor	196
VI.2.2	Thickness of the shaft-adhered layer	198
VI.3	Comparison of model predictions with published results	200
VI.3.1	Ferron et al. (1983)	200
VI.3.2	Ma & Taylor (1992, 1994)	202
VI.3.3	Lund & Tonnesen (1984)	206
VI.4	Comparison between predictions and the LMS results	208
VI.5	Comparison between predictions and the LOMT results	212
VI.6	Conclusion	215

CHAPTER VII	<i>Parametric study of the influence of lubricant supply conditions on bearing performance</i>	217
VII.1	Introduction	217
VII.2	Influence of lubricant feeding pressure	219
VII.3	Influence of lubricant feeding temperature	226
VII.4	Influence of the groove length ratio (a/b)	231
VII.5	Influence of the groove width ratio (w/d)	236
VII.6	Influence of the number of grooves	239
VII.7	Influence of the location of the grooves with respect to the load line	243
VII.8	Conclusion	252
CHAPTER VIII	<i>Overall conclusions and proposals for future work</i>	255
	<i>References</i>	263
	<i>Appendix I – calculations of the temperature profile in the Inlet section (exponential type)</i>	281
	<i>Appendix II – Finite Difference Solution of the Energy Equation</i>	285

*There's no point in being exact about something
if you don't even know what you're talking about.*

- John von Neumann

NOMENCLATURE

Latin Symbols

Symbol	Units	Description
a	m	Groove length (axial direction)
b	m	Bush length (axial direction)
c_d	m	Diametral clearance
c_r	m	Radial clearance
c_{mix}	-	Mixing coefficient used to obtain the leading edge temperature, T_{le}^+
C_p	J/kgK	Specific heat (constant pressure)
d	m	Nominal bearing diameter
e	m	Shaft eccentricity
e_s	m	Thickness of the layer of lubricant adhered to the shaft (Modified Effective Length model)
\bar{e}_{s0}	-	Fraction of the film height filled with the layer of lubricant adhered to the shaft (Modified Effective Length model)
\overline{EL}	-	Effective length ratio (fraction of the bearing length filled with liquid streamers for a given circumferential coordinate)
\overline{EL}_m	-	Modified Effective length ratio (same as \overline{EL} but corrected for the modified effective length model)
$F_1 \dots F_5$		Viscosity integrals
g	-	Switch function used in Elrod's formulation
h	m	Local film thickness
h_{min}	m	Minimum film thickness
h_{max}	m	Maximum film thickness
H_{amb}	W/m ² K	Global heat transfer coefficient between the bush and the ambient
H_{gr}	W/m ² K	Global heat transfer coefficient between the bush and the inner groove flow
i	-	Index of the grid points along the axial direction
j	-	Index of the grid nodes along the circumferential direction

k	-	Index of the grid nodes along the radial direction (fluid domain)
k_b	-	Index of the grid nodes along the radial direction (bush body domain)
K_{air}	W/mK	Thermal conductivity of the air
K_b	W/mK	Thermal conductivity of the bush body
K_l	W/mK	Thermal conductivity of the lubricant (liquid phase)
K_{eq}	W/mK	Equivalent thermal conductivity of the fluid (gaseous+liquid)
M_{shaft}	Nm	Shaft torque
M_{bush}	Nm	Bush torque
N	rpm	Shaft rotational speed
N_r	-	Total number of grid points along the radial direction (bush body domain)
N_x	-	Total number of grid points along the circumferential direction
N_y	-	Total number of grid points along the radial direction (fluid domain)
N_z	-	Total number of grid points along the axial direction (for half of the bearing)
O	-	Origin of the coordinate system $(O, \bar{x}, \bar{y}, \bar{z})$
O_r	-	Origin of the cylindrical coordinate system $(O_r, \bar{r}, \bar{\alpha}, \bar{\zeta})$
p	Pa	Hydrodynamic pressure within the film (relative to ambient pressure)
P_f	Pa	Lubricant feeding pressure (relative to ambient pressure)
P_{rupt}	Pa	Pressure at which film rupture occurs (considered as zero – ambient – in this work)
P	W	Power loss
q	W	Heat transfer rate
Q	l/min	Flow rate (volumetric)
Q_f	l/min	Lubricant feeding flow rate
r	m	Radial coordinate (bush body domain)
r_{gr}	m	Radial coordinate of the bottom face of the groove (equal to R_i + groove depth)
R_i	m	Nominal bearing radius / inner bush radius
R_e	m	Outer bush radius
T	°C	Temperature (fluid domain)
T_{amb}	°C	Ambient temperature – the average temperature of the bearing system environment
T_b	°C	Temperature (bush body domain)
T_{bush_avg}	°C	Average bush body temperature
T_f	°C	Lubricant feeding temperature
T_{le}	°C	Leading edge temperature – The average temperature of the lubricant leaving the groove and entering the bearing land

T_{is}	°C	Inlet section temperature – equal to T_{le} but corrected in order to account for the temperature of the whole axial extension of the bush and not just that corresponding to the groove extension
T_{max}	°C	Maximum bush temperature
u_x	m/s	Circumferential component of fluid velocity
u_y	m/s	Radial component of fluid velocity
u_z	m/s	Axial component of fluid velocity
U	m/s	Tangential velocity of the shaft surface
W	N	Applied load / Load carrying capacity
W_C	N	Resulting load along the direction of the line of centers
W_N	N	Resulting load along the direction normal to the line of centers
W_s	Pa	Specific Load (The load divided by the projected area of the bush ($b \cdot d$))
w	m	Groove width (circumferential direction)
x	m	Circumferential coordinate of the unwrapped geometry
y	m	Radial coordinate (fluid domain)
z	m	Axial coordinate

Greek Symbols

Symbol	Units	Description
α	deg	Circumferential coordinate – angle measured from the center of the +90° groove
β	N/m ²	Constant used in Elrod's algorithm based on the concept of the Bulk modulus of a liquid lubricant
β_v	-	Thermoviscosity coefficient of a lubricant
ε	-	Eccentricity ratio
φ	deg	Attitude angle
Φ	-	Viscous dissipation parameter of the energy equation
γ	deg	Angle measured from the position of maximum film thickness
θ	-	Variable used in the hydrodynamic pressure / continuity calculations through the Elrod algorithm
θ'	-	Liquid fraction (volumetric)
λ	-	Dummy variable of y/η used in Eq. III-44
μ_l	Pa·s	Dynamic viscosity of the lubricant
μ_{eq}	Pa·s	Equivalent dynamic viscosity of the liquid+gaseous flow at the ruptured film region used for the solution of the equivalent thermal problem

μ_f / μ_0	Pa·s	Dynamic viscosity of the lubricant at feeding temperature
μ_g	Pa·s	Dynamic viscosity of the gaseous mixture (considered as being that of the air)
ν	cSt	Kinematic viscosity of the lubricant
ρ_l	kg/m ³	Density of the liquid lubricant (continuous film)
ρ_g	kg/m ³	Density of the gaseous mixture (considered as being that of the air)
$(\rho C_p)_{eq}$	kg/m ³	Equivalent group of properties (density times specific heat) of the liquid+gaseous flow at the ruptured film region used for the solution of the equivalent thermal problem
ω	s ⁻¹	Angular velocity of the shaft

Subscripts

<i>axial</i>	Corresponding to the lateral edges of the groove
<i>bkf</i>	Corresponding to back flow (oil leaving the groove through the trailing edge, in the upstream direction)
<i>cv</i>	Control volume
<i>Hte</i>	Subscript of the convective heat transfer rate at the inner groove face located at the coordinate of the trailing edge
<i>Hle</i>	Subscript of the convective heat transfer rate at the inner groove face located at the coordinate of the leading edge
<i>Hbottom</i>	Subscript of the convective heat transfer rate at the inner groove face located at the bottom
<i>i</i>	index of the grid points along the axial direction (except in the case of R_i - Nominal bearing radius).
<i>is</i>	Inlet section of a bearing land (the whole bush section at the coordinate of the leading edge of the groove)
<i>j</i>	Index of the grid nodes along the circumferential direction
<i>k</i>	Index of the grid nodes along the radial direction (fluid domain)
<i>k_b</i>	Index of the grid nodes along the radial direction (bush body domain)
<i>le</i>	Corresponding to the leading edge of a groove (downstream edge) or its circumferential coordinate
<i>out</i>	Corresponding to flow rate leaking from the bearing through its edges
<i>rvf</i>	Corresponding to reverse flow (oil entering the leading edge of the groove coming from downstream)
<i>te</i>	Corresponding to the trailing edge of a groove (upstream edge) or its circumferential coordinate
<i>x</i>	Along Circumferential coordinate

<i>y</i>	Along radial coordinate (fluid domain)
<i>z</i>	Along axial coordinate

Abbreviations

<i>BEM</i>	Boundary Element Method
<i>Br</i>	Brinkman number
<i>CFD</i>	Computational Fluid Dynamics
<i>CJC</i>	Cold Junction Compensation
<i>EHL</i>	Elasto-hydrodynamic Lubrication
<i>EL</i>	Effective Length model
<i>EL_m</i>	Modified Effective Length model
<i>FDM</i>	Finite Difference Method
<i>FEM</i>	Finite Element Method
<i>FFT</i>	Fast Fourier Transform
<i>FH</i>	Film Height model
<i>FVM</i>	Finite Volume Method
<i>GB</i>	Gas Bubble model
<i>GRE</i>	Generalized Reynolds Equation
<i>HD</i>	Hydrodynamic
<i>ISOADI</i>	Theoretical approach proposed by some authors consisting on considering an isothermal shaft and an adiabatic bush
<i>ITS-90</i>	International Temperature Scale of 1990
<i>JFO</i>	Jacobson-Floberg-Olson theory
<i>LMS</i>	Solid Mechanics Laboratory of Poitiers University
<i>LOMT</i>	Machine Elements and Tribology Laboratory of Minho University
<i>NIST</i>	National Institute of Standards and Technology (USA)
<i>PL</i>	Power Loss
<i>Pe</i>	Peclet number
<i>Re</i>	Reynolds number
<i>RE</i>	Reynolds Equation
<i>RFP</i>	Relaxation factor used in the pressure field iterative process
<i>RFT</i>	Relaxation factor used in the fluid temperature field iterative process
<i>RFT_b</i>	Relaxation factor used in the bush temperature field iterative process
<i>RPM</i>	Revolutions Per Minute

<i>TEC</i>	Thermal expansion coefficient
<i>TEHD</i>	Thermoelastohydrodynamic
<i>THD</i>	Thermohydrodynamic
<i>Tol_P</i>	Tolerance used in pressure calculations through the Elrod Algorithm
<i>Tol_T</i>	Tolerance used in lubricant temperature calculations
<i>Tol_{Tc}</i>	Tolerance used in bush temperature calculations
<i>UM</i>	University of Minho
<i>UP</i>	University of Poitiers

NON-DIMENSIONAL VARIABLES AND GROUPS

Brinkman number

$$Br = \frac{\mu_f U^2}{K_{eq} T_f}$$

Bulk modulus [Pa]

$$\beta = \frac{\mu_f R_i U}{c_r^2} \bar{\beta}$$

Film thickness [m]

$$h = c_r \bar{h}$$

Flow rate [$\text{m}^3 \cdot \text{s}^{-1}$]

$$Q = c_r b U \bar{Q}$$

Heat transfer rate [W]

$$q = \rho_l C_{p_i} c_r b U T_f \bar{q}$$

Load [N]

$$W = \mu_f b U \left(\frac{R_i}{c_r} \right)^2 \bar{W}$$

Peclet number

$$Pe = \frac{[\rho c_p]_{eq} U c_r^2}{K_{eq} R_i}$$

Power Loss [W]

$$P = \frac{\mu_f b U^2 R_i}{c_r} \bar{P}$$

Pressure [Pa]

$$p = \frac{\mu_f R_i U}{c_r^2} \bar{p}$$

Reynolds number (nominal)

$$Re = \frac{\rho U c_r}{\mu_f}$$

Sommerfeld number

$$S = \left(\frac{R_i}{c_r} \right)^2 \frac{\Omega \mu_f}{2\pi W_s}$$

Spatial coordinates [m]

$$x = R_i \alpha \quad y = h \eta = c_r \bar{h} \eta \quad z = b \zeta \quad r = R_i \bar{r}$$

Temperature [K]

$$T = T_f \bar{T} \quad ; \quad T_b = T_f \bar{T}_b$$

Torque [N·m]

$$M_t = \frac{\mu_f b U R_i^2}{c_r} \bar{M}_t$$

Velocity [$\text{m}\cdot\text{s}^{-1}$]

$$\begin{cases} u_x = U\bar{u}_x \\ u_y = \frac{Uc_r}{R_i}\bar{u}_y \\ u_z = U\bar{u}_z \end{cases} \begin{cases} \dot{\alpha} = \frac{U}{R_i}\bar{\dot{\alpha}} \\ \dot{\eta} = \frac{U}{R_i}\bar{\dot{\eta}} \\ \dot{\zeta} = \frac{U}{b}\bar{\dot{\zeta}} \end{cases} \begin{cases} \bar{u}_x = \bar{\alpha} \\ \bar{u}_y = \eta \frac{\partial \bar{h}}{\partial \alpha} \bar{\alpha} + \bar{\eta} \bar{h} \\ \bar{u}_z = \bar{\zeta} \end{cases}$$

Viscosity [$\text{Pa}\cdot\text{s}$]

$$\mu = \mu_f \bar{\mu}$$

Viscosity integrals, F_i

$$\begin{cases} F_0 = \frac{\bar{h}c_r}{\mu_f} \bar{F}_0 \\ F_1 = \frac{\bar{h}^2 c_r^2}{\mu_0} \bar{F}_1 \\ F_2 = \frac{\bar{h}^3 c_r^3}{\mu_f} \bar{F}_2 \\ F_3 = \bar{F}_3 \end{cases} \begin{cases} F_4 = \frac{\bar{h}^2 c_r^2}{\mu_f} \bar{F}_4 \\ F_5 = \frac{\bar{h}c_r}{\mu_f} \bar{F}_5 \end{cases}$$

*Some say the cup is half empty, while others say it is half full.
In my opinion, both are wrong. The real problem is the cup is too big.
Sometimes all we need is a new perspective on an old problem.
- Donald Coduto (in "Foundation Design")*

CHAPTER I Introduction

Hydrodynamic journal bearings are machine elements used since the beginning of the industrial revolution for the support of rotating shafts. They are typically found in vehicles (both terrestrial, maritime and aerial), power plants (hydraulic, thermoelectric, nuclear, wind) and in general all mechanical systems with rotating shafts subjected to high surface speeds and/or applied loads (turbines, compressors, pumps, gear boxes, internal combustion engines, etc). Under such operating conditions their use generally constitutes the only practical option for the designer, since the other bearing types (namely, rolling bearings) would likely display unusually short life due to acute fatigue problems. Figure I-1a illustrates the typical range of operation for each bearing type, according to the operating conditions, as proposed by ESDU 65007.

1.1 Principles of operation

The basic function of Hydrodynamic journal bearings is to support radially loaded shafts, simultaneously allowing their free rotation with minimal drag and negligible wear. Their geometry is rather simple consisting of a (generally) metallic cylindrical shell, the bush, in which the shaft is seated and allowed to rotate freely within a small clearance.

A continuous flux of liquid lubricant is fed to the gap between the bush and the shaft through holes or axial grooves machined in the bush body, so that a thin film of lubricant is formed between the two surfaces, thus keeping them out of contact. Journal bearings with two axial grooves located at $\pm 90^\circ$ to the load line are widely used, especially when the shaft is expected to assume both directions of rotation. Some examples of this bearing type are displayed in Figure I-1b.

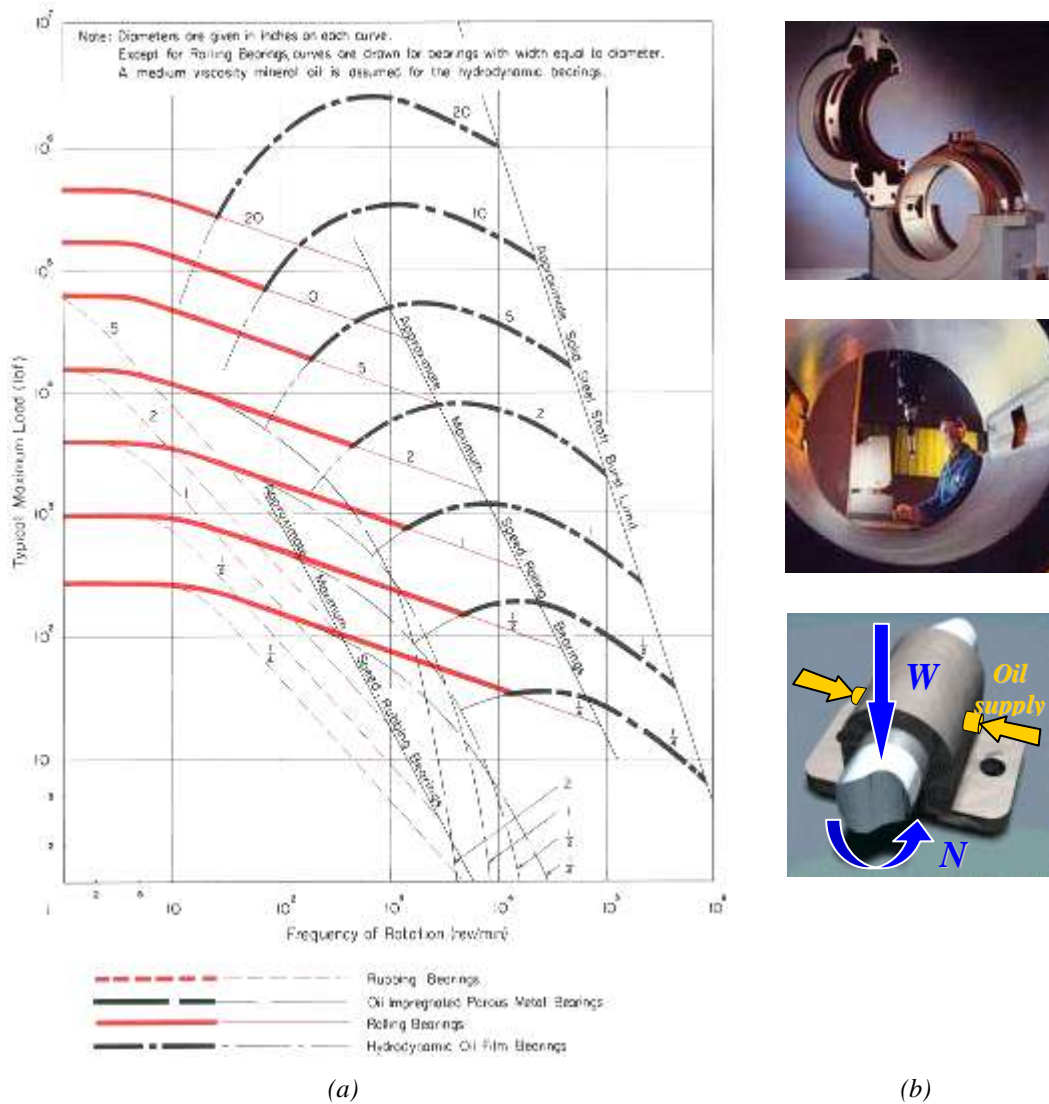


Figure I-1 – (a) Range of application of several bearing types (ESDU 65007); (b) examples of twin axial groove journal bearings (the lower image is schematic)

A sketch of a twin groove journal bearing under operation is presented in Figure I-2. The movement of the shaft surface relative to the inner bush surface causes the appearance of a positive pressure field generated hydrodynamically within the fluid, at the convergent portion of the gap. This effect, called the hydrodynamic lift, eventually compensates the applied load and causes the complete separation of both surfaces.

Once the full hydrodynamic regime has been achieved, the shaft rotates with a very low drag force and with virtually no wear under steady state operation. That is why the useful life of these components, if conveniently dimensioned, depends mainly on the frequency of starts and stops, the sole occasions where brief direct contact between bush and shaft is supposed to occur (especially if they are made under load).

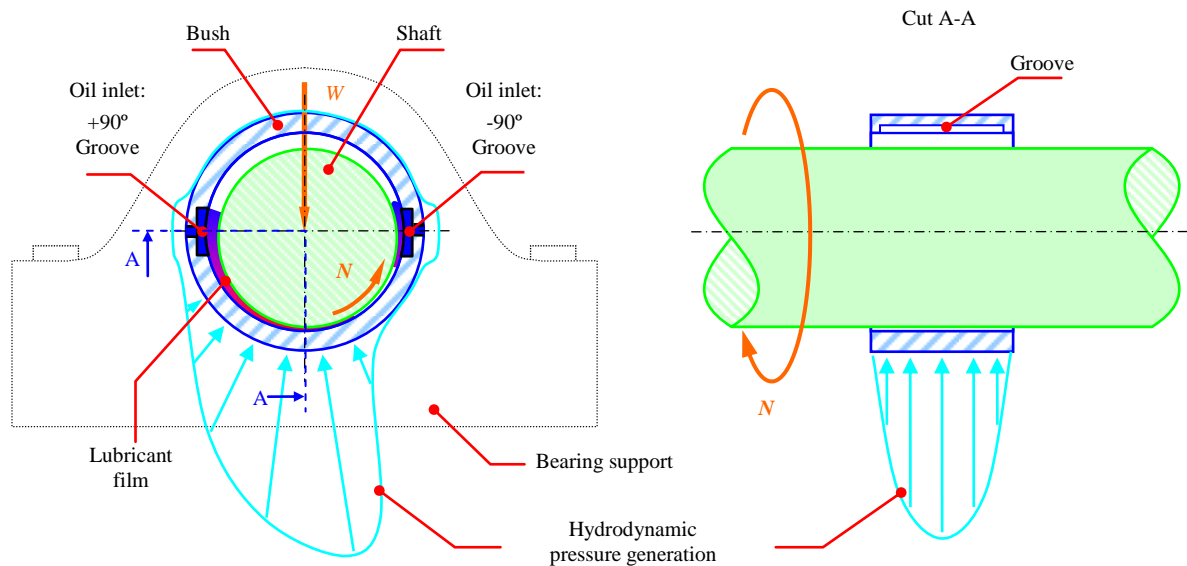


Figure I-2 -Outline of the hydrodynamic pressure generation in a twin groove journal bearing (a generic bearing support has been added).

1.2 The lubricant supply conditions

The lubricant supply conditions, which can vary significantly from case to case, affect the bearing behavior in several ways. In fact, the geometry and location of the grooves, the oil feeding pressure, P_f , and the oil feeding temperature, T_f , can influence significantly the pressure field, the flow patterns and the thermal behavior of the bearing system.

The lubricant feeding system is normally a closed circuit: the lubricant contained in the oil tank is fed to the bearing system through a pump, normally at a prescribed pressure, P_f . After leaking from the bearing, the oil is collected back into the oil tank. The control over the temperature at which the lubricant is fed to the bearing, T_f , depends on the effectiveness of the specific oil cooling system (if present), the capacity of the oil tank and the severity of the operating conditions, which can affect significantly the oil outlet temperature.

1.3 The performance prediction of hydrodynamic journal bearings

In recent years, mechanical design has been subjected to a considerable optimization effort, propelled by a more and more demanding global economy which requires an ever-growing reduction of conception and operating costs. At the same time, the need to achieve higher reliability standards in some critical applications, such as nuclear power plants, aerospace, automotive and medical applications, has required the machine design methods to become much more soundly based, relying on physically accurate models validated with extensive experimentation. The advent of computer-based simulation and the successive increase of

computation power further contributed to the improvement of machine element design techniques.

The accurate prediction of hydrodynamic journal bearing behavior is far more complex than what their simple geometry might initially suggest. In fact, the simultaneous pressure, flow and heat transfer calculations need to include the treatment of phenomena such as film rupture, dual phase flow, film reformation, forced and free convection, conduction, viscous dissipation, inner groove mixing and thermo-elastic distortion. The integrated modeling of these phenomena in a single algorithm displaying acceptable computation times does not seem a straightforward task.

The complexity of the problem has lead frequently to the use of oversimplified models. Particularly, the incorporation of lubricant supply conditions was normally made in an oversimplified way in most theoretical approaches or inclusively altogether disregarded. In fact, neglecting the effect of lubricant feeding pressure, feeding temperature or the actual geometry and location of grooves might explain some of the notable discrepancies found between many theoretical predictions and experimental measurements. These discrepancies seem to be especially acute in the case of twin groove journal bearings. The lack of comprehensive experimental data focusing on these issues might have also contributed for the lack of awareness on the important role which lubricant supply conditions play in bearing performance.

1.4 Outline of the present work

The aforementioned observations ultimately motivated the present work, which is in continuity with the previous work developed by the team on the analysis of journal bearing performance.

After a thorough assessment of the current state of the art of hydrodynamic journal bearing lubrication (CHAPTER II), a thermohydrodynamic (THD) model which realistically incorporates the influence of lubricant supply conditions on bearing performance was developed and applied to the twin groove journal bearing geometry (CHAPTER III). Additionally, an experimental test program was carried out in the Laboratory of Solid Mechanics of the University of Poitiers - LMS (CHAPTER IV) and in the Laboratory of Tribology and Machine Elements of the University of Minho - LOMT (CHAPTER V). This enabled a broad discussion of the role lubricant of supply conditions in the bearing behavior. After the validation task (CHAPTER VI), the theoretical model was used for a parametric study of the influence of lubricant supply conditions on the performance of twin groove journal bearings (CHAPTER VII). Finally, the major conclusions of the present work were summarized in CHAPTER VIII.

If you steal from one author, it's plagiarism.

If you steal from many, it's research.

- Wilson Mizner

CHAPTER II State of the art

II.1 Historical background

Hydrodynamic Journal Bearings are widely used since immemorial times as machine elements. However, lubrication theory only gave its first steps at the end of the Nineteenth century with works such as those of Hirn (1854) or Petrov (1883), which verified in his experiments that drag was actually caused by the shear rate within the fluid rather than by direct interaction between the two surfaces in relative motion. Moreover, Petrov discovered that viscosity, and not density, was the physical property responsible for drag and ultimately hydrodynamic lift. By the same time Beauchamp Tower (1883, 1885) was the first to study experimentally the relation between hydrodynamic pressure generation and the load capacity of train journal bearings. But properly, it may be stated that hydrodynamic lubrication theory began with the theoretical achievements of Sir Osborne Reynolds. The Reynolds equation (Reynolds, 1886), which he derived from the mass and momentum conserving equations under thin film conditions, governs hydrodynamic pressure generation and lubricant flow. This equation, which constituted a theoretical support for Tower's experimental findings, became the basis of modern hydrodynamic lubrication theory. Since then great achievements have been accomplished concerning the performance and reliability of lubricated machine elements. This was possible due to the long accumulated operative experience and the ever-growing theoretical achievements that persist to this day.

In the following sections, a description of the evolution and the current state of the art of hydrodynamic journal bearing performance analysis will be presented in its various theoretical and experimental aspects. A special focus will be put on the twin groove journal bearing, which is the geometry under study. Additional bibliography on the subject can be found in various books (Dowson, 1979; Pinkus, 1990), articles (Fillon et al, 1987; Khonsari, 1987; Tanaka, 2000) and PhD theses (Pierre, 2000; Costa, 2000; Bouyer, 2003).

II.2 Pressure and flow calculations

II.2.1 The early models

Before the advent of computers, scientific research on hydrodynamic lubrication kept its focus on the development of analytical models for the solution of the theoretical problem, namely the Reynolds equation solutions. Notable pioneer works were those of Sommerfeld (1904), with its long journal bearing theory. He derived an analytical solution for the Reynolds equation which neglects the effect of the bearing edges (infinitely long bearing approximation) as well as the occurrence of film rupture. However, this last approximation caused this theory to predict unrealistic load carrying capacities.

Gumbel (1914) improved Sommerfeld's solution by presenting the Half-Sommerfeld theory. In this approach, the negative pressures obtained at the divergent portion of the gap with the former theory are instead turned to zero. This approach tried to take into account the observed phenomenon in which the lubricant flow at the divergent portion of the bearing gap ruptures in several streamers and maintains itself at nearly ambient pressure instead of generating sub-ambient pressures as in the Sommerfeld Theory.

Swift (1931) and Stieber (1933) further improved the film rupture model by imposing a pressure gradient continuity at the rupture boundary. This way, both the pressure and its gradient are null at the rupture boundary. This condition seems to be physically accurate.

II.2.2 The short bearing approximation

Although the infinitely wide bearing may provide an acceptable approximation for bearings with length to diameter ratios over 1, such wide bearings are of limited use nowadays as they are prone to problems derived from misalignment. Ockvirk (1952) proposed the Short Bearing theory, an approximate method to predict the behavior of narrow bearings, which are more commonly used in industry and for which the long bearing theory provided poor results. This analytical solution was accomplished by neglecting the circumferential pressure gradients, which were assumed to be small in comparison with the axial pressure gradients.

These simplified analytical models using the short and the long bearing approximations were very popular and were still used in some recent theoretical works. Brown et al. (2000), Yang et al. (2001), Keogh and Khonsari (2001), Taylor (2004) and Song et al. (2005) have used the short bearing approximation on their works, while Deng and Brown (2008) and Wang and Khonsari (2008) applied the long bearing approximation. Reason and Narang (1982) combined

the two methods by means of a harmonic pressure average technique in order to obtain results which would be valid for the whole range of bearing widths. Similar approaches were made by Rao et al (2000, 2001) and Pereira et al (2007) concerning the dynamic problem.

Unfortunately, purely analytical approaches often lack the accuracy required in many applications as their use frequently implies an over-simplification of the problem. This is especially true when dealing with rather complex issues such as film rupture and reformation and the consideration of the lubricant supply conditions.

II.2.3 The advent of numerical methods and computer-based calculations

The appearance and the subsequent development of computers permitted the use of less simplified approaches based on numerical methods. The first computer-based solutions of the Reynolds equation were obtained by Raimondi and Boyd (1958) and Pinkus (1958), although simplified numerical methods were used before in such works as those of Christopherson (1941) or Frankel (1946). As computing systems became widespread, the algorithms based on numerical methods became the main performance analysis tool. This big leap in calculation capacity given by computer systems permitted, for instance, the rigorous treatment of film rupture and reformation as well as the consideration of thermal effects.

II.2.4 The Reynolds Model

The so-called “Reynolds Model” relies on the use of the Swift-Stieber conditions, also known as “Reynolds conditions” (described above) for the location of the film rupture boundary, along with the algorithm developed by Christopherson (1941). This algorithm is based on a finite difference solution of the Reynolds equation by the Gauss-Seidel method. The negative pressure nodes (which are the ruptured region nodes) are turned successively to zero in each iteration until convergence is achieved, while reformation is normally considered to occur at the position of maximum film thickness or at grooves. Due to its simplicity, the Reynolds model has been widely used in the analysis of plain journal bearings (Khonsari and Beaman, 1986; Boncompain, 1986) and tilting-pad journal bearings (Knight et al, 1990). There are still several recent works using the Reynolds Conditions (Brizmer et al, 2003; Siripuram and Stephens, 2004; Majumdar et al, 2004). However, these models generally provide poor predictions concerning flow rate due to the main shortcoming of the Reynolds conditions: They are not sufficient to assure mass conservation along the whole domain. To assure this,

additional care need be taken concerning the flow continuity within the ruptured film region and across film reformation boundaries.

II.2.5 The Jacobson-Floberg-Olson (JFO) mass-conserving algorithm

As mentioned earlier, neither the Half-Sommerfeld approach nor the Swift-Stieber/Reynolds conditions ensure, by themselves, mass conservation across the whole domain. In fact, the main problem of most non-conservative algorithms is that they rely solely on the solution of the pressure field within the full film region, without additional care concerning flow continuity at the ruptured film region where the Reynolds equation is not applicable. Within this region the pressure is simply imposed as being the rupture pressure, P_{rupt} , and no information concerning mass transport is retained. Therefore, mass conservation is lost, unless additional flow continuity computations are performed. It seems reasonable to affirm that the analysis of twin groove journal bearings, the case of the present study, will be even more sensible to mass conservation issues than single groove bearings, because one of the grooves will be normally located at the divergent portion of the film during normal operation. Under these conditions the accuracy of the location of the rupture and reformation boundaries will affect significantly the flow patterns obtained.

There are several algorithms which do account for mass continuity within the ruptured film region and across its boundaries, also known as mass conserving cavitation algorithms. The JFO theory (Jacobson and Floberg, 1957; and Olson, 1965) is one of the first successful mass-conserving algorithms for the solution of the Reynolds equation in journal bearings. According to this theory, and based on their experimental observations, the authors considered the ruptured film region to be at a uniform pressure, P_{rupt} , and therefore neglected the pressure-driven (Poiseuille) flow within the region. A purely drag-driven (Couette) flow of lubricant is considered to exist, being divided into an infinite number of streamers adhered to both shaft and bush surfaces. The remaining fraction of the axial length, the void fraction, is filled with an innocuous gaseous mixture. The rupture and reformation boundaries are found both through the Reynolds equation solved by the Christopherson algorithm and by flow continuity calculations. Rowe and Chong (1984) applied the JFO approach to the isoviscous analysis of a journal bearing. The ruptured film boundaries they obtained were somewhat inaccurate when compared with experimental data, possibly due to neglecting thermal effects, as defended by Pierre (2000).

Heshmat (1991) observed experimentally, along with the streamlet-type flow at the rupture region, the formation of a thin layer of lubricant adhered to the shaft surface within this region.

Mistry et al (1997) attributed this phenomenon to a balanced effect of surface tension and centrifugal forces and then changed the JFO reformation condition in order to take into account also the influence of the adhered layer to the shaft. He located the rupture and reformation boundaries more accurately than Rowe and Chong and discovered that the thickness of the adhered layer of fluid decreases with the increase of eccentricity and rotational speed. Therefore, this effect could be neglected under high loads, with the results becoming close to those obtained with the original JFO conditions.

The JFO model still provides far better results than the Reynolds model as shown in a work by Bayada (1983), where he found differences in flow rate above 50% between the two models under certain conditions. Although the original JFO approach is reported to be difficult to implement numerically (Elrod, 1981; Brewster, 1986; Claro, 1994), this model and its variants are still used currently as the base for many works, such as those of Zhao et al (2002) on the analysis of wavy thrust bearings, Bayada et al on the HD (2005) and EHD (2006) analysis of roughness effects in journal bearings, Wang and Khonsari (2006) on the analysis of coupled journal-thrust bearings, Michaud et al (2007) on the THD analysis of dynamically loaded journal bearings and Wang and Khonsari (2008) on the analysis of the effect of oil inlet pressure and inlet position of axially grooved infinitely long journal bearings.

II.2.6 Elrod's algorithm and its variants

a) Elrod and Adams, 1975

Another mass conserving model which implicitly implements the JFO conditions is the one proposed by Elrod and Adams (1975). The main goal of the authors was to arrive to a universal equation, valid throughout the whole domain, which would allow to obtain the pressure field and to locate the ruptured film boundaries, while still ensuring flow continuity.

Based on the slight compressibility found in liquid lubricants they performed an ingenious variable substitution in the compressible flow Reynolds equation, which yielded it valid throughout the whole bearing domain. Rather than the pressure field, the solution of the modified Reynolds equation yielded the relative density field, $\theta = \frac{\rho}{\rho_{rupt}}$. Within the full film region θ yielded directly the pressure field through a simple p - ρ relation based on the bulk modulus of the lubricant. Within the ruptured film region θ yielded the liquid fraction, which is the fraction of the gap effectively filled with lubricant.

The way this was carried out is rather ingenious and is detailed in the chapter dedicated to the theoretical model (section III.5.4). By now it is sufficient to say that this algorithm effectively treated the film rupture phenomena in a straightforward way, with the location of the rupture and reformation boundaries being determined automatically within Reynolds equation iterative process and with the JFO mass conserving conditions being implicitly applied.

b) Elrod, 1981

In order to improve the numerical performance of the Elrod and Adams (1975) model, Elrod (1981) proposed some major modifications to it. In fact, the differences between the two models are more profound than they might seem at a first glance. Actually, the two models were often inadvertently confused (as in the case of Han and Paranjpe, 1990). While the former model used in fact the variable density Reynolds equation, with the real density, ρ , being actually affected by the value of the pressure, within the latter model, however, the use of the compressibility of the lubricant was a simple analytical convenience: the resulting modified Reynolds equation of Elrod (1981) is, in practical terms, the incompressible version of the equation, only with a particular change of variable resembling the laws of liquid compressibility. As a consequence, the lubricant compressibility used does not actually affect the final pressure result but only the speed of the convergence process, as found by Miranda (1983) and Claro (1994).

A linear relationship between θ and the pressure was used, while a special form of the incompressible Reynolds equation was derived through a cell method, similar to the Finite Volume Method (FVM) approach. It relied on a flow rate balance made to an area of influence surrounding each node, where the Poiseuille and Couette components of flow rate were accounted for. A judicious choice of the finite difference scheme allowed a convenient numerical treatment of the problem.

This algorithm, adapted to the THD approach, has been chosen for the present analysis and is detailed in section III.5.5.

c) The popularity of Elrod's approach

The two algorithms previously described implement the rigorous JFO mass-conservative conditions in an easier way than the original JFO theory (Elrod, 1981; Brewe, 1986), have become very popular and have been used in a wide range of works.

Miranda (1983), using Elrod's Algorithm, developed a computer aided design procedure for journal bearings fed through an axial groove located at the maximum film thickness. Both the groove dimensions and the supply conditions were considered. Brewe (1986) successfully

adapted Elrod's algorithm to the dynamic analysis of journal bearings, by taking the film history into consideration. Later, Woods and Brewe (1989) incorporated multigrid techniques in the study of the stability of groove-less journal bearings submitted to cyclic conditions. Paranjpe and Goenka (1990) confirmed the superiority of the Elrod algorithm in relation to the Reynolds model concerning flow rate estimation, while Han and Paranjpe (1990) and later Paranjpe and Han (1994) used the Finite Volume Method (FVM) and adapted the Elrod algorithm for use with the THD approach.

d) Application to the analysis of lubricant supply conditions

Given its mass conservative nature and the implicit treatment of the ruptured film boundaries, the Elrod Algorithm seems especially well suited for the study of the influence of supply conditions such as lubricant feeding pressure and groove geometry and location. Claro and Miranda (1993), for instance, applied the Elrod Algorithm in conjunction with a multigrid technique to the study of journal bearings with several groove configurations and supply conditions. The real dimensions of the grooves were considered. Their analyses and experimental results were later used by Martin (1998) to build up diagrams for a rapid estimation of lubricant flow rate. Later, Costa et al (2003a) added the consideration of thermal effects to the analysis of single groove journal bearings.

e) Application to the analysis of the influence of surface roughness and surface micro-texturizing.

The use of mass-conserving algorithms such as Elrod's, has revealed recently to be preponderant also when analyzing such phenomena as the influence of roughness (Rao and Sawicky, 2005; Bayada et al, 2006) or the micro-texturizing of surfaces (Ausas et al, 2007 - see Figure II-1).

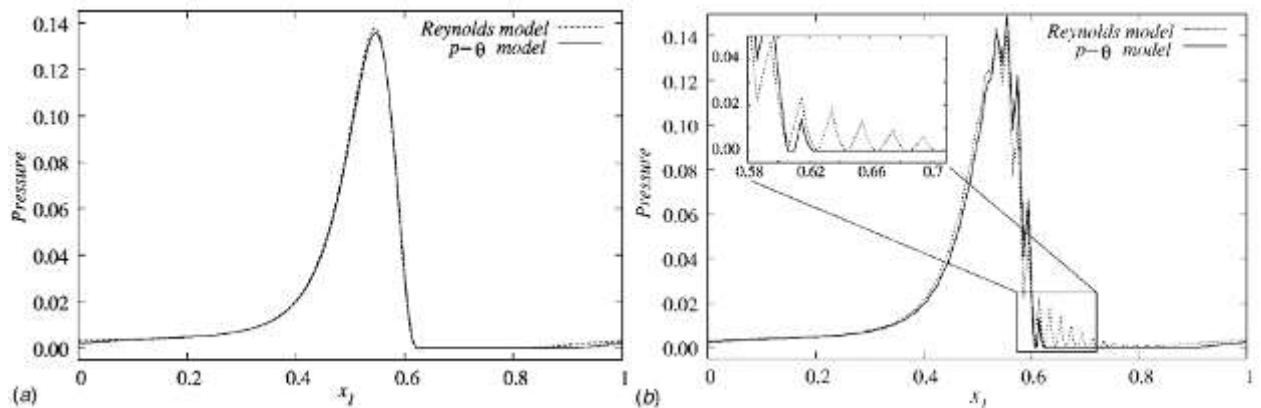


Figure II-1 - Pressure profile along the centerline for (a) the smooth case and (b) the textured bearing, calculated with Reynolds model and the mass-conserving $p-\theta$ model (Ausas et al, 2007).

In the latter work the authors compared the impact of the rupture model in the analysis of micro-textured lubricated journal bearings. They compared the non-mass-conservative Reynolds model to an algorithm based on Elrod's approach and found that when dealing with micro-textured surfaces, the Reynolds model yielded unphysical results and largely underestimated the cavitated area due to spurious film reformation.

These issues are further discussed in section II.5, where a revision of the current trends in journal bearing analysis has been presented.

f) Recent applications

Along with roughness and micro-texturizing effects, recent works have used also the Elrod algorithm for a wide range of subjects, such as the study of Hydrodynamic Herringbone Grooved Journal Bearings (Jang and Chang, 2000), the THD study of Thrust Washers (Yu and Sadeghi, 2002), the study of the dynamic characteristics of synchronously controlled hydrodynamic journal bearings (Rho and Kim, 2002), the analysis of misalignment in journal bearings (Bouyer and Fillon, 2003; Pierre et al, 2004), the THD analysis of a worn bearing (Fillon and Bouyer, 2004) the stability analysis of multilobe (Rao and Sawicky, 2003) and herringbone (Rao and Sawicky, 2005) journal bearings.

II.2.7 The models of Vijayaraghavan and Keith

Some developments to Elrod's approach have been subsequently proposed by some authors. Vijayaraghavan and Keith (1989) applied some changes to Elrod's formulation in order to improve the stability of the convergence process. Based on concepts that were used in transonic flow, they used a different differencing scheme for each domain. At the full film region, where the problem is elliptic (diffusion dominated), a centered differencing scheme was applied, while at the ruptured film zone the hyperbolic form of the equation (transport dominated) was treated with a backward difference scheme. This algorithm was also used later by several authors. For instance, Wang et al (2001) applied it to the THD study of journal bearings lubricated with couple stress fluids, while Talmage and Carpino (2002) used the model to study a plain journal bearing with flooded ends.

Later on, the same authors improved the model (Vijayaraghavan and Keith, 1990a, 1990b) through the use of Newton iteration, approximate factorization and multigrid techniques. This improved numerical stability over the alternating direction implicit scheme that was employed by Brewe (1986) for the time-dependent problem. This approach was applied to the study of the effect of misalignment and starvation (Vijayaraghavan and Keith, 1990c) and type and location

of oil groove (1992) on the performance of hydrodynamic journal bearings. In this work they concluded that the circumferential groove minimizes flow rate and power loss, while a groove located near the maximum film thickness optimizes the performance of a single axial groove journal bearing. Rao and Sawicky (2002) used this model recently to perform a linear stability analysis of a journal bearing, while Hirani (2005) and Hirani and Suh (2005) used this model within a multi-objective optimization technique through genetic algorithms.

II.2.8 Other models inspired in Elrod's theory

Other models were, to some extent, inspired on Elrod's approach. Kumar and Booker (1991, 1994) used a method that is suitable to use with the FEM and the Galerkin technique. P. Wang et al (2001, 2002) and Kucinski et al (2004) applied this model to their studies. Yu and Keith (1994, 1995) used the boundary element method (BEM) to solve the mass-conserving equation derived by Elrod. With this approach they avoided the oscillatory behavior which is sometimes found during the iterative process used by the FDM. Sahlin et al (2007) adapted Elrod and Adams' approach to accommodate for an arbitrary density–pressure relation. They applied it to the study of roughness and starvation effects.

II.2.9 Recent approaches to the pressure-flow problem in journal bearings

In order to obtain design charts for the maximum bearing shell and journal temperatures of twin groove journal bearings, Keogh et al (1997) solved the full Navier-Stokes and energy equations by the FVM and the SIMPLEC method of Van Doormal and Raithby (1984), though cavitation was restricted to an averaged treatment of the flows. They included simplified flow calculations at the region of the grooves. Unfortunately, although the CFD approach is more rigorous than the traditional Reynolds equation approach, the relatively small number of nodes used may have prevented a detailed observation of localized phenomena such as reverse flow.

Tanaka (2000) proposed a simplified method for the treatment of starvation in journal bearings (see Figure II-2), based on the JFO assumption of drag-driven flow at the ruptured film boundaries, symmetry considerations (both rupture and reformation at the groove start from the center to periphery) and mass balances. He obtained a good correlation with the experiments he performed for the extension of gaseous pockets. He concluded that shaft eccentricity can be severely increased due to starvation effects.

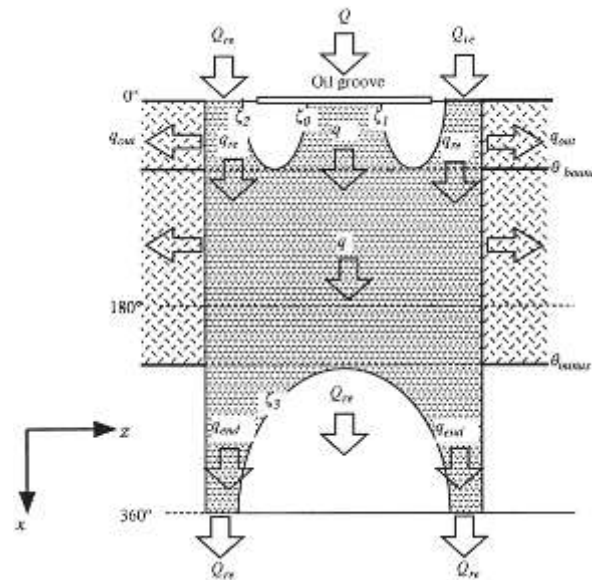


Figure II-2 – Starvation model of Tanaka (2000)

Groper and Etsion (2001, 2002) carried out a series of studies in order to investigate the reason for the pressure buildup at the ruptured film region near the reformation boundary of a submerged journal bearing. This phenomenon was observed experimentally by Etsion and Ludwig (1982) and also by Braun and Hendricks (1984).

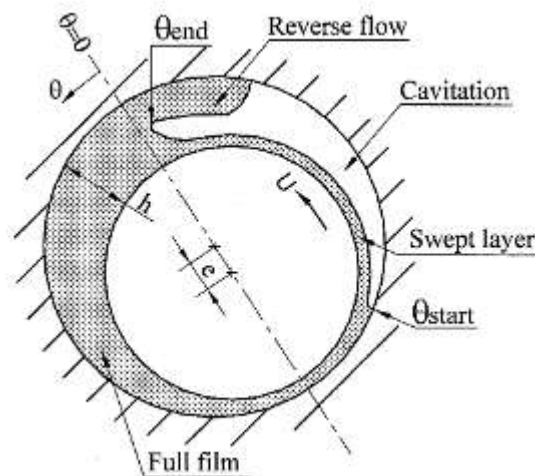


Figure II-3 – unsteady back flow region penetrating the ruptured film region (Groper and Etsion, 2002).

In the first work (Groper and Etsion, 2001) they concluded that neither the effect of the shear flow generated at the air bubble nor the effect of mass transfer process (air dissolved in the lubricant entering the cavitation bubble at film rupture and being reabsorbed at film reformation) were sufficient to explain the observed pressure buildup. In their second work (Groper and Etsion, 2002) they tested the possibility of back flow being the mechanism that explains this pressure build-up (see Figure II-3). In fact, the experimental works cited above had revealed the existence of a back flow phenomenon that penetrated into the ruptured film region and possessed an unsteadiness pattern in time, sometimes extending considerably upstream of reformation, sometimes collapsing and disappearing. They developed an algorithm

that allowed the estimation of the ruptured zone and the penetrating back flow. They concluded that in fact this phenomenon could be hold responsible for the pressure buildup occurring upstream of the reformation boundary.

Hatakenaka et al (2002a) derived a variant of the Reynolds equation that incorporates centrifugal effects for the analysis of the stability of high speed floating bush journal bearings. This type of bearing is frequently used in very high speed applications such as automotive turbochargers, where centrifugal effects are not negligible. They used the cavitation model of Koenke et al (1995), where the equivalent density and viscosity of the oil film is assumed to change gradually around the saturation pressure. A stepwise change from the values of the lubricant to those of the air at the saturating pressure occurs. They observed that centrifugal speed affects significantly the stiffness and damping coefficients, especially at high speeds.

Nassab and Moayeri (2002) carried out a THD 2-D and 3-D CFD approach applying the FVM through the SIMPLE algorithm of Patankar and Spalding (1972) to single groove journal bearings. In order to obtain a rectangular computational domain, they applied a conformal mapping scheme. The ruptured film region was treated as a uniform mixture of air and lubricant under Couette flow with equivalent properties according to the local fraction of fluid. The flow at the groove region was not calculated below the inner bush surface plane. Instead, an inlet fluid velocity was calculated at this boundary for each iteration. The model was successfully validated with experimental results of several authors. In a later work, Nassab (2005) added to the former model the effect of fluid inertia. He concluded that the presence of the inertia term increases the load capacity and attitude angle, while temperature is only marginally affected. Fluid inertia was found to have a substantial influence on the THD characteristics of a journal bearing if the bearing runs under low load, high speed and large clearance conditions, even at moderate values of the Reynolds number. In a very recent work, Nassab and Maneshian (2007 – see Figure II-7) used the same approach as the previous works to test three different rupture models, all of them based on the assumption of a single-phase fluid with equivalent properties that depend on the local fraction of lubricant. The numerical results showed that the model in which the liquid fraction was calculated based on continuity of the three-dimensional ruptured film flow is the one that best fits the experimental data in terms of lubricant pressure and temperature field. The thermal aspects of these models are detailed in section II.3.14f).

Cioc and Keith (2002) applied the space-time conservation element and solution element (CE/SE) method to 1-D journal bearing analysis for the first time. This mass-conservative algorithm was first proposed by Chang and To (1991). According to the authors, this method, which successfully dealt with the discontinuities occurring in transonic flow calculations as

sound waves and shock waves, seems to be particularly suitable for treating the flow in cavitating bearings, as it can simultaneously capture small and large discontinuities without introducing numerical oscillations in the solution. In this case the CE/SE method was applied to the 1D Reynolds equation through a method similar to the Elrod Algorithm (1981), implicitly incorporating the JFO assumptions. This method solves a set of integral equations derived directly from physical conservation laws and captures small and large flow discontinuities such as film rupture and reformation with negligible dissipation or dispersion. The authors claim that the CE/SE method is not only computationally efficient as it is conceptually simple and entirely explicit, but is also second-order accurate at the whole domain instead of just in the full film region. The authors compared the results of their model with those of Elrod (1981) and Vijayaraghavan and Keith (1989). They considered the CE/SE method to be the most accurate based on the differences observed between the models (as high as 10% in the pressure field). They attributed these differences to the lower numerical dissipation of the CE/SE model. Unfortunately, no comparison with experimental data has been performed. Therefore, the higher accuracy claimed for the CE/SE method still needs to be further confirmed. Later, Cioc et al (2003) applied the same CE/SE approach to plain journal and wave bearings, including the study of misalignment effects. On this occasion they used a triangular element mesh to solve the 2-D Reynolds equation. Again, only comparisons with other numerical results were presented. Although this model displayed a computational speed which was comparable with that of other transient models, it showed to be slower than other steady state models, as it relies on a time-dependent asymptotic solution for the steady state problem. As a conclusion it seems reasonable to affirm that, although the CE/SE approach seems to have a good potential to be used successfully in journal bearing analysis, the reliability and accuracy of its solutions should be further assessed through extensive experimental validation.

Nosov and Gomez-Mancilla (2004) developed a new approach for the estimation of the eccentricity threshold for the occurrence of film rupture, its location and number of streamers. Their approach is similar to an energy approach that was developed by Griffith (1920) on mechanics of fracture for elastic solids. In this approach, changes in the kinetic energy of the fluid near the rupture boundary are monitored and compared with the surface energy generated at the interfaces of fluid and gas. They reported a good agreement with the results of Khonsari and Booser (2001), although it remains more or less unclear the extent of this agreement. The main contribution from this work seems to be the estimation of the number of lubricant streamers at the ruptured zone based on physical principles and the estimation of a critical eccentricity under which no film rupture occurs. Nevertheless it remains unclear whether or not these two aspects were in fact validated by experimental evidence.

It can be seen that a wide variety of methods for the calculation of the hydrodynamic pressure and flow fields have been proposed along time, from the simple early analytical models to the recent full Navier-Stokes approaches. It seems that the solution of the Reynolds equation through the Elrod algorithm (1981) constitutes a good compromise between accuracy (mass-conserving algorithm) and the computational speed required for industrial design tools (non-CFD approach). That is why this approach was chosen for the present work, having been adapted for the inclusion of thermal effects. The state of the art of the analysis of such effects is described next.

II.3 Thermal effects

Although thermal effects in lubrication started being studied early by authors such as Hirn (1854) and Petrov (1900), a greater awareness for the importance of these effects arose by the time Kingsbury (1933) carried out an experimental and theoretical study in which he concluded that thermal effects were responsible for the large discrepancies between the experimental observations and the theoretical predictions for load carrying capacity of bearings.

II.3.1 The Global Thermal Model

Thermal effects in hydrodynamic lubrication started to be somehow taken into account in theoretical bearing analysis with the “Global Thermal Model” of Swift (1937). In this simplified theory, the lubricant is isoviscous. Based on a global energy balance, an average temperature and a corresponding average effective viscosity are estimated. Most subsequent isoviscous approaches were based on variations of Swift’s assumptions. Still nowadays the isoviscous approach is used with acceptable results for a limited range of operating conditions (Tanaka, 2000; Yu and Sadeghi, 2001; Stahl and Jacobson, 2001; Stahl, 2002; Talmage and Carpino, 2002; Johansson and Wettergren, 2004; Boedo and Booker, 2004). The isoviscous approach is sometimes the only reasonable choice when dealing with other theoretical complexities for which the THD approach would render the problem nearly untreatable or with excessive computational costs. It is also a reasonable option in preliminary and first-approach studies. However, the isoviscous approach does not provide a satisfactory response in cases where accurate predictions are needed, especially when high speeds and loads are present (Bouyer and Fillon, 2004). Under such conditions, the large amount of heat produced by viscous dissipation produces temperature gradients that are too high to be neglected. Moreover,

the isoviscous approach might dangerously underestimate critical performance parameters such as shaft eccentricity (Bouyer and Fillon, 2004).

II.3.2 The first approaches to the local thermal problem

The solutions of the energy equation under hydrodynamic incompressible flow appeared with the “Adiabatic Theory” of Cope (1949), which neglected solid body conduction and considered viscosity-temperature variation along the circumferential direction only. Zienkiewicz (1957) on the other hand, considered also the viscosity-temperature variation across the film thickness. This was the first model which computationally calculated both the pressure and the temperature fields of a hydrodynamic lubrication problem considering the viscosity variation across the film thickness.

II.3.3 The Generalized Reynolds Equation of Dowson

The rigorous unification of the thermal and the hydrodynamic effects in hydrodynamic lubrication theory was accomplished with the publication of the Generalized Reynolds Equation by Dowson (1962). This approach considers the local variation of density and viscosity due to temperature and its effect on the hydrodynamic pressure and velocity fields. The simultaneous solution of this equation and the energy equation with its boundary conditions constitutes the so-called Thermohydrodynamic (THD) problem or “Local Thermal Model”, in opposition to the “Global Thermal Model” described above. Naturally, some complexity arises from the fact that these two equations are coupled through the local lubricant viscosity. This property simultaneously depends on the temperature field and influences the lubricant flow, the hydrodynamic pressure generation and the heat generation by viscous dissipation.

II.3.4 Subsequent approaches to the THD problem

Since the Generalized Reynolds Equation was published, the equations which were the base for the THD problem were basically established. Much effort was deployed in the subsequent works based on this approach, in order to find the methods of solution that were most suitable and the boundary conditions which properly described the phenomena at stake. Often, many simplifying assumptions had to be made, especially in early works. Next, a description of the

main assumptions and simplifications made within the THD analyses of fluid film bearings is carried out.

II.3.5 The adiabatic condition at the bush-film interface

Concerning the treatment of the fluid-bush interface, Raimondi (1966) tested two different simplified boundary conditions at the inner wall of the bush: isothermal and adiabatic. While the isothermal condition was rejected for being too unrealistic, the adiabatic condition showed to be an acceptable first-approximation to the problem. As it significantly simplified the thermal problem, it was used in several subsequent works, such as those of Pinkus and Bupara (1979) or Smith and Tichy (1981).

More recently, the so-called ISOADI approach (Isothermal shaft and adiabatic inner bush surface) was used by some authors to develop a rapid THD tool for the design of plain journal bearings (Khonsari et al, 1996; Jang and Khonsari, 2004) and tilting pad journal bearings (Fillon and Khonsari, 1996). According to these works, the THD analysis with ISOADI boundary conditions provides an upper, conservative estimate of maximum bearing temperature. The results were presented in the form of non-dimensional charts and/or curve-fitted expressions. The use of two different non-dimensional constants named the temperature-rise parameters, which are measures of oil properties and shaft linear velocity, allowed the generalization of their THD approach for a wide range of geometries and operating conditions.

II.3.6 The continuity at the interface and the heat conduction in the bush

Instead of using an adiabatic condition, Dowson and Hudson (1964) applied the physically rigorous condition of heat flux continuity at the inner wall of a thrust bearing pad, along with the solution of Laplace's equation, which governs heat conduction, on the bush body. Shortly after, Dowson et al (1966) carried out an important experimental work on crown journal bearings (groove along the load line) where they measured the hydrodynamic pressure field and the temperature field at the inner surfaces of the bush and the shaft, and confirmed that there is a non negligible radial heat flux through the solid bodies that should be taken into account in theoretical analyses.

An important experimental work on twin groove circular journal bearings ($\pm 90^\circ$ to the load line) was carried out by Fitzgerald and Neal (1992). This work, which gave a significant contribution to the stock of thermal data concerning this bearing geometry, also analyzed in

depth the role of solid body conduction in bearing thermal behavior. They used two 76mm bushes with length to diameter ratios of 0.5 and 1, operating in conjunction with two different shafts which provided clearance ratios of 0.001 and 0.002. The axial grooves encompassed 0.8 of the bearing length. The tests were carried out at fixed feeding temperature and pressure, and covered a wide range of applied load and shaft speed. The thermocouples located both at the inner bush surface as well as the outer bush surface allowed an insight and estimation of isotherms. The axial temperature variation was found to be very small (less than 2°C) except at the vicinity of the grooves. The heat flux through the shaft was estimated to achieve a maximum of 10% of the total dissipated power for the smaller clearance ratio bearing. The Peclet number (expressing the convection to conduction ratio) was found to be the main indicator governing the fraction of the generated heat that flows through the bush body to the ambient, although the length to diameter ratio and the load were also found to be important secondary factors. The increase of these three factors contributed to the decrease of conductive heat fraction. For the conditions tested this fraction varied from 15% at large Peclet numbers to nearly 100% at very low Peclet numbers, low applied loads and large length to diameter ratios. This means that the heat flux through the bush is by no means negligible for a wide range of operating conditions, rendering the ISOADI approach highly inaccurate in many situations. The authors further observed that the minimum operating temperature was achieved for eccentricity ratios between 0.4 and 0.6, while the shaft temperature was found to be close to the maximum bush temperature for low eccentricities but substantially lower than this parameter for high eccentricities. The temperature inside the grooves was found to be much higher than the feeding temperature for low eccentricity cases and a few degrees higher than the feeding temperature in high eccentricity situations.

Due to what has been said before, the incorporation of the Laplace equation into the THD problem became more and more common. The 2-D (Costa et al, 2003a) or even purely radial heat conduction approaches were widely used (Safar and Szeri, 1974), although some authors opted for the full 3-D solution of the Laplace equation (Ferron et al, 1983; Boncompain et al, 1986; Tucker and Keogh, 1995; Pierre and Fillon, 2000).

According to Costa (2000) the use of a free convection boundary condition at the outer surface of a bearing was first proposed by Ezzat and Rhode (1974) and has been used since then in most analyses.

II.3.7 The axial temperature gradient

The experimental work of Dowson et al (1966) further reported that the axial temperature gradient was also rather small. This finding, also observed later by Ferron (1982) and Fitzgerald and Neal (1992), ultimately justified the wide use of 2-D thermal analyses of journal bearings restricted to the bearing midplane (Boncompain et al, 1986; Khonsari and Beaman, 1986; Ma and Taylor, 1992; Khonsari et al. 1996; Costa et al, 2003a) instead of more elaborate and computational-intensive 3-D approaches that were often used in cases where the axial symmetry could not be applied as, for instance, in the case of misaligned journal bearing analysis (Pierre et al, 2004; Bouyer and Fillon, 2003). The present work adopted this simplification.

II.3.8 Shaft temperature calculations

The experiments of Dowson et al (1966) and later Andrisano (1988) reported that while the circumferential variation of the inner bush surface was important, the circumferential variation of the shaft surface temperature was small and ultimately justified the assumption of an isothermal shaft by many authors. Some of them imposed a prescribed temperature (Ott and Paradissiadis, 1988; Gupta et al, 1990; Knight and Ghadimi, 1992), while others obtained the shaft temperature by equaling it to the average temperature of the bush surface (Safar and Szeri, 1974; Basri and Gethin, 1990) or through rigorous heat transfer calculations (Boncompain et al, 1986; Banwait and Chandrawat, 1998).

Another alternative was used by some authors (Mitsui, 1987; Rajalingham and Prabhu, 1987; Pascovici, 1993) that obtained the shaft temperature by assuming that a prescribed ratio of the total heat generated by viscous dissipation was absorbed by the shaft and lost to the exterior.

Finally, there were the works based on the assumption of no net heat flux at the fluid-shaft interface. This assumption can be seen as a midterm in practical bearing applications, where the shaft can act in some cases as a heat source (as in the case of a gas-turbine bearing located at the vicinity of the combustion chamber) and in some other cases as a heat sink (as in the case of a cryogenic pump) for the bearing system. This last approach was chosen by works such as those of Khonsari and Beaman (1986), Khonsari and Wang (1991), Ma and Taylor (1992), Pierre and Fillon (2000), Zhang et al (2000), Hatakenaka and Tanaka (2002), Costa et al, 2003a, Jang and Khonsari (2004) and was also chosen for the present work.

II.3.9 The Couette approximation

In order to simplify the coupling, due to pressure terms, between the Reynolds and the Energy equations, McCallion et al (1970) proposed the Couette approximation, which consisted in neglecting all pressure-related convective heat transfer terms in the energy equation and considering only the drag-driven flow as being responsible for convective heat transfer. Although this assumption simplified considerably the computational analysis, the results obtained for the temperature field were not considered satisfactory. A reason for this could also be other simplifications such as the weak treatment of shaft temperature, imposed as being the same as the average temperature of the inner bush surface. Other authors also used the Couette approximation (Pinkus and Bupara, 1979; Smith and Tichy, 1981; Ma and Taylor, 1994).

II.3.10 Treatment of cross-film phenomena

As said earlier, the first thermal models did not include a detailed study of the thermal phenomena occurring across the film thickness, with the cross-film variation of temperature and viscosity fields being frequently disregarded. These one-dimensional models, like those of Knight and Barret (1983) or Gupta et al (1990), although attractive due to their simplicity, revealed insufficient accuracy for many practical applications.

Lund and Hansen (1984) used a fourth order polynomial to represent the viscosity and the temperature variation across the film thickness of a twin groove journal bearing. They obtained temperature profiles which displayed a good correlation with experimental data at the loaded land of the bearing but poor at the unloaded land.

In their theoretical study, Rajalingham et al (1994) have put to evidence the importance of considering the thermal phenomena occurring across the thickness of the lubricant. In particular, the heat flux through the lubricant was found to depend strongly on its thermal conductivity. An increase in this factor provided maximum temperature decreases as high as 10°C.

Vijayaraghavan (1996) developed a method where properties across the film thickness, such as viscosity, were determined only at some points (*Lobatto* points) while their distributions across the thickness of the film were expressed by collocated Legendre polynomials. In this way, with only 3 different non-equidistant points in the film, a good correlation with experimental data was obtained in terms of temperature, except concerning the ruptured film region of twin groove journal bearings and sometimes at the region located downstream of grooves (see Figure II-4).

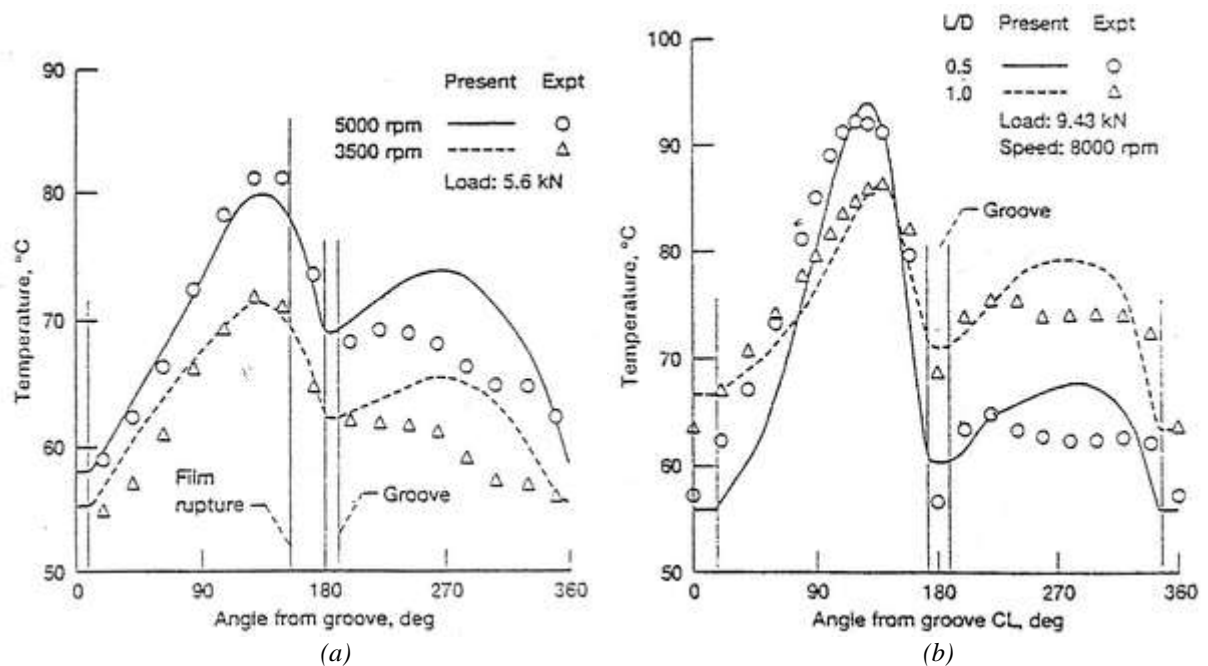


Figure II-4 – Predictions of Vijayaraghavan (1996) against the experimental results of (a) Lund and Tonnesen (1984) and (b) Fitzgerald and Neal (1992).

The model provided good agreement in terms of flow rate concerning single groove journal bearings. Unfortunately no comparisons between theoretical and experimental values of flow rate were presented for the twin groove journal bearing geometry.

Kumar and Booker (1994) proposed a model for the treatment of the ruptured film region that was best suited for the FEM. However, its over-simplification (the diffusive term and transverse temperature variation were neglected in the energy equation as well as the lubricant mixing effect at the groove) yielded poor agreement with experiments concerning maximum temperature and the temperature profile at the rupture film region. Nevertheless, some authors have applied this model to their FEM approaches (Wang, Keith and Vaidyanathan, 2001, 2002; Kucinski et al, 2004).

Clearly, the models which treat the phenomena occurring across the film thickness with more detail (Boncompain et al, 1986; Khonsari and Beaman, 1987; Ma and Taylor, 1994; Paranjpe and Han, 1994; Vijayaraghavan, 1996; Hatakenaka and Tanaka, 2002; Costa et al, 2003a) were the ones to provide a better correlation with experimental results. This is why the present model also considers the influence of viscosity across the film thickness.

II.3.11 Thermal mixing in the grooves

The Reynolds equation is based on the thin film assumption, where the pressure variation across the film thickness is neglected, and therefore it is not applicable within the groove regions. Instead, global heat and mass balances are often performed at the boundaries of groove

regions in order to estimate the so-called inlet section temperature, which is the average temperature of the fluid at the leading edge of a groove, imposed as boundary condition/initial value.

Smalley and McCallion (1966) were the first to include a heat balance at the groove region by taking into account both the effect of the feeding temperature and the recirculated hot oil coming from upstream and entering the groove region. From this balance they obtained the inlet region temperature, T_{is} . In this case, a uniform temperature profile was used. Since they used an over-simplified thermal model no satisfactory results were obtained.

Ettles (1968, 1969) carried out an analysis of the heat transfer processes occurring at the groove region based on the boundary layer theory and presented the Nusselt number (ratio of convection heat transfer to conduction heat transfer) as being a good indicator for the thermal processes occurring in this region.

Later works (Khonsari and Beaman, 1986; Heshmat and Pinkus, 1986; Ma and Taylor, 1992; Mistry et al, 1993) estimated the inlet zone temperature using similar mass and energy balances. They used also uniform temperature profiles along the film thickness.

Mitsui et al (1983) performed an experimental and theoretical work where they determined the inlet zone temperature using mass and energy balances in conjunction with a *mixing coefficient* which they derived from the measurement of the temperatures at the entry and exit regions. This mixing coefficient tries to quantify somehow the ratio of the hot oil coming from upstream which actually enters the groove region and mixes with the fresh supplied oil. Other authors, such as Hatakenaka and Tanaka (2002) used subsequently this mixing coefficient. Although reasonable agreement with experiment was found after coefficient tuning, experimentally derived coefficients pose a problem: it is unclear whether the optimal values found for the mixing coefficient will still be suitable for substantially different bearing geometries, groove configurations or supply conditions. Similarly, Heshmat and Pinkus (1986) carried out an extensive test program from which they derived a series of empirical equations in order to estimate the inlet temperature for both thrust bearings and journal bearings.

Boncompain et al (1984, 1986) and Banwait and Chandrawat (1998) proposed non-uniform inlet temperature profiles. They derived the coefficients of second and third order polynomials so that energy conservation and actual temperature at the shaft and bush surfaces were observed.

The use of non-uniform temperature profiles instead of uniform ones prevents temperature discontinuities at the interfaces and follows the typical continuity found in such physical phenomena as heat transfer. Mistry et al (1993) and later Costa (2000) have argued that the use

of non-uniform temperature profiles would have little effect on the maximum temperature obtained. However, not only these affirmations are based on the single groove journal bearing geometry only, but it can be argued also that the use of uniform inlet temperature profiles may be held responsible for the poor temperature correlation with experiments observed in these models at the region located immediately downstream of the groove. Moreover, the type of inlet temperature profile used also affects the flow patterns due to the temperature dependence of lubricant viscosity. Mistry et al (1993) found that the temperature profile chosen for the entry region can affect slightly the location of the maximum temperature of the bush.

Basri and Neal (1990) were the first to include a separate measurement of the flow rate at each groove of a twin groove journal bearing. This information is vital in order to validate models for this kind of bearing. The thermal mixing model at the groove greatly depends on the accuracy of the feeding flow rate. The authors of this study also stressed out the influence that the inlet region temperature profile might have on the calculated flow rate. They reported rather dissimilar flow rates in each groove, which highly depended on applied load and bearing length. They further reported that negative flow rate might have occurred at the +90° groove for low feeding pressure and high load, but no evidence on this phenomenon was provided. The present work has addressed this lack of knowledge both with experimental and theoretical evidence (CHAPTER VI and CHAPTER VII, respectively). Moreover, an original approach to the subject of inlet temperature profile has been advanced within the scope of the present work (section III.11.3). The consideration of the actual groove dimensions, which improves the assessment of the thermal behavior at the groove surroundings, has been also taken into account.

Chun and Ha (2001) analyzed the effect of mixing at the grooves for the turbulent flow occurring in high speed journal bearings and found that groove mixing should be always included in the analysis. Moreover, the wall temperature and the heat transfer were found to be of secondary importance to the mixing effectiveness within the groove and the resulting inlet temperature.

Additional discussion on the thermal mixing at the groove, now treated with the CFD approach, is still included in the next section.

II.3.12 The CFD approach

The inclusion of the groove region within the THD analysis cannot be carried out with the Reynolds equation. Instead, solutions of the Navier-Stokes equation, which take into account the pressure variation across the film thickness, need to be obtained. Moreover, the inclusion of

inertia or even vorticity and turbulence effects could further help to correctly assess the phenomena occurring within the groove regions. The Computational Fluid Dynamics (CFD) approach can deal conveniently with all these variables. The main drawback of CFD methods lies on being generally much more computationally intensive than traditional Reynolds approaches. Also, the accuracy of its results often requires the use of rather refined meshes.

Medwell and Gethin (1984) and later Gethin (1985, 1988) performed a TEHD analysis of twin groove journal bearings under high speed. Although they applied the rigorous turbulent Navier-Stokes approach, they did not include the treatment of the groove regions nor the ruptured film region. It seems reasonable to assume that this, along with the assumption of an adiabatic inner bush surface, was the reason for the poor correlation of their results with the experimental data of Gethin and Medwell (1985) in terms of inner bush surface temperature profile and flow rate (as high as 80%).

Keogh et al (1997) performed a CFD-based work on twin groove journal bearings (see also section II.2.9) and included flow and energy calculations within the groove region. The scope of this work, based on the same principles of an earlier work by Tucker and Keogh (1995), was to build design charts for twin groove journal bearings. This can be seen as an updated version, now through the CFD technique, of the THD method of Khonsari et al (1996 - see II.3.5). The work used the same non-dimensional factor approach, now for the twin groove journal bearing case. In order to build the design charts there was a need to compute a wide set of cases. This may have prevented the exploration of the full capabilities of the CFD approach within the groove region. In fact, no flow or energy calculations were performed at the inner portion of the groove, which is the region that is underneath the inner bush surface circumference. Instead, and as seen in Figure II-5, a constant feeding pressure and feeding temperature was imposed at the boundary defined by the bush inner surface circumference, while a radial flow through this boundary was calculated so that replenishment of an eventually ruptured film would be achieved.

Similarly to the previous work, in the CFD model of Nassab and Moayeri (2002) (see also section II.2.9) no calculations were performed in the inner region of the groove, below the inner bush surface circumference. Instead, an inlet fluid velocity was imposed at this boundary based on lubricant leakage at the outer bearing edges. The dissipative term was neglected within this region and the inlet zone temperature was obtained through a heat balance between the recirculated hot oil and the feeding oil. This model was successfully validated with experimental results from several authors, with the maximum bush temperature being slightly underestimated. Later, Nassab (2005) used the same approach but added the effect of fluid inertia. They found that, the temperature field was not significantly affected by fluid inertia.

However this factor was considered to affect the pressure field, increasing load carrying capacity, especially under the combined effect of low load, high speed and large clearance conditions.

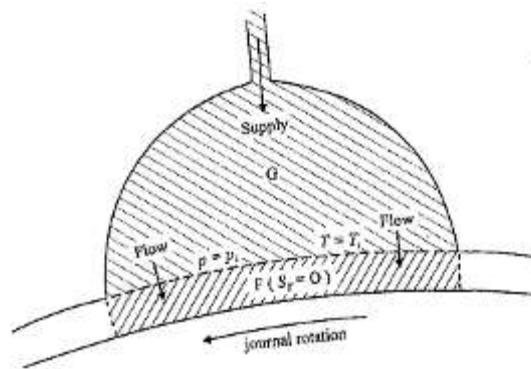


Figure II-5 – Simplified groove modeling proposed by Keogh et al (1997)

An analysis of what actually happens within the whole groove was carried out by Kosasih and Tieu (2004). They used commercial CFD packages in order to investigate the thermal mixing occurring with different groove geometries. They included turbulent and inertial effects when treating the groove interior. For the sake of simplicity they used adiabatic boundary conditions on both bush and shaft surfaces, which are rather unrealistic conditions, as explained in section II.3.5 and II.3.6. They used exaggerated feeding pressures (at least for hydrodynamic journal bearings) between 500kPa and 1500kPa. They found that the flows occurring within the groove interior are highly recirculating but have almost negligible effects on the thermal mixing. In fact, most of the injected cold oil did not immediately enter the oil film. The thermal mixing zone was found to extend to some distance beyond the grooves and in some cases to extend for almost the whole bearing length in the axial direction, although this conclusion might be a consequence of the high feeding pressures they considered. They found that the main parameters that govern the extent of mixing zones were the groove length and the feeding pressure. The extent of the thermal mixing zone did not seem to be affected by the groove shape. Finally, they extended their analysis to the full bearing gap through a multi-domain approach and studied the influence of groove size, location and bearing operating conditions on the bush temperature. For instance, when comparing the results for a groove located at -27° , 0 and 27° to the load line they found that the first configuration provided a 10% reduction in maximum temperature over the other two.

Jeddi et al (2005) used the FEM to study the effect of the feeding pressure and the runner velocity on the THD behavior of the lubricant in the groove of a journal bearing. They found these two factors to change significantly the flow and thermal patterns within the groove region, namely the temperature profile in the inlet section. However, they observed that this

temperature profile also depends strongly on the heat transfer through the bush and shaft. According to the authors, this influence still needs to be further assessed.

II.3.13 The treatment of reverse flow

In full hydrodynamic lubrication the surface speeds normally present cause the convective term of the energy equation (due to fluid movement) to become much greater than the diffusive term (due to conduction) in the circumferential direction. Therefore, it is common to neglect the conduction along this direction, causing the energy equation to become parabolic and therefore solved with a backward difference scheme, just as in time dependent problems. However, this method has problems when negative flow, also called reverse flow or back flow, occurs. This normally occurs in regions where intense adverse pressure gradients occur, such as upstream of a groove under high feeding pressure or upstream of the minimum film thickness zone under high eccentricity. In such cases, the simple backward difference scheme is unable to treat conveniently the reverse flow region. While many authors, especially the earlier ones, used coarse meshes which eventually prevented the observation of such phenomena, others, like Suganami and Szeri (1979) retained the circumferential conduction term and solved the energy equation in the elliptic form through the FEM.

Boncompain et al (1986), while maintaining the energy equation in the parabolic form, used a technique proposed by Richtmyer (1957) in which the domain of calculus is subdivided in two according to the direction of the flow. In the positive domain the backward difference scheme is used, while in the negative domain (reverse flow region) the forward difference scheme is deployed. When the calculations are being performed at one of the domains, the nodes of the opposite domain which are contiguous to the reverse flow boundary act as boundary condition nodes. This process is applied alternately to each domain until convergence is achieved. The authors reported this process as being stable and displaying a quick convergence. The present work used a similar approach (see section III.7).

Han and Paranjpe (1990) applied the FVM to the full 3D Reynolds and Energy equations, retaining all convective and conduction terms. This way, the resulting energy equation is in elliptical form and therefore the reverse flow region does not need to be treated separately. Naturally, retaining all diffusive and convective terms of the energy equation added considerable calculation effort. This was partly compensated by omitting solid body conduction through the ISOADI approach (explained in sections II.3.5 and II.3.6). Later, the same authors (Paranjpe and Han, 1994) extended their method by including heat conduction calculations in the bushing and by adding a heat balance at the groove region in order to take into account the

effect of recirculated hot oil. They partially validated the model with experimental data from Dowson et al (1966). A reasonable correlation with experiment was found, although flow rate was slightly underestimated, oil outlet temperature was overestimated and surprisingly no comparison of maximum bush temperature was performed.

Concerning the Finite Volume Method (FVM) applied to computational fluid dynamics and heat transfer, several alternative differencing schemes are presented in the book by Versteeg and Malalasekera (1995). For transport-dominated heat transfer, where regions with non-negligible diffusive term occasionally appear or where complex flow patterns such as reverse flow occur, they proposed the hybrid differencing scheme of Spalding (1972), as a good alternative to the standard upwind differencing. With the simple upwind difference scheme, a flow which is not aligned with the gridlines could originate the so-called *false-diffusion* error. The hybrid method avoids smearing by selecting the differencing scheme, central or upwind, according to the local Peclet number, which is a measure of the relative importance of convective terms over diffusive terms. Hatakenaka and Tanaka (2002) successfully solved the energy equation in the presence of reverse flow by applying the FVM through the hybrid technique to a two-lobe bearing.

Versteeg and Malalasekera (1995) still refer to other methods, such as the Power-law differencing scheme proposed by Patankar (1980) which also uses the Peclet number but in a more evolved way, or the higher order QUICK differencing scheme (Quadratic Upstream Interpolation for Convective Kinetics) proposed by Leonard (1979) which uses a three-point upstream weighted quadratic interpolation for cell face values.

II.3.14 The thermal model of the ruptured film zone

Although the gross heat generation occurs at the loaded region of the bearing, the thermal behavior of the ruptured film region has been reported by several experimental and theoretical works to exert a non negligible influence on the overall behavior of bearings (Etsion and Ludwig, 1982; Lund and Tonnesen, 1984; Knight and Niewiarowski, 1990).

As seen before, the ruptured film region has been almost always treated in a simplified way by authors, due to the complex phenomena that governs this region such as multi-phase flow, surface tension effects, sudden decompression near the rupture boundary and eventually vaporization, condensation, diffusion of dissolved gas out of and back into the lubricant, non-uniform pressure, complex flow patterns and shear within the gas bubble. It is true that the current advance in computational analysis makes it possible to deal with a lot of these complexities, although not all the phenomena are still completely understood. Nevertheless,

this exhaustive analysis is beyond the scope of most analyses, including that proposed by the current work, as they aim at obtaining solutions in a reasonably short time in order to incorporate them in bearing design procedures. Moreover, a much more detailed and accurate knowledge of the lubricant properties, operating conditions, geometric and supply parameters would be required so that the added detail could actually contribute for a better description of the phenomenon. This accurate knowledge of specific problem properties is clearly not what is usually found in the industrial environment.

Therefore, it is effectively important to assess the real extent of the influence of the various phenomena taking place and, as best as it is possible, to try taking into account the ones that may actually influence the bearing behavior in a more significant manner without rendering the problem too complex or even intractable in practical terms.

a) The Effective Length (*EL*) models

One of the thermal models used for the treatment of the ruptured film region is the so-called Effective Length model (*EL*), which is based on some of the assumptions of the JFO theory (see section II.2.5): The film at the divergent portion of the gap cannot withstand an adverse pressure gradient and ruptures into several streamers starting to flow under Couette (drag-driven) flow (see Figure III-5 in page 66). The sum of the lengths of all these streamers at a given section, which is obtained by flow continuity, becomes the effective length through which the heat transfer and the energy dissipation takes place. The remaining length is filled with gaseous cavities, through which no heat generation or heat transfer is considered to occur (according to the original model). Therefore, in approaches which neglect axial temperature gradients, the actual distribution and number of streamers will be unimportant for the thermal calculations, which will be averaged along the axial direction, being a function of the effective length of fluid.

Concerning full 3D energy approaches the effective length becomes a local parameter, coinciding with the local liquid fraction. Considering that the number of streamers is infinite (streamers with infinitesimal length uniformly distributed), the local liquid fraction is equivalent to a “local streamer density”. Such a local version of the *EL* model was used by Han and Paranjpe (1990) and later by Paranjpe and Han (1994) in their FVM approach to the 3D THD problem. The local liquid fraction was used as the weighting factor for the estimation of the equivalent lubricant properties.

Other variants of the *EL* model (Pierre and Fillon 2000; Costa et al, 2003a) also take into account the actual properties of the gaseous cavities allowing for radial conduction and even heat generation to occur within the gaseous cavities. In this case, the effective properties of the

fluid are obtained by an average of oil and air properties weighted with the liquid fraction. This can be seen as the equivalent problem of heat transfer occurring in parallel.

Models based on the Effective Length concept and its variants have been adapted by many authors to single groove journal bearings, (Ferron et al, 1983; Boncompain, 1984; Mistry et al, 1992; Pierre and Fillon, 2000; Costa et al, 2003a). Concerning twin groove journal bearing analysis, the *EL* model provided reasonable agreement with experiment at the loaded land but differences as high as 10°C at the unloaded land, the region where the film is generally ruptured (Lund and Hansen, 1984; Knight and Barret, 1987).

This model is further explored in the present work (see section III.10)

b) The Gas Bubble (*GB*) model

In order to improve the temperature profile at the ruptured film region provided by the *EL* model (Knight and Barret, 1983), Knight and Niewiarowski (1990) proposed a new algorithm called the *Gas Bubble (GB)* Model, where the lubricant within the ruptured film region does not shrink in length but instead a bubbly mixture of lubricant and gas is formed. The equivalent lubricant properties are then estimated through the bubbly lubrication theory of Khalil and Rhodes (1980). In this theory, many of the effective properties of the bubbly lubricant are obtained from weighted harmonic averages, where the weighting factor is the local lubricant fraction.

The resulting temperature profiles obtained by the authors at the ruptured film region were in better agreement with the experimental results of Lund and Tonnesen (1984) than the previous work, while the maximum bearing temperatures were underestimated in as much as 5°C. This model applied some simplifying assumptions, like imposing the shaft temperature (based on experimental measurements), considering constant lubricant viscosity across the film thickness and allowing the radial temperature profile to vary according to a second order polynomial.

Although some improvement over the *EL* model appeared to happen, the authors admitted that the *GB* model was less based on physical evidence than the *EL* model, which was based on experimental visualization of streamers at the rupture film region observed by authors such as Taylor (1964) and Floberg (1965). Moreover, only two different cases were tested against experimental data. There is no guarantee that good agreement with experiment would be kept for other operating conditions and geometrical characteristics. Nevertheless, authors such as Tucker and Keogh (1995), Nassab and Moayeri (2002) and Nassab (2005) adapted this model for their CFD works.

c) The Film Height (*FH*) and Cavity Height (*CH*) models

Knight and Ghadimi (1992) modified the *EL* model, based on the experimental observation by several authors that not all the lubricant at the ruptured film region flows along streamers but there is also a portion of it which adheres to the rotating shaft and completely covers it (Etsion and Ludwig, 1982; Heshmat, 1991). Since this adhered layer has no contact with the bush surface, the authors considered this layer to move uniformly at the speed of the shaft without any viscous dissipation. The thickness of the adhered layer was computed according to two different models. In the *CH* (Cavity Height) model the height of the bubble remains a constant, imposed, fraction of the local gap height. In the *FH* (Film Height) model the thickness of the adhered layer is imposed and kept constant throughout the ruptured film region. The remaining lubricant is considered to flow in streamlets under Couette flow just like the *EL* model. The model is sketched in Figure II-6a), along with the comparison of the *FH* model with the experimental results of Lund and Tonnesen (1984) for several values of the layer thickness ratio in Figure II-6b)

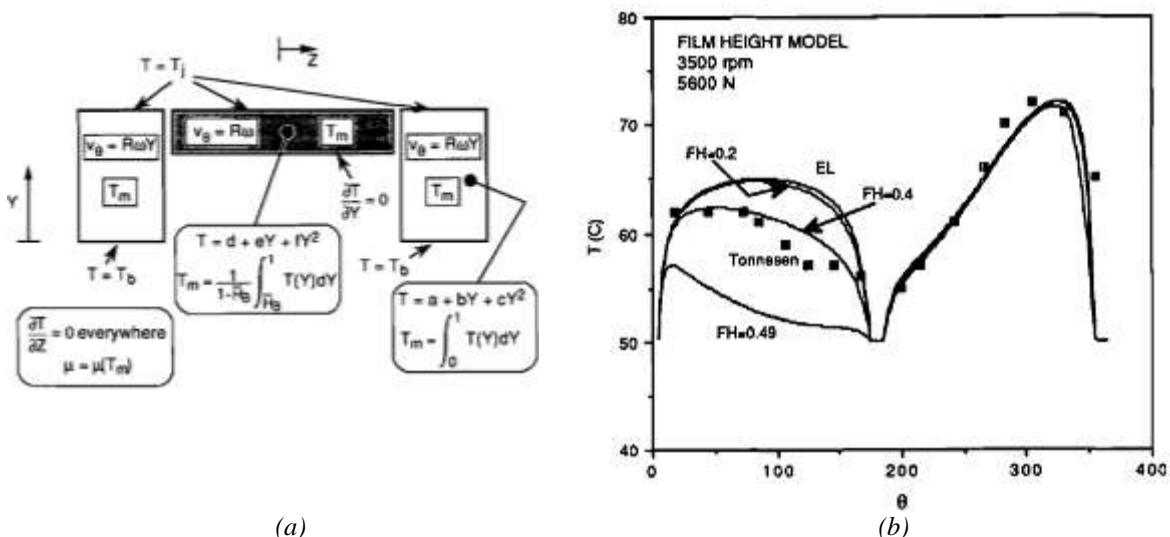


Figure II-6 – (a) Outline of the model proposed by Knight and Ghadimi (1992); (b) comparison of the *FH* model with the experimental results of Lund and Tonnesen (1984) for several values of the layer thickness ratio (Knight and Ghadimi, 1992).

A parametric optimization of the height factors used in each model was then carried out. Both models provided acceptable temperature predictions of both the loaded and the unloaded lands of the bearing for the cases tested. The *FH* model was considered to be the best of the two, as it provided slightly better results than the other model, being also more physically consistent with reality.

Later, Knight and Ghadimi (2001) complemented their former theory with the experimental observation of cavities and streamers through a glass bush. They measured the streamer widths and estimated the size of the adhered layer that should be present in order to satisfy flow

continuity. Their findings support the existence of an adhered layer, which varies in size from 11 to 32% of the gap height at rupture initiation. Their theoretical work had provided a value of 42% which provided the best agreement between theory and experiment over a variety of cases.

A model inspired in this approach has been proposed in the present work (section III.10.2)

d) The Separation Model of Ma and Taylor

Ma and Taylor (1992, 1994, 1995) proposed a new approach which tried to reproduce the strong temperature fade observed by some authors (Booser and Wilcock, 1988, Heshmat and Pinkus, 1986) just upstream of grooves, at the ruptured film region.

Booser and Wilcock (1988) had explained the temperature fade observed in the ruptured film zone, through three mechanisms: (a) heat removal by the shaft, which acted as a regenerative recuperator, removing heat from hot areas and delivering it to cold areas, (b) heat losses by conduction through the bush body and (c) reduction of the viscous heat generation due not only to the reduction of the total effective length of the film but also due to the phenomena observed by Heshmat and Pinkus (1986) of the formation of a thin layer of fluid adhering to the shaft with a nearly uniform velocity profile.

Based on the previous observations, Ma and Taylor proposed the *Separation Model*, where they admit that the ruptured film, which often extends up to the -90° groove edge, leaves room to a back-flow of fresh oil coming from this groove. This backflow is admitted to flood the whole separation cavities and then to mix with the recirculated hot oil contained within the ruptured film. The heat generation by viscous dissipation is neglected within the ruptured film region, while the thermal calculations are made through geometric considerations and elementary mass and energy balances.

The physical significance of assuming that the ruptured film region is supposedly fully flooded with fresh oil instead of a gaseous phase, as traditionally admitted, is arguable. It is true that some authors (Etsion and Ludwig, 1982; Heshmat and Pinkus, 1986) have observed experimentally an unsteady and nearly cyclic phenomenon occurring within the ruptured film region of a journal bearing which consisted on a growing backflow region gradually creeping upstream and then collapsing. Therefore, it seems reasonable to admit that the back-flow region could, in fact, extend further upstream into the ruptured film region than previously supposed: However, it is not likely that the backflow region would completely flood the cavities. This would be even less likely to occur under low feeding pressure or under high shaft speeds, where backflow is unlikely to occur.

The results provided by this model were nevertheless promising. The temperature fade before the downstream groove recorded by their experiments was successfully reproduced with reasonable detail both with circular and elliptical bearing geometries. Nevertheless, the temperature profile at the unloaded land of the bearing predicted by their approach often displayed a dissimilar trend in comparison to their experimental results. Still, the absolute difference between theoretical and experimental results within this region can be considered as fairly acceptable. Some of their experimental results have been used in the validation of the present theoretical work (see section VI.3.2).

Concerning twin groove circular journal bearings, flow rate was very well predicted under low feeding pressure (67kPa) and strongly under-predicted under high feeding pressure (134kPa). This could be explained taking heed that neither realistic prediction of the film reformation was considered nor flow continuity was assured in this study. This weakness of the model could be even more apparent in situations where film rupture could occur further away from grooves. This could happen in situations where the angle between the groove plane and the load is other than $\pm 90^\circ$. Therefore, a mass conserving algorithm would be advisable.

The same authors still carried out an experimental investigation of the thermal behavior of circular and elliptical bearings for a wide range of operating conditions (Ma and Taylor, 1996). Finally they used their theoretical model to compare the static performance of different fixed profile bore journal bearings. They compared 3-lobe, 4-lobe and twin groove circular, elliptical and offset-half journal bearings. They found that the circular bearing had the best overall static performance, whereas the four-lobe profile had the poorest. The circular bearing displayed the lowest peak pressure, although it was the profile with the highest load carrying capacity. The lubricant flow rate required by the offset-half and the elliptical bearing was found to be much higher than that of the other three configurations. Hussain et al (1996) performed a similar comparison using the model of Mistry et al (1992).

e) Other studies focused on the temperature fade before film reformation

Syverud (2001) carried out an experimental study of the temperature fade at the rupture zone using a bearing operating in an environment with sub-ambient pressure. He observed that the temperature drop across the rupture was more pronounced when in the presence of sub-ambient pressure. He detected pressures higher than ambient within the cavitation zone while the bearing was operated at sub-ambient pressure and explained it as being consequence of the oil evaporation. This phenomenon, which requires high enthalpies, would ultimately explain the temperature drop observed in the rupture zone of journal bearings. A secondary explanation

was attributed to isentropic decompression of the gases in the oil. This is an explanation which is an alternative to the back flow effect advanced by Ma and Taylor (1992) described earlier in the previous section.

The theoretical work of Groper and Etsion (2002 – see section II.2.9), on the other hand, seems to support Ma and Taylor's assumption of temperature fade being due to a back-flow tongue that flows from the groove and creeps upstream into the cavities of the ruptured film region, at least to some extent. Their work was not focused on the thermal phenomena but rather on the pressure buildup observed by Etsion and Ludwig (1982) at the end tip of the ruptured film region. They successfully reproduced this pressure buildup through an algorithm that allowed the calculation of the cavitation shape, the penetration of the back flow into the cavitation zone and the pressure distribution inside the cavitation zone of a submerged journal bearing. This model is rather elaborate and includes the treatment of complex phenomena such as surface waviness instability (Kelvin-Helmholtz instability model) which explains the observed instability of the back flow tongue. At a first glance, it does not seem a straightforward task to successfully incorporate this model into usual THD journal bearing analyses.

f) The rupture models of Nassab et al

Nassab and Moayeri (2002– see sections II.2.9 and II.3.12) carried out a THD study of single groove journal bearings through the CFD approach (SIMPLE algorithm). The ruptured zone was treated as a uniform mixture of air and lubricant with effective properties according to the local liquid fraction, in a similar fashion (weighted harmonic mean) to the Gas Bubble (*GB*) model of Knight and Niewiarowski (1990 – see section II.3.14c). In a later work, where inertia effects were included (Nassab, 2005), load capacity and attitude angle were found to be affected by fluid inertia under low load, high speed and large clearance conditions, while temperature was only marginally affected.

Very recently, Nassab and Maneshian (2007) tested three different thermal models of the ruptured zone. While still considering the ruptured film, for flow calculations, as a uniform mixture of air and lubricant, they applied three different ruptured film region thermal models which did not necessarily used the same assumptions of flow calculations. In fact, in the first two models the thermal calculations were performed on the assumption that the fluid adheres to the shaft, with a few weak bonded streamlets touching the bush body (see Figure II-7). This assumption was based on the experimental findings of Heshmat (1991) already described in section II.3.14c).

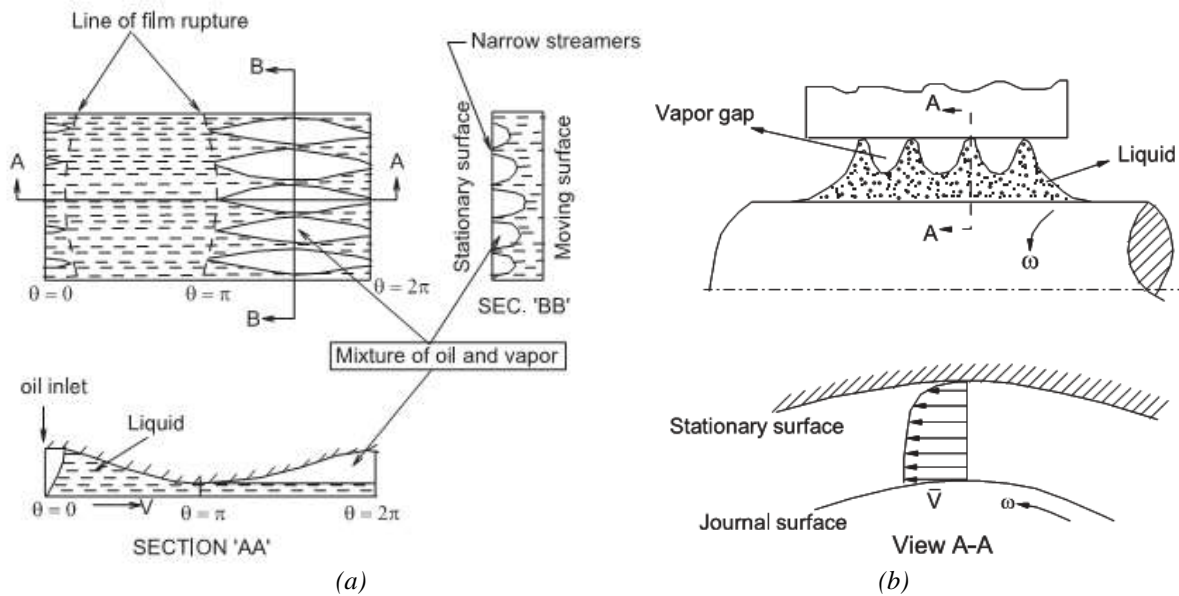


Figure II-7 – (a) The mechanism of film rupture and (b) Oil streamlets in the ruptured film region of the bearing as presented by Heshmat (1991) and later used in the models of Nassab and Maneshian (2007).

- i) In the first model, any heat generated by viscous dissipation is neglected with the assumption that the streamers are too weakly bonded to the stationary surface so that their velocity gradient is negligible (Figure II-7b). The properties, such as viscosity and thermal conductivity, are calculated similarly to their previous works (*GB* model). The thickness of the lubricant layer is obtained by continuity and considering a uniform velocity distribution for the liquid layer. The axial flow within the cavitated region is neglected. This model was found to systematically under-predict temperature profiles recorded in the experimental works of Mistry et al (1992), Mitsui et al (1986) and Ferron et al (1983). As a consequence, the maximum pressure of Ferron's bearing was over-predicted. This seems to render the assumption of no viscous dissipation at the ruptured film region as overtly inadequate.
- ii) The second model is similar to the first, but viscous dissipation within the gaseous phase is also considered, while still neglecting the viscous dissipation within the liquid phase. Although the viscosity of air is very small compared to that of current liquid lubricants the authors justify this assumption on the base that a very strong velocity gradient (from zero to the liquid surface velocity, which is considered to be approximately the shaft surface velocity) occurs across a very small thickness. Here, a linear velocity profile across the gas cavity is considered. The convective terms in the energy equation are computed based on the velocity field obtained by the momentum equation but the dissipation term is calculated with linear velocity for the vapour flow using the specific vapour property. Surprisingly, the inclusion of the viscous shear effect within the gaseous cavities had a significant effect on the estimated temperature profiles, raising temperature

globally and almost eliminating the underestimation of temperature that was observed with the previous model. Also the maximum pressure was much better estimated.

- iii) Unlike the previous two, the third model took into account the axial flows occurring at the ruptured film region. Furthermore, viscous dissipation was considered in the whole ruptured film region using mean properties of the mixture and with the velocity field which was obtained from the numerical solution of the Navier–Stokes equations. In order to calculate the liquid fraction, parabolic velocity profiles along the circumferential and the axial direction are considered. This model was similar to that used by Nassab and Moayeri (2002) which used linear velocity profiles in the circumferential direction instead. It provided slightly better results than the second model and therefore was considered to be the best performing model.

These results seem to point out that neglecting entirely the heat generation through viscous dissipation provides a rather under-predicted temperature profile. On the other hand, the best behaving model was the one which considered the lubricant to be a homogeneous mixture of oil and air, something which contradicts experimental evidence (Heshmat, 1991). The other two models, which provided poorer results seem, therefore, more physically accurate, except that in reality the streamers attached to the bush stationary surface should actually have a non-negligible viscous dissipation. In fact, the assumption made by the authors of the streamlets being weakly bonded to the stationary surface seems not physically accurate. This would imply the occurrence of some sort of wall slip, which is not likely to occur with typical lubricants and shaft surfaces. Therefore, it seems reasonable to assume that the models which are based on physical evidence could approach and even outperform the less physically accurate third model if viscous dissipation within the lubricant streamers would be taken into account in some way.

g) The finger-type cavitation model of Hatakenaka and Tanaka

Hatakenaka and Tanaka (2002) proposed a rupture zone algorithm that was inspired in the method used by Boncompain et al (1986), where a Couette flow of finger-type lubricant streamers separated by air cavities was considered. One of the differences of the new model in comparison to Boncompain's approach was the use of the FVM with the hybrid differentiation scheme (see section II.3.13) which, according to the authors, permitted convergence even with large regions under reverse flow. The other main difference was that the heat fluxes were calculated in the lubricant streams and in the cavities completely separately, with each of the thermal conductivities of the lubricant and the air being considered. In Boncompain's approach, however, when a computational cell contained both a streamlet part and a gas part, equivalent properties (namely thermal conductivity) based on the local fraction of liquid were used.

Hatakenaka and Tanaka sustained that the use these equivalent properties originated non-negligible inaccuracies to the heat transfer problem.

They validated their model with an experimental temperature profile obtained by Ma and Taylor (1994) for an elliptical journal bearing (see Figure II-8) and obtained a good correlation. However, it must be noted that the authors have tuned the values of some properties that were not specified in the experimental work (oil viscosity-temperature index, groove mixing coefficient, convective heat transfer coefficient from bearing pad to the ambient and shaft temperature) in order to obtain a good agreement with the measurements. Although the tuning was limited within reasonable property ranges, the legitimacy of this approach remains somewhat questionable, even taking into account that the authors also carried out a parametric study of the influence of each of the four parameters on the final results. For instance, variations larger than $\pm 5^\circ\text{C}$ were recorded when varying the value of the shaft temperature by $\pm 10^\circ\text{C}$.

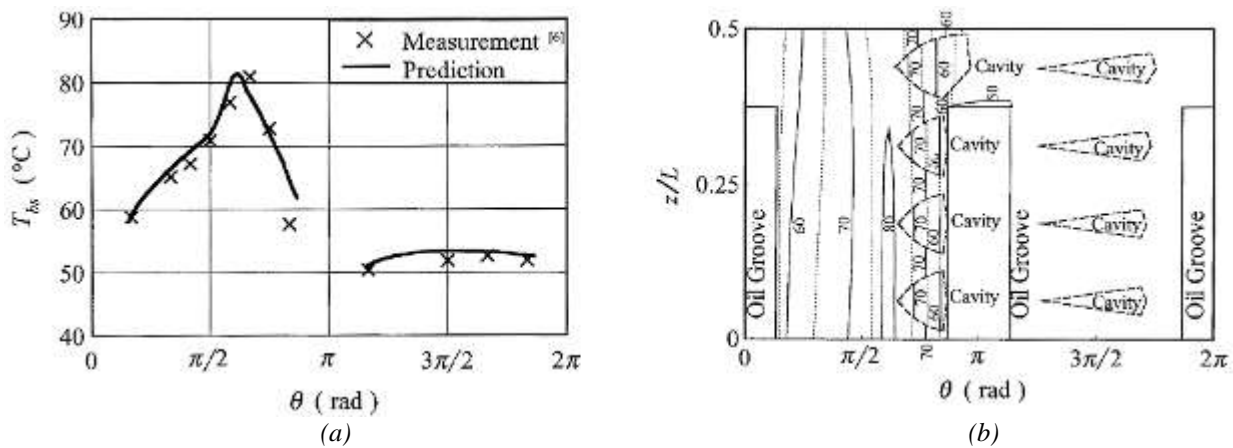


Figure II-8 – Comparison between theory (Hatakenaka and Tanaka, 2002) and experiment (Ma and Taylor, 1994) for (a) temperature profile at the midplane of an elliptical bearing and (b) corresponding location of cavities and temperature field (taken from Hatakenaka and Tanaka, 2002)

The authors reported that the chosen number of streamers did not affect significantly the results. This is a logical result since no axial heat exchange between liquid and gaseous cavities was considered. As a final remark, the suitability of this model will only be effectively assessed when a comparison with detailed experimental results is made.

II.3.15 The consideration of thermal and elastic deformations

Up to the eighties deformation studies were mainly limited to ball bearings (Bouyer, 2003). In fact, authors such as Rhode and Oh (1975) reported that the influence of thermal and elastic deformations on the performance of journal bearings operating under full hydrodynamic regime would be negligible when compared with the effect of transverse viscosity variations.

Nevertheless, these effects began to be incorporated more often in Journal bearing analysis since several experiments, like those of Ferron et al (1983), detected that the bearing gap could change considerably due to these effects.*

Medwell and Gethin (1984) while analyzing high speed twin groove journal bearings applied the simplified differential thermal expansion concept, in which an operating clearance based on an estimated average temperature of shaft and bush bodies was used. Afterwards, Gethin (1985) used the FEM to obtain both the pressure and displacement fields, considering a 2-D distortion model. These works pointed out for a significant influence, under high speed and high applied load, of thermo-elastic effects in flow rate, load carrying capacity and temperature distribution. Nonetheless, the correlation of flow rate and temperature profiles with the experimental data of Gethin and Medwell (1985) was poor.

Boncompain et al (1986) while maintaining a 3D Reynolds equation solution by the finite difference method (FDM) added the elastic and thermal deformation calculations at the midplane through the Finite Element Method (FEM). They found that the THD approach overestimated the maximum pressure obtained in Ferron's experiments (Ferron, et al, 1983), while the Thermoelastohydrodynamic (TEHD) approach provided a good prediction of this parameter.

Sinhasan and Chandrawat (1990) analyzed the performance of a twin groove journal bearing through the FEM and compared the results given by four different approaches: HD, EHD, THD and TEHD (3D). They obtained ever-increasing eccentricity values with each model, respectively. Unfortunately, no bush temperature data was presented, only shaft temperature. Furthermore, the model was weakly validated since only eccentricity-load results were compared against experimental data (obtained by Ferron et al, 1983).

Khonsari and Wang (1991) used the same FDM+FEM approach of Boncompain et al (1986) to analyze the two-dimensional case. Although they found also significant differences concerning the maximum pressure obtained by the THD and TEHD approaches, they found negligible differences between the results of the two models for axial flow rate and maximum temperature.

* The EHD and TEHD analyses described in this section should not be confused with the Elasto-Hydrodynamic Lubrication theory (EHL) typical of thin film lubrication of non-conformal surfaces under high specific loads (of the order of magnitude of the GPa). Here the EHD and TEHD analyses refer to the HD and the THD analyses with the inclusion of thermal and/or elastic deformations induced by the temperature field and/or the hydrodynamic pressure field.

Fillon et al (1992) carried out a TEHD and experimental study of a tilting-pad journal bearing and found that the thermal and mechanical deformations can change significantly the performance of these variable geometry bearings and that the deformations of all components (pads, body of support and shaft) should be taken into account. Monmosseau and Fillon (2000) further concluded that these effects can even lead to seizure at fast startups under conditions such as low bearing clearance and low feeding temperature.

The recent works which take into account deformation are mainly those that analyze:

- Tilting-pad journal bearings (Monmosseau et al, 1998; Reddy et al, 2000; Monmosseau and Fillon, 2000; Chang et al, 2002)
- Soft layered journal bearings (Elsharkawy et al, 2001) and thrust bearings (Markin et al, 2003; Glavatskih and Fillon, 2006),
- Dynamical loaded bearings - mainly engine connecting-rod bearings (Piffeteau et al, 2000; Kim and Kim, 2001; Fattu et al. 2006; Michaud et al, 2007)
- Plain journal bearings under severe operating conditions like high load and/or speed (Zhang et. al, 2000; Bouyer et al, 2004), strong misalignment (Bouyer 2003) or even under mixed lubrication including roughness effects (Shi and Wang, 1998; Wang et al, 1998; Zhang, 2002; Wang et al, 2002; Dobrica and Fillon, 2006a).

Bouyer and Fillon (2004) evaluated the relevance of the TEHD model in the analysis of a plain journal bearing subjected to severe operating conditions. Their deformation calculations were performed through the use of a compliance matrix that was previously obtained, based on the linearity of the problem, from individual FEM calculations of unit loads/heat fluxes at each node. They concluded that the THD approach provides acceptable results for normal operating conditions (surface velocities up to 30m/s and specific loads up to 10MPa). For operating conditions above these limits they recommend either the use of a full TEHD approach or the differential thermal expansion approach (use of an average operating radial clearance) used by Medwell and Gethin (1984). Taking these considerations into account, this latter model was adopted in the present work as a good compromise between simplicity and accuracy.

II.3.16 The Influence of lubricant supply conditions on thermal behavior

The inclusion of realistic lubricant supply conditions in journal bearing analyses can raise some theoretical difficulties, depending on the model used. While some models neglect the influence of supply conditions altogether, others use simplified approaches consisting on:

- Imposing full film reformation at the maximum film thickness position as in the Half-Sommerfeld approach (Gumbel, 1914).
- Considering grooves of infinitesimal width (no circumferential extension) (Bou Said, 1985).
- Considering grooves of finite width but extending to the full length of the bush body (Knight and Ghadimi, 1992; Rajalingham and Prabhu, 1987; Pierre and Fillon, 2000).
- Considering finite size grooves but imposing flow rate or no feeding pressure (ambient) (Rajalingham and Prabhu, 1987).
- Neglecting or oversimplifying the thermal phenomena occurring at the groove region, such as the effect recirculated hot oil, feeding temperature, reverse flow (oil that reenters the groove from downstream) or back flow (fresh oil that flows upstream from the groove).

Boncompain (1984) and later Boncompain et al (1986) modified the model of Ferron et al (1983) in order to include the consideration of the actual value of the feeding pressure, but they did not consider the actual groove dimensions in their study.

Knight et al (1985) analyzed the influence of feeding pressure in the performance of twin groove journal bearings through the FEM. They used a 1D energy equation and described the axial pressure profile through second order polynomials. They found that the feeding pressure affects the maximum temperature decreasing it, especially at low Sommerfeld numbers. The increase in feeding pressure was found to increase flow rate significantly and power loss slightly.

So and Sieh (1987) analyzed the cooling effect of the lubricant feeding pressure on the temperature profile of twin groove journal bearings. They used a bearing with small grooves and allowed the temperature to vary along the circumferential and the axial direction but not across the film thickness. They obtained significant axial temperature gradients due to the reduced dimensions of the groove and they concluded that the increase of the feeding pressure caused a decrease of the maximum temperature and a significant increase in flow rate. The latter parameter was found to be poorly correlated with the experimental data of Tonnesen and Hansen (1981), especially at high eccentricities.

Gethin and Gethin and El-Deihi (1987, 1990, 1991 and 1992) carried out a series of theoretical and experimental studies on high speed, twin groove journal bearings in order to assess the influence of the position of the two diametrically opposed axial grooves relatively to the load direction.

Gethin and El-Deihi (1987) first carried out an isoviscous simplified FEM approach to the Turbulent Reynolds equation, where assumptions such as full bearing length reformation and

ambient pressure were imposed at the groove region. They tested five different load angles (0° , 45° , 90° , 135° and 180°) and found that the maximum load capacity was obtained when the grooves were orthogonal to the load line (90°). In the cases where the grooves were aligned with the load line (0° , 180°), the load carrying capacity was only 25% of the load obtained in the 90° case (for an eccentricity ratio of 0.9). Power loss was found not to depend significantly on the load angle.

Gethin and El-Deihi (1990, 1991) added a rather simplified thermal analysis to their former model and also carried out validation experiments. Viscosity and temperature variations were taken into account along the circumferential and axial direction only. No heat conduction through the solid bodies was calculated. Instead, a simplified dissipation model based on an estimated heat removal factor was used. Backflow and groove axial outlet flow were also neglected. As a result of all these simplifications, the model yielded rather poor results concerning the temperature profiles, with differences in maximum temperature sometimes above 20°C . The model failed to reproduce the decreasing temperature trend found experimentally at the ruptured film region. The side flow leakage was largely underestimated (sometimes cut to one third of the experimental value), especially for the lower shaft speeds tested, which are closer to the laminar flow regime (5000rpm). Curiously, the power loss and the maximum film thickness were best predicted under these conditions. This work referred briefly to the eventuality of negative flow rate occurring at one of the grooves. This can occur when the pressure buildup zone is close to one of the grooves. They addressed this problem in their model by changing the way the heat balance at the grooves was undertaken. This issue is thoroughly addressed in the current work both experimentally and theoretically.

The last work by El-Deihi and Gethin (1992) on the effect of loading direction on the performance of journal bearings consisted in a more rigorous THD approach in comparison to the former works. Viscosity and temperature were allowed to vary along the thickness and heat conduction through the solid bodies was considered. The shaft temperature was imposed as being equal to the mean film temperature, while at the leading edge of the groove the inlet temperature was calculated through a heat balance. The use of such a groove mixing model proved to be determinant for the improvement of the results. With this new model a much better agreement with experiment was found for the temperature profile. However, huge differences between theory and experiment continued to be detected in flow rate.

Chun and Lalas (1992) analyzed the influence of feeding pressure and feeding temperature on the performance of both semi-circumferential and axially grooved journal bearings. However, their approach did not consider transverse viscosity variation and did not ensure flow continuity.

Claro and Miranda (1993) and Claro (1994) carried out a thorough theoretical and experimental assessment of the influence of lubricant supply conditions on the performance of circular journal bearings with several groove configurations, including twin axial groove journal bearings. Although their approach was based on the Global Thermal Model (Swift, 1937), they used a mass conservative algorithm (Elrod, 1981) and considered the actual dimensions of the grooves. Later, Costa et al extended this approach taking into account thermal effects and studied theoretically (Costa et al, 2003a) and experimentally (Costa et al, 2000, 2003b) the influence of lubricant supply conditions on the performance of single groove journal bearings. They found that often neglected parameters such as the real value of the feeding pressure and the actual groove geometry and location can influence significantly bearing performance.

Ma and Taylor (1995) used their theoretical approach based on the *Separation Model* (1992, 1994a - see section II.3.14d) and also carried out some experimental work in order to study the influence of feeding temperature and feeding pressure on the performance of twin groove elliptical bearings. They found that the increase of feeding temperature yielded significantly higher values of the maximum temperature and flow rate and significantly lower values of power loss. On the other hand, increasing feeding pressure caused an important increase in flow rate, and moderate decreases in maximum bush temperature and power loss.

Vijayaraghavan et al (1996) analyzed the effect of lubricant supply starvation on the THD performance of a journal bearing with a single axial groove. They used the model developed by Vijayaraghavan and Keith (1996 – see section II.2.7) and concluded that a judicious selection of the groove location could reduce substantially the flow rate and the power loss without a deleterious effect in load carrying capacity.

Keogh and Khonsari (2001) analyzed the influence of oil inlet conditions on the THD performance of fully circumferentially grooved journal bearings. They used a simplified axial averaging technique that enabled the groove pressure and the entry temperature to the lubricant film to be explicitly incorporated into the lubricant energy equation and reported that the mixing effect must be always taken into account.

As a final remark, it may be concluded the experimental works focusing on twin groove journal bearings are scarce or incomplete, namely in what concerns the influence of supply conditions. Effectively, Tonnesen and Hansen (1981) and Lund and Tonnesen (1984) carried out a good experimental work on these bearings, but with fixed supply conditions. The same can be said of the work by Fitzgerald and Neal (1992), which also lacks some other important data such as shaft eccentricity. Basri and Neal (1990) were the only authors to present individual measurements of flow rate at each groove, but only for two test conditions. Gethin and El-Deihi

(1990, 1991) presented very interesting experimental results of the behavior of a twin groove journal bearing under several load angles. Unfortunately the speeds tested were normally too high to consider a laminar regime. Finally, Ma and Taylor (1992, 1996) presented experimental results for this bearing type but omitted the main lubricant properties. Furthermore, the bearing they tested possessed unusually large grooves, spanning 55° each. It seems that an experimental work testing a wide range of lubricant supply conditions still needs to be done.

II.4 Numerical methods and Programming tools

In the last decades the numerical methods, the programming tools and the theoretical approaches used in journal bearing analysis have been increasing in sophistication and complexity from day to day.

II.4.1 Numerical methods

The Finite Element Method (FEM), which is widely used in solid and structural mechanics, has been used in hydrodynamic lubrication since several decades from now. Normally it is the method chosen in approaches which include thermal or elastic deformations, or in cases with more complicated geometries and unstructured meshes (Bou Saïd, 1985; Gethin, 1987).

The Finite Difference Method (FDM) which was used in the earlier works is still very popular. This is due not only to its simplicity and straightforwardness but also due to its proved ability to treat the complexities of the THD problem. Furthermore, many efficient HD and THD approaches which are still used today were originally developed with this method and have been object of notable development. Even nowadays many new models are based in the FDM, as seen in previous sections. If mastered correctly, the algorithms based on the FDM can provide results with an accuracy and efficiency comparable to other methods. This method is especially suited for simple geometries with structured meshes (as is the case of plain journal bearings) and it is more promptly implemented than the FEM. All these reasons, along with the accumulated expertise of the research group with the method, led to the choice of the FDM method for the present work.

Lately, the Finite Volume Method (FVM) has also gained popularity within the tribology field. This method (which relies also in the FDM derivative approach) has the advantage of being based on the conservation of properties across the elementary cell boundaries, which makes it intrinsically conservative (Versteeg and Malalasekera, 1995). The FVM is also widely applied in Computational Fluid Dynamics (CFD) analyses, having had a great development in the last

decades. The Pressure/flow calculations of the present work (The Elrod Algorithm) were based on a method relying in mass conservation computations which shares the philosophy of the FVM.

There are also other, less used, numerical methods, such as the Boundary Element Method (BEM), (Yu and Keith, 1994; Durany et al, 2005) or the more recent mesh-less methods (Li et al, 2004).

II.4.2 Programming tools

The theoretical models can be implemented either through compiler-based programming languages such as FORTRAN and C, by commercial solvers such as FLUENT or through high-level programming environments such as MATLAB. The choice of the best solution is highly dependent on the scope of the work.

Although there are some very advanced commercial numerical solvers, they often lack the flexibility needed to solve many specific THD lubrication problems. This is so concerning, for instance, the application of specific rupture models, boundary conditions or simplifying assumptions. Also, commercial packages normally display limited programming capabilities or simply lack them altogether.

High level programming environments such as MATLAB display many advanced numerical tools. However, these tools are reported as being too slow for the more computational intensive applications, especially in the presence of loops. Such is the case of the present model.

The reference works in lubrication analysis are still built from scratch by means of powerful compiler-based programming languages such as C or FORTRAN. This latter programming language is especially suited for numerical methods. The newer versions, FORTRAN 90/95, display very powerful algebra intrinsic functions. For instance, they are able to handle matrixes as single entities and perform many advanced operations. This programming language was chosen for the present work.

Recent developments in numerical performance were made through parallel computing. This technique can drastically reduce computation times and is being used not only in powerful computer clusters, but also in single computer calculations, as the multi-core and multi-processor computers are becoming widespread. It is starting to be used also in the field of THD lubrication. For instance, Wang and Tsai (2006) have assessed the performance of multi-thread programming using FORTRAN 95 and the OpenMP portable parallel programming paradigm in a dual core processor. They applied the approach to the THD analysis of a thrust pad and

found that the program coded in thread-level parallelism could use effectively the multi-core computing resources.

The present model still did not implement this programming paradigm. Actually, the processing time might become a critical factor for the present model mainly due to the high amount of cases to test (as when building design charts and when performing parametric studies) more than due to the actual duration of each test. It is worth noting that the resources of a computer cluster (dirac.fisica.uminho.pt) were efficiently used for the queuing and simultaneous running of several different test conditions.

II.5 Current trends in journal bearing analysis

Although journal bearing analysis has now reached its maturity, many new fields of research still continue to appear. An ever growing sophistication in theoretical and experimental approaches has not ceased to this day, with recent works covering a wide range of areas.

Before concluding this chapter, a revision of the current trends in journal bearing analysis is briefly presented. Even if some of the subjects are not directly related to those treated in the present work, it seems useful to provide some insight to the orientation which is currently being given to the hydrodynamic journal bearing research. It is expected that this will help in apprehending the wider context under which the present work is inserted.

II.5.1 Non-Newtonian effects, namely due to lubricant additives

Raghunandana et al (2001), Wang, Keith and Vaidyanathan (2002) and Osman (2004) studied the effect of non-Newtonian lubricants in the stability of journal bearings.

Several authors studied the performance of journal bearings lubricated with couple-stress fluids (Wang, Zhu and Wen, 2001, 2002; Wang, Zhu and Gui, 2002; Guha, 2004; Ma, Wang and Cheng, 2004; Chiang, Hsu, Lin, 2004; Elsharkawy, 2005).

An interesting result is that the couple stress fluids, for instance, not only tend to yield an increase in load capacity and a decrease in friction coefficient compared with Newtonian lubricants, but also produce normally a lower bearing temperature field and side leakage.

Others studied the effect of Micro-polar lubricants (Das et al, 2002, 2004, 2005; Wang and Zhu, 2006; Nair et al, 2007).

The Non-Newtonian effects were also investigated in conjunction with roughness effects in mixed lubrication by Zhang (2002) and Wang, Keith and Vaidyanathan (2002).

II.5.2 Roughness and micro-texture effects

The study of the influence of roughness effects has gained momentum in recent times. Generally such effects are neglected within thick film lubrication analyses. However, when under mixed lubrication regime or in the presence of especially thin films, this effect needs to be conveniently assessed.

Guha (2000) studied the combined effect of isotropic roughness and misalignment on the steady-state characteristics of misaligned hydrodynamic journal bearings. Rao and Sawicky (2005) studied the effect of roughness on journal bearing stability. Bayada et al (2005, 2006) included in their analysis the effect of macro and inter-asperity film rupture through an average flow model and a mass-conserving rupture model (see Figure II-9). The use of a mass conserving film rupture model was found to be important in order to conveniently treat roughness effects.

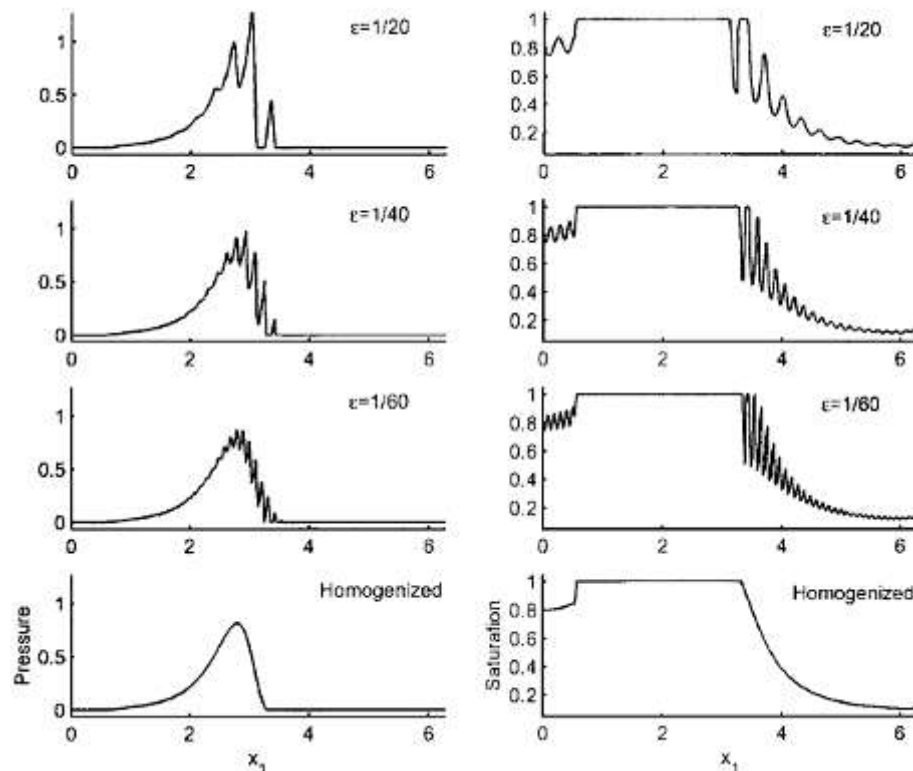


Figure II-9 – Influence of periodic roughness on Pressure and saturation at midplane, for different periods of the roughness and in the homogenized case (Bayada et al, 2005). Macro and inter-asperity film rupture has been considered.

Dobrica and Fillon (2006a) proposed a mixed-EHD deterministic model and compared it with the stochastic lubrication model of Patir and Cheng (1978). Brenner et al (2007) used the Lattice-Boltzmann Method in order to study a real surface with roughness obtained with the application of an optical interference technique.

The ability to apply protruding or recessed micro-textures or patterns through laser engraving, chemical erosion or photolithography has lead to the tribological assessment of the ability of

these patterns to provide extra load carrying capacity, reduce power loss or reduce surface contact and wear.

Some authors, which used the Reynolds equation with the Swift-Stieber conditions such as Siripuram and Stephens (2004) or Tala-Ighil and Fillon (2007) found a positive effect in the application of micro-texturizing of surfaces both in terms of load carrying capacity and power loss.

Others, like Arghir et al (2003), Sahlin et al (2005), or Kraker et al (2007) used the CFD approach and obtained an increase in load carrying capacity, which they attributed to the effect of fluid inertia (see Figure II-10 for Sahlin et al results).

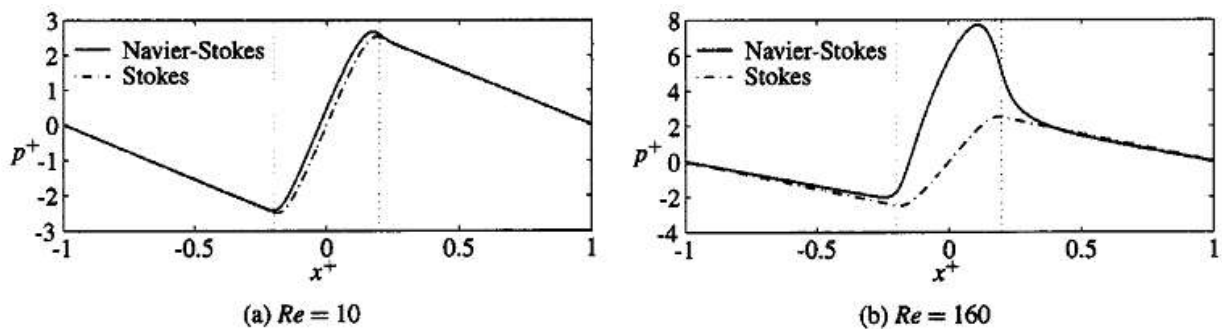


Figure II-10 – Influence of the inclusion of inertial effects into the CFD analysis on the pressure profile generated in a cylindrical texture, for two Reynolds numbers (Sahlin et al, (2005).

However, Dobrica and Fillon (2009) presented a work in which they object to the findings of the previous authors. Specifically, they object to the claim that the Reynolds equation would not be valid for modeling textured surfaces because inertia-related effects would explain, fully or partially, the hydrodynamic lift observed experimentally in parallel textured sliders. The main argument Dobrica and Fillon present is that the supposed beneficial effect of inertia for load capacity claimed by these authors was erroneously obtained once they limited their study to a single texture and wrongly assumed periodic boundary conditions.

In order to prove their objection, Dobrica and Fillon carried out a series of rigorous CFD calculations to a group of textures instead of a single one (see Figure II-11), and found that results were in fact quite different from those obtained with a single texture and that the use of periodic boundary conditions in such cases would be fundamentally wrong. Actually they found that the inertia effects could inclusively be deleterious for load capacity. Furthermore, they concluded that the load carrying capacity improvement provided by texturizing (which is verified experimentally) should be mainly explained by a step-like effect similar to the one found in step/pocket bearings, already predicted through the Reynolds equation.

Dobrica and Fillon carried out a parametric study on the differences found between the CFD and the Reynolds results for several texture aspect ratios and Reynolds numbers. They found

that the Reynolds equation can be applied in textured sliders, as long as λ is sufficiently large, and Re sufficiently small. They finally proposed a method for adding inertia effects into the Reynolds equation, which, in a simple manner, improved significantly the model rendering it valid for the majority of practical applications.

Ausas et al (2007 - see section II.2.6e) found that the film rupture model can be important for the accuracy of the results when incorporating roughness or micro-texture effects. These authors compared the results provided by the mass-conservative Elrod-Adams model to the non-conservative Reynolds model and found that the use of a mass-conservative rupture algorithm is vital for a correct assessment of roughness and micro-texturing effects due to the errors committed in the estimation of inter-asperity film rupture with the non-conserving algorithm. The differences between the two models are seen in Figure II-1 (page 11).

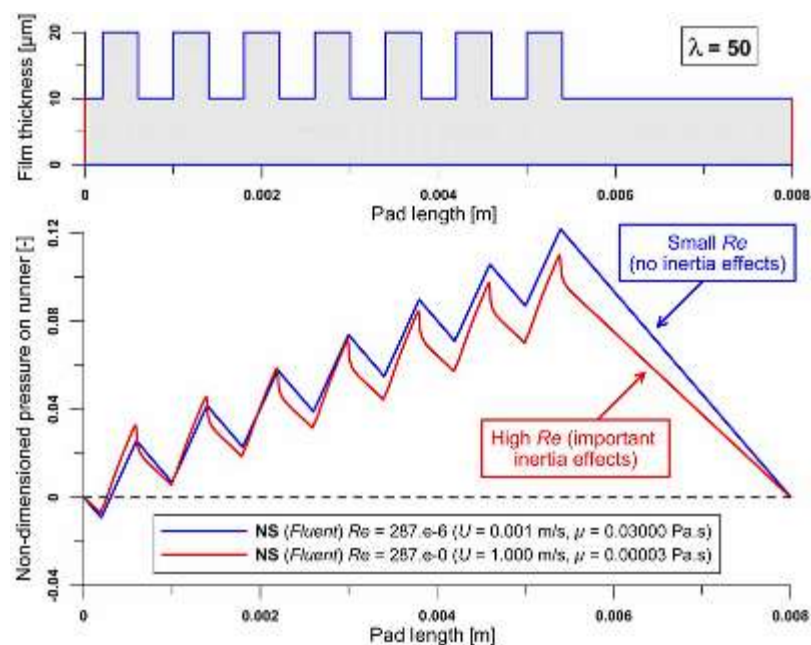


Figure II-11 - Inertia effects in a partially textured (inlet texture) parallel slider (Dobrica and Fillon, 2009).

Tønder (2004) used the average flow Reynolds equation of Patir and Cheng (1978) to study the improved performance (higher load capacity and lower drag) found in thrust bearings with partial texturing at the inlet region. The partial texturing technique was further studied by Marian et al (2007), Rahmani et al (2007) and Glavatskih et al (2005), which confirmed experimentally that micro-patterned thrust bearing pads can reduce by as much as 10% the friction coefficient, decrease the maximum pad temperature by as much as 5°C and increase slightly the load carrying capacity.

Kraker et al (2007) proposed a multi-scale approach for the treatment of both the macro and micro effects in lubrication. The local (micro) flow effects for a single surface pocket/texture were analyzed using the full Navier–Stokes equations with both inertia and micro-cavitation effects. With this, flow factors were derived and added to the macroscopic smooth flow

problem, modeled by the Reynolds equation. To account for an additional pressure buildup in the texture cell due to inertia effects, a pressure gain was introduced at the macroscopic level. They also studied the effect of pockets located at the moving surface. Of course, this approach displays the shortcomings already noted by Dobrica and Fillon (2009 – see discussion in the previous pages).

Other very recent works on micro-textured surface effects are those of Fowell et al (2007), Li and Chen (2007) and Dobrica et al (2007). In this latter work an important discussion has been opened, since the authors claim that the texturizing density which would maximize the performance of a partially textured bearing would be the limit value (100%). This would coincide with the pocket bearing geometry (see Figure II-12). Therefore, the partial texturizing becomes questionable as a suitable mean for the sole objective of improving the load capacity and power loss of hydrodynamic bearings, since a pocket could provide equal or even higher performance at a much cheaper cost.

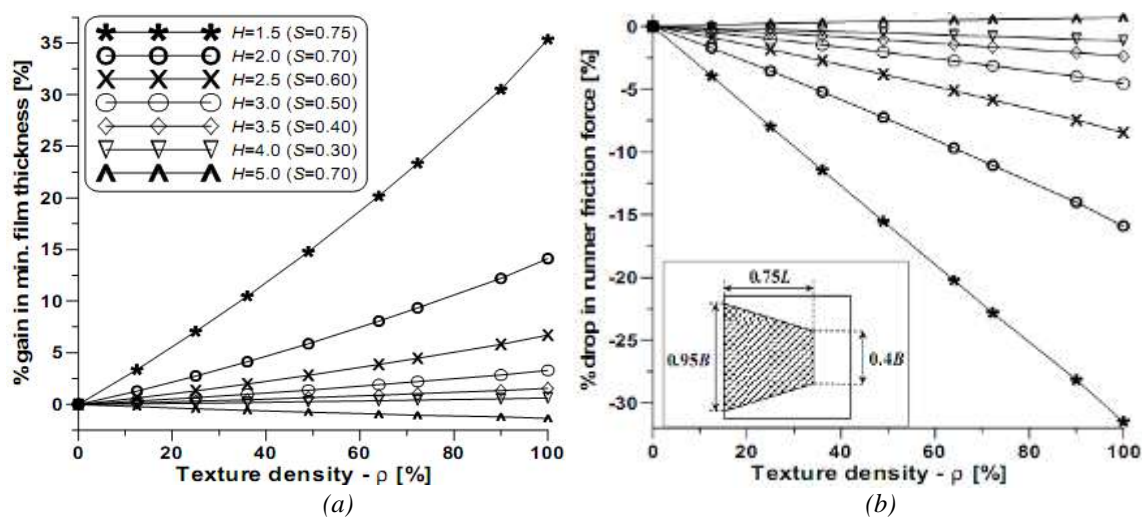


Figure II-12 – Influence of the texture density on (a) the gain in minimum film thickness and (b) the drop in friction force (Dobrica et al, 2007). 100% corresponds to a pocket.

II.5.3 The analysis of Inertia effects

As it has been said, several recent works have focused on the effect of fluid inertia in journal bearing analysis, such as those of Arghir et al (2003), Sahlin et al, (2005), Kraker et al (2007) and Dobrica and Fillon (2006b, 2009).

Kakoty and Majumdar (2000, 2002) have concluded that the effect of inertia is generally negligible in steady state analysis but cannot be neglected in dynamic analysis. Other works also analyzed this effect (Frêne et al, 2006; Shyu et al, 2000; Nassab, 2005 – see section II.3.14f).

II.5.4 Thermal analysis of dynamically loaded journal bearings

Numerous recent works have focused on the dynamic behavior of journal bearings. While some works focused on the estimation of dynamic coefficients (Rao et al, 2000, 2001; Sawicky and Rao, 2001; Mourelatos, 2001), several others performed TEHD analyses in order to study the behavior of connecting rod bearings under dynamic load (Stefani and Rebora, 2002; Souchet et al, 2004; Wang et al, 2004; Fattu et al, 2006; Michaud et al, 2007). For instance, Stefani and Rebora (2002) investigated the influence of the bolt preload on the performance of this kind of bearings.

Sawicky and Rao (2001) carried out an investigation on the acceptable limits of linear bearing dynamic coefficients analyses and applied it to twin groove journal bearings, while Rao and Sawicky (2002, 2003) analyzed the influence of considering cavitation in journal bearing linear stability analysis and concluded that indeed with the inclusion of a mass conservative algorithm there is a significant variation in the trend of dynamic characteristics of a plain cylindrical journal bearing. The stability threshold increases with increase in feeding pressure in the case of a grooved journal bearing.

II.5.5 Optimization techniques in bearing design

The ever-growing computational performance and the advent of many general purpose multi-objective optimization methods gave way to many recent innovative works which try to find the optimum set of geometrical and/or operating conditions for journal bearings. Many of these studies may constitute a very useful tool for bearing design.

Wang, Ho and Cha (2000) exemplify the use of unconstrained nonlinear programming methods, lattice search and simplex methods in the optimization of two or more design variables of elliptical, thrust and aerostatic bearings.

Hashimoto and Matsumoto (2001) optimized an elliptical bearing performance by finding the ideal vertical and horizontal radial clearances, bearing length to-diameter ratio and bearing orientation angle that minimized the weighted sum of maximum averaged oil film temperature rise, leakage oil flow rate, and the whirl onset speed for a high-speed range of journal rotational speed. They used a hybrid optimization technique combining the direct search method and the successive quadratic programming.

Yang et al (2001) applied the artificial life concept to the optimization of short bearing operating conditions. The concept is inspired in the survival of organisms and species within ecosystems found in nature. Analogies with concepts such as the search for resources within a

neighborhood, migration, energy adsorption and spending, age increasing, reproduction and death are deployed in the analysis. The micro-interaction of organisms with each other in the artificial life's world ultimately leads the artificial organisms to find all global optimums and produce the emergent colonization for all the optimums that minimize the objective function. According to the authors this is the main strength of this method in relation with other methods which often converge to local optimums rather than global optimums. They chose as design variables the radial clearance, the length to diameter ratio and the effective viscosity. Then, they specified the constraints applied to the state variables, the minimum and maximum values admitted for several parameters such as load, rotational speed, eccentricity ratio, maximum film pressure, maximum film temperature, or friction force. Then they built the objective function, in this case a weighted sum of fluid film temperature rise and lubricant feeding flow rate. Finally they applied the artificial life algorithm in order to find the optimum variables that minimize the objective function, while still respecting the constraints. Later, Song et al (2005) proposed the enhanced artificial life algorithm, which updates the previous model with the random-tabu method, which prevents the method of converging to a local minimum.

Boedo and Eshkabilov (2003) used genetic algorithms in order to determine the optimal shape of journal bearings. These algorithms are also based in analogies with natural phenomena such as genetic mutations and combinations along generations. The authors state that this method proved to be superior to the classical random search methods and comparable to other traditional optimization techniques.

Hirani (2004) tested the three-level Taguchi method and the Pareto optimality concept. A little later Hirani and Suh (2005) added a genetic algorithm in conjunction with Pareto analysis and axiomatic design. First guesses were made through analytical isoviscous solutions, followed by the application of the rigorous Reynolds solution through the mass-conserving algorithm of Vijayaraghavan and Keith (1990). In this approach the simultaneous minimization of power loss and lubricant flow rate was pursued within the imposed restraints

Zengeya and Gadala (2007) proposed a hybrid optimization technique that uses a genetic algorithm to converge to the global minimum and sequential quadratic programming for an accurate location of the minimum point. They used the THD approach of Jang and Khonsari (2004).

Swanson (2005) used sequential quadratic programming in order to derive the optimal shape of a fixed geometry journal bearing in terms of stability. Through an objective function based on the rigid rotor whirl-speed ratio he obtained a rather complex optimal shape for the inner

surface of the bush. This shape would be impossible to derive through trial/error guesses. He used an isoviscous approach based on the FEM.

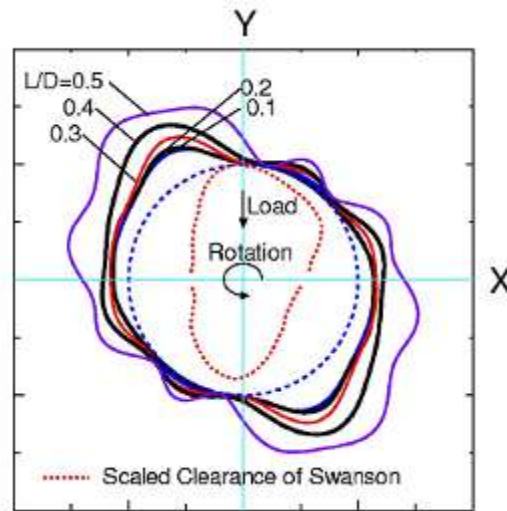


Figure II-13 – Comparison between the optimized bearing clearance of Swanson (2005) and those proposed by Matsuda et al (2007).

Matsuda et al (2007) tried to improve Swanson's results by providing geometries which would be stable over a wider range of conditions (see Figure II-13).

Unlike Swanson's method of adding small surface offsets to the film thickness, the authors used a Fourier series to represent an arbitrary circumferential clearance configuration. The optimization method then tries to find the Fourier coefficients that minimize the performance index. This performance index consists on the sum of the whirl-frequency ratios over a wide range of eccentricity ratios. Therefore this method becomes, according to the authors, more general than Swanson's approach.

II.5.6 Influence of form defects and wear

Another research field which has been recently explored is the analysis of out-of-control or off-design bearing characteristics. For instance, Fillon and Bouyer (2004) assessed the THD performance of a worn plain journal bearing and discovered that wear defects can in some cases improve bearing performance by decreasing maximum temperature and power loss. In an earlier work (Bouyer and Fillon, 2003) they also verified that local wear defects could actually improve the THD Performance of a Misaligned Plain Journal Bearing. Very recently, Bouyer et al (2007) studied the influence of wear on the behavior of a two-lobe hydrodynamic journal bearing subjected to numerous start-ups and stops and concluded that although the bearing behavior was affected by wear, it still remains useable and safe.

Mishra (2007a, 2007b) analyzed the effect of the non-circularity of the bush bore, with an elliptical deformation being considered. He assessed the effect of the degree of non-circularity on the THD behavior of the bearing. As non-circularity increased the temperature was found to decrease, accompanied by an increase of flow rate.

Fillon, Dmochowski and Dadouche (2007) explored the sensitivity of tilting pad journal bearing performance to manufacturing tolerances, with the variation of the bearing clearance and the geometrical preload of the bearing being the most influential parameters. The film thickness was found to be highly sensible to manufacturing errors under low speed and high applied load.

II.5.7 Innovative journal bearing solutions

Several innovative approaches to journal bearing analysis, design and control are described in recent publications.

New active bearing control procedures are proposed by Chowdhury (2000), Rho and Kim (2002) and Nicoletti and Santos (2003).

Custom tailored geometry bearing design method were proposed by Swanson (2005) and Matsuda et al (2007), as already described in section II.5.5.

Inlet textured thrust bearings were studied by Tønder (2004), Marian et al (2007), Rahmani et al (2007) and Glavatskih et al (2005) as described in point II.5.2.

Pandazaras and Petropoulos (2001) investigated the suitability of convex and concave bushings and concluded that a specific critical concavity waviness amplitude could lead to a quasi-uniform axial pressure distribution which minimized friction.

Martin and Parkins (2002) studied the performance of a continuously adjustable hydrodynamic bearing which can balance a range of loads in any direction and still maintain negligible rotor eccentricity through non-equal pad adjustments.

Based on the concept of highly hydrophobic surfaces where the no-slip condition typically used in hydrodynamic lubrication is no longer valid, several authors have proposed innovative bearing designs based on a judicious location of slip/no-slip surfaces. Spikes (2003) studied the half-wetted thrust bearing by adapting the Reynolds equation to both partial slip and no slip surface conditions. He concluded that this bearing geometry combines a good load support that results from fluid entrainment with very low friction due to very low or zero Couette flow. Similar studies were performed by Wu et al (2006) and Li et al (2006), while Choo et al (2007a, 2007b) confirmed experimentally a reduction in friction which should be attributed to

the occurrence of wall slip at the hydrophobic surface (mica coated with a self-assembled silane monolayer).

The partial wetted bearing approach was also applied to journal bearings by Fortier and Salant (2005), which concluded that the judicious application of slip to a journal bearing's surface can indeed lead to improvement of bearing performance. However, according to these authors the wall slip effect can be neglected for high eccentricities (above 0.92). Ma et al (2007) carried out a similar study and concluded that a slip zone located at the inlet region improves the performance of the bearing, namely by increasing load carrying capacity and decreasing the friction coefficient.

Other innovative bearing systems which are being currently studied are the magnetized journal bearings lubricated with ferrofluid (Osman et al, 2001; Kuzhir, 2008), the wavy bearings (Zhao et al, 2002; Dimofte et al, 2000, 2005), electro-rheological journal bearings (Peng and Zhu, 2003) and the hybrid (hydrodynamic + magnetic) journal bearing which can achieve the low starting torque of permanent magnetic bearings and still display the medium to high load carrying capacity of typical hydrodynamic bearings, all in a single bearing arrangement (Hirani and Samanta, 2007).

II.6 Conclusions

A review of the historical background and the current state of the art of hydrodynamic journal bearing analysis have been presented. The main theoretical and experimental achievements that were accomplished in the analysis of the performance of journal bearings in general, and twin groove journal bearings in particular, have been highlighted.

Clearly, the bases of the THD analysis of journal bearings are now solidly established. Although this field has been thoroughly studied by many authors, there is still insufficient correlation between theory and experiment in many aspects. Furthermore, there have been some works on similar subjects which displayed contradictory conclusions. The revision article of Tanaka (2000) on Recent THD analyses and designs of thick-film bearings has highlighted this problem and suggested that an effort of synthesizing past theoretical achievements should be undertaken in order to arrive to solidly validated models which would become readily available as reliable tools for bearing performance analysis and design.

As seen in this chapter, realistic supply conditions such as the actual groove geometry and location, lubricant feeding pressure and lubricant feeding temperature, have been often neglected or oversimplified in most theoretical models. This has limited the analysis of

important related phenomena such as the occurrence of reverse-flow at the inlet region, lubricant back-flow to the region which is located upstream of grooves, the mixing at the grooves, the inlet temperature profile, the occurrence of film rupture and reformation and the feeding flow rate. Also, experimental works focusing on twin groove journal bearings are also scarce or incomplete, namely in what concerns the influence of supply conditions.

The present work tries to address some of these concerns. More than trying to open new research fields still not studied until now, or embarking in the discussion of the latest state-of-the-art subjects such as those presented in II.5, it seems that an effort should be put on the development of an extensively validated model which could allow a better understanding of some of the mechanisms which can significantly affect the performance of common hydrodynamic journal bearings, and are still not thoroughly studied or satisfactorily dominated.

The decision of focusing the present study on twin groove journal bearings was based not only on the fact that this bearing geometry has received much less attention than single groove cases, but also because more acute theoretical discrepancies have been observed for this bearing geometry in comparison, for instance, with single groove journal bearings. In fact, most theoretical models do not conveniently represent the temperature field in the ruptured film region and in the vicinity of grooves, and largely overestimate flow rate. Moreover, there are specific issues related to twin groove configuration, such as flow rate partition between the grooves and the occurrence of negative flow rate at one of the grooves, which are still not sufficiently studied.

The theoretical and experimental study of both the HD and THD performance of single groove journal bearings, with particular emphasis on the influence of supply conditions was carried out in the past by the present team. This chapter has put into light that a similar study focused on twin groove journal bearings is needed.

*As far as the laws of mathematics refer to reality, they are not certain.
As far as they are certain, they do not refer to reality.*

- Albert Einstein

CHAPTER III Theoretical Model

III.1 Introduction

The present chapter describes the theoretical model that was developed for the analysis of the performance of twin groove journal bearings. The motivation of this work is presented in the introductory chapter of this thesis, while its full justification is thoroughly explained in CHAPTER II. Basically, the main aims of this task were:

- To improve the accuracy of bearing behavior predictions provided by existing theoretical models;
- To develop a computer program which could constitute the core of a future bearing design tool that would provide theoretically solid results within a time lapse compatible with typical design requirements. Based on inputs like the bearing geometry (diameter, clearance, width, groove dimensions), the working conditions (speed, load/eccentricity) and the supply conditions (feeding pressure, feeding temperature) the model should provide a reliable estimation of the relevant performance parameters such as shaft locus, pressure field (especially P_{max}), temperature field (especially T_{out} and T_{max}), flow rates, shaft torque and power loss.
- To assess the role of lubricant supply conditions on bearing performance, promoting the awareness of industrial designers and of the research community for their relevance.

In order to accomplish the aforementioned tasks, a suitable methodology was pursued:

- A Thermohydrodynamic (THD) approach was implemented. It was based on the simultaneous solution of the Generalized Reynolds Equation and the Energy Equation within the fluid domain and the Laplace equation within the bush body domain.
- Care was taken in order to realistically incorporate lubricant supply conditions into the analysis: the real dimensions of the grooves were considered in pressure and flow calculations, mass and energy conserving algorithms were deployed.

- Models for the ruptured film region and the lubricant mixing at the grooves were derived.
- A simplified thermo-elastic model was deployed.
- Suitable boundary conditions were pursued.
- In order to globally optimize algorithm flexibility, numerical performance and portability, a compiler-based programming language (FORTRAN 90/95) was preferred over existing commercial packages.
- A careful validation of the theoretical model with comparisons between its results and experimental data is presented subsequently in CHAPTER VI.
- Subsequently, an extensive parametric study to assess the influence of lubricant supply conditions on bearing performance was carried out, being presented in CHAPTER VII.

Various theoretical approaches were tested along the time. Although this chapter describes mainly the final stage of the model, the process by which previous approaches were discarded or updated is occasionally described.

III.2 Basic Assumptions

The following simplifying assumptions have been considered:

- i) The domain is continuous and incompressible, with the fluid displaying a Newtonian behavior;
- ii) The flow is within the laminar regime, the effect of fluid inertia and gravity is neglected (Small Reynolds number);
- iii) The bearing operates under steady state regime. Shaft speed, applied load, feeding pressure and feeding temperature are assumed to be constant;
- iv) The bush and the shaft are perfectly cylindrical, homogeneous, impermeable and aligned;
- v) Hydrodynamic pressure is constant along the film thickness (c_r is small – thin film approximation);
- vi) The effect of the bearing curvature is neglected ($c_r \ll R_s$);
- vii) No slip occurs between the fluid and the solid interfaces;
- viii) All lubricant properties are independent of temperature (except lubricant viscosity) and pressure;

- ix) The flow regime is considered to be full hydrodynamic, with no contact between surfaces occurring;
- x) The surfaces are considered to be hydrodynamically smooth, that is, roughness effects are considered as negligible;
- xi) The shaft and the bush bodies are considered as non-deformable under the action of hydrodynamic pressure and centrifugal forces. Thermal expansion is considered to be uniform and proportional to the average temperature of each body, affecting only the value of the diameters and not the cylindricity of the surfaces;
- xii) The axial temperature gradients are neglected;
- xiii) The only heat transfer mechanisms occurring within the film are conduction, convection and viscous dissipation (Heat transfer due to radiation, phase change or compression/depression is neglected).

III.3 Lubricant properties

For the pressure and temperature range normally found in journal bearings operating under the full hydrodynamic lubrication regime, the viscosity of typical mineral base oils can be considered to depend mainly on temperature (Motosh, 1963, ESDU84031, 1984, Vijayaraghavan and Brewe, 1998), while properties such as density, specific heat and thermal conductivity may be considered as approximately constant (Cameron, 1986, Richmond et al, 1984).

Mineral base oils usually display a dynamic viscosity, μ , which tends to decrease with increasing temperature with an approximately exponential trend. The Reynolds exponential law of viscosity (Reynolds, 1886) is often used for such lubricants. However practical, the exponential law has been reported to yield poor results when the two reference temperatures upon which the curve is built, are more than 20K apart (Pierre, 2000) and for temperatures outside of the reference temperature interval.

The McCoull and Walther expression is another popular expression for the modeling of lubricant viscosity-temperature law:

$$\log_{10}[\log_{10}(v + 0.6)] = n - m \log_{10}(T) \quad \text{Eq. III-1}$$

n and m are coefficients which can be determined from the viscosity measured at two different reference temperatures [K], while v is the kinematic viscosity [cSt - mm²/s], which is a function of the dynamic viscosity μ [Pa·s] and of the density ρ [kg/m³]:

$$\nu = \frac{\mu}{\rho} \cdot 1 \times 10^{-6} \quad [cSt] \quad \text{Eq. III-2}$$

With the McCoull-Walther expression the viscosity values obtained for temperatures higher than the reference temperatures do not fall as steeply as with the Reynolds curve. This expression was therefore adopted.

III.4 Journal bearing geometry

III.4.1 Basic geometry

Under steady state operation, a lubricated shaft rotating at an angular speed ω and submitted to a load W assumes an eccentric position relative to the bush within the bearing gap, as depicted in Figure III-1.

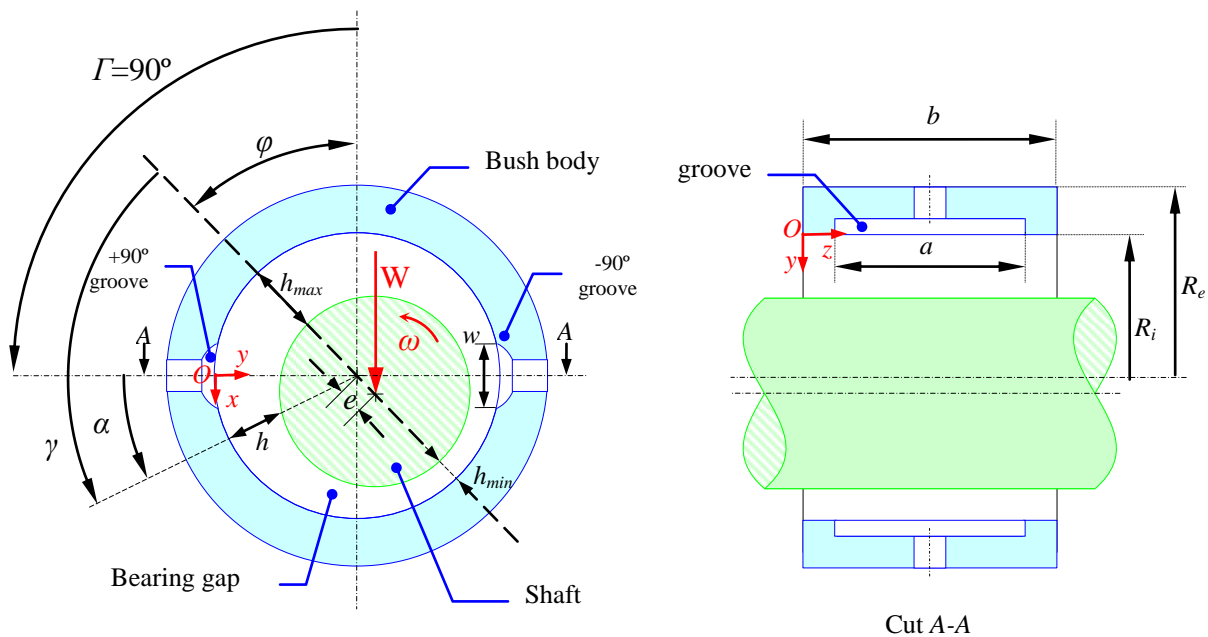


Figure III-1 – Outline of a twin groove journal bearing under steady state regime with its main geometrical features.

The relative position of the shaft and bush centerlines, also called the shaft locus, is defined by the attitude angle ϕ , (the angle between the load line and the line of centers) and the eccentricity e (the distance between the two centerlines). Eccentricity is normally represented in relation to the radial clearance, c_r , as the eccentricity ratio, ε :

$$\varepsilon = \frac{e}{c_r} \quad \text{Eq. III-3}$$

Assuming non-deformable shapes, ε can vary between 0 (concentric shaft) and 1 (shaft in contact with the bush surface). Taking into account that $c_r \ll R_i$, an approximate expression for the film thickness, $h(x)$, excluding the groove regions, can be derived:

$$\begin{aligned} h(x) &= c_r(1 + \varepsilon \cos \gamma) = c_r \left[1 + \varepsilon \cos \left(\frac{x}{R_i} + \Gamma - \varphi \right) \right] \Rightarrow \\ \Rightarrow h(\alpha) &= c_r \left[1 + \varepsilon \cos \underbrace{(\alpha + \Gamma - \varphi)}_{\gamma} \right] \end{aligned} \quad \text{Eq. III-4}$$

With γ being the angular coordinate with origin in the maximum film thickness (h_{max}), α being the angular coordinate used in the present work (with origin in the center of the upstream groove), Γ being the angular location of the groove axis relative to the load line (in the present work this angle was normally 90°) and φ is the attitude angle. These angles are represented in Figure III-1.

The lubricant is supplied to the bearing at a constant feeding pressure P_f and feeding temperature T_f , through two diametrically opposed axial grooves with length a and width w , as shown in Figure III-1.

III.4.2 The unwrapped bearing and the fluid domain

Taking into account the assumptions described before, namely the negligible curvature assumption ($c_r \ll R_i$) and the absence of centrifugal, inertial/gravitational effects, the fluid domain may be represented by the unwrapped bearing geometry displayed in Figure III-2, with the coordinate system $(O, \vec{x}, \vec{y}, \vec{z})$ and defined as:

$$\begin{cases} 0 \leq x \leq 2\pi R_i \\ 0 \leq y \leq h(x) \\ 0 \leq z \leq b/2 \end{cases}$$

The shaft surface is separated from the inner bush surface by the variable thickness $h(x)$ which is obtained from the actual eccentricity ratio and attitude angle through Eq. III-4.

The symmetry of the problem allows the calculations to be performed in one half of the bearing geometry only. No calculations are performed within the groove regions (here seen surrounded by boxes) since the thin film assumption under which the Reynolds equation is based is not

applicable in those regions. Only heat and mass balances are to be performed across the boundaries of the groove regions, as explained later on (section III.11).

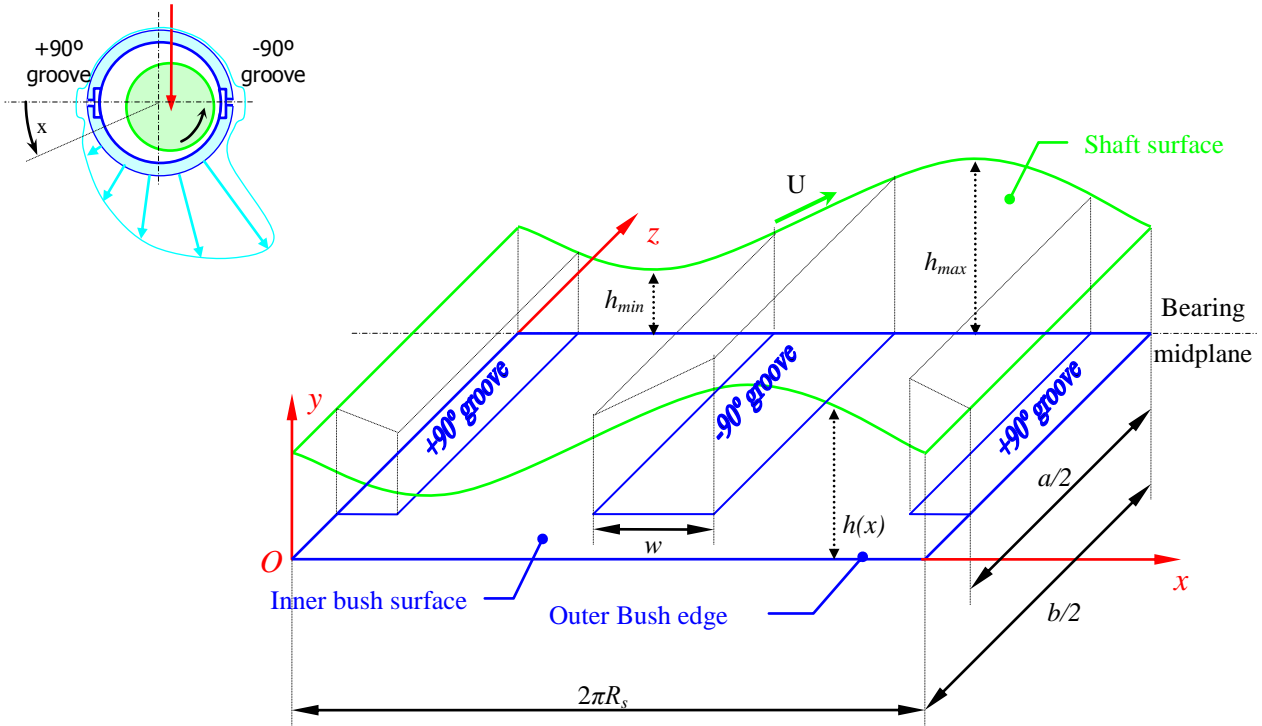


Figure III-2 – Fluid domain (unwrapped bearing geometry) including coordinate system.

III.4.3 Non-dimensional analysis and coordinate transformation

In order to facilitate the analysis, a coordinate transformation based on the normalization of the domain was deployed. The use of non-dimensional analysis in a rectangular, normalized reference domain permits the use of structured orthogonal rectangular meshes. Hence, the dimensional domain represented by the unwrapped bearing geometry in Figure III-2 is transformed into the normalized reference domain represented in Figure III-3.

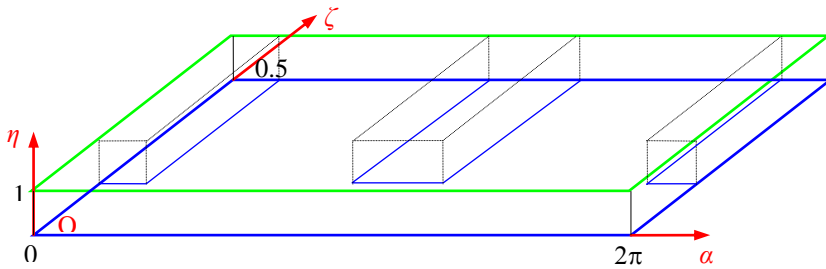


Figure III-3 –Normalized reference domain (non-dimensional coordinates).

The normalized reference domain has the coordinate system $(O, \bar{\alpha}, \bar{\eta}, \bar{\zeta})$ defined as:

$$\begin{cases} 0 \leq \alpha \leq 2\pi \\ 0 \leq \eta \leq 1 \\ 0 \leq \zeta \leq 1/2 \end{cases}$$

The following non-dimensional variables and groups were established:

$$\begin{aligned} h &= c_r \bar{h} \quad ; \quad T = T_f \bar{T} \quad ; \quad \mu = \mu_f \bar{\mu} \\ p &= \frac{\mu_f R_i U}{c_r} \bar{p} \quad ; \quad \beta = \frac{\mu_f R_i U}{c_r} \bar{\beta} \quad ; \quad Q = U c_r b \bar{Q} \end{aligned}$$

The coordinate system of the rectangular reference domain is obtained through a variable transformation:

$$x = R_i \alpha \quad ; \quad y = h \eta = \bar{h}(\alpha) c_r \eta \quad ; \quad z = b \zeta \quad \text{Eq. III-5}$$

It should be noted that the transformation of the y coordinate includes a non-constant term, $\bar{h}(\alpha)$, which displays a non-linear dependence on the α coordinate (recall Eq. III-4):

$$\bar{h}(\alpha) = 1 + \varepsilon \cos(\underbrace{\alpha + \Gamma - \varphi}_{\gamma}) \quad \text{Eq. III-6}$$

The Jacobian matrix, J , of the variable transformation can be built by taking into account the following derivation rule:

$$\frac{\partial}{\partial x_i} [f(\alpha, \eta, \zeta)] = \frac{\partial f}{\partial \alpha} \frac{\partial \alpha}{\partial x_i} + \frac{\partial f}{\partial \eta} \frac{\partial \eta}{\partial x_i} + \frac{\partial f}{\partial \zeta} \frac{\partial \zeta}{\partial x_i} \quad \text{Eq. III-7}$$

Where x_i is an arbitrary coordinate of a Cartesian coordinate system and f is a function of the new coordinates α, η, ζ .

Hence, the Jacobian matrix of the variable transformation defined by Eq. III-5 is easily obtained:

$$J = \begin{bmatrix} \frac{\partial \alpha}{\partial x} & \frac{\partial \alpha}{\partial y} & \frac{\partial \alpha}{\partial z} \\ \frac{\partial \eta}{\partial x} & \frac{\partial \eta}{\partial y} & \frac{\partial \eta}{\partial z} \\ \frac{\partial \zeta}{\partial x} & \frac{\partial \zeta}{\partial y} & \frac{\partial \zeta}{\partial z} \end{bmatrix} = \begin{bmatrix} \frac{1}{R_i} & 0 & 0 \\ -\frac{\eta}{R_i \bar{h}} \frac{\partial \bar{h}}{\partial \alpha} & \frac{1}{c_r \bar{h}} & 0 \\ 0 & 0 & \frac{1}{b} \end{bmatrix} \quad \text{Eq. III-8}$$

The velocity components of the unwrapped bearing geometry are written in a particular non-dimensional form defined as follows:

$$\begin{cases} u_x = U\bar{u}_x \\ u_y = \frac{Uc_r}{R_i}\bar{u}_y \\ u_z = U\bar{u}_z \end{cases} \quad \text{Eq. III-9}$$

These velocity components should not be confused with those of the normalized rectangular reference domain:

$$\begin{cases} \dot{\alpha} = \frac{\partial \alpha}{\partial t} \\ \dot{\eta} = \frac{\partial \eta}{\partial t} \\ \dot{\zeta} = \frac{\partial \zeta}{\partial t} \end{cases} \quad \begin{cases} \bar{\alpha} = \frac{R_i}{U}\dot{\alpha} \\ \bar{\eta} = \frac{R_i}{U}\dot{\eta} \\ \bar{\zeta} = \frac{b}{U}\dot{\zeta} \end{cases} \quad \text{Eq. III-10}$$

The relationship between the non-dimensional velocity components $\bar{u}_x, \bar{u}_y, \bar{u}_z$ and the non-dimensional velocity components of the reference domain $\bar{\alpha}, \bar{\eta}, \bar{\zeta}$ can be inferred after some mathematical manipulation:

$$\begin{cases} \bar{u}_x = \bar{\alpha} \\ \bar{u}_y = \eta \frac{\partial \bar{h}}{\partial \alpha} \bar{\alpha} + \bar{\eta} \bar{h} \\ \bar{u}_z = \bar{\zeta} \end{cases} \quad \text{Eq. III-11}$$

The non-trivial relationship between \bar{u}_y and $\bar{\eta}$ is a natural consequence of the deformation of the domain from its original form (the unwrapped bearing) to its rectangular form (the reference domain).

A full list of the non-dimensional variables and groups is shown in page xxi.

III.5 Pressure and velocity field

III.5.1 Hydrodynamic lift

Hydrodynamic lubrication is based on the ability of a fluid to be dragged between two surfaces in relative motion and to keep them separated even in the presence of a load which tends to draw them together. This is possible only due to lubricant viscosity, which is a property of the fluid which allows the transmission of moment between adjacent layers of fluid molecules,

through shear stress. This means that shaft motion might actually drag a continuous flux of lubricant capable of remaining placed between the two surfaces, keeping them out of contact.

The hydrodynamic lift phenomenon is physically translated in the appearance of a pressure field within the fluid at the convergent portion of the bearing gap, which equilibrates the applied load. This, along with the subsequent film rupture at the divergent portion of the film is depicted in Figure III-4.

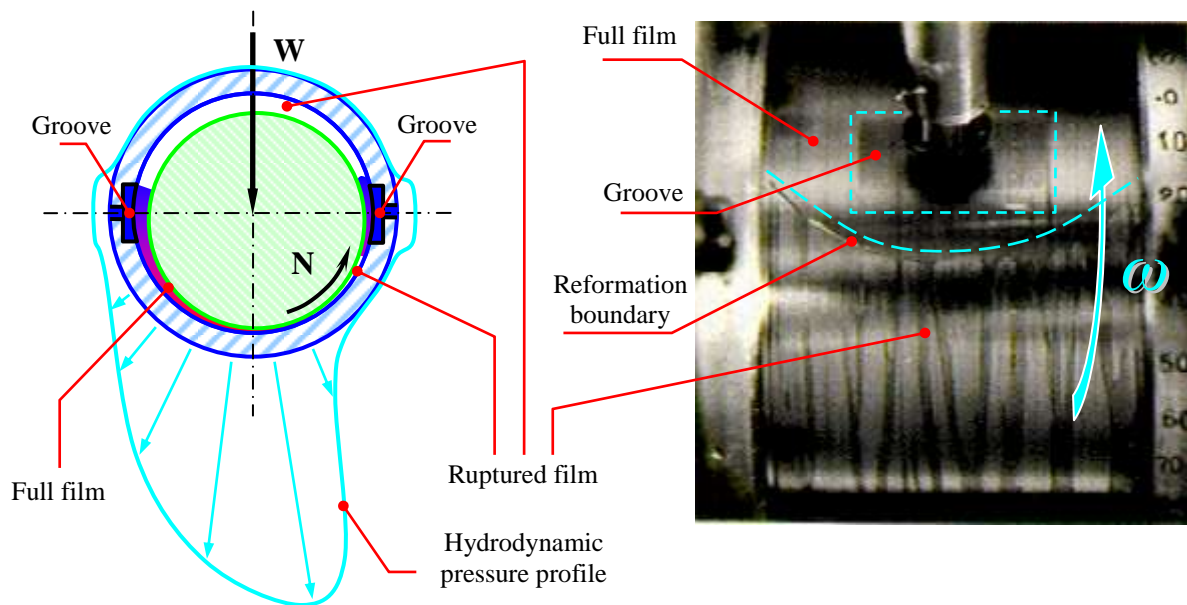


Figure III-4 – Outline of the hydrodynamic pressure generation occurring at the convergent region of the gap (full film region) and film rupture at the divergent region of the gap (Picture of a glass bush in the right hand side taken from Miranda, 1983).

III.5.2 Film rupture and reformation

At the divergent portion of the gap the pressure falls nearly to zero (atmospheric pressure) and the lubricant film breaks into a series of streamers separated by gaseous cavities, as photographed in Figure III-4 and sketched in Figure III-5. Within this region the pressure remains approximately equal to the ambient pressure, with lubricant flowing only due to drag.

It is convenient to consider, like in the case of the JFO theory (see section II.2.5), that the lubricant flows along an infinite number of streamers which are attached both to the shaft and the bush surfaces and possess a Couette flow pattern. These streamers of infinitesimal thickness are separated by gaseous ones without mixing with each other. This means that at any given location the gap is filled with a fraction of liquid, θ .

In reality, some authors have observed (Etsion and Ludwig, 1982, Heshmat, 1991) that not all the oil is present in such streamers but there is also a portion of it forming a thin layer of

lubricant which adheres to the shaft surface but is detached from the bush surface. This layer is dragged by the shaft and can be considered to share its surface velocity, U . Within the scope of the pressure field computations of the present work, the effect of this thin layer adhered to the shaft has been neglected, although it has received some attention within the scope of the thermal model.

The film rupture phenomenon is often called by several authors as gaseous cavitation or simply cavitation. However, the name cavitation does not seem convenient in this case because it is normally associated with phenomena involving transient vaporization of a liquid due to a sudden depressurization, or involving the sudden release of air or gas dissolved in a liquid. This is not normally the case in oil lubricated journal bearings operating under steady state. In this work this region has been called simply the ruptured film region.

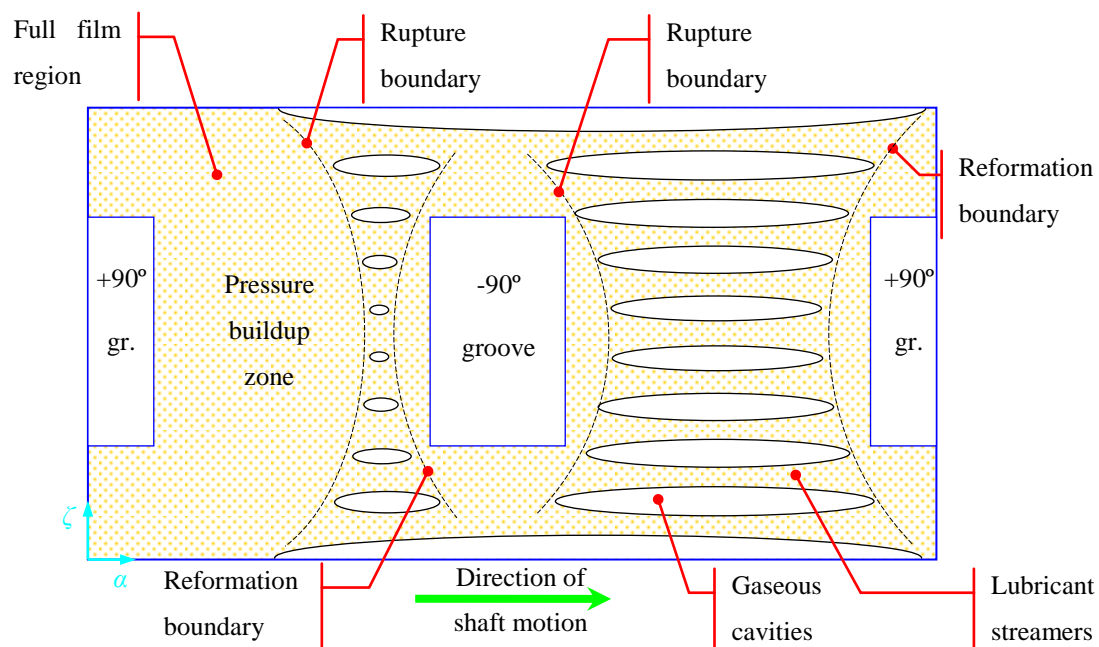


Figure III-5 – film rupture and reformation.

Film reformation occurs mainly in the vicinity of oil grooves or in the convergent portion of the film. The gap becomes flooded by lubricant either due to the lubricant supplied through the grooves or simply due to the reduction of the thickness of the gap at the convergent part of the film which eventually causes the flooding of the gap. The exact location of the reformation border depends not only on the operating conditions but also on factors such as the groove dimensions and the lubricant feeding pressure. The film reformation boundary is faintly observed in the photograph displayed in Figure III-4, located upstream of the groove.

The phenomenon of film rupture is complex and has been studied and modeled by several authors. Their main contributions have been described in CHAPTER II.

III.5.3 The Generalized Reynolds Equation

The hydrodynamic pressure and the velocity field within an arbitrary fluid flow are accurately described through the solution of the complete Navier-Stokes equations (NSE). However, the assumptions mentioned earlier, such as the pressure uniformity across the film thickness (thin film assumption) and the negligible contribution of inertia effects when compared with viscous effects (low Reynolds number), allow the use of the Generalized Reynolds Equation (GRE) for laminar regime derived by Dowson (1962 – recall section II.3.3). This equation, which is now used as the basis of most THD lubrication analyses, is an updated version of the classical Reynolds equation (RE) (Reynolds, 1886), but now incorporating thermal effects, such as the variation of temperature and viscosity across the thickness of the film:

$$\frac{\partial}{\partial x} \left[\rho_l F_2 \frac{\partial P}{\partial x} \right] + \frac{\partial}{\partial z} \left[\rho_l F_2 \frac{\partial P}{\partial z} \right] = U \frac{\partial}{\partial x} [\rho_l h F_3] \quad \text{Eq. III-12}$$

The GRE expresses the mass balance of liquid lubricant across the boundaries of an infinitesimal control volume.

The left hand terms account for the pressure-driven (Poiseuille) component of the flow in the circumferential (x) and axial (z) directions, while the right hand term accounts for the drag-driven (Couette) component of the flow, which in the present case develops along the circumferential (x) direction only.

The viscosity integrals F_i account for the effect of lubricant viscosity variation across the film thickness (y direction):

$$F_0 = \int_0^h \frac{1}{\mu_l} dy \quad ; \quad F_1 = \int_0^h \frac{y}{\mu_l} dy \quad ; \quad F_2 = \int_0^h \frac{y}{\mu_l} \left(y - \frac{F_1}{F_0} \right) dy \quad ; \quad F_3 = 1 - \frac{F_1}{h F_0} \quad \text{Eq. III-13}$$

Where μ_l is the viscosity of the liquid lubricant.

The boundary conditions are the following:

$$\begin{cases} p = p_f & \text{at the groove regions} \\ p = 0 & \text{at the bush edges} \end{cases} \quad \text{Eq. III-14}$$

With p_f being the lubricant feeding pressure.

Transposing Eq. III-12 into the normalized reference domain the following non-dimensional form of the GRE is obtained:

$$\frac{\partial}{\partial \alpha} \left[\rho_l \bar{h}^3 \bar{F}_2 \frac{\partial \bar{P}}{\partial \alpha} \right] + \left(\frac{R_s}{b} \right)^2 \frac{\partial}{\partial \zeta} \left[\rho_l \bar{h}^3 \bar{F}_2 \frac{\partial \bar{P}}{\partial \zeta} \right] = \frac{\partial}{\partial \alpha} [\rho_l \bar{h} \bar{F}_3] \quad \text{Eq. III-15}$$

With the non-dimensional viscosity integrals being defined as follows:

$$\overline{F}_0 = \int_0^1 \frac{1}{\overline{\mu}_l} d\eta \quad ; \quad \overline{F}_1 = \int_0^1 \frac{\eta}{\overline{\mu}_l} d\eta \quad ; \quad \overline{F}_2 = \int_0^1 \frac{\eta}{\overline{\mu}_l} \left(\eta - \frac{\overline{F}_1}{\overline{F}_0} \right) d\eta \quad ; \quad \overline{F}_3 = 1 - \frac{\overline{F}_1}{\overline{F}_0} \quad \text{Eq. III-16}$$

With

$$F_0 = \frac{\overline{h}c_r}{\mu_f} \overline{F}_0 \quad ; \quad F_1 = \frac{\overline{h}^2 c_r^2}{\mu_f} \overline{F}_1 \quad ; \quad F_2 = \frac{\overline{h}^3 c_r^3}{\mu_f} \overline{F}_2 \quad ; \quad F_3 = \overline{F}_3 \quad \text{Eq. III-17}$$

Although simpler than the full Navier-Stokes approach, the solution of the GRE still poses a good deal of complexity since it is coupled with the solution of the energy equation via the dynamic viscosity, μ . Furthermore, the GRE is not applicable, by itself, within the ruptured film region. In CHAPTER II the solutions proposed by many authors in order to overcome this limitation, along with their strengths and weaknesses, have been briefly described. For instance, it is worth recalling the so-called *Reynolds model* (section II.2.4) which allows the solution of the GRE by the application of the Swift-Stieber conditions while setting to zero all negative pressure nodes obtained in each iteration. Although practical, the *Reynolds model* does not ensure mass conservation across the whole domain and does not locate the film reformation boundary accurately. Therefore, this model did not seem suitable for the task of incorporating realistic supply conditions in the bearing analysis, which was one of the scopes of the present work.

The algorithms which do ensure mass conservation across the whole domain, such as those proposed by Elrod and Adams (1975) and Elrod (1981), seemed clearly the ones best suited for the present work, as already justified in CHAPTER II.0. Although the latter approach was chosen, it seemed important also to describe the former for the sake of clarity. In fact, too often these two approaches were confused between each other and their fundamental differences have seldom been completely apprehended.

III.5.4 The Elrod-Adams algorithm

Often, the cause for the non conservative character of some models is that their analysis is limited to the evaluation of the pressure field. Since the GRE is not valid within the ruptured film region, the information concerning flow rates within this region must be monitored somehow. Some authors proposed algorithms which did ensure flow continuity within this region, like the

JFO theory (recall section II.2.5). At the rupture boundary the principle of mass conservation is expressed as follows:

$$\frac{\partial p}{\partial n} = 0 \quad ; \quad p = p_{rupt} \quad \text{Eq. III-18}$$

With n being the direction normal to the rupture boundary. These are the Swift-Stieber conditions, also adopted by the JFO theory and many other approaches.

The Swift-Stieber conditions at the rupture are necessary but not sufficient to ensure mass conservation. At the locus of film reformation Jacobsson inferred that, according to the JFO assumptions, mass conservation would require the following to be true (for an isoviscous analysis):

$$\frac{h^2}{12\mu} \frac{\partial p}{\partial n} = \frac{V_n}{2} (1 - \theta^-) \quad \text{Eq. III-19}$$

Where V_n is the surface velocity along direction n and θ^- is the liquid fraction upstream of the boundary, that is, the fraction of the gap filled with lubricant. The computational implementation of this condition is not straightforward, namely when tracing the locus of the reformation interface between grid points and when evaluating the pressure derivative contained in the expression (Elrod, 1981). This is why the reformation condition defined by *Eq. III-19* has been seldom used in theoretical analyses.

The work of Elrod and Adams (1975) allowed the implicit use of the JFO conditions in a much more practical and implicit way. They sought after an algorithm which would allow the automatic handling of the ruptured film region. They devised a single universal equation which would handle simultaneously and automatically:

- the pressure generation within the full film region
- the lubricant mass flow conservation within the ruptured film region

This has been achieved by proposing a modified Reynolds equation which would change its character within the ruptured film region, becoming a simple mass balance equation adapted to the streamlet-like isobaric Couette flow occurring at this region.

They made use of the slight compressibility found in liquid lubricants and deployed a substitution variable, θ , which stands as the relative density of the lubricant:

$$\theta = \frac{\rho}{\rho_{rupt}} \quad \text{Eq. III-20}$$

With ρ being the density at the local pressure p and ρ_{rupt} being the density of the liquid at the pressure at which film rupture takes place. This pressure is known to be close to ambient pressure and was set to zero (ambient).

While θ is defined throughout the whole domain, it is calculated in different ways whether within the full film or the ruptured film region:

- Within the full film region the density of the fluid is related to the local pressure through the Bulk Modulus of the lubricant, β , which represents an inverse measure of the compressibility of a liquid. Therefore, θ will be equal or slightly higher than unity in the full film region, obeying to the following law:

$$\beta = \rho \frac{\partial p}{\partial \rho} \Leftrightarrow \beta = \theta \frac{\partial p}{\partial \theta} \quad \text{Eq. III-21}$$

- At the ruptured film region the pressure (P_{rupt}) is constant and therefore the density of the liquid phase (ρ_{rupt}) is also constant. Nevertheless, the film is ruptured into a series of streamers separated by gaseous cavities. Therefore, the relative density of the mixture, θ , is approximately equal to the local fraction of liquid. Within the ruptured film region θ can vary between two limits: 0, which would correspond to the limit case of no lubricant present within the gap (only the gaseous phase present), and 1, which would correspond to a full film with no gaseous phase present within the gap, at a pressure equal to P_{rupt} .

Based on Eq. III-21, the following relation applies, for an arbitrary coordinate x_i :

$$\frac{\partial p}{\partial x_i} = \frac{\beta}{\theta} \frac{\partial \theta}{\partial x_i} \quad \text{Eq. III-22}$$

Substituting Eq. III-20 and Eq. III-22 into Eq. III-15, the following equation (in non-dimensional form) is easily obtained:

$$\frac{\partial}{\partial \alpha} \left[g \bar{\beta} \bar{h}^3 \bar{F}_2 \frac{\partial \theta}{\partial \alpha} \right] + \left(\frac{R_i}{b} \right)^2 \frac{\partial}{\partial \zeta} \left[g \bar{\beta} \bar{h}^3 \bar{F}_2 \frac{\partial \theta}{\partial \zeta} \right] = \frac{\partial}{\partial \alpha} \left[\theta \bar{h} \bar{F}_3 \right] \quad \text{Eq. III-23}$$

This is the compressible flow generalized Reynolds equation adapted to the Elrod-Adams algorithm. It can be seen that a switch function, g , whose value is either 1 or 0 has been added:

$$\begin{cases} g = 0 & \text{for } \theta < 1 \quad (\text{ruptured film region}) \\ g = 1 & \text{for } \theta \geq 1 \quad (\text{full film region}) \end{cases} \quad \text{Eq. III-24}$$

This function activates or nullifies the Poiseuille (pressure) terms of the modified Reynolds equation, whether within the full film region (where $\theta \geq 1$) or within the ruptured film region (where $0 < \theta < 1$) respectively.

With this approach, a single equation is used across the whole domain, with the rupture zone being obtained automatically (nodes where $\theta < 1$). During the iterative solution process (Successive Over-Relaxation Gauss-Seidel applied to a finite difference discretization), the only care needed is to update the switch function at all the nodes after each iteration, according to the new values of θ .

Once convergence has been achieved, the pressure field is directly obtained from θ through an expression which results from the integration of *Eq. III-21* and the addition of the switch function in order to generalize its application to the whole domain:

$$P = P_{Rupt} + g\beta \ln \theta \quad \text{Eq. III-25}$$

The Elrod-Adams algorithm successfully determines the pressure field with an automatic handling of the ruptured film region, while still ensuring the mass-conservation of the liquid phase. However, the use of realistic values of β (of the order of 10^9 N/m²) can sometimes make the convergence of the iterative process difficult, especially when recesses and grooves are included in the geometry.

While it is true that the use of smaller values of β tends to facilitate convergence, this may constitute a problem, since the Elrod-Adams algorithm uses, in fact, the compressible flow version of the Reynolds equation and, therefore, the value of β used could actually influence the final result if the lubricant is allowed to be excessively compressible (β too low). Pierre (2000), which has used the THD version of the Elrod-Adams algorithm, reported that the use of values between 10^8 and 10^{10} N/m² did not change significantly the final results.

III.5.5 The Elrod algorithm

In order to improve the numerical performance of the Elrod and Adams (1975) model, Elrod (1981) proposed an approach apparently very similar to that used in his previous work with Adams, but which is actually quite different in nature.

While the former model relied on the compressible flow version of the Reynolds equation (*Eq. III-15*), in the latter model, however, the flow is treated, in practical terms, as incompressible.

Often, the incompressible character of this algorithm has not been fully understood because there are several apparent similarities between the two models which can be deceiving. For instance, Elrod used again the variables θ and β . However, in the new algorithm these variables are no longer linked with density, that is, *Eq. III-21* and *Eq. III-22* are no longer used.

Concerning the variable β , it no longer needs to be identified necessarily with the physical property called the bulk modulus of the lubricant as in the former model. In this latter model it may be regarded merely as a constant of proportionality between \bar{p} and θ in the full film region;

Regarding the variable θ :

- Within the ruptured film region θ still represents the liquid fraction;
- Within the full film region θ turns out to be, in essence, a mere substitution variable which is proportional to the local pressure, with β being the constant of proportionality, defined as follows:

$$p = p_{rupt} + g\beta(\theta - 1) \quad \text{Eq. III-26}$$

Which in non-dimensional form (and considering P_{rupt} as ambient) yields:

$$\bar{p} = g\bar{\beta}(\theta - 1) \quad \text{Eq. III-27}$$

This expression has been chosen so that continuity is maintained around $\theta=1$, where θ changes its character and the *Heaviside* switch function g shoots abruptly from 0 to 1.

It can be seen that *Eq. III-26* displays some similitude with the one used in the Elrod-Adams model (*Eq. III-25*). In fact, this new expression turns out to be a linearization of *Eq. III-25* for $\theta \approx 1$.

In this new algorithm the value of β used does not actually affect the final pressure result but only the proportionality between \bar{p} and θ . This can be graphically observed in a parametric study presented at the end of this chapter (section III.14.4). When using isoviscous models incorporating Elrod's algorithm, Miranda (1983) and Claro (1994) had already reported no significant differences between results obtained with very dissimilar values of β .

The ability to choose an arbitrary value for β is a clear advantage over the Elrod-Adams algorithm. A judicious choice of β can indeed improve the convergence process as it will be discussed below. This reason ultimately led to the choice of this approach in detriment of the one proposed by Elrod and Adams.

a) Control volume method

The generalized Reynolds equation results from a balance of Couette and Poiseuille mass fluxes of liquid lubricant applied to an arbitrary infinitesimal control volume:

$$\underbrace{\frac{\partial}{\partial \alpha} \left[\overline{h^3 F_2} \frac{\partial \overline{p}}{\partial \alpha} \right]}_{\text{Due to circumferential Poiseuille flow}} + \underbrace{\left(\frac{R_i}{b} \right)^2 \frac{\partial}{\partial \zeta} \left[\overline{h^3 F_2} \frac{\partial \overline{p}}{\partial \zeta} \right]}_{\text{Due to axial Poiseuille flow}} = \underbrace{\frac{\partial}{\partial \alpha} \left[\overline{h F_3} \right]}_{\text{Due to circumferential Couette flow}} \quad \text{Eq. III-28}$$

Elrod did not use directly this equation. Instead, he went a step back in the process and after defining control volumes around each computational node (see Figure III-6) and deriving specially tailored finite difference expressions for the calculation of Poiseuille and Couette flows, carried out a mass balance across the borders of each control volume. In this way, Elrod obtained a Reynolds-type finite difference equation which is mass-conservative and valid throughout the whole domain.

This cell method is quite similar to the Finite Volume Method (FVM) approach and shares its intrinsic conservativeness as well as its ability to deal with field discontinuities (Versteeg and Malalasekera, 1995, Cosmi, 2003) as in the case of film reformation. Similarly to Costa et al (2003), a THD version of Elrod’s approach has been proposed for the present work.

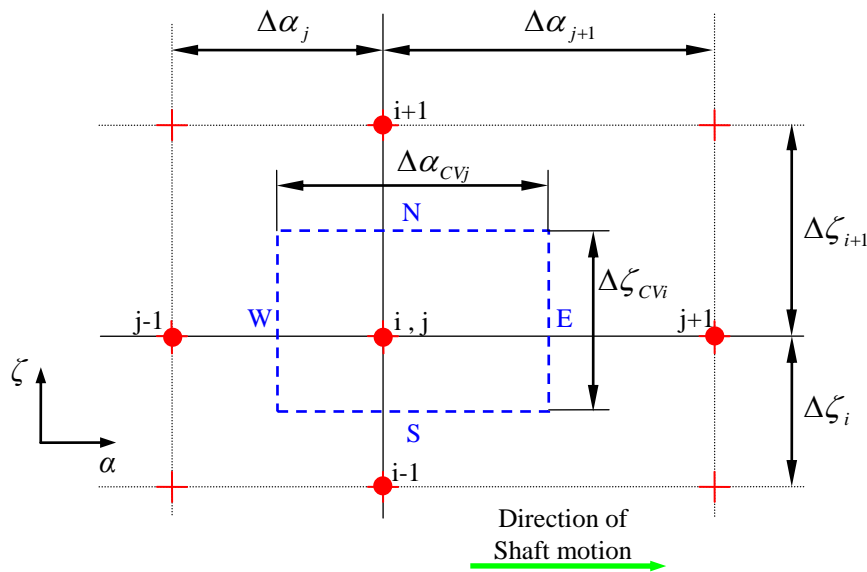


Figure III-6 – Elementary cell for an arbitrary node of an arbitrary rectangular mesh.

The dimensions of the faces of the control volume are the following:

$$\begin{cases} \Delta \alpha_{cvj} = \frac{\Delta \alpha_j + \Delta \alpha_{j+1}}{2} \\ \Delta \zeta_{cvi} = \frac{\Delta \zeta_i + \Delta \zeta_{i+1}}{2} \end{cases} \quad \text{with} \quad \begin{cases} \Delta \alpha_j = \alpha_j - \alpha_{j-1} \\ \Delta \zeta_i = \zeta_i - \zeta_{i-1} \end{cases} \quad \text{Eq. III-29}$$

In order to carry out the mass balance on the cell surrounding the central point, the Couette and Poiseuille components of the liquid flow crossing the four faces of the cell (N, S, E, W) should be accounted for.

The finite difference expressions chosen should be suited for application at the whole domain, that is, for control volumes located either at the full film region, at the ruptured film region or at the boundary between the two.

Adapting Elrod's approach to the THD case, the following expressions are proposed:

b) Couette flow across the West (W) face:

The drag-driven (Couette) non-dimensional mass flux of lubricant appears at the right side of the Reynolds equation (Eq. III-28) and is represented by the term $\bar{h}\bar{F}_3$, which is valid within the full film region only. Within the ruptured film region, only a fraction θ of the gap is effectively filled with liquid lubricant. Therefore, in this region the Couette mass flux per unit area is represented by $\theta\bar{h}\bar{F}_3$.

Through a judicious use of the switch function g (defined earlier in Eq. III-24) it is possible to derive a single finite difference expression which is valid throughout the whole reference domain and which yields the non-dimensional flow rate of the liquid portion of the Couette flow crossing the west face of a cell:

$$\bar{Q}_\alpha|_{Cou}^W = \left[\theta_{j-1}\bar{h}_{j-1}(1-g_{j-1})\bar{F}_{3j-1} + g_{j-1}\bar{h}_{j-1}\bar{F}_{3j-1} + \frac{g_j g_{j-1}}{2}(\bar{h}_j\bar{F}_{3j} - \bar{h}_{j-1}\bar{F}_{3j-1}) \right] \cdot \Delta\zeta_{CVi} \quad \text{Eq. III-30}$$

Note that the notation has been abbreviated (since the index i is unchanged in this expression, variables such as $\theta_{i,j-1}$, $\theta_{i,j}$, $\theta_{i,j+1}$ are written simply as θ_{j-1} , θ_j , θ_{j+1}).

By analyzing this expression it can be seen that it accommodates the following particular cases:

- The upstream node, $j-1$, is located within the ruptured film region ($g_{j-1}=0$):

$$\bar{Q}_\alpha|_{Cou}^W = (\theta_{j-1}\bar{h}_{j-1}\bar{F}_{3j-1}) \cdot \Delta\zeta_{CVi} \quad \text{Eq. III-31}$$

- The upstream node, $j-1$, is located within the full film region ($g_{j-1}=1$) but not the downstream node, j ($g_j=0$):

$$\bar{Q}_\alpha|_{Cou}^W = (\bar{h}_{j-1}\bar{F}_{3j-1}) \cdot \Delta\zeta_{CVi} \quad \text{Eq. III-32}$$

- Both nodes are located within the full film region ($g_{j-1}=g_j=1$):

$$\bar{Q}_\alpha \Big|_{Cou}^W = \frac{\bar{h}_j \bar{F}_{3j} + \bar{h}_{j-1} \bar{F}_{3j-1}}{2} \cdot \Delta \zeta_{Cvi} \quad Eq. III-33$$

c) Couette flow across the East (E) face:

Similarly, the Couette portion of the flow across the east face is given by:

$$\bar{Q}_\alpha \Big|_{Cou}^E = \left[\theta_j \bar{h}_j (1 - g_j) \bar{F}_{3j} + g_j \bar{h}_j \bar{F}_{3j} + \frac{g_j g_{j+1}}{2} (\bar{h}_{j+1} \bar{F}_{3j+1} - \bar{h}_j \bar{F}_{3j}) \right] \cdot \Delta \zeta_{Cvi} \quad Eq. III-34$$

d) Couette flow across the North (N) and South (S) faces:

The Couette flow is purely circumferential, therefore,

$$\bar{Q}_\alpha \Big|_{Cou}^N = \bar{Q}_\alpha \Big|_{Cou}^S = 0 \quad Eq. III-35$$

e) Poiseuille flow across the West (W) face:

The pressure-driven (Poiseuille) mass flux is accounted at the left side of the Reynolds equation (Eq. III-28). Performing the $\bar{p} - \theta$ variable substitution defined by Eq. III-27 and taking into account that only the circumferential gradient of the pressure contributes to the mass flux across the west (W) face of the cell, the following finite difference expression has been derived for the whole domain:

$$\bar{Q}_\alpha \Big|_{Poi}^W = \bar{\beta} \left(\frac{\bar{h}_{j-1} + \bar{h}_j}{2} \right)^3 \bar{F}_{2W} \left[\frac{g_{j-1} (\theta_{j-1} - 1) - g_j (\theta_j - 1)}{\Delta \alpha_j} \right] \cdot \Delta \zeta_{Cvi} \quad Eq. III-36$$

with \bar{F}_{2W} being the value of the viscosity integral \bar{F}_2 at the west face, estimated by a third order interpolation. This expression accommodates the following particular cases:

- Both nodes are located within the ruptured film region ($g_{j-1}=g_j=0$):

$$\bar{Q}_\alpha \Big|_{Poi}^W = 0 \quad Eq. III-37$$

- Both nodes are located within the full film region ($g_{j-1}=g_j=1$):

$$\bar{Q}_\alpha|_{Poi}^W = \bar{\beta} \left(\frac{\bar{h}_{j-1} + \bar{h}_j}{2} \right)^3 \bar{F}_{2W} \left[\frac{\theta_{j-1} - \theta_j}{\Delta\alpha_j} \right] \cdot \Delta\zeta_{CVi} \quad \text{Eq. III-38}$$

- Only one of the nodes is within the full film region (either g_j or $g_{j-1}=1$):

$$\bar{Q}_\alpha|_{Poi}^W = \bar{\beta} \left(\frac{\bar{h}_{j-1} + \bar{h}_j}{2} \right)^3 \bar{F}_{2W} \left[\frac{(\theta_{j/j-1} - 1)}{\Delta\alpha_j} \right] \cdot \Delta\zeta_{CVi} \quad \text{Eq. III-39}$$

f) Poiseuille flow across the East (E) face:

Similarly, the pressure-driven flow rate across the east face of the control volume is given by:

$$\bar{Q}_\alpha|_{Poi}^E = \bar{\beta} \left(\frac{\bar{h}_{j+1} + \bar{h}_j}{2} \right)^3 \bar{F}_{2E} \left[\frac{g_j(\theta_j - 1) - g_{j+1}(\theta_{j+1} - 1)}{\Delta\alpha_{j+1}} \right] \cdot \Delta\zeta_{CVi} \quad \text{Eq. III-40}$$

where \bar{F}_{2E} is the value of the viscosity integral \bar{F}_2 at the east face of the control volume, again obtained through a third order interpolation.

g) Poiseuille flow across the North (N) face:

The contribution of the Poiseuille component to the flow across the north face is given by:

$$\bar{Q}_\zeta|_{Poi}^N = \left(\frac{R_i}{b} \right)^2 \cdot \bar{\beta} \cdot \bar{h}_j^3 \cdot \bar{F}_{2j} \left[\frac{g_i(\theta_i - 1) - g_{i+1}(\theta_{i+1} - 1)}{\Delta\zeta_{i+1}} \right] \cdot \Delta\alpha_{CVj} \quad \text{Eq. III-41}$$

Note that, again, the notation has been abbreviated (since the index j is unchanged in this expression, variables such as $\theta_{i-1,j}$, $\theta_{i,j}$, $\theta_{i+1,j}$ are written simply as θ_{i-1} , θ_i , θ_{i+1}).

h) Poiseuille flow across the South (S) face:

Similarly, the following expression applies to the pressure-driven flow across the south face of the control volume:

$$\bar{Q}_\zeta|_{Poi}^S = \left(\frac{R_i}{b} \right)^2 \cdot \bar{\beta} \cdot \bar{h}_j^3 \cdot \bar{F}_{2j} \left[\frac{g_{i-1}(\theta_{i-1} - 1) - g_i(\theta_i - 1)}{\Delta\zeta_i} \right] \cdot \Delta\alpha_{CVj} \quad \text{Eq. III-42}$$

i) Mass balance

Finally, a mass balance across the control volume faces must be performed:

$$\bar{Q}_\alpha \Big|_{Cou+Poi}^E - \bar{Q}_\alpha \Big|_{Cou+Poi}^W + \bar{Q}_\zeta \Big|_{Cou+Poi}^N - \bar{Q}_\zeta \Big|_{Cou+Poi}^S = 0 \quad Eq. III-43$$

The result is a finite difference equation similar in essence to the generalized Reynolds equation, valid throughout the whole domain, which becomes:

- a central differenced elliptic equation virtually identical to the generalized Reynolds equation within the full film region;
- a backward differenced parabolic equation which governs a striated lubricant Couette flow and ensures mass conservation of the liquid portion of the flow within the ruptured film region.

A successive over-relaxation scheme can be used to solve the resulting system of equations (by putting $\theta_{i,j}$ into evidence), and obtain the θ field. During the iterative process the switch function g simply needs to be updated in every node after each iteration. Once convergence has been achieved, the pressure field is obtained directly from the θ field through *Eq. III-27*.

III.5.6 Velocity field

The velocity field must be computed as it affects the convective and the dissipative terms of the energy equation (presented ahead, in section III.7). There are models which consider the existence of a single homogeneous mixture of lubricant and gas with averaged properties (Knight and Niewiarowski, 1990, Costa et al, 2003a). However, in the present work there is not a homogeneous mixture flow but rather a flow of a virtually infinite number of liquid and gaseous streamers occurring in parallel. Although the fraction of each phase can actually vary locally, each one of them is considered not to mix with the other and to retain its own properties (density, viscosity, etc).

The Elrod algorithm is based on the continuity computations for the liquid portion of the flow only. Actually, the gaseous phase flow is altogether irrelevant for the determination of the velocity profiles and the various lubricant flow rates that need to be determined. It is therefore important to note that the pressure and flow calculations must be performed on the basis of the liquid portion of the flow only. Given the model adopted, the use of averaged fluid properties in flow calculations would be erroneous. Nevertheless, this does not mean that the gaseous phase might not actually influence the global thermal behavior of the bearing and that averaged properties should not be used in the calculation of the equivalent thermal problem. This influence is actually included exclusively in the thermal model and described in section III.10.

The velocity field governs both the convective and the dissipative term of the Energy equation. When integrated along a given section the velocity profile normal to that section also provides the flow rate across that section.

The calculation of the velocity profiles when considering variable transverse viscosity (the case of the THD analysis) includes the calculation of two viscosity integrals in addition to the ones presented earlier in Eq. III-13:

$$\left\{ \begin{array}{l} F_4 = \int_0^y \frac{\lambda}{\mu_l} d\lambda \\ F_5 = \int_0^y \frac{1}{\mu_l} d\lambda \end{array} \right. \quad \left\{ \begin{array}{l} \overline{F}_4 = \int_0^\eta \frac{\lambda}{\overline{\mu}_l} d\lambda \\ \overline{F}_5 = \int_0^\eta \frac{1}{\overline{\mu}_l} d\lambda \end{array} \right. \quad \text{with} \quad \left\{ \begin{array}{l} F_4 = \frac{\overline{h}^2 c_r^2}{\mu_f} \overline{F}_4 \\ F_5 = \frac{\overline{h} c_r}{\mu_f} \overline{F}_5 \end{array} \right. \quad \text{Eq. III-44}$$

with λ being a dummy variable of y or η , whether within the real or the reference domain, respectively.

The circumferential and axial components of the velocity field, which are derived from the GRE, are as follows:

$$\left\{ \begin{array}{l} u_x = \frac{\partial p}{\partial x} \left(F_4 - \frac{F_1 F_5}{F_0} \right) + U \frac{F_5}{F_0} \\ u_z = \frac{\partial p}{\partial z} \left(F_4 - \frac{F_1 F_5}{F_0} \right) \end{array} \right. \quad \text{or} \quad \left\{ \begin{array}{l} \overline{u}_x = \overline{h}^2 \frac{\partial \overline{p}}{\partial \alpha} \left(\overline{F}_4 - \frac{\overline{F}_1 \overline{F}_5}{\overline{F}_0} \right) + \frac{\overline{F}_5}{\overline{F}_0} \\ \overline{u}_z = \frac{R_i}{b} \overline{h}^2 \frac{\partial \overline{p}}{\partial \zeta} \left(\overline{F}_4 - \frac{\overline{F}_1 \overline{F}_5}{\overline{F}_0} \right) \end{array} \right. \quad \text{Eq. III-45}$$

The radial component of the lubricant velocity field, u_v , although usually small when compared with the other two components, can influence substantially the heat transfer across the film given the thin gap existing between the bush and the shaft surface.

Bearing in mind that no pressure gradient is considered to exist across the film thickness, the radial displacement of the fluid is obtained simply by applying the continuity equation to the liquid portion of the film:

$$\left\{ \begin{array}{l} \frac{\partial u_x}{\partial x} + \frac{\partial u_y}{\partial y} + \frac{\partial u_z}{\partial z} = 0 \quad \Leftarrow \quad \theta \geq 1 \text{ (full film)} \\ \frac{\partial(\theta u_x)}{\partial x} + \frac{\partial(\theta u_y)}{\partial y} + \frac{\partial(\theta u_z)}{\partial z} = 0 \quad \Leftarrow \quad \theta < 1 \text{ (ruptured film)} \end{array} \right. \quad \text{Eq. III-46}$$

It can be seen that within the ruptured film region only a fraction, θ , of the film is effectively filled with lubricant and contributes for the continuity computations. Within the normalized reference domain the equations can be rewritten, after some manipulation, as:

$$\left\{ \begin{array}{l} \frac{\partial \bar{u}_x}{\partial \alpha} - \frac{\eta}{\bar{h}} \frac{\partial \bar{h}}{\partial \alpha} \frac{\partial \bar{u}_x}{\partial \eta} + \frac{1}{\bar{h}} \frac{\partial \bar{u}_v}{\partial \eta} + \frac{R_i}{b} \frac{\partial \bar{u}_z}{\partial \zeta} = 0 \quad \Leftarrow \quad \theta \geq 1 (\text{full film}) \\ \frac{\partial(\theta \bar{u}_x)}{\partial \alpha} - \frac{\eta}{\bar{h}} \frac{\partial \bar{h}}{\partial \alpha} \frac{\partial(\theta \bar{u}_x)}{\partial \eta} + \frac{1}{\bar{h}} \frac{\partial(\theta \bar{u}_v)}{\partial \eta} + \frac{R_i}{b} \frac{\partial(\theta \bar{u}_z)}{\partial \zeta} = 0 \quad \Leftarrow \quad \theta < 1 (\text{ruptured film}) \end{array} \right. \quad \begin{array}{l} \text{Eq. III-47} \\ \text{Eq. III-48} \end{array}$$

The former equations may be easily converted into a single one, valid throughout the bearing domain, by introducing a new variable, θ' , based on the function *minimum*, which stands as the liquid fraction:

$$\theta' = \min(1; \theta) \quad \text{Eq. III-49}$$

Hence,

$$\frac{\partial(\theta' \bar{u}_x)}{\partial \alpha} - \frac{\eta}{\bar{h}} \frac{\partial \bar{h}}{\partial \alpha} \frac{\partial(\theta' \bar{u}_x)}{\partial \eta} + \frac{1}{\bar{h}} \frac{\partial(\theta' \bar{u}_v)}{\partial \eta} + \frac{R_i}{b} \frac{\partial(\theta' \bar{u}_z)}{\partial \zeta} = 0 \quad \text{Eq. III-50}$$

The radial velocity \bar{u}_v can be obtained from these equations with a simple integration along η .

Bearing in mind that the normalized bush and shaft walls are considered to be impermeable and are both normal to the radial direction, η , the radial component of the non-dimensional velocity at the reference domain, $\bar{\eta}$, will obey to the following boundary conditions:

$$\left\{ \begin{array}{l} \bar{\eta} = 0 \quad \text{for} \quad \eta = 0 \\ \bar{\eta} = 0 \quad \text{for} \quad \eta = 1 \end{array} \right. \quad \text{Eq. III-51}$$

Recalling the relationship between the non-dimensional velocity \bar{u}_v and the non-dimensional velocity of the transformed reference domain $\bar{\eta}$ (defined earlier in Eq. III-11), these boundary conditions can be expressed in terms of \bar{u}_v in order to be easily applied to Eq. III-50:

$$\left\{ \begin{array}{l} \bar{u}_v = 0 \quad \text{for} \quad \eta = 0 \\ \bar{u}_v = \frac{\partial \bar{h}}{\partial \alpha} \quad \text{for} \quad \eta = 1 \end{array} \right. \quad \text{Eq. III-52}$$

This sometimes can be confusing because while \bar{u}_v is a non-dimensional value (recall its definition in Eq. III-9), it has not received the variable transformation defined in Eq. III-5 as in the case of $\bar{\eta}$.

Since only one integration of Eq. III-50 is performed, only one of these conditions (the first has been chosen) needs to be applied, the second condition being automatically attained. Actually,

the difference between the theoretical value prescribed by the second condition of Eq. III-52 and the actual value obtained after the integration will be a measure of the numerical accuracy of the velocity field calculations.

III.5.7 Flow rate calculations

The lubricant feeding flow rate (the flow of lubricant fed to the bearing through each groove) is an important design parameter. The prediction of this parameter is important not only because it can help the selection of the oil feeding system, but also because it is a parameter which deeply affects the lubrication efficiency and the bearing cooling. The accuracy of the temperature field predictions can depend significantly on the accuracy of the prediction of flow rate. There are also other auxiliary flow rates which have to be computed, for instance, in order to carry out the thermal analysis in the groove regions.

The lubricant feeding flow rate is obtained through a mass balance of the liquid phase crossing the boundaries which define the groove region and are represented in Figure III-7.

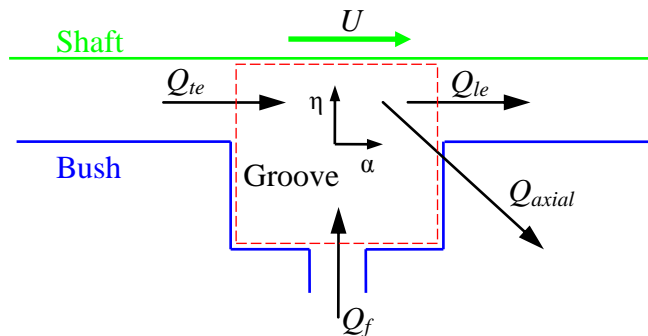


Figure III-7 – Flow balance around a groove

The mass balance yields:

$$Q_f = Q_{axial} + Q_{le} - Q_{te} \quad \text{Eq. III-53}$$

Where Q_f is the feeding flow rate, Q_{axial} is the axial flow rate, corresponding to the side leakage of the groove, Q_{le} is the flow rate across the leading edge of the groove and Q_{te} is the flow rate across the trailing edge of the groove, which corresponds to the recirculated flow rate, that is, the hot lubricant which reaches the trailing edge of the groove coming from upstream.

One possible method for calculating these various flow rates would be to integrate the velocity profiles along a specific section. This method was, in fact, used in the present work at an initial stage. However, the control volume method used for the prediction of the pressure field through the Elrod algorithm (see section III.5.5a) already computed the Couette and Poiseuille flow

rates crossing the faces of the control volumes surrounding each computational node. This information could be easily used in order to compute the relevant flow rates. Not only this approach seems to be more globally coherent, but it also has the advantage of avoiding the incorporation of the numerical errors which necessarily appear in the calculation of the velocity field.

Figure III-8 shows the control volumes in the groove region. The flow rate is obtained by selecting control volumes which contain the corresponding groove edge and the summing up the Poiseuille and the Couette flow rates which cross the appropriate face.

The non-dimensional flow rate across the trailing edge of the groove is calculated at the west face of control volumes encompassing this edge. Taking into account the expressions defined in section III.5.5a) for the Couette and Poiseuille flows across this face (Eq. III-30 and Eq. III-36) the following expression applies:

$$\bar{Q}_{te} = 2 \cdot \left[\frac{1}{2} \bar{Q}_{\alpha}(i_{gr}, j_{te})_{Cou+Poi}^W + \sum_{i=i_{gr}+1}^{N_z-1} \bar{Q}_{\alpha}(i, j_{te})_{Cou+Poi}^W + \frac{1}{2} \bar{Q}_{\alpha}(N_z, j_{te})_{Cou+Poi}^W \right] \quad Eq. III-54$$

The flow rate across the leading edge of the groove is calculated in a similar way, now at the East face of the control volumes encompassing this edge (Eq. III-34 and Eq. III-40):

$$\bar{Q}_{le} = 2 \cdot \left[\frac{1}{2} \bar{Q}_{\alpha}(i_{gr}, j_{le})_{Cou+Poi}^E + \sum_{i=i_{gr}+1}^{N_z-1} \bar{Q}_{\alpha}(i, j_{le})_{Cou+Poi}^E + \frac{1}{2} \bar{Q}_{\alpha}(N_z, j_{le})_{Cou+Poi}^E \right] \quad Eq. III-55$$

Finally, the axial flow rate, which is calculated at the South faces of the control volumes located in the lateral edge of the groove, only includes de Poiseuille term (given by Eq. III-42):

$$\bar{Q}_{axial} = 2 \cdot \left[\frac{1}{2} \bar{Q}_{\zeta}(i_{gr}, j_{le})_{Poi}^S + \sum_{j=j_{le}+1}^{j_{le}-1} \bar{Q}_{\zeta}(i_{gr}, j)_{Poi}^S + \frac{1}{2} \bar{Q}_{\zeta}(i_{gr}, j_{le})_{Poi}^S \right] \quad Eq. III-56$$

Note that all flow rates have been multiplied by two because the calculations were performed for one half of the bearing length only.

There are some flow rates, however, which need to be calculated by integrating the velocity profile. This is the case of the flow rates corresponding to back flow and reverse flow, where only a part of the radial extension (where the circumferential velocity is negative) is to be accounted for.

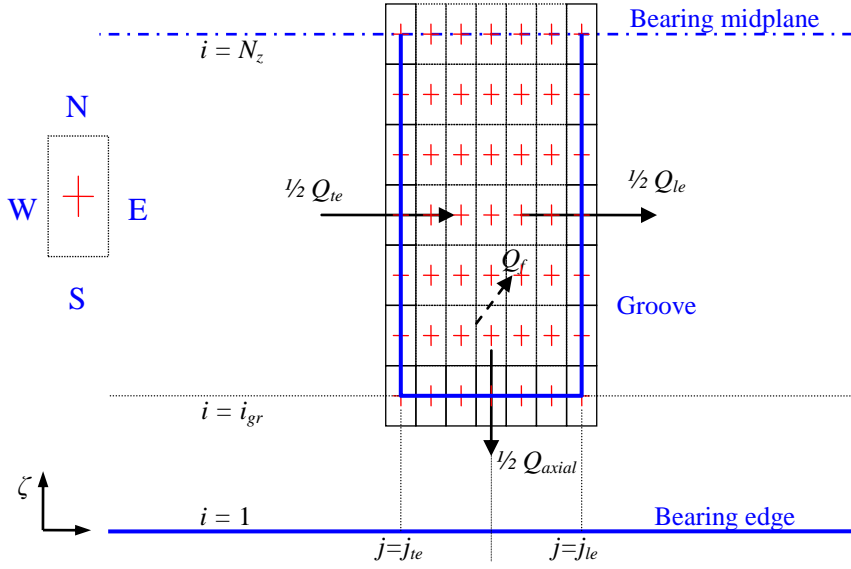


Figure III-8 –Flow rate calculations with the control volume method used in the Elrod algorithm

The circumferential flow rate across a given section comprised between two axial positions z_i (ζ_i) and z_f (ζ_f) and two radial positions y_i (η_i) and y_f (η_f) is obtained in dimensional and non-dimensional form as follows:

$$Q = \int_{z_i}^{z_f} \int_{y_i}^{y_f} u_x \theta' dy dz \Rightarrow \bar{Q} = \bar{h} \int_{\zeta_i}^{\zeta_f} \int_{\eta_i}^{\eta_f} \bar{u}_x \theta' d\eta d\zeta \quad \text{Eq. III-57}$$

Note the presence of the term θ' defined by Eq. III-49, which accounts for the liquid fraction of the flow.

Similarly, an axial flow rate across a given section comprised between x_i (α_i) and x_f (α_f) yields:

$$Q = \int_{x_i}^{x_f} \int_{y_i}^{y_f} u_z dy dx \Rightarrow \bar{Q} = \frac{R_i}{b} \int_{\alpha_i}^{\alpha_f} \int_{\eta_i}^{\eta_f} \bar{h} \bar{u}_z d\eta d\alpha \quad \text{Eq. III-58}$$

III.6 Introduction to the thermal problem

The influence of the heat generated by viscous dissipation and the temperature gradients present within the lubricant are only negligible for a limited number of cases, such as low load, low speed tests.

The Thermohydrodynamic (THD) analysis incorporates thermal effects into hydrodynamic lubrication theory. It encompasses the heat transfer analysis at the fluid domain through the Energy equation and usually also at the domain of the solid bodies through the Laplace equation. Boundary conditions are then established at the interfaces, while some regions, such

as the groove regions, are sometimes treated through mass and energy balances. An extended description of the treatment given to thermal effects in literature has been made in section II.3.

In the present analysis the temperature field is considered not to change significantly in the axial direction and therefore thermal calculations are performed at the bearing midplane only. A discussion on the suitability of this option can be found in section II.3.7.

The reference domains at which numerical calculations are carried out are presented in Figure III-9. The reference fluid domain, where the energy equation is solved, was already described earlier in section III.4.3.

The reference bush body domain, where the heat conduction problem is solved, corresponds to the unwrapped bush body represented in the non-dimensional cylindrical coordinate system $(O_r, \bar{r}, \bar{\alpha}, \bar{\zeta})$ (see top right of Figure III-9). The original rectangular shape of the grooves has been slightly deformed in order to comply with the mesh lines. The holes through which oil reaches the grooves and which are normally drilled through the bush body, have not been considered in the present analysis, even if they are located at the plane where the 2D calculations are performed (midplane). This decision was made taking into account that the diameter of such holes is normally much lower than the bush length. Additionally, without the elimination of such an obstacle, the heat transfer across bearing lands would be impossible to reproduce with the 2D approach considered.

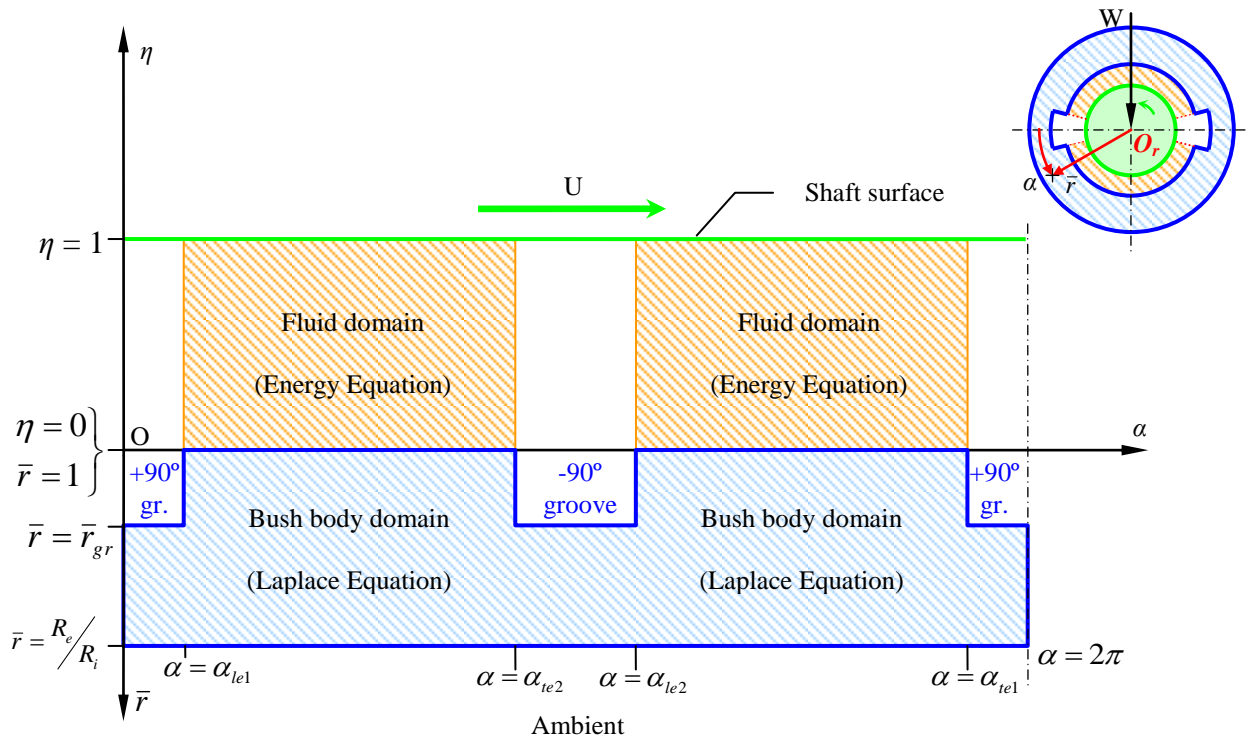


Figure III-9 – Unwrapped reference domains used in thermal calculations (midplane of the non-dimensional unwrapped bearing).

III.7 The energy equation

The lubricant viscosity and the presence of velocity gradients cause the appearance of shear stresses within the fluid. These stresses are responsible for the heat generation by viscous dissipation. This heat is propagated across the fluid mainly through conduction and convection (heat transport due to fluid motion). The Energy equation governs these phenomena within the fluid domain:

$$\underbrace{(\rho c_p)_{eq} \left[u_x \frac{\partial T}{\partial x} + u_y \frac{\partial T}{\partial y} + u_z \frac{\partial T}{\partial z} \right]}_{\text{convective term (convection)}} = \underbrace{K_{eq} \left[\frac{\partial}{\partial x} \left(\frac{\partial T}{\partial x} \right) + \frac{\partial}{\partial y} \left(\frac{\partial T}{\partial y} \right) + \frac{\partial}{\partial z} \left(\frac{\partial T}{\partial z} \right) \right]}_{\text{diffusiveterm (conduction)}} + \underbrace{\Phi}_{\text{dissipative term}} \quad \text{Eq. III-59}$$

with

$$\begin{aligned} \Phi = \mu_{eq} & \left[2 \left(\frac{\partial u_x}{\partial x} \right)^2 + 2 \left(\frac{\partial u_y}{\partial y} \right)^2 + 2 \left(\frac{\partial u_z}{\partial z} \right)^2 - \frac{2}{3} \left(\frac{\partial u_x}{\partial x} + \frac{\partial u_y}{\partial y} + \frac{\partial u_z}{\partial z} \right)^2 + \right. \\ & \left. + \left(\frac{\partial u_x}{\partial y} + \frac{\partial u_y}{\partial x} \right)^2 + \left(\frac{\partial u_y}{\partial z} + \frac{\partial u_z}{\partial y} \right)^2 + \left(\frac{\partial u_z}{\partial x} + \frac{\partial u_x}{\partial z} \right)^2 \right] \end{aligned} \quad \text{Eq. III-60}$$

with $(\rho c_p)_{eq}$, K_{eq} and μ_{eq} being the equivalent properties of the single/twin-phase flow (the product of density by specific heat, heat conduction coefficient and dynamic viscosity (explained further along this chapter). Within the full film region these properties coincide with those of the liquid lubricant. Within the ruptured film region there is a dual phase flow (liquid and gaseous streamers flowing in parallel) and the equivalent properties are obtained through a specific thermal model, which is described further ahead this chapter (section III.10).

For the present work, some simplifying assumptions were considered:

- The axial temperature gradient is neglected $\left(\frac{\partial T}{\partial z} \cong 0 \right)$. This assumption which was justified earlier in section II.3.7 allows the calculations to be performed at the midplane of the bearing only ($z=b/2$).
- The circumferential and axial diffusive terms may be neglected when compared with the respective convective terms (Frêne et al, 1990; Pinkus, 1990). This is generally true in practical lubrication cases, since the average speed at which the lubricant is transported across its respective characteristic length is much higher than the average speed at which the heat is transferred by conduction across the same characteristic length (high Peclet number).

- The only relevant dissipative terms are the ones based on the transverse gradients of the circumferential and axial velocities, $\frac{\partial u_x}{\partial y}$ and $\frac{\partial u_z}{\partial y}$ (Pinkus, 1990). Furthermore, due to symmetry considerations and bearing in mind that the shaft is considered to be perfectly aligned with the bush, the latter term is null at the midplane.

Taking into account the aforementioned assumptions, the Energy equation becomes:

$$(\rho c_p)_{eq} \left[u_x \frac{\partial T}{\partial x} + u_y \frac{\partial T}{\partial y} \right] = K_{eq} \frac{\partial^2 T}{\partial y^2} + \mu_{eq} \left(\frac{\partial u_x}{\partial y} \right)^2 \quad Eq. III-61$$

And in the non-dimensional reference domain, the variable transformation yields:

$$Pe \left[\bar{u}_x \frac{\partial \bar{T}}{\partial \alpha} + \left(\frac{\bar{u}_y}{\bar{h}} - \frac{\bar{u}_x \eta}{\bar{h}} \frac{\partial \bar{h}}{\partial \alpha} \right) \frac{\partial \bar{T}}{\partial \eta} \right] = \frac{1}{\bar{h}^2} \frac{\partial^2 \bar{T}}{\partial \eta^2} + Br \frac{\bar{\mu}_{eq}}{\bar{h}^2} \left(\frac{\partial \bar{u}_x}{\partial \eta} \right)^2 \quad Eq. III-62$$

with Pe and Br being the Peclet number and the Brinkman number, respectively:

$$Pe = \frac{(\rho c_p)_{eq} U c_r^2}{K_{eq} R_i} \quad ; \quad Br = \frac{\mu_f U^2}{K_{eq} T_f} \quad Eq. III-63$$

As long as \bar{u}_x is positive, *Eq. III-62* may be solved with a backward differencing scheme as an initial value problem in the α direction. However, reverse flow phenomena can sometimes occur (recall section II.3.13). In this case, *Eq. III-62* may be solved with a domain separation approach, such as that proposed by Boncompain et al (1986), outlined in Figure III-10.

This algorithm may be summarized as follows:

- The positive and negative domains of \bar{u}_x are solved separately with backward and forward differences, respectively;
- The nodes at each side of the common boundary of the two domains serve as initial/boundary condition nodes when the calculations are performed at the opposite domain.
- The calculations are repeated for each domain until the solutions of the two domains are harmonized in the vicinity of their common boundary.

The numerical solution proposed by Boncompain et al (1986) and later applied by Costa et al (2003) consists on a semi-implicit procedure which is detailed in Appendix II.

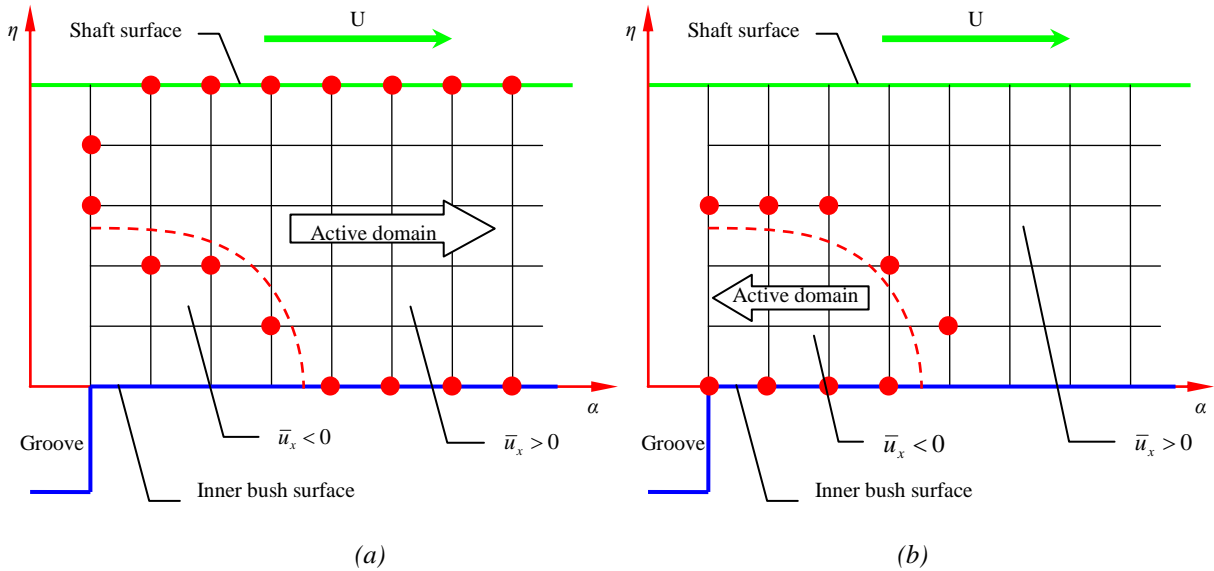


Figure III-10 – Domain separation algorithm used in the presence of reverse flow: (a) backward difference scheme at the positive velocity domain and (b) forward difference scheme at the negative velocity domain (red dotted nodes are used as initial/boundary conditions in each case).

III.8 The Laplace equation

The Laplace equation is a particular form of the Energy equation containing the diffusive (conduction) terms only. It governs the conductive heat transfer within the bush body, which is considered to be cylindrical, homogeneous and isotropic.

The fact that, within the fluid domain, the film is thin when compared with the curvature radius, has allowed unwrapping the geometry and treating it with a Cartesian coordinate system. However, within the bush body domain the thickness is not small when compared with the radius of curvature and therefore the curvature of the bush body must be retained. Therefore, the reference domain of the bush body is represented in cylindrical coordinates. The Laplace equation, which governs the temperature field along the bush body, T_b , thus yields:

$$\frac{\partial^2 T_b}{\partial r^2} + \frac{1}{r} \frac{\partial T_b}{\partial r} + \frac{1}{r^2} \frac{\partial^2 T_b}{\partial \alpha^2} + \frac{\partial^2 T_b}{\partial z^2} = 0 \quad \text{Eq. III-64}$$

Where α and z are the angular and axial coordinates (which coincide with those defined earlier for the fluid domain) and r is the radial coordinate with origin at the bush centerline.

Taking into account that the axial temperature gradient has been neglected and performing a non-dimensional transformation, one obtains:

$$\frac{\partial^2 \bar{T}_b}{\partial \bar{r}^2} + \frac{1}{\bar{r}} \frac{\partial \bar{T}_b}{\partial \bar{r}} + \frac{1}{\bar{r}^2} \frac{\partial^2 \bar{T}_b}{\partial \alpha^2} = 0 \quad \text{with} \quad \begin{cases} T_b = T_f \bar{T}_b \\ r = R_i \bar{r} \end{cases} \quad \text{Eq. III-65}$$

This is an elliptical partial differential equation which can be discretized through a central finite difference scheme:

$$\bar{T}_{j,kb} = \frac{(\bar{T}_{j,kb+1} - \bar{T}_{j,kc} - 1) \cdot \left(\frac{1}{2\bar{r}_{kb}\Delta\bar{r}} + \frac{1}{\Delta\bar{r}^2} \right) + \frac{\bar{T}_{j+1,kb} - \bar{T}_{j-1,kb}}{\bar{r}_{kb}\Delta\alpha_j}}{2 \left[\left(\frac{1}{\bar{r}_{kc}\Delta\alpha_j} \right)^2 + \frac{1}{\Delta\bar{r}^2} \right]} \quad \text{Eq. III-66}$$

This equation can be solved iteratively, for instance, with the Successive Over-Relaxation method:

$$\bar{T}_{j,kb}^{(n)} = \bar{T}_{j,kb}^{(n-1)} + RFT_b (\bar{T}_{j,kb}^{(calculated)} - \bar{T}_{j,kb}^{(n-1)}) \quad \text{Eq. III-67}$$

where $n-1$ and n are the previous and the current iterations respectively, while RFT_b is the relaxation factor used in the solution of the Laplace equation.

III.9 Thermal boundary conditions

The final solution of the THD problem is highly dependent on the boundary conditions chosen. There are simplified analyses using the isothermal, adiabatic or the ISOADI boundary conditions (see section II.3.5 and subsequent sections) which are handy in situations where a massive number of simulations must be performed, as when constructing design charts. These analyses tend to yield poor results in cases where large amounts of heat are generated or when the bulk of the heat generation is rather localized instead of being more or less evenly dispersed. The use of boundary conditions which are as physically realistic as possible is therefore advisable. An outline of the ones used in the present work is presented in Figure III-11. The thermal behavior of the groove region and the prediction of the inlet section temperature profile $\bar{T}(\eta)$ are described in a different section (III.11).

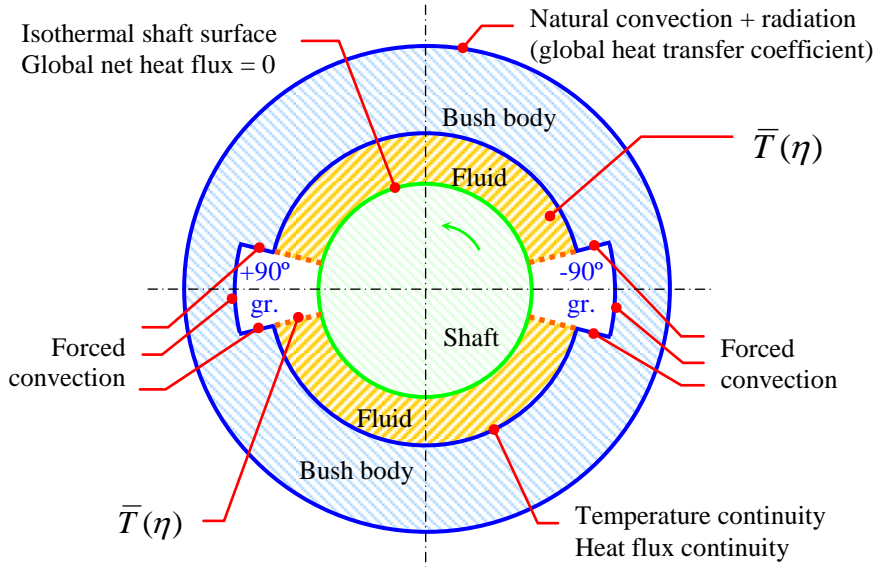


Figure III-11 – Boundary conditions used in the solution of the Energy equation at the fluid domain and of the Laplace equation at the bush body domain

III.9.1 Bush – film interface

The temperature fields at the fluid domain, $\bar{T}(\alpha, \eta)$, and at the solid domain $\bar{T}_b(\alpha, \bar{r})$ are calculated separately. Nevertheless these domains possess a common border. At this border the temperature and the heat flux continuity conditions are enforced:

$$\left\{ \begin{array}{l} T|_{y=0} = T_b|_{r=R_i} \Rightarrow \bar{T}|_{\eta=0} = \bar{T}_b|_{\bar{r}=1} \\ K_{eq} \frac{\partial T}{\partial y} \Big|_{y=0} = -K_b \frac{\partial T_b}{\partial r} \Big|_{r=R_i} \Rightarrow \frac{K_{eq}}{c_r \bar{h}} \frac{\partial \bar{T}}{\partial \eta} \Big|_{\eta=0} = -\frac{K_b}{R_i} \frac{\partial \bar{T}_b}{\partial \bar{r}} \Big|_{\bar{r}=1} \end{array} \right. \quad \begin{array}{l} Eq. III-68 \\ Eq. III-69 \end{array}$$

where K_{eq} and K_b are the equivalent thermal conductivity of the fluid (either single or twin phase) and the thermal conductivity of the bush body, respectively.

III.9.2 Groove inner walls

Within the groove the lubricant is considered to be at a constant temperature, T_{gr} . The flow in this region can be highly recirculating (Kosasih and Tieu, 2004; Jeddi et al, 2005) promoting the convective heat transfer across the groove walls. The heat flux continuity across the trailing edge wall, the leading edge wall and the bottom wall of the groove yields respectively:

$$\left\{ \begin{array}{l} K_b \frac{\partial T_b}{\partial x} = -H_{gr}(T_b - T_{gr}) \\ K_b \frac{\partial T_b}{\partial x} = H_{gr}(T_b - T_{gr}) \\ K_b \frac{\partial T_b}{\partial r} = H_{gr}(T_b - T_{gr}) \end{array} \right. \quad \left\{ \begin{array}{l} x = x_{te} \\ R_i \leq r \leq r_{gr} \\ x = x_{le} \\ R_i \leq r \leq r_{gr} \\ x_{te} \leq x \leq x_{le} \\ r = r_{gr} \end{array} \right. \quad \begin{array}{l} \text{Eq. III-70} \\ \text{Eq. III-71} \\ \text{Eq. III-72} \end{array}$$

Or in non-dimensional form:

$$\left\{ \begin{array}{l} \frac{K_b}{R_i} \frac{\partial \bar{T}_b}{\partial \alpha} = -H_{gr}(\bar{T}_b - \bar{T}_{gr}) \\ \frac{K_b}{R_i} \frac{\partial \bar{T}_b}{\partial \alpha} = H_{gr}(\bar{T}_b - \bar{T}_{gr}) \\ \frac{K_b}{R_i} \frac{\partial \bar{T}_b}{\partial \bar{r}} = H_{gr}(\bar{T}_b - \bar{T}_{gr}) \end{array} \right. \quad \left\{ \begin{array}{l} \alpha = \alpha_{te} \\ 1 \leq \bar{r} \leq \bar{r}_{gr} \\ \alpha = \alpha_{le} \\ 1 \leq \bar{r} \leq \bar{r}_{gr} \\ \alpha_{te} \leq \alpha \leq \alpha_{le} \\ \bar{r} = \bar{r}_{gr} \end{array} \right. \quad \begin{array}{l} \text{Eq. III-73} \\ \text{Eq. III-74} \\ \text{Eq. III-75} \end{array}$$

The convective heat transfer which is here seen in the perspective of the bush body (the heat lost by the bush to the oil within the groove), should be also taken into account when performing the thermal calculations under the perspective of the oil within the groove (Thermal balance of the groove – section III.11.1). Otherwise, an unrealistic heat sink would appear in the system.

III.9.3 Bush – ambient interface

The outer surface of the bush is in contact with the ambient and exchanges heat with it. This heat flux occurs mainly through convection and radiation. A global heat transfer coefficient between the bush and the ambient, H_{amb} , is therefore used:

$$\begin{aligned} & K_b \frac{\partial T_b}{\partial r} = -H_{amb}(T_b - T_{amb}) \quad \{r = R_e \Rightarrow \\ \Rightarrow & \frac{K_b}{R_i} \frac{\partial \bar{T}_b}{\partial \bar{r}} = -H_{amb}(\bar{T}_b - \bar{T}_{amb}) \quad \left\{ \bar{r} = \frac{R_e}{R_i} \right. \end{aligned} \quad \text{Eq. III-76}$$

III.9.4 Shaft - film interface

There are several ways of treating heat transfer phenomena occurring at the shaft which were already described in section II.3.8. The one chosen for the present analysis has been to consider

the experimentally backed hypothesis of an approximately isothermal shaft surface. The shaft temperature is obtained by considering that the global net heat flux across the shaft surface is zero (a midterm between existing applications where the shaft acts either like a heat source or a heat sink). This condition is expressed as follows:

$$y = h \Rightarrow \begin{cases} T = T_{shaft} \\ \int_0^{2\pi} \left(K_{eq} \frac{\partial T}{\partial y} \right) dx = 0 \end{cases} \quad \text{or} \quad \eta = 1 \Rightarrow \begin{cases} \bar{T} = \bar{T}_{shaft} \\ \int_0^{2\pi} \left(\frac{K_{eq}}{\bar{h}} \frac{\partial \bar{T}}{\partial \eta} \right) d\alpha = 0 \end{cases} \quad \begin{array}{l} \text{Eq. III-77} \\ \text{Eq. III-78} \end{array}$$

The fluid conductivity, K_{eq} , has been retained inside the integral because it is not necessarily a constant (it can vary at the ruptured film region according to the local liquid fraction, as described in section III.10). \bar{T}_{shaft} is obtained by substituting the derivative by a backward difference expression and solving the numerical integral expression in order to \bar{T}_{shaft} .

III.10 Thermal modeling of the ruptured film region

A revision of the most important thermal models of the ruptured film region has been already presented in section II.3.14. Concerning twin groove journal bearings, most theoretical models have reported large discrepancies between theoretical and experimental temperature profiles in the ruptured film region. In spite of being a rather inactive region in terms of pressure generation and thus load carrying capacity, its role in the global thermal behavior of the bearing is not negligible and should be modeled conveniently.

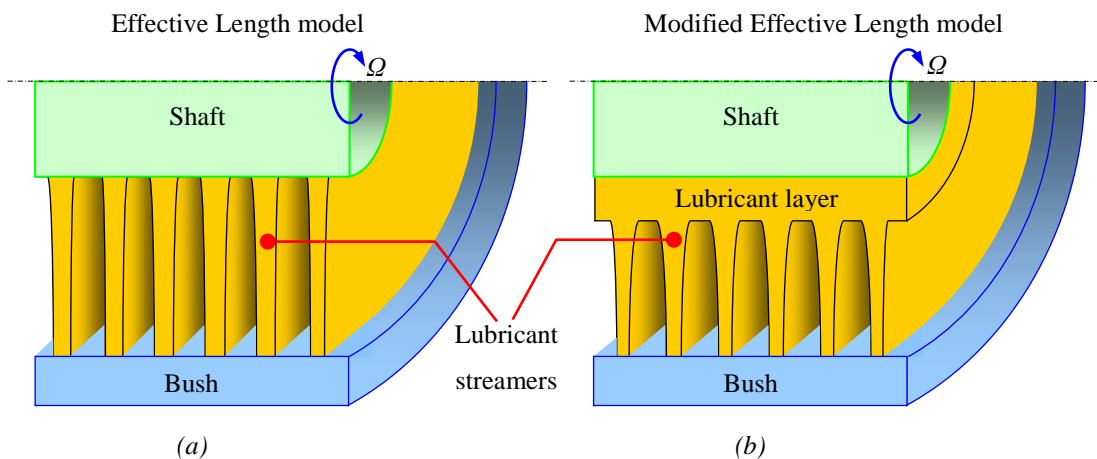


Figure III-12 – Outline of the lubricant flow in the ruptured film region according to (a) the Effective Length model and (b) the modified Effective Length model, which incorporates the influence of a layer of liquid attached to the shaft surface (the clearance has been exaggerated).

The Elrod Algorithm not only allows a mass-conservative prediction of the pressure field but also allows the location of the ruptured film region and the corresponding liquid fraction, θ' . Two alternative thermal models which take advantage from the knowledge of this information

have been developed in the present work. One is based on the Effective Length (*EL*) concept (recall section II.3.14a), adapted to the Elrod Algorithm. The second model proposes a modification to the former in which the influence of a layer of lubricant adhered to the shaft has been included. Figure III-12 sketches these two approaches.

III.10.1 Effective Length (*EL*) model

The *EL* concept relies on the assumption that in the ruptured film region the pressure is uniform and the liquid lubricant flows under the form of streamers which are attached to both shaft and inner bush surface and are separated by gaseous cavities, as depicted in Figure III-12(a). Therefore the liquid lubricant occupies only a fraction of the bearing length, the so-called effective length of lubricant, where the bulk of the heat transfer and heat generation phenomena takes place. Within the ruptured film region, the fraction of the bearing length filled with liquid lubricant can be obtained from the integration of the variable θ used in the Elrod Algorithm:

$$\overline{EL} = 2 \int_0^{\frac{1}{2}} \theta' d\zeta \quad \text{with} \quad \theta' = \min(1, \theta) \quad \text{Eq. III-79}$$

Assuming that no heat exchange exists between the liquid and the gaseous streamers (no axial heat flow), the heat transfer and viscous dissipation phenomena occur in parallel at each medium and the global thermal behavior of the dual phase flow may be calculated by considering that the gaseous streamers share the same temperature field and velocity profile of the liquid phase.*

The total convective heat flux is the sum of the partial heat fluxes in each phase. Thus, the convective term of the Energy equation (Eq. III-61) is:

$$\begin{aligned} & \overline{EL} \cdot \rho_l c_{pl} \left[u_x \frac{\partial T}{\partial x} + u_y \frac{\partial T}{\partial y} \right] + (1 - \overline{EL}) \cdot \rho_g c_{pg} \left[u_x \frac{\partial T}{\partial x} + u_y \frac{\partial T}{\partial y} \right] = \\ & = (\rho C_p)_{eq} \left[u_x \frac{\partial T}{\partial x} + u_y \frac{\partial T}{\partial y} \right] \end{aligned} \quad \text{Eq. III-80}$$

with

$$(\rho C_p)_{eq} = \overline{EL} \cdot \rho_l c_{pl} + (1 - \overline{EL}) \cdot \rho_g c_{pg} \quad \text{Eq. III-81}$$

* In reality, this is an approximation since the gaseous cavities have a closed geometry and therefore the flow patterns within them must necessarily be different from the Couette flow of the liquid streamers.

The same can be done concerning the diffusive term:

$$\begin{aligned} \overline{EL} \cdot K_l \frac{\partial^2 T}{\partial y^2} + (1 - \overline{EL}) \cdot K_g \frac{\partial^2 T}{\partial y^2} &= \\ = K_{eq} \frac{\partial^2 T}{\partial y^2} & \end{aligned} \quad \text{Eq. III-82}$$

with

$$K_{eq} = \overline{EL} \cdot K_l + (1 - \overline{EL}) \cdot K_g \quad \text{Eq. III-83}$$

Finally, the dissipative term is also obtained from the sum of the contributions of both phases:

$$\begin{aligned} \overline{EL} \cdot \mu_l \left(\frac{\partial u_x}{\partial y} \right) + (1 - \overline{EL}) \cdot \mu_g \left(\frac{\partial u_x}{\partial y} \right) &= \\ = \mu_{eq} \frac{\partial^2 T}{\partial y^2} & \end{aligned} \quad \text{Eq. III-84}$$

with

$$\mu_{eq} = \overline{EL} \cdot \mu_l + (1 - \overline{EL}) \cdot \mu_g \quad \text{Eq. III-85}$$

The present thermal model renders the Energy Equation (Eq. III-62) valid throughout the whole fluid domain.

It should be stated that these equivalent properties (namely the equivalent viscosity) are only applicable to the thermal calculations. The properties used for the pressure and flow calculations are those of the liquid portion of the flow, as explained before.

III.10.2 Modified effective length (EL_m) model

The EL model assumes that within the ruptured film region all the lubricant flows along lubricant streamers attached to both the shaft and the inner bush surface (recall Figure III-12a). Therefore, for this model the flow is considered to be entirely of the Couette type. Nevertheless, it has already been noted that, in reality, a portion of the lubricant actually adheres to the moving surface of the shaft flowing at an approximately uniform velocity – the shaft surface velocity. The influence of this thin layer of lubricant, represented in Figure III-12(b), is neglected in most approaches, namely the EL approach. However, its influence on the thermal behavior might be significant. In fact, the portion of the lubricant contained in this

layer does not contribute significantly to viscous dissipation. Therefore, it is anticipated that the predicted temperature fade within the ruptured film region will be more pronounced if the influence of this layer of lubricant is taken into account.

Based on similar considerations, Knight & Ghadimi (1992) proposed the Film Height (FH) and Cavity Height (CH) models (see section II.3.14c). Nevertheless, they used an over-simplified 2D imposing shaft temperature and neglecting important phenomena such as transverse viscosity variation.

Adapting the pressure/continuity calculations (Elrod's algorithm) in order to include the influence of a shaft-adhered lubricant layer is not a straightforward task. Besides the differences in the circumferential velocity field, it is likely that the inclusion of this effect would yield a marginal effect over the pressure field (maybe a slight change in the location of the film reformation boundaries). Nevertheless, an adaptation solely of the thermal model incorporating the influence of such phenomenon can still be implemented without too much effort. Therefore, the approach adopted in the present work was to include the shaft-adhered lubricant layer phenomenon within the scope of the thermal calculations, while keeping unchanged the pressure/flow calculations.

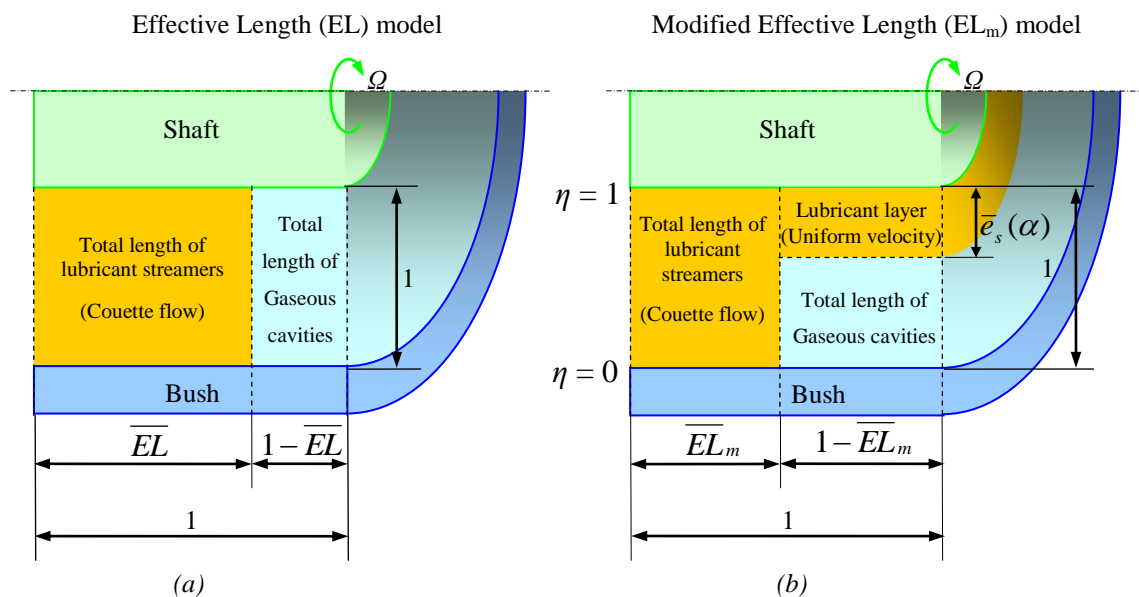


Figure III-13 – Outline comparison between the (a) Effective Length model and (b) the modified Effective Length model.

A new variable, \overline{EL}_m , is therefore introduced. Like \overline{EL} , \overline{EL}_m also accounts for the fraction of the bearing length effectively filled with lubricant streamers, but it is computed taking into account that a part of the lubricant actually flows along the shaft-adhered layer and not along the streamers. These concepts are schematically illustrated in Figure III-13.

Assuming that the circumferential flow rate across a given section is equal for both models, it is possible to derive the new variable \overline{EL}_m from \overline{EL} and from the thickness of the lubricant layer, which occupies a fraction $\bar{e}_s(\alpha)$ of the gap.

Within the streamlet flow, the velocity profile is of Couette type and therefore approximately linear. Therefore,

$$u_x(y) \approx \frac{y}{h}U \Rightarrow \bar{u}_x(\eta) \approx \eta \quad \text{Eq. III-86}$$

Within the shaft-adhered layer the velocity is considered to be uniform and equal to the shaft surface velocity:

$$u_x \approx U \Rightarrow \bar{u}_x \approx 1 \quad \text{Eq. III-87}$$

Therefore, the following equality applies:

$$\overline{Q}_{EL} = \overline{Q}_{EL_m} \Rightarrow \bar{h}\overline{EL} \int_0^1 \eta d\eta = \bar{h}\overline{EL}_m \int_0^1 \eta d\eta + \bar{h}(1 - \overline{EL}_m) \bar{e}_s(\alpha) \quad \text{Eq. III-88}$$

This yields the following relationship:

$$\overline{EL}_m = \frac{\overline{EL} - 2\bar{e}_s(\alpha)}{1 - 2\bar{e}_s(\alpha)} \quad \text{Eq. III-89}$$

Naturally, it can be seen that when the layer thickness tends to zero, the EL_m model reduces to the EL model. Furthermore, the maximum allowable value of the layer thickness $\bar{e}_s(\alpha)$ will correspond to $\overline{EL}_m = 0$, that is, will correspond to $\bar{e}_s(\alpha) = \frac{1}{2}\overline{EL}(\alpha)$. This is so because the average velocity of the Couette flow is about one half of that of the layer.

It seems plausible to admit that the thickness of the shaft adhered layer, e_s , will not vary significantly along the circumferential direction, given the assumptions concerning the ruptured film region (namely the absence of axial flow) that were made. Therefore, the knowledge of the fraction of the gap occupied by the layer at the rupture front, \bar{e}_{s0} , is sufficient to define the problem. With the layer thickness, e_s , being constant, the local fraction of the gap occupied by the layer, $\bar{e}_s(\alpha)$, will vary according to the following relation:

$$\begin{aligned}
e_s &= \bar{e}_{s0} \cdot h(\alpha_{rupt}) = \bar{e}_s(\alpha) \cdot h(\alpha) \Leftrightarrow \\
\Leftrightarrow \bar{e}_s(\alpha) &= \bar{e}_{s0} \cdot \frac{\bar{h}(\alpha_{rupt})}{\bar{h}(\alpha)}
\end{aligned}
\tag{Eq. III-90}$$

The value adopted for \bar{e}_{s0} must be imposed. A parametric study to find the \bar{e}_{s0} value that optimizes the correlation between theoretical and experimental results has been carried out and is presented further ahead (see section VI.2.2). Since \bar{e}_{s0} appeared to display a dependence on the eccentricity ratio, (something which was also supported by some experimental measurements), a ε - \bar{e}_{s0} curve has been proposed.

Once \bar{e}_{s0} has been selected, the new equivalent properties of the flow can be, finally, estimated. They will depend not only on the modified effective length ratio of the specific circumferential coordinate, but also on the radial coordinate, that is, whether in the presence of a pure streamlet flow or of a streamlet + shaft-adhered layer combined flow.

a) Equivalent fluid properties for $0 \leq \eta < 1 - \bar{e}_s(\alpha)$

By inspecting Figure III-13b it can be seen that within this radial range a fraction of the bearing length (\overline{EL}_m) is filled with lubricant streamers under Couette flow, while the remaining length fraction ($1 - \overline{EL}_m$) is filled with gaseous streamers/cavities. Therefore, the equivalent properties of this flow are derived in a way which is similar to that used by the standard EL model:

$$\left\{ \begin{aligned}
(\rho C_p)_{eq} &= \overline{EL}_m \cdot \rho_l c_{p_l} + (1 - \overline{EL}_m) \cdot \rho_g C_{p_g} && \text{Eq. III-91} \\
K_{eq} &= \overline{EL}_m \cdot K_l + (1 - \overline{EL}_m) \cdot K_g && \Leftrightarrow 0 \leq \eta < 1 - \bar{e}_s(\alpha) \quad \text{Eq. III-92} \\
\mu_{eq} &= \overline{EL}_m \cdot \mu_l + (1 - \overline{EL}_m) \cdot \mu_g && \text{Eq. III-93}
\end{aligned} \right.$$

b) Equivalent fluid Properties for $1 - \bar{e}_s(\alpha) \leq \eta \leq 1$

Within this radial range no gaseous phase is present. While a fraction of the bearing length (\overline{EL}_m) is filled with lubricant flowing under the form of streamers with Couette flow, the remaining length fraction ($1 - \overline{EL}_m$) is occupied by a layer of lubricant with uniform velocity profile (see Figure III-13b). Since the whole length of the bearing is filled with liquid lubricant, the resulting equivalent flow properties $(\rho C_p)_{eq}$ and K_{eq} will naturally coincide with those of

the liquid phase. The same cannot be said concerning the equivalent viscosity, μ_{eq}^* . The shaft-adhered layer of lubricant does not contribute to viscous dissipation (no velocity gradient is present). Therefore, only the fraction of the liquid contained within the streamers, \overline{EL}_m , should be accounted for the prediction of μ_{eq} . Hence,

$$\left\{ \begin{array}{l} (\rho C_p)_{eq} = \rho_l c_{p_l} \\ K_{eq} = K_l \\ \mu_{eq} = \overline{EL}_m \cdot \mu_l \end{array} \right. \quad \Leftrightarrow \quad 1 - \bar{e}_s(\alpha) \leq \eta \leq 1$$

Eq. III-94

Eq. III-95

Eq. III-96

These are the properties which should be used in the solution of the energy equation (Eq. III-62).

III.11 Thermal modeling of the groove region

The assumptions which are the base of the Reynolds equation, namely the “thin film” assumption ($h \ll R_i$) are not valid within the groove regions. One option is to treat this region in a global fashion by carrying out a global thermal balance in which the heat fluxes across the boundaries of the groove region are accounted for. Another option would be to carry out a full CFD analysis within these regions. These two approaches have been used by different authors as described earlier in Sections II.3.11 and II.3.12, respectively.

One of the aims of the present work is to sketch an outline for a future design tool. Such tool should be able to yield reliable results within a time frame compatible with current industrial demands. Clearly, a global approach (even though detailed) to the groove mixing problem seemed to be the best option.

The present approach takes into account:

- all major inlet and outlet heat fluxes due to lubricant flow across the boundaries of the groove region;
- the heat fluxes due to forced convection between the bush body and the inner groove lubricant flow;
- the influence of the actual groove dimensions, namely the groove length ratio, a/b ;

* It seems important to stress that this viscosity is used in the dissipative term of the energy equation only. The viscosity used in the calculation of the pressure field (GRE) and the velocity profiles corresponds to that of the liquid phase.

- the occurrence of fresh oil backflow (upstream of the groove) and reverse flow (downstream of the groove);
- the influence of the occurrence of negative feeding flow rate (hot oil reflux) in one of the grooves;
- the existence of a non-uniform temperature profile at the inlet section (leading edge of the groove).

An outline of the heat fluxes crossing the boundaries of the groove region is presented in Figure III-14.3.

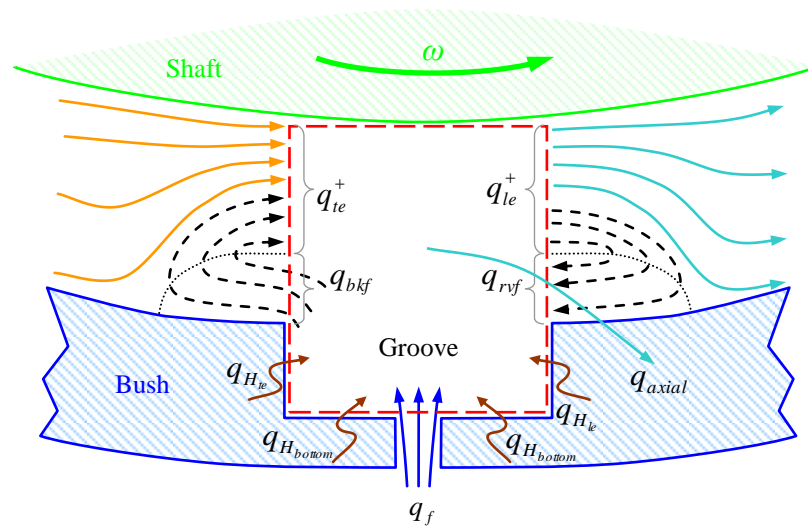


Figure III-14 – Heat fluxes across the boundaries of the groove region in the presence of back flow upstream and reverse flow downstream of the groove.

Where q_{te}^+ and q_{le}^+ are the heat transfer rates, in [W], corresponding to the positive flow rate respectively at the trailing and leading edges of the groove, q_{ryf} and q_{bkf} are the heat transfer rates corresponding to the reverse-flow and the back-flow phenomena, q_{axial} is the heat transfer rate due to the axial flow exiting the groove and q_{H_i} quantifies the convective heat transfer between the oil within the groove and the bush body.

III.11.1 Global thermal balance

The non-dimensional heat transfer rate is defined as follows:

$$q = \rho_l C_{p_l} c_r b U T_f \bar{q}$$

Eq. III-97

A global thermal balance across the groove region (box defined by the dotted red line) of Figure III-14 yields, in non-dimensional terms, the following equality of heat transfer rates (absolute values are used in order to avoid signal confusion):

$$\bar{q}_{le}^+ + \bar{q}_f + \bar{q}_H + |\bar{q}_{rvf}| = \bar{q}_{le}^+ + |\bar{q}_{bkf}| + \bar{q}_{axial} \quad \text{Eq. III-98}$$

Some of these heat transfer rates are obtained through the integration of the heat flux along the corresponding surfaces:

$$\bar{q}_{le}^+ = \frac{2\bar{h}}{\rho_l C_{p_l}} \int_{\zeta_{gr}}^{\zeta_{gr}^{1/2}} \int_{\eta_{bkf}}^{\eta_{bkf}^1} (\rho C_p)_{eq} \cdot \bar{u}_x(\alpha_{le}, \eta, \zeta) \cdot \bar{T}(\alpha_{le}, \eta) \cdot d\eta d\zeta \quad \text{Eq. III-99}$$

$$\bar{q}_{rvf} = 2\bar{h} \int_{\zeta_{gr}}^{\zeta_{gr}^{1/2}} \int_0^{\eta_{rvf}} \bar{u}_x(\alpha_{le}, \eta, \zeta) \cdot \bar{T}(\alpha_{le}, \eta) \cdot d\eta d\zeta \quad \text{Eq. III-100}$$

while others are simply obtained by:

$$\bar{q}_f = \bar{Q}_f \cdot \bar{T}_f \quad \text{Eq. III-101}$$

$$\bar{q}_{le}^+ = \bar{Q}_{le}^+ \cdot \bar{T}_{le} \quad \text{Eq. III-102}$$

$$\bar{q}_{bkf} = \bar{Q}_{bkf} \cdot \bar{T}_{bkf} \quad \text{Eq. III-103}$$

$$\bar{q}_{axial} = \bar{Q}_{axial} \cdot \bar{T}_{axial} \quad \text{Eq. III-104}$$

Finally, the total heat transfer rate by forced convection across the groove walls, \bar{q}_H , is obtained by the sum of the partial heat fluxes integrated along the surface of each one of the groove walls (side walls were neglected):

$$\bar{q}_H = \bar{q}_{H_{te}} + \bar{q}_{H_{le}} + \bar{q}_{H_{bottom}} \quad \text{Eq. III-105}$$

$$\bar{q}_{H_{te}} = \frac{H_{gr} R_i a}{\rho_l C_{p_l} c_r b U} \int_1^{\bar{r}_{gr}} [\bar{T}(\alpha_{te}, \bar{r}) - \bar{T}_{gr}] \cdot d\bar{r} \quad \text{Eq. III-106}$$

$$\bar{q}_{H_{le}} = \frac{H_{gr} R_i a}{\rho_l C_{p_l} c_r b U} \int_1^{\bar{r}_{gr}} [\bar{T}(\alpha_{le}, \bar{r}) - \bar{T}_{gr}] \cdot d\bar{r} \quad \text{Eq. III-107}$$

$$\bar{q}_{H_{bottom}} = \frac{H_{gr} R_{gr} a}{\rho_l C_{p_l} c_r b U} \int_{\alpha_{te}}^{\alpha_{le}} [\bar{T}(\alpha, \bar{r}_{gr}) - \bar{T}_{gr}] \cdot d\alpha \quad \text{Eq. III-108}$$

Where a is the groove length, H_{gr} is the convective heat transfer coefficient and \bar{T}_{gr} is the non-dimensional inner groove temperature.

It is important to stress that the incorporation of this effect into the analysis seems important. Otherwise, a heat sink would exist in the calculations, since groove convection would be considered on the side of the bush conduction calculations but not on the side of groove oil

calculations. In fact, when in some tests this parameter was excluded from the thermal balance of the groove, a decrease of several degrees in maximum bush temperature was observed. Surprisingly, the use of such procedure is frequently found in literature. Under such conditions, the use of large convection coefficients is likely to be prohibitive (the creation of a large heat sink would affect too deeply the temperature field). This may be a reason for the rather small values of H_{gr} (between 50 and 100W/m²K) usually found in most analyses. These values are in the lower range of the typical values found in forced convection with oil as a fluid (between 100 and 1000W/m²K).

The inclusion of this effect in both sides of the thermal calculations (solid and fluid) caused the sensitivity of the value chosen for the convection coefficient to cease to be as critical for the global temperature level as it used to be. Under these conditions the value of H_{gr} was found to affect mainly the temperature trend in the vicinity of grooves rather than the maximum temperature.

In the present work a value of 750W/m²K was chosen for H_{gr} . This value, which was already used by some authors (Monmosseau et al, 1998) seemed to be especially appropriate: not only it appeared to be in better agreement with the physical phenomenon (the highly recirculating flow found within the groove regions will significantly promote convection), but it also provided a better correlation between theoretical and experimental temperature profiles (the strong temperature fade experimentally found in the vicinity of grooves was better predicted – see CHAPTER VI). Nevertheless, it is suggested that a theoretical/experimental investigation should be carried out in order to find realistic values of H_{gr} for typical groove geometries and bearing operating conditions.

III.11.2 Mixing coefficient and inner groove temperature

The thermal balance is not sufficient, by itself, to determine the non-dimensional average temperatures corresponding to the outward lubricant flows, \bar{T}_{le} , \bar{T}_{bkf} , \bar{T}_{axial} , and the inner groove temperature, \bar{T}_{gr} . While an accurate and univocal calculation of these values could actually be carried out through a full CFD solution of the thermal mixing at the groove regions, it would be at the expense of an indubitably computer-intensive solution.

A good, practical alternative consists on assuming that these four temperatures are correlated. Ultimately, they will all depend on the main inward fluxes, that is, those corresponding to the hot, recirculated lubricant flow coming from upstream and the fresh lubricant entering the groove. If a perfect groove mix is achieved, then all four outward temperatures will be virtually

identical. However, if the mix is not perfect, that is, if some of the recirculated hot oil dragged by the moving shaft fails to mix up with the cooler groove lubricant, then it is expected that \bar{T}_{le} will be higher than \bar{T}_{gr} , \bar{T}_{bkf} or \bar{T}_{axial} . Regardless of the mixing efficiency, it seems reasonable to assume that \bar{T}_{bkf} and \bar{T}_{axial} will be close to \bar{T}_{gr} . Therefore, it was assumed that:

$$\bar{T}_{axial} = \bar{T}_{bkf} = \bar{T}_{gr} \quad \text{Eq. III-109}$$

This is the same as admitting that the recirculated hot oil either mixes with the groove oil or is dragged towards the entry section, without flowing backward or being axially deflected. An outline of the mixing process is sketched in Figure III-15.

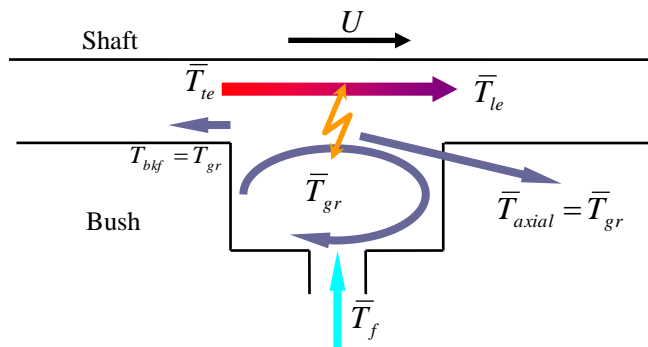


Figure III-15 – Outline of the thermal mixing model within the groove region

A mixing coefficient, c_{mix} is therefore introduced:

$$\bar{T}_{gr} = c_{mix} \bar{T}_{le} + (1 - c_{mix}) \bar{T}_f \quad \text{Eq. III-110}$$

The value chosen for c_{mix} is bounded by two theoretical limits:

- The lower limit is zero. This would imply that all recirculated hot oil would be re-fed to the next bearing land without the occurrence of any heat exchange with the groove oil, that is, $\bar{T}_{gr} = \bar{T}_f$.
- The upper limit is 1. This would indicate that all recirculated hot oil would perfectly mix with groove oil so that all outward groove fluxes would display the same temperature, that is, $\bar{T}_{gr} = \bar{T}_{le}$.

The mixing efficiency within a groove is likely to depend on factors such as the groove geometry, the shaft speed and the feeding pressure. The derivation of a physically-backed coefficient is out of the scope of the present work. A fixed value has been selected after a brief parametric study (see section VI.2.1).

It is now possible to obtain the leading edge temperature, \bar{T}_{le} , from the thermal balance expressed in Eq. III-98 (the absolute values are used in order to avoid signal confusion):

$$\bar{T}_{le} = \frac{\bar{q}_{te}^+ + \bar{q}_H + \bar{Q}_f \bar{T}_f + |\bar{q}_{rvf}| - (|\bar{Q}_{axial}| + |\bar{Q}_{bkf}|)(1 - c_{mix})\bar{T}_f}{c_{mix}|\bar{Q}_{axial}| + c_{mix}|\bar{Q}_{bkf}| + \bar{Q}_{le}^+} \quad \text{Eq. III-111}$$

It can be seen that although \bar{q}_H is also a function of \bar{T}_{gr} (see Eq. III-105 and subsequent ones), for the sake of simplicity this relationship has not been made explicit. The iterative nature of the algorithm permits the estimation of \bar{q}_H with the value of \bar{T}_{gr} obtained in the previous iteration. Once the process approaches convergence, the influence of this approximation will become negligible.

III.11.3 The occurrence of negative flow rate at one of the grooves

The previous calculations were based on the rather common sense notion of a positive feeding flow rate. While this assumption is always true concerning single groove journal bearings, it might not apply in the case of multi groove bearings under certain operating conditions and for one of the grooves.

Indeed, the phenomenon of negative flow rate or hot oil reflux at one of the grooves, in which hot oil flows out of the bearing gap through one of the grooves, was observed during the experimental test program and has been thoroughly analyzed in CHAPTER V. This phenomenon has been barely treated or even referenced in previous works. To the author's knowledge, only Gethin and El-Deihi (1990, 1991) introduced a slight modification to their model in order to handle this possibility, but in a simplified way.

There is a phenomenon associated with the negative flow rate which has never been documented in previous literature: when negative flow rate occurs at one of the grooves, the hot oil flows out of the bearing through that groove and then flows backward in the feeding hoses until it mixes with the fresh oil feeding before it reenters the system through the opposite groove (see Figure III-16). As a consequence of this hot oil reflux at one of the grooves, an effective rise of the feeding temperature at the opposite groove occurs. This curious effect has been documented experimentally in the present work and can be observed, for instance, in Figure V-26 (page 171).

In order to incorporate this phenomenon into the analysis, two separate corrected feeding temperature values (one for each groove) must be considered. If the flow rates at each groove

are positive, then these two values will be equal to \bar{T}_f . Otherwise, a thermal balance must be carried out to the control volume represented in the figure by the dotted box.

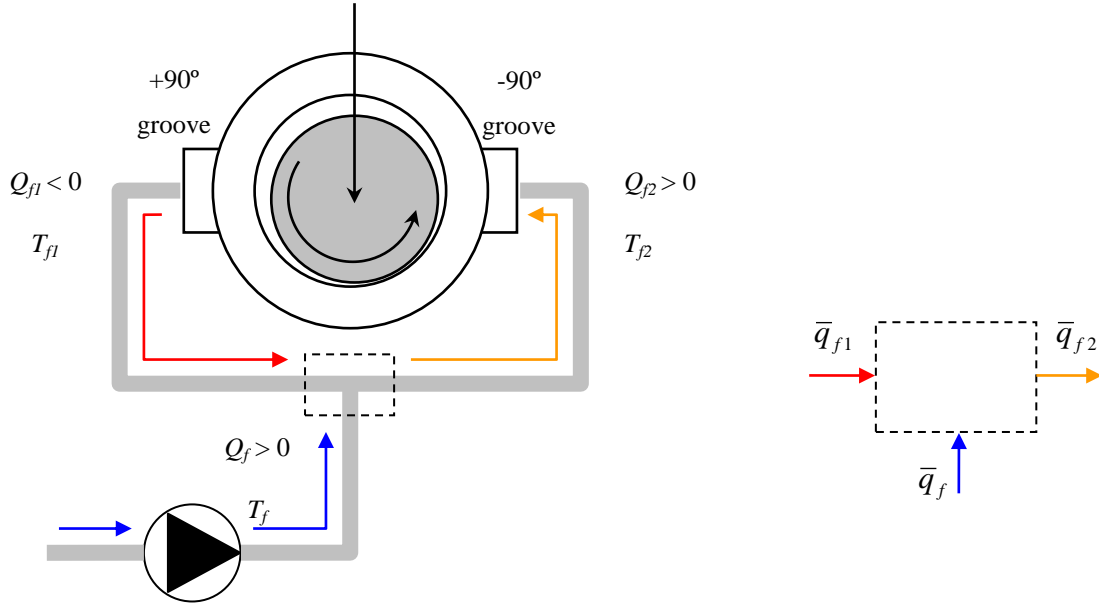


Figure III-16 – Occurrence of negative flow rate at the $+90^\circ$ groove which causes an effective rise of the feeding temperature at the -90° groove.

In the presence of hot oil reflux, for instance, at the $+90^\circ$ groove (as sketched in Figure III-16), the effective feeding temperature at the -90° groove, \bar{T}_{f2} will be obtained by:

$$\bar{T}_{f2} = \frac{\bar{Q}_f \bar{T}_f - \bar{Q}_{f1} \bar{T}_{f1}}{\bar{Q}_{f2}} = \frac{(\bar{Q}_{f1} + \bar{Q}_{f2}) \cdot \bar{T}_f - \bar{Q}_{f1} \bar{T}_{f1}}{\bar{Q}_{f2}} \quad (\bar{Q}_{f1} < 0) \quad \text{Eq. III-112}$$

Now \bar{T}_{f1} is not properly a feeding temperature (because oil is getting out of the bearing rather than entering it) but is actually the temperature of the exiting hot oil. Again, the absence of a full CFD analysis of the groove region requires an estimation of this value based on simplifying assumptions and a thermal balance. While the thermal balance represented in Eq. III-98 still applies when $\bar{Q}_{f1} < 0$, some of the temperatures which enter in that balance must be estimated differently. Under these conditions, the mixing coefficient, c_{mix} , loses its physical significance.

In the absence of fresh oil entering the system, the temperature of the outward fluxes will depend only on the recirculated oil heat transfer rate, \bar{q}_{te}^+ , and the reverse flow heat transfer rate, \bar{q}_{rvf} , if it exists. Under these conditions it seems reasonable to consider that all outward fluxes will display a temperature similar to the groove temperature, that is:

$$\bar{T}_{f1} = \bar{T}_{gr} = T_{le}^+ = \bar{T}_{axial} = \bar{T}_{bkf} \quad \text{Eq. III-113}$$

Applying these assumptions to Eq. III-98, yields:

$$\bar{T}_{le}^+ = \frac{\bar{q}_{te}^+ + \bar{q}_H + |\bar{q}_{rvf}|}{\bar{Q}_{le}^+ + |\bar{Q}_{bkf}| + \bar{Q}_{axial} - \bar{Q}_{f1}} \quad (\bar{Q}_{f1} < 0) \quad \text{Eq. III-114}$$

Neglecting this effect will cause an under-prediction of the maximum bush temperature. The effectiveness of this approach can be verified, for instance, in section VI.3.2.

III.11.4 Incorporating the influence of the groove length into the 2D approach

The 2D THD approach used in the present work is especially suited for large groove bearings. In these bearings the axial variation of the temperature at the inlet section (the whole axial section at the circumferential coordinate of the groove leading edge) may be neglected. Under these conditions, the midplane temperature is fairly representative of the average temperature of that section. This is not necessarily so in the case of small grooved bearings (a/b well below unity), where the midplane temperature might no longer be representative of the average temperature of the whole inlet section. Nevertheless, a corrective measure may still be deployed in order to extend the applicability of the model for small groove bearings.

A new variable called the average temperature of the inlet section (\bar{T}_{is}) was defined. Unlike the temperature at the leading edge of the groove, \bar{T}_{le}^+ which was estimated at the previous section, \bar{T}_{is} reflects the average temperature of the whole section and not just that of the lubricant exiting the groove. Figure III-17 displays an outline of the approach taken.

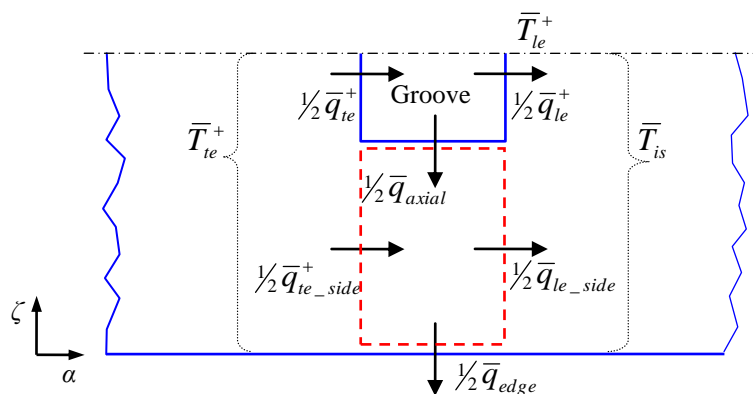


Figure III-17 – Outline of the thermal balance carried out to determine the average inlet section temperature, \bar{T}_{is} , which incorporates the influence of the groove length ratio, a/b .

Being the average temperature of the whole inlet section, \bar{T}_{is} is obtained from the following relationship:

$$(\bar{Q}_{le}^+ + \bar{Q}_{le_side}) \cdot \bar{T}_{is} = \bar{q}_{le}^+ + \bar{q}_{le_side} \Leftrightarrow \bar{T}_{is} = \frac{\bar{Q}_{le}^+ \bar{T}_{le}^+ + \bar{Q}_{le_side} \bar{T}_{le_side}}{\bar{Q}_{le}^+ + \bar{Q}_{le_side}} \quad Eq. III-115$$

The temperature of the oil located at the portion of the bearing length which is not covered by the groove, \bar{T}_{le_side} , may be estimated by carrying out a thermal balance across the red dotted box of Figure V-17:

$$\bar{Q}_{te_side} \bar{T}_{te} + \bar{Q}_{axial} \bar{T}_{axial} = \bar{Q}_{edge} \bar{T}_{edge} + \bar{Q}_{le_side} \bar{T}_{le_side} \quad Eq. III-116$$

Considering \bar{T}_{edge} as being equal to \bar{T}_{le_side} and applying the flow conservation law to the control volume, the following expression is derived:

$$\bar{T}_{le_side} = \frac{\bar{Q}_{te_side} \bar{T}_{te} + \bar{Q}_{axial} \bar{T}_{axial}}{\bar{Q}_{te_side} + \bar{Q}_{axial}} \quad Eq. III-117$$

The incorporation of the groove length effect just described is likely to cause a slight overestimation of the midplane temperature just downstream of the grooves. Nevertheless, a global improvement of the correlation is expected (namely concerning the estimation of T_{max}), especially in the case of bearings with narrow grooves (small a/b ratio). In fact, the parametric study of the influence of lubricant supply conditions presented in CHAPTER VII included the analysis of the groove length ratio (section VII.4). The results obtained for a wide range of a/b (between 0.3 and 0.875), seem to confirm the usefulness of the approach just described.

III.11.5 Temperature profiles at the inlet section

As seen in section II.3.11, there has been some debate on whether the temperature profiles at the inlet sections (leading edge of the groove) should be regarded as uniform or not. For the sake of simplicity, most of the previous analyses have considered a uniform profile, with the inlet section temperature being either imposed or estimated through a thermal balance. The claim of some authors which stated that the use of non-uniform temperature profiles would not affect significantly the results still needs to be conveniently assessed, particularly concerning multi-groove geometries.

The impossibility of obtaining a perfect mixing at the grooves points out to the existence of a significant transverse temperature gradient at the inlet section. The experimental finding, described previously, of the existence of a layer of lubricant attached to the shaft at the ruptured film region further indicates that some serious cross-film temperature gradients might be found.

It is expectable that the temperature of the fluid which is closer to the shaft will be less affected by the mixing process at the groove than that which is closer to the radial position of the inner bush surface. At the leading edge of the groove, the fluid in contact with the wall will share its temperature, \bar{T}_{bush_le} . Therefore an inlet section temperature profile curve varying between \bar{T}_{bush_le} and T_{shaft} and displaying an average temperature compatible with the thermal balances made in the groove region should be built. An infinite number of curves are able to comply with these conditions as long as their shape can adapt to in order to comply with various conditions such as the thermal load at the inlet section (see previous sections). However, not all of them will be equally suitable.

a) Previously tested curves

Some curve families were tested in the present work:

- A *bi-uniform* profile, as depicted in Figure III-18a, was tested. It consisted simply of a profile with two different uniform temperature levels (one at \bar{T}_{bush_le} and the other at \bar{T}_{shaft}). The level would change at a radial position which would be such that the resulting average temperature (obtained by integration) would coincide with \bar{T}_{is} . However, the discontinuity in the temperature at the boundary between the two levels combined with the discrete nature of the mesh frequently yielded instabilities which prevented convergence. Therefore this curve family was discarded in favor of continuous curves.

- Several polynomial curves such as quadratic, cubic and even fourth degree ones were also tested in the present work. However, the resulting fit sometimes yielded unrealistic temperature profiles such as those displaying temperatures lower than the inner groove temperature or even lower than the feeding temperature.

- A cubic/uniform family of curves was also derived (Figure III-18b,c). This mixed curve possessed a cubic polynomial portion and a uniform portion. The goal was to have a continuously adaptable curve which could be treated analytically. The shape of the resulting curve somewhat resembled what would be expected in reality: a hotter layer of lubricant closer to the shaft surface (less affected by groove mixing), and a cooler, more efficiently mixed lower portion. These curves were indeed implemented with success into the present analysis.

However, their analytical deduction was somewhat laborious and the large expressions obtained are not quite mathematically elegant. For the sake of simplicity, this curve family was also discarded.

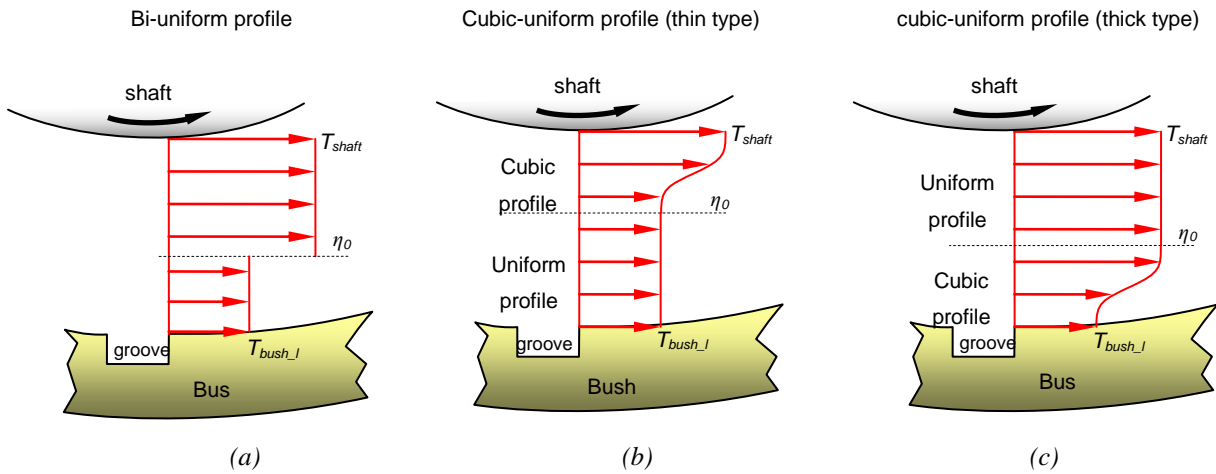


Figure III-18 – Previously tested inlet section temperature profiles (a) bi-uniform, (b) cubic/uniform (thin type) and (c) cubic/uniform thick type.

b) Exponential profile

The main requirement of the inlet temperature profile is that its corresponding average temperature should coincide with the average temperature of the inlet section, \bar{T}_{is} , which was obtained from the thermal balances performed to the groove regions (sections III.11.3 and III.11.4). \bar{T}_{is} is likely to lie between the bush and the shaft temperatures at the inlet section (\bar{T}_{bush_le} and T_{shaft}). Therefore, a good curve family would be one which could vary smoothly between a *thin* profile where, in the limit, $\bar{T}(\alpha_{le}, \eta) = \bar{T}_{bush_le}$ and a *thick* profile where, in the limit, $\bar{T}(\alpha_{le}, \eta) = T_{shaft}$.

After some testing, the following family of exponential-type curves was derived:

$$\bar{T}_{exp}(\alpha_{le}, \eta) = A + B \cdot \frac{e^{C\eta} - 1}{e^C - 1} \tag{Eq. III-118}$$

The constants *A* and *B* are so that:

$$\left\{ \begin{aligned} \bar{T}_{exp}(\alpha_{le}, 0) &= \bar{T}_{bush_le} \end{aligned} \right. \tag{Eq. III-119}$$

$$\left\{ \begin{aligned} \bar{T}_{exp}(\alpha_{le}, 1) &= T_{shaft} \end{aligned} \right. \tag{Eq. III-120}$$

Therefore, the exponential inlet temperature profile will have the following formula:

$$\bar{T}_{\text{exp}}(\alpha_{le}, \eta) = \bar{T}_{bush_le} + (\bar{T}_{shaft} - \bar{T}_{bush_le}) \cdot \frac{e^{C\eta} - 1}{e^C - 1} \quad \text{for } \bar{T}_{bush_le} < \bar{T}_{is} < \bar{T}_{shaft} \quad \text{Eq. III-121}$$

The value of C will depend on the magnitude of \bar{T}_{is} :

- As \bar{T}_{is} gets closer to the lower limit (\bar{T}_{bush_le}) the value of C which will provide a profile with an average temperature equal to \bar{T}_{is} will tend to $+\infty$.
- As \bar{T}_{is} gets closer to the higher limit (\bar{T}_{shaft}) the value of C which will provide a profile with an average temperature equal to \bar{T}_{is} will tend to $-\infty$.

Figure III-19 shows that, depending on the value of C , the resulting temperature profile will be thicker or thinner, reflecting, respectively, the higher or the lower magnitude of the thermal load coming from upstream.

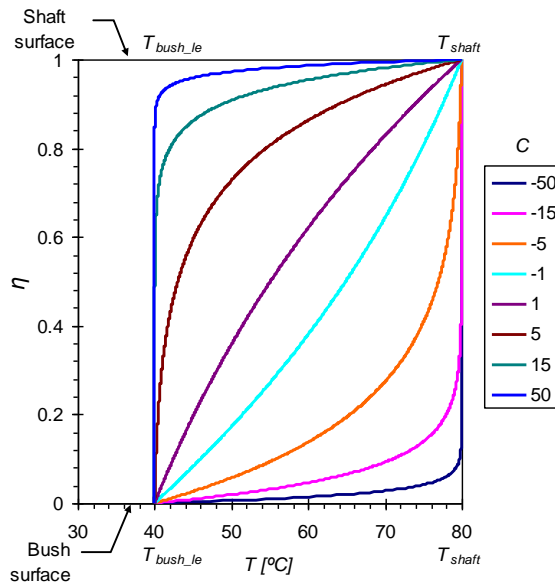


Figure III-19 – Exponential temperature profiles corresponding to several values of C and for $T_{bush_le}=40^{\circ}\text{C}$ and for $T_{shaft}=80^{\circ}\text{C}$.

The calculation of the value of C which yields an inlet temperature profile with an average temperature equal to \bar{T}_{is} is not straightforward and is presented in Appendix I.a).

b.1) Special cases where $\bar{T}_{is} \leq \bar{T}_{bush_le}$ or $\bar{T}_{is} \geq \bar{T}_{shaft}$

It was observed that sometimes \bar{T}_{is} would be lower than \bar{T}_{bush_le} or higher than \bar{T}_{shaft} , in which case, the exponential curve previously described could not be applied. Also, when \bar{T}_{is} would be too close to these limits, the algorithm became unstable. To avoid these problems, a lower

(C_{lim}^-) and a higher limit (C_{lim}^+) were imposed for C . This means that \bar{T}_{is} is also limited by $\bar{T}_{is\text{lim}}^-$ and $\bar{T}_{is\text{lim}}^+$, which are calculated based on C_{lim}^+ and C_{lim}^- , respectively (see Appendix I.b):

$$C_{\text{lim}}^- < C < C_{\text{lim}}^+ \quad \Rightarrow \quad \bar{T}_{is\text{lim}}^- < \bar{T}_{is} < \bar{T}_{is\text{lim}}^+ \quad \text{Eq. III-122}$$

C is not allowed to go beyond these limits. If necessary, an additional component (a 2nd degree polynomial profile) will be added so that the sum of the two curves will display an average temperature still equal to \bar{T}_{is} .

The following expression is proposed for the polynomial component of the curve (see deduction in Appendix I.b)

$$\bar{T}_{\text{Poly}}(\alpha_{le}, \eta) = 6(\bar{T}_{is\text{lim}}^{-/+} - \bar{T}_{is}) \cdot (\eta^2 - \eta) \quad \text{Eq. III-123}$$

For $\bar{T}_{is} \leq \bar{T}_{is\text{lim}}^-$ C will be constant and equal to its higher limit (C_{lim}^+) and the global profile will be:

$$\bar{T}(\alpha_{le}, \eta) = \bar{T}_{bush_le} + (\bar{T}_{shaft} - \bar{T}_{bush_le}) \cdot \frac{e^{C_{\text{lim}}^+ \eta} - 1}{e^{C_{\text{lim}}^+} - 1} + 6(\bar{T}_{is\text{lim}}^- - \bar{T}_{is}) \cdot (\eta^2 - \eta) \quad \text{Eq. III-124}$$

For $\bar{T}_{is} \geq \bar{T}_{is\text{lim}}^+$ C will be constant and equal to its lower limit (C_{lim}^-) and the global profile will be:

$$\bar{T}(\alpha_{le}, \eta) = \bar{T}_{bush_le} + (\bar{T}_{shaft} - \bar{T}_{bush_le}) \cdot \frac{e^{C_{\text{lim}}^- \eta} - 1}{e^{C_{\text{lim}}^-} - 1} + 6(\bar{T}_{is\text{lim}}^+ - \bar{T}_{is}) \cdot (\eta^2 - \eta) \quad \text{Eq. III-125}$$

In the present work C_{lim}^- and C_{lim}^+ were imposed to be -15 and 15, respectively.

III.12 Differential thermal expansion compensation

The feeble clearances which are typical of hydrodynamic lubrication applications might be significantly affected by the thermal expansion of the interacting bodies, especially in the presence of high thermal gradients and pairs of materials with dissimilar thermal expansion coefficients.

A review of the various theoretical approaches to this phenomenon, as well as the justification for the approach chosen for the present work has been already carried out in section II.3.15. The chosen approach relies on the differential thermal expansion compensation concept. Instead of carrying out a full FEM analysis of the thermal expansion of the 3D system, which is

out of the scope of this work, an estimation of the average thermal expansion of both bush and shaft bodies is carried out on the basis of their respective average temperature. This yields a simple clearance correction based on the variation of the shaft radius and the inner bush radius:

$$c_r = c_{r_ref} + R_{i_ref} (T_{bush_avg} - T_{ref}) \cdot TEC_{bush} - R_{shaft_ref} \cdot (T_{shaft} - T_{ref}) \cdot TEC_{shaft} \quad Eq. III-126$$

Where T_{ref} is the reference temperature at which the geometrical parameters were measured (usually 20°C), TEC is the respective thermal expansion coefficient of each material and T_{bush_avg} is the average bush body temperature. The value of the radial clearance, c_r , and the variables and groups which depend on it are updated after each temperature field iteration. This addition to the model was found to be frankly positive for improving the correlation between theoretical and experimental results, especially in terms of flow rate.

III.13 Main performance parameters

The main scope of the model is to provide a reliable prediction of the main performance parameters of journal bearings submitted to specific operating conditions. This information provides precious insight to bearing behavior and may be useful for bearing design.

a) Maximum pressure, maximum temperature

The maximum pressure and the maximum temperature are directly obtained from the respective profiles. These two parameters can affect the mechanical resistance of the bearing material (namely the integrity of the coatings). If excessive, the latter parameter would induce a local fall in lubricant viscosity which could ultimately lead to contact and could also be responsible for lubricant degradation.

b) Eccentricity ratio and minimum film thickness

The eccentricity ratio, ε , and the minimum film thickness, h_{min} (recall section III.4.1) are two interconnected parameters related by:

$$h_{min} = c_r (1 - \varepsilon) \quad Eq. III-127$$

They are key factors in bearing behavior analysis as they provide an estimate of how close the system is from its limit of safe operation.

c) Load carrying capacity, attitude angle

The shaft locus (eccentricity ratio, attitude angle) depends on the operating conditions such as shaft speed and applied load. The present model carries out the inverse problem, which consists on finding the load (the load carrying capacity) corresponding to a given eccentricity. An iterative process is then carried out in order to find the eccentricity and the attitude angle which ultimately generate the pressure field which compensates the prescribed load.

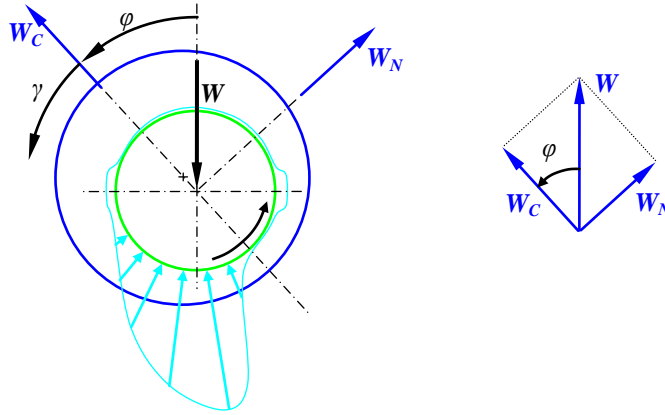


Figure III-20—Load components: along the line of centers (W_c) and normal to the line of centers (W_n).

The load is obtained by calculating the resultant of the pressure field along two orthogonal directions: the direction of the line of centers and its normal, as displayed in Figure III-20. In non-dimensional form this yields:

$$\left\{ \begin{array}{l} \bar{W}_C = 2 \int_0^{2\pi^{0.5}} \int_0^{2\pi^{0.5}} [\bar{p}(\gamma, \zeta) \cos \gamma] d\zeta d\gamma \\ \bar{W}_N = -2 \int_0^{2\pi^{0.5}} \int_0^{2\pi^{0.5}} [\bar{p}(\gamma, \zeta) \sin \gamma] d\zeta d\gamma \\ \bar{W} = \sqrt{\bar{W}_C^2 + \bar{W}_N^2} \end{array} \right. \quad \text{Eq. III-128}$$

Based on the new load components, a new value of the attitude angle, φ , may be estimated:

$$\varphi = \tan^{-1} \left(\frac{\bar{W}_N}{\bar{W}_C} \right) \quad \text{Eq. III-129}$$

This new value of φ will be used to calculate a new pressure field, then a new load, then a new attitude angle and so on, until convergence of φ is achieved (see algorithm description in section III.14.1).

d) Shaft torque, bush torque and power loss

The shaft torque and the corresponding power loss are important design parameters. In fact, a non-negligible fraction of the energy losses in power plants is due to bearing systems. An optimization of these parameters is therefore desirable.

The non-dimensional values of the shaft torque and the bush torque are given by:

$$\bar{M}_{shaft} = 2 \int_0^{2\pi} \int_0^{0.5} \frac{1}{h} \left(\bar{\mu} \frac{\partial \bar{u}_x}{\partial \eta} \right)_{\eta=1} d\zeta d\alpha$$

Eq. III-130

$$\bar{M}_{bush} = 2 \int_0^{2\pi} \int_0^{0.5} \frac{1}{h} \left(\bar{\mu} \frac{\partial \bar{u}_x}{\partial \eta} \right)_{\eta=0} d\zeta d\alpha$$

The power loss is given by:

$$P = M_{shaft} \cdot \omega = M_{shaft} \cdot \frac{U}{R_i} \Rightarrow \bar{P} = \bar{M}_{shaft}$$

Eq. III-131

III.14 Numerical procedure

To implement the theoretical model described earlier, a computer program was built using the FORTRAN 90/95 programming language. The capabilities of this compiler-based language have been already described in section II.4, where a brief revision of the programming tools and numerical methods more frequently applied in hydrodynamic journal bearing analysis was carried out.

The program was compiled with INTEL FORTRAN 10.0 and run on a Linux Cluster (see <http://hawk.fisica.uminho.pt/dirac.html> for details) with 6 Intel Xeon dual-processor units. Although the program was not written for parallel processing, it was possible to use the cluster at full charge by queuing and running multiple jobs of the same program for different test conditions.

Since many details of the numerical procedure have been already revealed in the previous sections, only a global overview of the numerical algorithm is given here. The selection of the mesh parameters and convergence criteria, which was based on a comprehensive parametric study is also detailed at the end of this section.

III.14.1 Algorithm description

The global numerical algorithm is outlined in the flowchart represented in Figure III-21(a), with the portion corresponding to the thermal calculations being detailed in Figure III-21(b).

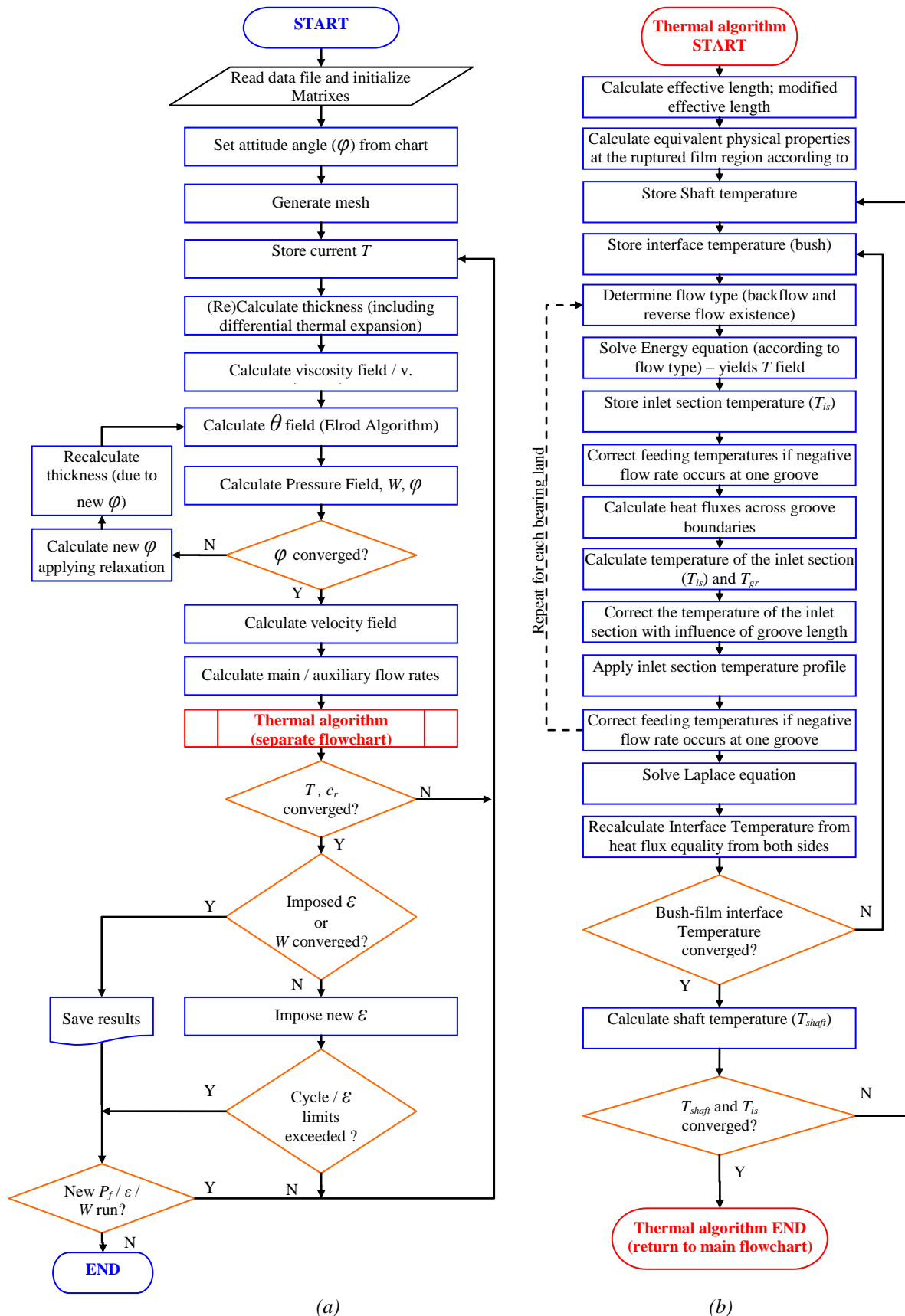


Figure III-21 – Flowchart of (a) the global numerical algorithm and (b) the thermal algorithm, which is part of the former.

The global solution algorithm is outlined as follows:

- 1. Beginning of program**
2. The input data is read from a formatted text file containing the various operating conditions, the lubricant supply conditions, the choice of the models which are to be used, the geometrical data, the physical and thermodynamic properties of the bodies and the lubricant, the mesh parameters and the tolerances. Multi-run sessions (sequential testing of several values of eccentricity/load and/or feeding pressure) are also possible;
3. Matrixes are initialized;
4. A first guess of the attitude angle, φ , is made based on the charted results of the isoviscous model of Claro et al (1993);
5. The coarse mesh is generated (a refined mesh will be applied later, after eccentricity has converged for the first time);
- 6. Beginning of the global cycle;**
7. The film thickness, h , is (re)calculated (Eq. III-4); the differential thermal expansion is also accounted for (Eq. III-126);
8. The viscosity field to be used in the hydrodynamic calculations is estimated based on the local temperature field (Walther equation - Eq. III-1);
- 9. Beginning of the attitude angle (φ) cycle;**
10. The θ field is calculated through the Elrod Algorithm (Eq. III-43);
11. The pressure field, the load carrying capacity, W , and the new attitude angle, φ , are calculated from Eq. III-27, Eq. III-128 and Eq. III-129, respectively;
12. If φ has converged, exit the φ cycle. Otherwise, a new value of φ is obtained, applying relaxation, the thickness is recalculated (Eq. III-4) and the φ cycle restarts (return to point 9.);
- 13. End of the attitude angle (φ) cycle;**
14. Once the pressure field has converged, the velocity field is calculated (Eq. III-45, Eq. III-50);
15. The main and auxiliary flow rates are obtained from the Elrod Algorithm flows (Eq. III-54 to Eq. III-56) or by integration of the velocity profiles (Eq. III-57, Eq. III-58);
16. The effective length (EL - Eq. III-79) and modified effective length (EL_m - Eq. III-89) are calculated;

17. The equivalent physical properties are estimated based on EL / EL_m , according to the ruptured film region model (Eq. III-81, Eq. III-83, Eq. III-85, Eq. III-91 to Eq. III-96);
- 18. Beginning of outer thermal cycle (shaft temperature cycle);**
19. The current value of the Shaft surface temperature, T_{shaft} , is stored;
- 20. Beginning of inner thermal cycle (interface temperature cycle);**
21. The current values of the bush-film interface temperature profile are stored;
- 22. Beginning of the cycle which is repeated for each bearing land;**
23. The flow is classified according to the existence of negative velocity in the bearing land, whether it be downstream of a groove (reverse flow) or upstream of a groove (back flow);
24. The Energy Equation (Eq. III-62) is solved according to the previous flow classification;
25. The previous value of the inlet section temperature, T_{is} is stored and the effective feeding temperatures are corrected if negative flow rate occurs at one groove (Eq. III-112, Eq. III-113);
26. The heat transfer rates across the groove boundaries are calculated: They correspond to the positive flow rate at the trailing edge of the groove (q_{te}^+ - Eq. III-99) and leading edge of the groove (q_{le}^+ - Eq. III-111), to the reverse-flow flow rate (q_{rvf} - Eq. III-100) and the back-flow flow rate (q_{bkf} - Eq. III-103), to the axial flow rate exiting the groove (q_{axial} - Eq. III-104, Eq. III-109) and to the heat flux across the inner groove walls due to convection (q_{H_i} - Eq. III-105 - Eq. III-108).
27. The new values of the groove leading edge temperature, T_{le} (Eq. III-111 or Eq. III-114 when applicable), and the inner groove temperature, T_{gr} (Eq. III-110 or Eq. III-113 when applicable), are obtained from the thermal balance across the groove boundaries;
28. The inlet section temperature, T_{is} , is obtained from Eq. III-115. It corrects the leading edge temperature, T_{le} , incorporating the influence of groove length;
29. A new inlet section temperature profile (exponential) is fitted (Eq. III-121 or Eq. III-124 or Eq. III-125);
30. The effective feeding temperatures are again corrected if negative flow rate occurs at one of the grooves (Eq. III-112, Eq. III-113);

31. End of the cycle which is repeated for each bearing land (cycle back to point 22. if applicable);

32. The Laplace equation is solved at the whole bush body (*Eq. III-66 / Eq. III-67*) applying the boundary conditions defined by *Eq. III-68* thru *Eq. III-76*;

33. The bush-film interface is recalculated based on the continuity of heat flux (*Eq. III-69*);

34. If the bush-film interface temperature has converged, the program exits the inner thermal cycle. Otherwise, this cycle restarts (point 20.);

35. End of inner thermal cycle;

36. A new shaft surface temperature, T_{shaft} , is obtained from the no-net global heat flux condition (*Eq. III-78*);

37. If convergence of T_{shaft} and of T_{is} at both grooves has been achieved, the program exits the outer thermal cycle. Otherwise, this cycle restarts (point 18.);

38. End of outer thermal cycle;

39. If the relative difference between the new temperature field and the old one is higher than the tolerance or if the corrected radial clearance (*Eq. III-126*) has not converged, the program cycles back to the beginning of the global cycle (point 6.)

40. If the load carrying capacity has converged to the imposed load or if eccentricity has been imposed, then the results are saved in formatted text documents.

41. If eccentricity has not been imposed and the load carrying capacity still did not converge to the imposed load, then a new value of ε is imposed;

42. If the maximum number of cycles or the eccentricity limits have been exceeded or if more runs are in queue, then the program cycles back to the beginning of the global cycle (point 6.);

43. If no more runs are in queue, the program exits the global cycle;

44. End of global cycle;

45. End of program.

III.14.2 Mesh selection

The choice of suitable mesh parameters is not as straightforward as it might seem at first sight. A given mesh might be sufficient for some test cases but be unsuitable for some other specific

cases. For instance, phenomena such as lubricant reverse flow are only observable with the use of fine meshes. Coarse meshes might also be unsuitable in cases where, for instance, the objective is to accurately predict a temperature profile more than to merely estimate the maximum temperature.

Most existing theoretical results in literature were obtained with the use of rather coarse meshes. The approach here used relies on the use of more refined meshes, whose parameters were obtained through a systematic parametric optimization. This optimization was made iteratively, in the sense that whenever a new optimum value for a specific parameter was elected, all previous tests (the optimization of the other parameters) had to be repeated, now incorporating the new value. Therefore, the optimization charts presented below for each parameter, correspond to the final iteration of the process, that is, they are already built with the final, optimized values of all the other parameters.

The parametric optimization tests were performed for the case of the LMS bearing ($N=4000\text{rpm}$, $T_f=40^\circ\text{C}$, $P_f=140\text{kPa}$, see details in Table IV-1) testing three different eccentricity ratios (0.3, 0.6 and 0.9). The results presented here correspond to highest eccentricity case, which is the worst case scenario not only because working conditions are more extreme but also because phenomena such as reverse flow tend to occur mostly within the higher range of eccentricity.

The performance parameters monitored during the optimization were the used CPU time, maximum bush temperature, total lubricant feeding flow rate, shaft temperature, maximum pressure, attitude angle and load capacity. Only the first four parameters are here detailed.

a) Circumferential nodes, N_x

The normalized reference domain has been presented already in Figure III-3. The circumferential coordinate, α , develops along the direction of the shaft motion. The N_x circumferential nodes are distributed along two regions, each with uniform mesh. The spacing of the nodes located within the region comprised by the circumferential coordinate of grooves is about half of the spacing of the nodes outside those regions.

After the temperature field has totally converged for the first time, an additional refinement in the circumferential direction is performed: In the present case, the two cells in the vicinity of the upstream and downstream edges of grooves are refined by a factor of six (N_x does not account for these additional nodes).

The results concerning maximum bush temperature (T_{max}), Total flow rate (Q_f), load capacity (W) and total CPU time are presented in Figure III-22. They show that N_x is the mesh parameter

which affects most significantly the results. For instance, with 61 nodes the load capacity is overestimated by nearly 8% in relation to the highest accuracy test (401 nodes).

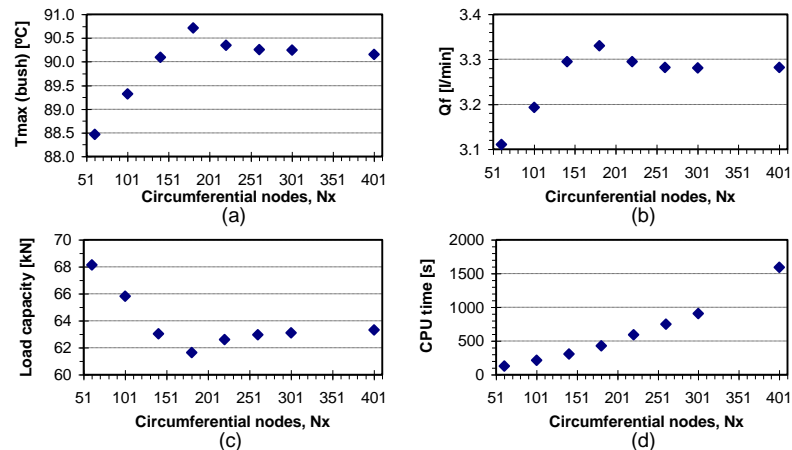


Figure III-22 – Effect of the number of circumferential nodes N_x , in (a) maximum bush temperature, (b) Total flow rate, (c) Load capacity and (d) total CPU time used to run three consecutive eccentricity cases (results are presented for the last case only, $\varepsilon=0.9$). Chosen: $N_x=221$.

The value chosen for N_x was 221 nodes. With this choice, T_{max} , Q_f and W are distant 0.2%, 0.4% and 1.1% from the values corresponding to the highest accuracy test, respectively. This value seems to be a good compromise between accuracy and processing time, and is certainly much greater than most existing published theoretical results.

b) Axial nodes, N_z (half bush length)

Due to symmetry reasons, the calculations need only to be performed in half of the bearing length. The nodes are distributed along this half length as evenly as possible. A limitation to this is that the lateral edge of the grooves should coincide with a line of nodes and there should be a minimum of four nodes between this line and the edge of the bush in order to accurately estimate the pressure gradients. Therefore, two different node spacings are defined for the two regions which are separated by the straight line defined by lateral edges of the grooves.

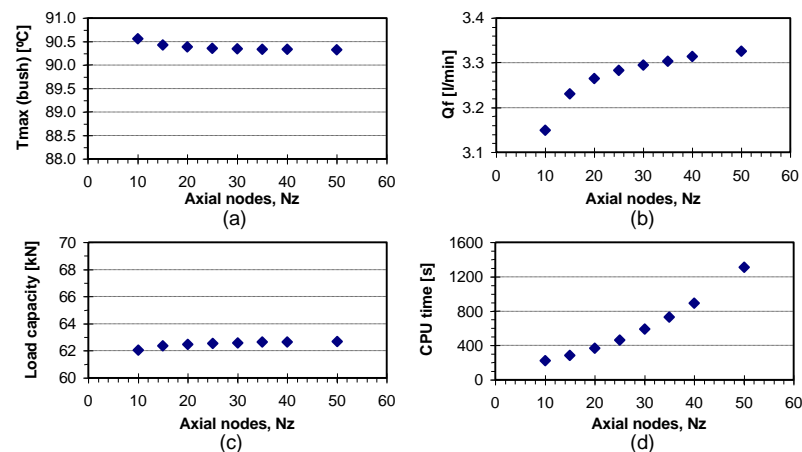


Figure III-23 – Effect of the number of axial nodes N_z , in (a) maximum bush temperature, (b) Total flow rate, (c) Load capacity and (d) total CPU time used to run three consecutive eccentricity cases (results are presented for the last case only, $\varepsilon=0.9$). Chosen: $N_z=30$.

By inspecting Figure III-23 it can be observed that the variation of N_z affects mainly the flow rate and the CPU time. In terms of flow rate, the value chosen, $N_z=30$, yields a difference of less than 1% in relation to the highest accuracy test, while T_{max} and W are virtually identical between both cases.

c) Radial nodes in the fluid domain (N_y)

The radial mesh of the fluid domain is used in the flow and heat transfer computations. By inspecting Figure III-24 it can be seen that, except for very low values, all parameters are only moderately affected by the choice of N_y .

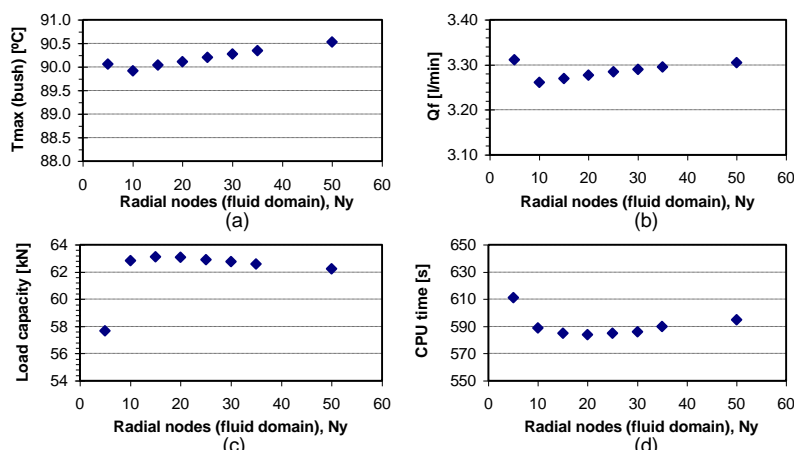


Figure III-24 – Effect of the number of radial nodes in the fluid domain N_y , in (a) maximum bush temperature, (b) Total flow rate, (c) Load capacity and (d) total CPU time used to run three consecutive eccentricity cases (results are presented for the last case only, $\varepsilon=0.9$). Chosen: $N_y=35$

Surprisingly, the computation time is nearly unaffected by the number of radial nodes used. The choice of $N_y=35$ yielded differences to the highest accuracy test of 0.2%, 0.3% and 0.6%, in T_{max} , Q_f and W , respectively.

d) Radial nodes in the bush body domain (N_r)

The number of nodes in the radial direction of the bush body, N_r , is expected to affect the accuracy not only of the conductive heat transfer calculations (Laplace equation) but also of the temperature and heat flux continuity conditions (recall section III.9). As Figure III-25d indicates, the computation time is only moderately affected by the choice of N_r . This enabled the selection of a value for this parameter ($N_r=35$), which yielded maximum differences to the highest accuracy test ($N_r=50$) of less than 0.3%, for all parameters analyzed and within a reasonable computation time lapse.

As a concluding remark to this section, it might be stated that, taking into account the small randomness found in the results (even at very high eccentricities), along with the small differences found between the results obtained with the final mesh and the finest meshes tested, the present algorithm seems to be particularly robust.

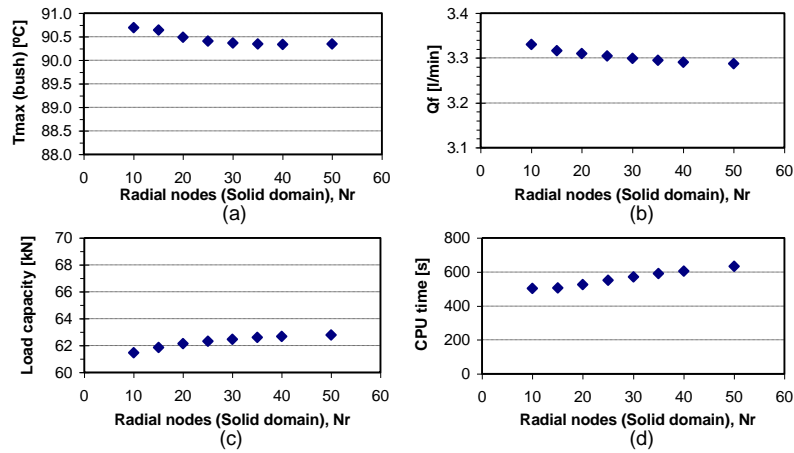


Figure III-25 – Effect of the number of radial nodes in the bush body domain, N_r , in (a) maximum bush temperature, (b) Total flow rate, (c) Load capacity and (d) total CPU time used to run three consecutive eccentricity cases (results are presented for the last case only, $\varepsilon=0.9$). Chosen: $N_r = 35$.

III.14.3 Convergence criteria

A parametric study of the influence of the convergence criteria (the maximum allowable error between iterations) used in the various algorithms is displayed in Figure III-26.

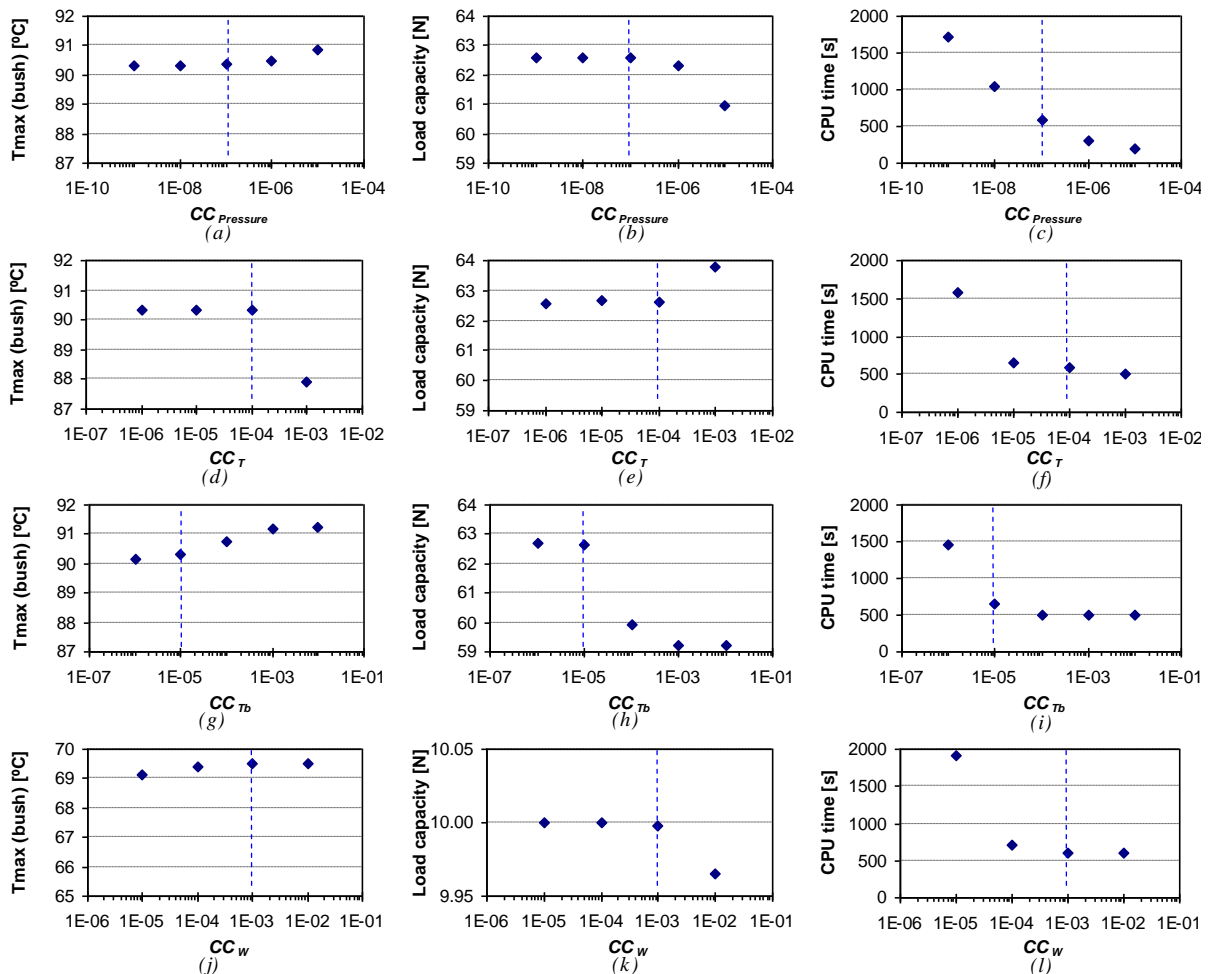


Figure III-26 – Effect of the convergence criteria on maximum bush temperature, load capacity and total CPU time, for (a)(b)(c) the pressure field, (d)(e)(f) the fluid temperature field, (g)(h)(i) bush temperature field and (j)(k)(l) load.

The conditions used were the same used for the mesh selection (LMS bearing with $\varepsilon=0.9$), except when testing the load convergence criterion (LMS bearing with $W=10\text{kN}$). The use of tighter values increases exponentially the computation time.

The convergence criterion used for pressure field calculations ($CC_{Pressure}$) was defined to be 10^{-7} , yielding differences to the highest accuracy test of less than 0.1% in T_{max} and Load capacity. Similar values were obtained with the chosen convergence criterion for the temperature field of the fluid ($CC_T=10^{-4}$). Concerning the bush temperature calculations, a value of $CC_{Tb}=10^{-5}$ was necessary to reduce the differences to the highest accuracy test below 0.2%. Finally, the convergence criterion for load ($CC_W=10^{-3}$) was chosen as a good compromise between accuracy and computation time.

III.14.4 Elrod Algorithm constant (β)

In section III.5.5 it was justified why the value of the bulk modulus variable, β , used in the works of Elrod and Adams (1975) and later Elrod (1981), needed to be physically realistic in the former model, but could assume an arbitrary value in the latter model. In this case, the value chosen for β would not affect the pressure field but only its proportion with the Elrod variable (θ) and the convergence of the process. Although the reasons pointed in that section seem sufficient to prove this claim, a material proof in support of it could be helpful. Figure III-27 displays the results for a wide range of values of the constant β .

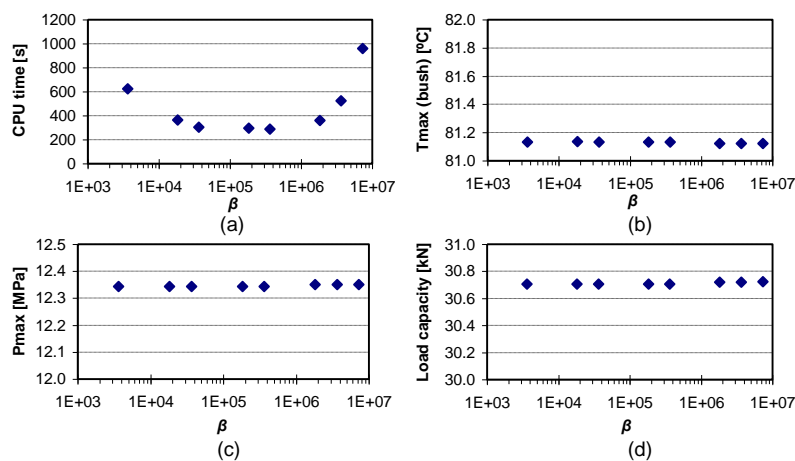


Figure III-27 - Effect of the bulk modulus constant, β , from Elrod's algorithm on (a) CPU time, (b) maximum bush temperature, (c) maximum pressure and (d) load capacity (LMS bearing for $\varepsilon=0.8$, $P_f=140\text{kPa}$, $T_f=40^\circ\text{C}$)

These results show that the value chosen for β does not actually affects the final results but only the convergence speed. This is a very convenient feature of the algorithm, since it was only possible to achieve convergence with values of β which were far from being physically realistic

(which would correspond to about 10^8). The optimal value for β was found to be in the 10^5 range.

III.15 Conclusions

A theoretical model for the analysis of the steady state performance of twin groove journal bearings has been developed.

Based on input data such as the physical properties of the lubricant and the bearing components, the operating conditions, the geometric configuration of the bearing and the lubricant supply conditions, the model is expected to provide the main performance parameters relevant to bearing design and performance analysis, such as the hydrodynamic pressure and temperature profiles, oil flow rate, minimum film thickness, eccentricity, attitude angle, shaft torque, and power loss.

The model incorporates the full Thermohydrodynamic (THD) analysis and treats realistically the lubricant supply conditions, namely taking into consideration the lubricant feeding pressure, the feeding temperature and the actual groove dimensions.

A computer program was built using a compiler-based language (FORTRAN 95) in order to treat numerically the various phenomena intervening in the model which are expressed through partial differential equations, mass balances and energy balances.

The hydrodynamic pressure field was obtained through the solution of the Generalized Reynolds Equation through a control volume method inspired in the Elrod Algorithm (Elrod, 1981);

The viscous dissipation and the heat transfer analysis within the fluid were treated through the solution of the Energy Equation within the fluid with a finite difference based semi-implicit method. The lubricant viscosity was allowed to vary across the thickness of the film.

The problem of the heat conduction within the bush body was solved through the Laplace equation and the Successive Over-Relaxation method (finite differences).

The groove regions received special treatment through a refined thermal balance in which all relevant heat fluxes were taken into account: those corresponding to convective heat transfer from the bush body to the groove oil, those corresponding to the hot recirculated oil flow coming from the upstream land, to the reverse flow coming from the downstream land, to oil back flow going upstream of the groove and to lubricant feeding flow. A mixing coefficient was also introduced;

Several shapes for the inlet section temperature profile were tested;

The ruptured film region (also known as the cavitated region) was treated with the use of a model relying on the Effective Length concept. Additionally, an alternative model which incorporates the influence of the experimentally observed phenomenon of a shaft-adhered lubricant layer was proposed.

The thermal expansion suffered by the components was modeled with a simplified approach (the differential thermal expansion approach).

An extensive optimization of the mesh parameters and the convergence criteria has been carried out. In this study, the coherence of the results seems to confirm the robustness of the numerical algorithm. The validation of the model with experimental data is presented in a separate chapter.

As a concluding remark, it should be stated that special attention was given to the coherent treatment of the domain normalization, non-dimensional analysis and the compatibility of Elrod's approach with the assumptions made. This was an especially important task as these aspects were too often mistreated in previous analyses. This appears to be an important contribution of the present work, which ultimately justified the extended length of the chapter.

Experience serves not only to confirm theory, but differs from it without disturbing it; it leads to new truths which theory only has not been able to reach.

- D'Alembert

CHAPTER IV Experimental work at the University of Poitiers (LMS)

IV.1 Introduction

Experimental investigations on hydrodynamic journal bearings have been carried out over several decades. The study of the influence of oil supply conditions has been undertaken by several authors, especially in relation to single groove plain journal bearings. Here, it is worth mentioning the work of Dowson et al. (1966), who studied the effect of the feeding temperature on the bearing temperature distribution. Majumdar and Saha (1974), using a journal bearing with a single axial groove located at the position of maximum film thickness, analyzed the effect of feeding pressure on the bush temperature distribution. Mitsui et al. (1983), varying the feeding temperature and the oil thermoviscosity, analyzed the cooling effect of the feeding oil on a single axial groove plain journal bearing. Syverud and Tanaka (1997) also studied the effect of feeding temperature by using a system to heat and cool the shaft in order to study the heat transfer mechanisms inside the bearing. Finally, Costa et al. (2000) investigated the influence of the supply conditions, including groove length and location, on bearing performance.

Experimental work concerning two axially grooved journal bearings is scarcer. The existence of an additional groove dramatically affects the flow patterns and the temperature field inside the bearing. Difficulties in theoretical modeling arise in flow and temperature calculations, especially near the grooves. Nevertheless, these bearings have a higher load capacity than variable geometry (tilting pad) bearings, being suitable for steady-regime operation. They permit the rotation of the shaft in both directions. The inclusion of the downstream groove permits them to work at a lower temperature than in the case of single groove bearings. The work of Lund and Tonnesen (1984) is often referred to as it is one of the first well documented experimental works focusing on temperature measurements for this type of bearing. However, the scope of this work did not encompass the study of the supply conditions. Claro (1994) carried out a parametric study on the influence of the supply conditions, which also included

this bearing geometry, in order to validate an isothermal model for bearing performance analysis. This work was not focused on thermal measurements. Gethin and El-Deihi (1990) studied the effect of the groove location on the performance of two axial groove bearings. They concluded that small changes in the groove location can cause significant changes in the pressure and temperature. Fitzgerald and Neal (1992) provide results for the temperature fields at the shaft and bush surfaces for various rotational speeds and applied loads, using fixed supply conditions. Finally, Ma and Taylor (1995) carried out a series of tests with two grooved elliptical bearings to assess the influence of feeding temperature and pressure on bearing performance.

In relation to studies of the influence of oil feeding pressure and feeding temperature in 2-grooved journal bearings, the experimental data available is clearly scarce. The aim of the present work is to address this lack of experimental data in order to ensure a better understanding of the influence of supply conditions on bearing performance. Current theoretical models still do not give good estimates of the temperature evolution at the unloaded lobe of the bearing. It is anticipated that a better understanding of the combined effect of the two grooves on the temperature field will improve theoretical modeling, thereby allowing better predictions to be made about the thermal behavior of bearings.

IV.2 Bearing Test Rig and experimental procedure

Figure IV-1 shows the test rig of the LMS-Poitiers. This rig has been used for a good deal of experimental work, from the study of thermal effects in journal bearings by Ferron, Frêne and Boncompain (1983) to the recent study of the effect of misalignment on the performance of journal bearings by Bouyer and Fillon (2002). A description of the experimental layout has previously been presented in these studies. Thus, only a brief description is necessary here.

The equipment allows the operating conditions (rotational speed and applied load) to be controlled, as well as the supply conditions (oil feeding pressure and temperature). The measured parameters were the following: oil flow rate, temperature fields at the oil-bush and oil-shaft interfaces, oil outlet temperature, bush body temperature at different locations, position of shaft center relative to the bush center, hydrodynamic pressure along the mid-plane of the inner surface of the bush, and bush torque.

The instrumented bearing system is detailed in Figure IV-2. The shaft is driven by a 21kW variable speed DC motor via a transmission belt. The speed is regulated with an accuracy of ± 5 rpm, by an electronic controller connected to the data acquisition and control system. The shaft

is supported by three precision preloaded rolling bearings that provide a stable and stiff mode of operation for the whole system.

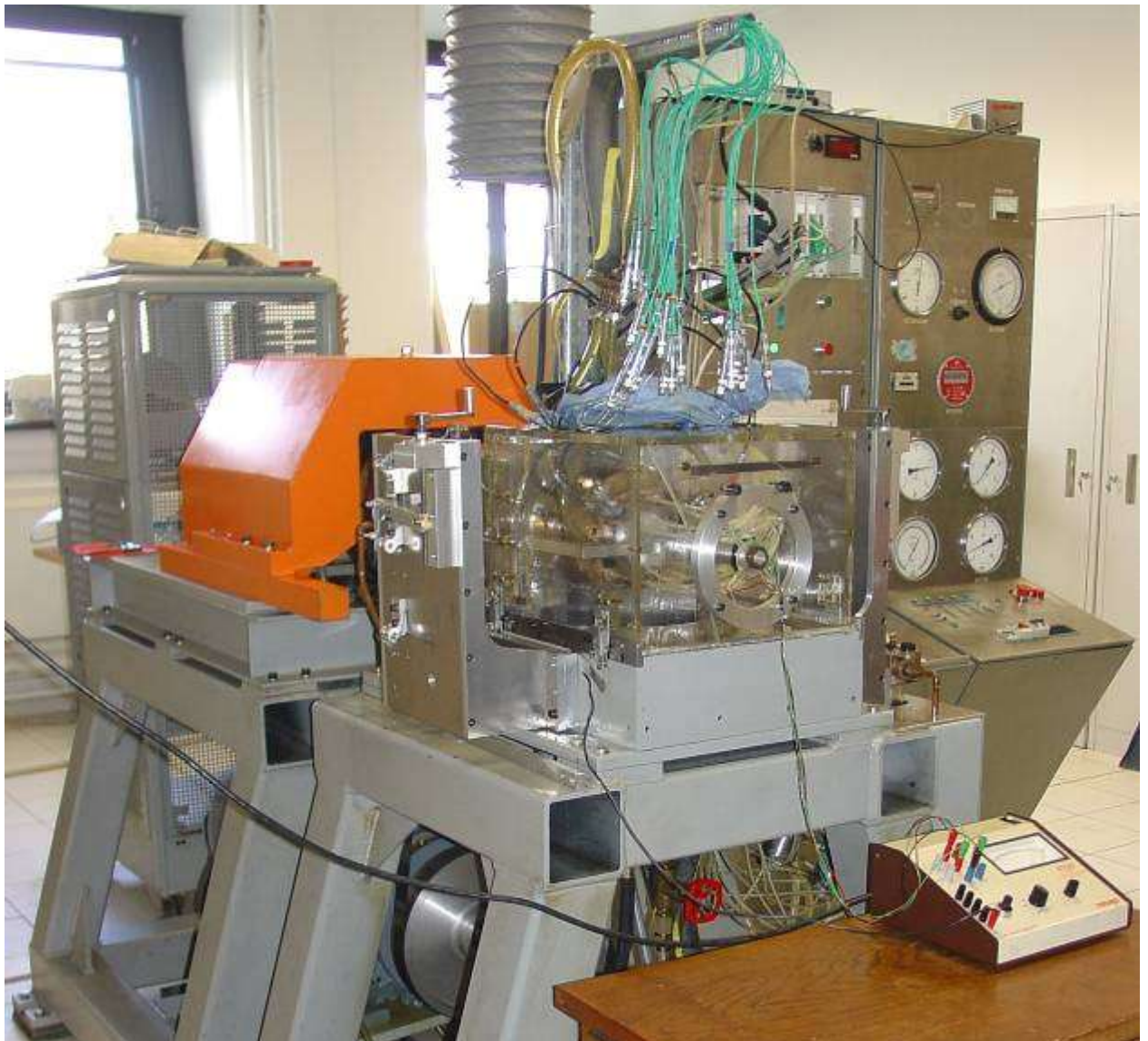


Figure IV-1 Overview of the test rig

The inner part of the bush, depicted in Figure IV-3, was specially designed for the present work. It is built of bronze and is designed to be inserted in a pre-existent sleeve whose purpose is to permit the testing of different bush geometries in the same experimental machine. In Figure IV-2 the two components can be seen already mounted. The shaft is made of 100C6 steel. The diametral clearance is $171 \pm 5 \mu\text{m}$ (20°C).

The loading system relies on a pneumatic cylinder that acts on the bearing sleeve. The load is applied to the bush along the vertical direction with an error of $\pm 0.2\text{kN}$. Between the loading system and the bearing there is a spherical hydrostatic bearing as well as a flat one (see Figure IV-2). These ensure that a perfectly aligned load is applied to the bush body without parasitic torques. The lower part of the bush was machined to form the mating surface of the spherical bearing. This bearing system allows accurate measurements of the bush torque to be made.

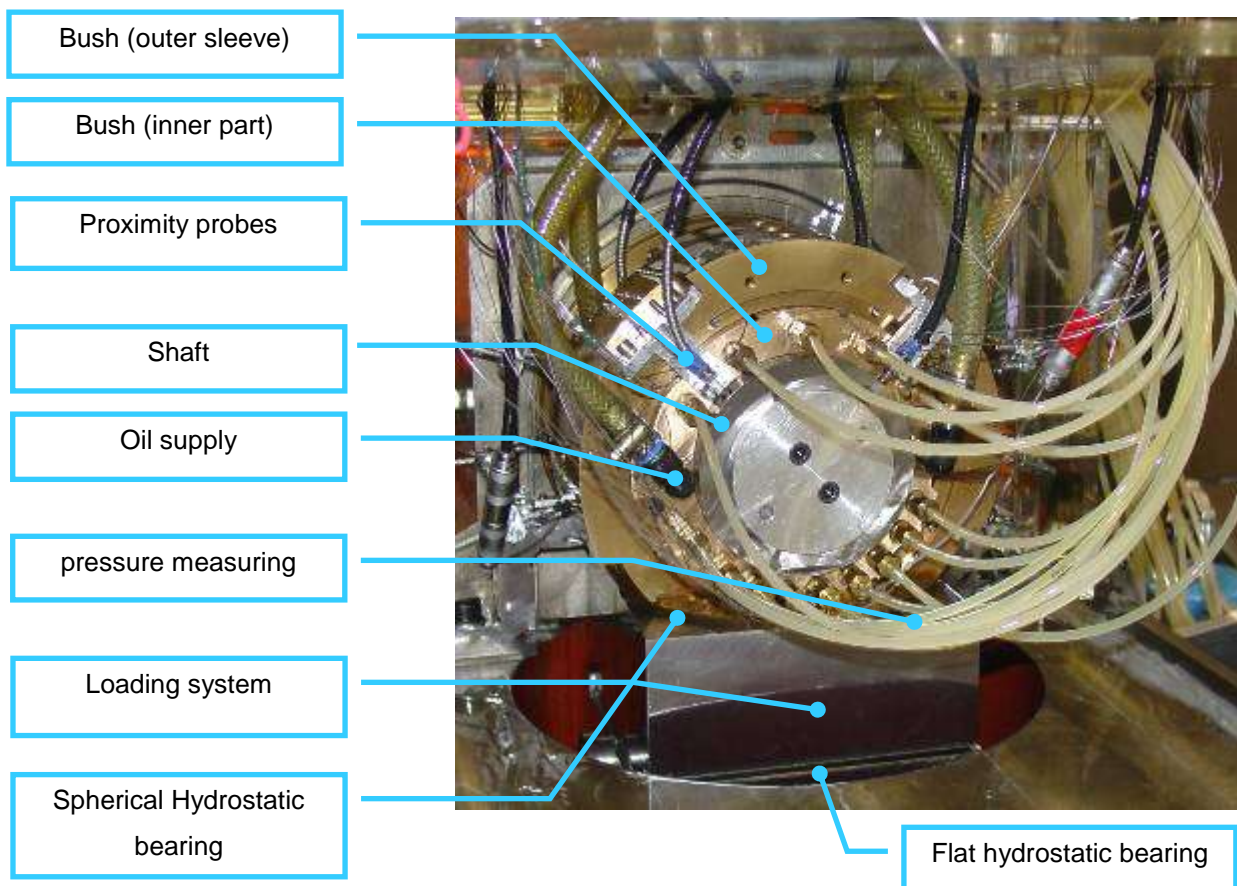


Figure IV-2 – Detail of the bearing system

The feeding pressure is regulated by a precision restrictor valve and monitored by a Bourdon pressure gauge, with an error of ± 0.004 MPa, located at the oil distribution collector. The feeding temperature is regulated via a cryothermostat serving the oil tank. Its value is monitored by a thermocouple located in the oil distribution collector and is kept within a range of $\pm 0.5^\circ\text{C}$ from the set point.

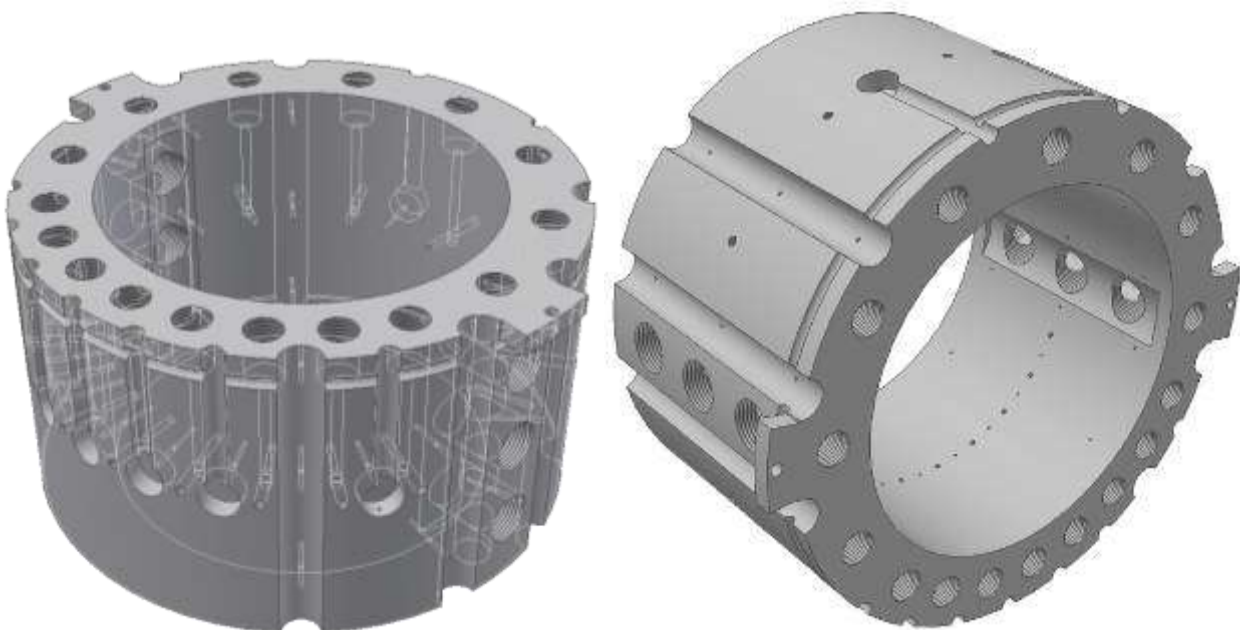


Figure IV-3 - 3D drawings of the inner part of the bush

The measurements were always made under a steady-state regime. In order to achieve this, start-up times were set for thermal stabilization. Between tests, parameters such as temperature and flow-rate were monitored until stabilization occurred.

The oil flow rate was measured by an electric pulse gear flow meter attached to the data acquisition system, with an accuracy of ± 0.05 l/min. The temperature field was monitored by THERMOCOAX type K thermocouples inserted in 0.5mm metal sleeves and attached to a data acquisition system with signal conditioning. The accuracy of the measured values is $\pm 0.7^\circ\text{C}$. The temperature at the oil-bush interface was measured at the locations depicted in Figure IV-4. The sleeved thermocouples are placed inside fully drilled holes. The active part of the thermocouple is flush with the inner surface of the bush. In addition, thermocouples were positioned so as to measure the oil outlet temperature, the ambient temperature (environment temperature around the bearing) and the bush body temperature at two different locations. The temperature at the oil-shaft interface was also measured at three different points by type K thermocouples connected to the system by a rotary joint.

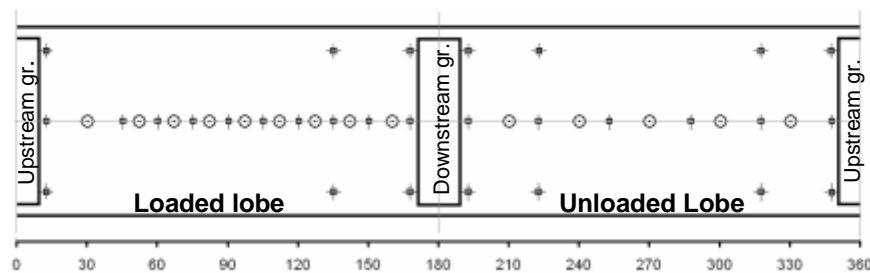


Figure IV-4 – Angular location of the thermocouples (\oplus) and pressure holes (\odot) at the inner surface of the bush.

The hydrodynamic pressure profile was measured by precision Bourdon pressure gauges attached via manifold valves to a series of 1mm holes drilled in the bush mid-plane, as detailed in Figure IV-4. The measured pressure was generally greater than 30% of the total range of each pressure gauge. The measuring uncertainties are $\pm 0.01\text{MPa}$ for pressure values lower than 0.1MPa and $\pm 3\%$ for higher values.

The relative shaft position was obtained with the help of two pairs of Eddy Current proximity probes located at $\pm 45^\circ$ to the load line, on both sides of the bearing. The sensitivity of each sensor ranges from 7 to 7.63mV/ μm . The accuracy of the displacement measurements was $\pm 5\mu\text{m}$. These measurements were corrected taking into consideration the estimated thermal deformation of the system. The locus of the shaft center is relative to a reference test where the absolute position of the shaft has been obtained from an (early version) of the theoretical model developed in the present work. A specific reference test was used for each rotational speed. Therefore, the calculated position of the shaft centerline in relation to the bush centerline should be looked as relative to the reference position chosen for that specific rotational speed.

weighted average of the mean inner surface temperature (70%) and the temperature given by a thermocouple located inside the bush, 2 mm from its outer surface (30%). It was observed that the estimate of the thermal deformation is affected by the method of calculation adopted.

A rough estimation of the mechanical deformations for the maximum load tested (10kN) was performed with a FEM commercial solver, as seen in Figure IV-6. Since the maximum displacement was around 0.5 μm , this effect was neglected in shaft locus measurements.

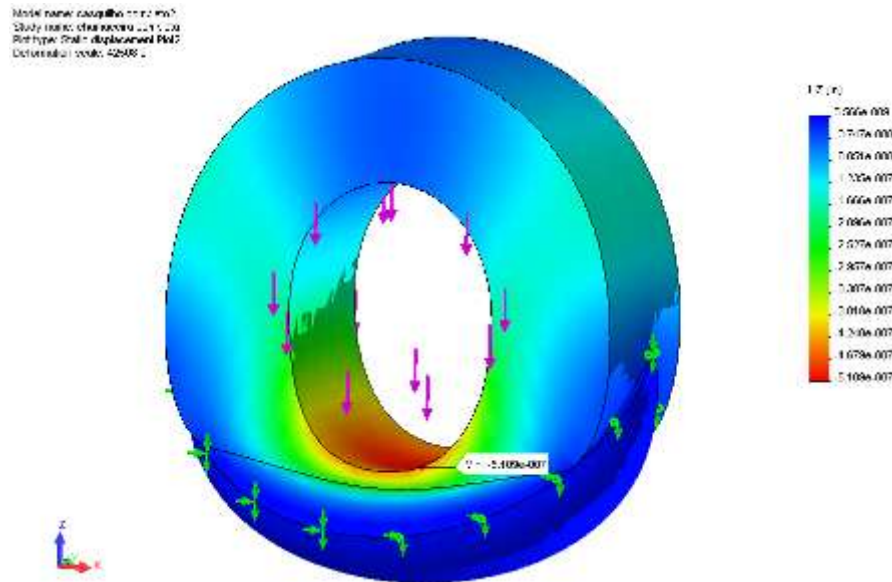


Figure IV-6 – Estimation of the vertical displacements caused by a load of 10kN applied to the LMS bearing with FEM solver CosmosWorks (simplified geometry; load type used was “Bearing Loads”).

A static sensor was used to measure the torque applied to the bush, T_b . Power loss, P , depends rather on the shaft torque, therefore, P was obtained from the following formula:

$$P = [T_b + e \cdot W \cdot \sin(\varphi)] \cdot \omega \quad \text{Eq. IV-5}$$

Where e is the shaft eccentricity, W is the applied load, φ is the attitude angle and ω is the angular velocity. Repeatability of the tests was checked. Each test was repeated at least once on a different occasion. Differences in maximum pressure and maximum temperature were, respectively, less than $\pm 0.01\text{MPa}$ and $\pm 1^\circ\text{C}$ in most cases. The accuracy of bush torque measurements was found to be significantly affected by the instrumentation attached to the bearing (thermocouple wires, proximity probe wires, oil feeding and oil measurement hoses), making it difficult to set the zero of the scale. Sometimes measurements between corresponding tests yielded differences as high as $0.5\text{N}\cdot\text{m}$. The values obtained should therefore be regarded with caution.

The geometric parameters and operating conditions, as well as lubricant properties, are presented in Table 1.

Table IV-1 - Bearing geometry, operating conditions, and lubricant properties

			Value/Span
Rotational speed	N	rpm	1000, 3000, 4000
Applied load	W	kN	2, 10
Feeding pressure	P_f	kPa	70, 140, 210
Feeding temperature	T_f	°C	35, 40, 50
Bush inner diameter (nominal)	d	mm	100
Bush outer diameter (including sleeve)	D	mm	200
Bush length	b	mm	80
Groove length	a	mm	70
Circumferential extension of each groove	w	mm	16
Diametral clearance (20°C)	C_d	μm	171
Lubricant viscosity (40°C)	μ_{40}	Pa.s	0.0293
Lubricant viscosity (70°C)	μ_{70}	Pa.s	0.0111
Lubricant thermal conductivity	K_l	W/mK	0.13
Bush thermal conductivity	K_b	W/mK	50
Lubricant density	ρ	kg/m ³	870
Lubricant specific heat	C_p	J/kgK	2000
Ambient temperature (inside protection box)	T_{amb}	°C	30 to 55

IV.3 Results and Discussion

Results concerning the influence of the feeding pressure and feeding temperature on bearing performance for different sets of working conditions will be presented and analyzed. Tests were carried out for two values of applied load: 2kN and 10kN. The former value is very low for the bearing under consideration, but is of theoretical interest. Three different values of the shaft rotation speed were considered: 1000, 3000 and 4000rpm. Three different values of both the feeding pressure and feeding temperature were tested: 70, 140, 210 kPa and 35, 40, 50°C, respectively. In each case, the measured parameters were: hydrodynamic pressure and temperature fields, oil flow rate, bush torque, and position of the shaft center relative to the bush. The power losses in the bearing were deduced from the measured torque.

IV.3.1 Effect of changes in feeding pressure

a) Hydrodynamic pressure distribution and position of shaft center

Figure IV-7 represents the hydrodynamically generated pressure profile at the mid-plane of the bearing. This was obtained from tests at two different feeding pressures (70 and 210 kPa) and under two different loads (2 and 10kN). The maximum pressure is also given for the high loaded case in Figure IV-7c. The angle origin is located at the center of the upstream groove: the two feeding grooves here are called the upstream and downstream grooves, depending on whether the groove is located upstream or downstream of the minimum film thickness. The

lower and upper halves of the bush here are called the loaded and the unloaded lobes of the bush, reflecting the different contribution of the hydrodynamic pressure field in the two lobes.

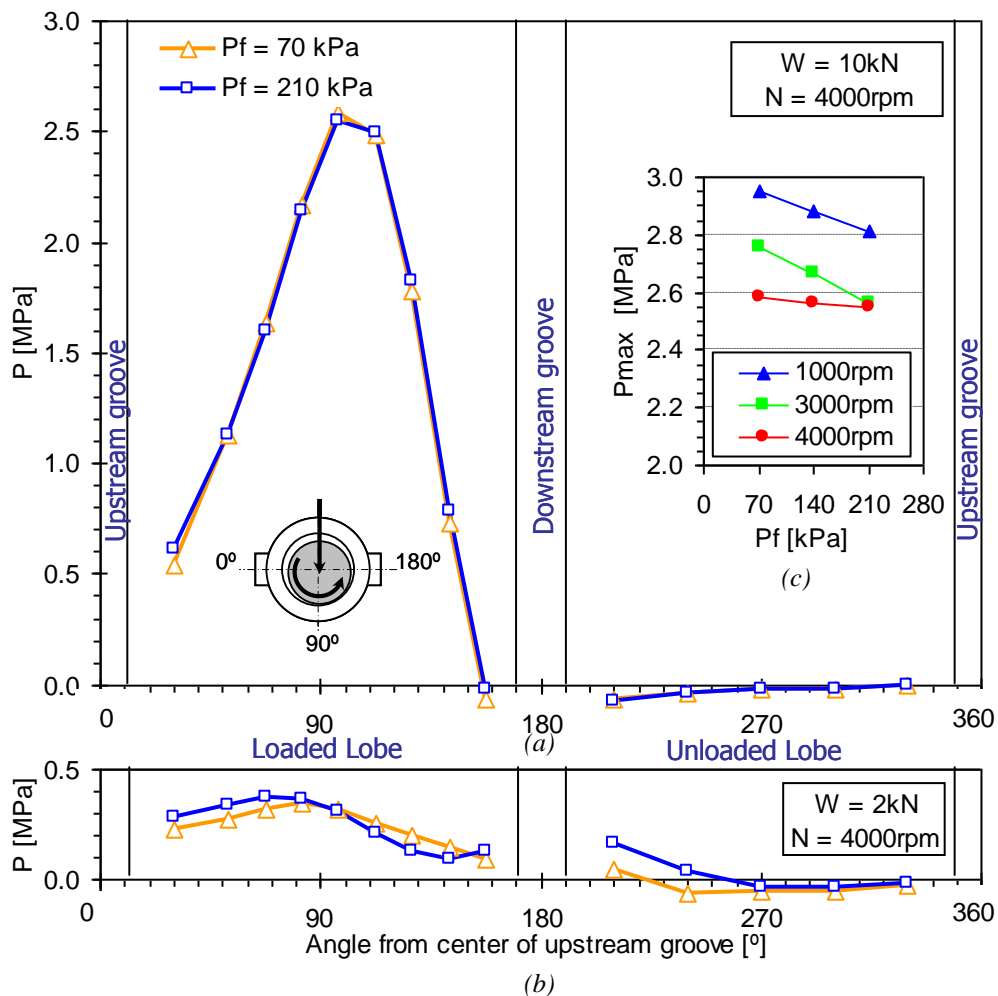


Figure IV-7 - Pressure profiles for (a) 10kN, 4000rpm tests, (b) 2kN, 4000rpm tests, and (c) maximum pressure values ($T_f = 40^\circ\text{C}$).

In Figure IV-8 it can be seen that the pressure build-up at the loaded lobe is followed by the rupture zone where cavitation takes place. Under high load (10kN, Figure IV-7a) the pressure starts at a negative (sub-ambient) value in the unloaded lobe, gradually reaching zero. Similar pressure profiles have been obtained by Lund and Tonnesen (1984). Under low load (2kN, Figure IV-7b) the pressure is still positive after the downstream groove. This is so because the film rupture takes place further downstream due to the lower eccentricity. It can also be observed that an increase in feeding pressure further delays the film rupture.

The differences between pressure profiles for different feeding pressures are small, but it can be noted from Figure IV-7c, that for the tests with a load of 10kN, the maximum pressure decreases with the increase in both feeding pressure and rotational speed. This is in good agreement with Figure IV-8, where it can be observed that the eccentricity decreases and the attitude angle increases with rises in the value of those parameters. This means that the load capacity of the bearing has improved. Under these conditions, lower pressure peaks and wider

positive pressure zones generally occur. Reasons for the increase in load capacity with feeding pressure can be related to the hydrostatic lift caused by the high feeding pressure. The extension of the continuous film zone, caused by the increase in the amount of oil, also contributes to this phenomenon.

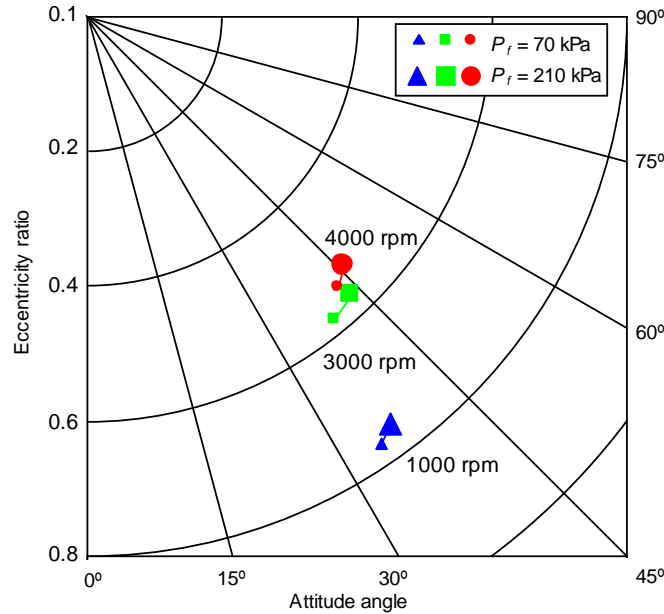


Figure IV-8 - Locus of the shaft center in relation to the bush center ($W = 10\text{kN}$; $T_f = 40^\circ\text{C}$).

For low loads (2kN), the rise in feeding pressure caused a wider extension of the continuous film associated with a wider zone of positive pressure at the unloaded lobe (Figure IV-7b). This causes an increase in power loss that can be confirmed in Figure IV-9. Under high loads (10kN, Figure IV-9b), the power loss did not change significantly with the increase in feeding pressure. A reason for this may be the fact that the full film region does not seem to change significantly with the increase in feeding pressure, as seen in Fig. 5(a).

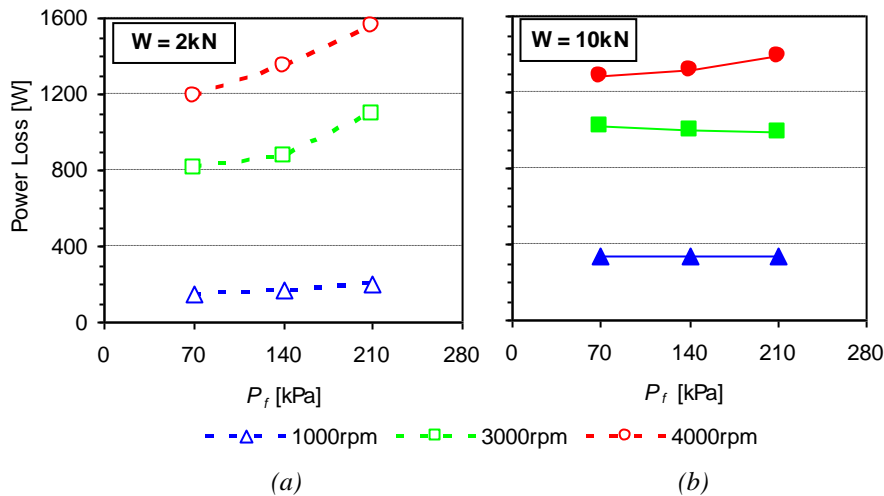


Figure IV-9 - Influence of speed and feeding pressure on power loss for (a) $W = 2\text{kN}$, (b) $W = 10\text{kN}$ ($T_f = 40^\circ\text{C}$)

b) Oil flow rate

Figure IV-10 shows the significant increase in oil flow rate with increasing feeding pressure. The same tendency is observed for increasing rotational speed (increase in the Couette effect) and applied load (increase in pressure gradients which promote oil leakage and renewal). The largest relative change in the oil flow rate is obtained using the lowest rotational speed (1000rpm), and it increases by 104% when the feeding pressure is increased from 70 to 210kPa.

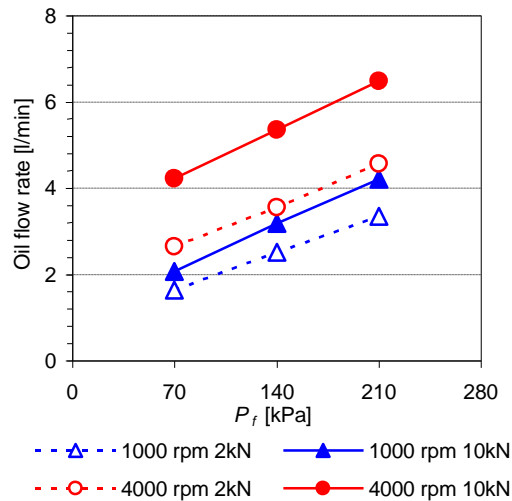


Figure IV-10 – Influence of feeding pressure on oil flow rate for variable rotational speed and applied load ($T_f = 40^\circ\text{C}$).

c) Temperature distribution

Figure IV-11 shows the temperature profiles at the mid-plane of the bush inner surface for two different values of applied load and feeding pressure. The shaft temperatures are also displayed.

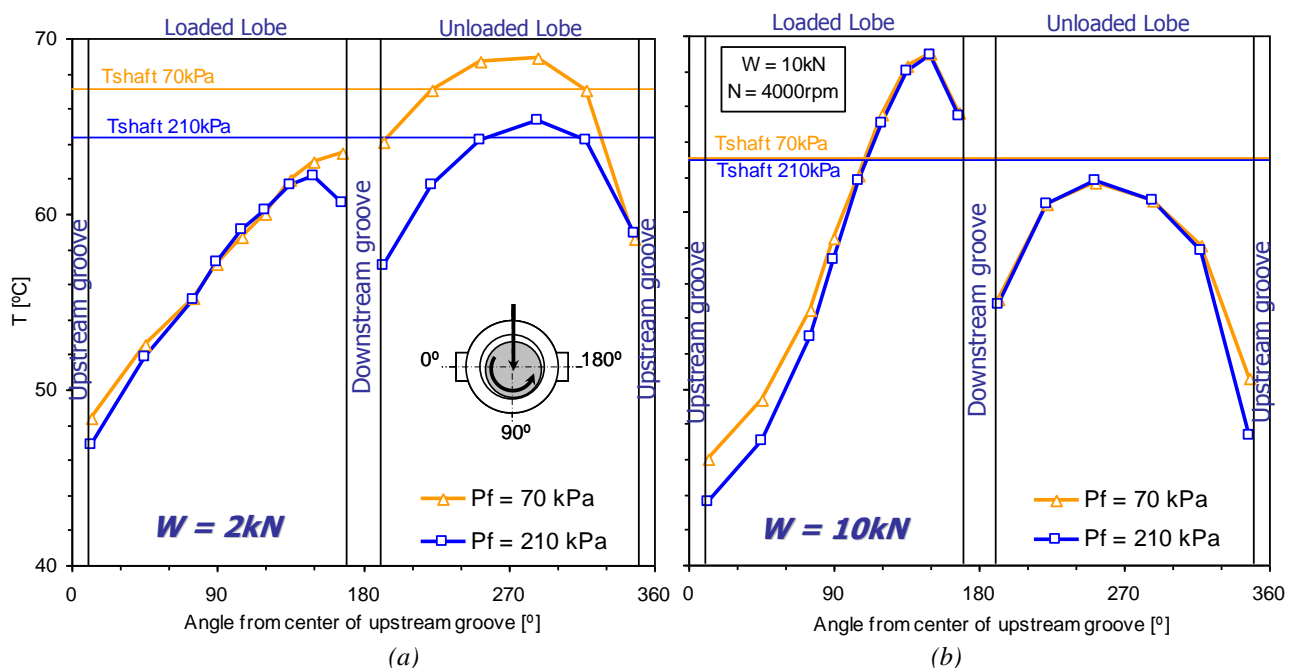


Figure IV-11 - Influence of the feeding pressure on the temperature profile at the mid-plane of the bush-film interface, for a load of (a) 2kN and (b) 10kN ($N = 4000\text{rpm}$; $T_f = 40^\circ\text{C}$)

For the lowest load value (2kN, Figure IV-11a), the maximum temperature occurs in the unloaded lobe. In this case there is a significant temperature drop across the upstream groove (10.2°C and 12.0°C for feeding pressures of 70kPa and 210kPa, respectively), while the cooling effect of the downstream groove is only significant if the feeding pressure is high (3.6°C for 210kPa). For the highest applied load (10kN, Figure IV-11b) the maximum temperature is located in the loaded lobe. Here the temperature drop across the upstream groove is less pronounced (4.6°C and 3.8°C for feeding pressures of 70kPa and 210kPa, respectively), while the cooling effect of the downstream groove becomes more effective. The high pressure gradient in the loaded lobe promotes an increase in oil flow outwards, causing an increase in oil renewal at the downstream groove even at low feeding pressures. The temperature fall across this groove was about 10.5°C independently of the value of feeding pressure. Under low loads, however, much of the oil is recirculated, so the downstream groove contributes only poorly to the cooling of the bearing unless the feeding pressure is high. Therefore, the increase in feeding pressure had a positive effect in terms of lowering the maximum temperature of the bearing only under low load conditions. Figure IV-12a shows that the strongest decrease in the maximum temperature (3.5°C) occurs with a rotational speed of 4000rpm. The same trend was observed with the shaft surface temperature, as depicted in Figure IV-12 b. However, the oil outlet temperature always decreased with the increase in feeding pressure, as shown in Figure IV-12c. The maximum decrease (4.7°C) is obtained for the high speed / low load conditions.

Under low loads and low feeding pressures, the inner bush surface temperature profile approaches that of a bearing with a single axial groove located at 90° in relation to the loading line.

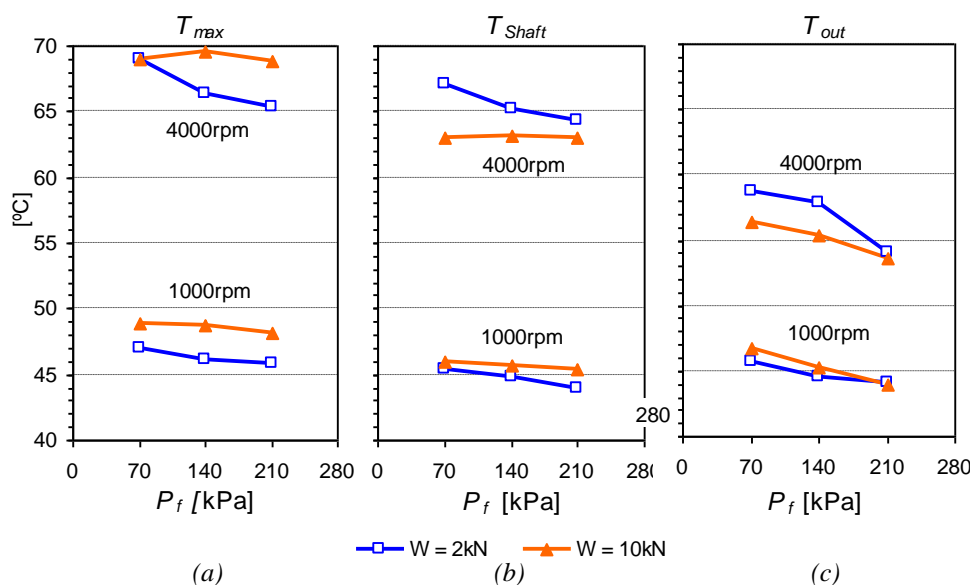


Figure IV-12 - Influence of the oil feeding pressure on (a) the maximum temperature at the bush-film interface, (b) the mean shaft-film interface temperature and (c) the oil outlet temperature ($T_f = 40^\circ\text{C}$).

Results in the literature for this kind of bearings (for instance, Mitsui et al, 1983) showed that the location of maximum temperature tends to move towards the upstream direction as the load increases. For sufficiently high loads, the temperature peak will eventually occur before the downstream groove, as observed in Figure IV-11b for the 10kN tests. This explains why, under high applied loads (10kN), the increase in feeding pressure does not seem to significantly affect the maximum temperature at the bush and shaft interfaces. The main differences between 10kN tests lie in the upstream groove region. On the other hand, under low load (2kN), the increase in feeding pressure lowers the temperature both before and after the downstream groove, as is shown in Figure IV-11a.

IV.3.2 Influence of changes in feeding temperature.

a) Hydrodynamic pressure distribution and position of shaft center

Hydrodynamic pressure profiles at the mid-plane of the bush inner surface are presented in Figure IV-13, for a load of 10kN and two rotational speeds (1000 and 4000 rpm) and feeding temperatures (35 and 50°C).

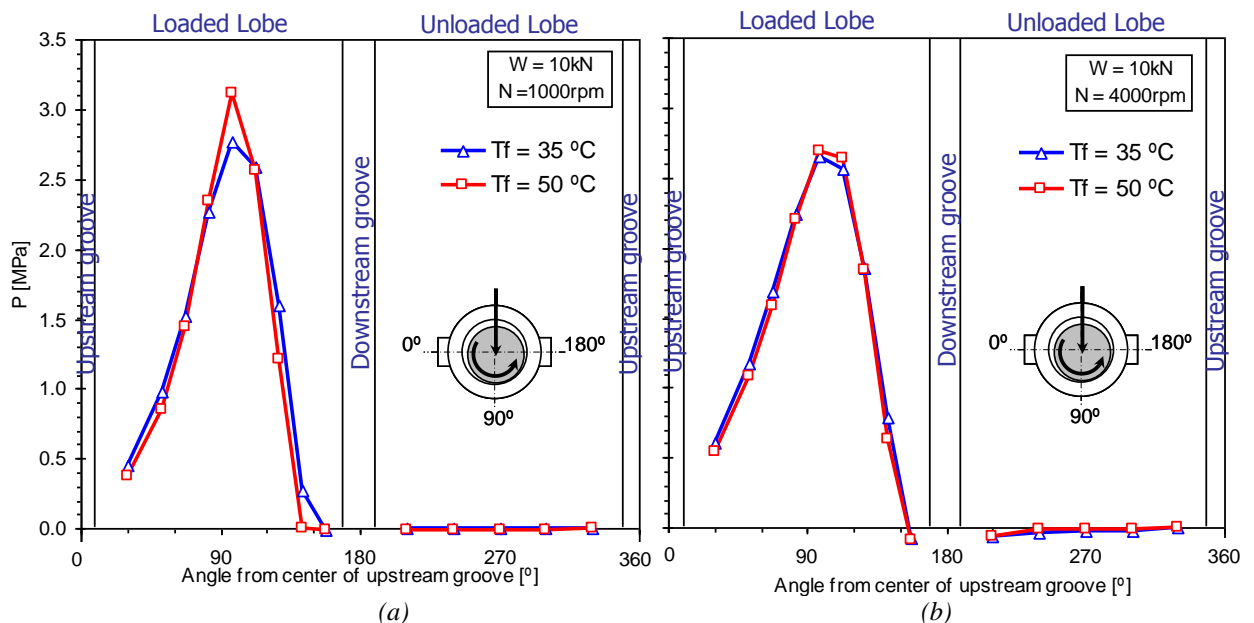


Figure IV-13 - Influence of the feeding temperature on the pressure profiles at the mid-plane of the bearing for (a) $N = 1000\text{rpm}$ and (b) $N = 4000\text{rpm}$ ($W = 10\text{kN}$; $P_f = 140\text{kPa}$)

One can note that the increase of feeding temperature yields greater pressure peaks and causes the pressure build-up zones to have slightly smaller angular extent, this being more pronounced at low rotational speed. This is associated with a decrease in the bearing load carrying capacity (higher operating eccentricity) due to increasing bearing temperature and subsequent lower viscosity, as is confirmed in Figure IV-14.

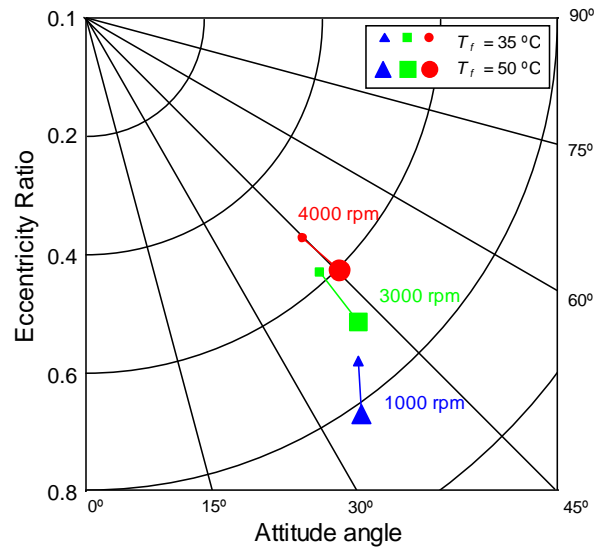


Figure IV-14 - Locus of the shaft center in relation to the bush center ($W = 10\text{kN}$; $P_f = 140\text{kPa}$).

b) Oil flow rate and Power loss

Figure IV-15 represents oil flow rate as a function of the feeding temperature, rotational speed (1000 and 4000rpm) and applied load (2 and 10kN). Increasing applied load promotes oil renewal as a consequence of the greater pressure gradients present in the lubricant film. Similarly, the increase in feeding temperature causes a drop in oil viscosity, thus increasing flow rate. The increase in oil flow rate varies from 1.0 to 1.3 l/min when the temperature increases from 30°C to 50°C, depending on operating conditions.

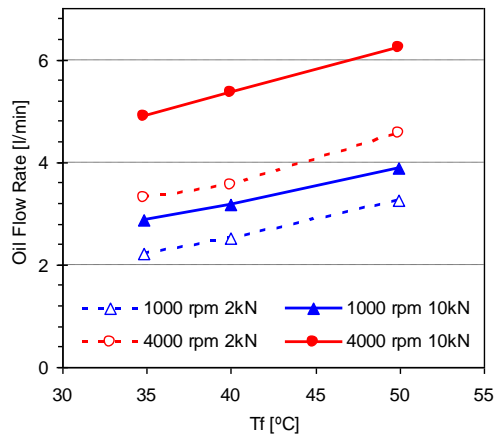


Figure IV-15 - Influence of oil feeding temperature in oil flow rate ($P_f = 140\text{kPa}$).

Power loss decreases with increasing feeding temperature, as shown in Figure IV-16a. This is due to the decrease of oil viscosity in the film, thus reducing lubricant shear rate. Under high loads, however, the increase of feeding temperature also increases significantly the eccentricity ratio (recall Figure IV-14). This effect, which causes the appearance of large velocity gradients through the film thickness, seems to counterbalance the above effect and leads to the power loss stability with variations in feeding temperature. When the feeding temperature increases

from 35 to 50°C the decrease in power loss varies from 18 to 55% for the 2 kN case and from 0 to 9% for the 10 kN, depending on the rotational speed.

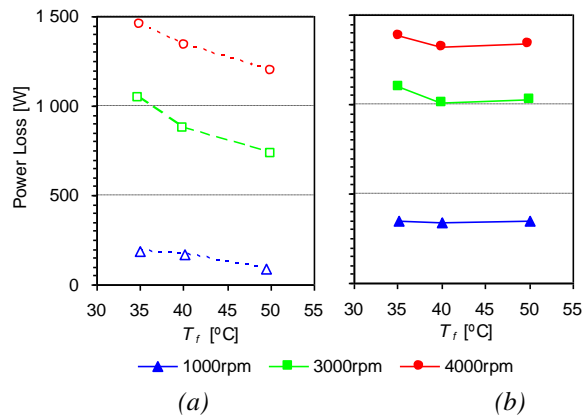


Figure IV-16 - Influence of oil feeding temperature on power loss for an applied load of (a) 2kN and (b) 10kN ($P_f = 140\text{kPa}$).

c) Temperature distribution

Figure IV-17 shows the temperature profiles at the mid-plane of the bush-film interface for a set of operating conditions and feeding temperatures. Shaft temperatures are also displayed (light horizontal lines).

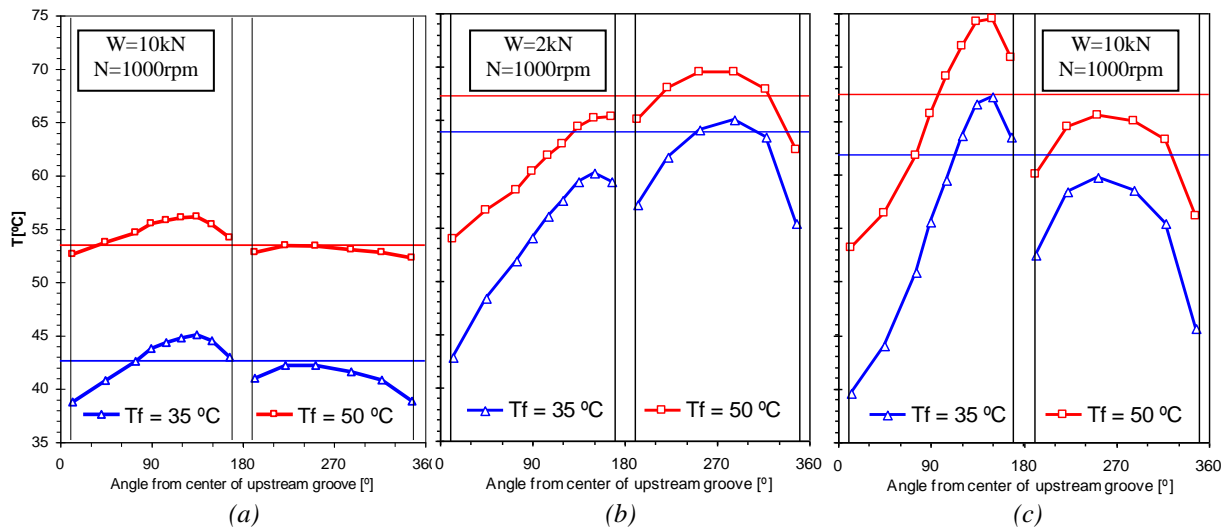


Figure IV-17 - Temperature profiles at the mid-plane of the bush-film interface for three different feeding temperatures with (a) $W = 2\text{kN}$, $N = 4000\text{rpm}$, (b) $W = 10\text{kN}$, $N = 1000\text{rpm}$, (c) $W = 10\text{kN}$, $N = 4000\text{rpm}$ ($P_f = 140\text{kPa}$)

The results for lightly-loaded conditions (low load and high velocity) are depicted in Figure IV-17 a. The general temperature profile obtained has already been discussed in association with Figure IV-10. Figure IV-17b,c show the temperature profiles for a low (1000rpm) and a high (4000rpm) rotational speed, the applied load here being 10kN. The temperature profiles exhibit the same trend of variation for all values of feeding temperature tested.

Increasing feeding temperature resulted in the increase of the bush-film interface temperature. However, the increase in maximum bush-film interface temperature was always less than the

corresponding increase in oil feeding temperature. For $N = 4000\text{rpm}$ (Figure IV-17c), the increase of the former was between 30% (low load) and 50% (high load) of the increase recorded for the feeding temperature. Increasing rotational speed caused a general increase in bush-film interface temperature, due to the increase in energy dissipation.

It can also be noted that, as the feeding temperature increased, the temperature decrease across the groove zones was smaller, because of the hotter feeding oil entering the grooves.

Comparing the three figures, it can be observed that the higher the eccentricity ratio, the further upstream the maximum temperature occurs. This could be due to the fact that, as eccentricity increases, the film becomes more divergent. This promotes the appearance of film rupture further upstream (compare the pressure profiles in Figure IV-13a and Figure IV-13b, and the corresponding eccentricity ratios in Figure IV-14). The heat generated in cavitated films is very low compared with the heat generated in continuous lubricant film, as it contains as it contains gas bubbles which have low viscosity.

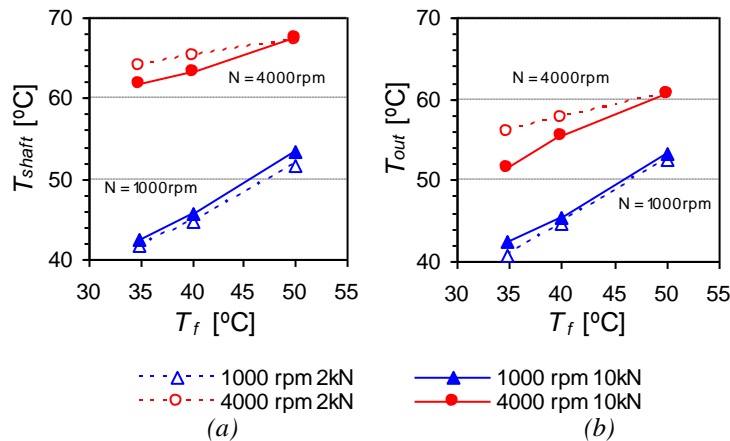


Figure IV-18 - Influence of oil feeding temperature on (a) the mean shaft-film interface temperature and (b) the oil outlet temperature ($P_f = 140\text{kPa}$)

The temperature of the shaft-film interface (T_{shaft}) presented in Figure IV-18a and the oil outlet temperature (T_{out}) presented on Figure IV-18b are significantly affected by shaft speed. T_{shaft} is only slightly affected by load, while the effect of this parameter on T_{out} is only significant at low values of the feeding temperature and high rotational speed. At low speed ($N=1000\text{rpm}$) T_{shaft} is very close to T_{out} . At high speed ($N=4000\text{rpm}$), T_{shaft} is significantly higher than T_{out} .

Comparing the values of T_{shaft} with the corresponding temperature profiles, presented earlier in Figure IV-17, it can be noted that the shaft temperature is very close to the maximum temperature for low load tests (2kN, Figure IV-17a). In high load tests (10kN, Figure IV-17b,c) however, T_{shaft} is 5 to 8°C below the maximum temperature and always above the peak temperature achieved at the unloaded lobe. This difference could be due to the fact that in low load tests the shaft is almost concentric with the bush while, under high load tests, there is a

highly convergent-divergent lubricant film. This yields more localized heat generation near the region of minimum film thickness. Under low loads however, the heat generation is less concentrated, and there is a low rate of oil renewal. Under these circumstances a greater thermal uniformity is expected, with T_{max} being closer to the value of T_{shaft} .

IV.4 Conclusions

Experimental investigations of the influence of the feeding temperature and pressure on the steady-state performance of a two-grooved plain journal bearing were carried out for a set of operating conditions. Results concerning the temperature and pressure fields inside the bearing, oil flow rate, power loss, and the position of shaft center have been presented above and discussed. The following conclusions can be drawn:

- i) Increasing feeding temperature increases oil flow rate, shaft eccentricity and maximum temperature. The observed increase in maximum temperature is significantly lower than the corresponding increase in feeding temperature.
- ii) Shaft temperature and oil outlet temperature were mainly affected by feeding temperature and rotational speed. At high shaft speeds, the mean shaft temperature is significantly higher than the outlet temperature.
- iii) The increase in feeding pressure yields an increase in oil flow rate, a decrease in oil outlet temperature and a slight increase in the attitude angle and minimum film thickness.
- iv) Under low applied loads the cooling effect of the upstream groove is apparent, while the cooling effect of the downstream groove is only significant at high feeding pressures. Maximum temperature occurs in the unloaded lobe of the bearing, being only slightly higher than the mean shaft surface temperature.
- v) Under high applied loads the cooling effect of the upstream groove becomes weaker, while the cooling effect of the downstream groove is significant no matter the value of the feeding pressure. Maximum temperature occurs at the loaded lobe of the bearing, and was found to be 4 to 8°C higher than the shaft surface temperature for the conditions tested.

The major difference between a thing that might go wrong and a thing that cannot possibly go wrong is that when a thing that cannot possibly go wrong goes wrong, it usually turns out to be impossible to get at and repair.

- Douglas Adams (in "Mostly Harmless")

CHAPTER V Experimental work at the University of Minho

V.1 Introduction

The present chapter describes the experimental work carried out with the test rig at the Tribology Laboratory of the University of Minho (LOMT). This work is complementary of the experimental work carried out at the Solid Mechanics Laboratory of the University of Poitiers (LMS). In fact, while the LMS rig has the advantage of performing pressure profile and shaft temperature measurements, the LOMT rig allows the separate measurement of the flow rate in each groove. Additionally, several bearing geometries could be tested with the LOMT rig. The nominal bearing diameters of the two systems were also diverse.

Both works have the aim of providing a better understanding of the behavior of twin groove journal bearings in order to contribute to the improvement of bearing design and operation. In particular, these results were used within the scope of the present work for the validation and the refinement of the theoretical model, which puts a special emphasis on the analysis of the influence of lubricant supply conditions.

As already mentioned in CHAPTER II, the theoretical and especially the experimental published work focusing on the influence of supply conditions is rather scarce. Particularly, some issues such as the knowledge of the flow rate distribution along each groove, the comparison between the performance of single and twin groove bearings or a thorough investigation of the role of the lubricant supply conditions covering most of the factors which are related to them (feeding pressure, feeding temperature, clearance, etc) is practically non-existent. This work tries to address these issues.

The capabilities of the existing rig have been improved, namely the measurement of the flow rate at each groove, a thorough investigation on the role of each groove in the performance of twin groove journal bearings has been carried out.

V.2 Bearing test rig

V.2.1 Overview of the rig

The rig used in the present study has been used already in several experimental works, namely the PhD works of Claro (1994) and Costa (2000), but has been significantly modified for the present work. A detailed description of the core apparatus has been already presented by the former works and therefore the description of the rig given here will focus mainly on the updated components and on the new experimental approaches.

Figure V-1 shows a general view of the bearing test rig.



Figure V-1 – Bearing test rig of the Tribology Laboratory of the University of Minho.

The following operative parameters can be regulated:

- Rotational speed
- Applied load
- Lubricant feeding pressure
- Lubricant feeding temperature.

The following performance parameters can be measured (mainly through data acquisition):

- Temperature at the film-bush interface

- Lubricant outlet temperature
- Feeding temperature (before ramification) and temperature upstream of each groove
- Pressure inside each groove
- Total lubricant flow rate
- Lubricant flow rate at each groove
- Shaft locus.
- Motor consumption (measured only in some tests).

An outline of the test rig is presented on Figure V-2.

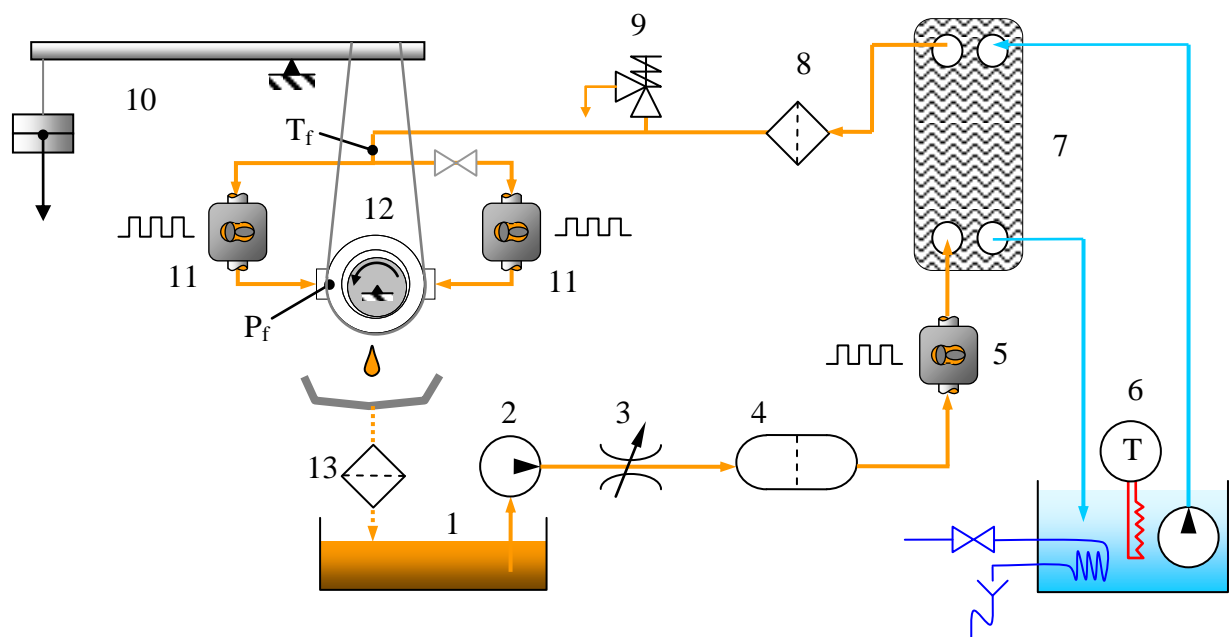


Figure V-2 - Overview of the test rig. (1) – Oil tank ; (2) - gear pump; (3) - flow regulation valve; (4) - pulse damping chamber; (5) electric pulse gear flow meter (total flow rate); (6) – temperature controlled water bath with outer circulation; (7) - plate heat exchanger; (8) – Filter; (9) - relief valve; (10) - loading system; (11) - electric pulse gear flow meters; (12) – Instrumented bearing system; (13) – Filter.

The lubricant coming from the tank (1) is pressurized through a gear pump (2). The lubricant then passes through a valve that regulates lubricant flow (3), a pulse damping chamber (4) and an electric pulse gear flow meter (5) which measures total flow rate.

In order to regulate the feeding temperature (T_f), the lubricant passes through a plate heat exchanger (7) whose primary circuit consists on a water circuit coming from a temperature controlled water bath with outer circulation (6).

Before the split into each groove, the lubricant still passes through a Y filter (8) and a relief valve (9). At each branch electric pulse gear flow meters (11) record the flow rate entering each groove of the bearing system (12).

The loading system (10) relies on dead weights which act on the bush body through a cantilever and a steel cable. The load is applied upwards to the bush body and therefore, a reaction force of equal value and opposite direction acts on the shaft, which is only allowed to rotate.

The lubricant leaking from the bearing gap returns to the tank after being filtered (13).

V.2.2 Bushes and shafts

Three bronze bushes with different lengths and groove widths and two stainless steel shafts with different clearances were used in the present study. All were designed and manufactured specifically for the present work, with the exception of one of the shafts (Shaft V1). Their main geometric characteristics are presented in Table V-1.

The various bush and shaft combinations allow the study of the influence of bearing length, groove length and clearance. The differences in diameter between the three bushes are not negligible as intended. Therefore, the influence of each parameter cannot be totally isolated.

Table V-1 – Geometric parameters and metrological characterization of the bushes and shafts used in the work

	Geometric parameters					With Shaft V1		With Shaft V2	
	Outer diameter D [mm]	Inner diameter d [mm]	Bush length to diameter ratio b/d	Groove length ratio a/b	Groove circumferential extension w/d	Clearance C_d [μm]	C_d/d ($\times 10^{-3}$)	Clearance C_d [μm]	C_d/d ($\times 10^{-3}$)
Bush B1	100	50.091	0.8	0.8	0.2	72	1.44	94	1.87
Bush B2		50.104	0.8	0.5		86	1.71	107	2.14
Bush B3		50.073	0.5	0.8		54	1.08	76	1.51
Shaft V1	50.019								
Shaft V2	49.997								

Metrologic data such as cylindricity and roughness are presented in Table V-2. The diameters and the cylindricity of the components were measured using a coordinate measuring machine (Mitutoyo BHN706) with a resolution of $0.1\mu\text{m}$ and repeatability between 1.4 and $1.8\mu\text{m}$, depending on the axis of measurement. The roughness was measured through a mechanical profile meter (Mahr-Perthen S5P Perthometer) with a resolution of $0.001\mu\text{m}$.

Table V-2 – Metrological data of the bushes and shafts

	Metrology				
	Cilindricity [μm]	R_a [μm]	R_{max} [μm]	R_z [μm]	R_T [μm]
Bush B1	21	0.4	3.5	3.1	3.7
Bush B2	10	0.5	6.4	3.8	6.6
Bush B3	6	0.6	5.7	4.2	5.7
Shaft V1	3	0.5	7.9	4.8	8.4
Shaft V2	10	0.7	7.9	5.5	7.9



Figure V-3 - the shaft V2 and the bush B3.

The shafts, one of them shown in Figure V-3, were made of steel (X22-CrNi17) and were rigidly mounted through two preloaded conical rolling bearings, assuring a good stiffness to the system (Claro, 1994). The excess axial and radial clearances were eliminated by using a rectified spacer ring that was machined down to an adequate thickness.

The bushes were made of bronze (RG5-CuSn5ZnPb). Care was taken in order to suitably incorporate the lubricant feeding system and the pressure, the proximity and the temperature sensors, as shown in Figure V-4 and Figure V-5.

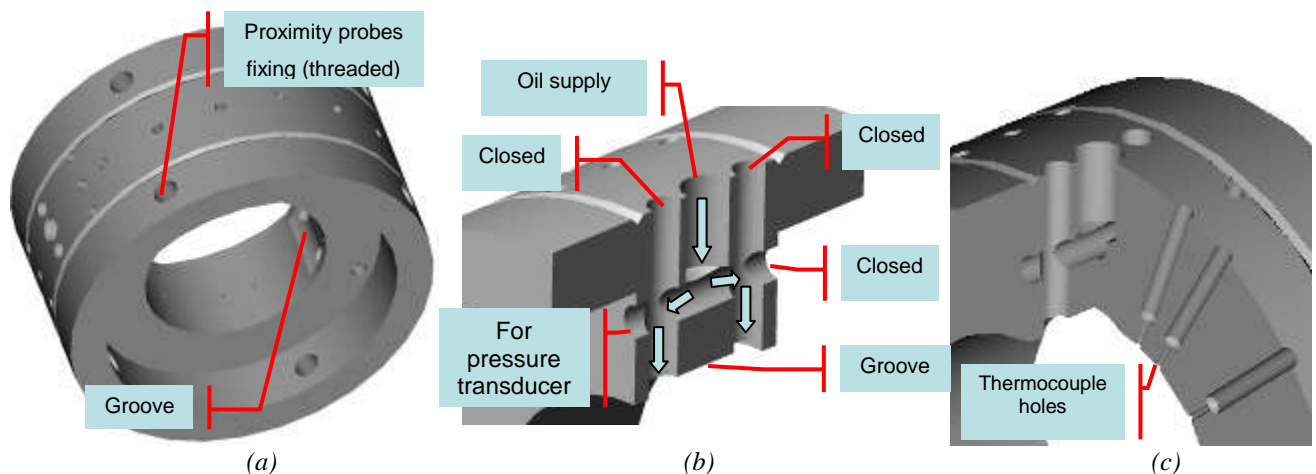


Figure V-4 – 3D drawings of one of the bushes: (a) general view; (b) detail of the thermocouple holes; (c) detail of the feeding system.

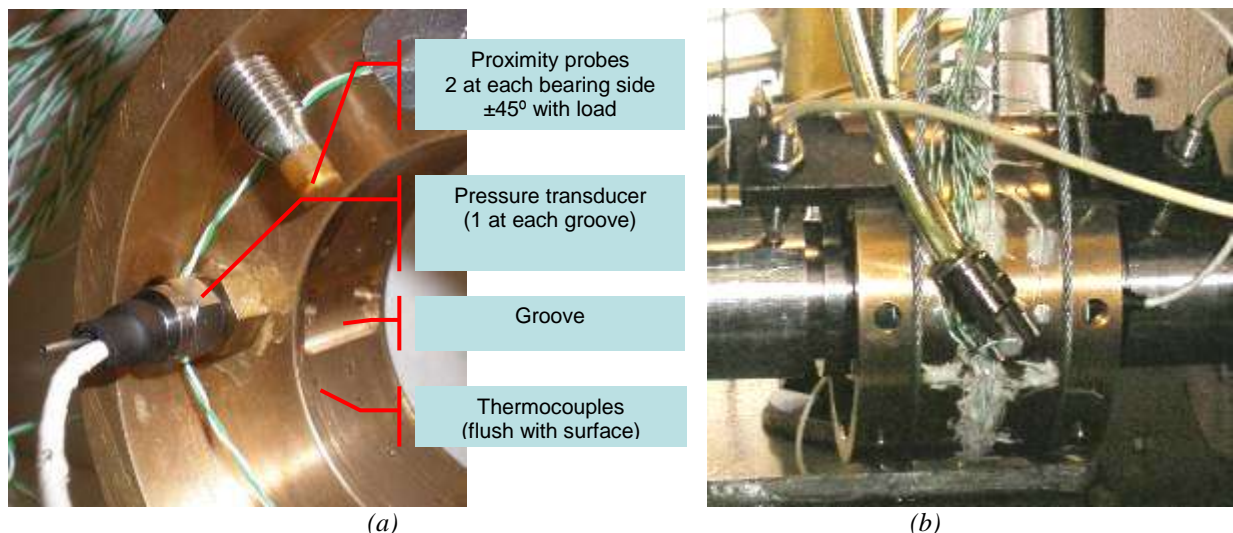


Figure V-5 – (a) detail of sensor mounting (bush B3); (b) instrumented and loaded bush (B1) with alternative proximity probe mounting.

V.2.3 Shaft motion control

The shaft was driven by a *Leroy-Somer* 0.95kW variable speed motor through a transmission belt (1:3 transmission ratio). The speed of the motor was regulated through an inverter drive

(Telemecanique Rectivar VA3). The speed of the shaft, which can vary from 0 to nearly 5000rpm, was kept within a range of ± 15 rpm of the nominal rotational speed. A contactless optical tachometer with a repeatability of ± 1 rpm was used to periodically assess the rotational speed (see experimental procedure in section V.3).

V.2.4 Loading system

The loading system is depicted in Figure V-6. It consists of a rod acting as a cantilever between the calibrated weights at one side and the bush body at the opposite side.

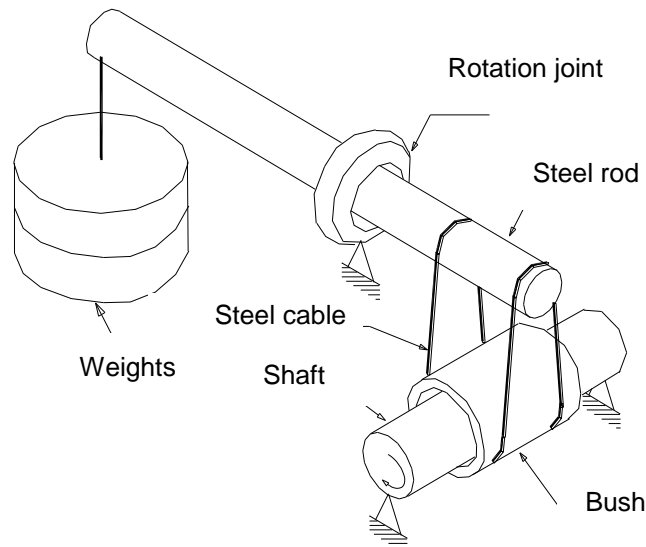


Figure V-6 – Loading system (adapted from Costa, 2000)

According to Costa (2000), the system was calibrated with a load cell whose non-linearity and hysteresis were found to be less than $\pm 0.04\%$ and $\pm 0.03\%$ of the whole scale (0.5 to 4kN) respectively, according to the NIST standards and the norm EN 10002-3(1994). The obtained relation between the total mass, M , of the calibrated weights and the resulting applied load, W , was the following:

$$W[N] = (40.9 + 9.12 \cdot M[kg]) \cdot 9.81 \quad \text{Eq. V-1}$$

V.2.5 Lubricant feeding system and feeding pressure regulation

The lubricant feeding circuit has already been sketched in Figure V-2. The lubricant is supplied to the bearing through a gear pump with a nominal flow rate of 0.6 l/s at 1.6MPa, which is moved by a 0.37 kW electric motor. The pressure fluctuations are smoothed through a pulse damper chamber located downstream of the pump and the regulating valve.

The lubricant is filtered both before and after passing through the bearing system. The lubricant feeding lines are attached to the bearing system through quick fit chromed brass elbows which are free to rotate.

Since the present study does not encompass the study of the performance of the lubricant, standard ISO-VG32 non-additivated oil was selected and used throughout the tests. The properties of this oil (GALP HIDROLEP 32) are displayed in Table V-3.

Table V-3 – Lubricant characteristics (GALP HIDROLEP 32)

Parameters		Units	Value
Lubricant properties			ISO VG 32
- Dynamic viscosity at 30°C	μ_{30}	Pa.s	0.0467
- Dynamic viscosity at 40°C	μ_{40}	Pa.s	0.0283
- Dynamic viscosity at 75°C	μ_{75}	Pa.s	0.0083
- Dynamic viscosity at 100°C	μ_{100}	Pa.s	0.0048
- Viscosity index	V.I.	-	106
- Specific Heat	C_p	J/kgK	2000
- Density (at 20°C)	ρ	kg/m ³	873
- Thermal conductivity	k	W/mK	0.13

A fine adjustment valve regulates the lubricant flow so that the prescribed feeding pressure (P_f) is kept within ± 2 kPa of the setpoint.

The feeding pressure is measured through miniature transducers whose tip is inserted in the interior of each groove, as depicted in Figure V-4b and Figure V-5a. The feeding pressure is considered to be the highest value of the two (usually occurring at the +90° groove). The sensors are piezo-resistive transducers (DRUCK PDCR200 miniature series) and are attached to digital process indicators (Druck DPI 280). The combined non-linearity and hysteresis of the system is $\pm 0.3\%$ and the temperature effects encompass a total error band of 1.5% from 10°C to 60°C. The zero of the indicator was reset before each test session. In order to reduce the random error and the excessive oscillation of the displayed values, a moving average of the last 25 readings was set to be displayed every 0.5 seconds. Additionally, an external 5VDC buzz alarm was incorporated into the system for security reasons, being activated both below 40kPa and above 500kPa.

V.2.6 Feeding temperature regulation system

The feeding temperature (T_f) was regulated via a water thermostatic bath with outer circulation (HAAKE C10) passing through a plate heat exchanger (20 plate Alfa Laval DOC52) in order to heat the lubricant. The temperature of the bath was regulated so that T_f was kept within a range of $\pm 0.2^\circ\text{C}$ from the set point.

T_f was checked by a thermocouple located in the main feeding line, just upstream of the point where the flow is separated in two branches in order to feed each groove. Additionally, two other thermocouples were located just before each groove entrance (Figure V-5b).

In the rare cases where oil cooling was needed (high speed tests with low feeding temperature), an external circuit of water flowing at ambient temperature was allowed to pass through a secondary coil in order to cool the thermostatic bath (see Figure V-2).

In spite of the inherent thermal inertia of this system (the sensor is away from the regulation device) it was possible to maintain a quite stable and accurate feeding temperature. This should be due not only to the bath's thermostat efficiency in maintaining a very stable bath temperature (due to power modulation, oscillations were as low as $\pm 0.1^\circ\text{C}$) but also due to the fact that the heat exchanger is largely over-dimensioned, if one takes into account the rather small flow rates which are at stake.

V.2.7 Data acquisition system

a) Acquisition Card

The signal coming from the thermocouples, the flow meters and the proximity probes was recorded by a data acquisition card installed in a PC. The card *Keithley DAS-801* possesses 8 analog input channels (either single-ended or differential), with a 12 bit Analog-to-digital converter (ADC), 40kHz of maximum sample rate, a maximum measuring range of $\pm 10\text{V}$ in bipolar mode (for the minimum gain of 0.5) and $+10\text{V}$ in unipolar mode. The accuracy of the system is reported to be $\pm 0.01\%$ of the full scale ($\pm 1\text{bit}$ typical).



Figure V-7 – Data acquisition control panel – thermocouples and CJC sensors.

The software used for the interaction between the PC and the data acquisition card was the Keithley ExcelLinx, which works as an add-on within the Microsoft Excel environment (see Figure V-7). This allowed a straightforward acquisition and post-processing of the measurements within the same environment.

b) Multiplexing cards

In order to overcome the 8 channel limitation, two of the channels were multiplexed into 8 new channels each, through two Keithley EXP-800 multiplexer cards. Sixteen thermocouples were attached to this system. These cards are suitable for thermocouple measurements as they include Cold Junction Compensation (CJC), which consists on precision thermistors ($24.4\text{mV}/^\circ\text{C}$) which record the reference temperature (the temperature of the location where thermocouples are attached) that is used to compute the total temperature measured by each thermocouple.

The multiplexer cards allow the application of high gain (500x), something which is especially useful when dealing with the typical low output voltage of thermocouples measuring moderate temperature differentials, as in the present study.

c) Electrical calibration of the system

The main drawback of multiplexing systems is that they might influence slightly the measurements due to tiny signal losses. In fact, this effect was observed: For the same input voltage slightly different values were obtained with each multiplexer card. A voltage difference equivalent to 3°C was recorded between the measurements of each card. To palliate this error source the gains were set to their maximum (500x). Additionally, an electrical calibration of the system was carried out.

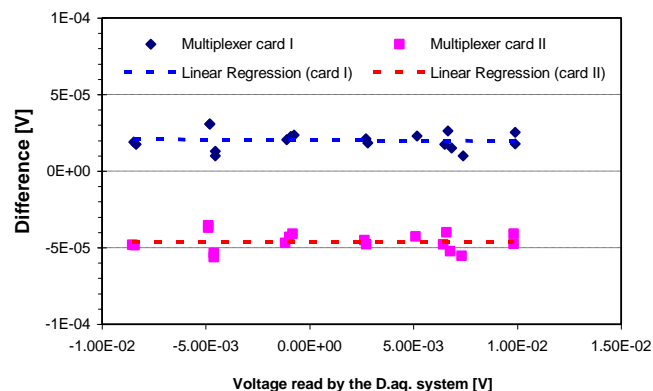


Figure V-8 - Difference between the voltage acquired by the Data Acquisition card and its accurate measurement with a precision voltmeter.

A DC power supply with variable output was attached to all 16 channels of the multiplexer system. Voltages within the expected working range of type K thermocouple were acquired

simultaneously by the card and by a precision multimeter with a resolution of $0.1 \mu\text{V}$. It was found that the signal needed only a zero correction for each card (-2.05×10^{-5} and $+4.57 \times 10^{-5} \text{V}$ respectively). This can be easily confirmed in Figure V-8 by the nearly horizontal least squares linear regression lines. This means that the error is independent of the magnitude of the measured value.

d) Sensor switching

It was necessary to measure a number of parameters that was actually higher than the number of channels. The solution found was to attach 2 different sensors to the same input channel and to commute them between measurements through manual switches. This allowed the alternate signal acquisition of two different sensors using one single channel. In particular, this was applied to the alternate measurement of flow rate and shaft locus (proximity probes).

V.2.8 Temperature measurement

a) Thermocouple locations

The temperature was measured using thermocouples located as follows:

- In the main feeding pipe (upstream of flow ramification to each groove) and in the pipes feeding each groove.
- At the oil exit, 180° to the load line (see Figure V-9b)
- At the locations of the bush-film interface depicted in Figure V-9a
- At the ambient – hanging freely at a distance of approximately 100mm from the bush.
- The thermocouples were positioned (glued) flush with the inner bush surface as seen in Figure V-9b.

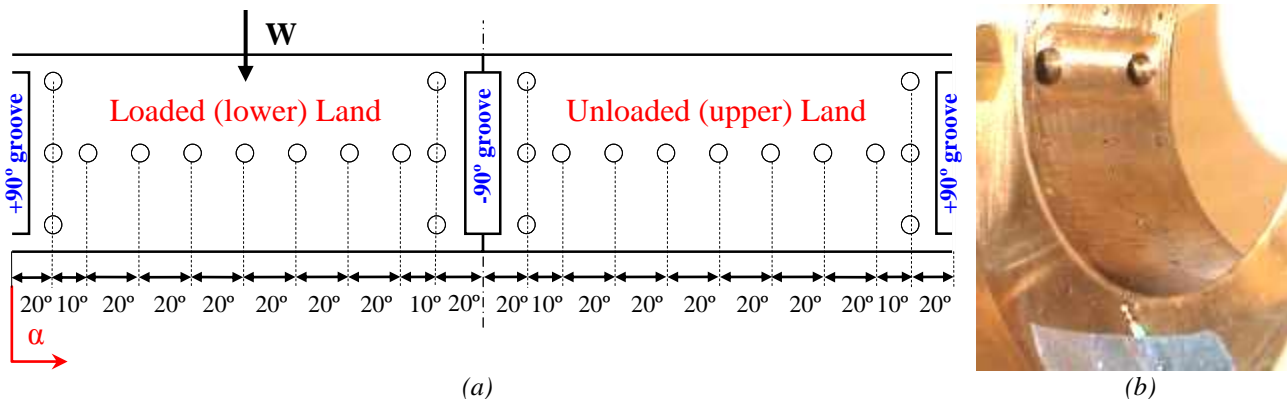


Figure V-9 – (a) - Thermocouple distribution along the inner surface of the bush (planified view) (b) – detail of the outlet temperature thermocouple and some of the thermocouples located at the inner bush surface (bush B3).

b) Thermocouple specifications

Initially, thermocouples were manufactured in the laboratory with existent thermocouple wire. Nevertheless, neither TIG soldered nor tin brazed thermocouple heads provided sufficient repeatability. Therefore, commercial type K (Nickel/Chromium - Nickel/Aluminum) PTFE insulated thermocouples (RS 219-4315) were installed. These thermocouples display a reported repeatability of $\pm 0.75\%$. Since the temperature differentials typical of the tests performed is rather small, several solutions were tested in order to improve the repeatability of the temperature measurements, which is described below.

c) Custom thermocouple calibration

The compliance with the standard calibration curve for type K thermocouples[§] was checked and it was found that the thermocouples overestimated the actual temperature by a proportional factor, as seen in Figure V-10. This happened even after the electrical calibration of the data acquisition system was applied, as described in the previous section. Fortunately, rather than a random, non-controllable error, this was a systematic error, and to a certain extent, could be corrected. Therefore, it made sense to perform a custom calibration curve based on actual temperature observations rather than using the standard curve for type K thermocouples.

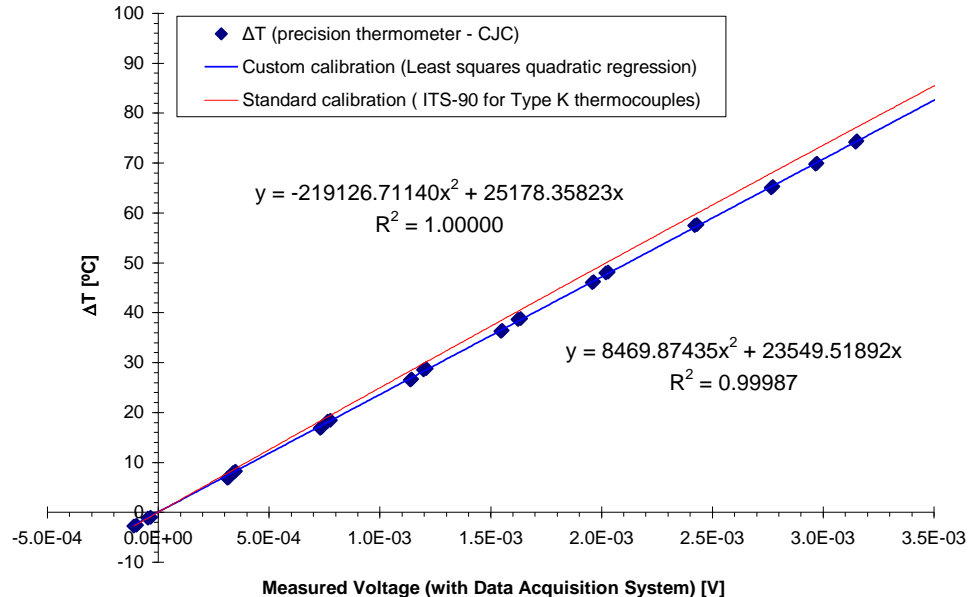


Figure V-10 – Comparison between the standard type K thermocouple calibration curve and the custom calibration curve obtained for the thermocouples used in the study.

While the thermocouples were immersed in the thermostatic bath, the temperature was registered with a precision mercury bulb thermometer (resolution of 0.1°C) and the signal was measured by the data acquisition system. The calibration curve was obtained by quadratic

[§] NIST ITS-90 Table for type K thermocouples in http://srdata.nist.gov/its90/download/type_k.tab

regression of the average of the measurements of all the thermocouples, as seen in Figure V-10. This curve makes the correspondence between the measured voltage and the corresponding ΔT (the actual temperature minus the reference temperature provided by the *CJC* sensor). In order to build the curve, several measurements were made over a temperature range of 20 to 100°C (corresponding approximately to a ΔT between -5°C and 75°C). The scattering of the average signal around the calibration curve was very low: generally less than $\pm 0.3^\circ\text{C}$ and never above $\pm 0.6^\circ\text{C}$. The standard deviation of the values measured by all the 16 thermocouples was always below 0.16°C . This means that about 70% of the values were within $\pm 0.16^\circ\text{C}$ of the average value and about 95% were within $\pm 0.32^\circ\text{C}$, admitting a normal distribution of the error (Lyons, 1991).

d) Cold junction temperature uniformization

Another problem related to the accuracy of temperature measurements was some data scattering due to slight differences of the cold junction temperature of each thermocouple (temperature at the connector side). Ideally, this temperature should be the same for all the thermocouples and equal to the *CJC* sensor temperature. However, the heating caused by the electronic components originated temperature gradients along the thermocouple connector card. By cooling the multiplexer enclosure with a dedicated fan, the differences between thermocouples were significantly mitigated.

e) Averaging and noise filtering

To reduce random error, temperature values were always obtained from an average of 100 measurements for each thermocouple at an acquisition rate around 500Hz. Some noise overshoots were often detected in the signal, especially in high speed tests. This noise was effectively filtered by calculating the average signal with a trimmed mean, by rejecting the 10% data further outside the average. An example of signal noise is presented in Figure V-11.

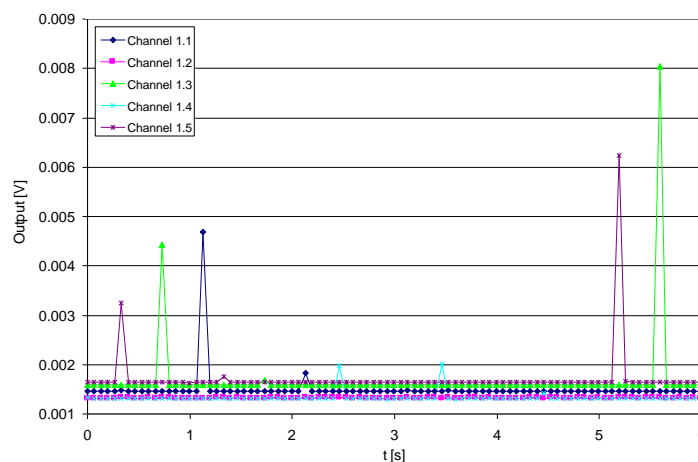


Figure V-11 - Example of signal noise in thermocouple data acquisition (Bearing B1V1; $N=4000\text{rpm}$; $W=5\text{kN}$; $T_f=40^\circ\text{C}$; $P_f=250\text{kPa}$)

V.2.9 Lubricant flow rate measurement

As noted in the State of the art Chapter, one of the novelties of this work is the accurate and systematic measurement of the flow rates entering through each groove. In the particular case of twin groove journal bearings, the study of the flow rates in each groove has been almost always disregarded, with the exception, to the author's knowledge, of the work by Basri and Neal (1990), where they presented a limited set of results which included a separate measurement of the flow rate at each groove.

The lubricant flow rate is an important performance parameter because the pumping system dimensioning is based on this parameter. Furthermore, it is an important factor for the validation of numerical models for the prediction of bearing performance.

a) Multiple flow meter approach

The original LOMT rig possessed an electrical pulse (Hall effect) gear flow meter (Hydrotechnik ZD2-030) which proved its suitability for single groove bearing tests (Claro, 1994, Costa, 2000). However, with twin groove journal bearings the flow rate at each groove may be significantly different, as shown by Basri and Neal (1990).

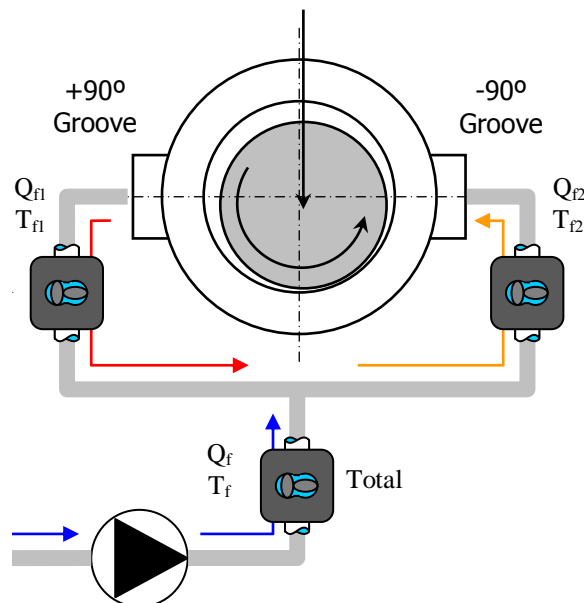


Figure V-12 – Outline of the flow meter scheme used for the measurement of the flow rate at each groove. Example of the occurrence of negative flow rate at the +90° groove.

The experience with the test program carried out in the University of Poitiers (LMS-UP) showed that the lack of knowledge of the flow rate distribution along the grooves limited significantly the analysis of the results. This knowledge is important for a deep understanding of the phenomena taking place inside the bearing gap and to correctly model both the flow and the heat transfer occurring in bearings. Furthermore, some evidence pointed out to a possible

inversion of the direction of flow occurring in one of the grooves (hot oil reflux). These unexpected observations dictated the necessity of acquiring two additional flow meters.

Only the conjugation of three different flow meters (1 total + 2 partial) allows detecting with confidence the occurrence of negative flow rate at one of the grooves. This is so because the difference in the signal provided by the flow meters for positive and negative flow is undistinguishable. Therefore, total flow rate as well as partial flow rates should be measured. The solution adopted is presented in Figure V-12.

b) Flow meter and electric circuit description

Two Macnaught M1RSP-1R elliptical gear flow meters were chosen. These flow meters display a repeatability of 0.03%. Unlike the existing total flow meter, which is based on a Hall effect sensor and needs a 10V (DC) power supply, the new partial flow meters rely instead on a Reed Switch system that opens/closes every 1ml approximately. Therefore, as these are passive sensors which act merely as switches, an electrical circuit with a +5V DC signal was deployed. To avoid undetermined electrical states due to open circuits (when the switch is in the off position); a pull-up system with a $27\text{k}\Omega$ resistance was built, as shown in Figure V-13.

When the Reed switch is in the opened position, no electrical current exists. Therefore no voltage fall happens across the resistance and therefore a +5V signal is measured by the data acquisition. When the switch closes, the + and – poles of the channel enter in short circuit yielding a zero voltage measurement.

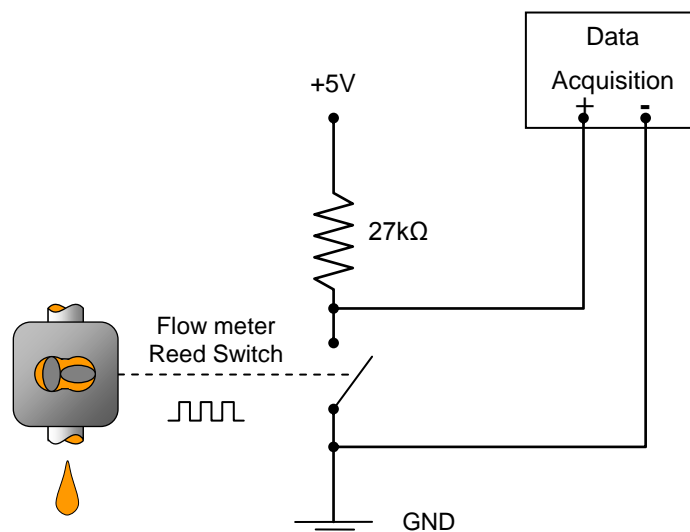


Figure V-13 – Outline of the electrical circuit built for the data acquisition of the signal from the flow meters (rectangular wave) caused by the Reed Switch of the flow meters, including pull-up system to avoid undetermined electrical states.

The value of the resistance was chosen so that only a small current (0.1mA) would be obtained with the switch closed. A sample of the signal coming from the three flow meters is presented in Figure V-14.

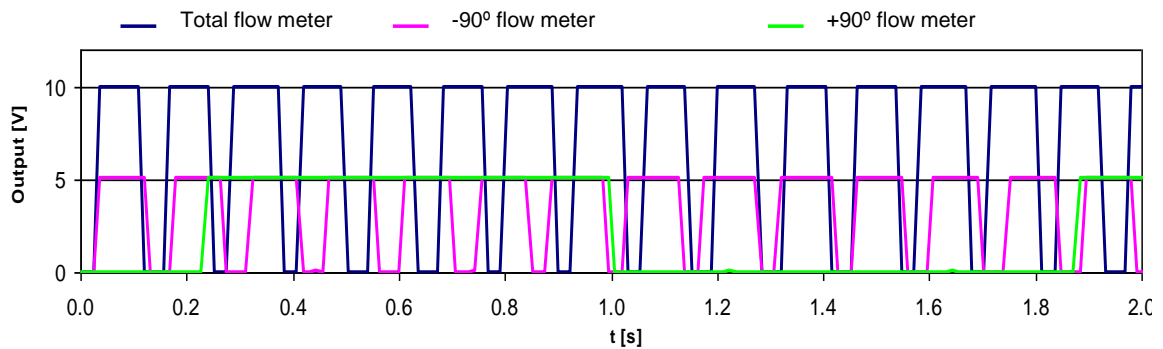


Figure V-14 – Signal coming from the gear flow meters ($B1-V1$, $N=4000rpm$, $W=5kN$, $T_f=40^\circ C$, $P_f=250kPa$).

c) Calibration

The calibration of each flow meter was carried out with a 1000ml graduated glass that was filled at two different flow rates. Each measurement was based on a total number of pulses between 700 and 900.

d) Method used for determining the flow rate

Initially, a simple method for the estimation of flow rate was deployed: it consisted in counting the total number of waves. Within Excel, this was made automatically by identifying the total number N of 0 to 5V pulses. The total number of complete waves would be $N-1$, which divided by the total data acquisition time would yield the average wave frequency. The multiplication of this value by the calibration factor (in liters per pulse) would yield the flow rate (in liters per second). This straightforward method, which gave acceptable results for large flow rates or very long acquisition times showed to be unsuitable for the present work. This kind of error can be better understood by looking at Figure V-15, where two cases of very different flow rates would yield the same calculated flow rate according to this method: it can be seen that only one full wave (two upward pulses) would be identified in both cases during the total data acquisition time.

On the contrary, if the useful time lapse is accounted for (the time lapse between the first and the last recorded pulse), a much more accurate wave frequency is obtained, even with only one complete wave recorded (see Figure V-15):

$$F [\text{pulses} / \text{s}] = \frac{\text{pulses} - 1}{\text{useful time lapse}} \quad \text{Eq. V-2}$$

With this new method, the accuracy of the estimation is much less dependent on the total amount of waves recorded, but will depend mainly on the magnitude of the data acquisition

time step, as it determines the accuracy of the location of the pulses. As the total number of detected pulses increases, this error becomes more and more negligible. In fact, with this new method differences less than 0.3% between the sum of the two partial flow rates and the total flow rate were normally obtained.

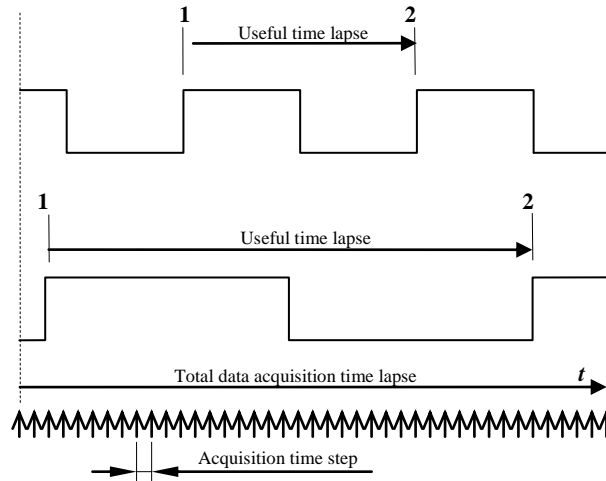


Figure V-15 – Outline of the wave frequency calculation for two different cases.

The flow rate measurements for the three flow meters were based on 3000 scans at an acquisition rate of 250Hz. This means that the flow rate calculation for each flow meter was based on 1000 scans at an acquisition time step of $3/250$ (0.012 seconds).

V.2.10 Shaft locus measurement

a) Relevance of shaft locus measurements

The relative position of the shaft and bush centerlines, often expressed in terms of eccentricity ratio and attitude angle, is one of the most important performance parameters of bearing systems. For instance, the eccentricity ratio provides an estimation of the minimum film thickness. This is a vital parameter to assess how close the bearing system is from severe contact and eventually general failure, in a given situation.

Too small eccentricities might also be deleterious for bearing performance, as they tend to cause excessive temperature, bearing instability and may put to evidence an under-optimized (excessively conservative) bearing design. The knowledge of the shaft locus is also fundamental in vibration, stability and dynamic analyses of journal bearings.

b) Description of the measuring system

In this work two pairs of proximity probes (*Bently Nevada 3300 NSv*) located at $\pm 45^\circ$ to the load line, on both sides of the bearing, were used. Depending on the bearing length, the sensors

were mounted in two different ways, as shown in Figure V-5. The configuration used with the larger bushes (B1 and B2 - Figure V-5b) was necessary in order to prevent the probes of getting near of the grooved part of the shaft.

Figure V-16 displays an outline of the sensor disposition and the coordinate system used. These are non-contact sensors based on the *Eddy Current* effect. Each sensor was attached to a *Bently Nevada 3300 XL NSv / 7200 Proximator*, their power supply and signal conditioning unit.

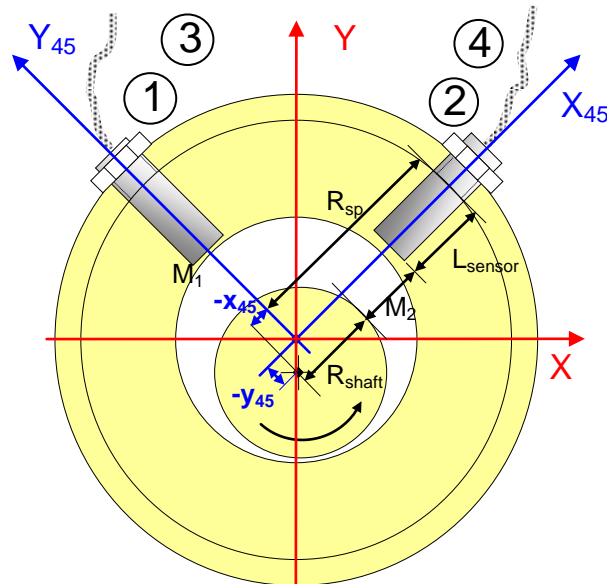


Figure V-16 – Outline of the proximity probes 1 and 2 disposition (probes 3 and 4 are unseen, located at the opposite side of the bearing)

This is the standard sensor type used in rotating shaft applications. Their non-contact characteristics and their high sensitivity within a small range of operation (around 1.5mm) make them more suited for recording the small displacements which are typical of these applications than, for instance, contact-based sensors such as LVDT's.

c) Measurement difficulties

In spite of the popularity of Eddy current probes, it is known that factors such as sensor and target temperatures, nearby metallic bodies, target geometry, thermal and mechanical elastic deformations affect significantly this sensor response (Bently Nevada Corporation, 2001, Glavatskih et al, 2001). Many authors have reported their difficulty to compensate these effects in their experimental works (Ferron et al, 1983, Gethin and Medwell, 1985, Basri and Neal, 1990, Claro and Miranda, 1993, Costa, 2000). Some of them even discarded the presentation of their results due to these problems (Basri and Neal, 1990). There are also many reference works which simply omit this kind of measurement (Mitsui et al, 1986, Ma and Taylor, 1992, Fitzgerald and Neal, 1992). The pursue of alternative film thickness measurement methods observed in some recent works (Glavatskih et al, 2001, Kasolang and Dwyer-Joyce, 2008) is an

evidence of the difficulty experienced still nowadays in order to obtain reliable results in this field. Similar difficulties were experienced in the present work. Nevertheless, some workarounds, which are described below, were deployed in order to mitigate some of these effects.

d) Calibration

The system was calibrated against a target cylinder of the same material and diameter of the test shaft. The probe was fixed to an unmovable support, while the target was attached to a movable block whose distance from the probe was regulated through a fine threaded bolt and checked with a micrometric dial indicator. 25 measurements between 0 and 1.3mm (one measurement each 50 μm) were recorded, with obtained sensitivities around 7.5mV/ μm . It is worth noting that, since the calibration measurements were made through the data acquisition system, the final calibration curve already takes into account the influence of both the sensors and the measuring system. Unfortunately, no practical solutions allowing a calibration of the sensors when located at their normal operation locations, and under their normal operation temperatures, were devised.

e) Measuring methodology and compensation of external influences

The estimation of the relative shaft position is a very sensible task: the gap between the shaft and bush surface is of the order of the tens of microns, with the displacements which are to be determined being of that order of magnitude. As a consequence, there is a need to correct the standard calculations with the influence of the various factors that might affect the measurements.

e.1) Measurement through a reference position

Considering the axis system presented in Figure V-16, the coordinate X_{45} of the shaft centerline relative to the bush centerline can be expressed as:

$$X_{45} = R_{sp} - M_2 - R_{shaft} - L_{sensor2} \quad \text{Eq. V-3}$$

Where R_{sp} is the radius of the location of the sensor support, M_2 is the measurement provided by the probe 2 (the probe which is aligned with the X_{45} axis), R_{shaft} is the radius of the shaft and $L_{sensor2}$ is the length of the free portion of probe 2.

The induced X_{45} displacements caused by Y_{45} displacements (and vice-versa) should be very small due to the small clearance ratio and therefore have been neglected.

It should be noted that the expression above is not useful by itself to determine the shaft locus, namely because L_{sensor} is normally unknown. However, if it is used in a relative manner (in

relation to a reference position), this problem ceases to exist. Therefore, in order to know the actual shaft centerline position for a given test, a reference position is selected, with their coordinates, which are known beforehand or imposed, being associated with the corresponding distances recorded by the sensor for that reference position. Then, subsequent shaft locations will be determined based on that reference:

$$X_{45} = X_{45 REF} - \Delta M_2 \quad \text{Eq. V-4}$$

$$Y_{45} = Y_{45 REF} - \Delta M_1 \quad \text{Eq. V-5}$$

where ΔM is the difference between the actual test measurement and the reference test measurement.

A simple reference position could be, for instance, a loaded shaft under rest, which, theoretically, would display an eccentricity ratio of 1 and an attitude angle of exactly 180° . In reality, however, the use of such a reference position has not provided good results. Instead, it is common to use the measurements of one particular test as the reference and assume that the actual coordinates of that test are known beforehand (they may be obtained with a theoretical model). This approach has been used in the present work.

e.2) Differential thermal expansion compensation

One of the factors which affect the measurements is the thermal expansion suffered by the shaft, the bush and the probe. If the thermal expansion of the elements is to be taken into account, then all the factors of Eq. V-5 will become variable and therefore the expression becomes, for each axis:

$$X_{45} = X_{45 REF} + \Delta R_{sp} - \Delta M_2 - \Delta R_{shaft} - \Delta L_{sensor2} \quad \text{Eq. V-6}$$

$$Y_{45} = Y_{45 REF} + \Delta R_{sp} - \Delta M_1 - \Delta R_{shaft} - \Delta L_{sensor1} \quad \text{Eq. V-7}$$

The variation of the distances R_{sp} , M , R_{shaft} and L_{sensor} will be a function of the temperature differential observed between the current test and the reference test and the thermal expansion coefficient for each component. Although L_{sensor} continues to be unknown, only a rough estimation of this distance (the sensor head typically extends itself up to a distance of about a millimeter from the shaft surface) is necessary in order to provide a sufficiently accurate value for ΔL_{sensor} .

e.3) Elastic deformation compensation

In order to estimate the influence that elastic deformations due to bearing loading could have in the shaft locus measurements, the bearing was modeled in a 3D environment (SolidWorks) and tested with a Finite Element (FEM) package (CosmosWorks). The bush geometry, which was

modeled with a significant degree of detail, was cut at the two vertical symmetry planes, as shown in Figure V-17.



Figure V-17 – Finite Element simulation of the elastic displacements suffered by the bush (B3) and the cable subjected to a 5kN load, (a) meshing and boundary conditions ; (b) elastic deformation displacements (magnified 1500 times). Note: Taking into account symmetry, simulation was made only with $\frac{1}{4}$ of the bearing.

A distributed vertical load (axially constant) with a parabolic shape (zero at the extremities, maximum at the middle) was applied to the lower half of the inner bush surface so that the resultant load was equal to the applied load.

In order to provide realistic restraints to the FEM calculations, an assembly of bush + supporting cable was used. A simple boundary condition of non penetration was used between the cable and the bush body, while the upper extremity of the cable was set to unmovable. The symmetry condition was imposed at the symmetry cuts of both bush and cable.

For the highest load (5kN) the maximum displacements within the bush body were less than $2\mu\text{m}$ for the B1 and B2 bush geometry. However, the inner diameter of the narrow bush B3 ($b/d=0.5$) suffered variations of about $11\mu\text{m}$ both along the horizontal (decrease) and the vertical (increase) directions. Therefore, the elastic deformations can be neglected in the large bush cases (B1 and B2) but are important in the case of the narrow bush (B3), as variations account for 15% of the diametral clearance.

The relative displacements of some specific nodes of the bush body were recorded in order to estimate the global effect of mechanical deformation on the response of each sensor. This compensation was applied to all tests.

e.4) Final remarks on shaft locus measurements

It was observed that the measurements were more consistent when compared to results obtained in the same test session. Therefore, large test sessions, especially when performing parametric studies were performed every time it was possible.

Repeatability was improved when the probes were kept at a constant axial position in relation to the shaft. This procedure was later added to the standard experimental procedure.

In spite of all the care taken in order to compensate the various factors affecting the measurements, as described in this chapter, it was not possible to obtain completely satisfactory signal compensation. This could be due to factors such as the variation of the sensor response with temperature, the variability of material properties (non-isomorphous), and to the fact that the calibration could not be performed *in situ* (with the probes installed at their normal working location). Therefore, all shaft locus measurements of this work should be regarded mainly as indicative, especially when comparing results with very different operating conditions such as load, shaft speed or feeding temperature.

V.3 Detailed procedure followed during test sessions

The experimental procedure is presented below. Some of its steps appeared along the process as a consequence of accumulated experience.

LOMT General experimental procedure.

1. Turn on electrical power. Note: The power supply to sensors, computer and all the data acquisition system should be turned on at least one day before the beginning of the test sessions and remain on until the end of the test season in order to improve the thermal and electrical stability of the components;
2. Reset the zero of the pressure transducers;
3. Turn on lubricant feeding pump and lubricant heating system;
4. Turn on motor control system (after confirming that the manifold is set at zero);
5. Begin writing test report (date, startup time, operative parameters, observations);
6. Confirm that the bearing is unloaded and the feeding pressure is above 200kPa;
7. Turn the shaft a couple of times for an initial wetting of the bush/shaft;
8. Align load 90° with the grooves and retrieve the cantilever relief support;
9. Acquire proximity probe signal under rest;

10. Initiate shaft motion while alleviating the load by pressing the cantilever downwards. (this is done in order to mitigate contact and wear during startup);
11. Readjust feeding pressure during the startup process (do not let it fall under 100kPa);
12. Activate motor consumption measurement (turn on multimeter and retrieve current by-pass);
13. Let system warm-up during at least 20 minutes, depending on the test speed;
14. During the stabilization readjust periodically the shaft speed (displays tendency to increase gradually), the feeding pressure (considered as the highest value of the two grooves), the feeding temperature (measured before the bifurcation to the two grooves) and the axial position of the bush (align proximity probes with marks);
15. When steady state has been achieved (negligible temperature fluctuations) recheck speed (within ± 15 rpm), feeding pressure (within ± 2 kPa), feeding temperature (within $\pm 0.2^\circ\text{C}$) and axial position;
16. Activate proximity sensors selectors and acquire signal (average of 2000 scans at 10kHz) ;
17. Activate flow meter selectors and acquire signal (3000 scans at 250Hz - duration of approx 36 seconds) – Excel calculates the number of complete rectangular waves and respective time lapse (eliminates time corresponding to incomplete waves) ;
18. During flow meter data acquisition, write the time of the measurement, speed, load, feeding pressure (re-confirm it is within ± 2 kPa) and motor consumption (A);
19. Confirm flow rate error is within 1% (typical error is below 0.5%). If error is not negligible, one of the flow meters should be displaying a faulty electrical connection (check it) or negative flow rate is occurring in one of the grooves;
20. Acquire thermocouple signal (average of 100 scans at 481Hz, with rejection of the 10% most deviated values to eliminate noise overshoots) and re-confirm that feeding temperature is within $\pm 0.2^\circ\text{C}$;
21. Save results in a different page, eliminating formulas and links to other cells;
22. Test is complete;
23. Set new test operating conditions. If load or speed should increase, then increase previously the feeding pressure for security reasons;
24. If additional tests are to be performed, restart the procedure in point 14. Depending on the magnitude of the change on the operating conditions, the stabilizing time may vary.

- Stabilization after changes in feeding pressure should be much quicker than after changes in speed or feeding temperature;
25. After the last test has been concluded, unload the bearing, reduce gradually the speed and the feeding pressure;
 26. Before shaft stops completely, alleviate load by pressing downwards the cantilever (at the side of the bearing) until shaft stops, to mitigate contact and wear;
 27. Turn off the oil pump;
 28. When feeding pressure is close to nil, acquire proximity probe signal (could be useful for posterior data analysis);
 29. Unload the bearing by applying the cantilever support;
 30. Turn off the oil bomb, the oil heating system and the motor control system;
 31. Save files and write pertinent test notes.
 32. The End

V.4 Results and discussion

V.4.1 Test program

The test program that was carried out in the LOMT rig is presented on Table V-4. Four different combinations of bushes and shafts were used. These bearings have two axial grooves located at $\pm 90^\circ$ to the load line.

The speed (N) varied between 1000rpm and 4000rpm, while the applied load (W) varied between 0.4kN and 5kN. The feeding pressure (P_f) had a maximum range between 50kPa and 400kPa. The feeding temperature varied between 29°C and 58°C.

In some tests the -90° groove was deactivated (no lubricant supplied to this groove). It seems reasonable to assume that such bearing arrangement will perform similarly to a bearing with a single axial groove located at $+90^\circ$ to the load line.

These tests allowed the analysis of the influence on bearing behavior of W , N , P_f , T_f , bearing clearance (c_d), and number of grooves. The analysis of the influence of groove length ratio (a/b) and bearing length ratio (b/d) was initially intended. However, this analysis was later discarded because, contrary to expected, the machining of the various bushes yielded slightly different inner bush diameters. This caused the clearances of the different bearing systems to be too dissimilar to allow the comparison of results corresponding to different bearings.

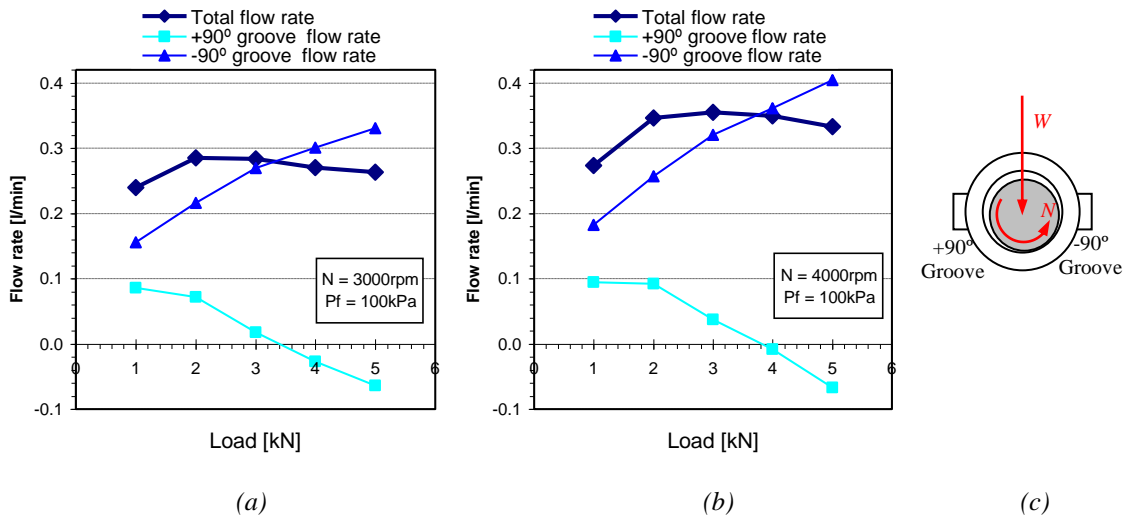


Figure V-18 – Total flow rate and flow rate at each groove for (a) $N=3000rpm$ and (b) $N=4000rpm$ (bearing B1V1, $P_f=100kPa$, $T_f=40^\circ C$). (c) bearing outline

The total oil flow rate curves show a typical evolution with load, as presented in other works (Fitzgerald and Neal, 1992, Ma and Taylor, 1992), with an initial increase, stabilization and a smooth decline.

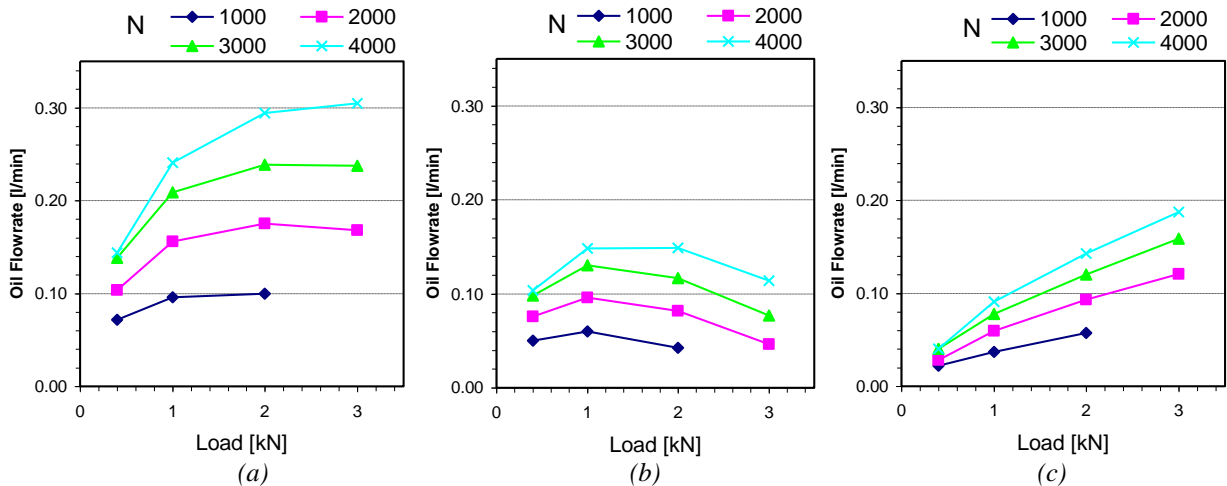


Figure V-19 – (a) – Total flow rate; (b) - $+90^\circ$ groove flow rate; (c) - -90° groove flow rate (bearing B2V1, $P_f=100kPa$, $T_f=29.5^\circ C$).

It is interesting to note that the two grooves display a totally different behavior with loading conditions. As load increases, the following occurs at each groove:

- -90° groove: The flow rate at this groove begins with its lowest values, then increases consistently. This behavior can be explained by the fact that, as load increases, a higher hydrodynamic pressure tends to occur on the lower land of the bearing. This causes an increase in oil leakage with its subsequent renewal at this groove, which is the one located immediately downstream of the pressure buildup zone. Furthermore, as load increases the change in shaft locus causes the gap at the -90° groove to increase, while the pressure buildup zone tends to develop on a smaller angular extension, away from

the -90° groove region. These two phenomena further facilitate the oil entrance through this groove. This is sketched in Figure V-21.

- $+90^\circ$ groove: This groove displays a totally different behavior. Although a smooth increase of flow rate with increasing load is still observed for the lowest eccentricity cases (from 0.4kN to 1kN with bearing B2V1, which is one of the long bearings, $b/d=0.8$ – see Figure V-19b), the flow rate starts decreasing consistently when load increases above 1kN. Furthermore, for high eccentricity cases the flow rate from the $+90^\circ$ groove became negative. This means that rather than flowing into the bearing clearance, oil flows out of the bearing through the $+90^\circ$ groove (Figure V-18). The decrease of this flow rate with increasing load is associated with the corresponding change of location and magnitude of the hydrodynamic pressure field, as sketched in Figure V-21. As load increases there is an increase in eccentricity and a decrease in attitude angle, as depicted in Figure V-22 for the B3V1 bearing case. This causes the hydrodynamic pressure to increase, with the pressure buildup zone moving upstream, closer to the $+90^\circ$ groove region. Above some critical load, the pressure generated in the $+90^\circ$ groove region exceeds the value of the feeding pressure. This causes some of the oil to flow out of the bearing through the oil groove. In the case of bearing B2V1 (Figure V-19) this phenomenon did not occur. This should be due to the lower specific loads present (load did not exceed 3kN and b/d is greater than that of B3V1).

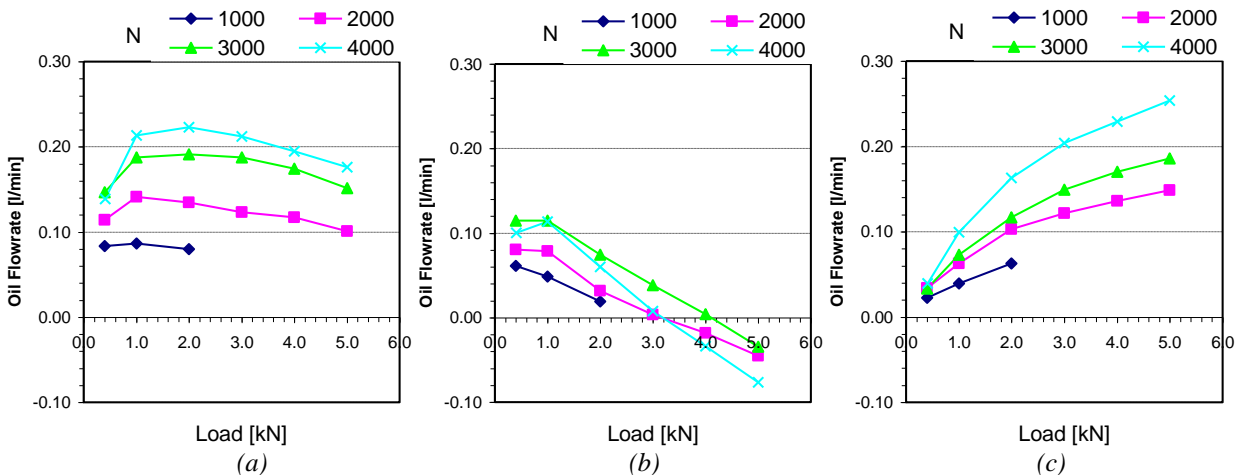


Figure V-20 - (a) – Total flow rate; (b) - $+90^\circ$ groove flow rate; (c) - -90° groove flow rate (bearing B3V1, $P_f=100\text{kPa}$, $T_f=29.1^\circ\text{C}$).

The occurrence of negative flow rate at one of the grooves is undesirable for various reasons. Concerning lubrication needs, the region near the location of minimum film thickness (h_{min}) is the critical one. When flow rate at the $+90^\circ$ groove is negative, oil is being supplied only at the non-active part of the film, where it will increase power loss due to viscous dissipation. At the same time, oil is being retrieved from the film instead of being supplied to it, just upstream of

the location where it is mostly needed. Furthermore, this happens under severe operating conditions (high eccentricities) further rising the failure risk of the system.

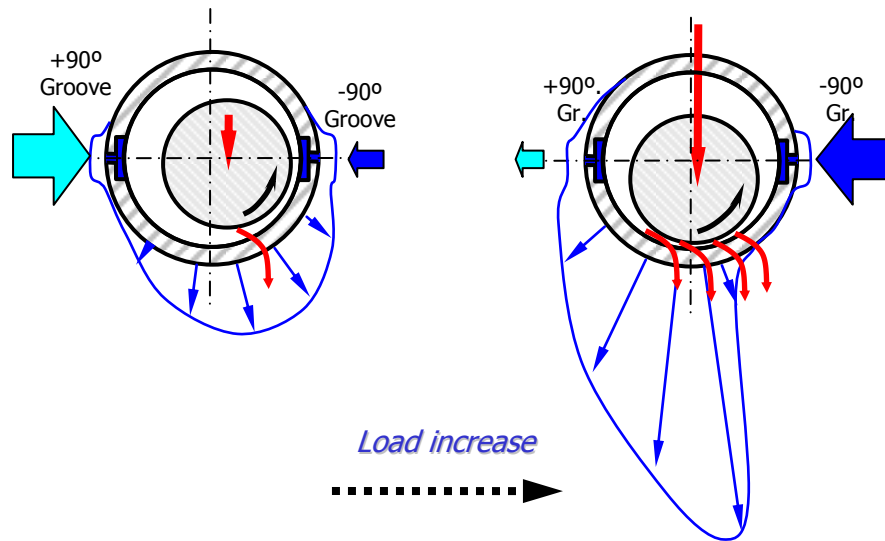


Figure V-21 – Schematic representation of the mechanism responsible for the occurrence of negative flow rate at the $+90^\circ$ groove as load increases.

The impact of the occurrence of negative oil flow rate can be further assessed by analyzing the temperature field, which is deeply affected by the way the oil is delivered to the system.

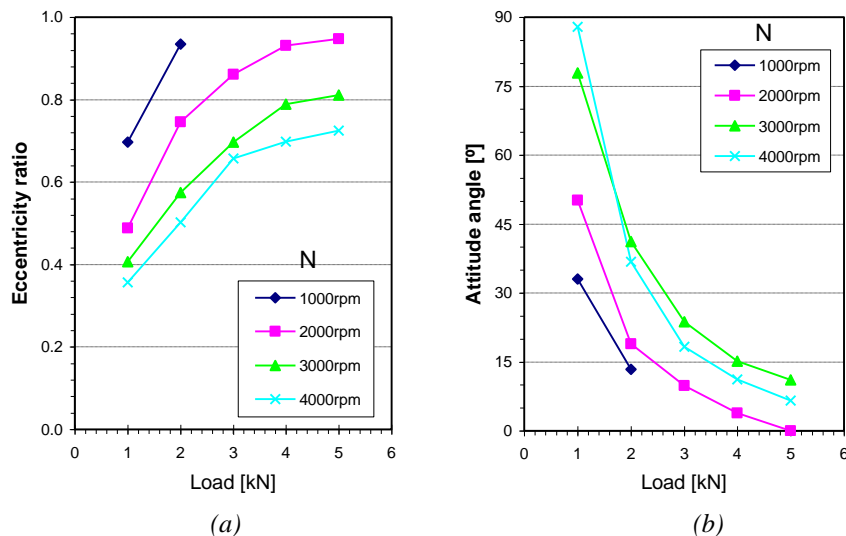


Figure V-22 – Measurements of (a) eccentricity ratio and (b) Attitude angle as a function of speed and load (Bearing B3V1, $P_f=100\text{kPa}$, $T_f=29.5^\circ\text{C}$, reference test - 2000rpm, 1kN). Note: due to large measuring uncertainties, these values should be regarded mainly as indicative.

b) Temperature field

b.1) Influence of shaft speed on the temperature field

The way shaft rotational speed and applied load influence the temperature profiles at the midplane of the film-bush interface is presented in Figure V-23 for the bearing B3V1. In this Figure it can be observed the strong influence that shaft speed exerts on the global temperature level, which increases strongly with increasing speed. In fact, the heat generated by viscous

dissipation is a direct function of the velocity gradient across the film thickness, with the drag (Couette) component, being the major contributor in normal hydrodynamic bearing applications. In general, the increase of shaft speed tends to improve the load carrying capacity of bearings. In other words, the bearing tends to operate at lower eccentricities, further away from seizure conditions. However, if shaft speed is increased above a certain threshold, the added heat generated by viscous dissipation might originate such temperature levels that the loss of lubricant viscosity due to this would eventually induce a net loss of load carrying capacity.

It can be observed in Figure V-23 that the temperature span becomes wider as speed increases, with the cooling effect of grooves becoming stronger.

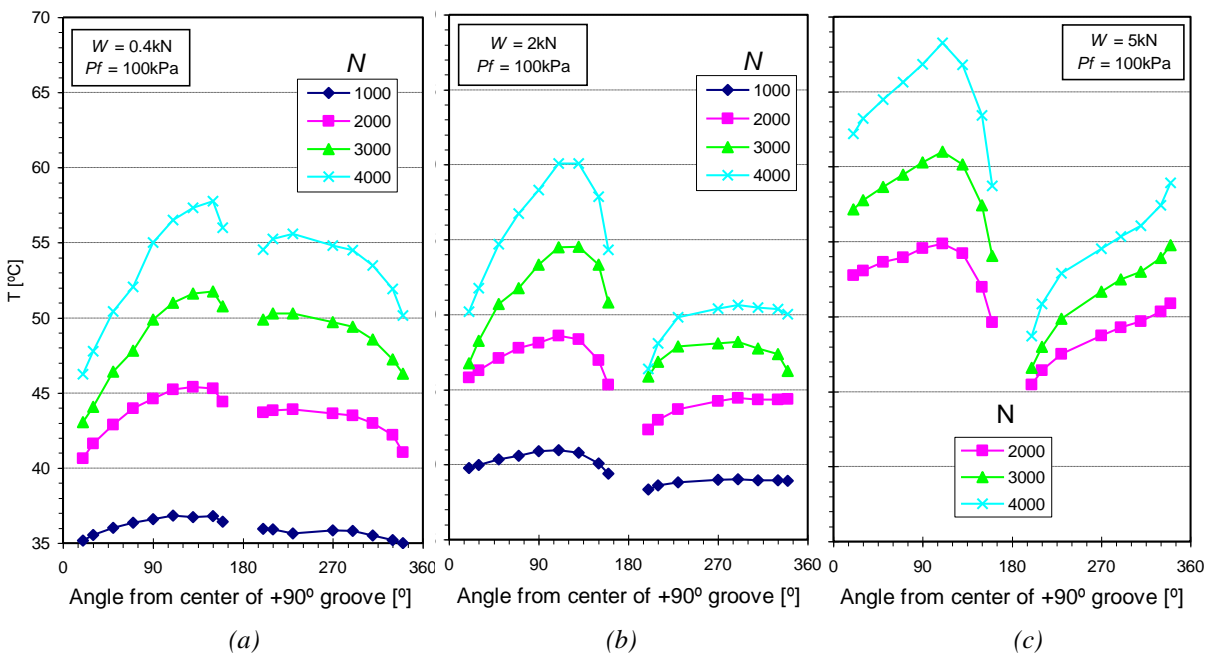


Figure V-23- Temperature at the midplane of the inner bush surface for different shaft speeds and a load of (a) $W=0.4\text{ kN}$, (b) $W=2\text{ kN}$ and (c) $W=5\text{ kN}$ (Bearing B3V1, $P_f=100\text{ kPa}$, $T_f=29.5^\circ\text{C}$)

b.2) Influence of applied load on the temperature field

The temperature curves corresponding to 2000rpm and 4000rpm tests with the same bearing (B3V1) are shown as a function of applied load in Figure V-24 (a) and (b) respectively. These curves deserve a detailed observation in order to understand better the effect of load on bearing temperature:

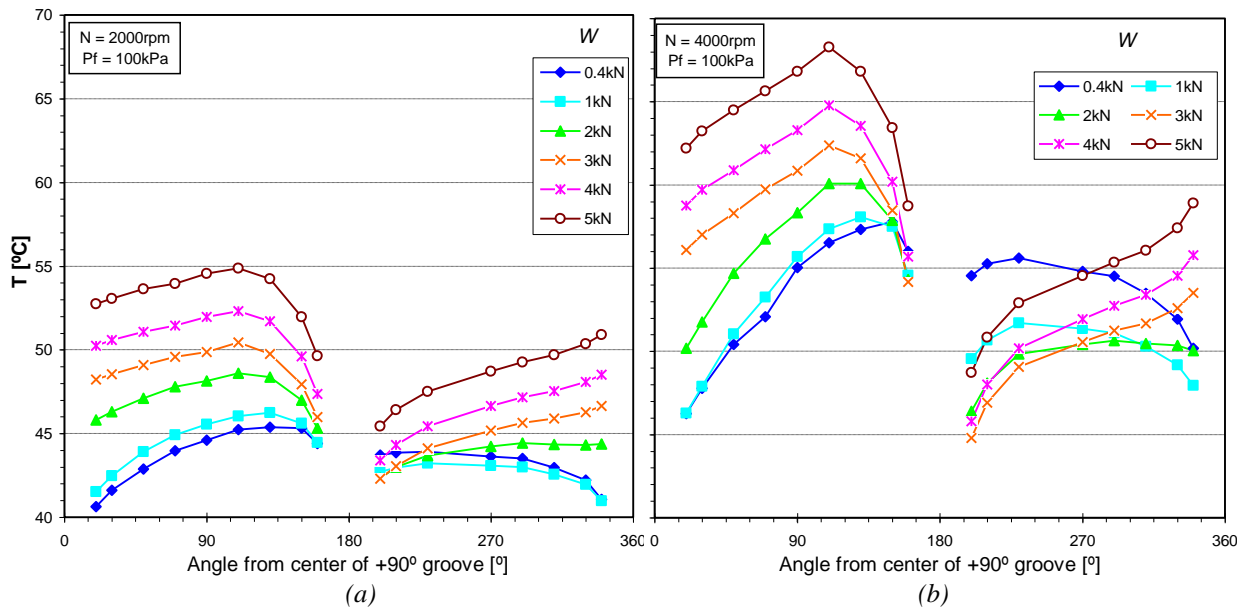


Figure V-24 - Temperature at the midplane of the inner bush surface for different loads and a speed of (a) $N=2000\text{rpm}$ and (b) $N=4000\text{rpm}$ (Bearing B3V1, $P_f=100\text{kPa}$, $T_f=29.5^\circ\text{C}$).

At low load (0.4kN):

- The maximum temperature (T_{max}) occurs near the -90° groove's edge, at an angular distance of about 20° . This is so because lightly loaded bearings tend to display high attitude angles. This causes the minimum film thickness, and therefore T_{max} , to be located relatively near the groove region.
- There is only a slight temperature decrease between T_{max} and the -90° groove entry (1°C and 2°C respectively for 2000rpm and 4000rpm tests), followed by a temperature fall across this groove which is even smaller. The small cooling effect of this groove for low loads is linked with the low flow rate detected at this groove in such cases (recall Figure V-20b). As a consequence, the maximum temperature at the loaded land of the bearing is only slightly higher (1.5°C and 2°C respectively for 2000rpm and 4000rpm) than that of the unloaded land.
- Slightly after the -90° groove the temperature profile displays a decreasing trend. This trend results from the balance of several factors. On one hand, there are the heat losses by conduction to the bush body that may overcome at some point the heat generation within the film, which is small in this region. On the other hand, fresh oil backflow coming from the $+90^\circ$ groove can also be responsible for some temperature decrease in its vicinity.
- The global temperature fade observed across the $+90^\circ$ groove surroundings is more pronounced when compared with that occurring at the opposite groove, especially in the lowest eccentricity test (4000rpm). This is in good agreement with the proportion of flow rate values between the two grooves, (Figure V-20b, c). In order to facilitate comparisons, the values of T_{max} and of the temperature change across grooves are detailed in Figure V-25(a) and (c), respectively. Lubricant outlet temperature (T_{out}) is also presented in Figure V-25b.

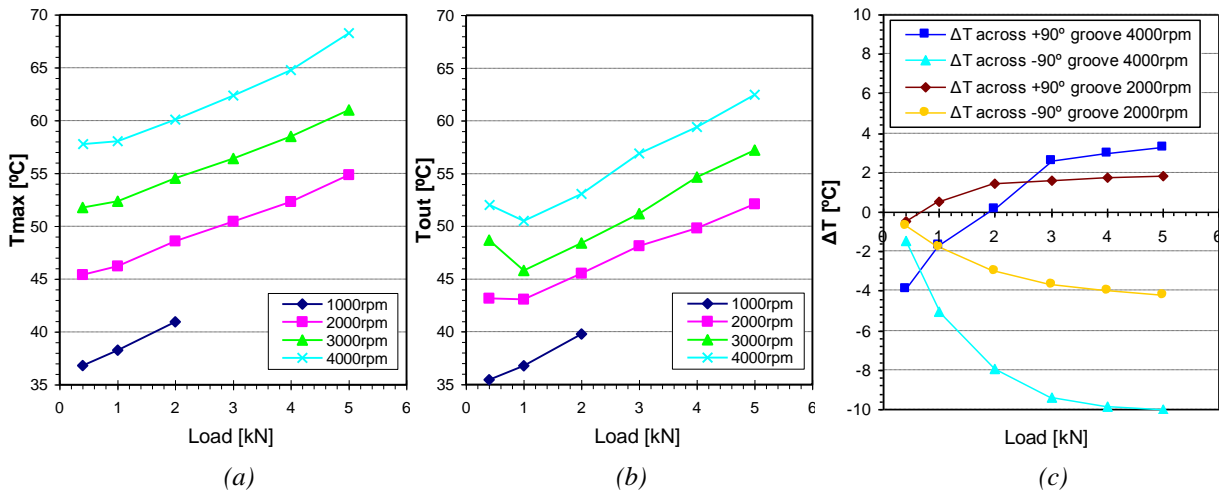


Figure V-25 – (a) Maximum bush temperature; (b) lubricant outlet temperature ; (c) Temperature fall across each groove for 2000 and 4000rpm (Bearing B3V1, $P_f=100\text{kPa}$, $T_f=29.5^\circ\text{C}$)

As load increases:

- There is an increase in T_{max} (see Figure V-25a) linked to the increase in eccentricity (recall Figure V-22a) and therefore, of heat dissipation. It is interesting to note that the curves for the various speeds are rather parallel with each other, displaying an increase on T_{max} around 10°C across the whole load span (from 0.4kN to 5kN) for all speeds. This yields an increase of 2°C in T_{max} for each 1kN increase in applied load.

- T_{max} occurs further upstream. This could be explained by the decrease in attitude angle (recall Figure V-22b), that causes the region where heat dissipation is more intense to occur further upstream. The occurrence of fresh oil backflow coming from the -90° groove might also contribute to this.

- It can be seen in Figure V-25c that the temperature fall observed both upstream and across the -90° groove becomes more pronounced as load increases. For instance, in the 2000rpm tests the temperature fall across this groove increases from 0.7°C (0.4kN) to 4.2°C (5kN). In 4000rpm tests the cooling effect of this groove increases even more from 1.5°C (0.4kN) to 10°C (5kN). This is mainly explained by the flow rate increase in this groove already observed in Figure V-20c.

- In the unloaded region of the bearing there is a gradual change of trend from decreasing temperature profiles at low loads to increasing temperature ones at high loads. Again, the flow rate patterns can explain this behavior. As flow rate at the $+90^\circ$ groove decreases with increasing load, as already seen in Figure V-20b, the cooling effect of this groove tends to diminish and eventually disappear. Above a certain load (between 1kN and 2kN, depending on shaft speed) the cooling effect of the $+90^\circ$ groove was so low that no noticeable temperature fall across the $+90^\circ$ groove region was observed in Figure V-25c. Another factor contributing for the increasing trend of the temperature profile at the unloaded zone under high loads, is that

even taking into account that this is mainly a ruptured film region, there should still exist non-negligible heat generation by viscous dissipation because at high loads a significant amount of lubricant has been fed to this region through the -90° groove (Figure V-20c).

The influence of negative flow rate on the effective feeding temperature

Surprisingly, the occurrence of negative flow rate (hot oil reflux) at the $+90^\circ$ groove for the higher loads tested (4kN and 5kN) had consequences at the opposite groove. This is clearly seen in Figure V-26a,b,c, which displays the lubricant temperature measured at the main lubricant feeding pipe (considered to be the actual feeding temperature) and at each one of the branches which feed the two grooves, just upstream of bearing entry.

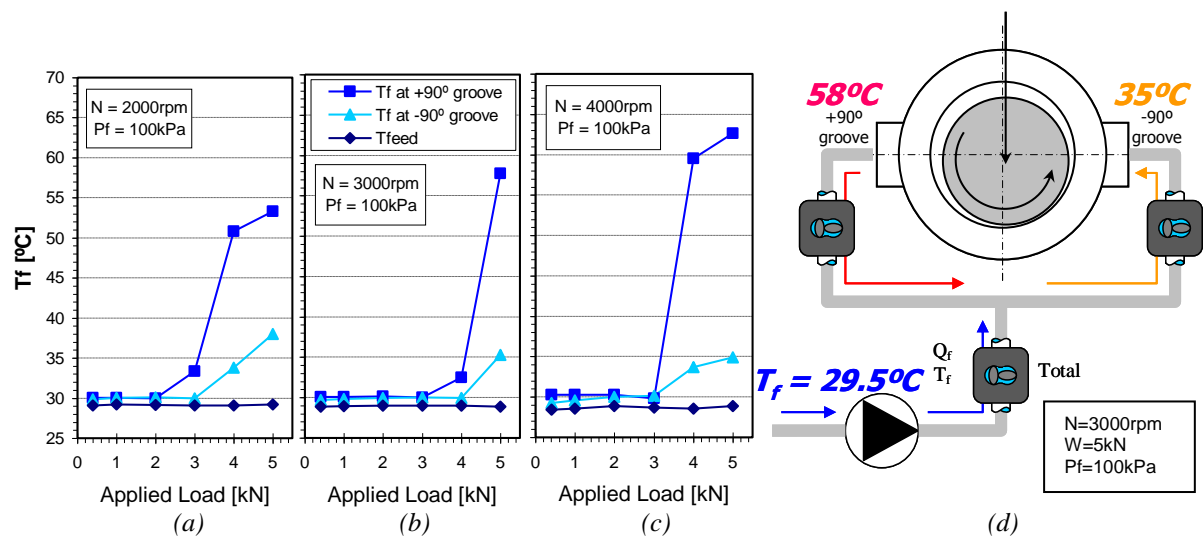


Figure V-26 – Effective rise of feeding temperature at the -90° groove due to the occurrence of negative flow rate at the $+90^\circ$ groove for (a) $N=2000\text{rpm}$, (b) $N=3000\text{rpm}$ and (c) $N=4000\text{rpm}$. (d) - Schematic representation for the case where $N=3000\text{rpm}$ and $W=5\text{kN}$ (Bearing B3V1, $P_f=100\text{kPa}$, $T_f=29.5^\circ\text{C}$).

Figure V-26d sketches what happened in one of the tests where negative flow rate occurred ($N=3000\text{rpm}$, $W=5\text{kN}$, details in Figure V-26b). Due to negative flow rate (-0.035l/min – see Figure V-19b) occurring at the $+90^\circ$ groove, hot oil (58°C) flowed out of the bearing through this groove. It then mixed with the new oil ($T_f=29.5^\circ\text{C}$) inside the feeding system piping and entered through the -90° groove at a temperature of 35°C , which is 5.5°C higher than the original feeding temperature. This effective feeding temperature rise is noticeable in Figure V-24, where it can be seen that the temperature immediately downstream of the -90° groove tends to decrease with increasing load until negative flow occurs (4kN and 5kN tests for both speeds). From here on, the opposite is observed. This effective rise in feeding temperature caused by hot oil reflux further increases the risk of bearing seizure. This phenomenon has not been reported by any study until now, to the author's knowledge, and therefore it is not being taken into account in current bearing design procedures and performance prediction models.

The effect of hot oil reflux in the temperature field can also be appreciated in Figure V-27 for the case of bearing B1V1. Under low loads (1kN, 2kN) a moderate temperature fade can still be observed upstream of the -90° groove, denoting the cooling effect of the oil supply. However, for high loads (3kN, 4kN and 5kN) this temperature fade disappears and the temperature displays a continuously increasing trend along the whole extension of the unloaded land. This denotes the absence of cooling effect in the $+90^\circ$ groove, due to the small (3kN case) or even negative (4kN, 5kN cases) flow rate in this groove. This can be confirmed by recalling the corresponding flow rate charts in Figure V-18.

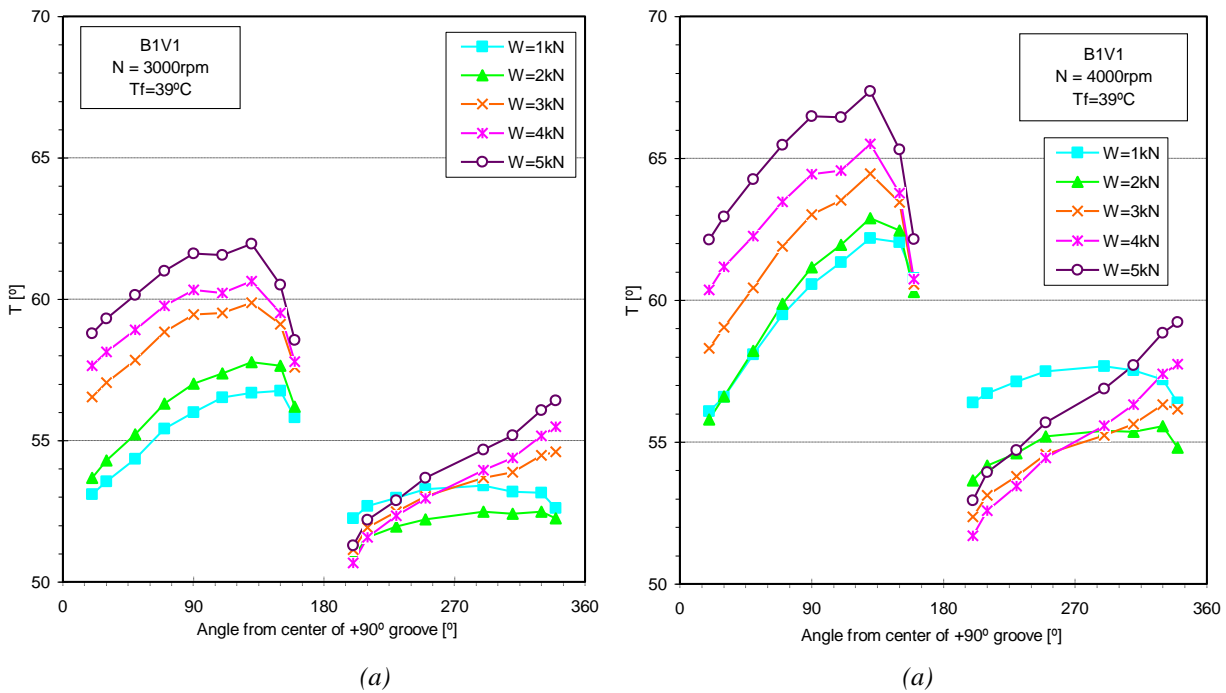


Figure V-27 Temperature profile at the midplane of the inner bush surface, for two different shaft speeds and four different applied loads (bearing B1V1, $P_f=100\text{kPa}$, $T_f=38.5^\circ\text{C}$).

V.4.3 Influence of feeding pressure

The lubricant feeding pressure, P_f , is a parameter which affects significantly bearing performance, namely because it strongly influences the lubricant flow rate and therefore the effectiveness of lubrication and bearing cooling. Furthermore, the amount of lubricant present in the bearing gap also affects heat generation by viscous dissipation and power loss. In this section it will be also shown how the value of this parameter could sometimes be critical to avoid bearing seizure under severe operating conditions.

a) Lubricant flow rate

Figure V-28 shows the evolution of flow rate with increasing oil feeding pressure, P_f , for the lowest (0.4kN) and the highest (5kN) load tested under two different shaft speeds (2000rpm and 4000rpm).

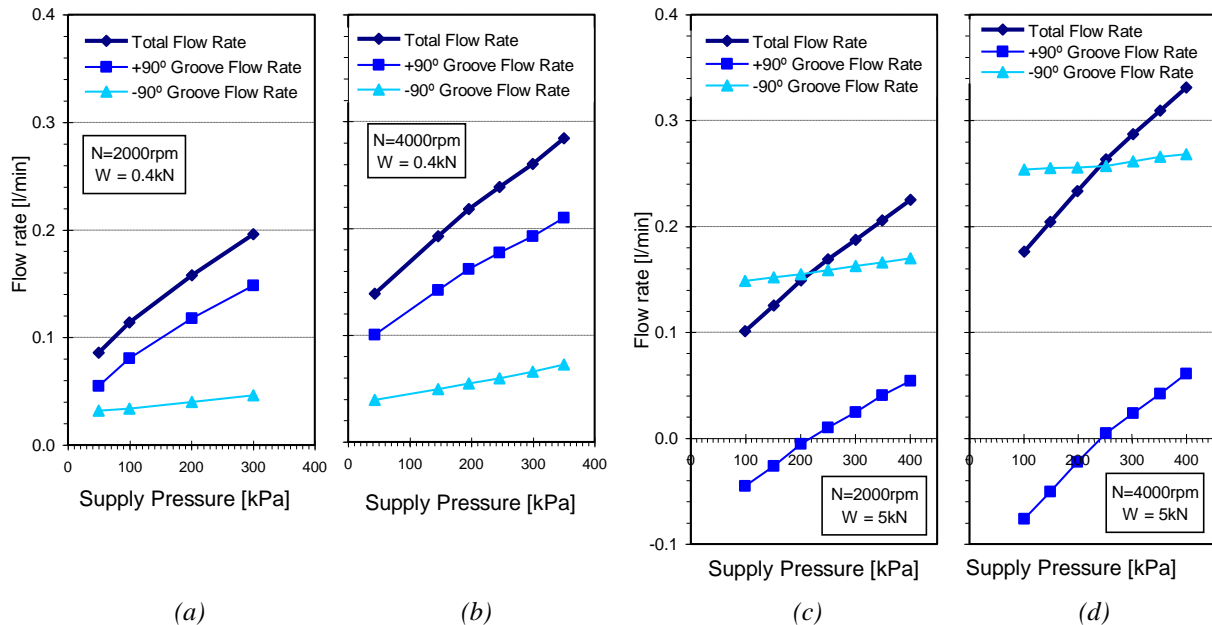


Figure V-28 – Influence of feeding pressure on lubricant flow rate for two different shaft speeds and loads (Bearing B3V1, $T_f = 29.5^\circ\text{C}$).

It can be seen that all the curves display an approximately linear trend with similar average increasing rates. For instance, the total flow rate increases with P_f at a rate between 0.4 and 0.5 l/min per MPa for all cases depicted in Figure V-28, being slightly higher for 4000rpm than 2000rpm tests. It is interesting to note that the main contribution to the increase of total flow rate with increasing P_f comes always from the +90° groove.

a.1) Lightly loaded bearing (0.4kN)

Under low load (Figure V-28a,b) the +90° groove flow rate is significantly higher than that of the opposite groove and is also more sensible to the increase of P_f than that of the opposite groove. Nevertheless, for 2000rpm the proportion of the +90° flow rate relative to the total flow rate increases slightly (from 64% to 76% of the total flow rate), while for 4000rpm this proportion remains nearly unchanged (from 72% to 74% of total flow rate).

a.2) Heavily loaded bearing (5kN)

Under high load (Figure V-28c,d) the flow rate is supplied to the bearing mainly through the -90° groove. However, when P_f increased four times from 100kPa to 400kPa, this flow rate increased only 6% and 15% for 2000rpm and 4000rpm tests respectively. On the contrary, the flow rate at the +90° groove was strongly dependent on the value of P_f . Low values of P_f

induced a negative flow rate in this groove, as already discussed. For feeding pressures above 200kPa and 250kPa, respectively, for 2000rpm and 4000rpm tests, negative flow rate ceased to occur and flow rate increased linearly with P_f , approaching 20% and 25% of the total flow rate for the highest value of P_f tested (0.4 MPa). This means that the negative flow rate problem can be effectively eliminated simply by increasing the value of the feeding pressure above a certain threshold.

b) Eccentricity ratio

Figure V-29 shows the influence of feeding pressure on eccentricity ratio, for the highest load tested (5kN) at three different shaft speeds (2000rpm, 3000rpm and 4000rpm). As said earlier, the shaft locus results should be used with caution and be regarded mainly as qualitative, as they are prone to large systematic errors (see previous section of this chapter on the methodology used in shaft locus measurement). Nevertheless, the relative differences between tests carried out at similar loads and speeds can be analyzed with some more confidence. For instance, it may be stated that the increase of P_f consistently yielded a decrease of eccentricity for all speeds tested. A 0.07 reduction in eccentricity ratio between the 100kPa and the 400kPa tests can be considered as important, taking into account that at low values of P_f the shaft was very close to contact. This confirms that the elimination of negative flow rate by increasing the feeding pressure is beneficial to bearing operation and that the value of P_f under extreme operating conditions might play a critical role in avoiding bearing seizure.

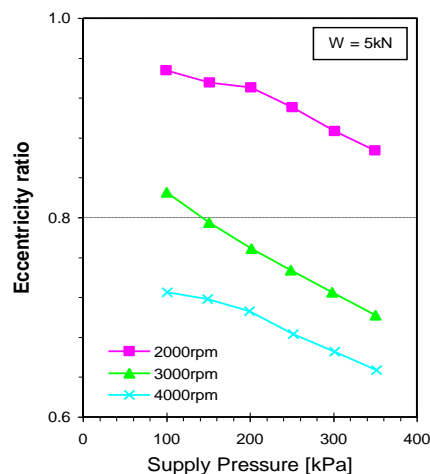


Figure V-29 - Influence of lubricant feeding pressure on eccentricity ratio for $W=5\text{kN}$ three different shaft speeds (Bearing B3V1, $T_f=29^\circ\text{C}$). Note: due to large measuring uncertainties, these values should be regarded mainly as indicative.

c) Temperature field

The temperature profiles at the midplane of the bush-film interface for the lowest (0.4kN) and the highest (5kN) load tests and feeding pressures of 50kPa and 300kPa, are presented in Figure V-30.

Results for maximum temperature (T_{max}) and lubricant outlet temperature (T_{out}) are also detailed in Figure V-31.

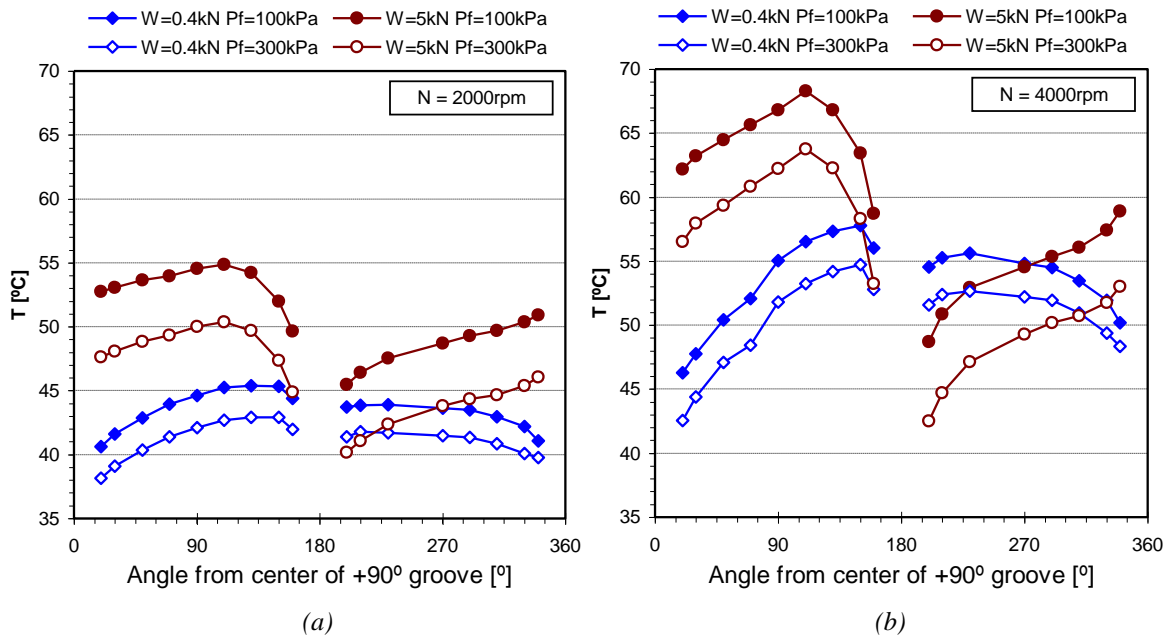


Figure V-30 - Influence of feeding pressure on the temperature profile at the midplane of the bush-film interface for two different applied loads (0.4 and 5kN) and (a) $N=2000\text{rpm}$; (b) 4000rpm (Bearing B3V1, $T_f=29^\circ\text{C}$)

It can be seen in Figure V-30 that P_f undoubtedly affects the temperature level of the bearing, although the temperature profiles corresponding to different values of P_f display a very similar trend, as they are nearly parallel to each other.

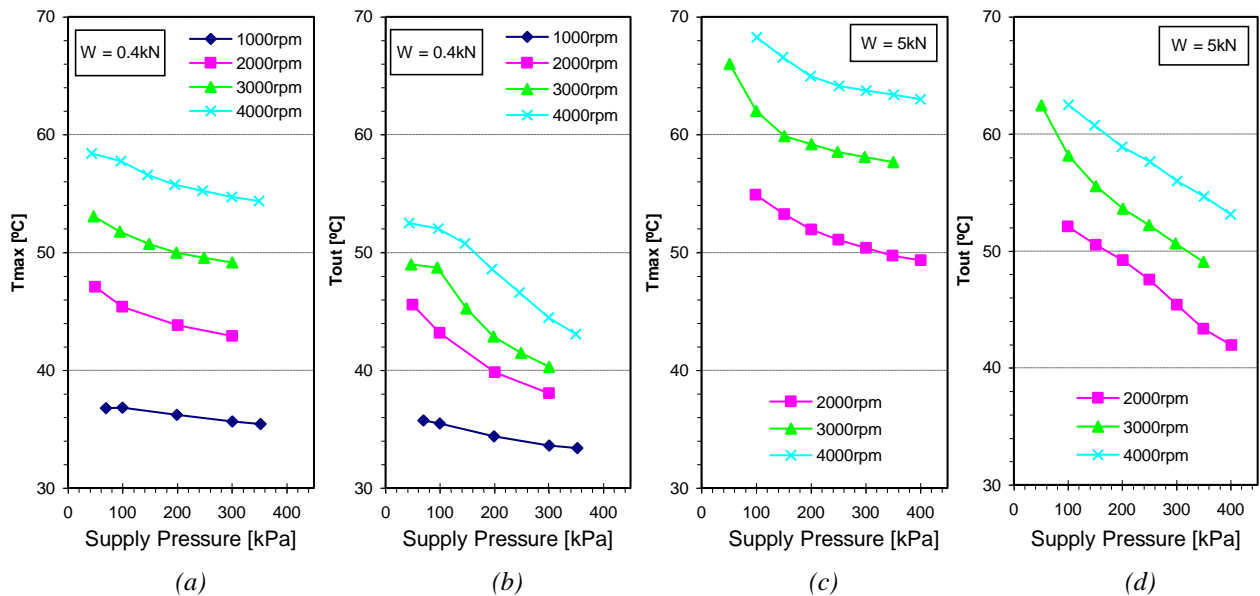


Figure V-31 – Influence of lubricant feeding pressure on the maximum temperature and on the lubricant outlet temperature for several shaft speeds and for two different applied loads (0.4kN and 5kN); (Bearing B3V1, $T_f=29^\circ\text{C}$)

Analyzing Figure V-31 it can be seen that the increase of P_f yields the decrease of both T_{max} and T_{out} , with the latter decreasing more intensely than the former (the decrease of T_{max} over the whole range of P_f was roughly a half of that observed for T_{out}). The general temperature

decrease is due to the increase in flow rate already observed in Figure V-28. Therefore, it is natural that T_{out} , which is a good indicator of the mean lubricant temperature, decreases more intensely than T_{max} .

T_{max} is particularly affected by P_f at high load (5kN) and in the lower range of P_f . This is the region of the chart where the tests with negative flow rate at the $+90^\circ$ groove are located. As explained earlier, in these tests the hot lubricant flowing out of the bearing gap through the $+90^\circ$ groove mixed with the fresh lubricant at the feeding piping effectively raising the temperature of the lubricant supplied to the opposite groove. This feedback phenomenon contributed to a global rise of the bearing temperature. As P_f increased this phenomenon was mitigated and eventually disappeared. This is illustrated in the diagrams of Figure V-32, which represent the T temperature at the main feeding pipe and at the ramification to each groove.

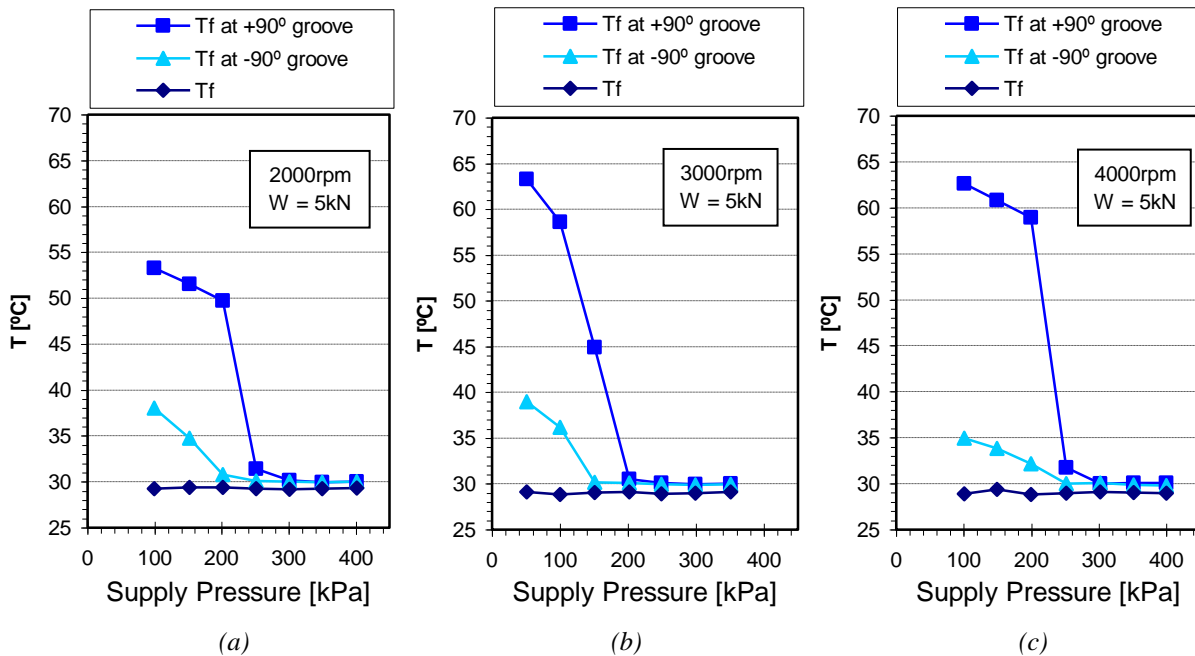


Figure V-32 - Oil feeding temperature increase due to negative flow rate at the upstream groove for three different shaft speeds (Bearing B3V1, $T_f=29^\circ\text{C}$).

The cases for which a negative flow rate occurred can be easily detected because both grooves displayed temperatures that fairly exceeded the feeding temperature, T_f (29°C). For instance, in the 2000rpm test with the lowest P_f (100kPa, Figure V-32a), it can be seen that the hot oil that was flowing out of the upstream groove had a temperature around 53°C . After mixing with the fresh oil supply (29°C) at the feeding system pipes that it caused a 9°C increase in the temperature of the lubricant supplied to the -90° groove (38°C). Figure V-32a further shows that when P_f was increased to 100kPa and 150kPa this temperature decreased to 35°C and 31°C respectively. In all these three tests the $+90^\circ$ groove flow rate was negative, as seen previously in Figure V-28a. With P_f values of 250kPa and higher, the negative flow rate disappeared in the

2000rpm tests and so did its effect on the feeding temperature rising. Similar analyses apply to the data obtained at 3000 and 4000rpm presented in Figure V-32.

V.4.4 Influence of feeding temperature^{**}

Lubricant viscosity, which strongly depends on local temperature, is the parameter responsible for hydrodynamic pressure generation within the fluid. Therefore, the variation of feeding temperature, T_f , is likely to exert a strong influence not only on the temperature field, the power loss and the flow patterns, but also on the bearing eccentricity and ultimately on the load carrying capacity of the bearing. It is true that feeding the lubricant at low T_f tends to maximize bearing cooling efficiency and load capacity even if it is at the expense of a slightly higher power loss caused by the added drag. However, in the absence of an efficient oil cooling system, it is not always possible to keep T_f as low as desired, especially under severe operating conditions, where large amounts of heat are generated by viscous dissipation. Under these conditions the high T_f values raise the seizure risk not only because dangerously high eccentricities might be induced, but also because thermal distortion will further facilitate localized contact due to the thermal crowning of surfaces. A loss in lubricant viscosity also tends to reduce damping, promoting an unstable operation.

A suitable knowledge of the actual influence of T_f on bearing performance would therefore be of great help. Some previous theoretical and experimental works have addressed this issue, although with bearing types which were different from those tested in the present work. Mitsui et al (1983) and Costa et al (2003a, 2003b) focused their studies on single groove journal bearings, while Ma and Taylor (1995) studied the elliptical bearing. Recent work by the team on a different test rig has already started to address the lack of knowledge on lubricant supply conditions such as lubricant feeding pressure and feeding temperature (Brito et al, 2006, 2007a). However, the lack of knowledge concerning the proportion of the flow fed through each groove somewhat limited the discussion. One of the main contributions of the tests carried out in the rig of Minho University is the ability to perform an accurate flow measurement of the individual flow rates entering each one of the grooves. This knowledge has proved to be a major contribution for the understanding of twin groove journal bearing behavior.

Several loads (from 0.4kN to 5kN), shaft speeds (2000rpm and 4000rpm) and bearing geometries (B3V1 and B2V1) were tested. The Lubricant feeding pressure was kept at 100kPa, while the feeding temperature took four different values (29/29.5°C, 39°C, 48.5°C, 58°C).

^{**} This section is based on an article presented in IBERTRIB 2009, held in Coimbra, Portugal, in May 2009.

a) Shaft locus

Figure V-33 shows the influence of the feeding temperature on the eccentricity ratio, ϵ , for two different bearing geometries and a fixed shaft speed (4000rpm). It can be seen that ϵ increases with the increase of T_f . This happens due to the loss of viscosity suffered by the hotter lubricant, which decreases the load carrying capacity of the bearing. For the same working conditions, Bearing B2V1 displays a lower eccentricity than bearing B3V1 due to the lower specific load (the two bearings have dissimilar lengths – they display b/d ratios of 0.8 and 0.5, respectively).

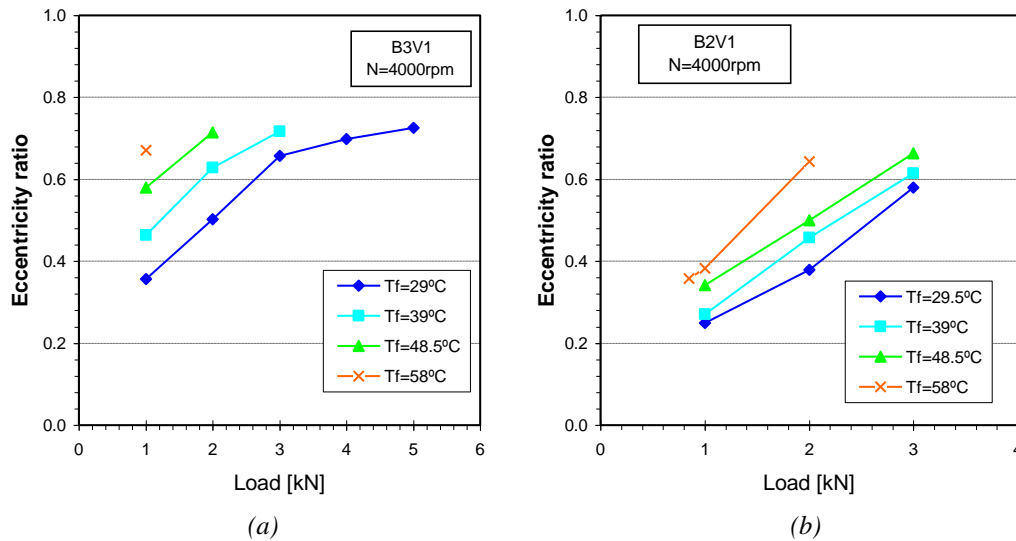


Figure V-33 – Influence of lubricant feeding temperature on the eccentricity ratio of (a) Bearing B3V1 and (b) Bearing B2V1 (N=4000rpm, Pf=100kPa). Note: due to measuring uncertainties, these values should be regarded mainly as indicative.

b) Lubricant flow rate

Flow rate results (total flow rate and partial flow rates at each groove) corresponding to several working conditions and T_f values are presented in Figure V-34 thru Figure V-36.

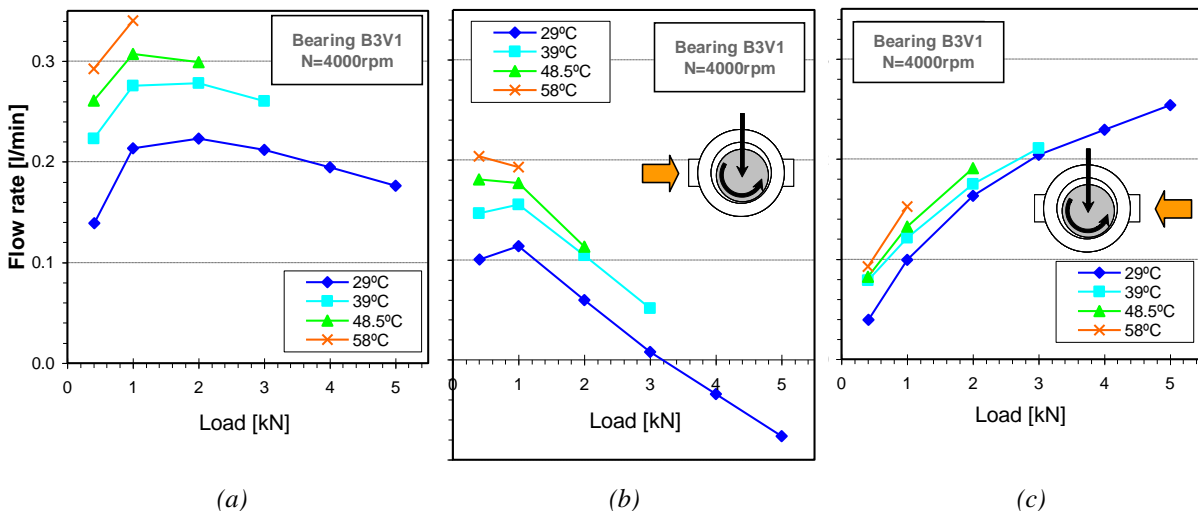


Figure V-34 – Influence of feeding temperature on (a) Total flow rate, (b) +90° groove flow rate and (c) -90° groove flow rate (Bearing B3V1, N=4000rpm, Pf=100kPa).

For the 4kN and 5kN tests, it is interesting to note, again, the occurrence of negative flow rate at the groove located at the convergent portion of the film (the $+90^\circ$ groove – see Figure V-34b).

It can be seen that the total flow rate tends to increase with increasing T_f , especially in the lower range of applied load. For instance, for the lightest load tested (0.4kN), the total flow rate and the flow rate at each groove of bearing B3V1 approximately doubled as T_f changed from 29° to 58°C (see Figure V-34a). The reason for this could be explained as follows. On one hand, the increase of T_f yields a decrease in lubricant viscosity which promotes the oil flow. On the other hand, by inspecting the eccentricity chart displayed in Figure V-33, it can be seen that the increase of T_f brought an increase in shaft eccentricity. It is a known fact that within the lower eccentricity range the increase of ε is normally associated with an increase in total flow rate (Brito et al, 2007a).

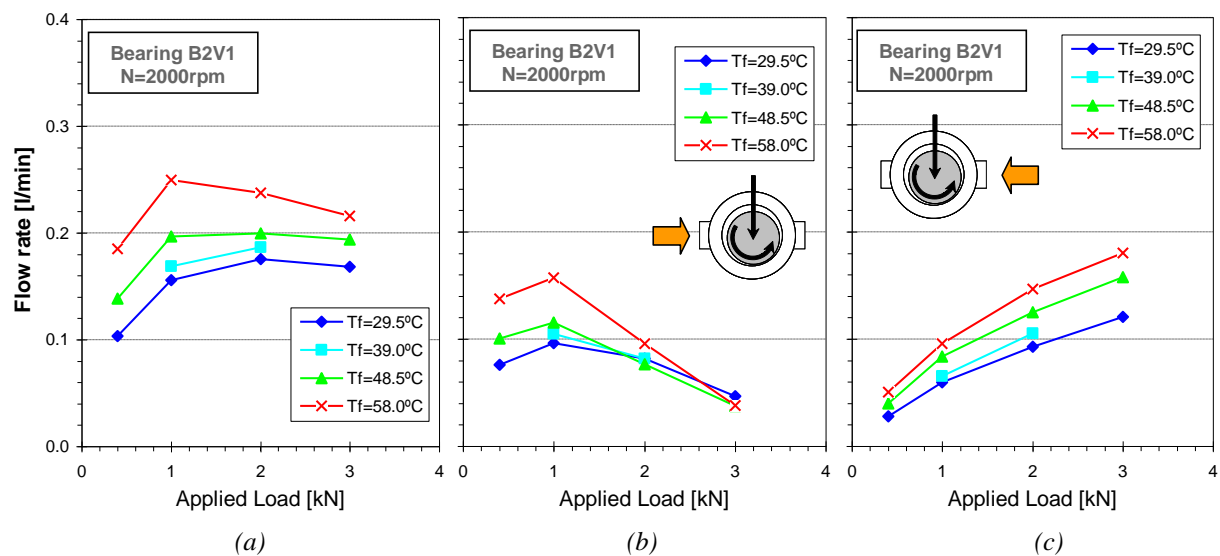


Figure V-35 – Influence of feeding temperature on (a) Total flow rate, (b) $+90^\circ$ groove flow rate and (c) -90° groove flow rate (Bearing B2V1, $N=2000\text{rpm}$, $P_f=100\text{kPa}$).

For higher loads, however, the increase of the total flow rate with increasing T_f tends to be mitigated, with the flow rate curves for each T_f getting closer to each other. Inclusive, the increase of T_f lead in some cases to the decrease of the flow rate at the $+90^\circ$ groove, as Figure V-35b and Figure V-36b depict. This occurred with combinations of high T_f and high load, which corresponded to the tests with the highest eccentricity, as seen in Figure V-33b. Again, this is in agreement with what was already observed in previous sections, that within the high eccentricity range, the $+90^\circ$ groove flow rate tends to decrease with increasing eccentricity. Therefore, it may be stated that T_f has an influence on flow rate which is analogous to that of load, in the sense that both influence eccentricity in the same way.

Unfortunately, there are no results available in order to assess the influence of T_f in the negative range of the $+90^\circ$ groove flow rate. However, by observing the trends of the curves in

Figure V-35b and Figure V-36b it can be advanced that the increase of T_f should actually lower the critical load at which the negative flow rate phenomenon starts occurring.

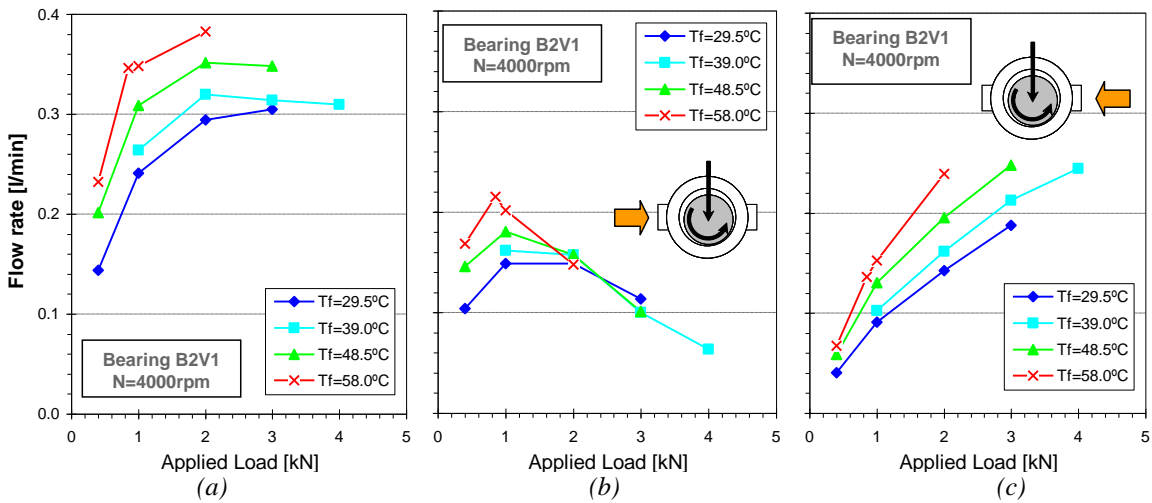


Figure V-36 – Influence of feeding temperature on (a) Total flow rate, (b) +90° groove flow rate and (c) -90° groove flow rate (Bearing B2V1, $N=4000rpm$, $P_f=100kPa$).

c) Temperature field

Figure V-37 displays the temperature profiles at the midplane of the inner bush surface of bearing B3V1 for three different values of load (0.4kN, 1kN and 2kN) and four different values of feeding temperature (29°C, 39°C, 48.5°C, 58°C).

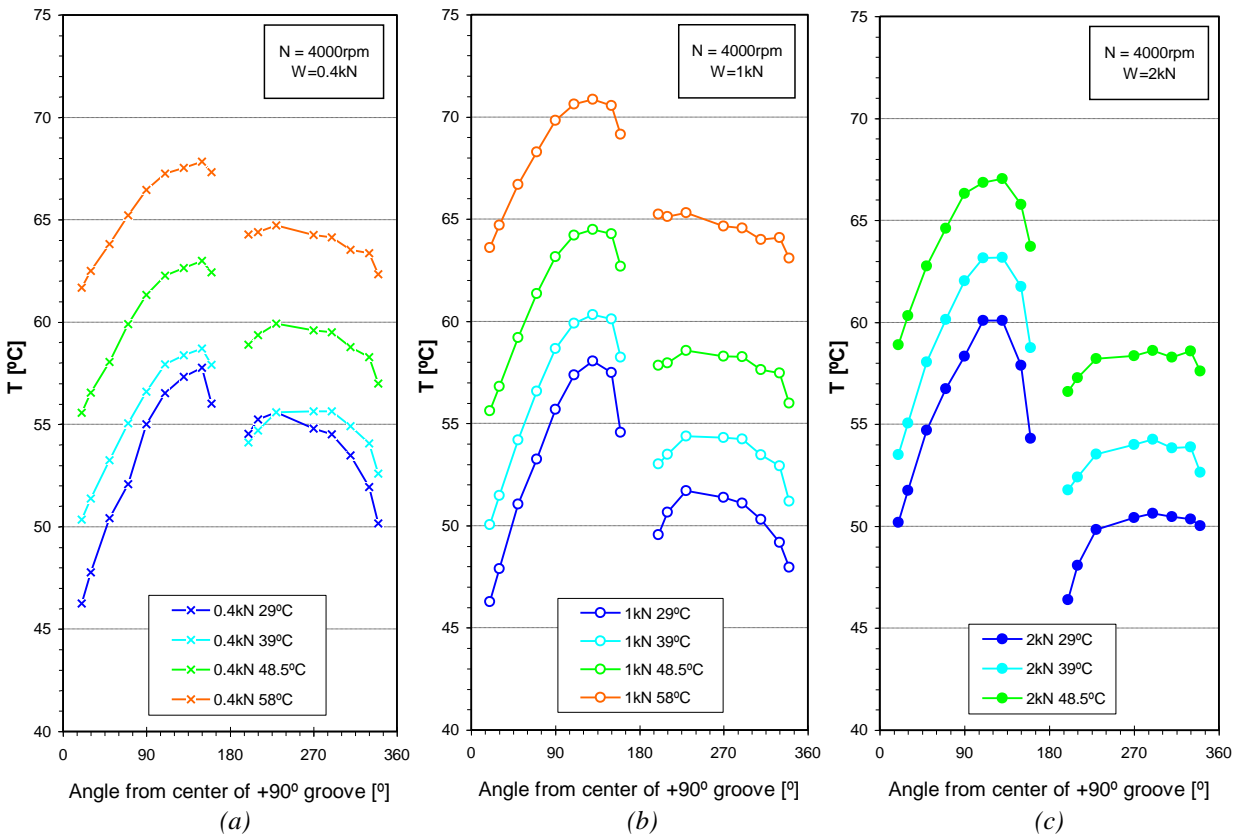


Figure V-37 – Influence of lubricant feeding temperature on the temperature profile at midplane of the inner bush surface for (a) $W=0.4kN$, (b) $1kN$ and (c) $2kN$ (Bearing B3V1, $N=4000rpm$, $P_f=100kPa$).

The profiles corresponding to the different values of T_f although very different in level are similar in trend. Some differences may be observed at the vicinity of grooves. The lower is T_f , the stronger is the temperature depression observed around these regions, both before and after the grooves. This causes the temperature span of each curve to decrease as T_f increases.

Figure V-38a, which summarizes the maximum bush temperature for each test, shows that the increase of T_{max} is smaller than the corresponding increase of T_f . The same applies to the lubricant outlet temperature, as displayed in Figure V-38b.

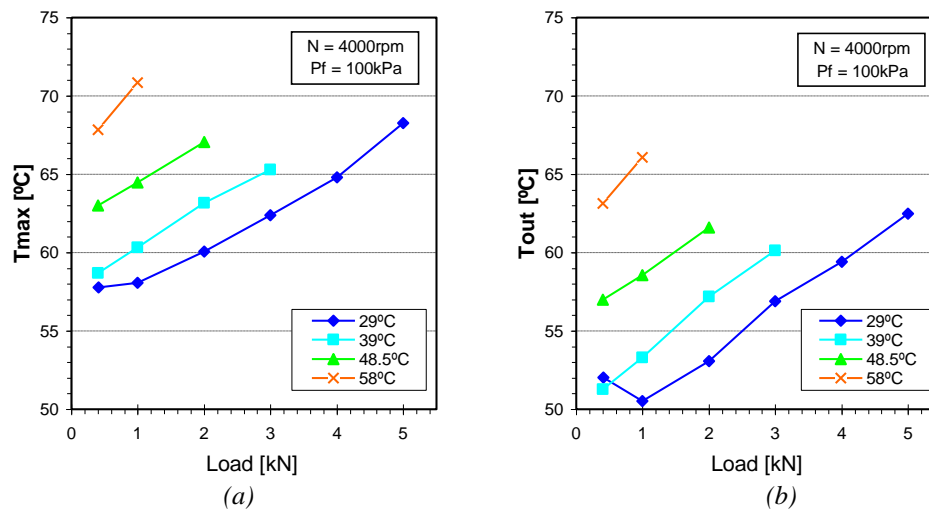


Figure V-38 Influence of lubricant feeding temperature on (a) bush maximum temperature and (b) lubricant outlet temperature (Bearing B3V1, $N=4000 \text{ rpm}$, $P_f=100 \text{ kPa}$).

It is interesting to note in the lowest load tests (0.4 kN - Figure V-37a) that the temperature profile corresponding to the lowest T_f (29°C) is very close to the temperature profile of the test with a T_f 10°C higher (39°C). Not only the maximum bush temperature difference is only 0.9°C, as detailed in Figure V-38a, but also the lubricant outlet temperature for the lower T_f test (29°C) is actually slightly higher than that of the higher T_f test (39°C - Figure V-38b). This might have happened because the higher lubricant feeding temperature was eventually compensated by the increase of the flow rate. In fact, Figure V-34 shows that when T_f increased from 29°C to 39°C the flow rate increased 60% (from 0.14 l/min to 0.22 l/min), the greatest increase recorded in the chart. This ultimately leads to a similar cooling effect for both tests. Additionally, when T_f increased there was an eccentricity increase (Figure V-33a) and it is known that within the very low eccentricity range, an increase in eccentricity actually yields a general decrease on bearing temperature.

A temperature decrease with increasing eccentricity in the low eccentricity range was observed, for instance, with the tests carried out with bearing B2V1 under variable load, whose results are displayed for $N=2000 \text{ rpm}$ (Figure V-39) and for $N=4000 \text{ rpm}$ (Figure V-40). It can be seen that there was a reduction in T_{max} when increasing the load (and therefore eccentricity)

from 0.4kN to 1kN in the lowest T_f tests. Inclusively, T_{max} is highest for the lowest load in tests with $T_f=29.5^\circ\text{C}$ and $N=4000\text{rpm}$ (Figure V-40a,c).

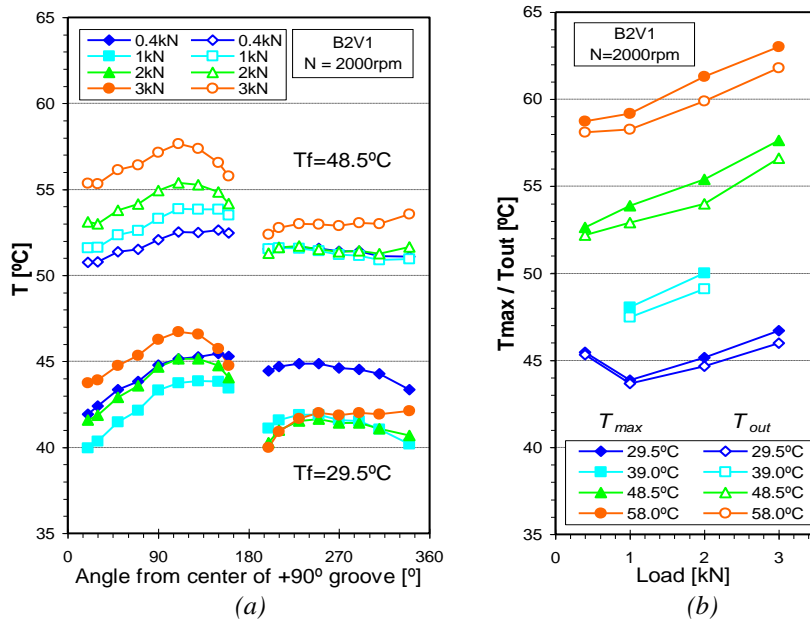


Figure V-39 – (a) Temperature profile at the midplane of the inner bush surface for different loads and two different feeding temperatures and (b) Influence of feeding temperature on maximum bush temperature and lubricant outlet temperature (Bearing B2V1, $N=2000\text{rpm}$, $P_f=100\text{kPa}$).

By inspecting Figure V-40, it can be seen that, for the same load, the increase of T_f globally increased the temperature level, with this variation being more pronounced at the loaded land of the bearing than at the unloaded land. Again, it can be said that the increase of T_f has an effect on the trend of the temperature profiles which is comparable to the effect of load increase and to the effect speed decrease, which is linked to the increase of eccentricity usually observed in all of these situations.

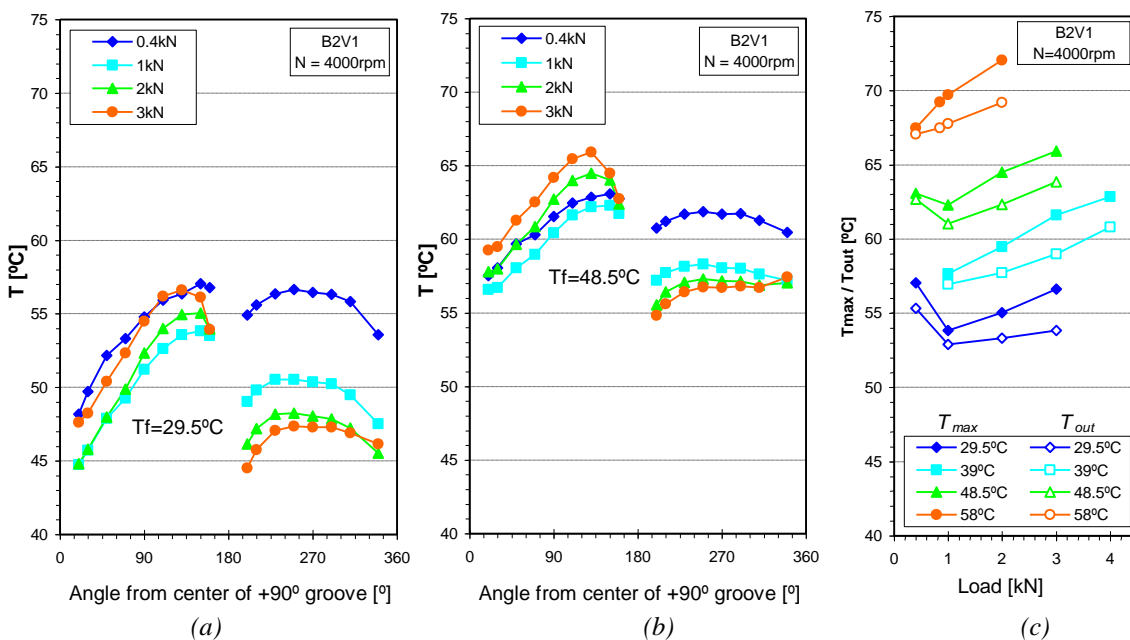


Figure V-40 – Temperature profile at the midplane of the inner bush surface for different loads and (a) $T_f=29.5^\circ\text{C}$ and (b) $T_f=48.5^\circ\text{C}$. (c) Influence of feeding temperature on maximum bush temperature and lubricant outlet temperature (Bearing B2V1, $N=4000\text{rpm}$, $P_f=100\text{kPa}$).

d) Concluding remarks

This study points out to the overall conclusion that under lightly loaded conditions a moderate increase of T_f might indeed prove beneficial in terms of reducing the power loss without compromising the safe operation of the system. This would clearly not be the truth in the case of heavily loaded bearings. Not only is it not guaranteed that any actual reduction in power loss will be obtained with the increase of T_f , but also the risk of seizure would be greatly amplified.

The individualized measurement of the flow rate, which allowed the detection of rather dissimilar flow rates at each groove (that could even reach negative values in one of them), showed that lubrication effectiveness might not be as good as the value of the total flow rate would suggest. The increase of T_f under such conditions would lower the critical load at which seizure is likely to occur.

V.4.5 Influence of bearing clearance

The radial clearance of a bearing system, c_r , which is the difference between the bush inner radius and the shaft radius, is a very important design variable, since it affects deeply the flow patterns and the viscous dissipation within the bearing gap. Generally, decreasing the clearance of a bearing tends to increase its load carrying capacity because the velocity gradients, which are responsible for hydrodynamic lift, become more intense. However, this happens just up to a certain point. If the clearance is excessively low, thermal effects might become prevalent, with the heat generated by viscous dissipation causing a fall in load capacity. A bearing clearance might also be suitable under a range of working conditions but become unsuitable out of that range.

To study the effect of this parameter on the bearing behavior tests were carried out with bush B2 and the two different shafts V1 and V2. The resulting bearing systems B2V1 and B2V2 displayed radial clearances (c_r) of 43 μm and 54 μm at 20°C, respectively, as shown in Table V-1. This corresponds to clearance ratios (c_r/R_i) of 1.71×10^{-3} and 2.14×10^{-3} respectively.

a) Lubricant flow rate

Results for flow rate for the two bearing systems are presented in Figure V-41. All flow rates increase significantly when increasing clearance. The 25% increase in clearance from bearing B2V1 to bearing B2V2 yielded increases of between 50% and 60% in total flow rate, between 40% and 55% for the -90° groove flow rate and between 60% and 70% for the +90° groove flow rate. These increases which are much greater than the increase of c_r are in agreement with theory (ESDU 84031, 1984).

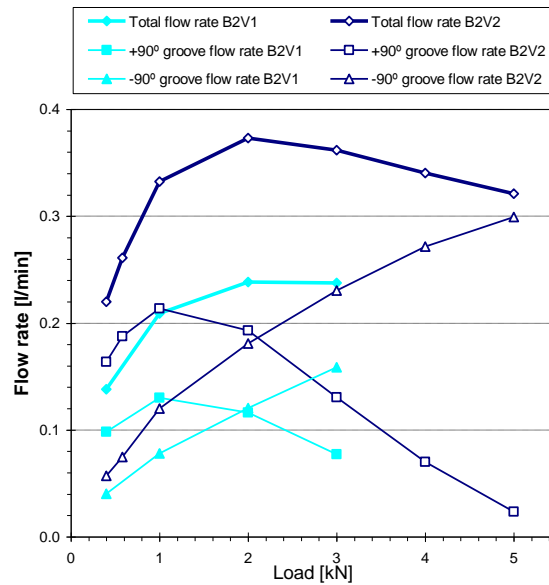


Figure V-41 –Influence of bearing clearance on lubricant flow rate (bearings B2V1 and B2V2, $N=3000\text{rpm}$, $P_f=100\text{kPa}$, $T_f=29.5^\circ\text{C}$)

b) Temperature field

The thermal results for the two bearings under similar operating conditions are displayed in Figure V-42. Comparing the temperature profiles of bearings B2V1 and B2V2 (Figure V-42a and b, respectively) it can be seen that the increase of c_r yielded similar temperature profiles but a decrease of the temperature level. T_{max} decreased between 3°C for the highest load (3kN) and nearly 6°C for the lowest load (0.4kN). This temperature decrease is explained both by the reduction of heat generation by viscous dissipation and by the increase in flow rate. The influence of the latter factor can be easily observed in the vicinity of the grooves, where the temperature fade is more marked than in the rest of the bearing circumference.

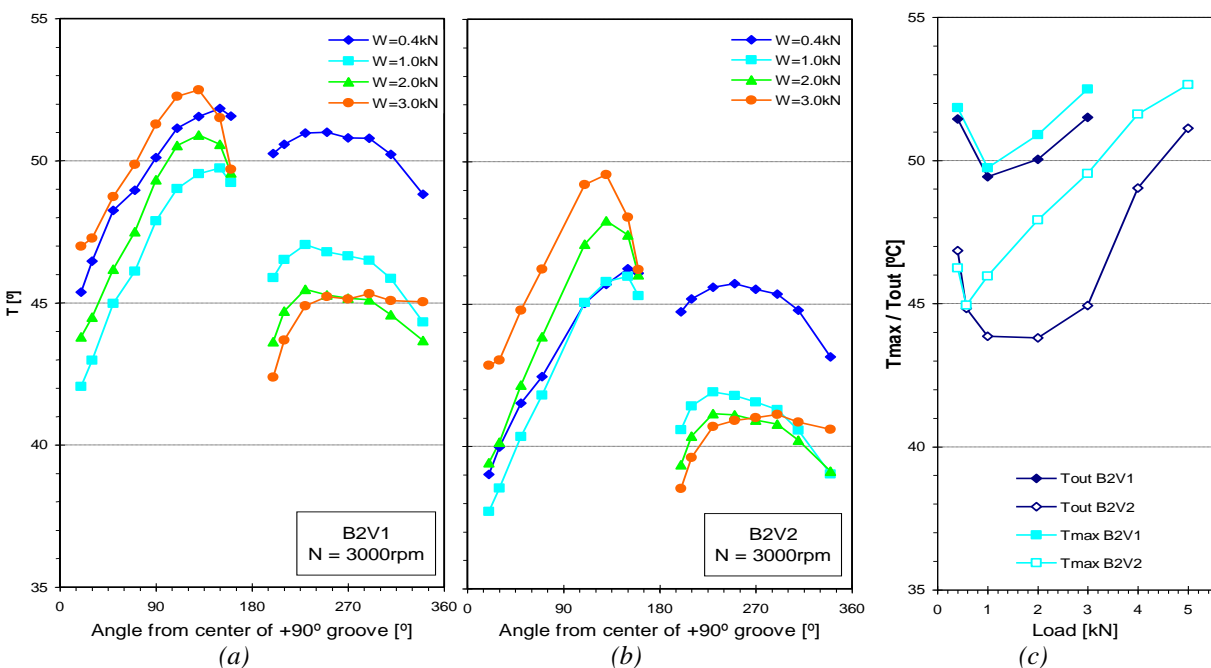


Figure V-42 – Influence of bearing clearance on the temperature profile at the midplane of the inner bush surface for (a) bearing B2V1 and (b) bearing B2V2. (c) Maximum bush temperature and lubricant outlet temperature ($N=3000\text{rpm}$, $P_f=100\text{kPa}$, $T_f=29.5^\circ\text{C}$).

The difference between T_{max} and T_{out} was always below 1°C for bearing B2V1, and as high as 4.6°C for bearing B2V2, as seen in Figure V-42c. Curiously, the trend of variation of T_{out} is approximately symmetrical to the trend of the curve corresponding to the +90° groove flow rate of Figure V-41. This suggests that the decrease of T_{out} could be intimately associated with the increase of flow rate at this groove.

V.4.6 Influence of the number of grooves

It is rather commonsense to affirm that a twin groove arrangement provides a more efficient lubrication and a cooler operation than a bearing with a single groove located at +90° to the load line, but little evidence has been found in support of this claim. Furthermore, there are no experimental works, to the author's knowledge, that compare the performance of single and twin axial groove bearings with similar geometry.

As already explained, the single groove bearing is in reality the twin groove bearing with the lubricant supplied to the +90° groove only to perform this study. The oil feeding to the opposite groove was shut with a valve. This way, although this groove has not been eliminated, it is expected that its influence will be marginal since the inactive groove is located in the unloaded region of the bearing. On the other hand, one great advantage of this procedure is that it becomes possible to test and compare the two different groove profiles (single and twin) with exactly the same geometric shape (namely with the same clearance), and within the same test session.

a) Lubricant flow rate

The total flow rate and the flow rate through each groove are displayed in Figure V-43 for two different feeding pressures (100kPa and 250kPa).

It is interesting to note that the total flow rate is nearly the same for both single and twin groove bearings. Only a slight difference appears as load increases, with the single groove bearing displaying slightly lower flow rate values (5% and 9% maximum, respectively for 100kPa and 250kPa tests). It is natural that these differences are greater under higher loads, because these are the tests where the additional groove (-90° groove) is more active: at high loads this groove is located at a very low pressure region, the ruptured film region. Here, the resistance to inward lubricant flow is lowest, causing a great part of the lubricant to enter the bearing gap through this groove instead of through the groove which feeds the loaded region of the bearing (+90° groove).

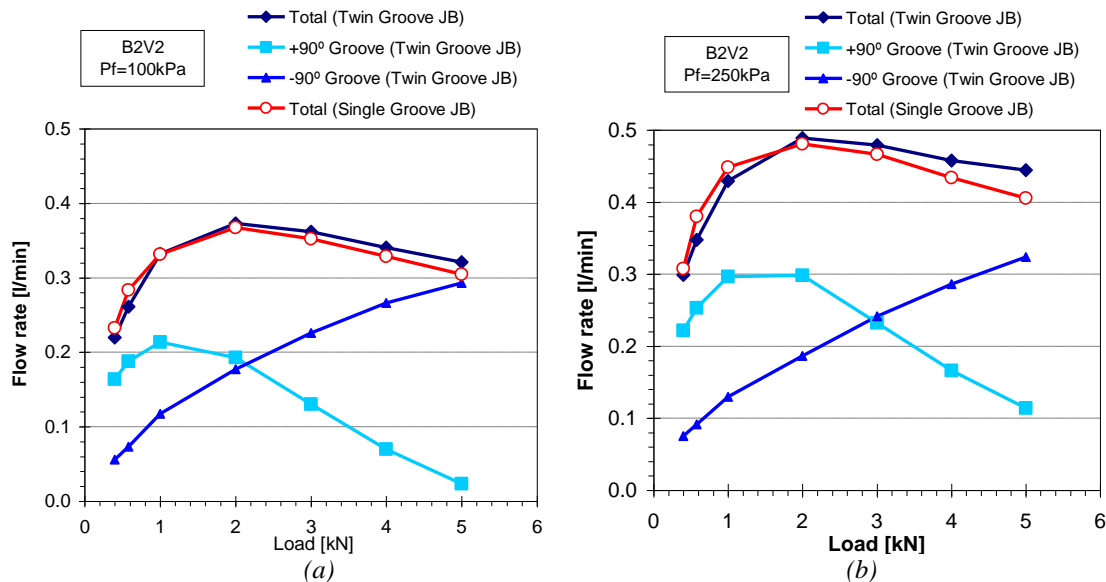


Figure V-43 – Influence of the number of grooves on the lubricant flow rates for (a) $P_f=100\text{kPa}$ and (b) $P_f=250\text{kPa}$ (Bearing B2V2, $N=3000\text{rpm}$, $T_f=29.5^\circ\text{C}$).

It can be concluded that when increasing the number of grooves from 1 to 2 the lubricant supplied directly to the active region of the bearing through the $+90^\circ$ groove decreases, while the lubricant starts being supplied to the unloaded land of the bearing through the -90° groove. It can be seen clearly in Figure V-43a that the flow rate pattern of the twin groove bearing can be problematic at high loads and low values of P_f : in the highest load test displayed in this figure the $+90^\circ$ groove flow rate was nearly zero. This means that the critical region of the bearing (the region of minimum film thickness) is poorly lubricated, even admitting that some of the lubricant coming from the upper land is recirculated. Observing the trend of $+90^\circ$ groove flow rate curve it may be estimated that negative flow rate would be likely to occur at loads above 6kN (this has not been tested). On the contrary, in the 5kN test the single groove journal bearing still displayed a $+90^\circ$ groove flow rate of 0.31l/min, which is only 17% lower than the maximum measured flow rate (2kN test).

b) Shaft locus

The effect of the number of grooves, load and feeding pressure on the shaft eccentricity ratio and attitude angle is displayed in Figure V-44. The increase of feeding pressure has a positive influence in shaft eccentricity ratio, reducing it as much as 0.06 (Figure V-44a). On the other hand, changing the groove profile from a single to a twin groove arrangement exerted the opposite effect, rising eccentricity for loads above 1kN. This deleterious effect is amplified as load increases, with a maximum increase of 0.06, from 0.87 to 0.93 for the highest load/lowest P_f tested.

In spite of the fact that the absolute values of eccentricity are to be taken mainly as qualitative since they are prone to a high degree of uncertainty, nevertheless the relative differences

between tests, especially between single and twin groove tests carried out at similar operative conditions, may be analyzed with some confidence.

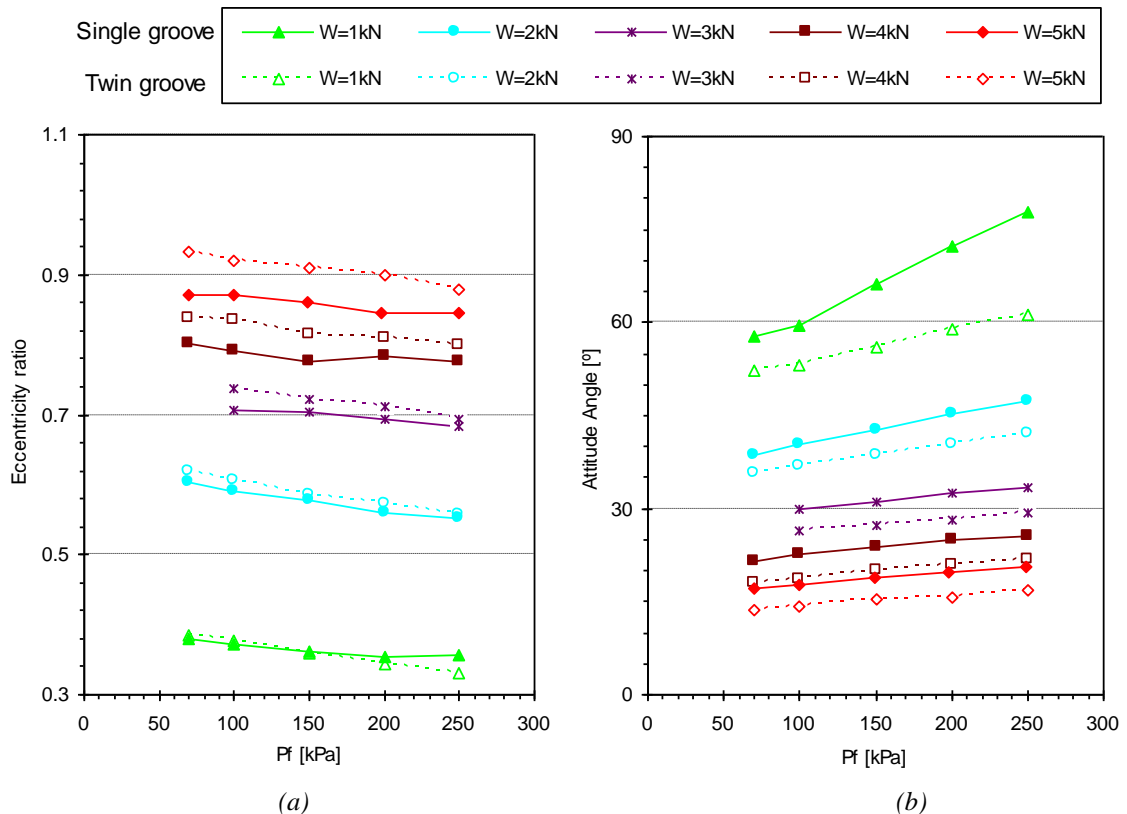


Figure V-44 – Influence of groove number on (a) eccentricity ratio and (b) attitude angle, for several loads and feeding pressures (Bearing B2V2, $N=3000\text{rpm}$, $T_f=29.5^\circ\text{C}$).

The eccentricity increase due to the increase in number of grooves and the decrease in P_f was always accompanied by a decrease in attitude angle, as seen in Figure V-44b.

c) Temperature field

The influence of groove number on the temperature profile at the midplane of the inner bush surface is presented in Figure V-45 for two different loads and feeding pressures. A separate analysis of low load (0.4kN) and high load (5kN) results is carried out below.

c.1) Lightly loaded bearing ($W=0.4\text{kN}$):

- Under low loads there is little change in the temperature trends between the single and the twin groove configuration. Only a slight temperature fall across the -90° groove was observed in the twin groove bearing case. This fall, which was of 1.2°C at a feeding pressure of 100kPa (Figure V-45a), is hardly distinguishable from that observed with a feeding pressure 2.5 times higher (1.4°C - Figure V-45b). This is in agreement with the fact that the -90° groove flow rate at low loads was small both for low and high feeding pressures (0.05 and 0.07l/min respectively for $P_f=100\text{kPa}$ and $P_f=250\text{kPa}$ – see Figure V-43).

- In spite of being moderate, the effect of the activation of the -90° groove was sufficient to move the maximum temperature location from the unloaded land, as in the case of the single groove bearing, to the loaded land of the bearing. Increasing the number of grooves yielded a decrease of 1.1°C in T_{max} for 100kPa and of 1.5°C for 250kPa .

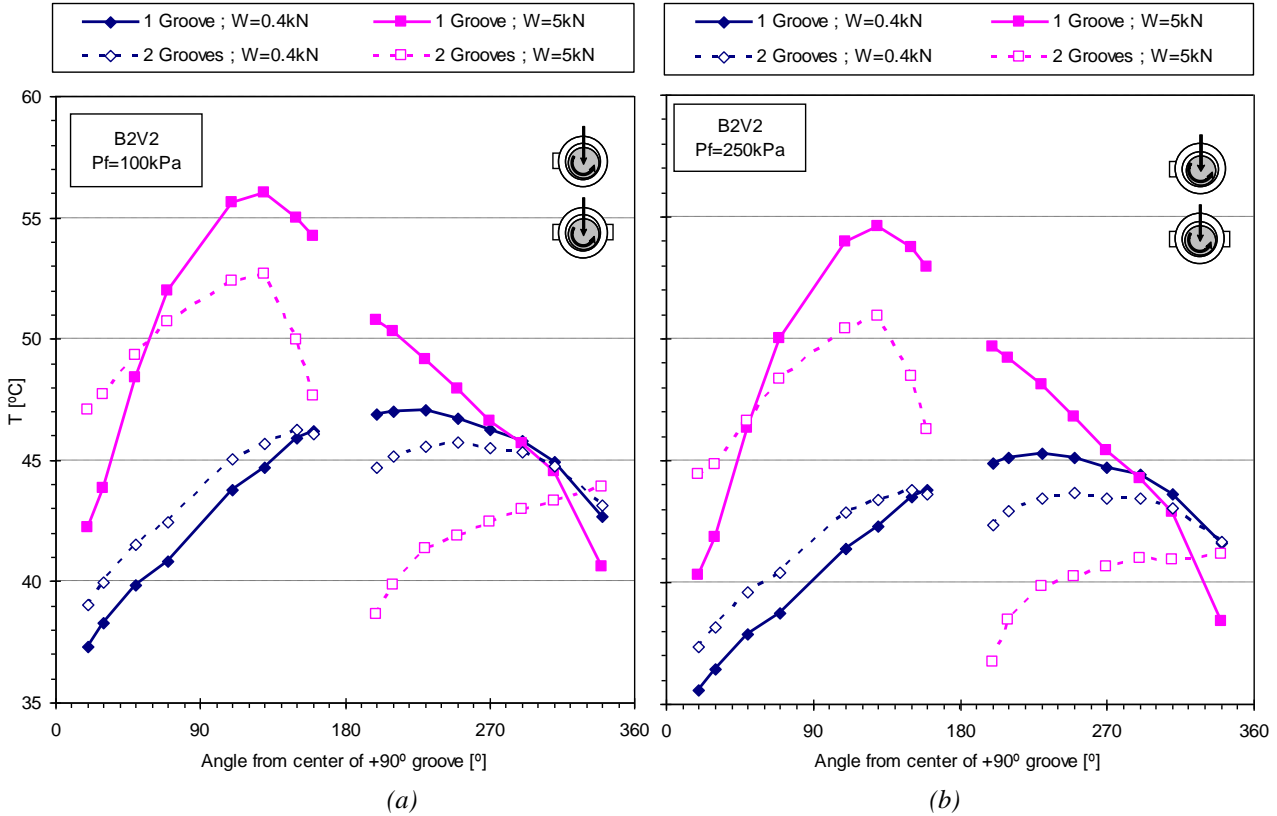


Figure V-45 – Influence of groove number on the temperature profile at midplane of the inner bush surface for two different loads and (a) $P_f=100\text{kPa}$ and (b) $P_f=250\text{kPa}$ (Bearing B2V2, $N=3000\text{rpm}$, $T_f=29.5^\circ\text{C}$).

c.2) Heavily loaded bearing ($W=5\text{kN}$):

Under high loads the differences between the single and the twin groove bearing are patent both at low (100kPa - Figure V-45a) and high (250kPa - Figure V-45b) feeding pressure.

- The cooling effect of the -90° groove is clear. When this groove is active (twin groove case) not only the temperature falls steeply across it, with a temperature decrease above 9°C , but also the maximum bush temperature is lowered by about 3.5°C . Such cooling effect is explained by the high flow rate at this groove (see Figure V-43).

- A very diverse cooling effect of the $+90^\circ$ groove is apparent when comparing the two cases. The temperature at the vicinity of the groove region is lower in the single groove case than in the twin groove case. In the latter case there is even a significant increase of the temperature between the thermocouples located immediately upstream and downstream of this groove. Nevertheless when comparing Figure V-45a and Figure V-45b, some cooling of the bush body can still be perceived because the increasing trend of the temperature curve at the unloaded land (between 180° and 360°) is less steep for the higher P_f test. This indicates that some

cooling still exists, nonetheless. Again these differences are only explained with the knowledge of the flow rates at each groove given by Figure V-43.

The evolution of bush maximum temperature and the lubricant outlet temperature with load is presented in Figure V-46, for both groove configurations (single and twin) and for two different values of P_f (100kPa and 250kPa).

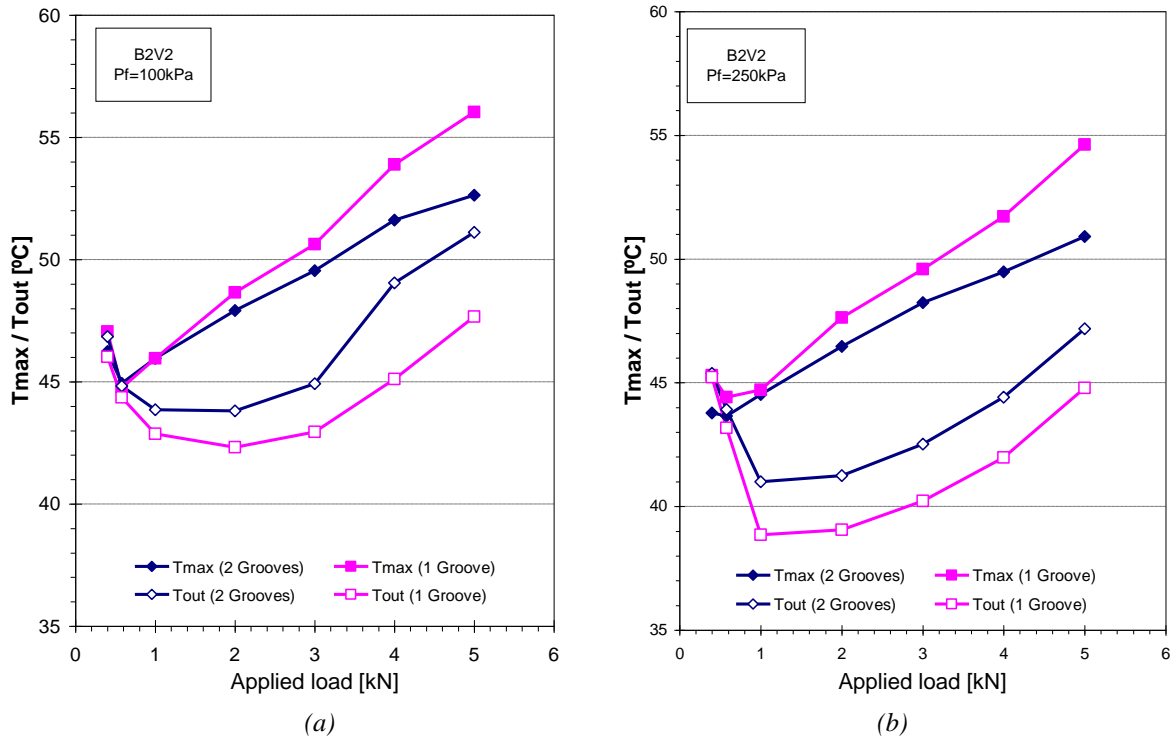


Figure V-46 – Influence of groove number on the maximum bush temperature and on the lubricant outlet temperature as a function of load and (a) $P_f=100\text{kPa}$ and (b) $P_f=250\text{kPa}$ (Bearing B2V2, $N=3000\text{rpm}$, $T_f=29.5^{\circ}\text{C}$)

T_{max} suffers an initial decrease with increasing load but above 0.6kN begins increasing consistently. T_{out} also displays an initial decrease with increasing load, a minimum between 1 and 2kN, and an ascending trend for higher loads. This happens for both groove configurations (single and twin). The trend of T_{out} with load displays some parallel with the inverse of the trend of the $+90^{\circ}$ flow rate (recall Figure V-43). When this flow rate increases with increasing load, T_{out} tends to decrease, and vice versa. Therefore, T_{out} seems to be intimately connected with the cooling efficiency of the $+90^{\circ}$ groove flow rate.

It is interesting to note that although T_{max} was always higher for the single groove configuration, T_{out} is almost always higher with the twin groove configuration, except in some lightly loaded tests. The reason for this may be explained again by interconnection found between T_{out} and the $+90^{\circ}$ groove flow rate that was noted in the previous paragraph. In fact, this flow rate is stronger in the case of the single groove bearing.

d) Motor consumption

The total motor electrical consumption was recorded in some test sessions with a portable multimeter. The results are displayed in Figure V-47. Although the motor consumption depends on more factors than just the effect of the bearing system, it can provide some insight on the relative influence of applied load and feeding pressure and, particularly, on the impact of the number of grooves, in bearing performance.

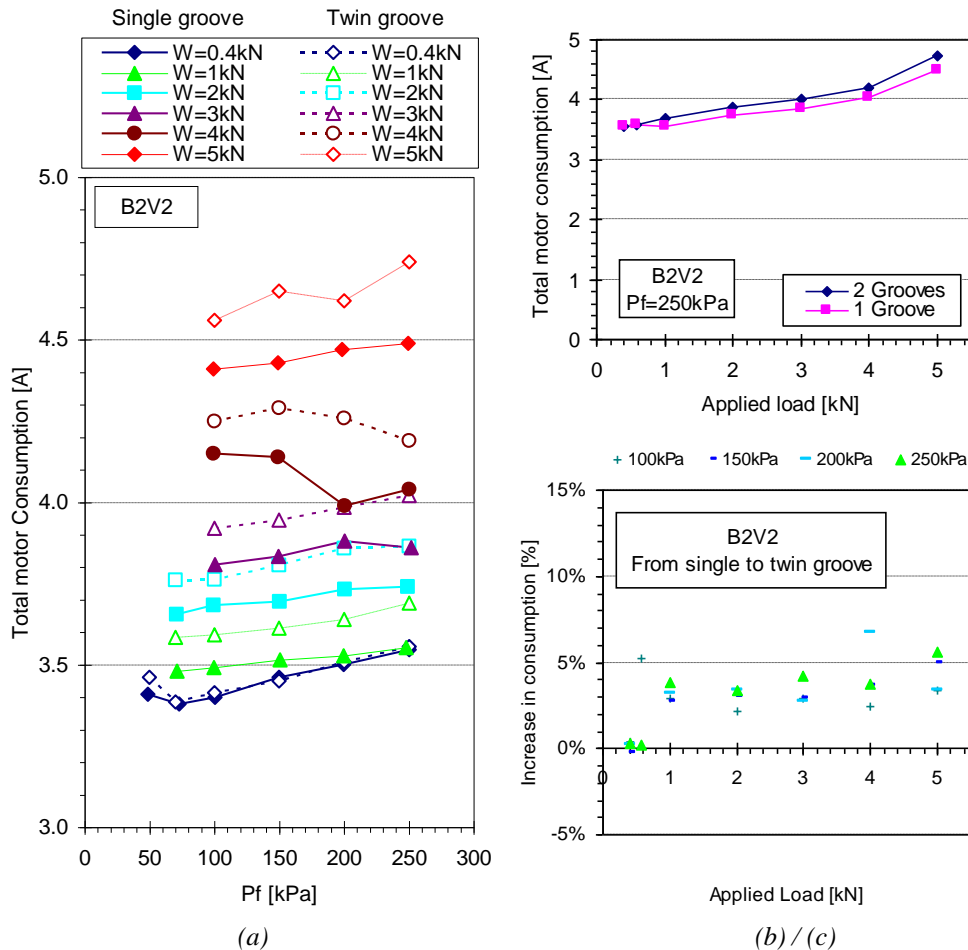


Figure V-47 – Influence of number of grooves on the total motor consumption (a) as function of feeding pressure and (b) as function of load, for $P_f=250\text{kPa}$. (c) Percentage increase of the total motor consumption due to the increase of the number of grooves (Bearing B2V2, $N=3000\text{rpm}$, $T_f=29.5^\circ\text{C}$).

In Figure V-47a, the total motor consumption is displayed as a function of feeding pressure, for several loads and for the two groove configurations (single and twin). Figure V-47b shows the motor consumption as a function of load for one value of feeding pressure ($P_f=250\text{kPa}$). By analyzing Figure V-47a it can be observed that:

- Under low loads there is a general ascending tendency of the consumption with the increasing feeding pressure. This smooth increase of the electrical consumption, typically around 50mA for each 100kPa, is due to the increase of the viscous dissipation: As P_f increases, more lubricant is present in the bearing gap. This happens both with single and twin groove bearings.

- Under high applied loads (above 3kN) the results are more scattered and this poses difficulties for the data analysis. In fact, under high loads there are two opposing effects present when increasing P_f : the higher drag which would be expected with increasing must be balanced with the increase of the effectiveness of the lubrication when P_f is increased (lubricant starvation is minimized and eccentricity is reduced). In the limit, an excessively low feeding pressure combined with a small groove length ratio (0.5) could inclusively induce the appearance of local contact (mixed lubrication regime inception), which would clearly affect the negatively not only power loss but also the safety of operation and bearing life.

- The consumption was almost always higher with the twin groove bearing than with the single groove bearing, as can be observed in all three figures. Particularly, Figure V-47c, which represents the percent increase in electric consumption when changing from a single to a twin groove configuration, shows that the differences are fairly consistent for most cases. The twin groove bearing displayed consumptions which were normally 2% to 5% higher than those obtained with the single groove bearing. Exceptions to this were the very low load tests, with negligible differences between the two groove configurations.

Several causes can be pointed out to explain why twin groove journal bearings generally display a higher consumption than single groove bearings. While the unloaded region of the twin groove bearing is filled with lubricant that was supplied trough the -90° groove, this is not the case with single groove bearings. On the contrary, the lubricant which leaked out of the bearing at its active region is not compensated until the $+90^\circ$ groove. Therefore, little lubricant is present within the ruptured film region of single groove bearings. This reduces the viscous dissipation within this region, unlike twin groove bearings. Also twin groove bearings display a slightly higher working eccentricity than single groove bearings (recall Figure V-44a).

As a conclusion, it is not straightforward to conclude which of the groove configurations, single or twin, should be used preferentially. However, based on the present investigation, it seems reasonable to assume with some confidence that the twin groove journal bearing can be problematic under combinations of high eccentricity and low feeding pressure, causes slightly more power loss and a higher lubricant outlet temperature than bearings with a single groove located at $+90^\circ$ to the load line. Nevertheless, the twin groove bearing tends to display a lower maximum bush temperature and allows the rotation of the shaft in both directions, which could be a design requisite. Further investigation would be needed in order to generalize these conclusions.

V.5 Conclusions

In this chapter the experimental work carried out in the Tribology Laboratory of Minho University has been presented. A description of the test rig, with special emphasis on its new and updated capabilities, has been carried out. The experimental procedure has been fully described.

Results concerning total flow rate, flow rate through each groove, shaft locus, inner bush surface temperature, lubricant outlet temperature, and motor consumption have been presented and discussed for a range of operating and supply conditions, and geometric characteristics. An investigation on the influence of load, speed, feeding pressure, feeding temperature, bearing clearance and number of grooves on bearing performance has been undertaken.

The conjunction of all the factors mentioned provided a notable aid to the understanding of the phenomena taking place, particularly, the understanding of the role of each groove and of the supply conditions in bearing performance. This, along with the creation of an extensive repository of bearing performance data which would help the validation of theoretical bearing models, were the main aims of the present experimental work.

Some particularities of this work include, to the author's knowledge, the first thorough investigation of the flow rate distribution through each groove of twin groove journal bearings, the first documented report of the phenomenon of negative flow rate occurring at one of the grooves of twin groove bearings and the first experimental comparison of the performance of single and twin groove journal bearings with identical geometry.

For the geometry and working conditions tested the following conclusions can be drawn:

1. In the range of applied load studied, the measured total flow rate in the bearing was approximately the same for single and twin groove journal bearings. For the twin groove arrangement, the partial flow rates through each groove varied dramatically with increasing load.
2. For twin groove bearings in the very low eccentricity range the flow rate in the +90° groove tends to increase up to a maximum, after which it starts decreasing consistently with increasing eccentricity.
3. At high eccentricities the flow entering through the +90° groove is significantly lower than that on the -90° groove, providing poor cooling. For the tests with high eccentricity and low feeding pressure the measured flow rate at the +90° groove was negative and had an impact on the temperature of the lubricant supplied to the opposite groove, raising this temperature.

4. Under the high loading conditions mentioned above, the increase in oil feeding pressure prevented the occurrence of negative flow rate in twin groove bearings, thus eliminating the risk of surface contact. A single groove arrangement also prevents this phenomenon to happen.
5. The flow rate in the -90° groove of twin groove bearings is low at low eccentricities, providing, therefore, a poor contribution to the bearing cooling. However, the flow rate at this groove increases consistently with eccentricity, becoming the main contributor to the total flow rate at high eccentricities.
6. The increase in feeding temperature yields an increase in eccentricity, flow rate and maximum temperature. The latter increase is smaller than the corresponding increase in T_f .
7. The increase in clearance yielded significant increases in all flow rates and a decrease in maximum temperature and, especially, in lubricant outlet temperature.
8. In the cases tested the increase in groove length yielded an increase in the total flow rate but a decrease in the flow rate supplied to the active region of the bearing through the $+90^\circ$ groove.
9. The twin groove journal bearing displays a lower maximum temperature but higher outlet temperature and eccentricity than the single groove journal bearing.

Trust, but verify.

-Ronald Reagan

(Signing with Gorbachov the treaty for the eradication of intermediate-range nuclear weapons, December 8th, 1987).

CHAPTER VI Model validation

VI.1 Introduction

Hydrodynamic journal bearing lubrication analysis is already in a mature state, with many models having been proposed over the last decades. However, one frequent shortcoming of existing theoretical models is their lack of a comprehensive validation carried out with a broad range of experimental data. Actually, this seems to be a frequent weakness of the scientific research in many fields. While some models lack any kind of validation whatsoever (Keogh et al, 1997), some others have relied on a validation based on a single experimental temperature profile (Knight and Ghadimi, 1992). Nevertheless, there are good examples of comprehensive model validation, like the work carried out by Vijayaraghavan (1996), where he compared the predictions of his model against temperature, flow rate and power loss results from four different experimental works (Mitsui, 1987; Ferron, 1983; Lund and Tonnesen, 1984; Fitzgerald and Neal, 1992).

The results obtained with the current theoretical model have been thoroughly tested against reputable experimental published results (Ferron et al, 1983, Lund and Tonnesen, 1984; Ma and Taylor, 1992, 1994) and also against those obtained in the present work. A summary of the main characteristics of the experimental tests used in the present validation is presented in Table VI-1.

VI.2 Tuning of parameters

Before proceeding with the validation task it was necessary to set the values of some model-specific parameters, such as the mixing coefficient or the thickness of the shaft-adhered lubricant layer used in the modified effective length (EL_m) model.

Table VI-1 – Bearing geometries, operating conditions, and lubricant properties of the tests used in the validation of the model.

Parameters		Units	Ferron et al.	Ma & Taylor	Lund & Tonnesen	LMS	LOMT B2V2
Geometrical bearing characteristics							
- Inner bush diameter (nominal)	d	mm	100	110	100	100	50
- Outer Bush diameter	D	mm	200	200	200	200	100
- Bush width / diameter ratio	b/d		0.8	0.7	0.55	0.8	0.8
- Groove number ; angle with load line			1 groove 0°	2 grooves ±90°	2 grooves ±90°	2 grooves ±90°	2 grooves ±90° 1 groove +90°
- Groove length / bush length ratio	a/b		0.875	0.78	0.8	0.875	0.5
- Groove circumfer. extension / diam. ratio	w/d		0.157	0.48	0.175	0.18	0.2
- Bearing radial clearance (at 20°C)	C_r	µm	145	94	69	86	53.5
- Clearance ratio (at 20°C)	C_r/R_s	$\times 10^{-3}$	2.90	1.70	1.37	1.71	2.14
Oil properties							
- T1		°C	40	45	50	40	30
- T2		°C	70	80	90	70	75
- Dynamic viscosity at temperature T1	μ_{T1}	Pa.s	0.0280	0.0228	0.0183	0.0293	0.0467
- Dynamic viscosity at temperature T2	μ_{T2}	Pa.s	0.0085	0.0067	0.0056	0.0111	0.0083
- Specific Heat	C_p	J/kgK	2000	2000	2000	2000	1943
- Density	ρ	kg/m ³	860	850	850	870	875
- Thermal conductivity	k	W/mK	0.13	0.13	0.15	0.13	0.13
Operating conditions							
- Rotational speed	N	krpm	2, 4	4	3.5, 5	1, 2, 3, 4	3
- Applied load	W	kN	4, 6	1.69, 8.47, 16.94 25.41, 33.88	5.6	2, 6, 10	0.4, 1, 2, 3, 4, 5
- Specific load	$W/(bd)$	MPa	0.5, 0.75	0.2, 1, 2, 3, 4	1	0.25, 0.75, 1.25	0.2, 0.5, 1, 1.5, 2, 2.5
Supply conditions							
- Oil supply pressure	P_f	kPa	70	67, 134	135	70, 140, 210	100
- Oil supply temperature	T_f	°C	40	45*	50	40	30

* - The lubricant supply temperature used by Ma & Taylor was based on an average of 4 thermocouples. In case they were not located upstream of the flow ramification to each groove, and in the presence of hot oil reflux at one of the grooves (which occurred in some cases), the temperature measured by the thermocouples is significantly higher than the one at which the lubricant was originally supplied to the system. This means that it is likely that in some tests the oil was supplied below T_f (see discussion in the corresponding section)

VI.2.1 Mixing factor

In the absence of a full thermal and CFD flow calculation inside the grooves, the use of the mixing coefficient (c_{mix}) which has been described in section III.11.2, tries to quantify the effectiveness of the thermal mixing between the various flows inside the grooves. If the mixing is low, it means that the recirculated hot oil will hardly mix with the cooler groove oil before reentering the bearing gap. On the contrary, if there is a high degree of mixing inside the grooves, the recirculated hot oil will perfectly mix with the groove oil, and so all outward fluxes will display a similar temperature, which will also coincide with the inner groove temperature. It is important to stress that this factor is not used as a substitute of the groove’s thermal balance, which is also performed.

Several c_{mix} values have been tested against some of the experimental results obtained with the LMS bearing (see Table V-1 for details). Comparisons for two different loads (2kN and 10kN) and c_{mix} values (0.1 and 0.75) are presented in continuation.

Figure VI-1, presents the results obtained with the lowest load (2kN). The poor agreement of the temperature profile at the lower land of the bearing regardless of the value of c_{mix} should be due to the underestimation of the flow rate at the +90° groove, but this issue is treated further

ahead on section VI.4. What now seems important to stress here is that the lowest value of c_{mix} (0.1) provides a perfect fit for such important design parameters as the shaft temperature (T_{shaft}) and the maximum bush temperature (T_{max}). The overall temperature trend is also best estimated with the lowest value of c_{mix} . Furthermore, the $+90^\circ$ groove temperature obtained with the highest value of c_{mix} (0.75) is clearly unrealistic because it is much higher than the temperatures recorded immediately downstream of this groove.

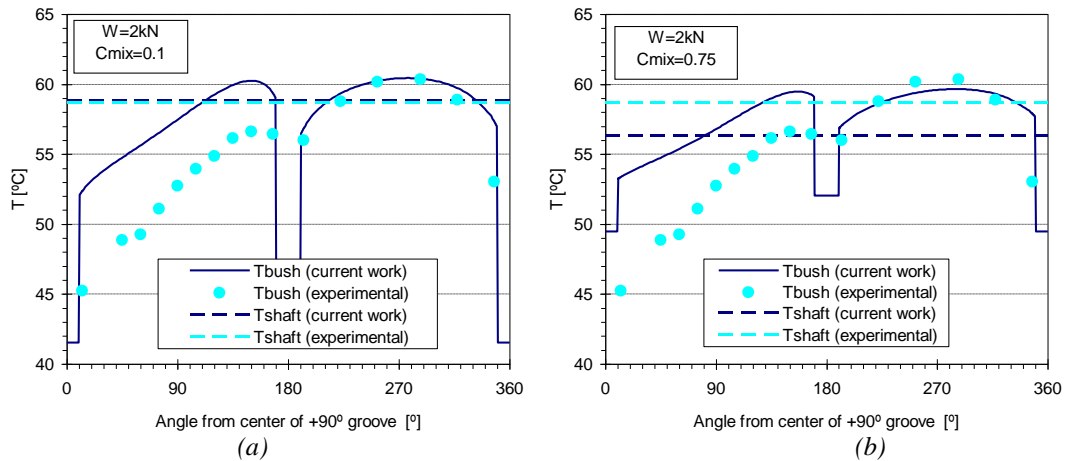


Figure VI-1 – Comparison between theory and experiment in order to analyze the Influence of the mixing coefficient, C_{mix} , on the bush inner surface temperature profile and the shaft temperature for (a) $C_{mix} = 0.1$ and (b) $C_{mix} = 0.75$ (LMS bearing, $N=3000\text{rpm}$, $W=2\text{kN}$, $P_f=140\text{kPa}$, $T_f=40^\circ\text{C}$ – see Table V-1).

For the 10kN load case, Figure VI-2 shows that the influence of c_{mix} is smaller, although the lower mixing value (0.1) yields, again, a more realistic shaft temperature and groove temperature, at the expense of a slightly overestimated T_{max} . The lower value of c_{mix} (0.1) has been adopted for the present work. This small mixing coefficient is in agreement with the CFD study of Kosasih and Tieu (2004), which concluded that the flows occurring within the groove interior are highly recirculating but have almost negligible effects on the thermal mixing (see section II.3.12).

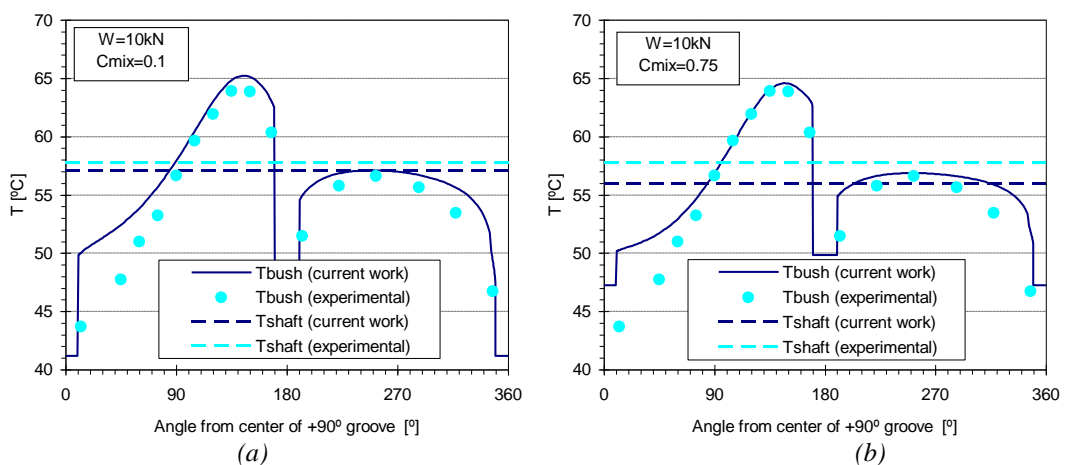


Figure VI-2 - Comparison between theory and experiment in order to analyze the Influence of the mixing coefficient, C_{mix} , on the bush inner surface temperature profile and the shaft temperature for (a) $C_{mix} = 0.1$ and (b) $C_{mix} = 0.75$ (LMS bearing, $N=3000\text{rpm}$, $W=10\text{kN}$, $P_f=140\text{kPa}$, $T_f=40^\circ\text{C}$ – see Table V-1).

VI.2.2 Thickness of the shaft-adhered layer

In section III.10.2 a modified effective length thermal model for the ruptured film region has been proposed. This model considers that in the ruptured film region a portion of the lubricant flows along streamers with Couette flow, while another portion of the flow adheres to the moving journal surface flowing at a uniform speed (the shaft speed).

The thickness of the lubricant layer is considered to remain constant and equal to a certain fraction of the gap, \bar{e}_{s0} at the location of its formation (at film rupture). This fraction could be chosen as a specific constant value. However, it was observed that with low eccentricity tests the experimental temperature profiles are best fitted with theoretical results in which high values of \bar{e}_{s0} were used and vice versa. This work is summarized in Figure VI-3, which displays the layer thickness ratio \bar{e}_{s0} that best fits the experimental temperature profiles of several authors as a function of the theoretical eccentricity ratio. This figure also displays the experimental measurement of the thickness of a shaft-adhered layer performed by Knight and Ghadimi (2001).

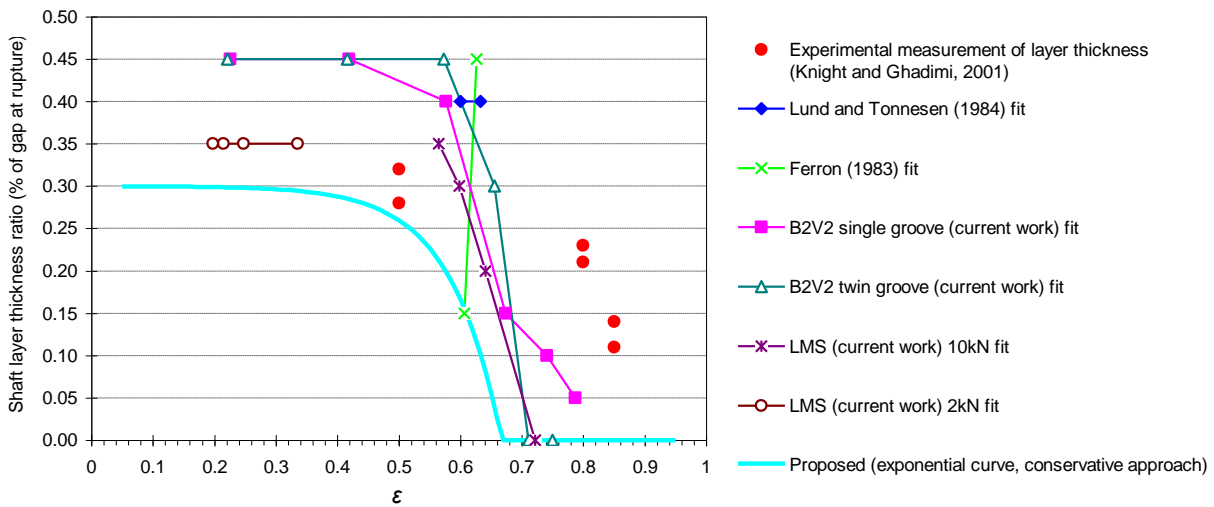


Figure VI-3 - Shaft layer thickness ratio, \bar{e}_{s0} (% of gap at rupture) which best fits the experimental temperature profiles of several works; experimental measurement of thickness ratios (red dots); proposed eccentricity ratio - thickness ratio curve (light blue line).

Instead of assuming a fixed value for \bar{e}_{s0} irrespective of eccentricity, a curve acting as a lower envelope of the theory-experimental best fits was built. This exponential-based curve turns out to be a conservative estimate of the ideal thickness ratio and has the following formula:

$$\bar{e}_{s0}(\varepsilon) = \max\left(0; 0.3 - 10^{-4} \cdot e^{12\varepsilon}\right) \tag{Eq. VI-1}$$

The adequacy of this new approach can be assessed by analyzing Figure VI-4 and Figure VI-5, which compare the results obtained with:

- (a) - no shaft layer (which corresponds to the effective length, EL, model);
- (b) - a shaft layer occupying 45% of the gap at the rupture location, which is close to the theoretical limit - all lubricant attached to the shaft ($\bar{e}_{s0}=0.5$);
- (c) – The case of \bar{e}_{s0} being a function of eccentricity (Eq. VI-1).

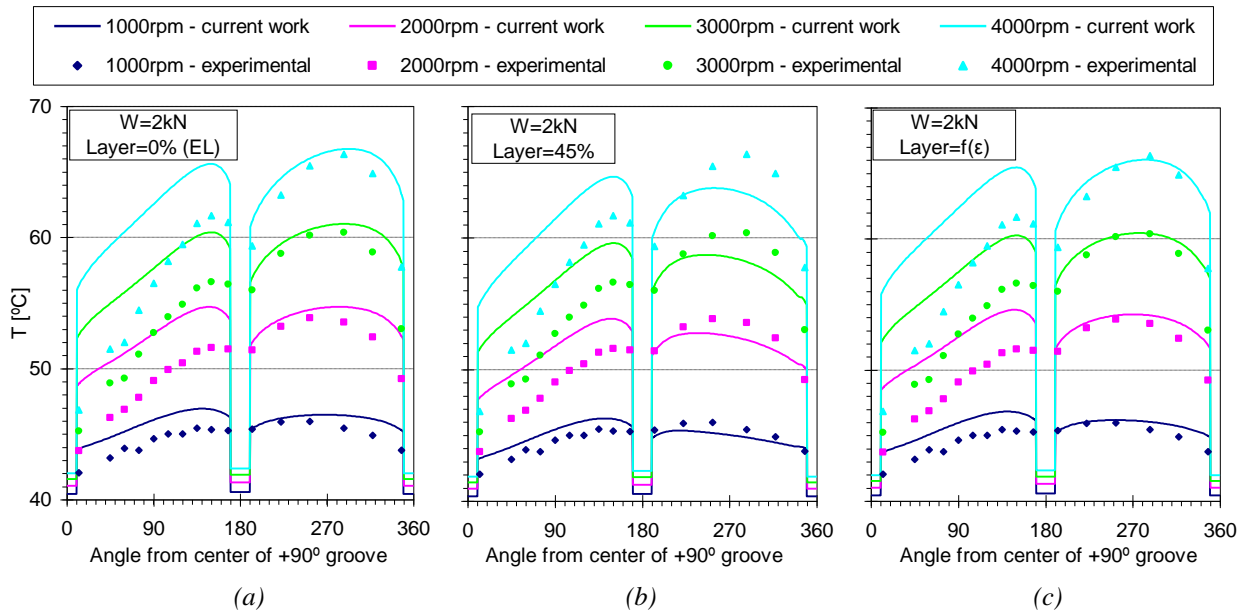


Figure VI-4 – Comparison between theory and experiment using (a) an effective length model, (b) a modified effective length model with a shaft layer ratio of 0.45 and (c) a modified effective length model with a shaft layer ratio which is a function of eccentricity (LMS bearing, $W=2\text{kN}$, $P_f=140\text{kPa}$, $T_f=40^\circ\text{C}$)

Although it can be seen that the fit is not always optimum, the correlation between theoretical and experimental results is improved in comparison with the *EL* model. For instance, it can be concluded from in Figure VI-5 that the overestimation of the temperature of the lowest eccentricity test (4000rpm), was slightly reduced when switching from the *EL* model to the new approach. This happened without worsening the temperature correlation of the highest eccentricity test (1000rpm), which was already underestimated with the *EL* model.

If a fixed value of \bar{e}_{s0} would be used, either a temperature overestimation of the low eccentricity tests or an underestimation of the high eccentricity tests would be obtained.

A slightly less conservative curve (like changing the left asymptote of the curve from 0.30 to 0.35) would further improve most results. But for the sake of security, Eq. VI-1 will be kept unchanged for now.

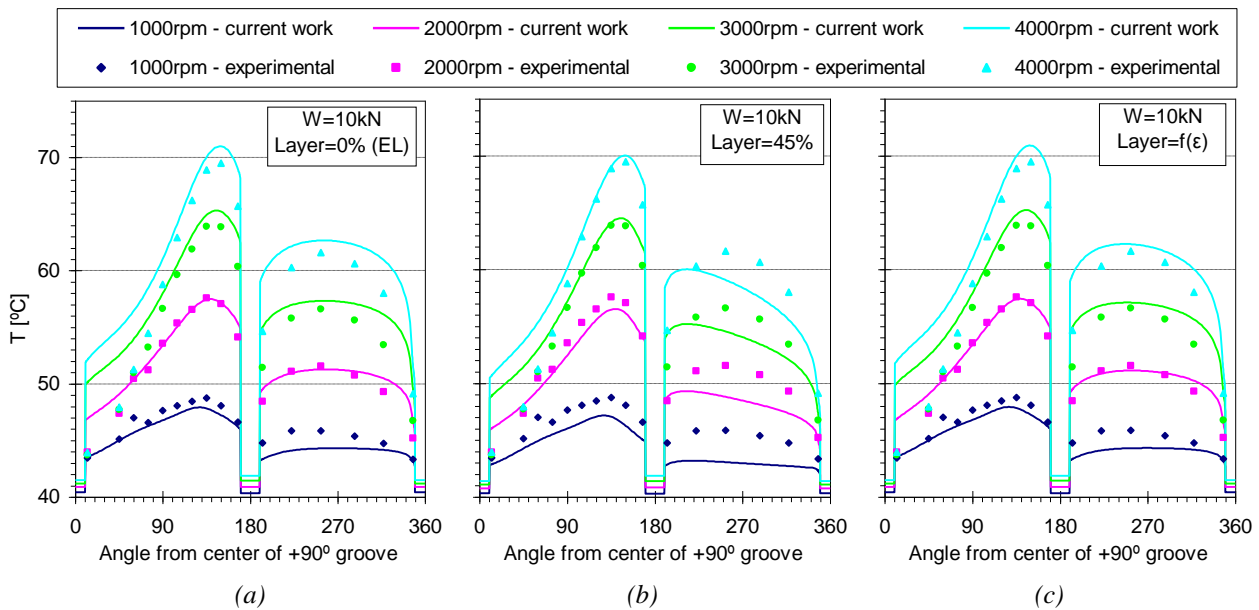


Figure VI-5 – Comparison between theory and experiment using (a) an effective length model, (b) a modified effective length model with a shaft layer ratio of 0.45 and (c) a modified effective length model with a shaft layer ratio which is a function of eccentricity (LMS bearing, $W=10\text{kN}$, $P_f=140\text{kPa}$, $T_f=40^\circ\text{C}$)

VI.3 Comparison of model predictions with published results

VI.3.1 Ferron et al. (1983)

The experimental results of Ferron's crown bearing (Ferron et al, 1983) have been widely used for the validation of hydrodynamic bearing models. This has the advantage of allowing the comparison of the theoretical models of several different authors (although this comparison will not be performed here).

Figure VI-6a) displays the temperature profiles at the inner bush surface for two different operating conditions. A very good theoretical-experimental correlation is obtained for maximum temperature (T_{max}) with differences of around 1°C . The temperature trend is fairly well predicted for both cases except in the region immediately downstream of the groove. This may have happened due to the fact that, while the experimental values were measured at the midplane of the bearing, the theoretical approach performs averaged thermal calculations on the whole section: not only the thermal calculations are only 2D, but also the effect of finite grooves was incorporated into the analysis (see section III.11.4).

The pressure results (Figure VI-6b) are in perfect agreement with the experimental data. The slightly underestimation of the pressure peak should be due to the mechanical deformation caused by the hydrodynamic pressure field which tends to palliate the value of the maximum pressure.

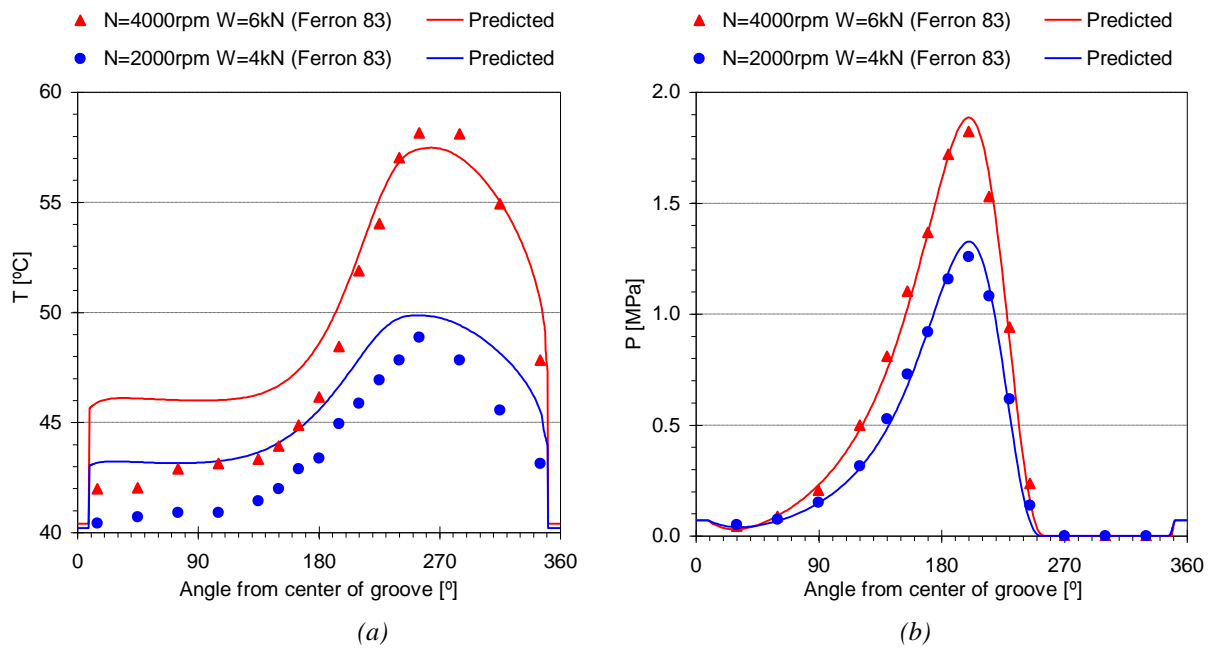


Figure VI-6 – Comparison between theory and experiment (Ferron et al, 1983) under two different conditions, for (a) inner bush surface temperature profile and (b) pressure profile at the midplane of the bearing.

Figure VI-7a) displays a comparison between theoretical and experimental eccentricity ratio. Taking into account that the measurement of this parameter is normally associated with some degree of uncertainty, the small differences between theory and experiment can be neglected. The same cannot be said when analyzing the flow rate charts in Figure VI-7b). Differences in flow rate of 23% and 26% are observed for the two tests (2000rpm/4kN and 4000rpm/6kN test). In fact, this is one of the performance parameters which are more difficult to predict accurately in journal bearing analysis (Ma and Taylor, 1992; El-Deihi and Gethin, 1992), even with mass conservative algorithms such as the present one. Inclusive, popular bearing design tools such as ESDU item n. 84031 provide flow rate estimates which correlate better with other theoretical analyses than with experimental results. This is especially true in the case of twin groove journal bearings.

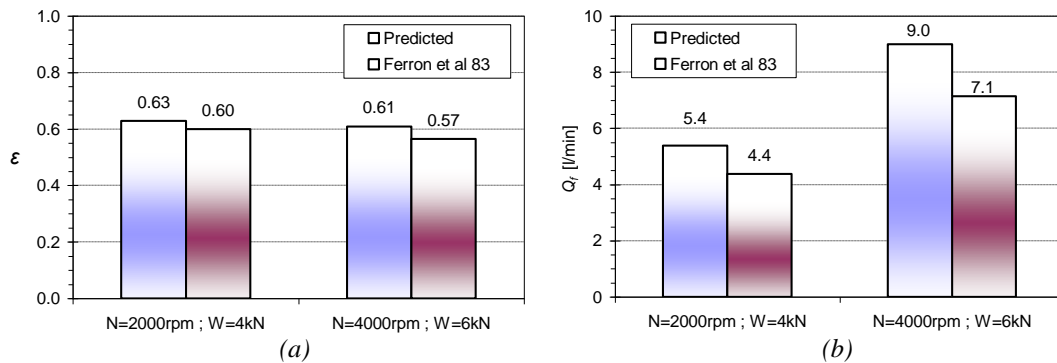


Figure VI-7 - Comparison between theory and experiment (Ferron et al, 1983) under two different conditions, for (a) eccentricity ratio and (b) lubricant feeding flow rate.

The lack of accuracy in the prediction of flow rate might be due, in the first place, to a wrong estimation of the local gap geometry (due to form defects, to misalignment, to errors in the

measurement of the bearing clearance, to the absence of a rigorous estimation of the thermal and mechanical deformations which can significantly affect the geometry of the bearing gap). There are also the intrinsic limitations of the Reynolds equation and the way film rupture, film regeneration and the twin phase flow are handled. A broad discussion on these issues has been presented in CHAPTER II.

In spite of the differences found, the overall agreement between the theoretical and Ferron's results may be deemed as fairly satisfactory.

VI.3.2 Ma & Taylor (1992, 1994)

A wealth of experimental results on twin groove journal bearings (circular and elliptical) can be found in the publications by Ma and Taylor (1992, 1994). They used these tests for the validation of their own theoretical work (the so-called *separation model*, which has been described in section II.3.14d).

One particularity of these tests it is that the bearing they used has huge axial grooves, with an angular extension of 55 degrees each. This detail has more consequences than one can imagine at first glance, as it facilitates the appearance of negative flow rate at the +90° groove for high eccentricities. This hot lubricant reflux, which flows back into the feeding system pipes was experimentally documented for the first time, to the author's knowledge, by Brito et al (2007) and is also presented in section V.4. The influence this phenomenon exerts on bearing performance has been also incorporated into the present analysis (see section III.11.3. One of the consequences of this hot lubricant reflux at one of the grooves is that it mixes with the new fresh lubricant coming from the feeding system, thus rising the temperature of the oil before it is fed to the opposite groove. In this way, the temperature of the oil fed to the positive flow rate groove is actually higher than the temperature at which the oil came from the exterior.

When the lubricant reflux phenomenon takes place some confusion on the correct value of T_f may arise, depending on the location of the thermocouples through which the lubricant feeding temperature, T_f , is monitored:

- Method I - T_f is the temperature measured at the main feeding pipe

It seems reasonable to consider that T_f represents the temperature of the oil supplied to the whole system, irrespective of the phenomena taking place inside the system. In accordance with this, T_f should be monitored at the main feeding pipe, before lubricant is derived to feed the two grooves. In this case, if oil reflux occurs at the +90° groove, then the temperature of the lubricant supplied to the opposite groove will be higher than T_f , due to the mixing effect just

described. This effect has been simulated in Figure VI-8a) for the three highest loads, where oil reflux occurred at the +90° groove (as displayed in Figure VI-8c).

For the highest load test ($W_S=4\text{MPa}$) the simulation shows that oil at 59°C refluxed from the +90° groove back into the feeding pipes, mixed with the fresh oil at 45°C and was re-fed to the -90° groove at nearly 50°C. This would correspond to a 49°C average of the 2 grooves.

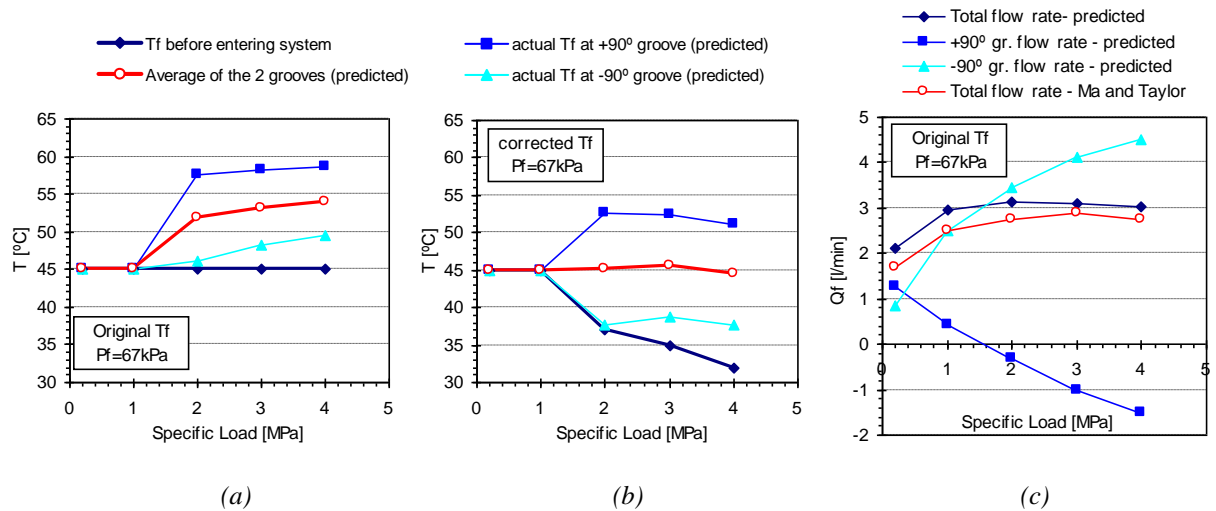


Figure VI-8 – Prediction of the effect of two different methods of the evaluation of T_f applied to Ma and Taylor's tests: (a) T_f (45°C) corresponds to the temperature of the lubricant before entering the system (method I); (b) T_f (45°C) corresponds to the average of the temperatures recorded just before each groove (method II); (c) Total flow rate and flow rate at each groove – theory vs. experiment (method I)

- Method II - T_f is the average of the temperatures measured at the entry of each groove

In some works, however, T_f is monitored downstream of the derivation to each groove, sometimes at the derivation itself, or near the entrance to each feeding groove. This method can be misleading in cases where oil reflux occurs. This seems to be the method used in Ma and Taylor's tests. In fact, according to their description of the experimental apparatus, T_f was set to be the average of four different thermocouple readings. The use of so many thermocouples seems to indicate that T_f was not monitored in the main feeding pipe, but rather at several different locations, most likely, downstream of the derivation to each groove. In such eventuality, when oil reflux occurs and mixes with the fresh oil feeding, the value of T_f would actually be a measure of the temperature of the mixing, or the average of the temperatures recorded near the entrance of each groove. As a consequence, the fresh oil supplied would actually have to be cooler than the prescribed T_f , so that the set-point for T_f would still be attained.

This hypothesis seems to be confirmed by the study presented in continuation.

Adapting the present model to method II (assumed to have been used in the experiments)

In order to adapt the theoretical model to the definition of T_f according to method II, the input variable T_f (which has the meaning of method I) will have to be lowered so that the resulting average of the two grooves (obtained at the end of the simulation) will correspond to the prescribed value for T_f . This approach was tested against Ma and Taylor's results, being presented in Figure VI-8b). According to the predictions, for the highest load, the fresh oil temperature must have been 32°C in order to allow the maintenance of an average temperature of 45°C.

The temperature profiles corresponding to three different cases were compared against theoretical results in which the two different definitions of T_f were tested. The results are presented in Figure VI-9 and correspond to specific loads of 0.2MPa, 2MPa and 4MPa. Oil reflux occurred in only the two highest load tests.

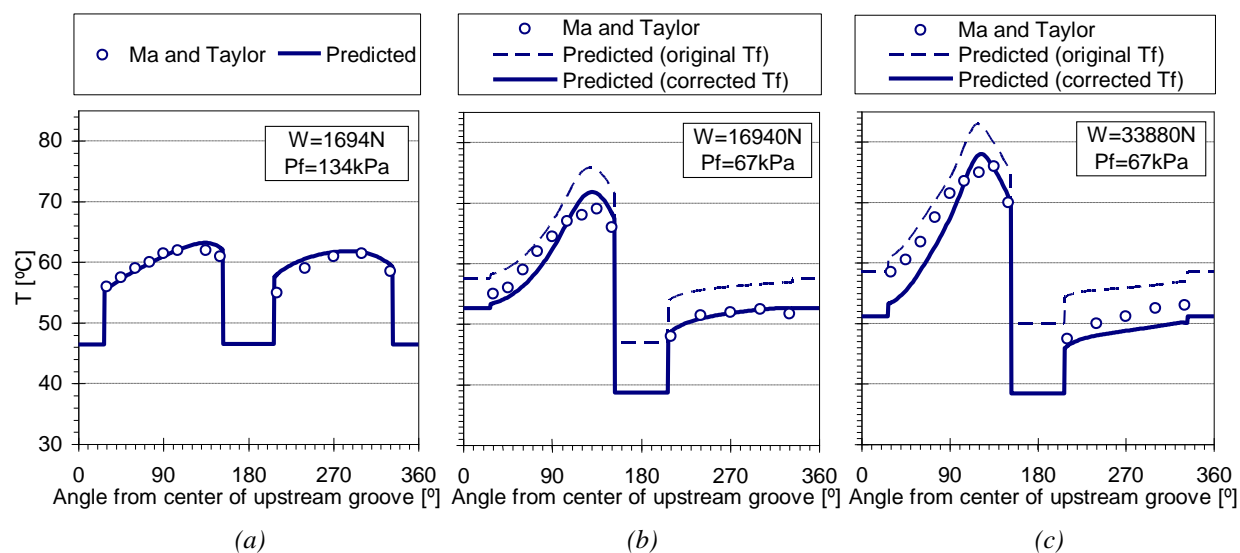


Figure VI-9 – Theoretical and experimental (Ma and Taylor) inner bush surface temperature profiles for three different test conditions. Two different ways of calculating T_f were used in the presence of oil reflux (cases b and c)

Only the assumption that Ma and Taylor's T_f measurements were made with a method similar to method II are able to explain why a perfect temperature correlation was obtained for a case where oil reflux did not occur (test with 0.2MPa Specific load, Figure VI-9a), while large discrepancies (7°C excess in T_{max}) were observed with method I in cases where oil reflux did occur (Figure VI-9b,c).

The differences between experimental and theoretical results using the two different definitions of T_f are clearer when analyzing the maximum temperature results (Figure VI-10).

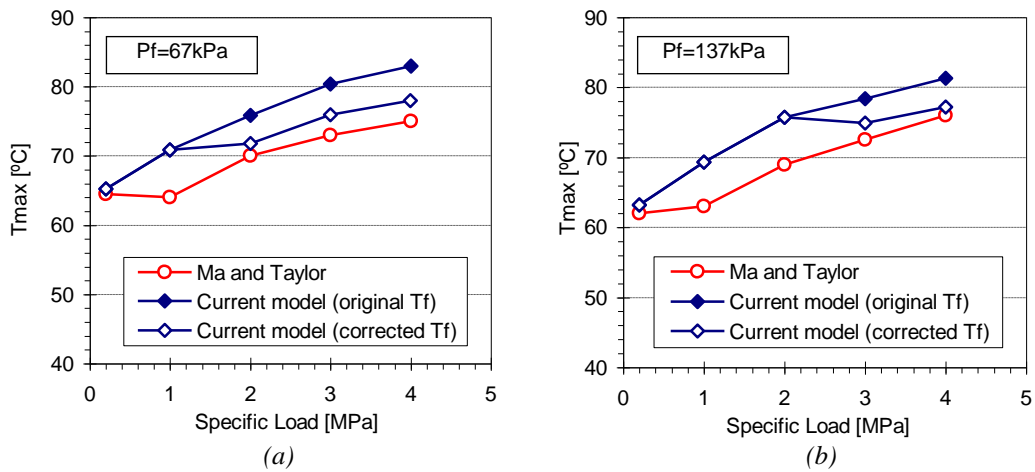


Figure VI-10 – Comparison between theory and experiment of maximum bush temperature for (a) $P_f=67\text{kPa}$ (oil reflux predicted for the three highest load tests) and (b) $P_f=137\text{kPa}$ (oil reflux predicted for the two highest load tests). In the presence of oil reflux two different definitions of T_f were tested.

Concerning the lowest feeding pressure test series ($P_f = 67 \text{ kPa}$, Figure VI-10a), It can be seen that when oil reflux is predicted to occur, the use of method II significantly improves the correlation between theory and experiment. However, the results for the 1MPa test are still poorly predicted, probably because oil reflux might have indeed occurred in this test but was still not predicted to occur by the model.

The same observations can be stated in relation to the highest feeding pressure test series ($P_f = 137 \text{ kPa}$, Figure VI-10b). For these tests oil reflux was only predicted for the two highest loads.

Similar comparisons are presented in Figure VI-11 for side leakage. Again, it can be seen that method II provides a very good correlation for the results whenever lubricant reflux was predicted.

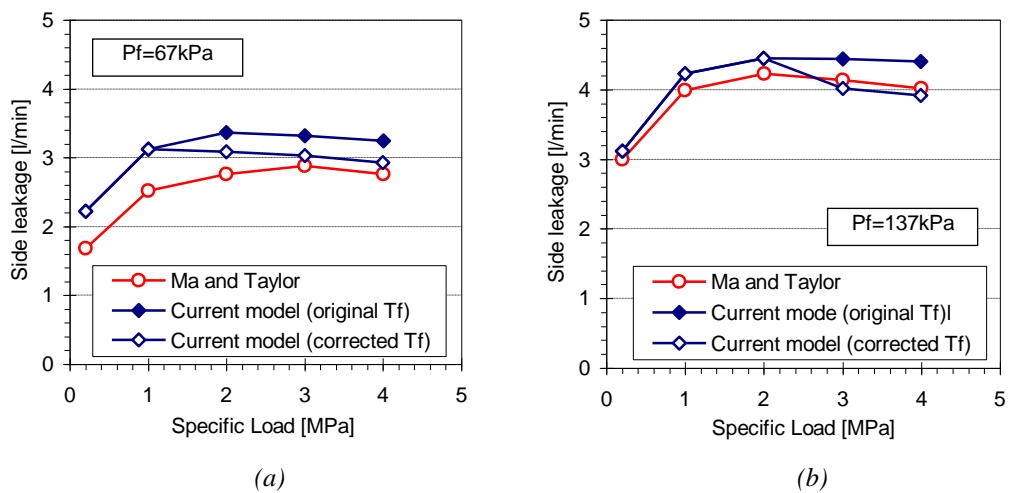


Figure VI-11 - Comparison between theory and experiment of Side leakage for (a) $P_f=67\text{kPa}$ (oil reflux predicted for the three highest load tests) and (b) $P_f=137\text{kPa}$ (oil reflux predicted for the two highest load tests). In the presence of oil reflux two different definitions of T_f were tested.

The flow rate predictions made by the current model are similar to those made by the model of Ma and Taylor (1992) for the lowest feeding pressure tests (67kPa). For the highest feeding pressure tests (137kPa) the current model also yielded a close correlation with experiment, as seen in Figure VI-11b. However, the theoretical predictions made by the authors of this experimental work (Ma and Taylor, 1992) strongly under-predicted the total flow rate. This seems to confirm that the present model is suitable to incorporate the influence of lubricant supply conditions.

The following concluding remarks may be drawn:

A careful analysis of the experimental results should be made whenever they are to be used in model validation. In this case, the method used for the monitoring of T_f proved to be critical.

The theoretical model was adapted in order to contemplate an alternative methods of measuring T_f , which was likely used in the experimental work. When using this alternative method the correlation between theory and experiment was very much improved. This supports the supposition that the method used by Ma and Taylor to monitor T_f was indeed method II (It was not possible to contact the authors to confirm this).

The model's capability of predicting and handling negative groove flow rate situations in a suitably manner has been confirmed.

A very good agreement of the total flow and the temperature trend at the unloaded land of the bearing was observed, something which is not always easy to obtain in twin groove journal bearing analysis.

VI.3.3 Lund & Tonnesen (1984)

Another reference work in the field of journal bearing testing is the one performed by Lund and Tonnesen (1984), which has also been used for model validation by several authors (Boncompain et al, 1986, Knight and Niewiarowski, 1990, Vijayaraghavan, 1996). The comparison between theory and experiment of the inner bush surface temperature profiles for two different test conditions is displayed in Figure VI-12.

T_{max} is very well predicted for both cases, with differences of around 1°C. The slight differences found in the temperature trend at the lower land of the bearing might be due to the thermal and mechanical deformations of the bearing geometry or simply due to the limitations of the 2D approach. Some differences are also observed at the upper land between 270° and the groove. Here the temperature profile displays a rather bizarre S shape depression which is not very common. It would be necessary to observe the experimental apparatus in order to check if some

other factor could be responsible for this. Nevertheless, a more intensely decreasing trend of the temperature profile at the upper land would be obtained with a less conservative calculation of the shaft layer thickness curve (Eq. VI-1).

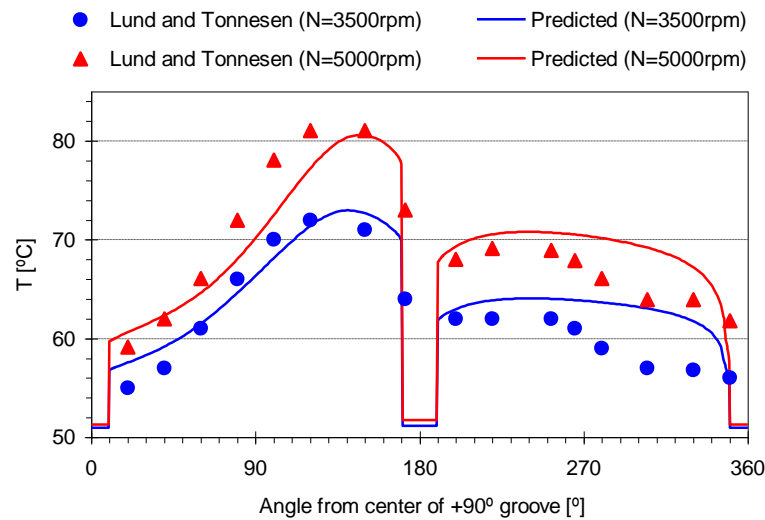


Figure VI-12 - Theoretical and experimental (Lund and Tonnesen) inner bush surface temperature profiles for a load of 5.6kN and two shaft speeds ($N=3500\text{rpm}$ and $N=5000\text{rpm}$).

The eccentricity ratio and shaft temperature correlations are presented in Figure VI-13. All values are predicted within a 10% margin. Concerning eccentricity ratio this margin falls within the typical uncertainty margin of this kind of measurements (recall section V.2.10).

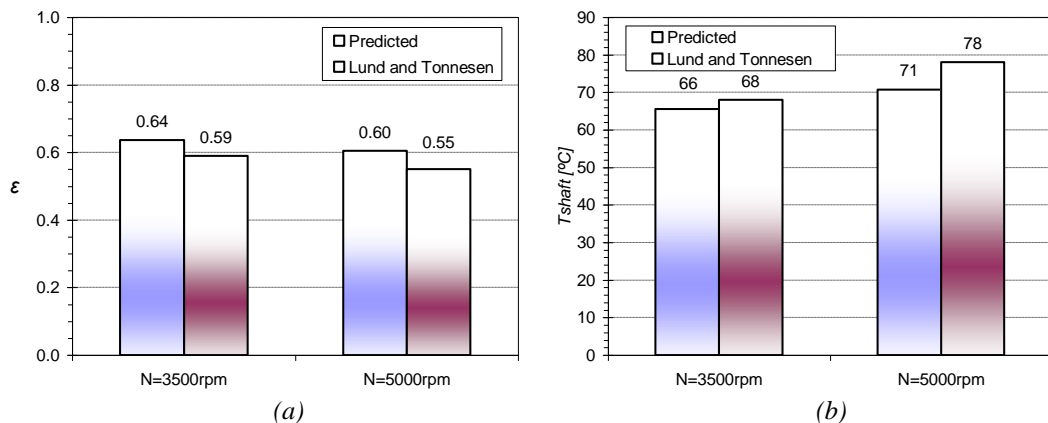


Figure VI-13 - Comparison between theory and experiment (Lund and Tonnesen) under two different shaft speeds, for (a) eccentricity ratio and (b) Shaft surface temperature.

Concerning T_{shaft} , the predictions underestimate by 2°C and 7°C the experimental values obtained in the 3500rpm and the 5000rpm tests, respectively. Only the latter difference is significant. This difference might be due to the way T_{shaft} is estimated (see section III.9.4: It is assumed that no net heat transfer occurs between the fluid and the shaft. The suitability of this assumption depends on the degree of insulation of the shaft from the exterior and on the proximity of heat sources or heat sinks which can alter the heat transfer balance between the shaft and the fluid. Therefore, the relevance of this 10% difference can be rather relative.

VI.4 Comparison between predictions and the LMS results

One of the main goals of the experimental part of the present work was to use the results for the validation of the model developed. In this section the results obtained at the test rig of the Solid Mechanics Laboratory of the University of Poitiers (LMS) are compared with the theoretical predictions. These experiments have been presented in CHAPTER IV0 and other publications (Brito et al, 2006, Brito et al 2007). The test conditions used in this section are presented in Table VI-1 at the beginning of this chapter. Sixteen different test conditions were used for this validation task, by combining four shaft speeds (1000, 2000, 3000 and 4000rpm) and three loads (2, 6 and 10kN). Tests performed at three different feeding pressures (70, 140 and 210kPa) were also used in the comparison for a fixed shaft speed (3000rpm) and two different loads (2kN and 10kN).

Results concerning the pressure profile at the midplane of the bearing are presented in Figure VI-14. Figure VI-14a displays the comparison between theory and experiment for three different loads (2, 6 and 10kN) at a constant shaft speed (3000rpm), while Figure VI-14b refers to two tests performed with a constant load (6kN) and two different speeds (1000rpm and 4000rpm). The predicted pressure seems to be slightly overestimated in all cases. Several reasons might explain this:

- On one hand, in the event of a slight misalignment the line of maximum pressure becomes slightly deviated from the midplane. This way the recorded values would not correspond to the maximum ones.
- The 2D nature of the thermal model and the viscosity field will certainly affect to some extent the axial distribution of the hydrodynamic pressure field.
- The thermal and mechanical deformations induced by the temperature field and by the pressure field could also play a role. It is known that the mechanical deformations tend to reduce the maximum pressure obtained. However, this mechanism is not sufficient by itself to explain why the hydrodynamic pressure field of low loaded tests is also overestimated. In this case, the looseness of the bearing system under such conditions may cause a more erratic, less predictable response.
- Other reasons for the difference between theory and experiment could be linked with the measurement method itself. While it is not possible that the pressure gauges would all be out of calibration, it would be possible that the holes drilled up to the inner bush surface in order to measure the pressure, could interfere in some way with the measurement, namely inducing a suction effect which would lower the recorded values. A suction effect can be observed, for instance, in Figure VI-14b, where the test with the

highest shaft speed displays a strong negative pressure (a minimum of -0.87bar was recorded) at the rupture region. This did not happen with the lowest speed test, (a minimum of -0.05bar was recorded).

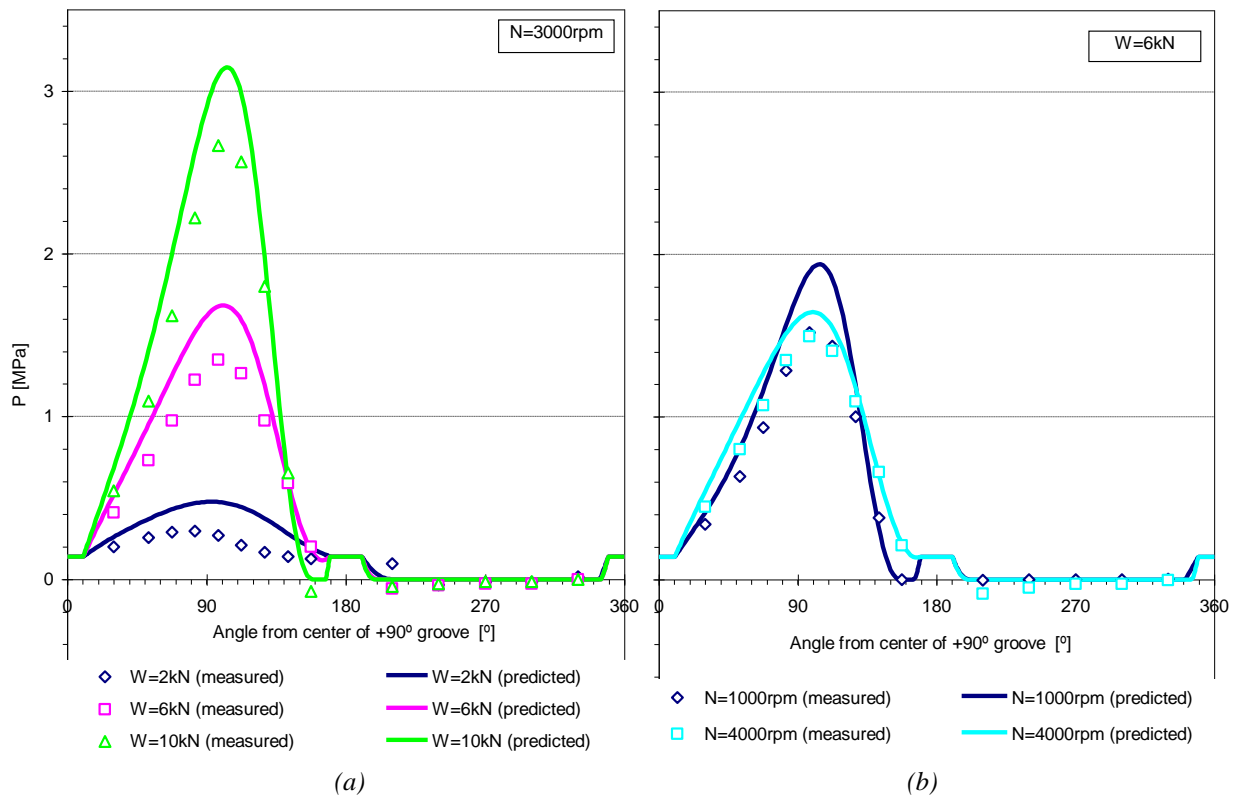


Figure VI-14 - Comparison between theoretical and experimental pressure profiles at the midplane of the bearing for (a) fixed shaft speed (3000rpm) and three values of applied load (2kN, 6kN, 10kN) and (b) fixed applied load (6kN) and two shaft speeds (1000rpm and 4000rpm). (LMS bearing, $P_f=140kPa$).

A very positive characteristic of the comparison between theoretical and experimental pressure profiles is the excellent correlation of the results at the vicinity of the location where film rupture starts (descending portion of the curve). This means that, except for the lowest load test, the location of film rupture is very well predicted.

The temperature profiles at the midplane of the bearing are presented in Figure VI-15 for different operating conditions. Also, charts summarizing the shaft temperature and the maximum temperatures (global T_{max} and T_{max} at each land of the bearing) are presented in Figure VI-16.

Taking into account the wide range of operating conditions tested, it may be stated that the quite good overall correlation is obtained: the prediction of the maximum temperature, a key performance parameter, is quite satisfactory (see also Figure VI-16b). The temperature trend at the upper (unloaded) land of the bearing is also very close to the experimental data, as can be seen in Figure VI-16d. This is an achievement which is certainly not common in existing twin groove journal bearing models. The predicted shaft temperature (Figure VI-16a) is also very close to the experimental values for almost all the tests.

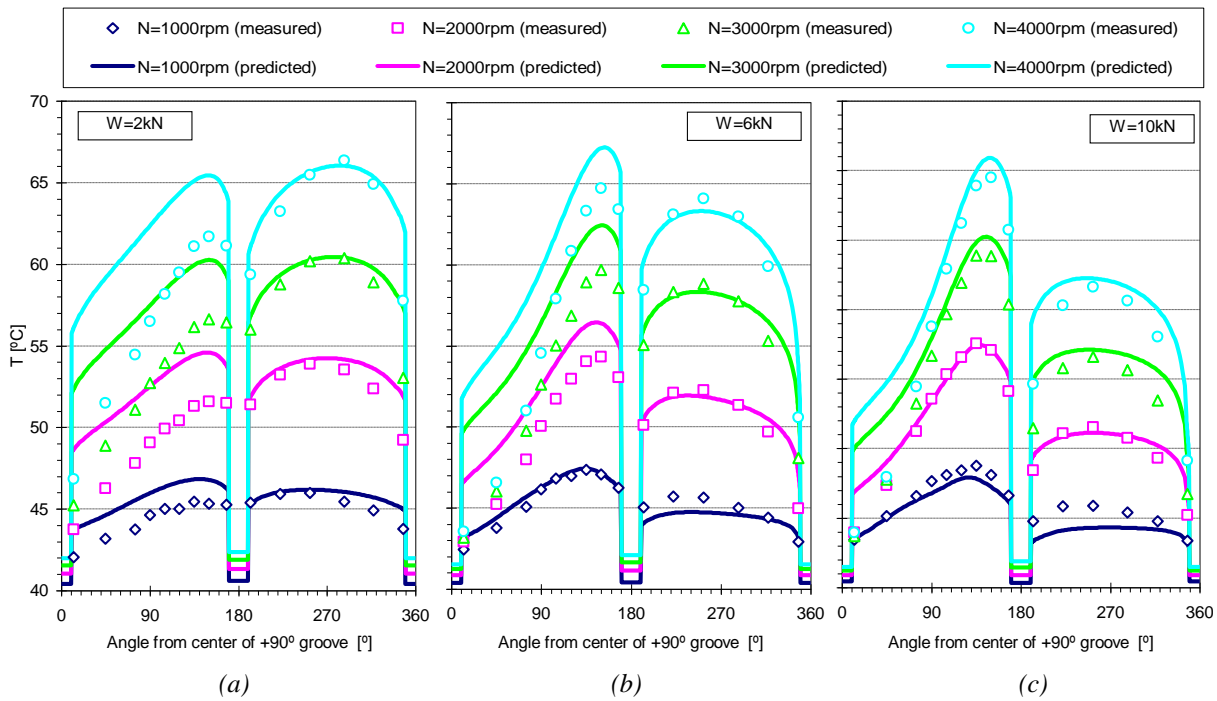


Figure VI-15 - Comparison between theoretical and experimental temperature profiles at the midplane of the inner bush surface for four different shaft speeds and an applied load of (a) 2kN, (b) 6kN and (c) 10kN. (LMS bearing, $P_f=140kPa$).

The temperature immediately downstream of the $+90^\circ$ groove is generally overestimated. It must be remembered that this is a 2D thermal approach which averages what happens along the axial extension of the bearing. Therefore it is natural that the correlation will not be totally realistic in the vicinity of grooves, because these are the locations where the temperature is least uniform along the axial direction.

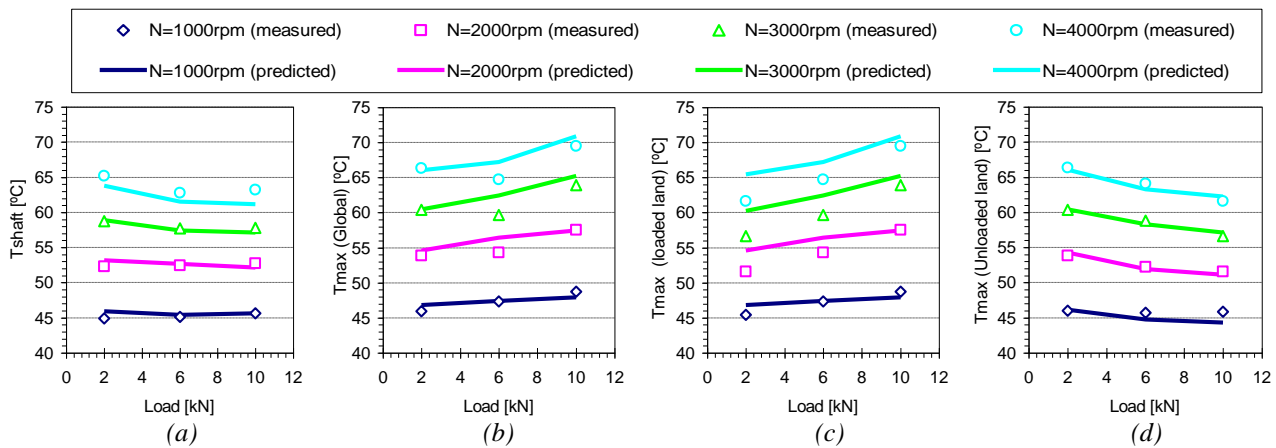


Figure VI-16 - Comparison between theory and experiment, for several loads and shaft speeds, of (a) Shaft surface temperature, (b) maximum bush temperature, (c) maximum bush temperature at the loaded (lower) land and (d) maximum bush temperature at the unloaded (upper) land of the bearing. (LMS bearing, $P_f=140kPa$).

For low eccentricity tests, the temperature at the loaded land is overestimated. This may be due to the strong underestimation of the flow rate (described in continuation). However, as load increases, this excess temperature disappears, probably because the weight of the flow rate at the $+90^\circ$ groove is smaller for higher eccentricities (Brito et al, 1997). Under such conditions, the influence of the global underestimation of the flow rate becomes weaker.

The fact that the maximum bush temperature is still accurately predicted even in the presence of a temperature overestimation at low loads, allows downgrading the importance of this problem.

In contrast with the rest of the results, a quite poor correlation is found for flow rate, as seen in Figure VI-17a). However, this strong underestimation of flow rate has a particularity: there is a nearly constant difference between the theoretical and the experimental values, as displayed in Figure VI-17b).

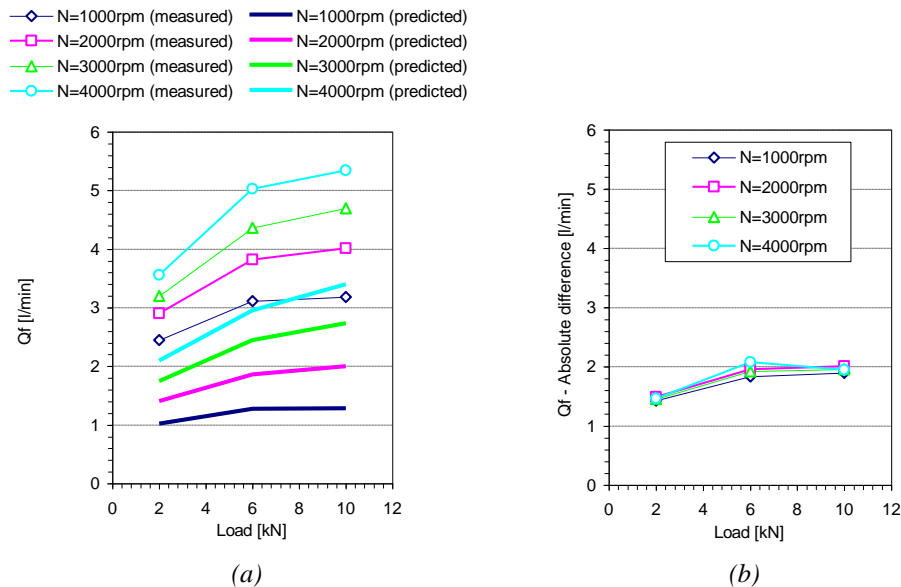


Figure VI-17- Comparison between theory and experiment, for several loads and shaft speeds, (a) of total lubricant feeding flow rate. (b) Difference between theoretical and experimental values. (LMS bearing, $P_f=140\text{kPa}$).

The following possible reasons for these differences were devised:

- An error in the estimation of the actual clearance: The flow rate is strongly dependent on the bearing clearance. The use, in the calculations, of a clearance lower than the real value would yield a significant underestimation of the flow rate. Cylindricity defects and the simplified estimation of the thermal expansion of the components used in the present work might have also contributed for the error found in flow rate.
- Intrinsic limitations of the theoretical approach: The modeling of the twin phase flow found at the ruptured film region is simplified. No pressure gradients are considered to exist at the ruptured film region. Therefore, only drag-driven (Couette) flow is considered to exist in this region. However, some experimental works (recall section II.2.9) have reported the existence of secondary flows coming from the grooves which are not considered in traditional theory, like the unsteady back flow bubble coming from a groove, which penetrates into the ruptured film region. These phenomena are

more likely to occur with twin groove journal bearings, which display a groove right in the midst of the ruptured film region.

Unfortunately, the crude underestimation of the flow rate in twin groove journal bearings is rather frequent in literature (ESDU item 84031, 1984, Ma and Taylor, 1992, El-Deihi and Gethin, 1992, Claro, 1994). This problem requires further investigation in the future.

The theoretical and experimental results were also compared for three values of the feeding pressure. The comparison is presented in Figure VI-18.

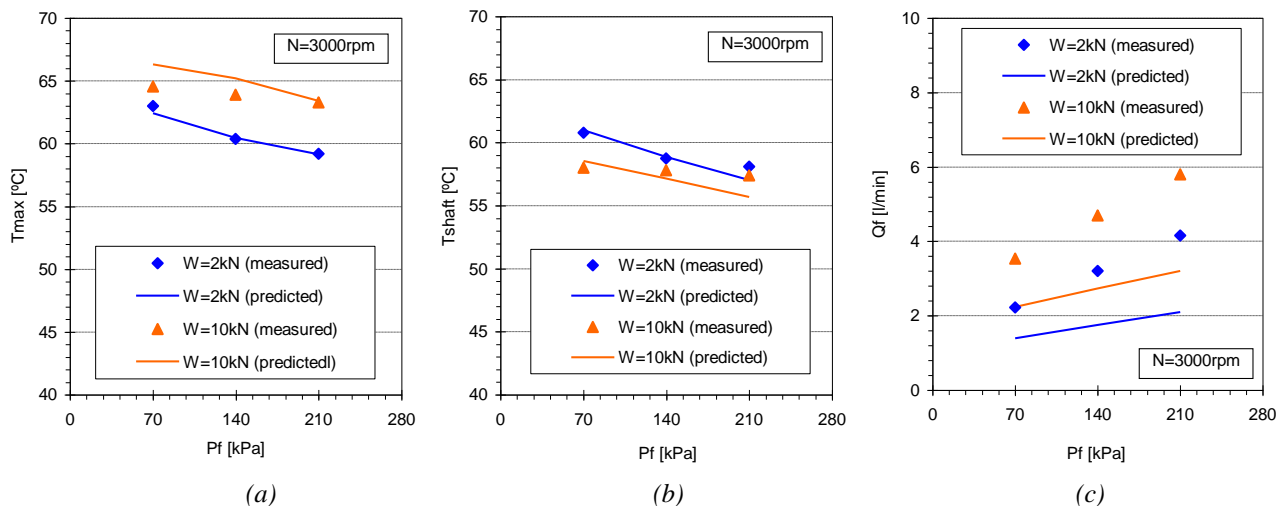


Figure VI-18 – Influence of lubricant feeding pressure on the correlation between theory and experiment, for two different loads, of (a) maximum bush temperature, (b) Shaft surface temperature and (c) total lubricant feeding flow rate. (LMS bearing, $N=3000$ rpm).

The trends of all predicted parameters are in fair agreement with experimental measurements. Again, both T_{max} and T_{shaft} are very well predicted, with the maximum differences being of the same order of magnitude of the uncertainty margin. Concerning total flow rate, it can be seen that the differences increase with increasing P_f .

As a concluding remark, it may be said that, except for flow rate, a very good correlation between theory and experiment has been obtained for a wide range of operating conditions. Further investigation on the flow rate predictions is needed.

VI.5 Comparison between predictions and the LOMT results

The experimental results obtained with the test rig of the Machine Elements and Tribology Laboratory of Minho University (LOMT) have been thoroughly analyzed in CHAPTER V.

This rig is capable of measuring not only the total flow rate but also the partial flow rates in each groove. The bushings, which are twin grooved, can be also tested with one of the grooves shut, thus resembling single groove bearings with a groove at $+90^\circ$ to the load line.

The LOMT bearings also display an important difference in relation to all the experimental results used in the present chapter: they have a much smaller diameter (50mm), which is at least one half of the others. This is positive in the sense that few experimental results exist for this range of bearing diameters. However, there are also some drawbacks: the smaller dimensions of the bearing tend to increase the relative weight of errors. The scaling effect tends to increase the relative weight of some sources of uncertainty (geometry and metrology-related uncertainty, proximity sensor response). The smaller mass of the system also makes it thermally less stable. Another drawback is the smaller stiffness of the system, which makes it subject to stronger mechanical deformations in the presence of high loads.

The general correlation obtained for the tests with the LOMT bearings was the least good among all the comparisons made so far. Figure VI-19 displays the comparison between the theoretical and experimental temperature profiles at the midplane of the bearing for a single groove configuration. Although the overall temperature trend is well predicted for the whole load range, the temperature level is significantly overestimated within the lower load range (Figure VI-19a) and quite accurately predicted for the higher load range (Figure VI-19c). This can be better evaluated by looking at the maximum bush temperature results for all tests which is displayed in Figure VI-20a.

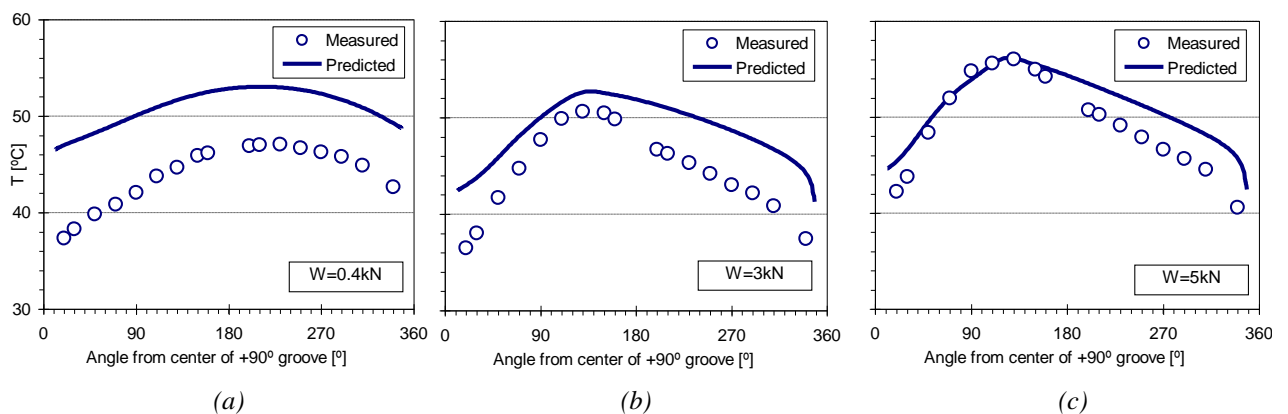


Figure VI-19 - Comparison between theory and experiment of the temperature profiles at the midplane of the inner bush surface of the bearing for an applied load of (a) 0.4kN, (b) 3kN and (c) 5kN. (single groove B2V2 bearing, $N=3000\text{rpm}$, $T_f=30^\circ\text{C}$, $P_f=100\text{kPa}$).

A temperature overestimation at low loads was already observed in the LMS series of comparisons (previous section), but this effect was more or less confined to the lower half of the bearing (see Figure VI-16c) and did not seem to affect T_{max} significantly. The underestimation of the flow rate was already pointed out as being responsible for the temperature excesses detected in the LMS bearing predictions. In the present case, the same underestimation of the flow rate has been detected (see Figure VI-20b). It seems that the effect of the flow rate underestimation on the temperature field has been significantly amplified due to the much smaller mass of the B2V2 bearing system which makes it thermally less stable.

Fortunately, journal bearings are seldom subjected to such low loads (the predicted eccentricity ratio for this case was around 0.2) as they become prone to instability. In such cases, preloaded bearings (lemon bore, offset halves) or tilting pad bearings are preferred.

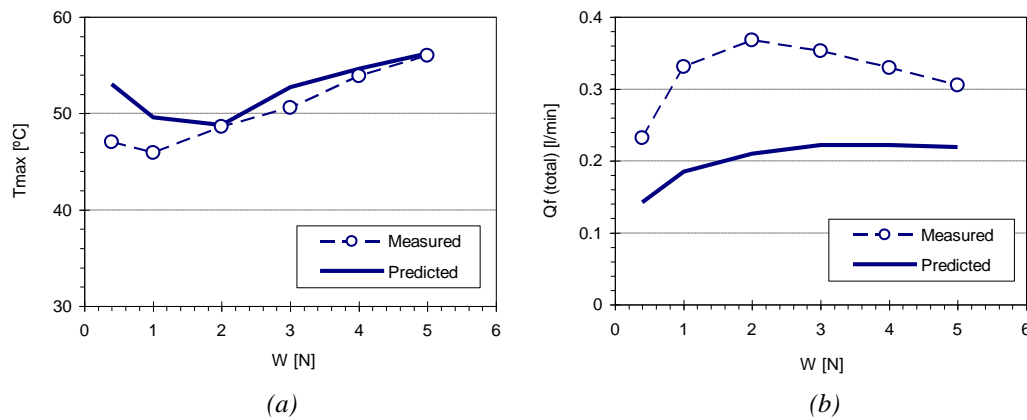


Figure VI-20 - Comparison between theory and experiment for (a) maximum bush temperature and (b) Total flow rate (single groove B2V2 bearing, $N=3000\text{rpm}$, $T_f=30^\circ\text{C}$, $P_f=100\text{kPa}$).

In continuation, similar results are presented, but now for the twin groove bearing arrangement. The same overestimation of the temperature field is observed in lightly loaded cases (Figure VI-21a). For higher loads (Figure VI-21b,c) the temperature trend is not so accurately predicted as in the case of the single groove bearing (Figure VI-19b,c). The temperature level predicted in the upper land of the bearing is generally over-predicted. This happens as a consequence of the strong under-prediction of the flow rate at the groove serving this land (-90° groove).

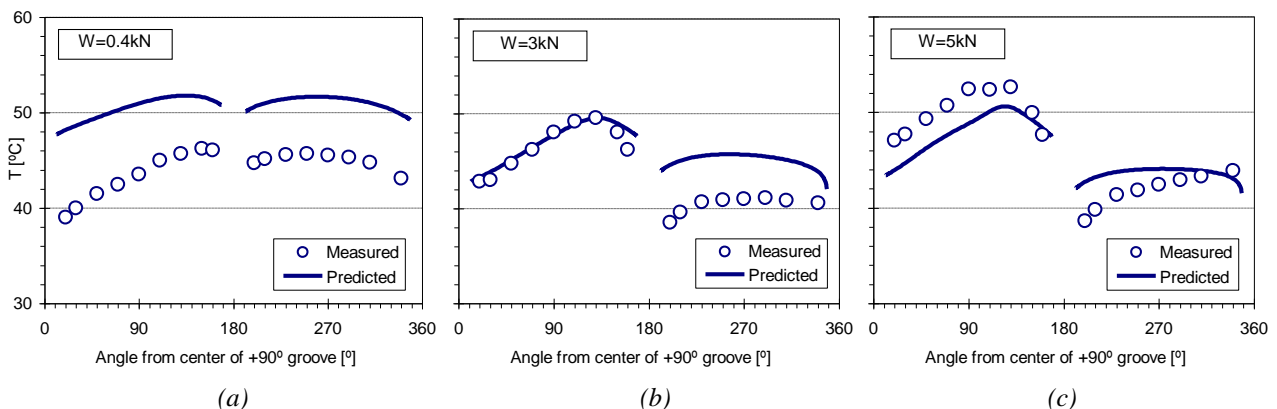


Figure VI-21 Comparison between theory and experiment of the temperature profiles at the midplane of the inner bush surface of the bearing for an applied load of (a) 0.4kN, (b) 3kN and (c) 5kN. (twin groove B2V2 bearing, $N=3000\text{rpm}$, $T_f=30^\circ\text{C}$, $P_f=100\text{kPa}$).

Figure VI-22a) shows that T_{max} goes from being clearly over-predicted, under low loads, into being slightly under-predicted for the highest loads. This transition occurs for a load around 3kN. Curiously, the flow rate at the groove which serves the land where T_{max} occurs (the $+90^\circ$ groove) goes from being under-predicted into being over-predicted, with the threshold being also the 3kN test. This can be seen by comparing the measured and the predicted flow rate of the $+90^\circ$ groove displayed in Figure VI-22b) and c), respectively. Actually, it was already

advanced in CHAPTER V0 that the flow rate at the $+90^\circ$ groove seemed to have a dominant role in the thermal behavior of twin groove journal bearings. This fact seems to explain the major differences between theoretical and experimental thermal predictions.

The oil reflux phenomenon described before (sections III.11.3 and V.4) and predicted in some of Ma and Taylor's tests (section VI.3.2) almost happened at this groove during the 5kN test (the flow rate at this groove was 0.02l/min, close to being negative - Figure VI-22b). However, the theoretical predictions were still far from anticipating it (0.08 l/min - Figure VI-22c). The lack of a detailed calculation of the thermal and mechanical deformations suffered by the bushing with the subsequent deformation of the local gap might explain this, at least in part. It is worth noting, however, that the trend of the flow rate curves is rather consistent with the trends observed experimentally.

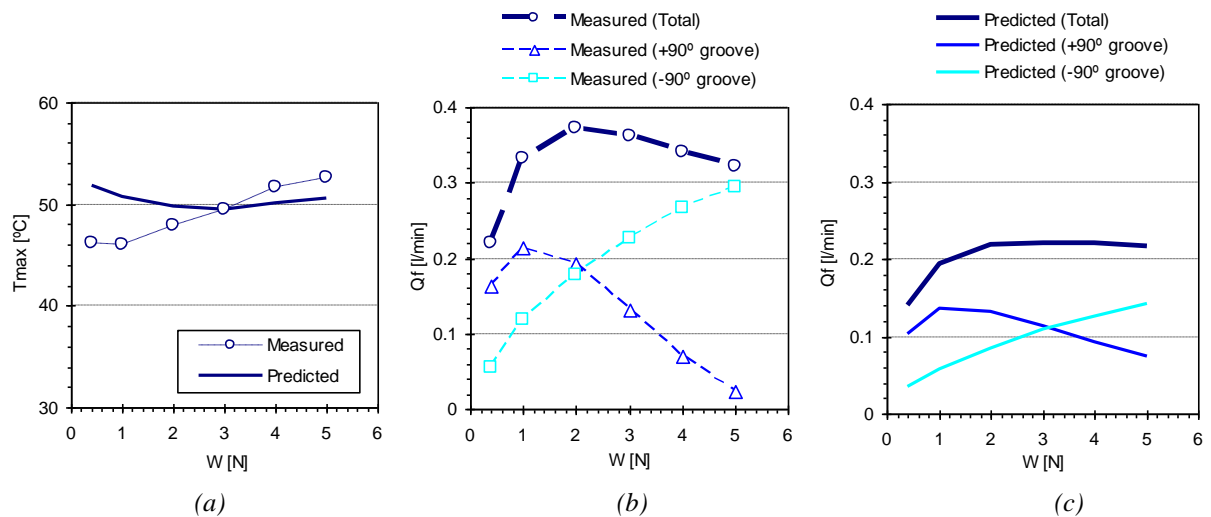


Figure VI-22 – (a) Comparison between theory and experiment of the maximum bush temperature as a function of load; (b) Measured flow rate (total and in each groove); (c) Predicted flow rate (total and in each groove). (twin groove B2V2 bearing, $N=3000\text{rpm}$, $T_f=30^\circ\text{C}$, $P_f=100\text{kPa}$)

It is clear that, for small diameter bearings, the accuracy of the predictions of the present theoretical model is highly dependent on the accuracy of the flow rate predictions at each groove.

VI.6 Conclusion

An extensive validation of the present theoretical model was undertaken. This validation was made with the help of widely known literature results (Ferron et al, 1983, Ma and Taylor, 1992, 1994, and Lund and Tonnesen, 1984) and also with experimental results from the current work.

The correlation between theory and experiment was generally quite satisfactory. The predictions of the most important design parameters such as the eccentricity ratio, maximum bush temperature and the shaft temperature were very close to the experimental measurements.

The predicted temperature trends were also in general agreement with experiment, inclusively at the upper half of the bearing, where a poor correlation has been obtained by most previous analyses.

A weakness of the model appears to be the under-estimation of the flow rate in some tests. Actually, this seems to be a general limitation of many current models, especially in the case of twin groove bearings. Nevertheless, although the absolute value of flow rate sometimes displayed a level which can be different from the experimental measurements, the trends of the total flow rate and of the partial flow rates in each groove were fairly consistent with the experimental ones. The possible reasons for these differences have been discussed and some suggestions of future model developments were proposed, such as the inclusion of a more realistic calculation of the thermal and mechanical deformations of the bearing.

The differences found in flow rate do not seem to affect significantly the prediction of bearing behavior. An exception is made for the case of smaller bearings (like the LOMT bearings), especially under low load: in fact, the low mass of these bearing systems might have caused the thermal calculations to be much more sensitive to the under-prediction of the flow rate. For low loads the under-prediction of flow rate resulted in an over-prediction of T_{max} . Fortunately, this bearing type is seldom used under light load conditions. For medium to high loads T_{max} was accurately predicted, with the main differences being obtained in the temperature trend at the unloaded land of the bearing.

A very positive achievement of the current model was the ability to predict and conveniently treat the occurrence of oil reflux in one of the grooves. This phenomenon, which can be rather deleterious for bearing performance has been hardly reported or treated in the past. Nevertheless, the critical load at which this phenomenon starts occurring is generally lower than that predicted by the current model.

In spite of the limitations noted, the current model seems apt to be used in the analysis of the performance of single and twin groove hydrodynamic journal bearings with realistic supply conditions.

*Every cold empirick, when his heart is expanded
by a successful experiment, swells into a theorist.*

- Samuel Johnson

CHAPTER VII Parametric study of the influence of lubricant supply conditions on bearing performance

VII.1 Introduction

Once the model has been validated it can finally be used in the performance analysis of single and twin groove journal bearings for a wide range of geometries and operating conditions. As it was discussed in the state of the art chapter, there is an insufficient knowledge on the influence which lubricant supply conditions exert on bearing performance. This is mainly due to the fact that most existing analyses are either non-conservative by nature (like the models base on the Reynolds conditions – see section II.2.4) or oversimplified in the way they treat the thermal problem and groove-related phenomena (absence of thermal mixing models, actual groove dimensions are often not considered). Moreover, the temperature trend typical of twin groove journal bearings has rarely been accurately reproduced.

The present model is conservative and incorporates a detailed THD analysis of the phenomena occurring both in the vicinity of grooves and in the ruptured film region. This, along with the encouraging results obtained in its validation, indicates that it is suited for the aim pursued in this chapter.

This parametric study assesses the influence of parameters which are related to the way lubricant is supplied to the system: the lubricant feeding pressure and temperature, groove length ratio (a/b), groove width ratio (w/d), number of grooves (single $+90^\circ$ vs. twin $\pm 90^\circ$) and location of the grooves with respect to the load line.

The study of each parameter was made for specific loads which ranged from around 0.1MPa up to around 10MPa. This encompasses the whole load range typical of practical applications, which, according to design procedures such as the ESDU 84031, normally goes up to 4-5MPa under normal conditions and up to 7-8MPa under specially controlled conditions (namely, for

very low surface roughness). In practical terms, nearly the whole range of eccentricity ratio (from 0.15 to 0.95 in 0.05 intervals) was tested for the study of most parameters.

The various test conditions are summarized in Table VII-1. When analyzing one specific parameter, all remaining parameters were kept unchanged, with the exception of load and speed. The charts which are represented as a function of specific load have a logarithmic scale. This has to do with the effect that load has on eccentricity, which is also logarithmic in trend (the sensitivity of ϵ to changes in W_s decreases with the increase of W_s).

Table VII-1 – Listing of the conditions used for the study of each parameter

			Parameter studied					
			Pf	Tf	a/b	w/d	1gr vs. 2gr	groove location w/ respect to load line
Geometric characteristics								
- Inner bush diameter (nominal)	d	mm	100	100	100	100	100	100
- Outer Bush diameter	D	mm	200	200	200	200	200	200
- Bush width / diameter ratio	b/d		0.8	0.8	0.8	0.8	0.8	0.8
- Groove number			2	2	2	2	1 ; 2	2
- Groove angle with load line			$\pm 90^\circ$	$\pm 90^\circ$	$\pm 90^\circ$	$\pm 90^\circ$	+90° ±90°	30° ; 60° 90° ; 120° 150°
- Groove length / bush length ratio	a/b		0.875	0.875	0.3 ; 0.6 0.875	0.875	0.875	0.875
- Groove width / diam. ratio	w/d		0.18	0.18	0.18	0.18 0.36	0.18	0.18
- Groove depth ratio (radial depth divided by the thickness of the bush)			0.2	0.2	0.2	0.2	0.2	0.2
- Bearing radial clearance (at 20°C)	C_r	μm	75	75	75	75	75	75
- Clearance ratio (at 20°C)	C_r/R_s	$\times 10^{-3}$	1.5	1.5	1.5	1.5	1.5	1.5
Oil properties								
- T1		°C	40	40	40	40	40	40
- T2		°C	70	70	70	70	70	70
- Dynamic viscosity at temperature T1	μ_{T1}	Pa.s	0.0293	0.0293	0.0293	0.0293	0.0293	0.0293
- Dynamic viscosity at temperature T2	μ_{T2}	Pa.s	0.0111	0.0111	0.0111	0.0111	0.0111	0.0111
- Specific Heat	C_p	J/kgK	2000	2000	2000	2000	2000	2000
- Density	ρ_l	kg/m ³	870	870	870	870	870	870
Heat transfer coefficients used								
- Global H.T. coefficient bush-ambient	H_{amb}	W/m ² K	50	50	50	50	50	50
- Global H.T. coefficient bush-groove oil	H_{gr}	W/m ² K	750	750	750	750	750	750
- Thermal conductivity of the air	k_{air}	W/mK	0.025	0.025	0.025	0.025	0.025	0.025
- Thermal conductivity of the lubricant	k_l	W/mK	0.13	0.13	0.13	0.13	0.13	0.13
Operating conditions								
- Rotational speed	N	krpm	1000;3000 5000	3000	3000	3000	3000	3000
- Specific load range (approx).	W_s	MPa	0.1 - 10	0.1 - 10	0.1 - 10	0.1 - 10	0.1 - 10	0.1 - 10
Supply conditions								
- Oil supply pressure	P_f	kPa	0; 50;100 150;200 250;300	100	100	100	100	100
- Oil supply temperature	T_f	°C	40	30 ; 40 50 ; 60	40	40	40	40

VII.2 Influence of lubricant feeding pressure

The experimental study of the effect of lubricant feeding pressure (P_f) on bearing performance was presented in the chapters dedicated both to the LMS and the LOMT test series (Chapters V and VI, respectively). It is interesting to observe that the same tendencies which were observed experimentally are now predicted for a wide range of operating conditions.

The main direct effect of increasing lubricant feeding pressure is the increase in flow rate. It has been shown already in the present work that, in the twin groove bearing case, the knowledge of the flow rate partition between the two grooves can be vital when trying to understand the bearing behavior. The evolution of total and partial flow rates with specific load (W_s) and P_f is presented in Figure VII-1 for a fixed shaft speed ($N=3000\text{rpm}$).

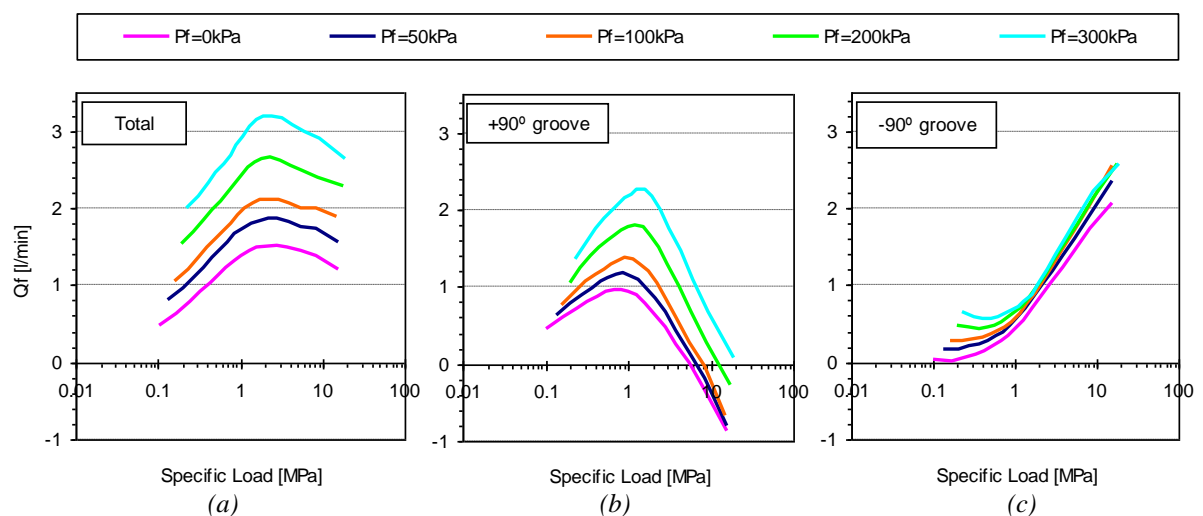


Figure VII-1 - Influence of specific load and lubricant feeding pressure on (a) total flow rate, (b) +90° groove flow rate and (c) -90° groove flow rate ($N=3000\text{rpm}$).

The same general tendencies that were observed experimentally in the LOMT test series were obtained:

- When increasing load, the total flow rate displays a clear increasing trend, followed by a smooth decline in the higher load range. The increase of P_f yields a proportional increase in flow rate, irrespective of load;
- When increasing load, the +90° flow rate displays the same initial increasing trend, but then followed by a steep, continuous decline. Inclusively, negative values (hot oil reflux) were obtained in the higher load range, especially for low P_f . The increase of P_f yields a proportional increase in flow rate irrespective of load and eventually prevents the occurrence of hot oil reflux through this groove;
- Except for the lower load range, the flow rate in the -90° groove displays a steady logarithmic increase. The influence of P_f is strong in the lower load range and is marginal for the higher load range.

The influence of shaft rotational speed, N , can be evaluated in Figure VII-2, where the flow rate results obtained for 1000rpm (a,b,c) and 5000rpm (d,e,f) are presented for varying specific load and three different P_f values (50, 100 and 300kPa).

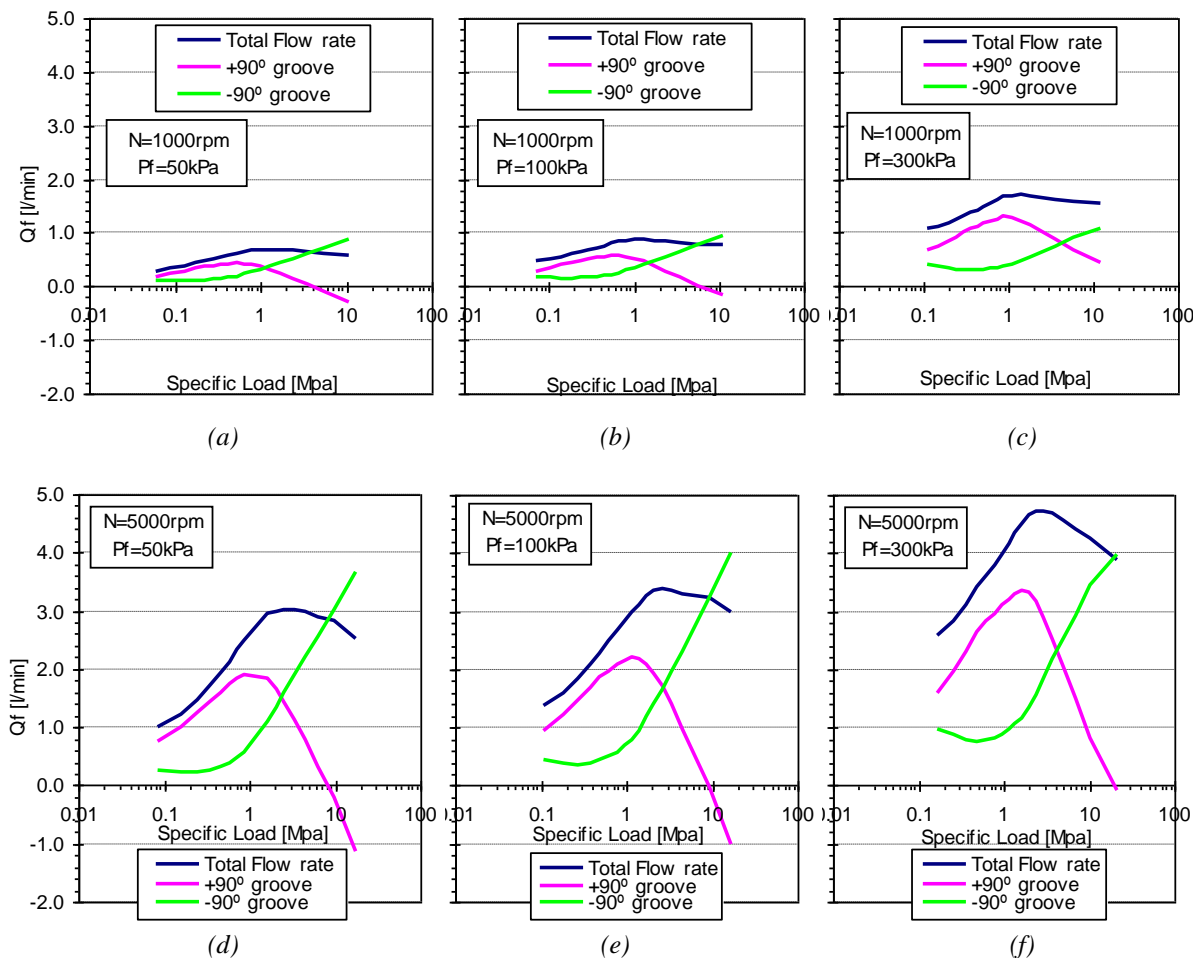


Figure VII-2 – Influence of specific load and lubricant feeding pressure on total flow rate and on the flow rate in each groove, for three different values of P_f and two different shaft speeds (1000rpm and 5000rpm).

It can be seen that the increase of N yields strong increases in flow rate, although this increase is smaller for the higher load range. Still, the critical W_s at which hot oil reflux starts occurring is magnified with the increase of N . This seems reasonable, because the increase of the Couette component of the flow reduces reverse flow phenomena, which are responsible for hot oil reflux.

One last series of flow rate charts (displayed in Figure VII-3) could help the understanding of the circumstances under which hot oil reflux starts occurring: curiously, for the lower P_f range, this phenomenon appears at around the same eccentricity for all speeds tested: around 0.86 for $P_f = 50\text{kPa}$ and around 0.90 for $P_f = 100\text{kPa}$. This corresponds to specific loads of around 4, 7 and 8 MPa for $P_f = 50\text{kPa}$, and of 6, 8 and 9.5MPa for 100MPa. In reality, these values should be lower: as seen in the validation task the present model seems to over-predict the critical load at which oil reflux starts occurring. Moreover, these results should be regarded with extra caution since some of these loads are already out of the safe range of operation recommended

for hydrodynamic journal bearings: Moreover, some of the assumptions made in the model become unsuitable.

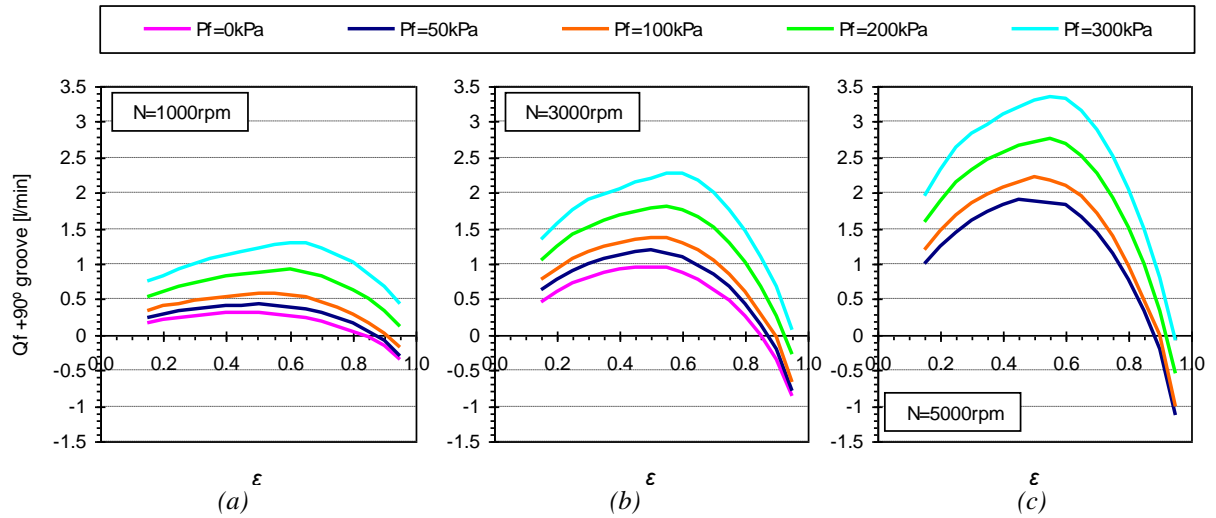


Figure VII-3 - Influence of eccentricity ratio and lubricant feeding pressure on the flow rate in the +90° groove for (a) $N=1000\text{rpm}$, (b) $N=3000\text{rpm}$ and (c) $N=5000\text{rpm}$.

Figure VII-4 shows, for two different values of P_f (100kPa and 300kPa), the evolution of the eccentricity ratio with both W_s and the Sommerfeld number, which is a non-dimensional number frequently used in bearing analysis.

It can be seen that the increase in P_f always reduces eccentricity. For instance, Figure VII-4a shows that the 3000rpm tests with $P_f=300\text{kPa}$ display eccentricities which are similar and in some cases even lower than those obtained in tests with $N=5000\text{rpm}$ and $P_f=100\text{kPa}$.

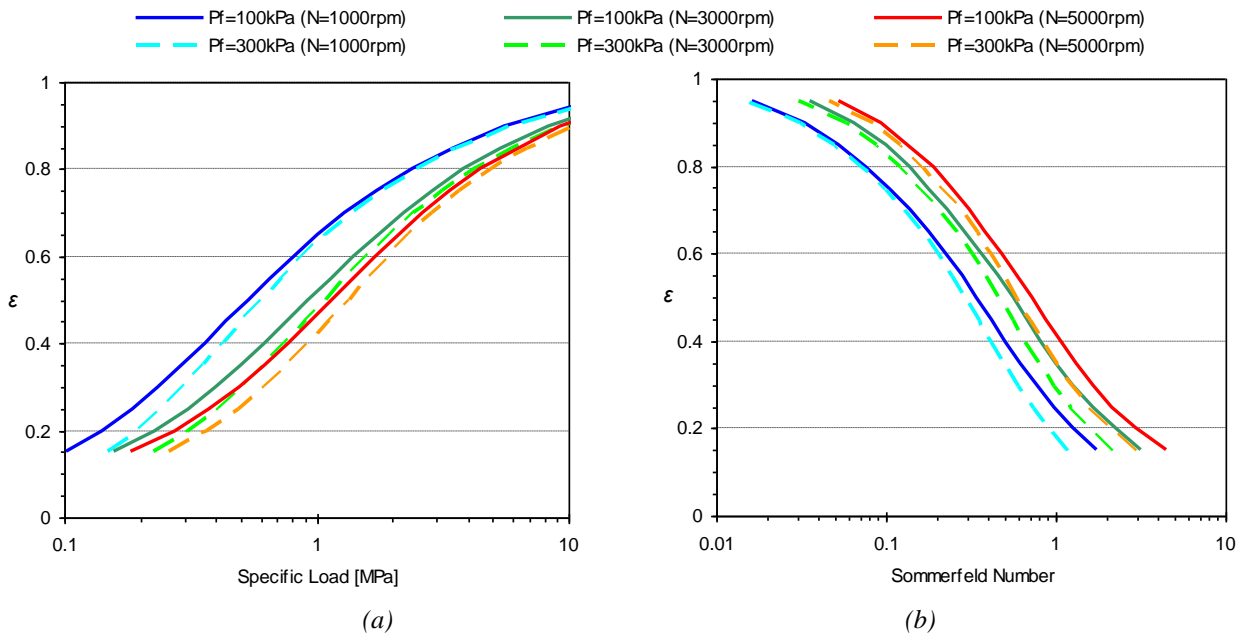


Figure VII-4 – Eccentricity ratio for several values of feeding pressure and rotational speeds as a function of (a) Specific load and (b) Sommerfeld number

A shaft locus plot and the corresponding minimum film thickness values are presented in Figure VII-5 for a fixed speed ($N=3000\text{rpm}$), several specific loads (from 0.1 to 10MPa) and six different values of P_f (from 50 to 300kPa).

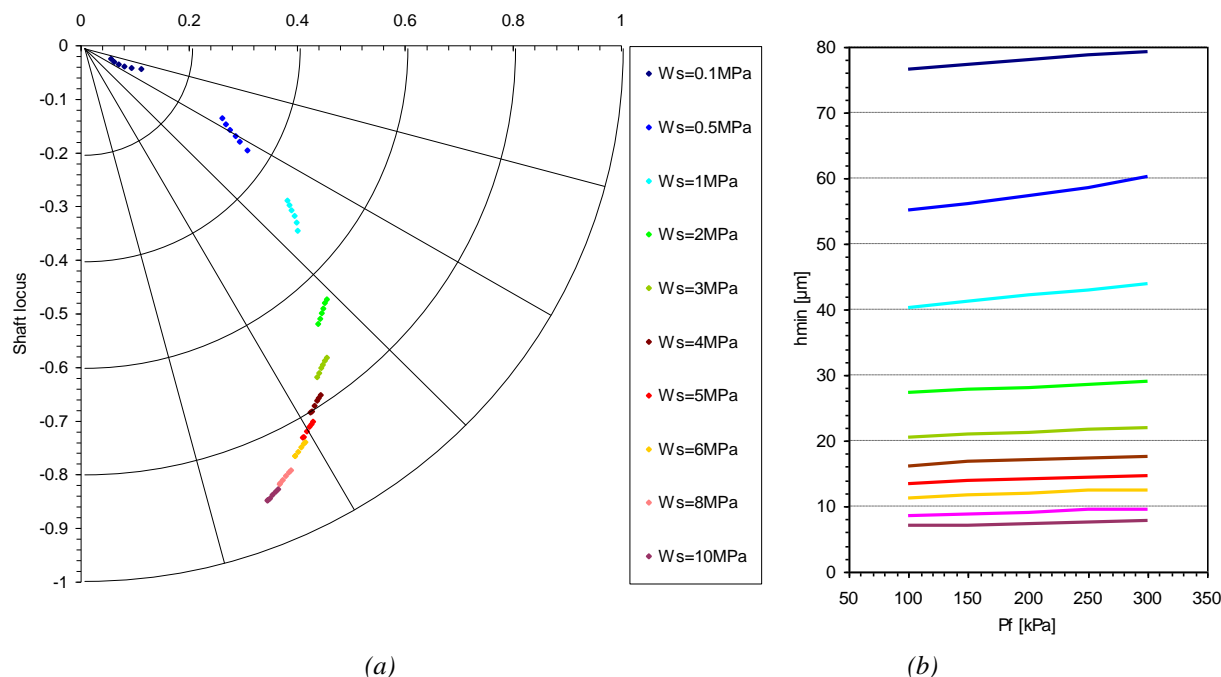


Figure VII-5 – (a) Shaft locus for several specific loads and six values of P_f (50, 100, 150, 200, 250, and 350kPa) and (b) minimum film thickness as a function of P_f and for several specific loads ($N=3000\text{rpm}$).

Although in the higher load range the differences in eccentricity between low and high P_f simulations might appear to be unimportant, in fact, within the high eccentricity range, bearing performance is highly sensitive to even small changes in ε . These, combined with the differences in thermal behavior, elastic deformations and possibly some misalignment could, inclusively, make the difference between the occurrence and the prevention of seizure in some cases. As a matter of fact, the critical role of P_f has been previously experienced during the LOMT experimental work (see section V.4.3).

The influence which P_f has on the temperature profile at the midplane of the inner bush surface can be assessed in Figure VII-6 for several specific loads. The same results, now grouped by load are also displayed, for three different W_s values, in Figure VII-7. The global trends which are normally obtained experimentally can also be clearly observed here:

- The increase of P_f leads to a decrease of the temperature level rather than to a change in trend (except when hot oil reflux occurred).
- The lowest T_{max} is obtained within the low eccentricity range but not with the lowest eccentricity case.

- As load increases, T_{max} starts being located at the unloaded land of the bearing and moves its location more and more upstream, while the temperature level at the unloaded land of the bearing tends to decrease.
- In the higher load range a curious temperature peak is formed. This should be due to the intense viscous dissipation occurring in the vicinity of the minimum film thickness region. Some experimental results also appear to display a similar feature (see Figure V-27).
- For the two highest load cases ($W_s = 8$ and 10MPa), the temperature profiles corresponding to the two P_f values display some differences because hot oil reflux was predicted to occur for $P_f=100\text{kPa}$ but not for 300kPa (see flow rate charts in Figure VII-1b). One of the differences is that when increasing P_f from 100 to 300kPa a sharp fall of the temperature inside the $+90^\circ$ groove was predicted. It decreased from around 65°C (denoting hot oil exiting the bearing gap through this groove - Figure VII-6a) to around 42°C (denoting cool feeding oil entering the bearing gap through this groove - Figure VII-6b). Another difference between the curves is the disappearance, when P_f increased from 100kPa to 300kPa , of the ever-increasing trend of the temperature profile at the unloaded land of the bearing which is typical when hot oil reflux occurs (see, for instance, the LOMT experimental results displayed in Figure V-23c). The disappearing of hot oil reflux due to the increase of P_f can also be seen in Figure VII-7c.

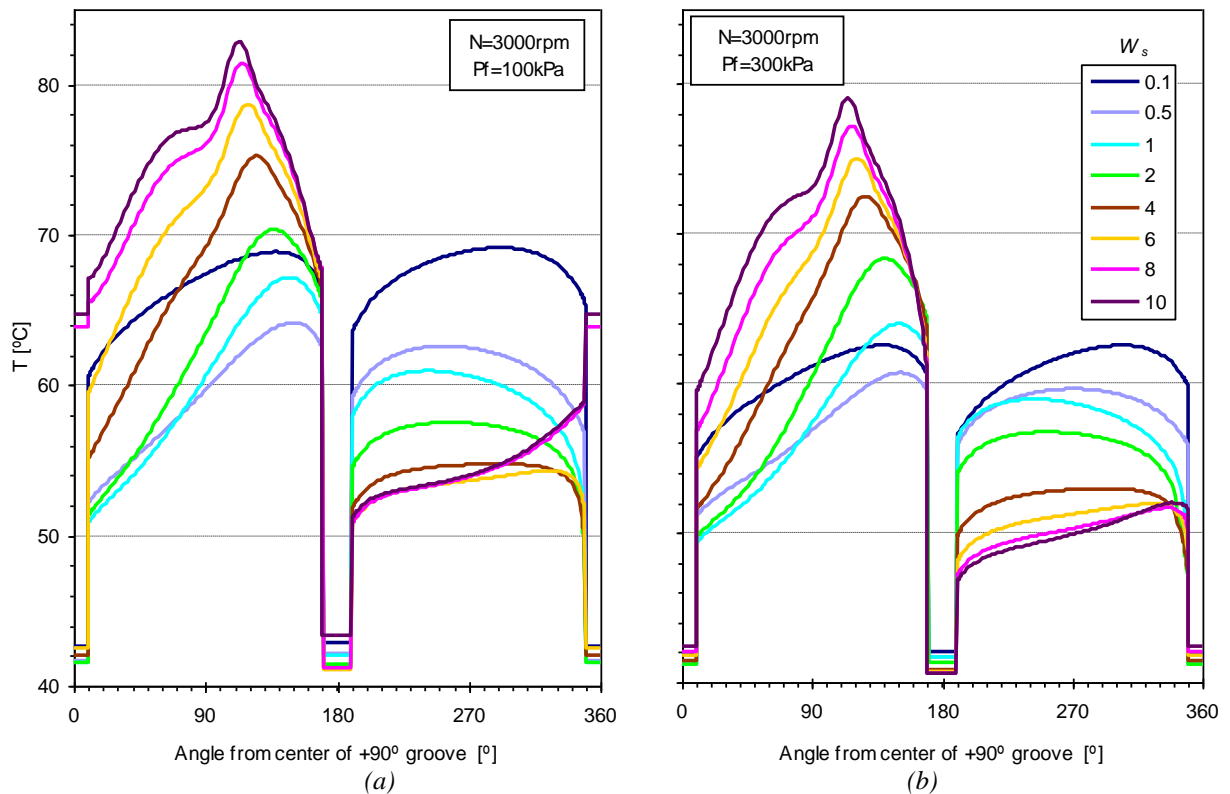


Figure VII-6 – Temperature profile at the midplane of the inner bush surface for several specific loads and (a) $P_f=100\text{kPa}$ and (b) $P_f=300\text{kPa}$ ($N=3000\text{rpm}$).

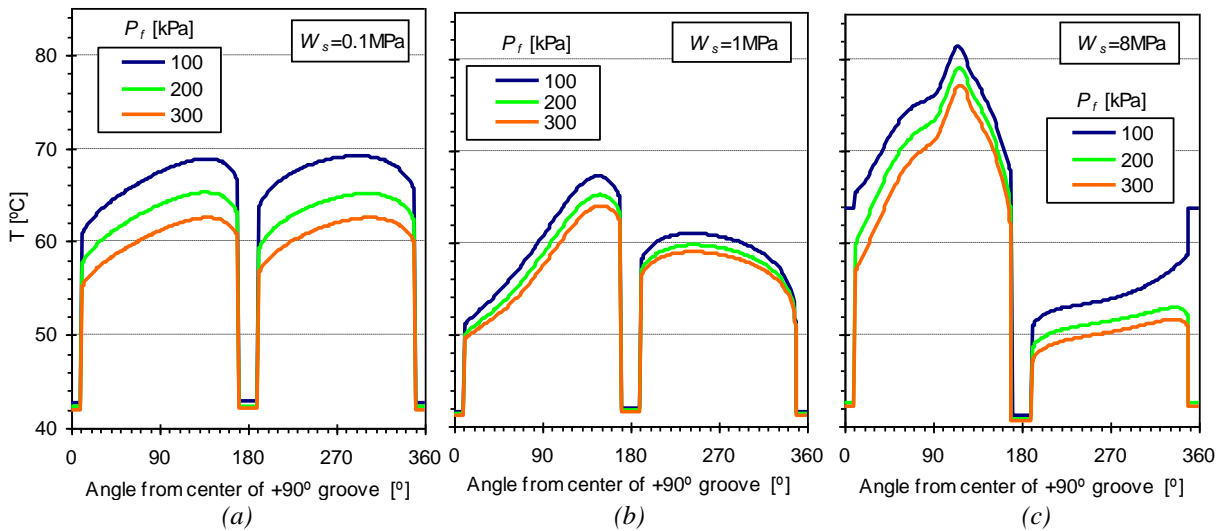


Figure VII-7 - Temperature profiles at the midplane of the inner bush surface for several feeding pressures and (a) $W_s=0.1\text{MPa}$, (b) $W_s=1\text{MPa}$ and (c) $W_s=8\text{MPa}$. ($N=3000\text{rpm}$).

Figure VII-8 summarizes the maximum temperatures predictions, which are represented as a function of eccentricity and specific load.

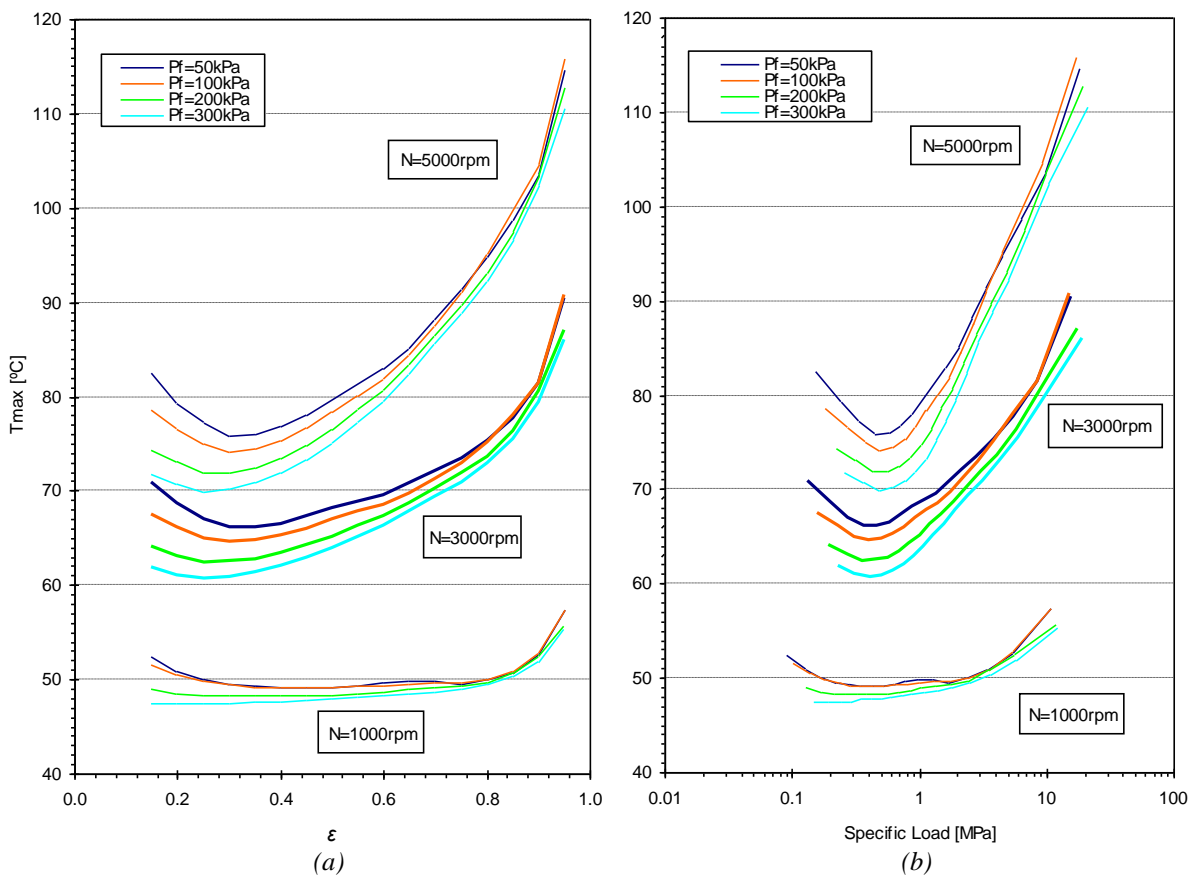


Figure VII-8 – Influence of feeding pressure on maximum bush temperature (a) for varying eccentricity and (b) for varying specific load.

The lowest value of T_{max} is not obtained for the lowest eccentricity but between 0.2 and 0.3 (corresponding to a specific load interval between 0.3MPa and 0.5MPa). Within the lower eccentricity range the increase of P_f yields a significant decrease in T_{max} . As load increases the influence which P_f has on T_{max} becomes weaker. However, in the higher eccentricity range

there is a point where some of the lower P_f curves start diverging for the remaining curves. This is when hot oil reflux starts occurring at the $+90^\circ$ groove. As explained before, this phenomenon causes a mixing and feedback effect where an effective rise in feeding temperature is obtained. This causes a global rise of the temperature level in the bearing which is also reflected in T_{max} .

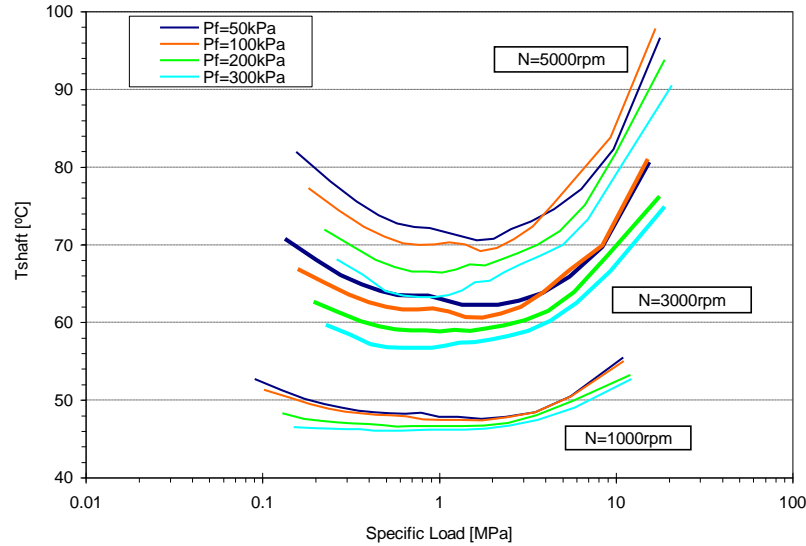


Figure VII-9 - Influence of feeding pressure on the temperature of the shaft surface for varying specific load

The effect of load, speed and P_f on the shaft surface temperature is presented in Figure VII-9. One particularity of T_{shaft} relatively to T_{max} is that its minimum is obtained for a much higher load, as T_{max} is much more affected by P_f in the low load range.

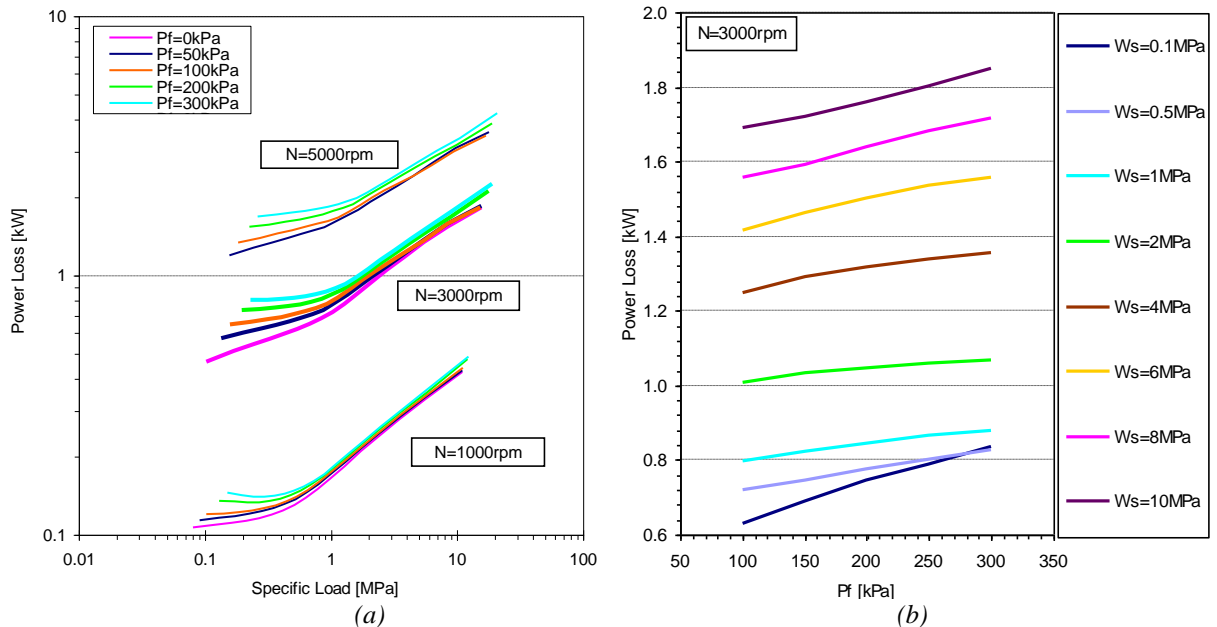


Figure VII-10 –Influence of feeding pressure and specific load on power loss, for (a) varying specific pressure and (b) varying P_f .

Figure VII-10 displays the influence of P_f on power loss. In Figure VII-10a it can be seen that the influence of P_f on power loss is more significant for low loads. For instance, when P_f was

increased from 100 to 300kPa in the case of a bearing with $W_s=0.1\text{MPa}$ and $N=3000\text{rpm}$, a 33% increase in power loss (from 0.65kW to 0.85kW – see Figure VII-10b) is predicted.

For higher loads ($W_s > 1\text{MPa}$) the influence of P_f seems to be smaller and less dependent of load. This can be also observed also in Figure VII-10b, with the power loss curves corresponding to specific loads above 1MPa displaying an increase in power loss of around 10% when increasing P_f from 100 to 300kPa.

As concluding remarks, it is worth stating that:

- The increase of P_f may be useful in reducing T_{max} and T_{shaft} , especially in the case of the lightly loaded bearings. However, this will be made at the expense of a significant increase in power loss.
- In the case of heavily loaded bearings, P_f displays a less deleterious effect on power loss but it is not as effective in reducing the temperature level as with low eccentricities. Nonetheless, P_f is a key factor in eliminating hot oil reflux at the $+90^\circ$ groove, and in slightly reducing eccentricity. Under severe operating condition these combined effects might prove decisive in preventing seizure.

VII.3 Influence of lubricant feeding temperature

Lubricant viscosity (μ_l), which strongly depends on local temperature, is the parameter responsible for hydrodynamic pressure generation within the fluid. Therefore, the variation of T_f is likely to exert a strong influence not only on the temperature field, the power loss and the flow patterns, but also on the bearing eccentricity and ultimately on the load carrying capacity of the bearing.

It is true that feeding the lubricant at low T_f tends to maximize bearing cooling efficiency and load capacity, even if it is at the expense of a slightly higher power loss caused by the added drag. However, in the absence of an efficient oil cooling system, it is not always possible to keep T_f as low as desired, especially under severe operating conditions where large amounts of heat are generated by viscous dissipation. Under these conditions the high T_f values raise the seizure risk not only because dangerously high eccentricities might be induced, but also because thermal distortion will further facilitate localized contact due to the thermal crowning of surfaces. Therefore a better understanding of the influence of T_f on bearing performance is needed. The impact that this factor has in bearing performance has been studied experimentally and discussed in sections IV.3.2 and V.4.4.

The changes in the viscosity field due to changes in T_f are likely to affect significantly the flow rates. Figure VII-11a,b,c shows the evolution of the global flow rate and the partial flow rates in each groove as a function of specific load, for three different values of T_f between 30°C and 60°C. It is interesting to compare what happens in each groove as T_f increases:

- Within the lower range of specific loads (below 2MPa) there is an increase in flow rate at the +90° groove as a consequence of the fall in lubricant viscosity with increasing T_f . This increase is smaller in the case of the -90° groove.
- Within the higher range of specific loads (above 2MPa) the increase of T_f yields a decrease of the flow rate in the +90° groove (which anticipates the critical specific load for the occurrence of hot oil reflux from 10MPa to 6MPa, when increasing T_f from 30°C to 60°C) and an increase of the flow rate in the -90° groove.

In order to better understand this behavior, it helps analyzing the flow rates as a function of eccentricity ratio, as displayed in Figure VII-11d,e,f. Now it can be seen that, actually, for a fixed eccentricity the increase of T_f always yields an increase in flow rate at the +90° groove. Therefore, the drop in the +90° groove flow rate with increasing T_f observed in Figure VII-11b, is actually a direct consequence of the eccentricity increase. In fact, it was already seen that, for high loads, the increase in eccentricity always caused the increase of the -90° groove flow rate and the decrease of the +90° groove flow rate.

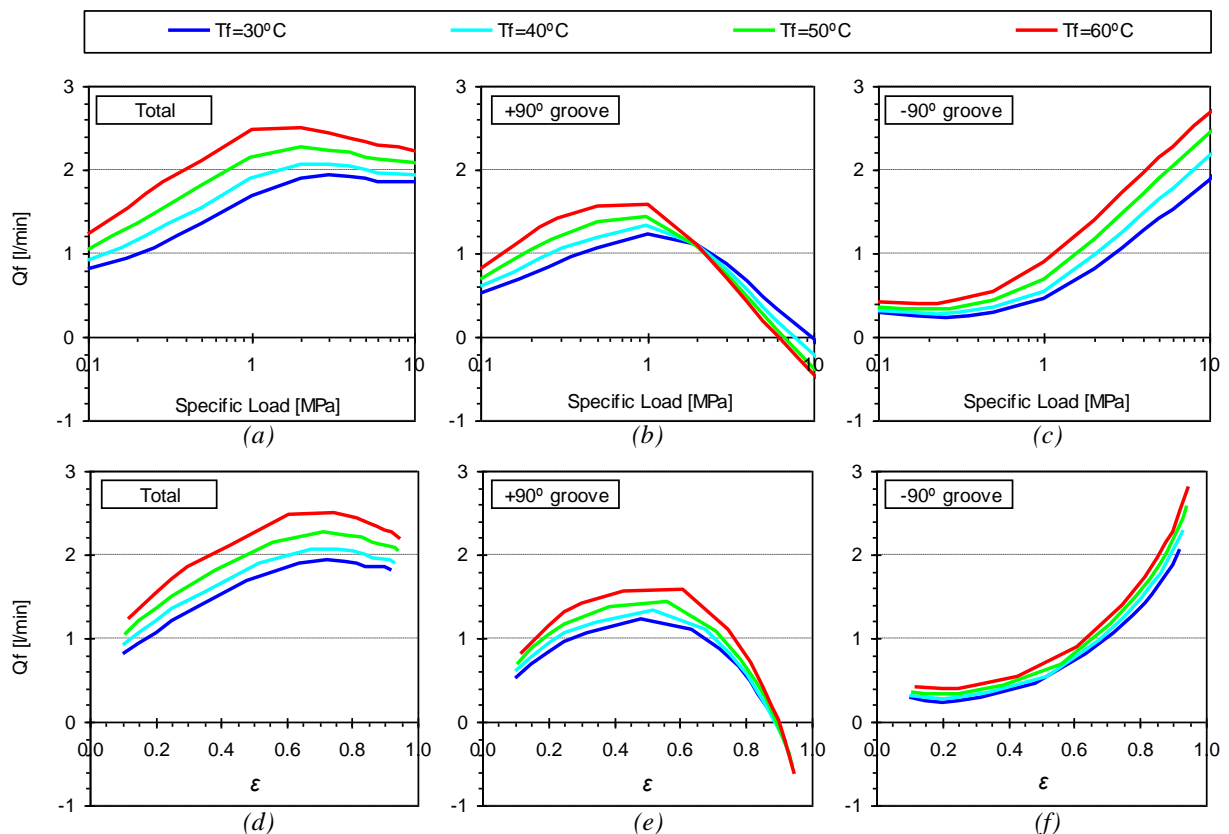


Figure VII-11 - - Influence of specific load / eccentricity and lubricant feeding pressure on (a)/(d) total flow rate, (b)/(e)+90° groove flow rate and (c)/(f) -90° groove flow rate.

The effect that T_f has on the eccentricity ratio, which is quite marked, can be seen in Figure VII-12 as a function of both W_s and the Sommerfeld number.

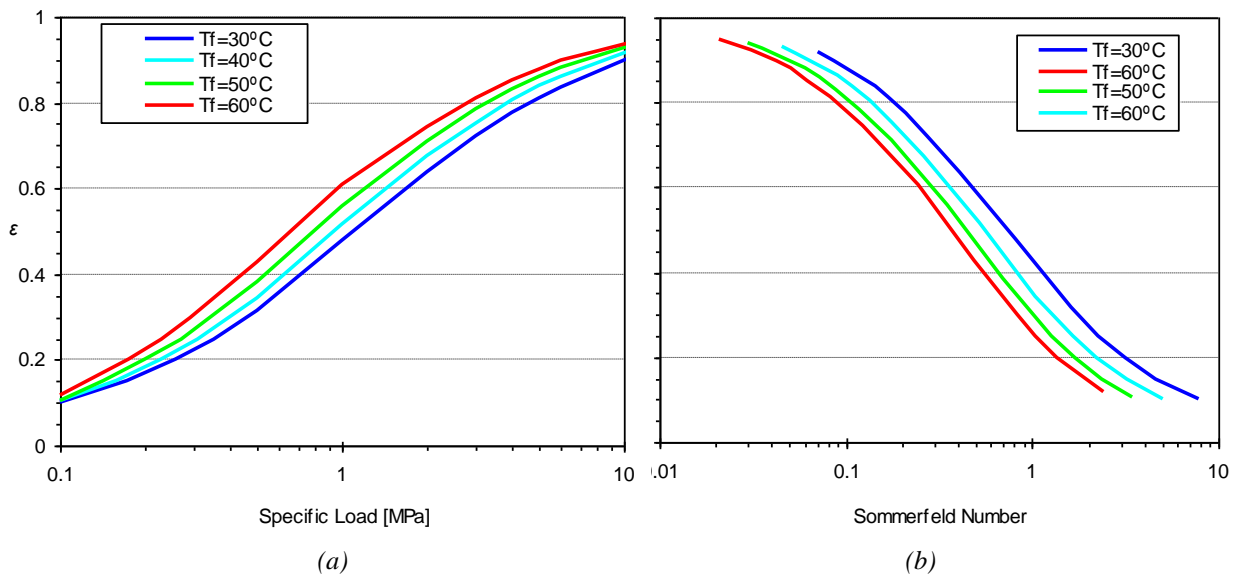


Figure VII-12 – Eccentricity ratio, for several values of feeding temperature, as a function of (a) Specific load and (b) Sommerfeld number.

The eccentricity charts can be complemented with the shaft locus chart, presented in Figure VII-13a, and the minimum film thickness as a function of T_f presented in Figure VII-13b.

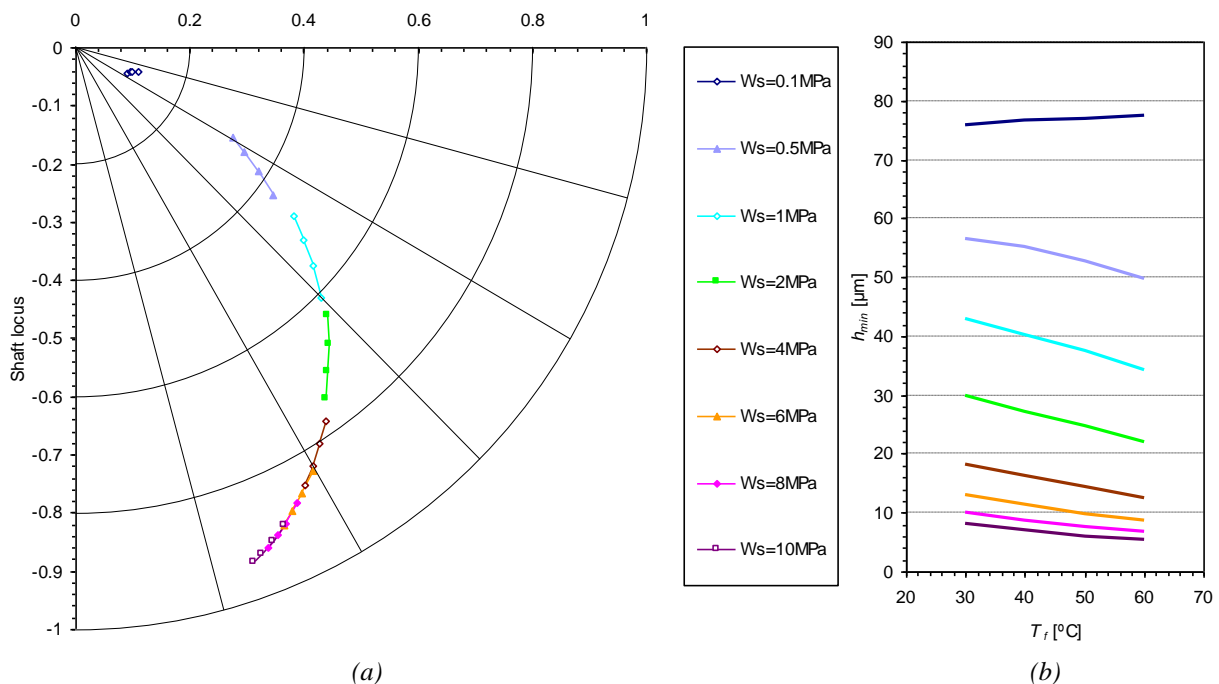


Figure VII-13– (a) Shaft locus for several specific loads and four values of T_f (30, 40, 50 and 60°C) and (b) minimum film thickness as a function of T_f and for several specific loads.

The decrease in eccentricity which is a consequence of the increase in T_f also affects the pressure field, increasing the maximum pressure (see Figure VII-14). This could also be deleterious as it amplifies the elastic distortions suffered by the bush body. This, along with the temperature extremes obtained in the vicinity of the minimum film thickness region could

accelerate the appearance of damage in the white metal coating which frequently covers the inner bush surface.

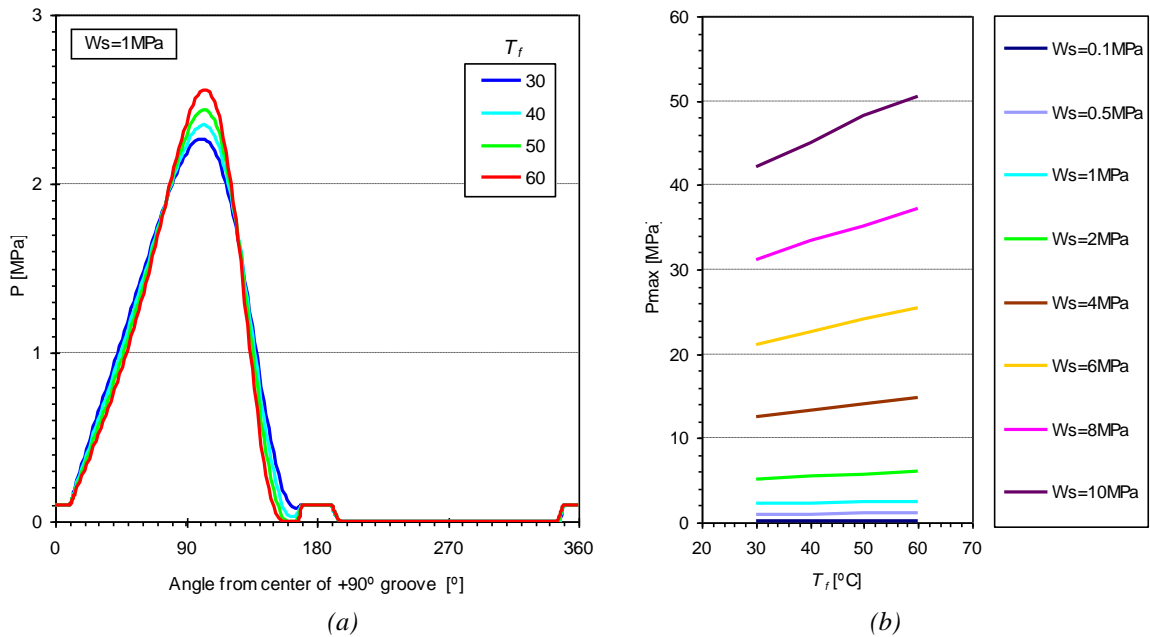


Figure VII-14 – Influence of feeding pressure on (a) the hydrodynamic pressure profile at the midplane of the bearing for $Ws=1MPa$ and (b) maximum pressure.

A comparison between the temperature profiles for T_f of 30°C and 60°C is presented in Figure VII-15 for a wide range of specific loads.

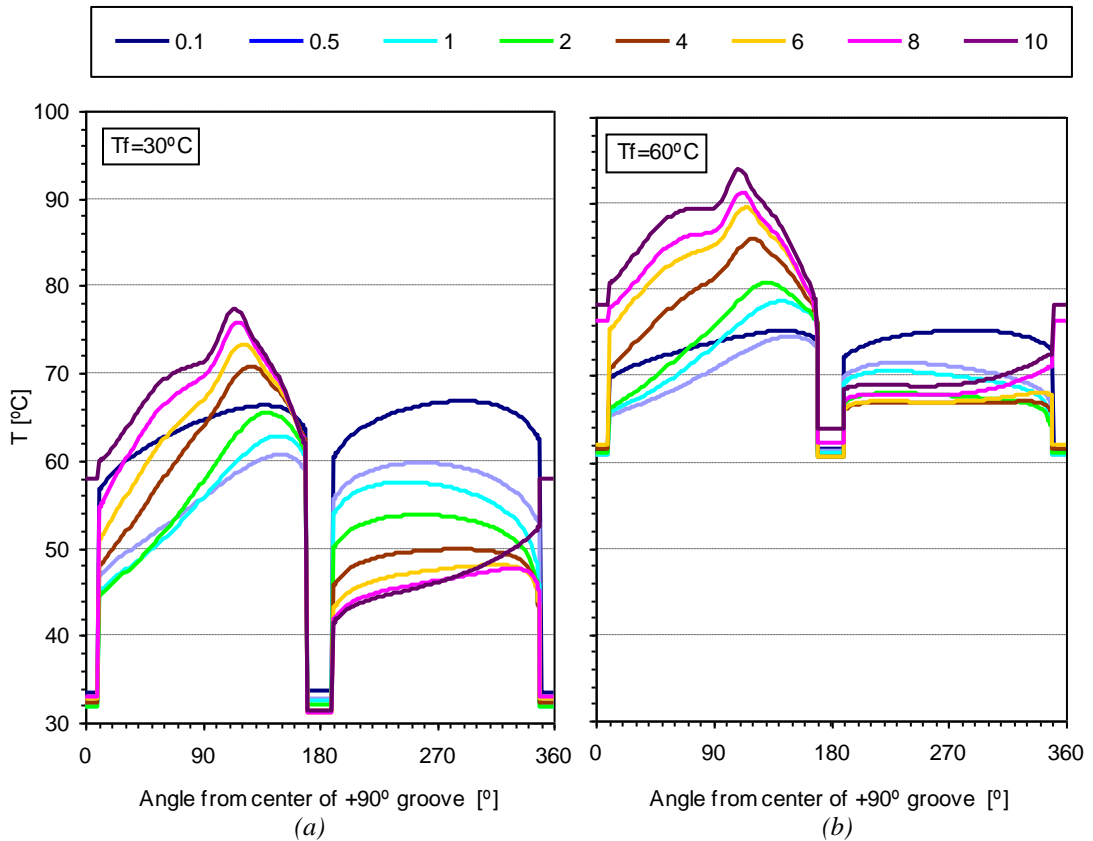


Figure VII-15 Temperature profile at the midplane of the inner bush surface for several specific loads and (a) $T_f=30^\circ C$ and (b) $T_f=60^\circ C$.

Again, and in accordance with the experimental observations, the increase in T_{max} is always much less than the corresponding increase in T_f . In this case, a 30°C increase in T_f yielded increases of 7°C for the lowest load case ($W_s = 0.1\text{MPa}$) and 15°C for the highest ($W_s = 10\text{MPa}$). Another interesting fact is that the T_f increase triggered the appearance of the hot oil reflux phenomenon in the test with $W_s = 8\text{MPa}$. This can be better appreciated in Figure VII-16b, where it is seen that this phenomenon was only prevented with $T_f = 30^\circ\text{C}$.

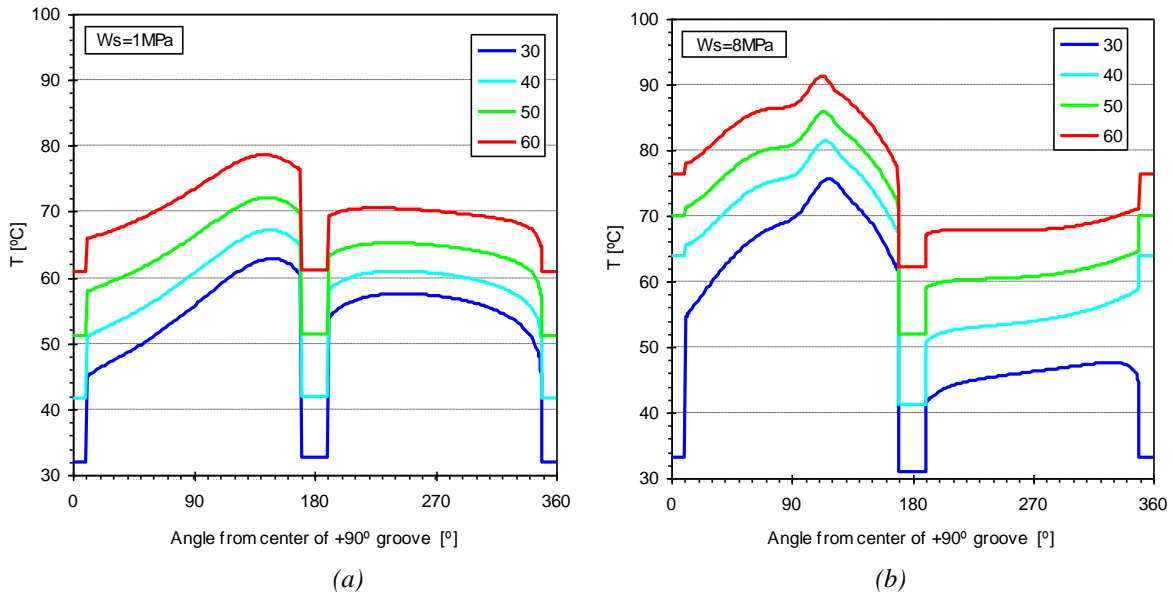


Figure VII-16 - Temperature profiles at the midplane of the inner bush surface for several feeding temperatures and (a) $W_s = 1\text{MPa}$ and (b) $W_s = 8\text{MPa}$.

The effect of T_f on the maximum temperature and shaft surface temperature is displayed in Figure VII-17a. Here it can be seen more clearly that the increase in T_{max} increase with increasing T_f is less pronounced in the low eccentricity range.

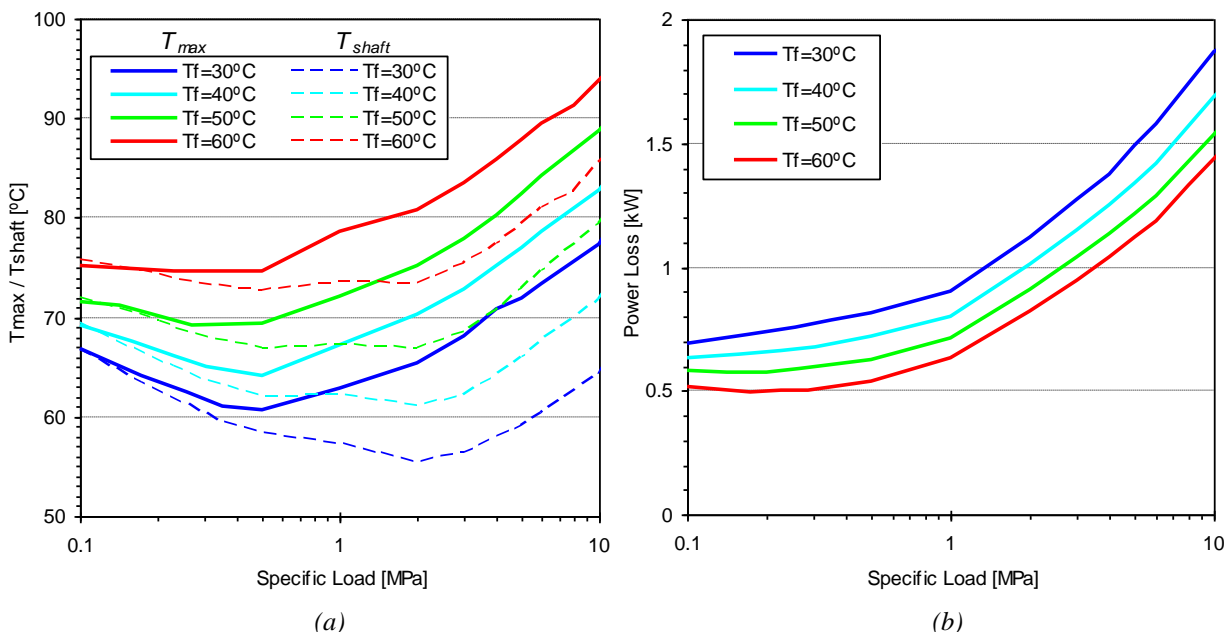


Figure VII-17 - Influence of feeding temperature on (a) maximum bush temperature and shaft surface temperature and (b) on power loss ($N = 3000\text{rpm}$).

The data also show that although for large eccentricities (higher load range) T_{shaft} is much lower than T_{max} , as the eccentricity reduces these values become similar. The experimental tests at the LMS have shown a similar pattern as seen, for instance, Figure IV-12a,b).

The influence of T_f in power loss is presented in Figure VII-17b. As expected, the viscosity reduction caused by the increase in T_f with temperature yielded a decrease of the viscous dissipation and, therefore, of the power loss. For instance, a 30% reduction in power loss may be obtained when increasing T_f from 30°C to 60°C, for a specific load of around 1MPa.

The influence of T_f on power loss is rather uniform, except for the low load range: here, the power loss values are more close to each other because the temperature levels corresponding to the various T_f cases are also more close to each other.

As expected, the feeding temperature has a marked effect on bearing performance. As concluding remarks it may be stated that:

- Under light loads a moderate increase of T_f might prove beneficial as it can reduce substantially the power loss. However this will be made at the expense of higher flow rate and increased thermal distortion.
- Under severe loading the increase of T_f might endanger safe operation due to the substantial increase in T_{max} , eccentricity and maximum pressure. Also, the flow rate at the groove which serves the active region of the bearing decreases significantly with the increase of T_f . The critical load at which hot oil reflux starts occurring is also lowered. The added distortion of the bodies (of both mechanical and thermal origin) further raises the risk of seizure, but indeed, this effect could not be evaluated with the present model.

VII.4 Influence of the groove length ratio (a/b)

In most practical cases the ideal axial groove length, a , would coincide with bearing length, b ($a/b=1$). This would, in principle, provide the most uniform delivery of lubricant to the whole axial extension of the bearing, thus optimizing lubrication efficiency and bearing cooling. However, this is not always possible, or at least not practical to do due to design constraints. For instance, in order to alleviate manufacturing costs, axial grooves are sometimes replaced by simple holes. Also, larger grooves normally require bigger pumping systems as they tend to increase oil flow rate. Larger grooves also tend to reduce the structural stiffness of the system, which might be an important parameter in some applications.

The present model neglects axial temperature gradients and therefore its predictions show some limitations when dealing with cases where significant axial temperature gradients are likely to appear. Nevertheless, the pressure and flow calculations are performed along the whole domain and, unlike most existing models, the actual groove dimensions are considered in calculations. Moreover, the thermal balances performed in the groove regions have incorporated the influence of a/b (see section III.11 and particularly paragraph d).

The hydrodynamic pressure fields obtained for two bearings with dissimilar a/b ratios (0.3 and 0.875) are presented in Figure VII-18.

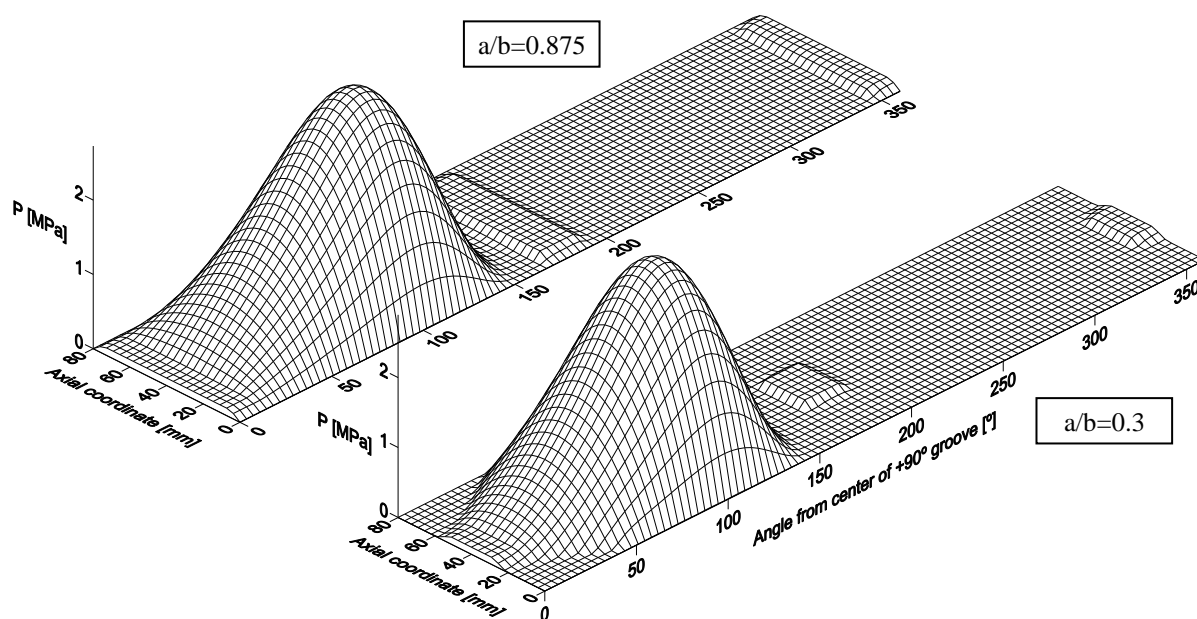


Figure VII-18 – Influence of the groove length ratio on the hydrodynamic pressure field ($W_s=1.1\text{MPa}$)

Some differences between the two cases may be appreciated:

- The two different groove geometries can be distinguished by the pressure plateaus, in the groove locations, corresponding to the feeding pressure, P_f .
- In the vicinity of the $+90^\circ$ groove and in the region downstream of it, it can be seen that there are some differences between the pressure fields obtained for the two cases: In the case of the large grooved bearing, the pressure is already positive along the whole axial length of the bearing. On the contrary, in the case of the small grooved bearing the pressure buildup only appears further downstream.

The observations made above can be better understood by analyzing the film rupture and reformation boundaries as well as the local liquid fraction, presented in Figure VII-19.

For the large groove bearing reformation extended to the whole bearing length immediately downstream of the circular coordinate of the trailing edge of the $+90^\circ$ groove (around 350°). However, the reduction in groove length caused film reformation to extend to the whole

bearing length only for an angular coordinate around 55°. Furthermore, it can be seen that the film rupture has been slightly anticipated.

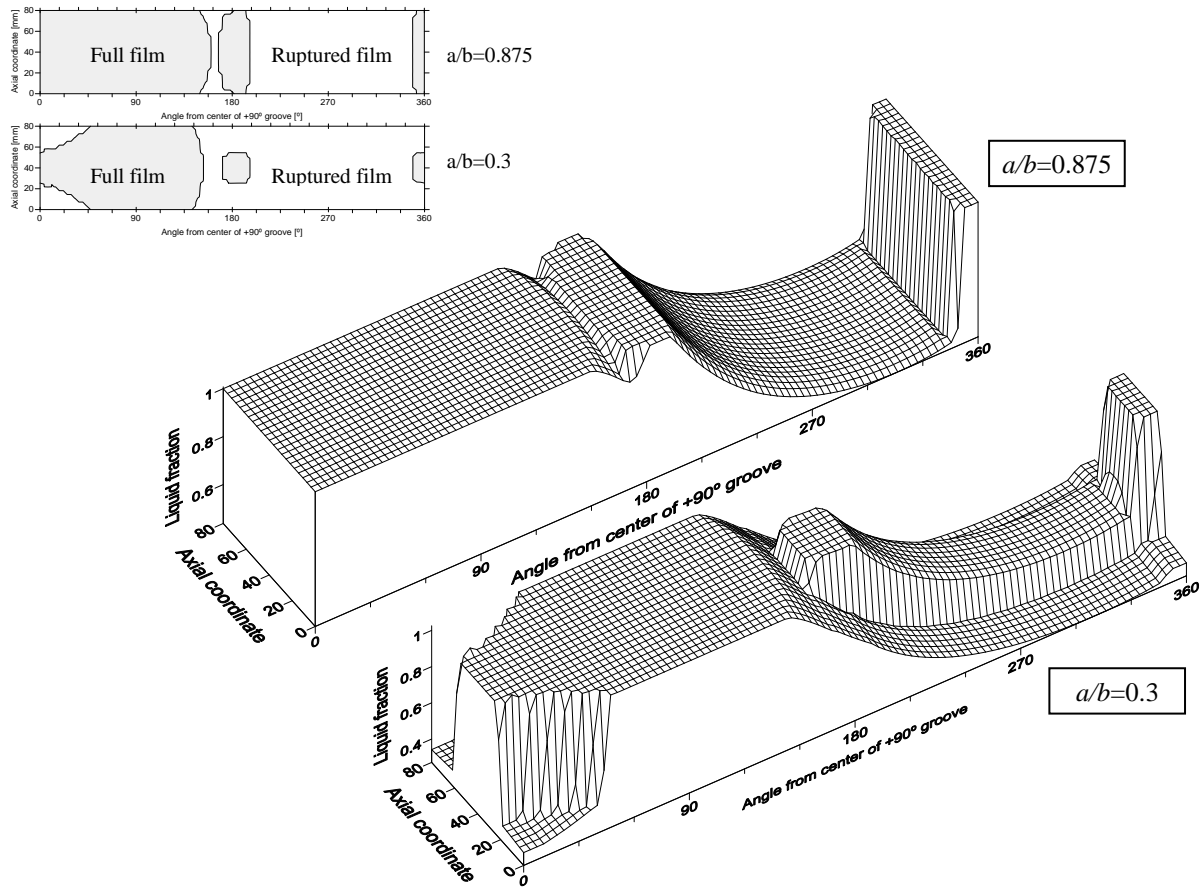


Figure VII-19 – Influence of the groove length ratio on the rupture boundaries (top left) and on the local liquid fraction (lower right) ($Ws=1.1MPa$).

The effect of the a/b ratio upon the flow rates can be observed in Figure VII-20. As expected, the total flow rate increases with the increase in a/b . In this case, it more than doubled when increasing a/b from 0.3 to 0.875.

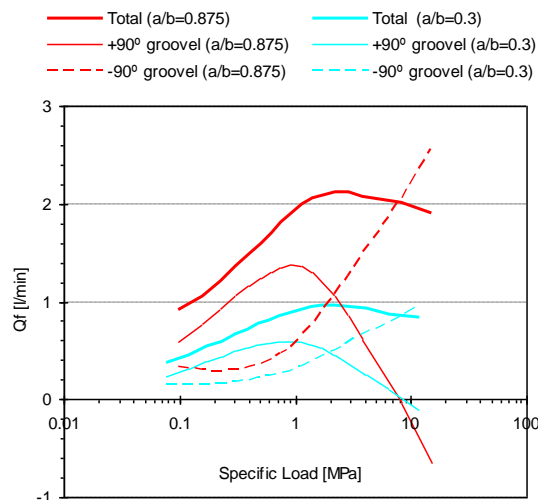


Figure VII-20 - Influence of the groove length ratio on the global flow rate and on the partial flow rates in each groove for varying Specific load.

An interesting characteristic of the $+90^\circ$ flow rate is that it increases with the increase of a/b only up to a certain threshold. This threshold coincides with the critical value of W_s at which hot oil reflux starts occurring. Curiously, this value did not change with the change of a/b . When it occurs, the negative flow rate effect is not less acute for the lower a/b . It seems that the critical load for the start of hot oil reflux might be more sensible to the circumferential coordinate of the groove limits (that depends on w/d) than to their axial coordinate (that depends on a/b). This is further explored in the next section.

The effect which a/b exerts on eccentricity and on shaft locus can be observed in Figure VII-21. The higher eccentricity displayed by the bearings with smaller grooves is a consequence of the differences in the hydrodynamic pressure field which have been pointed out before. These differences in the pressure field also tend to decrease the attitude angle (see Figure VII-21b) because the pressure loss at the starved region near the $+90^\circ$ groove causes the shaft to get closer to it.

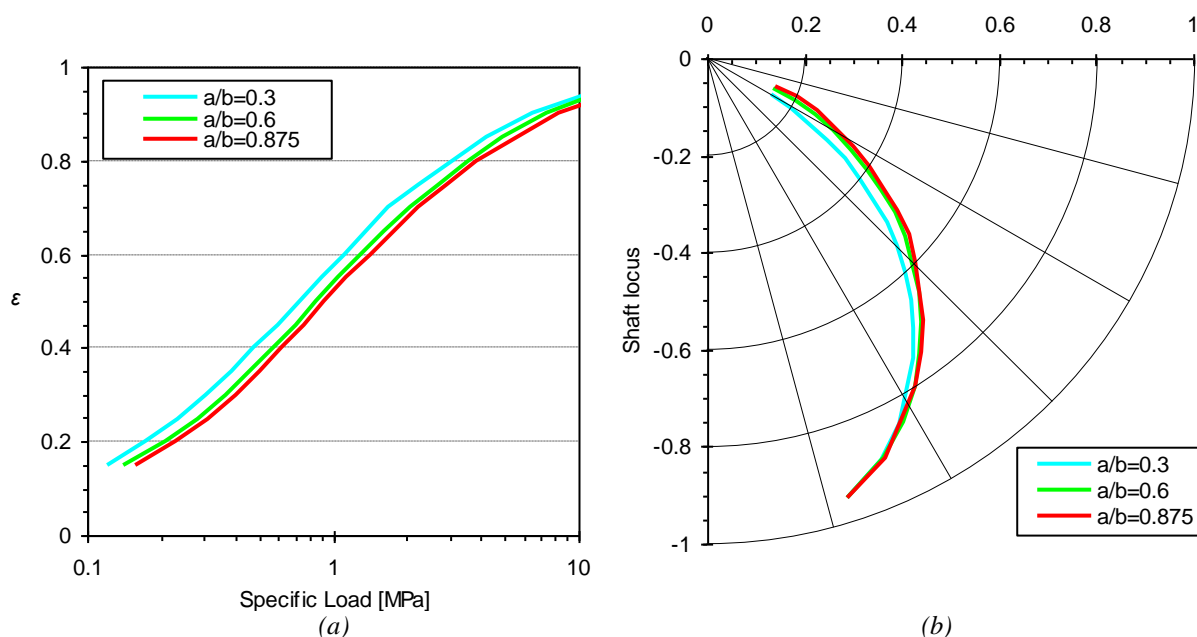


Figure VII-21 - Influence of the groove length ratio on (a) eccentricity ratio and (b) shaft locus, for varying specific load.

The effect which a/b has on the temperature field is displayed in Figure VII-22, which compares the inner bush surface temperature profile for two groove length ratios, and Figure VII-23a, which charts the maximum bush temperature and the shaft surface temperature values for three different values of a/b .

The different temperature level displayed by the three cases is mainly explained by the strong differences in flow rate and in part by the slight differences in eccentricity. It is anticipated that these differences should be even higher outside the bearing midplane, but indeed, the present model is not able to quantify this.

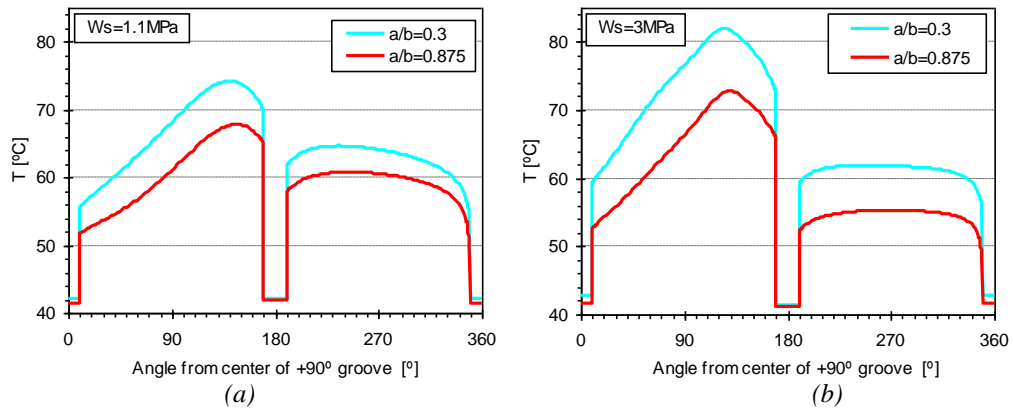


Figure VII-22 -Influence of the groove length ratio on the temperature profile at the midplane of the inner bush surface for (a) $W_s = 1.1 \text{ MPa}$ and (b) $W_s = 3 \text{ MPa}$.

The final parameter to be analyzed is again power loss (see Figure VII-23b). The lower lubricant flow rate, the smaller extension of the complete film and the higher temperature should explain the lower power dissipation observed for the smaller groove bearings.

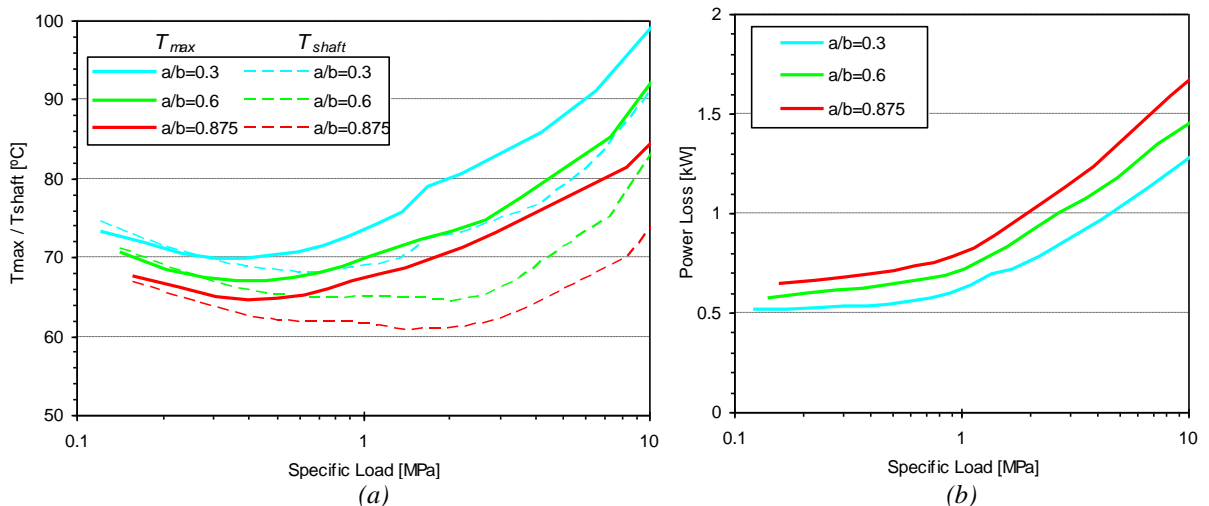


Figure VII-23-Influence of the groove length ratio on (a) maximum bush temperature and shaft surface temperature and (b) power loss.

As a conclusion it may be stated that the groove length ratio was found to affect bearing performance in several ways. Reducing the axial extension of the grooves is expected to cause:

- Some positive effects like the reduction in power loss and in pumping requirements. The reduction in total lubricant flow rate did not seem to affect the critical load at which hot lubricant reflux occurs at the $+90^\circ$ groove.
- Negative effects such as the reduction in load carrying capacity (eccentricity increase), oil starvation near the edges of the bearing, a global increase in temperature level and in general a less efficient bearing cooling, (reduced lubricant flow and stronger asymmetries in the bearing temperature field).

The addition of thermal calculations along the axial direction into the theoretical analysis would allow a much deeper insight into the influence of this parameter on bearing performance. It is therefore suggested that some of the future work would focus on such an improvement.

VII.5 Influence of the groove width ratio (w/d)

The influence of the circumferential extension of groove, also called the groove width, w , upon bearing performance is not as straightforward as it might appear at a first glance because it affects the behavior of the bearing at several different levels:

- The reduction of the angular extension of the film due to an increase in w/d causes a decrease in the total heat generation by viscous dissipation because the viscous dissipation within the groove regions is smaller (actually, it was neglected in the current model).
- The increase in w/d causes the oil within the groove to occupy a greater portion of the total circumferential extension of the gap. This induces a cooling effect which is not directly associated to lubricant flow rate: in fact, the portion of the shaft surface which is crossing the groove regions is cooled by the oil within the groove.
- Greater groove dimensions tend to improve the cooling of the bush body, through convection between the groove oil and the groove walls.
- A negative effect of increasing w/d is the loss of load supporting area. Nevertheless, since, in our case, the groove axes are in the plane perpendicular to the load line ($\pm 90^\circ$), it is likely that this effect will only start being relevant for very high w/d values (or for groove angles different from $\pm 90^\circ$ with the load line). In spite of this, it is likely that even small changes in w/d will affect the critical load at which the hot oil reflux phenomenon starts occurring, as it will be seen further along this section.

The following results, in which two different values of w/d (0.18 and 0.36) were tested, seem to be in accordance with the aforementioned observations.

The total and partial flow rates in each groove are presented in Figure VII-24a for the two w/d values. Curiously, the total flow rate was not significantly affected by the changes in w/d . However, when increasing w/d , the flow rate at $+90^\circ$ groove suffered a strong decrease, especially for specific loads higher than 0.3MPa, while the opposite happened in the -90° groove. As a consequence, the critical W_s for the occurrence of hot oil reflux was lowered from around 8MPa to about 4MPa when increasing w/d . When observing the evolution of the $+90^\circ$ groove flow rate as a function of eccentricity, it can be seen that this critical load corresponds

to an eccentricity ratio around 0.8. This is the lowest recorded eccentricity at which hot oil reflux was detected in this work.

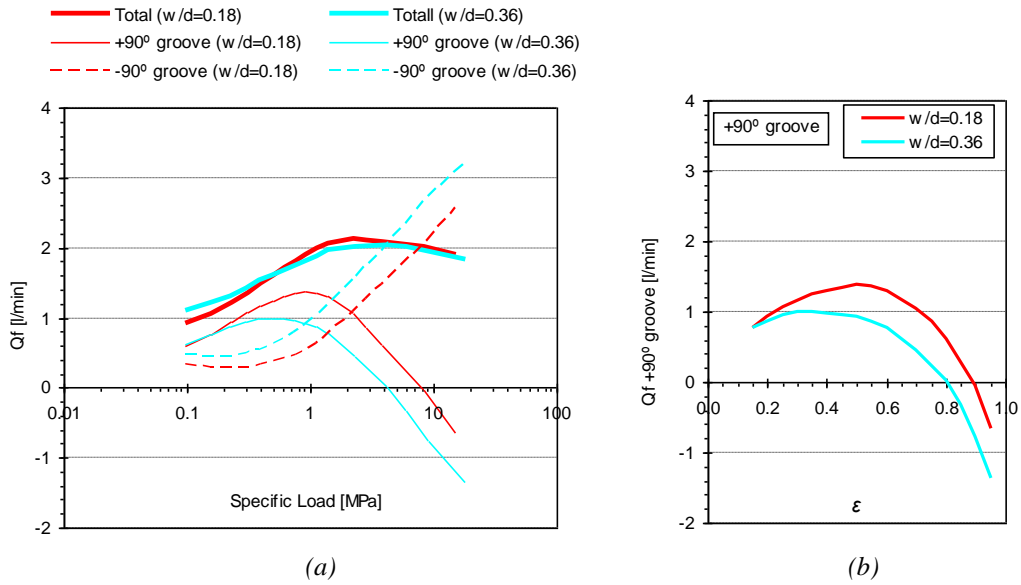


Figure VII-24 – Influence of groove width ratio on (a) the global flow rate and the partial flow rates in each groove for varying Specific load and (b) on the partial flow rate at the +90° groove for varying eccentricity.

In Figure VII-25a it can be seen that the influence of w/d on eccentricity is marginal. However, the attitude angle is significantly affected. This can be explained by noting that the main differences between the hydrodynamic pressure fields of the two cases should occur at the region immediately downstream of the +90° groove. The difference in groove width causes, for the bearing with the smallest groove, a pressure buildup region at a coordinate which for the other bearing still corresponds to the interior of the groove. This added region of pressure has a resultant force which is nearly perpendicular to the load line, thus affecting attitude angle without affecting significantly the eccentricity ratio.

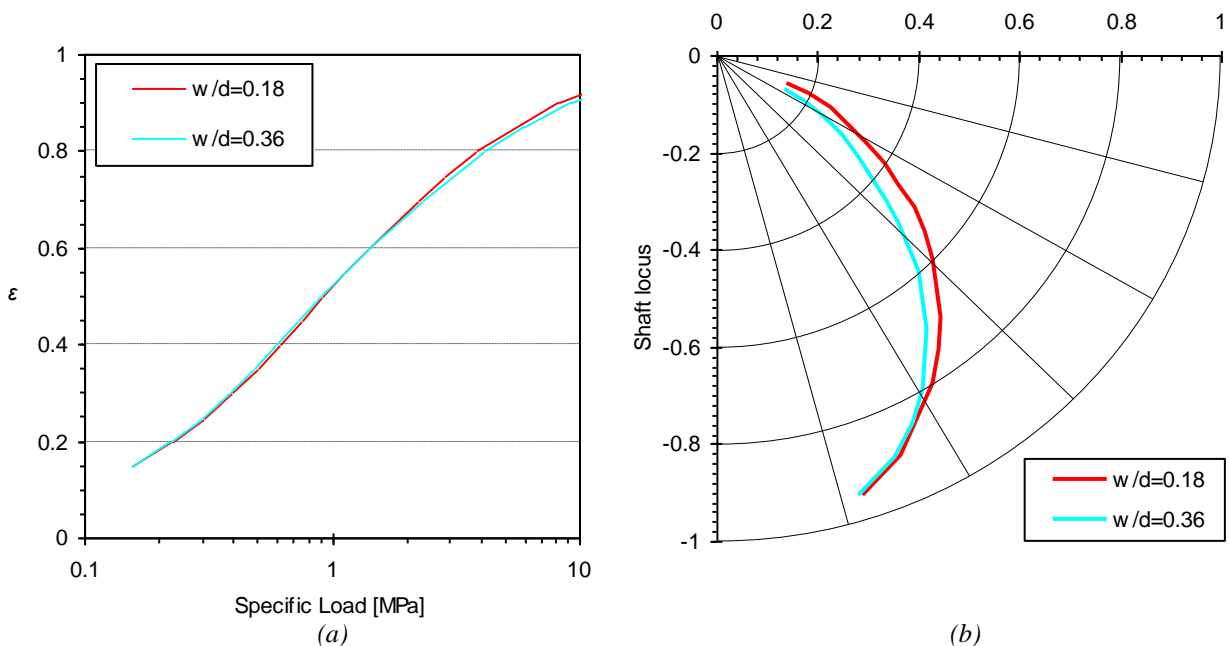


Figure VII-25 – Influence of groove width ratio on (a) Shaft locus and (b) eccentricity ratio.

The reasons pointed out at the beginning of this section justify why the increase of w/d causes the lowering of the temperature level. This can be observed in terms of the temperature profiles at the midplane of the inner bush surface (Figure VII-26) and of T_{max} and T_{shaft} (Figure VII-27a).

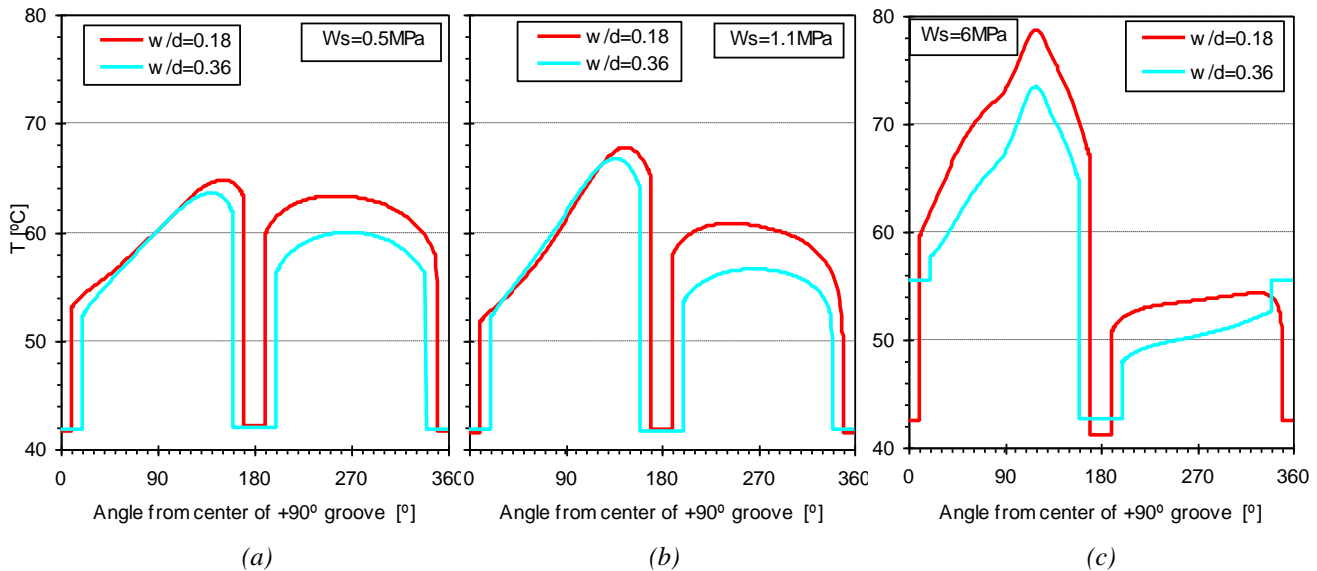


Figure VII-26 – Influence of groove width ratio on the temperature profiles at the midplane of the inner bush surface for (a) $W_s=0.5\text{MPa}$, (b) $W_s=1.1\text{MPa}$ and (c) $W_s=6\text{MPa}$.

Power loss, displayed in Figure VII-27b, is reduced with the increase of w/d . As explained above, this should be due to the decrease of viscous dissipation caused by the smaller angular extent of the oil film.

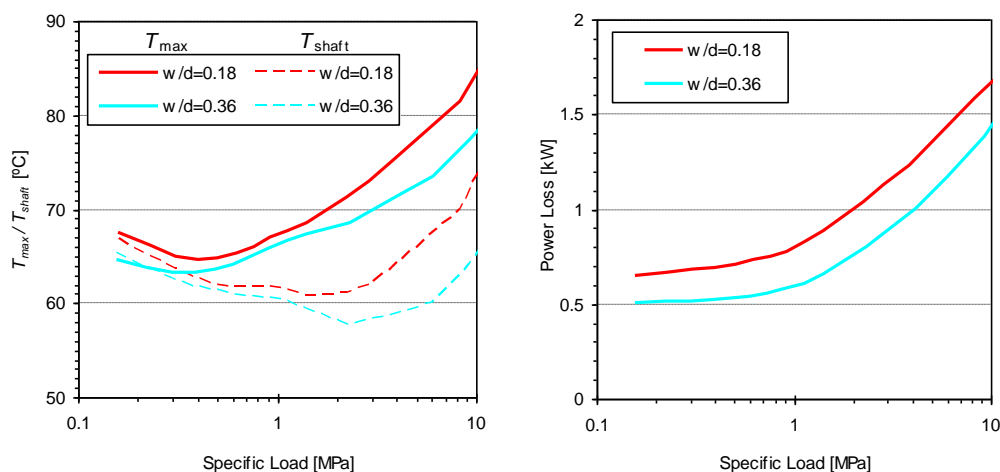


Figure VII-27- Influence of groove width ratio on (a) maximum bush temperature and shaft surface temperature and (b) on power loss.

As a conclusion, it seems that a moderate increase of w/d may indeed prove beneficial in most cases, as a reduction in temperature level and power loss is obtained without a significant increase in eccentricity. This might not apply for w/d values much higher than those tested and in the cases where the groove axis' plane is not perpendicular to the load line. Finally, the critical load for which oil reflux starts occurring is lowered with the increase of this parameter.

VII.6 Influence of the number of grooves

The comparison of the performance of single ($+90^\circ$) and twin groove ($\pm 90^\circ$) hydrodynamic journal bearings for the same operating conditions has seldom been made either theoretically or experimentally. The common sense perception that a twin groove bearing will operate at a lower temperature and with a more efficient lubrication than the single groove one still needs to be confirmed.

In the experimental work carried out at the LOMT, besides the tests involving twin groove bearings, an additional set of tests was carried out with one of these bearings but in which one of the grooves (the -90° groove) was shut, thus resembling a single groove journal bearing with one groove at $+90^\circ$ to the load line. These results, which have been presented in section V.4.6 were not totally conclusive in indicating the best groove configuration. The single groove bearing displayed always a higher temperature than the twin groove one, but appeared to display a slightly lower eccentricity for the highly loaded cases, particularly in cases where the hot oil reflux phenomenon was close to happen. However, this could not be confirmed with confidence due to the high level of uncertainty of the eccentricity measurements. A theoretical comparison between both cases would, therefore, be most welcome.

One of the great differences when increasing the number of grooves from 1 (at $+90^\circ$ to the load line) to 2 ($\pm 90^\circ$) is that the total flow rate, which in the former case was fed entirely through a single groove, is now redistributed through two grooves. Figure VII-28 compares the flow rate for both cases. It is interesting to acknowledge that the total flow rate is nearly the same for the two bearings along the whole load range, something which was also observed experimentally (see, for instance, Figure V-43).

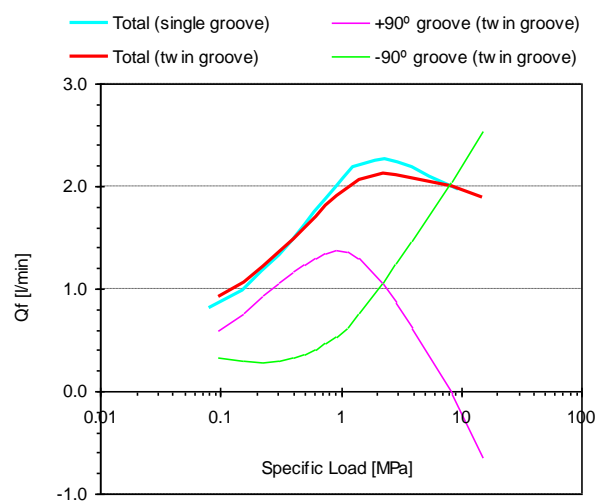


Figure VII-28 - Influence of the number of grooves on the lubricant flow rates (global and per-groove).

The eccentricity ratio obtained for the two different groove configurations is presented in Figure VII-29. It can be seen that, as load increases, the difference between the two cases

becomes more significant, with the single groove configuration always displaying the highest value.

Significant differences between the two groove configurations are found concerning attitude angle, as observed in Figure VII-29b. This is a well known characteristic of single groove bearings: the resulting force caused by the hydrostatic pressure in the groove region (the feeding pressure), is not being cancelled by a symmetrical force on the opposite side of the bearing, as it would happen with the twin groove case. Therefore, in the presence of a single groove bearing, the shaft centerline tends to move away from the +90° groove towards the opposite side, thus increasing the attitude angle.

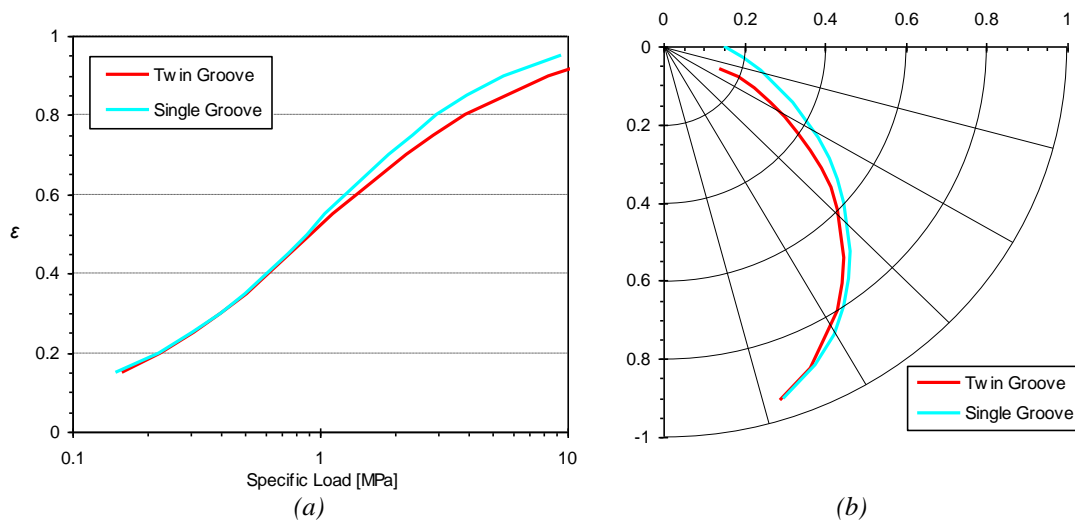


Figure VII-29 - Influence of the number of grooves on eccentricity ratio and shaft locus.

Subsequently, the temperature profiles at the inner bush surface (midplane) are presented alongside with the temperature field within the whole fluid and solid domain.

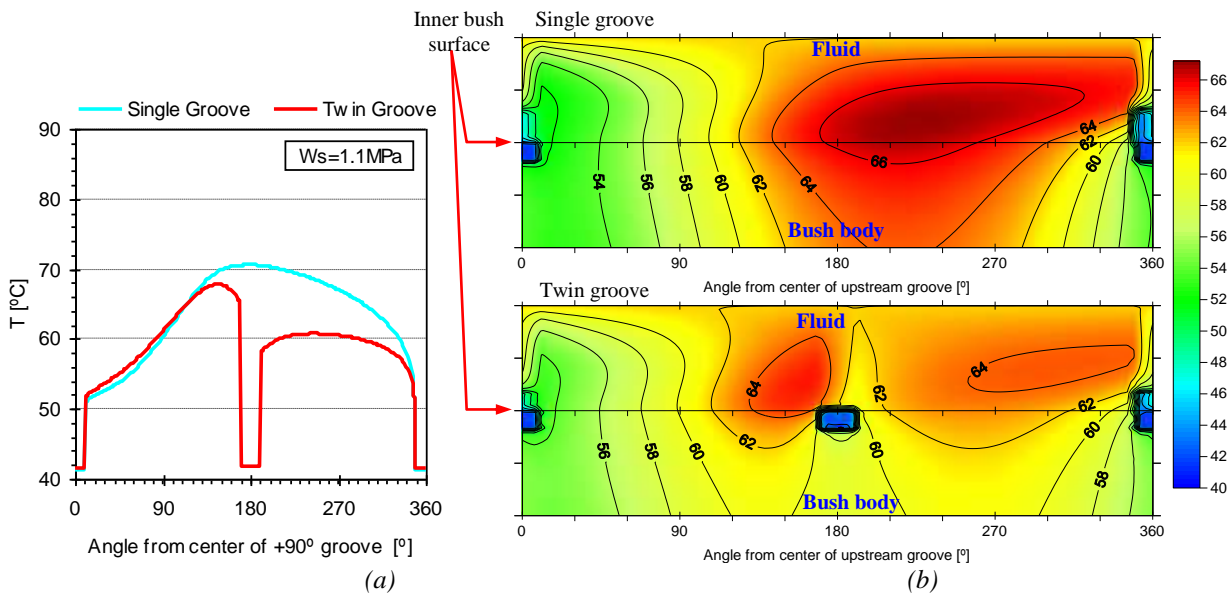


Figure VII-30 – Influence of the number of grooves on (a) the temperature profile at the midplane of the inner bush surface and (b) the midplane temperature field of the fluid domain and of the bush body domain ($W_s=1.1MPa$).

Figure VII-30 displays the temperature field for a specific load of 1.1MPa. It can be seen that the temperature at the loaded land of the bearing is similar for both cases except in the vicinity of the -90° groove. Here it is clear the added cooling effect obtained with the addition of the second groove, which extends to the whole unloaded land. Nevertheless, the difference in T_{max} is below 3°C .

The same data is presented in Figure VII-31, now for a much higher specific load ($W_s=3.9\text{MPa}$). The differences are quite significant (12°C in T_{max}). This can be better understood by taking into account the following chain of effects: the less efficient cooling of the single groove configuration causes a higher fluid temperature, which in turn causes a loss in lubricant viscosity, which originates higher eccentricity, thus aggravating the temperature excess.

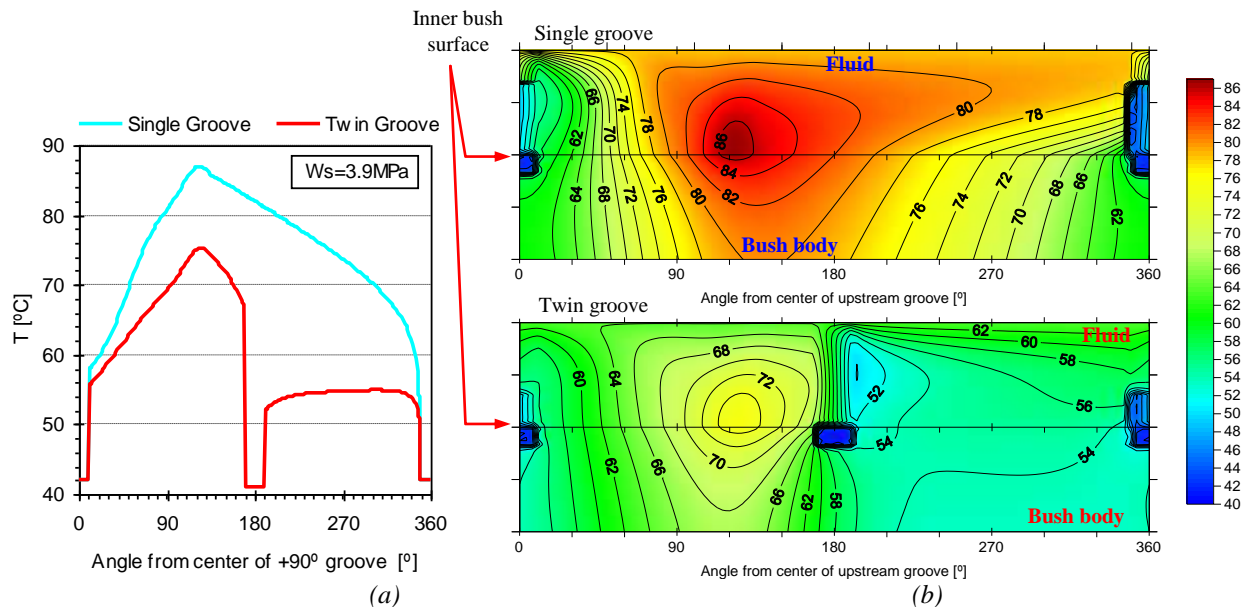


Figure VII-31 – Influence of the number of grooves on (a) the temperature profile at the midplane of the inner bush surface and (b) the midplane temperature field of the fluid domain and of the bush body domain ($W_s=3.9\text{MPa}$).

This dramatic divergence of the temperature levels of the two groove configurations with increasing load can be further observed in Figure VII-32a, which displays the evolution of T_{max} and T_{shaft} with W_s . Here it can be seen that the number of grooves also affects significantly T_{shaft} , with differences in T_{max} and T_{shaft} being as high as 25°C and 30°C , respectively.

These factors also deserve to be analyzed as a function of eccentricity ratio (Figure VII-32b). This can help isolating the temperature effects of the two factors which were pointed out as being responsible for the temperature rising (ineffective cooling and eccentricity increase). In fact, if eccentricity is kept constant, the differences in T_{max} and T_{shaft} are exclusively linked with the cooling efficiency. It can be seen that even cancelling the effect of eccentricity on

temperature there are still significant differences between the two cases (as much as 15 and 20°C for T_{max} and T_{shaft} , respectively).

The number of grooves also seems to significantly affect the power loss, as seen in Figure VII-32c. The reduction in this parameter when eliminating the -90° groove, as high as 25%, seems to be associated to the loss of viscosity (and therefore, of heat generation by viscous dissipation) suffered by the hotter oil. In the higher range of specific load, however, it is likely that power loss will be boosted as soon as mixed lubrication is initiated (this effect is not considered in the present model).

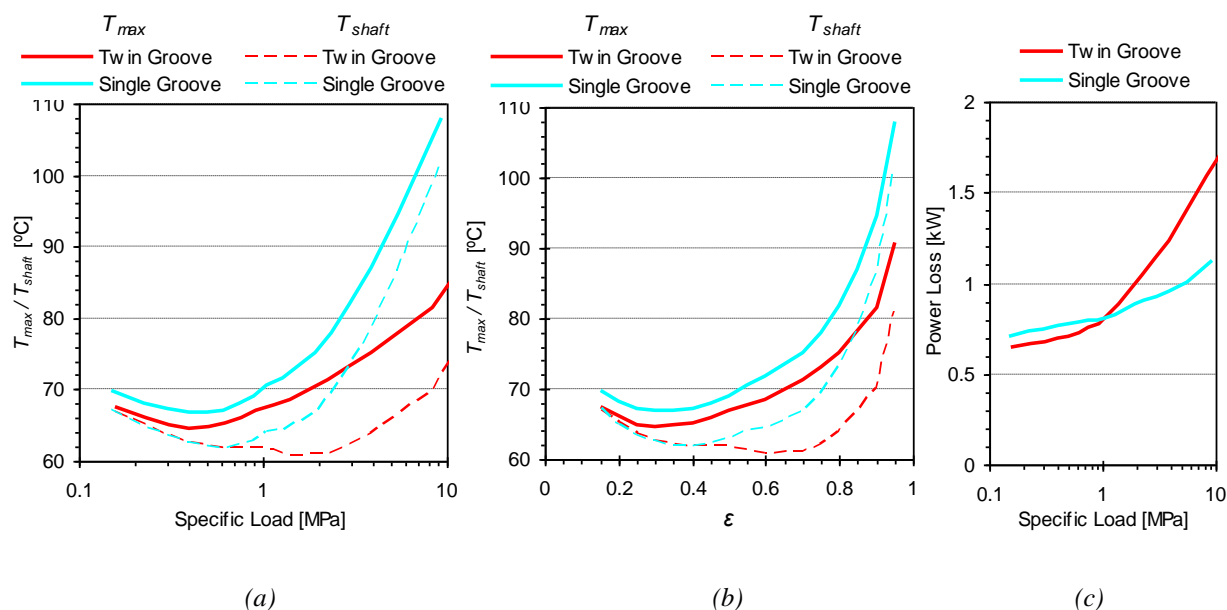


Figure VII-32 –Influence of the number of grooves on the maximum bush temperature and the shaft surface temperature as a function of (a) specific load and (b) eccentricity ratio. (c) Influence of the number of grooves in power loss.

As a concluding remark, it is worth noting that the results just presented indicate that the addition of the -90° groove causes the decrease of temperature level and eccentricity. This decrease becomes rather intense for higher loads. This is made at the expense of a higher power loss.

However, some caution should be taken with the generalization of these results. In fact, it has been observed before that the present model tends to over-predict the +90° groove flow rate in the high eccentricity range for the case of the twin groove bearing (see, for instance, Figure VI-22b,c). This over-estimation might be affecting significantly the predictions in some cases: if in reality the +90° groove flow rate is too small, starvation problems might start appearing and become dominant.

The overestimation of the +90° groove flow rate is also the reason why the model also tends to over-predict the critical load at which hot oil reflux problems start occurring. In the case studied, this phenomenon was predicted to occur for specific loads above 8MPa (Figure

VII-28). This problem, which is rather deleterious for bearing performance, namely for eccentricity, appears only in multi groove bearings.

Therefore, it is possible that in some situations the oil starvation caused by the splitting of the flow by two grooves instead of one might become a critical effect, making the twin groove bearing a poorer choice than the single groove bearing. In fact, this seems to be the case with, for instance, the experimental results obtained for the B2V2 LOMT bearing (see section V.4.6).

The incorporation of a 3D thermal analysis along with a more realistic estimation of the thermal and mechanical deformations of the bodies might enable a better prediction of bearing performance in such cases.

VII.7 Influence of the location of the grooves with respect to the load line

The angle between the axis of the grooves and the load line, here designated simply as the groove angle, Γ , is measured in the direction of shaft rotation, as seen at the top right of Figure VII-33. This angle is normally 90° in twin groove journal bearings. However, it can assume other values, namely when there is permanent or temporary change in the load direction.

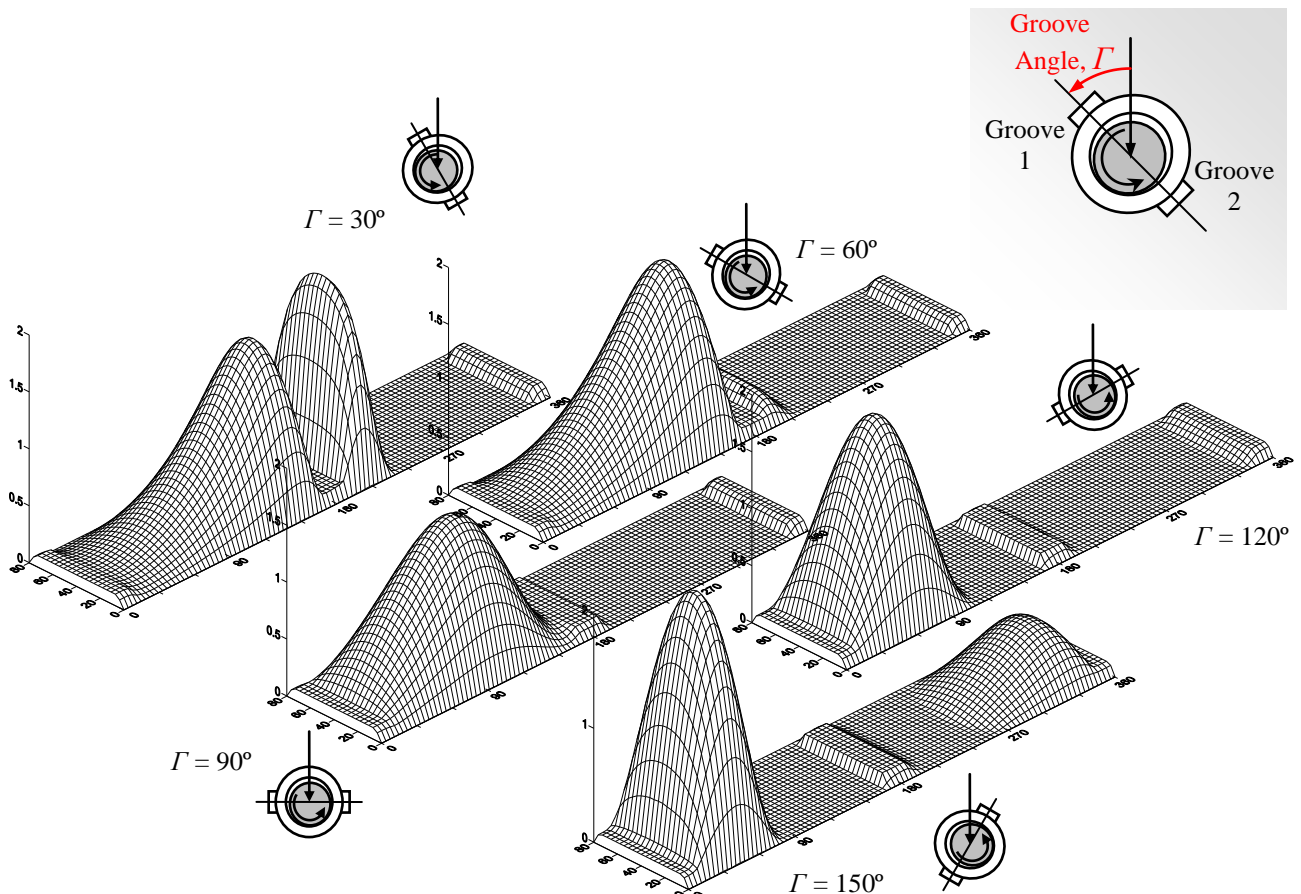


Figure VII-33 – Influence of the location of the grooves with respect to the load line on the hydrodynamic pressure field ($Ws=0.6\text{MPa}$).

The study of this parameter is likely to provide a deep insight into the role of each groove, and more generally, of lubricant supply conditions on bearing behavior. Additionally, it enables to confirm the robustness of the model, since a broad variation of parameters takes place, with some severe operating conditions occurring: strong pressure and temperature gradients often in the vicinity of grooves, strong reverse and back flow, hot oil reflux at one of the grooves, unusual film rupture and regeneration boundaries, unusual pressure and temperature profiles are likely to occur.

The effect of Γ upon the hydrodynamic pressure field is presented in Figure VII-33 for a fixed specific load ($W_s=0.6\text{MPa}$) and five different values of Γ (30° , 60° , 90° , 120° and 150°).

It can be seen that Γ interferes significantly with the hydrodynamic pressure field. In fact, there is no relevant hydrodynamic pressure generation within grooves because no thin convergent film is present. The grooves are considered to be at a constant pressure (the feeding pressure, P_f). Therefore, if the pressure in the vicinity is lower, lubricant feeding flow rate is positive. However, if the pressure outside the groove is higher than P_f , then oil will flow from the bearing gap into the groove and out of the bearing through the feeding pipe. It can be seen that for $\Gamma = 30^\circ$ and 150° , the main pressure buildup zone is clearly located in the vicinity of groove 1. This groove interferes deeply with the hydrodynamic pressure generation. In order to compensate this effect, the pressure level increases so that the same load is still supported.

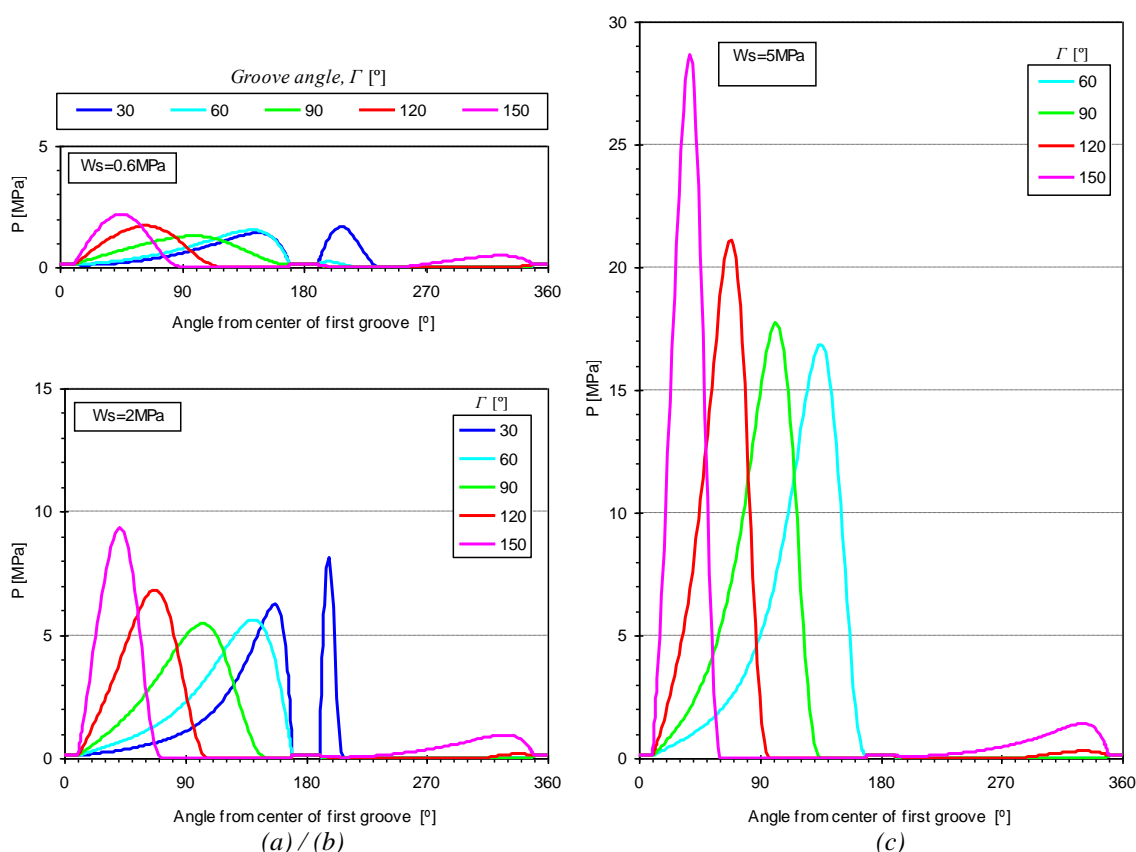


Figure VII-34— Influence of Γ on the hydrodynamic pressure profile at the midplane of the bearing for (a) $W_s=0.6\text{MPa}$, (b) $W_s=2\text{MPa}$ and (c) $W_s=5\text{MPa}$.

The pressure profiles at the midplane of the bearing are displayed in Figure VII-34 for three different loads, the first one corresponding to the same conditions presented in the previous figure. It can be seen that lower pressures are obtained in the cases where the grooves have the least interference with the pressure field.

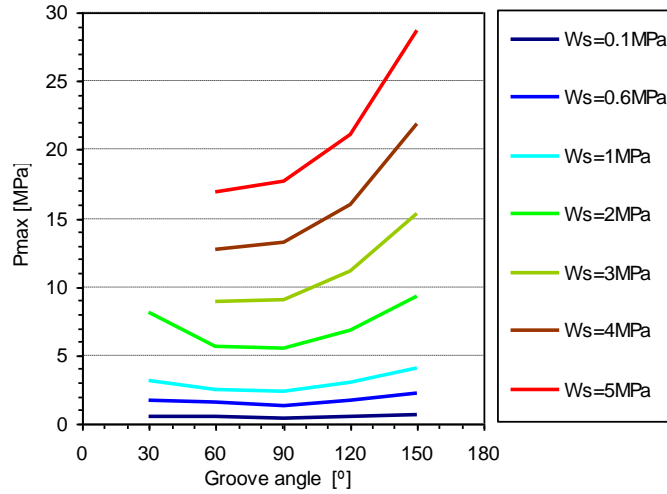


Figure VII-35 – Influence of Γ on maximum pressure for several values of specific load

Figure VII-35 summarizes the influence of Γ on the maximum pressure (P_{max}) for several specific loads. P_{max} can be regarded as a good indicator of the degree of interference of the grooves in the pressure field. It can be seen that for low loads P_{max} was minimized by the standard Γ , 90° . For loads higher than 3MPa, however, an angle of 60° yielded slightly lower values for P_{max} . The worse cases were those with the lowest (30°) and the highest (150°) value of Γ , precisely those cases which displayed pressure buildup zones more close to the grooves. In fact, no convergence could be achieved for 30° tests with specific loads above 2MPa due to excessive eccentricity.

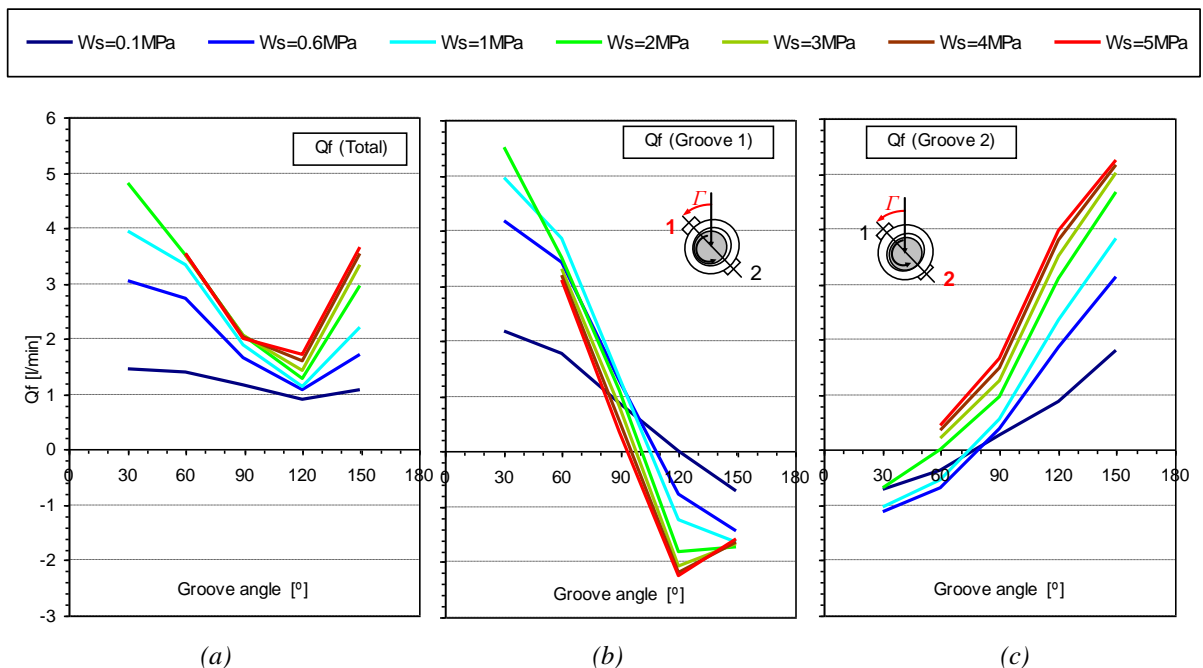


Figure VII-36 – Influence of Γ on (a) total flow rate, (b) flow rate in groove 1 and (c) flow rate in groove 2.

The effect of Γ on the total and partial flow rates for several loads is presented on Figure VII-36. It is clear that the knowledge of the total flow rate by itself is rather insufficient in order to characterize what happens. It is important to analyze what happens in each groove. The general trend found is that increasing Γ tends to decrease the flow rate at groove 1 (upstream groove) and tends to increase the flow rate at groove 2 (downstream groove). Hot oil reflux (negative flow rate) occurs on both grooves (although, naturally, never simultaneously). The flow rate trends are mainly explained by the relative magnitude of the pressure buildup zones and their location relatively to each groove. It is not clear why the decreasing trend of the flowrate in groove 1 is broken between 120° and 150° for the higher load range.

The evolution of these flow rates with specific load can also be analyzed for each value of Γ , as displayed in Figure VII-37.

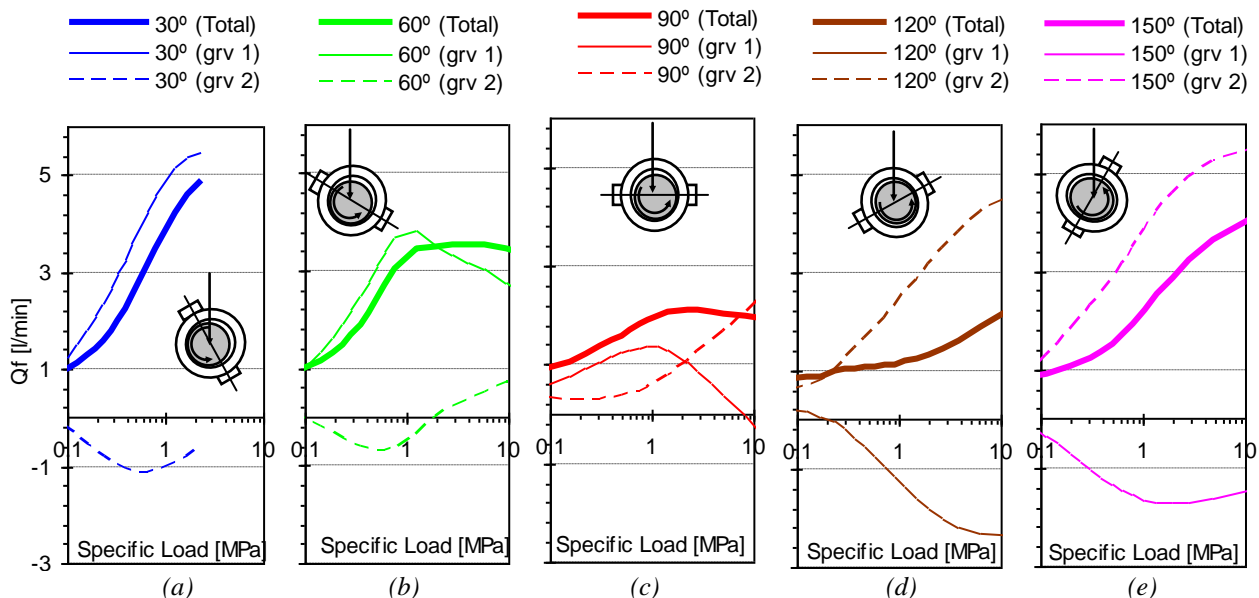


Figure VII-37 – total flow rate and partial flow rates in each groove for (a) $\Gamma=30^\circ$, (b) $\Gamma=60^\circ$, (c) $\Gamma=90^\circ$, (d) $\Gamma=120^\circ$ and (e) $\Gamma=150^\circ$.

It is interesting to analyze the totally different behavior at different groove angles and even, for the same Γ , the variation and the relative weight of the flow rate in each groove:

- In the case of the lowest Γ tests (30°), the flow rate at groove 1 is much higher than that at groove 2 which is always negative. This is so because the latter groove is right in the midst of the pressure buildup zone.
- For $\Gamma=60^\circ$ the flow rate at groove 2 is only negative for W_s lower than 2MPa. By increasing Γ this flow rate is always increasingly positive, while the flow rate at groove 1 is increasingly negative.
- For a groove angle of 90° (the usual value) the partial flow rates are equilibrated. However, oil reflux appears for specific loads above 8MPa. This is an undesirable

situation because the very high eccentricities present could risk the safety of the bearing.

- For $\Gamma=120^\circ$ and 150° the flow rate in groove 1 is negative for nearly the whole load range. This constitutes the least desirable situation, because oil is being retrieved from the bearing gap instead of being fed to it, just upstream of the region where it would be most necessary – the active land of the bearing and more precisely, the minimum film thickness region. Under high eccentricities this could even induce bearing seizure.

One of the consequences of hot oil reflux from one of the grooves is the effective rise of the feeding temperature in the opposite groove. In fact, the hot oil flowing out of the bearing gap through a groove mounts up the feeding pipes, then mixes with the fresh oil feeding (which is at a temperature T_f) and is re-fed to the opposite groove at a temperature which is actually higher than T_f . The incorporation of this effect into the analysis, as described in section III.11.3, is one of the novelties proposed in the present work.

The temperature of the hot oil reflux (higher temperature curve) and its effect upon the feeding temperature at the opposite groove (lower temperature curve) can be observed in Figure VII-38. Comparing these charts with the flow rate charts presented in Figure VII-37, it can be confirmed that when no reflux is present both values are equal to T_f (40°C). The actual temperature of the oil supplied to the positive flow rate groove will depend not only on the temperature of the hot oil reflux but also on the value of the flow rates.

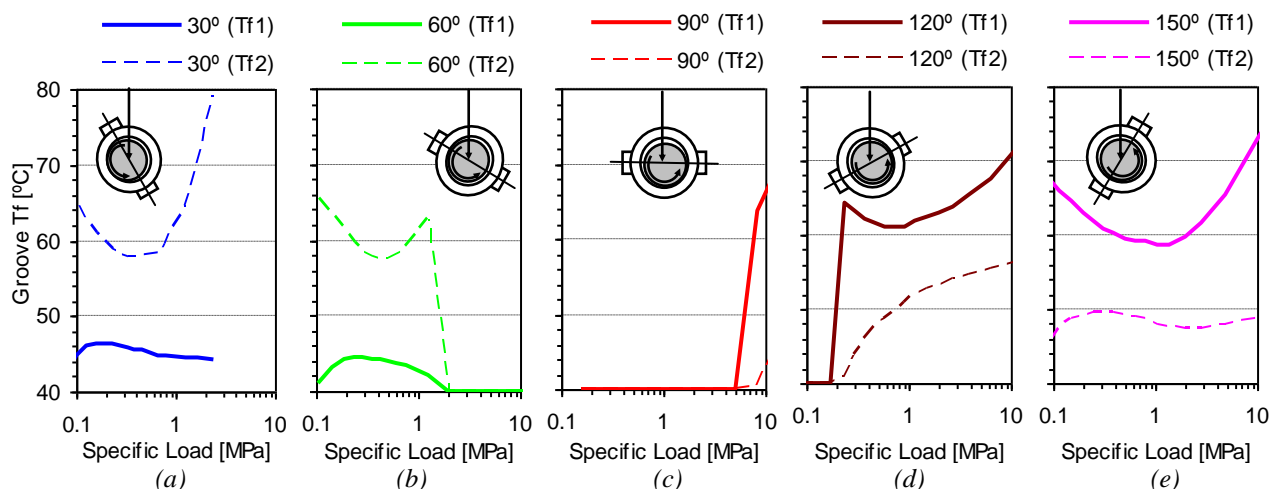


Figure VII-38 – Influence of negative flow rate in one of the grooves, on the effective feeding temperature of the opposite groove, for (a) $\Gamma=30^\circ$, (b) $\Gamma=60^\circ$, (c) $\Gamma=90^\circ$, (d) $\Gamma=120^\circ$ and (e) $\Gamma=150^\circ$. For each case, higher level curves denote the temperature of the hot oil reflux, while the lower level curves denote the temperature at which this hot oil is being re-supplied to the opposite groove after mixing with new oil feeding. When no reflux is present both values are equal to T_f .

The influence of Γ on eccentricity ratio is displayed in Figure VII-39. It has some parallel with the maximum pressure chart (Figure VII-35). Again, the highest values are obtained with the most extreme values of Γ (30° and 150°). The lowest Γ seems to be especially deleterious for

this parameter. The 60° tests also display an abnormal eccentricity but only within the lower, less dangerous, range of eccentricity. On the contrary, they display the best performance (lowest eccentricity) for the higher load range, even better than that for the 90° case. The reason for this change in trend should be linked with the changes in flow rate (see Figure VII-37b). In fact, the flow rate in groove 2 becomes positive for specific loads higher than 2MPa. For this value of specific load the eccentricity obtained is only slightly higher than the lowest value obtained for that load (corresponding to a $\Gamma=90^\circ$). This happened ultimately because the load increase pushed the pressure buildup zone away from groove 2, thus increasing flow rate at this groove.

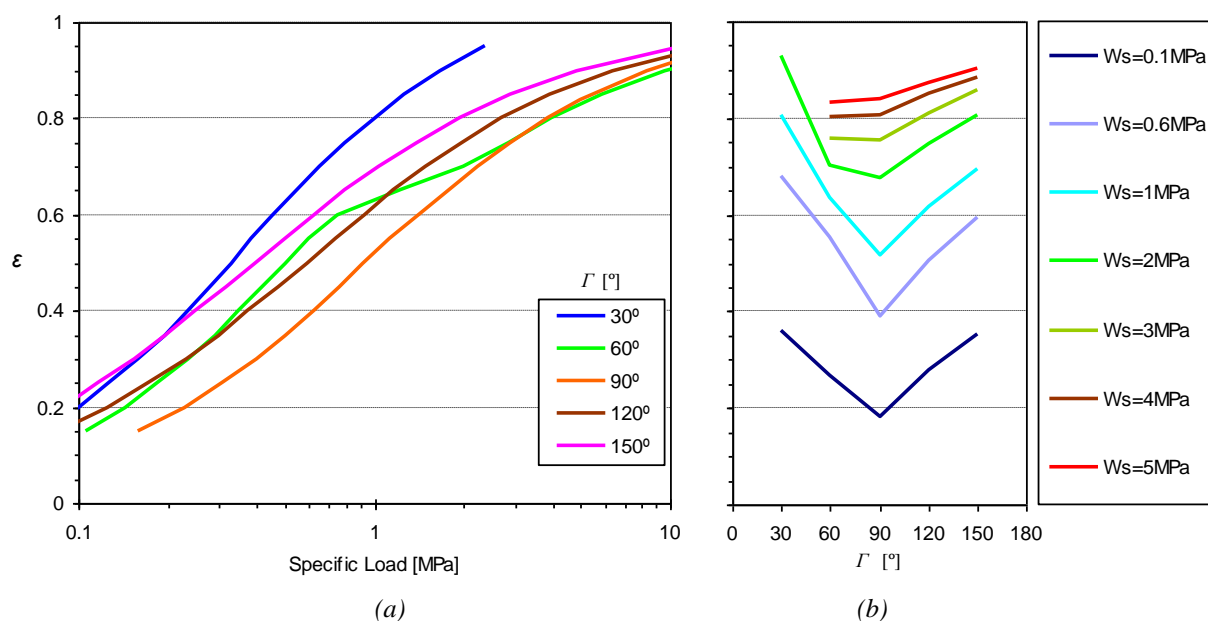


Figure VII-39 – influence of Γ in eccentricity ratio, (a) represented as a function of specific load for several values of Γ and (b) represented as a function of Γ for several values of specific load.

The temperature profiles corresponding to the various Γ values are presented in Figure VII-40 for three different specific loads (0.6, 2 and 5MPa). The following observations should be pointed out:

- The cases where oil reflux occurred in one of the grooves are easily recognizable because the temperature at the corresponding groove is very high and there is no temperature decrease across the groove. The general temperature level is also higher than that of the cases where no oil reflux occurs. This can be observed, for instance, for the lowest specific load case (0.6MPa - Figure VII-40a): the maximum temperature of the only case in which oil reflux was avoided (90°) is 4 to 5°C lower than all other cases.
- Concerning the 2MPa case (Figure VII-40b) it can be seen that the 30° test displays a much higher temperature than the others, in accordance with the excess in eccentricity

detected for this case (Figure VII-39b). Actually, the differences in the temperature levels of the tests performed with this load are closely related to the differences detected in eccentricity. The maximum temperature obtained for $\Gamma=60^\circ$ is already close to that obtained for $\Gamma=90^\circ$, because the flow rate in groove 1 has ceased to be negative. But because it is still close to zero, no significant temperature fall is detected across the groove. Also, the temperature level at the unloaded land of the bearing is much higher than that of the 90° case.

- The temperature levels of the tests carried out with the highest load (5MPa - Figure VII-40c) are also in fair agreement with the differences found in eccentricity. An exception is made in the case of the 120° test which, although recording a lower eccentricity than the 150° test, displays a slightly higher T_{max} (possibly because it displays a lower total flow rate and therefore less cooling). For this load a groove angle of 60° already provides a lower T_{max} than the 90° case.

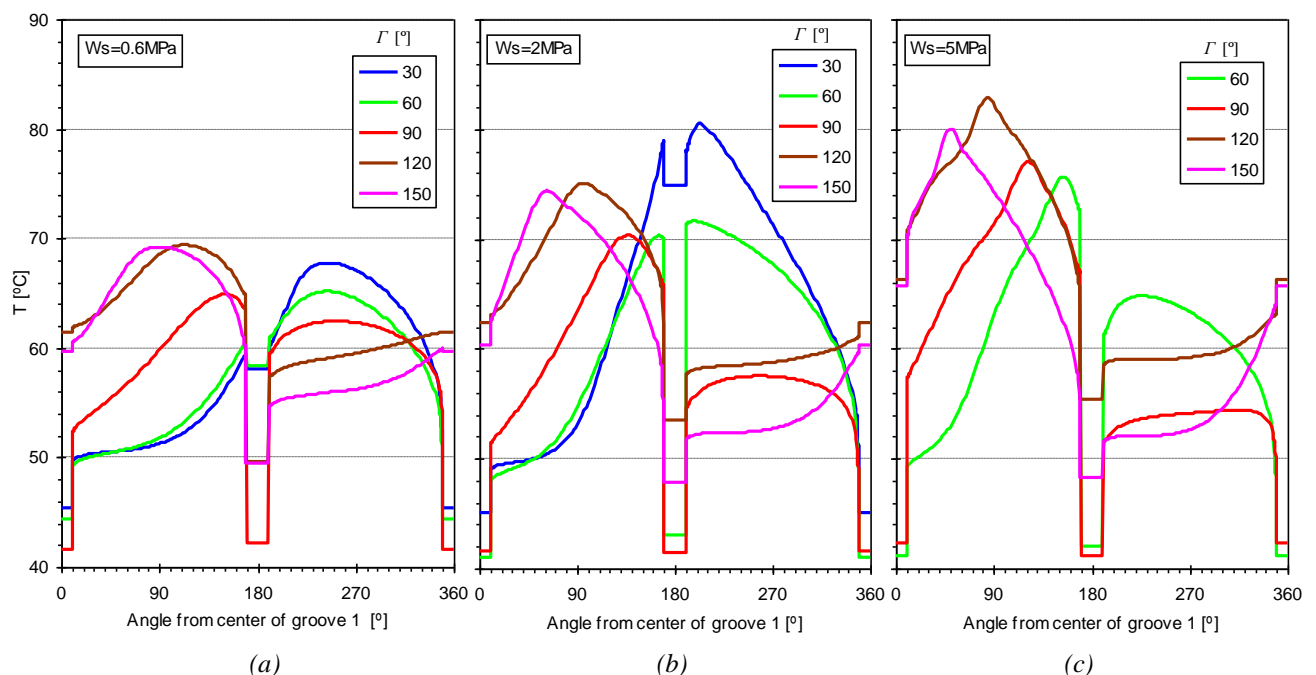


Figure VII-40 – Influence of Γ on the temperature profile at the midplane of the inner bus surface for (a) $W_s=0.6\text{MPa}$, (b) $W_s=2\text{MPa}$ and (c) $W_s=5\text{MPa}$

The influence of Γ in maximum temperature is presented in Figure VII-41 in three different ways. When presenting T_{max} as a function of eccentricity (Figure VII-41a), all the curves display a similar general trend, but of course, this can be deceiving, as the same eccentricity corresponds to very dissimilar load capacities depending on the value of Γ .

When analyzing T_{max} as a function of specific load (Figure VII-41b) it can be seen that the worst choices for Γ in terms of T_{max} are 30° then 120° then 150° . The minimum values for T_{max} are obtained for $\Gamma=90^\circ$ for specific loads between 1MPa and 3MPa. Out of this interval a

groove angle of 60° provides the lowest T_{max} . This can also be well appreciated in Figure VII-41c.

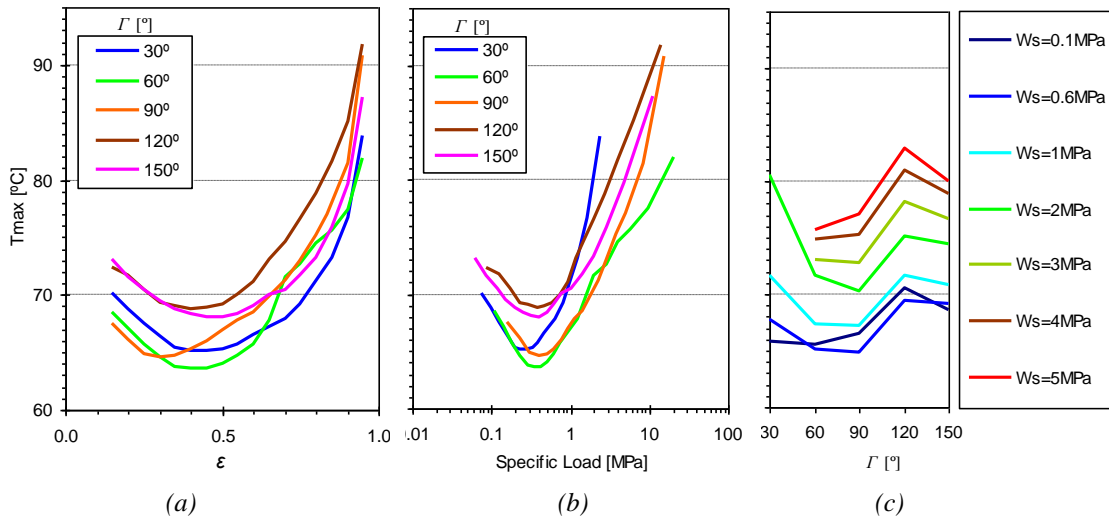


Figure VII-41 – influence of Γ in maximum temperature, (a) represented as a function of eccentricity for several values of Γ , (b) represented as a function of specific load for several values of Γ and (c) represented as a function of Γ for several values of specific load.

The shaft surface temperature is also presented as a function of the eccentricity ratio and specific load in Figure VII-42. The same remarks which were made in the discussion of T_{max} seem to apply.

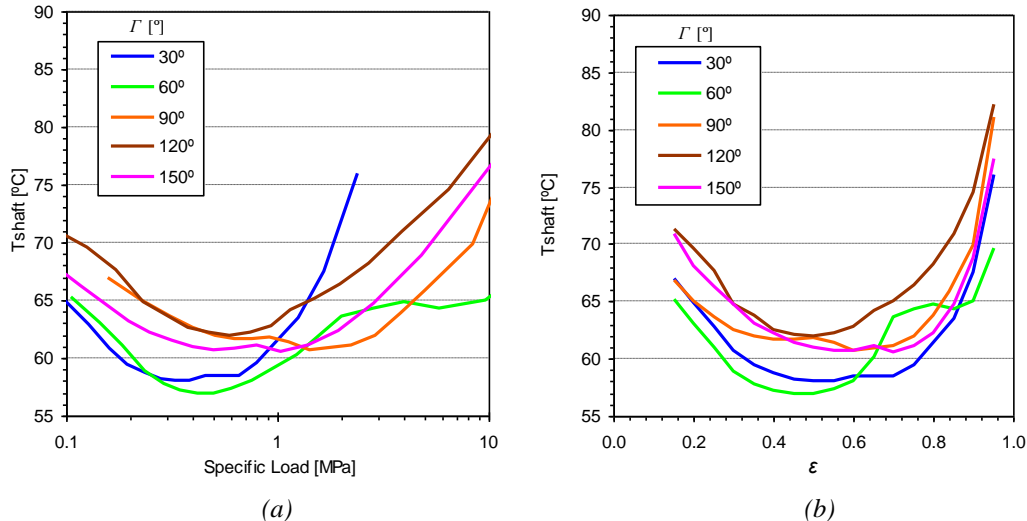


Figure VII-42 – influence of Γ in shaft surface temperature, represented as a function of (a) specific load and (b) of eccentricity.

Concerning power loss it seems useful to show again the evolution of this parameter with eccentricity, as it shows that the two seem to be intimately linked, with relatively small differences in power loss being obtained for a given eccentricity. However, it is also important to analyze this parameter as a function of the specific load. It can be seen that the more extreme values of Γ (30° and 150°) yield the highest power losses recorded. This is because these cases also displayed the highest eccentricity for a given load (see Figure V-40). The groove angles

which optimize power loss for the specific load range usually used with this kind of bearings, were 90° for W_s lower than 1.5MPa and 60° for higher loads (up to 6MPa).

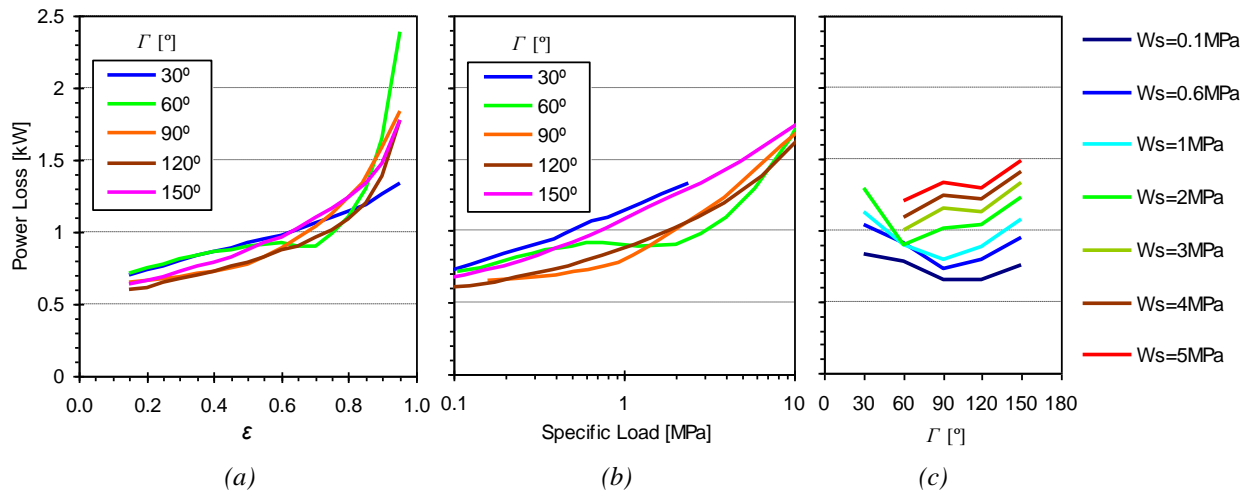


Figure VII-43 – influence of Γ in power loss, (a) represented as a function of eccentricity for several values of Γ , (b) represented as a function of specific load for several values of Γ and (c) represented as a function of Γ for several values of specific load.

As concluding remarks, it can be stated that:

- The groove angle was found to affect significantly most of the performance parameters. This had mainly to do with the influence of this parameter on the pressure profile: the proximity of grooves from the pressure buildup regions deeply affects the shape of the pressure profile, eccentricity and flow rates, which frequently become negative in one of the grooves (hot oil reflux). The analysis of what is actually happening in each groove separately was vital in order to understand the bearing behavior. The harsh conditions tested in this last parametric study seem to confirm the robustness of the present model.
- The bearing performance was found to strongly deteriorate with groove angles of 30° , 150° and 120° . In these cases negative flow rate (hot oil reflux) was detected in one of the grooves for nearly the whole range of loads tested.
- The optimum value of Γ possibly lies somewhere between 60° and 90° . In fact, for heavily loaded cases (W_s values higher than about 3MPa), eccentricity, T_{max} and power loss were all minimized with $\Gamma=60^\circ$, while for lower loads, a groove angle of 90° generally provided lower power losses, with T_{max} values similar to those obtained with a $\Gamma=60^\circ$.

VII.8 Conclusion

A parametric study of the influence of lubricant supply conditions on the performance of twin groove journal bearings has been performed using the model which was previously developed.

The main factors which can affect the lubricant feeding - lubricant feeding pressure and temperature, groove length ratio, groove width ratio, number of grooves and location of the grooves with respect to the load line - were investigated for a range of specific load which was extended beyond the range of practical applications. The main analyzed parameters were the flow rates (both total and in each groove), maximum temperature, shaft temperature, temperature profile at the midplane of the bearing, power loss, eccentricity ratio, shaft locus and minimum film thickness. In selected cases the temperature and pressure fields were also analyzed along the whole domain of calculus. It was found that:

- In general, the same trends and tendencies which were experimentally observed were predicted by the model. Despite the limitations pointed out in the validation chapter, the results obtained appear to be globally coherent, physically plausible, and with small randomness.
- The feeding pressure proved to be a critical factor in reducing the temperature level of the bearing and in preventing the occurrence of hot oil reflux, even if it was at the expense of a slightly higher power loss
- The increase of the lubricant feeding temperature proved to be beneficial under low loads (it decreased power loss) but especially dangerous under high loads as it strongly increases the eccentricity, T_{max} , P_{max} , and the thermal and mechanical distortions, while lowering the critical load for which hot oil reflux starts occurring.
- The use of smaller length grooves (lower a/b) yielded the decrease in power loss, but at the expense of a less efficient bearing cooling, a smaller extension of complete lubricant film and thus a lower load carrying capacity. The narrower range of the lubricant film combined with the stronger thermal crowning of surfaces due to cooling asymmetries might inclusively cause local contact.
- The increase of w/d induced a decrease in power loss and maximum bush temperature without a significant decrease in load carrying capacity. However, the critical load for which hot oil reflux starts occurring was lowered.
- When comparing single groove ($+90^\circ$ to the load line) and twin groove ($\pm 90^\circ$ to the load line) it was found that the addition of the -90° groove caused a decreased in the temperature level and in eccentricity, especially in the higher load range. There are also

negative effects of adding an extra groove, which are the increase in power loss and the appearance of hot oil reflux for high eccentricities.

- The location of the grooves with respect to the load line was found to affect strongly most performance parameters due to the strong interference of the grooves in the hydrodynamic pressure field. The optimum location of the groove axis seems to lie between 60° and 90° to the load line. When Γ falls out of this interval a substantial degradation of the performance is experienced (lower load capacity, higher T_{max}).

It may be stated with confidence that the lubricant supply conditions play an important role in the performance of hydrodynamic journal bearings and therefore should not be neglected in bearing analysis. Their optimization can result in substantial energy savings and reduced environmental impact. Truly, in some cases the supply conditions might even dictate the occurrence or the avoidance of bearing seizure.

"Mach 2 travel feels no different", a passenger commented on an early Concorde flight.

"Yes," Sir George replied. "That was the difficult bit".

*- Sir George Edwards, co-director of Concorde development.
(Quoted in Kenneth Owen, "Concorde, New Shape in the Sky").*

CHAPTER VIII Overall conclusions and proposals for future work

The present work was focused on the theoretical and experimental study of the performance of twin groove journal bearings operating under steady state, with a particular emphasis on the analysis of the influence of lubricant supply conditions.

In the present chapter, a summary of the main conclusions of the work, along with some proposals for future work, will be presented. More detailed conclusions can be found at the end of each chapter.

a) State of the art

After briefly introducing the subject under study in CHAPTER I, an extensive revision of the state of the art was carried out in CHAPTER II.

This revision has put into evidence that although the study of the performance of hydrodynamic journal bearings has now achieved a rather mature status, there are still some notable shortcomings which need to be addressed. Extensively validated codes are rare, while important discrepancies between theoretical and experimental results still persist to this day: the thermal behavior of journal bearings is, in most cases, not accurately predicted in the ruptured film region and in the vicinity of grooves; also there are large disparities in terms of flow rate. These shortcomings seem to be especially acute in the case of twin groove journal bearings.

One reason for the discrepancies found seems to be the over-simplified way in which lubricant supply conditions are incorporated into most analyses. The absence of an extensive experimental investigation on the role of these factors (namely on the role of grooves) might have played a role in the little attention given to such parameters in many theoretical analyses.

The aforementioned observations seem to justify the development of a model which would incorporate the following capabilities:

- Incorporation into the analysis of realistic lubricant supply conditions and the actual dimensions of the grooves.
- Accurate location of the film rupture and reformation borders through the use of mass-conservative algorithms.
- Thermal modeling of the groove regions and the ruptured film region.

Such a task, in line with the previous work made by the team, would be followed by a comprehensive experimental and theoretical investigation focused on the influence of lubricant supply conditions in twin groove journal bearing performance.

b) Development of the theoretical model

In CHAPTER III the development of a theoretical model based on the simultaneous solution of the Generalized Reynolds Equation (Elrod Algorithm), the Energy Equation and the Laplace Equation was detailed. Special care was taken in the following aspects:

- Coordinate transformation and the non-dimensional analysis;
- Realistic representation of the bearing geometry;
- Selection of appropriate boundary conditions;
- Thermal modeling of the grooves and the ruptured film regions;
- Selection of the most suitable mesh parameters and convergence criteria.

Some original, specific contributions of the present work appear to be, to the author's knowledge:

- An original discussion focusing on the fundamental difference in character between the Elrod and Adams (1975) and the Elrod (1981) approaches, which has been seldom apprehended in subsequent works;
- A new modified effective length model, proposed for the ruptured film region;
- The comprehensiveness of the thermal balances made in the groove regions, including the introduction of a mixing factor, the use of specially tailored inlet temperature curves, the inclusion of the influence of groove length and the discussion on the relevance of inner groove convection;

- The novel treatment of the phenomenon of negative flow rate in one of the grooves and its consequences on the opposite groove;

c) Experimental work

An extensive test program was carried out at the University of Minho and at the University of Poitiers. These tests covered a wide range of geometric parameters (different bearing diameters, bearing lengths and clearances, different groove dimensions, single/twin groove configurations); operating conditions (a broad range of shaft speeds and applied loads) and lubricant supply parameters (feeding pressure and feeding temperature). The results obtained not only provided a wealth of experimental data that was made available to the scientific community through several publications, but also allowed the validation and refinement of the theoretical model.

The careful analysis of the experimental results provided a deep insight into the parameters which affect most the bearing performance. Some new contributions of this work include, to the author's knowledge,

- The first extended investigation of the flow rate distribution through each groove of twin groove journal bearings, with the subsequent discussion of the role of each groove in bearing performance. The knowledge of the flow rate distribution through each groove proved to be determinant in the analysis of lubrication effectiveness and in understanding the thermal behavior. Actually, the two grooves display a completely dissimilar behavior, which was found to be strongly dependent on the value of the specific load.
- The first documented report of the phenomenon of negative flow rate (hot oil reflux) occurring at one of the grooves of twin groove bearings, under severe operating conditions. The appearance of this phenomenon induced a quick degradation of bearing performance, unpredicted by most existing theoretical models (but incorporated into the current model). The value of the feeding pressure was found to be determinant in preventing the appearance of this phenomenon.
- The first experimental comparison of the performance of single and twin groove journal bearings with identical geometry. This comparison has put into light some of the strengths and weaknesses of each groove configuration. Again, the pertinence of lubricant supply conditions was noticeable.

d) Model validation

The model was extensively validated with experimental results from the literature and with experimental results from the current work. The correlation between theory and experiment was generally quite satisfactory. Some highlights of the validation task are worth mentioning:

- A close prediction of the major design parameters - eccentricity ratio, maximum bush temperature and shaft temperature - was obtained, especially under medium to high applied loads (which, in reality, is the load range of practical interest).
- A close prediction of the thermal behavior of the bearing was obtained in most cases: The temperature fade which is normally observed in the vicinity of grooves, as well as the temperature trend in the unloaded land of the bearing, were successfully reproduced. In fact, many existing models fail to predict these trends adequately.
- The ability to predict and conveniently treat the occurrence of negative flow rate (hot oil reflux) in a groove.

The model still displays some weaknesses:

- For some operating conditions the lubricant flow rate was significantly under-predicted. This seems to be a common weakness of most current models, especially in the case of twin groove journal bearings, and couldn't still be totally eliminated in the current work, in spite of the substantial effort put in the task. Nevertheless, the influence of this underestimation seems to have affected primarily the performance predictions of smaller bearing systems, especially in the low load range (over-prediction of T_{max}).
- The critical load for which hot oil reflux starts occurring in one of the grooves appears to be over-predicted.

Despite the limitations described, the present model seems apt for the analysis of the performance of journal bearings with a realistic treatment of lubricant supply conditions.

e) Parametric study of the influence of lubricant supply conditions

After the conclusion of the numerical modeling task, a parametric study assessing the influence of lubricant supply conditions on the performance of twin groove journal bearing was carried out. The parameters under study were the lubricant feeding pressure, the lubricant feeding temperature, the groove length ratio, the groove width ratio, the number of grooves and the location of the grooves with respect to the load line.

The study of the influence of each parameter was carried out for a broad range of operating conditions, namely loading conditions (nearly the whole eccentricity range was encompassed in the study of most parameters).

The theoretical results obtained have confirmed the great importance of the supply conditions on the behavior of such bearings:

- The power loss was found to decrease with the increase of the lubricant feeding temperature (T_f), the groove length ratio (a/b), the groove width ratio (w/d) and with the decrease of the number of grooves (from 2 to 1) and lubricant feeding pressure (P_f). However, for the high eccentricity cases, this was normally obtained at the expense of an added risk of seizure. Under high loads, a groove angle (Γ) between 60° and 90° to the load line was found to minimize the power loss of twin groove journal bearings.
- The occurrence of hot oil reflux in one of the grooves was prevented with the increase of P_f and with the decreases of T_f and w/d . In the high load range, a slight decrease of Γ from the usual value of 90° down to 60° was also found to palliate this problem. Groove locations outside this interval tended to cause the appearance of negative flow rate in one of the grooves. The use of single groove bearings also eliminated this problem. The application of an anti-reflux valve at the entry of each groove might also be a good solution for the hot oil reflux problem.
- The maximum bush temperature (T_{max}) was lower with the twin groove bearing than with the single groove configuration. A decrease in T_{max} was also obtained with the decrease of T_f and with the increase of P_f (especially under low loads), w/d and a/b . A value of Γ between 60° and 90° was found to minimize T_{max} .
- Under severe operating conditions, the eccentricity was lower with the use of the twin groove bearing (as long as hot oil reflux did not occur). For these conditions the eccentricity was alleviated with the increase of P_f and a/b , and with the decrease of T_f . A value of Γ between 60° and 90° was again found to optimize bearing performance, minimizing eccentricity. Values outside this interval were found to significantly aggravate eccentricity.

It can be seen that an optimal balance between the obtention of a negligible risk, low power loss and savings in the total cost of the system (namely, due to the higher or lower capacity required for the oil pumping system and the oil cooling system) must be sought in order to reach the best solution for each specific application.

f) **Concluding remarks and proposals for future work**

The results provided by the validation task and the parametric study appear to display small randomness, to be physically coherent, in accordance with thermohydrodynamic lubrication theory and with the same general tendencies displayed by the experimental results. The model succeeded to compute the results corresponding to a wide range of operating conditions, including some which were particularly severe or uncommon, as when testing some groove angles. The model appeared to be capable of conveniently treating lubricant supply conditions and complex phenomena such as reverse flow, back flow and hot oil reflux, in a realistic way.

As seen during the validation task, the model still displays some limitations. Also, the results obtained for particularly severe operating conditions can sometimes render some of the assumptions made as inaccurate.

Some modifications to the model might further improve its accuracy being, therefore, suggested as future work:

- Inclusion of the axial temperature/viscosity variation: it's a natural evolvement of the present model. In fact, the realistic treatment of the bearing geometry which was already present in the pressure calculations makes this update especially useful. With this addition it is likely that the model would improve the prediction of the thermal behavior of the bearing in the vicinity of grooves and in the vicinity of the minimum film thickness region. This would also allow the study of the influence of effects such as misalignment, 3D form defects and non-standard geometries.
- Inclusion of a more realistic estimation of the thermal and mechanical deformations, namely through the use of influence/compliance matrixes, as made, for instance, by Bouyer and Fillon (2003). It is expected that this modification would improve significantly the predictions for severe operating conditions, where the strong temperature gradients and elastic deformations present might substantially alter the geometry of the gap. A more accurate prediction of the flow rates and of the critical load for the appearance of hot oil reflux might substantially depend on this modification.
- Extension of the assumptions made in the modified effective length model to the pressure calculations (currently, the effect of the existence of a shaft-adhered layer is only accounted for in the thermal calculations). This modification is likely to produce slightly different rupture and reformation boundaries. These slight differences might, however, produce less negligible modifications in flow rates. Furthermore, the model

- will become more coherent (same flow assumptions for pressure and temperature calculations);
- The deduction of physically backed values of the mixing factor, c_{mix} , and of the convective heat transfer coefficient within the grooves, H_{gr} , through CFD techniques, along with a deeper investigation on the real thickness of the shaft-adhered layer.
 - If the previous proposals do not succeed in improving the prediction of flow rates, a solution of the problem through a twin phase flow CFD model (such as the V.O.F. approach), including the flow calculations within the grooves is proposed.
 - The inclusion of non-newtonian effects in order to incorporate the influence of lubricant additives.

When drinking the water, don't forget those who dug the well
- Chinese proverb

REFERENCES

- Andrisano A. O., 1988, "An experimental investigation on rotating journal surface temperature distribution", ASME Journal of Tribology, Vol. 110, pp. 638-645
- Arghir M., Roucou N., Helene M. and Frêne J., 2003 "Theoretical analysis of the incompressible laminar flow in a macro-roughness cell". ASME J. Tribol., 2003, 125, 309–318.
- Ausas R., Ragot P., Leiva J, Jai M, Bayada G, 2007, "The Impact of the Cavitation Model in the Analysis of Micro-texturized Lubricated Journal Bearings", ASME JoT, 129, pp. 868-875.
- Ayres-Jr. F., 1957, "Theory and Problems of Differential and Integral Calculus", Schaum Publishing Co., USA.
- Banwait S. S., Chandrawat H. N. and Adithan M., 1998, "Effect of operating parameters on static and dynamic characteristics of a journal bearing under Thermohydrodynamic conditions". Proc. of 8th Nordic Symposium of Tribology- NORDTRIB'98, Vol. II, pp. 523-530.
- Basri S. and Gethin D.T., 1990, "A Comparative Study of the Thermal Behavior of Profile Bore Bearings", Tribology International, Vol. 23, pp. 265-276.
- Basri H. and Neal P.B., 1990, "Oil flow in axial groove journal bearings". In Proceedings of the Seminar on Developments in Plain Bearings for the '90s, IMechE Tribology Group, May 1990, pp. 11-17 (Mechanical Engineering Publications, London).
- Bayada G., 1983, Variational Formulation and Associated Algorithm for the Starved Finite Journal Bearing", ASME Journal of Lubrication Technology, 105, pp. 453-457.
- Bayada G., Chambat M., e El Alaoui M., 1990, "Variational formulations and finite elements algorithms for cavitation problems" ASME Journal of Tribology, Vol. 112, pp. 398-403.
- Bayada G., Martin S. and Vázquez C., 2005 "An Average Flow Model of the Reynolds Roughness Including a Mass-Flow Preserving Cavitation Model", ASME JoT, 127, pp. 793-802.
- Bayada G., Martin S. and Vázquez C., 2006, "Micro-roughness effects in (Elasto)hydrodynamic lubrication including a mass-flow preserving cavitation model", Tribology International 39, 1707–1718.
- Boedo S. and Eshkabilov S.L., 2003, "Optimal Shape Design of Steadily Loaded Journal Bearings using Genetic Algorithms", Tribology Transactions, 46:1, pp. 134-143.
- Boedo S. and Booker J.F., 2004, "Classical Bearing Misalignment and Edge Loading: A Numerical Study of Limiting Cases", 126, pp. 535-541.

- Boncompain R., 1984, "Les paliers lisses en régime thermohydrodynamique – aspects théoriques et expérimentaux", Thèse de Doctorat d'État, Université de Poitiers, France.
- Boncompain R., Fillon M. and Frêne J., 1986, "Analysis of thermal effects in hydrodynamic bearings", ASME Journal of Tribology, vol. 108, pp. 219-224.
- Booser E.R. and Wilcock D.F., 1988, "Temperature fade in journal bearing exit regions", ASLE Trans; 31:405–10.
- Bou Said B., 1985, "La lubrification a basse pression par le méthode des éléments finis. Application aux paliers", Thèse de doctorat, INSA de Lyon, France.
- Bouyer J. And Fillon, M., 2003, "Improvement of the THD performance of a misaligned plain journal bearing", ASME Journal of Tribology Vol. 125, pp.334-342.
- Bouyer J., 2003, "Étude des Performances Thermoélastohydrodynamiques de Paliers Soumis à des Conditions Sévères", PhD Thesis, Université de Poitiers, France.
- Bouyer J and Fillon M., 2004, "Relevance of the Thermoelastohydrodynamic model in the analysis of a plain journal bearing subjected to severe operating conditions", Proc. Instn Mech. Engrs Vol. 218 Part J: J. Engineering Tribology, pp. 365-377.
- Bouyer J., Fillon M., and Pierre-Danos I., 2007, "Influence of Wear on the Behavior of a Two-Lobe Hydrodynamic Journal Bearing Subjected to Numerous Startups and Stops", ASME Journal of Tribology Vol. 129, pp. 205-208.
- Braun M.J. and Hendricks R.C., 1984, "An Experimental Investigation of the Vaporous/Gaseous Cavity Characteristics of an Eccentric Journal Bearing", ASLE Trans., 27, pp. 1–14.
- Brenner G., Al-Zoubi A., Mukinovic M., Schwarze H. and Swoboda S., 2007 " Numerical Simulation of Surface Roughness Effects in Laminar Lubrication Using the Lattice-Boltzmann Method", ASME JoT, 129, pp. 603-610.
- Brewe, D.E., 1986, "Theoretical Modeling of the Vapor Cavitation in Dynamically Loaded Journal Bearing," ASME JoT, Vol. 108, No. 4, pp. 628-638.
- Brito F.P., Bouyer J., Fillon M., Miranda A.S., 2006a, "Influência da carga aplicada e da temperatura do óleo de alimentação no desempenho de uma chumaceira radial hidrodinâmica com dois sulcos axiais", Mecânica Experimental.13, pp.95-104. Originally presented at IBERTRIB - III Congresso Ibérico de Tribologia, June 16-17 2005, CD-ROM (ISBN 972-99596-0-9), Universidade do Minho – Guimarães.
- Brito F.P., Bouyer J., Fillon M., Miranda A.S., 2006b – "Experimental investigation on the thermal behavior and performance characteristics of a twin axial groove journal bearing as a function of applied load and rotational speed", 5th International Conference On Mechanics & Materials in Design - M2D'2006, Symposium on Wear and Lubrication In Design, FEUP, Porto, 24-26 July 2006. CD-ROM (ISBN 972-8826-10-9).
- Brito F.P., Bouyer J., Fillon M., Miranda A.S., 2006c - "Thermal behavior and performance characteristics of a twin axial groove journal bearing as a function of applied load and oil supply temperature", TRIBOLOGIA – Finnish Journal of Tribology, The Finnish Society for Tribology, 25/2006-3, pp. 24-

- 33 (originally presented at the 12th Nordic Symposium in Tribology - NORDTRIB 2006, Helsingør, Denmark, 6-9 June 2006. CD-ROM (ISBN 87-90416-19-8).
- Brito F.P., Bouyer J., Fillon M., Miranda A.S., 2007a, "Experimental Investigation of the Influence of Supply Temperature and Supply Pressure on the Performance of a Two Axial Groove Hydrodynamic Journal Bearing", *ASME Journal of Tribology*, 129, 2007, pp. 98–105. Originally presented at the STLE/ASME International Joint Tribology Conference, San Antonio, Texas, 23-25 October 2006, CD-ROM (ISBN 0-7918-3789-0).
- Brito F.P., Miranda A.S., Pimenta Claro J.C., Fillon M., 2007b, "The Role of Each Groove on the Behavior of Twin Axial Groove Journal Bearings", *IBERTRIB - Congreso Ibérico de Tribología, Escuela de Ingenieros, Bilbao*, June 20-21, 2007, CD-ROM.
- Brito F.P., Miranda A.S., Pimenta Claro J.C., Fillon M., 2008, "Experimental Study of the Influence of Groove Flow Rate on the Performance of a Single and a Twin Axial Groove Journal Bearing", *STLE Annual Meeting*, May 18-22, 2008, Cleveland Convention Center, Ohio, USA (Extended Abstract).
- Brito F.P., Miranda A.S., Pimenta Claro J.C., Fillon M., 2009, "The Role of Lubricant Supply Temperature on the Performance of Twin Groove Journal Bearings: An Experimental Study", *IBERTRIB – Congresso Ibérico de Tribologia*, 17-18th June 2009, Universidade de Coimbra, Portugal (CD-ROM)
- Brizmer V., Kligerman Y. and Etsion I., 2003, "A Laser Surface Textured Parallel Thrust Bearing", *Tribology Transactions*, 46:3, 397 – 403.
- Brown R.D., Drummond G. And Addison P.S., 2000, "Chaotic response of a short journal bearing", *Proc Instn Mech Engrs Vol 214 Part J*, 387-400.
- Buscaglia G., Ciuperca I. and Jai M., 2005, "The Effect of Periodic Textures on the Static Characteristics of Thrust Bearings", *ASME JoT*, 127, pp. 899-901.
- Chang S.C. and To, W.M., 1991, "A New Numerical Framework for Solving Conservation Laws The Method of Space-Time Conservation Element and Solution Element" NASA TM 104495. NASA, Cleveland, OH.
- Chang Q, Yang P., Meng Y. and Wen S., 2002, "Thermoelastohydrodynamic analysis of the static performance of tilting-pad journal bearings with the Newton–Raphson method", *Tribology International* 35, pp. 225–234.
- Chiang H.L., Hsu C.H. and Lin J.R., 2004, "Lubrication performance of finite journal bearings considering effects of couple stresses and surface roughness", *Tribology International* 37, pp. 297–307.
- Choo J.H., Glovnea R.P., Forrest A.K. and Spikes H.A., 2007a, "A Low Friction Bearing Based on Liquid Slip at the Wall", *ASME JoT*, 129, pp. 611-620.
- Choo J.H., Spikes H.A., Ratoi M., Glovnea R.P. and Forrest A.K. and 2007b, "Friction reduction in low-load hydrodynamic lubrication with a hydrophobic surface", *Tribology International*, 40, pp. 154–159.
- Chowdhury S.K.R., 2000, "A feed back control system for plain bearings using film thickness measurement", *Tribology International* 33, pp. 29–37.
- Christopherson D.G., 1941, "A New Mathematical Method for the Solution of Film Lubrication Problems", *Proceedings, Instn Mechanical Engineers*, 146, pp. 126-135.

- Chun, S. and Lalas, D., 1992, "Parametric study of inlet oil temperature of a half-circumferential grooved journal bearing. STLE Tribology Trans., 35, 213±224.
- Chun S.M. and Ha D.H., 2001, "Study on mixing flow effects in a high-speed journal bearing", Tribology International 34, 397–405.
- Cioc, S. and Keith JR., T.G., 2002 "Application of the CE/SE Method to One-Dimensional Flow in Fluid Film Bearings", Tribology Transactions, 45:2, 169 – 176.
- Cioc, S., Dimofte, F. and Keith JR., T.G., 2003, "Application of the CE/SE Method to Wave Journal Bearings", Tribology Transactions, 46:2, pp. 179-186.
- Claro J. C. P., 1994, "Reformulação do Método de Cálculo de Chumaceiras Radiais Hidrodinâmicas - Análise do Desempenho Considerando as Condições de Alimentação, Tese de doutoramento, Universidade do Minho.
- Claro J. C. P., Miranda A. S., 1990, "The performance of journal bearings with a single axial groove", ImechE Seminar: Developments in Plain Bearings for 90's, pp. 19-25
- Claro J. C. P., Miranda A. S., 1993, "Analysis of hydrodynamic journal bearings considering lubricant supply conditions", Proc. Inst. Mech. Eng., Part C, Vol. 207.
- Cope W.F., 1949, "The Hydrodynamical Theory of Film Lubrication", Proc. R. Soc. London, Ser. A, 197, pp. 201.
- Costa L., 2000, "Análise do Desempenho de Chumaceiras Radiais Hidrodinâmicas Considerando Efeitos Térmicos", Tese de doutoramento, Universidade do Minho
- Costa L., Miranda A. S., Claro J.C.P., Fillon M., 2000, "Temperature, Flow and Eccentricity Measurements in a Journal Bearing with a Single Axial Groove at 90° to the Load Line", Proc. 9th Nordic Symposium of Tribology NORDTRIB 2000, Vol 1, pp. 108-117.
- Costa L., Miranda A. S., Fillon M. and Claro J. C. P., 2003a, "An analysis of the influence of oil supply conditions on the Thermohydrodynamic performance of a single groove journal bearing", Proc. Inst. Mech. Eng., Part J: Journal of Engineering Tribology, Vol. 217, pp. 133-144
- Costa L., Fillon M., Miranda A. S. and Claro J. C. P., 2003b, "An Experimental Investigation of the Effect of Groove Location and Supply Pressure on the THD Performance of a Steadily Loaded Journal Bearing", ASME JoT, 122, pp. 227-232.
- Das S., Guha, S.K. and Chattopadhyay, A.K., 2002, "On the steady-state performance of misaligned hydrodynamic journal bearings lubricated with micropolar fluids", Tribology International 35 (2002) pp. 201–210.
- Das S., Guha, S.K. and Chattopadhyay, A.K., 2004, "Theoretical analysis of stability characteristics of hydrodynamic journal bearings lubricated with micropolar fluids", Proc. Instn Mech. Engrs Vol. 218 Part J: J. Engineering Tribology, pp. 45-56.
- Das S., Guha, S.K. and Chattopadhyay, A.K., 2005, "Linear stability analysis of hydrodynamic journal bearings under micropolar lubrication", Tribology International 38 pp. 500–507.
- Deng D. and Brown J, 2008, "A New Model for Transition Flow of Thin Films in Long Journal Bearings", Tribology Transactions, 51, 1-11

- Dimofte F., Proctor M.P., Fleming D.P., and Keith T.G. Jr., 2000, "Wave Fluid Film Bearing Tests for an Aviation Gearbox", 8th International Symposium on Transport Phenomena and Dynamics of Rotating Machinery, ISROMAC-8, Honolulu, HI, 26-30 March 2000, NASA/TM-2000-209766.
- Dimofte F., Fleming D.P., Anderson W.J. and Klein R. C., 2005, "Test of a Fluid-Film Wave Bearing at 350°C with Liquid Lubricants", *Tribology Transactions*, 48, pp. 515-521.
- Dobrica M. and Fillon M., 2006a, "Mixed Elastohydrodynamic Lubrication in a Partial Journal Bearing—Comparison Between Deterministic and Stochastic Models", *ASME JoT*, 128, pp. 778-788.
- Dobrica M. and Fillon M., 2006b, "Thermohydrodynamic Behavior of a Slider Pocket Bearing", *ASME JoT*, 128, pp. 312-318.
- Dobrica M., Fillon M., Pascovici M.D. and Cicone T., 2007, "Proceedings of the STLE/ASME International Joint Tribology Conference IJTC2007, October 22-24, 2007, San Diego, California, USA.
- Dobrica M. and Fillon M., 2009, "About the validity of Reynolds equation and inertia effects in textured sliders of infinite width", *Proc. IMechE Vol. 223 Part J: J. Engineering Tribology*, pp. 69-78.
- Dowson D., 1962, "A generalized Reynolds equation for fluid film lubrication". *International Journal Mech. Sc.*, Pergamon Press Ltd., 4, 159-170.
- Dowson D. and Hudson, J. D., 1964, "Thermohydrodynamic Analysis of the Infinite Slider Bearing", *Proc. I Mech. E.*, Vol, 3, pp, 34-51.
- Dowson D., Hudson J., Hunter B., and March C., 1966-67, "An experimental investigation of the thermal equilibrium of steadily loaded journal bearings. *Proc. Instn. Mech. Engrs.*, Pt 3B, 101, 70-80.
- Dowson D., Taylor C. M., Miranda A.S., 1985, "The prediction of liquid film journal bearing performance with a consideration of lubricant film reformation, part I and II", *Proc. ImechE*, Vol 119, C2, pp. 95-102, 102-111.
- Dowson D., 1979, "History of Tribology", Longmans Group Limited, London.
- Durany J., Pereira J., Varas F., 2005, "Análisis Termohidrodinámico de un Par Eje-Cojinete Combinando Métodos de Volúmenes Finitos y Elementos de Contorno", *IBERTRIB 2005 – III Congresso Ibérico de Tribologia*, 16-17 de Junho de 2005, Universidade do Minho, Guimarães, Portugal, CD-ROM (ISBN 972-99596-0-9)
- EI-Deihi, M.K.I. and Gethin, D.T., 1992, "A Thermohydrodynamic Analysis of a Twin Axial Groove Bearing Under Different Loading Directions and Comparison With Experiment," *ASME J. Tribol.*, 114, pp. 304–310.
- Elrod H. G., 1981, "A cavitation algorithm". *ASME Journal of Lubrication Technology*, 103, nº 3, 350-354.
- Elrod, H.G. and Adams, M.L., 1975, "A computer program for cavitation and starvation problem", *Cavitation and related phenomena in lubrication*, 1st Leeds-Lyon Symposium in on Tribology - 1974, pp. 37-44 (Mechanical Engineering Publications Limited, London).
- Elsharkawy A, and Guedouar L.H., 2001, "An inverse solution for finite journal bearings lubricated with couple stress fluids", *Tribology International* 34, 107–118.

- Elsharkawy A.A., 2005, "Effects of lubricant additives on the performance of hydrodynamically lubricated journal bearings", *Tribology Letters*, Vol. 18, No. 1, January, pp. 63-73.
- ESDU, item No. 65007, 1965, *General Guide to the Choice of Journal Bearing Type*, Engineering Sciences Data Unit (ESDU) International Plc., London.
- ESDU item No. 84031, 1984, "Calculation Methods for Steadily Loaded Axial Groove Hydrodynamic Journal Bearings", Engineering Sciences Data Unit (ESDU) International Plc., London.
- Etsion I. and Ludwig L.P., 1982, "Observation of Pressure Variation in the Cavitation Region of Submerged Journal Bearings," *ASME J. Lubr. Technol.*, 104, pp. 157–163.
- Ettles C., 1968, "Solutions for Flow in a Bearing Groove," *Proc. Inst. of Mech. Eng.*, Vol. 182, Part 3N, pp. 122-133.
- Ettles C.M., 1969, "Hot Oil Carry Over in Thrust Bearings". *Proc. IMechE Part 3L*, 184,75-81.
- Ezzat H.A. and Rohde S.M., 1974, "Thermal Transients in Finite Slider Bearings," *ASME Journal of Lubrication Technology*, 96, pp. 315–321.
- Fattu A. Hajjam M. and Bonneau D., 2006, "A New Model of Thermoelastohydrodynamic Lubrication in Dynamically Loaded Journal Bearings", *ASME JoT*, 128, pp. 85-95.
- Ferron J., 1982, "Contribution à l'étude de phénomènes thermiques dans les paliers hydrodynamiques", Thèse pour obtenir le titre de docteur de 3^{ème} cycle, Université de Poitiers, França.
- Ferron J., Frêne J. and Boncompain R., 1983, "A Study of the Thermohydrodynamic performance of a plain journal bearing. Comparison between theory and experiments". *ASME Journal of Lubrication Technology*, 105, 422-428.
- Fillon M., 1985, "Contribution à l'étude des phénomènes thermiques dans les Paliers à Patins Oscilants" PhD Thesis, Université de Poitiers, France
- Fillon M., Bligoud J.C and Frene J., 1992, "Experimental Study of Tilting-Pad Journal Bearings—Comparison with Theoretical Thermoelastohydrodynamic Results", *ASME JoT*, 114, pp. 579-588.
- Fillon M. and Khonsari M.M., 1996, "Thermohydrodynamic Design Charts for Tilting-Pad Journal Bearings", *ASME JoT*, 118, pp. 232-238.
- Fillon M., 1998, "Temperature effects in hydrodynamic bearings" *Actas das 6^{as} Jornadas Portuguesas de Tribologia*, Ramalho A., Universidade de Coimbra, Portugal, pp. 3.1-3.4
- Fillon M., and Bouyer J., 2004, "Thermohydrodynamic analysis of a worn plain journal bearing", *Tribology International* 37 pp. 129-136.
- Fillon M., Dmochowski W. and Dadouche A., 2007, "Numerical Study of the Sensitivity of Tilting Pad Journal Bearing Performance Characteristics to Manufacturing Tolerances: Steady-State Analysis", *Tribology Transactions*, 50:3, pp.387-400.
- Fitzgerald M. K., and Neal P. B., 1992, "Temperature distributions and heat transfer in journal bearings", *ASME Journal of Tribology*, Vol. 114, pp. 122-130.
- Floberg L., 1965, "On Hydrodynamic Lubrication with Special Reference of Sub-Cavity Pressures and Numbers of Streamers in Cavitation Region", *Acta Polytechn. Scand. Mech. Eng. Ser.*, 19.

- Fortier A.E. and Salant R.F., 2005, "Numerical Analysis of a Journal Bearing With a Heterogeneous Slip/No-Slip Surface", *ASME JoT*, 127, pp. 820-825.
- Fowell M., Olver A.V., Gosman A.D., Spikes H.A. and Pegg I., 2007, "Entrainment and Inlet Suction: Two Mechanisms of Hydrodynamic Lubrication in Textured Bearings", *ASME JoT*, 129, 336-347.
- Frankel A. 1946, "Calculation of the Performance Characteristics of Plain Bearings", *The Engineers Digest*, 7, pp. 133-138 and pp. 163-166.
- Frêne J., Arghir M., Constantinescu V., 2006, "Combined thin-film and Navier–Stokes analysis in high Reynolds number lubrication", *Tribology International* 39 pp. 734–747
- Frêne J., Nicolas D., Degueurce B., Berthe D. and Godet M., 1990, "Lubrification hydrodynamique – paliers et butées", *Collection de la direction des Études et Recherches d'Électricité de France*, 72, Editions Eyrolles, Paris, pp.354-358
- Gethin D.T., 1985, "An investigation into plain Journal Bearing Behavior including Thermoelastic Deformation of the Bush", *Proc Inst Mech Engrs* 119, C3 pp. 215-223.
- Gethin D.T. and Medwell, J.O., 1985, "An Experimental Investigation Into the Thermohydrodynamic Behavior of a High Speed Cylindrical Bore Journal Bearing.", *ASME JoT*, 107, pp. 538-543.
- Gethin D. T., 1987, "An application of the finite element to the Thermohydrodynamic analysis of a film cylindrical bore bearing running at high sliding speed", *ASME Journal of Tribology*, Vol. 109, pp. 283-289.
- Gethin D.T., 1987, "A Finite Element Approach to Analyzing Thermohydrodynamic Lubrication in Journal Bearings", *Tribology International*, 21:2, pp. 67-75.
- Gethin D. T., and El-Deihi, M. K. I., 1990, "Thermal behavior of a twin axial groove bearing under varying loading direction", *Proc. ImechE*, Part C. 204, pp. 77–90.
- Gethin D. T., 1996, "Modeling the Thermohydrodynamic behavior of high speed journal bearings", *Tribology International*, Vol 29, pp. 579-596.
- Glavatskih S.B., McCarthy D.M.C. and Sherrington, I., 2005, "Hydrodynamic Performance of a Thrust Bearing with Micro patterned Pads", *Tribology Transactions*, 48:4, pp. 492 – 498.
- Glavatskih S.B. and Fillon, M., 2006, "TEHD Analysis of Thrust Bearings with PTFE-Faced Pads", *ASME JoT*, 128, pp. 49-58.
- Griffith A.A., 1920, "The Phenomena of Rupture and Flow in Solids", *Philos. Trans. R. Soc. Lond.*, A221, pp. 163-198.
- Groper M. and Etsion I, 2001, "The Effect of Shear Flow and Dissolved Gas Diffusion on the Cavitation in a Submerged Journal Bearing", *ASME JoT*, 123, pp. 494-500.
- Groper M. and Etsion I, 2002, "Reverse Flow as a Possible Mechanism for Cavitation Pressure Build-up in a Submerged Journal Bearing", *ASME JoT*, 124, pp. 320-326.
- Guha S.K., 2000, "Analysis of steady-state characteristics of misaligned hydrodynamic journal bearings with isotropic roughness effect", *Tribology International* 33 pp. 1–12.

- Guha S.K., 2004, "A theoretical analysis of dynamic characteristics of Finite hydrodynamic journal bearings lubricated with coupled stress fluids", Proc. Instn Mech. Engrs Vol. 218 Part J: J. Engineering Tribology pp. 125-133.
- Gumbel, L., 1914, "Das problem der lagerreibung", Monatsblätter, Berliner Biezirks Verein Deutscher Ing., VDI n° 5, pp 97-104 e 109-120.
- Gupta G., Hammond C. R. And Szeri A.Z., 1990, "An approximate THD theory for journal bearings", ASME Journal of Tribology, Vol 112, pp. 224-229.
- Han T. and Paranjpe R., 1990, "A finite volume analysis of the Thermohydrodynamic performance of journal bearings", ASME Journal of Tribology, Vol. 112, pp.557-566.
- Hashimoto H. and Matsumoto K., 2001, "Improvement of Operating Characteristics of High-Speed Hydrodynamic Journal Bearings by Optimum Design: Part I— Formulation of Methodology and Its Application to Elliptical Bearing Design", ASME JoT, 123, pp. 305-312.
- Hatakenaka K. and Tanaka M., 2002, "Thermohydrodynamic performance of journal bearings with partial reverse flow and finger-type cavitation", Proc. IMechE, part J, Vol 216, pp. 315-325.
- Hatakenaka K., Tanaka M. and Suzuki K., 2002, "A Theoretical Analysis of Floating Bush Journal Bearing With Axial Oil Film Rupture Being Considered", ASME JoT, 124, pp. 494-505.
- Hatakenaka K. and Tanaka M., 2002 "Thermohydrodynamic performance of journal bearings with partial reverse flow and Finger-type cavitation", Proc Instn Mech Engr s Vol 216 Part J: J Engineering Tribology, pp. 315-325.
- Heshmat H., and Pinkus O., 1986, "Mixing Inlet Temperatures in Hydrodynamic Bearings", ASME JoT, 108, pp. 221-248.
- Heshmat, H., 1991, "The Mechanism of Cavitation in Hydrodynamic Lubrication" Tribol. Trans., 34, No. 2, pp. 177-186.
- Hirani H, 2004, "Multiobjective optimization of a journal bearing using the Pareto optimality concept", Proc. Instn Mech. Engrs Vol. 218 Part J: J. Engineering Tribology, pp. 323-336.
- Hirani H, 2005, "Multi-objective optimization of journal bearing using mass conserving and genetic algorithms", Proc. IMechE Vol. 219 Part J: J. Engineering Tribology, pp. 235-248.
- Hirani H, Suh N.P., 2005, "Journal bearing design using multi-objective genetic algorithm and axiomatic design approaches", Tribology International 38, pp. 481-491".
- Hirani H. and Samanta P., 2007, "Hybrid (hydrodynamic + permanent magnetic) journal bearings". Proc. IMechE Vol. 221 Part J: J. Engineering Tribology. Pp. 881-891.
- Hirn, G., 1854, "Sur les principaux phénomènes qui presentent les frottements médiats". Bull. Ind. Soc. Mulhouse, 26, 188-277.
- Hussain A., Mistry K., Biswas S. and Athre K., 1996, "Thermal Analysis of Noncircular Bearings", ASME JoT, 109, 246-254.
- Jacobson B. and Floberg L., 1957, "The Finite Journal Bearing, Considering Vaporization", Trans. Chalmers Univ. Technol., 190.

- Jakeman R. N., 1989, "A numerical analysis method based on flow continuity for hydrodynamic journal bearings", *Tribology International*, Vol. 17, pp. 325-333
- Jang G.H. and Chang D.I., 2000, "Analysis of a Hydrodynamic Herringbone Grooved Journal Bearing Considering Cavitation", *ASME JoT*, 122, pp. 103-109.
- Jang J.Y. and Khonsari M.M., 2004, "Design of bearings on the basis of thermohydrodynamic analysis", *Proc. Instn Mech. Engrs Vol. 218 Part J: J. Engineering Tribology*, pp. 355-363.
- Jeddi L, El Khelifi M. and Bonneau D, 2005, "Thermohydrodynamic analysis for a hydrodynamic journal bearing groove", pp. 263-274.
- Johansson L, and Wettergren H., 2004, "Computation of the Pressure Distribution in Hydrodynamic Bearings Using Newton's Method", 126, pp. 404-407.
- Kakoty S.K., 2000, "Effect of fluid inertia on stability of oil journal bearings", *ASME Journal of Tribology* Vol. 122, pp.741-745.
- Kakoty S.K. and Majumdar B.C., 2000, "Effect of fluid inertia on the dynamic coefficients and stability of journal bearings", *Proc Instn Mech Engrs Vol 214 Part J*, pp. 229-242.
- Kakoty, S.K. and Majumdar, B.C., 2002 "Effect of Fluid Film Inertia on Stability of Flexibly Supported Oil Journal Bearings: A Non-Linear Transient Analysis", *Tribology Transactions*, 45:2, pp. 253-257.
- Kasolang, S. and Dwyer-Joyce, R. S., 2008 "Observations of Film Thickness Profile and Cavitation around a Journal Bearing Circumference", *Tribology Transactions*, 51:2, 231 — 245.
- Keogh P.S., Gomiciaga R., Khonsari M.M., 1997, "CFD Based Design Techniques for Thermal Prediction in a Generic Two-Axial Groove Hydrodynamic Journal Bearing", *ASME JoT*, 119, pp. 428-435.
- Keogh P.S. and Khonsari, M.M., 2001, "Influence of Inlet Conditions on the Thermohydrodynamic State of a Fully Circumferentially Grooved Journal Bearing", *ASME JoT*, 123, 525-532.
- Khonsari M. And Beaman J., 1986, "Thermohydrodynamic analysis of laminar incompressible journal bearings", *ASLE Transactions*, Vol. 35, pp. 141-150.
- Khonsari, M.M. and Booser E.R., 2001, *Applied Tribology Bearing Design and Lubrication*, Wiley, New York.
- Khonsari M., Jang J., and Fillon M., 1996, "On the generalization of Thermohydrodynamic analysis of journal bearings". *ASME Journal of Tribology*, 118, 571-579.
- Khonsari M.M. and Wang, S.H., 1991, "On The Fluid-Solid Interaction in Reference to Thermoelastohydrodynamic Analysis of Journal Bearings" *ASME J. Tribol.*, 113, pp. 398-404.
- Kim B.J. and Kim K.W., 2001, "Thermo-Elastohydrodynamic Analysis of Connecting Rod Bearing in Internal Combustion Engine", *ASME JoT*, 123, pp. 444-454.
- Kingsbury A., 1933, "Heat Effects in Lubricating Films", *Mech Eng* 55, pp. 685-688.
- Knight J. D. And Barret L., 1983, "An approximate solution technique for multilobe journal bearings including thermal effects with comparison to experiment" *ASLE Transactions*, Vol. 26, pp. 501-508.
- Knight J. D. Barret L. and Cronan R.D., 1985, "The effects of Supply Pressure on Operating Characteristics of Two-Axial Groove Bearings", *STLE Tribology Transactions*, 28, pp. 336-342.

- Knight J.D., and Niewiarowski A.J., 1990, "Effect of Two Film Rupture Models on the Thermal Analysis of a Journal Bearing," ASME JoT, 112, pp. 183-188.
- Knight J. D. and Ghadimi P., 1992, "Effects of modified Effective length models of the rupture zone on the analysis of a fluid journal bearings", STLE Tribology Transactions, Vol.35, pp 29-36.
- Knight J. D. and Ghadimi P., 2001, "Analysis and observation of cavities in a journal bearing considering flow continuity", STLE Tribology Transactions, Vol.44, pp. 88-96.
- Koeneke C.E., Tanaka M., and Motoi H., 1995, "Axial Oil Film Rupture in High Speed Bearings Due to the Effect of the Centrifugal Force", ASME J. Tribol., 117, pp. 394–398.
- Kosasih P.B. and Tieu A.K., 2004, "An investigation into the thermal mixing in journal bearings", Proc. Instn Mech. Engrs Vol. 218 Part J: J. Engineering Tribology, pp. 379-389.
- Kraker A., van Ostayen R. A. J., van Beek A., Rixen D. J., 2007, "A Multi-scale Method Modeling Surface Texture Effects", ASME Journal of Tribology 129-2, pp. 221-449.
- Kucinski B.R., Fillon M., Frêne J., Pascovici M. D., 2000, "A transient Thermoelastohydrodynamic study of steadily loaded plain journal bearings using finite element method analysis" ASME Journal of Tribology Vol. 122, pp.219-226.
- Kucinski B.R., DeWitt K.J., Pascovici M.D., 2004, "Thermoelastohydrodynamic (TEHD) Analysis of a Grooved Thrust Washer", ASME JoT, 126, pp. 267-274
- Kumar A. and Booker J.F., 1991a, "A finite element cavitation algorithm". ASME Journal of Tribology, 113, 276-286.
- Kumar A. and Booker J.F., 1991b, "A Finite Element Cavitation Algorithm: Application/Validation," ASME JoT, 113, pp. 255–261.
- Kumar A. and Booker J. F., 1994, "A mass and energy conserving Finite element lubrication algorithm", ASME, JoT, 116, pp. 667-671.
- Kuzhir P., 2008, "Free boundary of lubricant film in ferrofluid journal bearings", Tribology International, 41, pp. 256–268.
- Leonard, B.P., 1979, "A Stable and Accurate Convective Modeling Procedure Based on Quadratic Upstream Interpolation", Comput. Methods Appl. Mech. Eng., Vol. 19, pp. 59-98.
- Li H.D., Liu B. and Li J., 2004, "Numerical Simulation of Taper Flat Slider Air Bearing Based on a Mesh-Free Method", IEEE TRANSACTIONS ON MAGNETICS, 40:4.
- Li J, and Chen, H, 2007, "Evaluation on Applicability of Reynolds Equation for Squared Transverse Roughness Compared to CFD", ASME JoT, 129, pp. 963-967.
- Li W.L., Chu H.M. and Chen M.D., 2006, "The partially wetted bearing—extended Reynolds equation", Tribology International, 39, pp. 1428–1435.
- Lund, J.W. and Tonnesen, J., 1984, 'An approximate analysis of the temperature conditions in a journal bearing. Part II: Application', ASME Journal of Tribology, Vol 106, No. 2, pp 237-245.
- Lund J.W., and Hansen P.K., 1984, "Approximate Analysis of the Temperature Conditions in a Journal Bearing", ASME JoT, 106:2, pp. 228–236.

- Lyons, L., 1991, "A Practical Guide to Data Analysis for Physical Science Students", Cambridge University Press.
- Ma M. T., Taylor C. M., 1992, "A theoretical and experimental study of thermal effects in a plain circular steadily loaded journal bearing", IMechE Seminar: Plain Bearings - Energy Efficiency and Design, Mech. Eng. Publications Ltd., London
- Ma M. T., Taylor C. M., 1994, "Prediction of temperature fade in cavitation region of two-lobe journal bearings", Proc. ImechE, Vol 208, pp. 133-139
- Ma M. T., Taylor C. M., 1995, "Effects of Oil Temperature on the Performance of an Elliptical Bearing", Proc. Of the 21st Leeds-Lyon Symposium on Tribology, 1994, Elsevier, Tribology series 30 pp.143-151.
- Ma M. T., Taylor C. M., 1996, "An experimental investigation of thermal effects in circular and elliptical plain journal bearings", Tribology International 29:1, pp. 19-26.
- Ma Y.Y., Wang W.H. and Cheng X.H., 2004, "A study of dynamically loaded journal bearings lubricated with non-Newtonian couple stress fluids", Tribology Letters, Vol. 17, No. 1, July, pp.69-74.
- Ma G.J., Wu C.W. and Zhou P., 2007, "Wall slip and hydrodynamics of two-dimensional journal bearing", Tribology International, 40, pp. 1056–1066.
- Majumdar B.C., Pai R. and Hargreaves D.J., 2004, "Analysis of water-lubricated journal bearings with multiple axial grooves", Proc. Instn Mech. Engrs Vol. 218 Part J, pp. 135-146.
- Marian V.G., Kilian M. and Scholz W., 2007, "Theoretical and experimental analysis of a partially textured thrust bearing with square dimples", Proc. IMechE Vol. 221 Part J: J. Engineering Tribology, pp. 771-778.
- Markin D. McCarthy D.M.C. and Glavatskih S.B., 2003, "A FEM approach to simulation of tilting-pad thrust bearing assemblies", Tribology International 36, pp. 807–814.
- Martin J.K. and Parkins D.W., 2002, "Theoretical Studies of a Continuously Adjustable Hydrodynamic Fluid Film Bearing", ASME JoT, 124, pp. 203-211.
- Matsuda K., Kijimoto S. and Kanemitsu Y., "Stability-Optimized Clearance Configuration of Fluid-Film Bearings", ASME JoT, 129, pp. 106-111.
- Martin F.A., 1998, "Oil flow in plain steadily loaded journal bearings: realistic predictions using rapid techniques", Proc Instn Mech Engrs Vol 212 Part J, pp. 413-425.
- Mccallion T. H., Yousif F. And Lloyd T., 1970, "The analysis of thermal effects in a full journal bearing", ASME Journal of Lubrication Technology, Vol. 92, pp. 578-588.
- Medwell J.D. and Gethin D.T., 1984, "Differential Expansion Problem in Journal Bearings", Proc. 10th Leeds-Lyon Symposium on Tribology, 1983, ed. D. Dowson et al. Butterworths Guildford pp. 297-301.
- Michaud P., Souchet D., and Bonneau D., 2007, "Thermohydrodynamic lubrication analysis for a dynamically loaded journal bearing", Proc. IMechE Vol. 221 Part J: J. Engineering Tribology, pp.49-61.
- Miranda A. S., 1983, "Oil Flow, Cavitation and Film Reformation in Journal Bearings, Including an Interactive Computer-Aided Design Study", PhD Thesis, University of Leeds
- Mishra, P. C., 2007a, "Thermal Analysis of Elliptic Bore Journal Bearing", Tribology Transactions, 50, pp. 137-143.

- Mishra, P. C., Pandey R.K., Athre K., 2007b, "Temperature profile of an elliptic bore journal bearing", *Tribology International* 40 453–458.
- Mistry K., Biswas S. and Athre A., 1992, "Study of profile and cavitation in a circular journal bearing" *Wear*, Vol. 159, pp 79-87
- Mistry K., Biswas S., Athre A., 1993, "Thermal Aspects of Plain Circular Bearing Under Moderately Loaded Conditions", *Proceedings of Eurotrib'93*, 4, pp19-24.
- Mistry K., Biswas S., Athre A., 1997, "A new Theoretical Model for Analysis of the Fluid Film in the Cavitating Zone of a Journal Bearing", *ASME JoT*, 119, pp. 741-746.
- Mitsui J., Hori Y. and Tanaka, M., 1983, "Thermohydrodynamic analysis of cooling effect of supply oil in circular journal bearings", *ASME Journal of Tribology*, 105, pp. 414–421.
- Mitsui J., 1987, "A Study of Thermohydrodynamic Lubrication in a Circular Journal Bearing", *Tribol. Int.*, 20, pp. 331–340.
- Monmosseau P., 1997, PhD Thesis, Université de Poitiers, France
- Monmosseau P., Fillon, M. and Frêne J., 1998, "Transient Thermoelastohydrodynamic Study of Tilting-Pad Journal Bearings - Application to Bearing Seizure", *ASME JoT* 120, pp.319-324.
- Monmosseau P. and Fillon, M., 2000, "Transient Thermoelastohydrodynamic analysis for safe operating conditions of a tilting-pad journal bearing during start-up", *Tribology International* 33 (2000) 225–231.
- Mourelatos, Z.P. 2001 "An Efficient Journal Bearing Lubrication Analysis For Engine Crankshafts", *Tribology Transactions*, 44:3, pp. 351-358.
- Nair K.P., Nair V.P.S. and Jayadas N.H., 2007, "Static and dynamic analysis of elastohydrodynamic elliptical journal bearing with micropolar lubricant", *Tribology International* 40 pp. 297–305.
- Nassab S.A.G. and Moayeri M.S., 2002, "Three-dimensional thermohydrodynamic analysis of axially grooved journal bearings", *Proc Instn Mech Engrs Vol 216 Part J: J Engineering Tribology*, pp. 35-47.
- Nassab S.A.G., 2005, "Inertia effect on the thermohydrodynamic characteristics of journal bearings", *Proc. IMechE Vol. 219 Part J: J. Engineering Tribology*, pp. 459-467.
- Nassab S.A.G, and Maneshian B., 2007, "Thermohydrodynamic analysis of cavitating journal bearings using three different cavitation models", *Proc. IMechE Vol. 221 Part J: J. Engineering Tribology*, pp. 501-513.
- Nicoletti R. and Santos, I.F., 2003. "Linear and non-linear control techniques applied to actively lubricated journal bearings", *J. SoundVibr.*, 206, 927–947.
- Nosov, V.R. and Gomez-Mancilla, J., 2004, "On the Appearance of Lubricant Film Rupture in Cylindrical Journal Bearings", *Tribology Transactions*, 47:2, pp. 233-238.
- Ockvirk F. W., 1952, "Short bearing approximation for full journal bearings", *NACA Tech note* 2808.
- Osman T.A., Nada G.S. and Safar Z.S., 2001, "Static and dynamic characteristics of magnetized journal bearings lubricated with ferrofluid", *Tribology International*, 34, pp. 369–380.
- Osman T.A., 2004, "Effect of lubricant non-Newtonian behavior and elastic deformation on the dynamic performance of finite journal plastic bearings", *Tribology Letters*, Vol. 17, No. 1, pp. 31-40.

- Ott H.H. and Paradissiadis G., 1988, "Analysis of Thermal Effects in Hydrodynamic Bearings" ASME JoT, 110, pp. 439-447.
- Pandazaras C.N. and Petropoulos G.P., 2001, "A computational study of hydrodynamically lubricated convex and concave journal bearings", Proc Instn Mech Engrs Vol 215 Part J, pp. 425-429.
- Paranjpe, R.S. and Goenka, P.K., 1990, "Analysis of Crankshaft Bearings Using a Mass-Conserving Algorithm," STLE Tribol. Trans., 33(3), pp. 333-344.
- Paranjpe R. and Han T., 1994, "A Study of the Thermohydrodynamic performance of steadily loaded journal bearings", STLE Tribology Transactions, Vol. 37, pp. 679-690.
- Pascovici M. D., 1993, "A Thermohydrodynamic analysis of journal bearings cooled through the shaft", Proceedings Eurotrib '93, Vol. 4, pp. 251-256.
- Patankar S.V. and Spalding, B.D., 1972, "A calculation procedure for heat, mass and momentum transfer in three-dimensional parabolic flows", Int. J. Heat Mass Transfer, 15, pp. 1787-1806.
- Patankar S. V., 1980, "Numerical Heat Transfer and Fluid Flow, McGraw-Hill, New York.
- Patir N. and Cheng H.S., 1978, "An Average Flow Model for Determine Effects of Three Dimensional Roughness on Partial Hydrodynamic Lubrication", ASME JOURNAL OF LUBRICATION TECHNOLOGY, Vol. 100, pp. 12-17.
- Peng J. and Zhu K.Q. "Effects of electric field on hydrodynamic characteristics of finite-length ER journal bearings", Tribology International, 39, pp. 533-540.
- Pereira R, Flores P., Machado G. and Claro J.C.P. "Computational Modeling of Dynamically Loaded Journal Bearings", IBERTRIB 2007 - Congreso Ibérico de Tribología, Escuela de Ingenieros, Bilbao, June 20-21, 2007, CD-ROM. "
- Petrov N.P., 1883, "Theoretical and Experimental Study of Mediate Friction: Parts I, II, III and IV", Reprinted in "Fluid film Lubrication: A century of Progress", Ed. Rohde et al, 1983, American Society of Mechanical Engineers, pp. 107-134.
- Pierre I., 2000, "Etude tridimensionnelle des effets thermohydrodynamiques Dans les Paliers Alignés et Mésalignés ", PhD Thesis, Université de Poitiers, France
- Pierre I. and Fillon M., 2000, "Influence of geometric parameters and operating conditions on the thermohydrodynamic behavior of plain journal bearings". Proc. Instn. Mech. Engrs, Pt J, Journal of Engineering Tribology, 214, 445-457.
- Pierre I., Bouyer J. and Fillon M, 2004 "Thermohydrodynamic Behavior of Misaligned Plain Journal Bearings: Theoretical and Experimental Approaches", Tribology Transactions, 47:4, pp. 594 - 604.
- Piffeteau S., Souchet D. and Bonneau D., 2000, "Influence of Thermal and Elastic Deformations on Connecting-Rod Big End Bearing Lubrication under Dynamic Loading", ASME JoT, 122, pp. 181-191.
- Pinkus O., 1958, "Solutions of Reynolds Equation for Finite Journal Bearings", ASME JoT, 80, pp. 858-864.
- Pinkus O. and Bupara S.S., 1979, "Analysis of Misaligned Grooved Journal Bearings", ASME J. Lubr. Technol., 101, pp. 503-509 (Discussion and Errata, 102, pp. 257-260).
- Pinkus O., 1990, "Thermal Aspects of Fluid Film Tribology". ASME Press, New York.

- Raghunandana K, Majumdar B.C., and Maiti R., 2001, "Stability of Flexibly Supported Oil Journal Bearings Using Non-Newtonian Lubricants: Linear Perturbation Analysis", ASME JoT, 123, pp. 651-654.
- Rahmani, R., Shirvani, A. and Shirvani, H, 2007, "Optimization of Partially Textured Parallel Thrust Bearings with Square-Shaped Micro-Dimples", Tribology Transactions, 50:3, 401 - 406
- Rajalingham C., and Prabhu B. S., 1987, "The influence of variation of viscosity with temperature on the steady state characteristics of journal bearings – simple analysis" Tribology International, Vol. 20, n° 5, pp 261-266.
- Rajalingham C., Blat R.R. and Xistris G.D., 1994, "The influence of Thermal Conduction Across the Film on the the THD Characteristics of a Plain Journal Bearing", ASME JoT, 116, pp. 397-399.
- Raimondi A.A. and Boyd J., 1958, "A solution for the finite journal bearing and its application to analysis and design" parts I, II and III, ASLE Trans., 1958, 1(1), 159-209.
- Raimondi A.A., 1966, "An Adiabatic Solution for the Finite Slider Bearing", ASME Transactions, 9:3, 283-298.
- Rao T.V.V.L.N., Biswas S., Hirani H. and Athre K., 2000, "An Analytical Approach to Evaluate Dynamic Coefficients and Nonlinear Transient Analysis of a Hydrodynamic Journal Bearing', Tribology Transactions, 43:1, 109-115
- Rao T.V.V.L.N, Biswas S. and Athre K., 2001, "A Methodology for Dynamic Coefficients and Nonlinear Response of Multi-Lobe Journal Bearings", Tribology Transactions, 44-1, 111-117.
- Rao T.V.V.L.N. and Sawicky J.T., 2002, "Linear Stability Analysis for a Hydrodynamic Journal Bearing Considering Cavitation Effects", Tribology Transactions, 45:4, pp. 450-456.
- Rao T.V.V.L.N and Sawicky J.T., 2003, "Dynamic Coefficient Prediction in Multi-lobe Journal Bearings Using a Mass Conservation Algorithm", Tribology Transactions, 46:3, pp. 414-420.
- Rao T.V.V.L.N and Sawicky J.T., 2005, "Stability Analysis of a Rough Journal Bearing Considering Cavitation Effects", ASME JoT, 127, pp. 112-119.
- Reason B. R. and Narang I. P., 1982, "Rapid design and performance evaluation of steady state journal bearings – A technique amenable to programmable hand calculators". Trans. STLE, 25(4), 429–444.
- Reynolds O., 1886, "On the theory of lubrication and its application to Mr. Beauchamp Tower's experiments, including an experimental determination of the viscosity of olive oil", Philosophical Trans., Royal Society, Vol. 177 (1886).
- Rho B.H. and Kim K.W., 2002, "A study of the dynamic characteristics of synchronously controlled hydrodynamic journal bearings", Tribology International 35 pp. 339–345.
- Rhode S.M. and Oh K.P. 1975, "A TEHD Analysis of a Finite Slider Bearing", ASME Journal of Lubrication Technology pp. 450-460.
- Richtmyer R. D., 1957, "Difference methods for initial value problems", Interscience Publishers Inc., New York.
- Rowe W. B. and Chong F. S., 1984, "A computational algorithm for cavitating bearings" Tribology International, Vol 17, n° 5, pp. 243-250.
- Sahlin F., Glavatskih S.B., Almqvist T. and Larsson R., 2005 "Two-Dimensional CFD-Analysis of Micro-Patterned Surfaces in Hydrodynamic Lubrication", ASME JoT, 127, pp. 96-102.

- Sahlin F., Almqvist A., Larsson R. and Glavatskih S., 2007, "A cavitation algorithm for arbitrary lubricant compressibility", *Tribology International* 40 pp. 1294–1300.
- Safar Z. and Szeri A., 1974, "Thermohydrodynamic Lubrication in Laminar and Turbulent Regimes," *Jour. of Lubr. Tech.*, 96, pp 48-56.
- Sawicki, J.T. and Rao, T.V.V.L.N., 2001, "Nonlinear Prediction of Rotordynamic Coefficients For a Hydrodynamic Journal Bearing", *Tribology Transactions*, 44:3, pp. 367-374.
- Shi F. and Wang Q., 1998, "A Mixed-TEHD Model for Journal-Bearing Conformal Contacts—Part I: Model Formulation and Approximation of Heat Transfer Considering Asperity Contact", *ASME JoT*, 120, pp. 198-205.
- Shyu, S.H., Talmage, G. and Carpino, M., 2000, "Comparison of Lubrication Models for Plane Slider Bearings", *Tribology Transactions*, 43:1, pp. 74-81.
- Sinhasan R., and Chandrawat H. N., 1990, "Analysis of Two-Axial Groove Journal Bearing Including ThermoelastoHydrodynamic Effects" *Tribol. Int.*, 22(5), pp. 347–353.
- Siripuram R.B. and Stephens L.S., 2004, "Effect of Deterministic Asperity Geometry on Hydrodynamic Lubrication", *ASME JoT*, 126, pp. 527-534.
- Smalley A.J. and McCallion, H., 1966, "The Effect of Journal Misalignment on the Performance of a Journal Bearing under Steady Running Conditions," *Proc. IMechE*, 181,3B, pp 39-48.
- Smith R.N. and Tichy J.A., 1981, "An Analytical Solution for the Thermal Characteristics of Journal Bearings", *ASME Journal of Lubrication Technology*, 103, pp. 443-452.
- So H. And Sieh J. A., 1987, "The cooling effects of supply oil on journal bearings for varying inlet conditions", *Tribology International*, Vol. 20, pp 79-89.
- Sommerfeld A., 1904, "Zur hydrodynamiscien Theorie der Schiermittelreibung" *Zeitschriif Mathematik Phisik*, Vol 50, pp. 97-155.
- Song, J.D., Yang B.S., Choi, B.G. and Kim, H.J., 2005, "Optimum design of short journal bearings by enhanced artificial life", *Tribology International* 38, 403–412
- Souchet D., Hoang L.V. and D Bonneau D, 2004, "Thermoelastohydrodynamic lubrication for the connecting rod big-end bearing under dynamic loading", *Proc. Instn Mech. Engrs Vol. 218 Part J: J. Engineering Tribology*, pp. 451-464.
- Spalding D.B., 1972, "A novel Finite-difference Formulation for Differential Expressions Involving Both First and Second Derivatives", *Int. J. Numer. Methods Eng.*, Vol. 4, p.551
- Spikes H.A., 2003, "The half-wetted bearing. Part 1: extended Reynolds equation", *Proc. Instn Mech. Engrs Vol. 217 Part J: J. Engineering Tribology*, pp. 1-14.
- Stahl J, 2002, "Narrow journal bearings", *Proc Instn Mech Engr s Vol 216 Part J: J Engineering Tribology*, pp. 346-346.
- Stahl J. and Jacobson B.O., 2001, "Design functions for hydrodynamic bearings", *Proc Instn Mech Engrs Vol 215 Part J*, pp. 405-416.

- Stefani F.A. and Rebori A.U., 2002, "Finite Element Analysis of Dynamically Loaded Journal Bearings: Influence of the Bolt Preload", *ASME JoT*, 124, pp. 486-493.
- Stieber W., 1933, "Das schimmlager hydrodynamische theorie des geihagers", VDI Verlag, Berlin
- Suganami T. and Szeri, A. Z., 1979, "A Thermohydrodynamic Analysis of Journal Bearings", *ASME JOURNAL OF LUBRICATION TECHNOLOGY*, Vol. 101, pp. 21-27.
- Swanson E., 2005, "Fixed-Geometry, Hydrodynamic Bearing with Enhanced Stability Characteristics", *Tribology Transactions*, 48:1, pp. 82-92.
- Swift H. W., 1931, "The stability of lubricant film in journal bearings", *Proc. Of Institution of Civil Engineers*, Vol. 23, 4809, pp. 267-322.
- Swift H. W., 1937, "Theory and experiment applied to journal bearing design", *ImechE*, General discussion on lubrication and lubricants, n° 1, pp. 309-316
- Syverud T., 2001, "Experimental investigation of the temperature fade in the cavitation zone of full journal bearings", *Tribology International* 34, pp. 859-870
- Tala-Ighil N., Maspeyrot P., Fillon M. and Bounif A., 2007, "Effects of surface texture on journal-bearing characteristics under steady-state operating conditions", *Proc. IMechE Vol. 221 Part J: J. Engineering Tribology*, pp. 622-633.
- Talmage G. and Carpino M., 2002, "Performance of a Plain Journal Bearing with Flooded Ends", *Tribology Transactions*, 45:3, pp. 310-317.
- Tanaka M., 1997, "Recent analysis and designs of thick-film bearings", *New directions in Tribology*, First World Tribology Congress, Mech. Eng. Pub. Ltd, London, pp. 411-433.
- Tanaka M., 2000, "Journal bearing performance under starved lubrication", *Tribology International* 33, pp. 259-264.
- Taylor G.I., 1964, "Cavitation in Hydrodynamic Lubrication", *Cavitation in Real Liquids*, in *Proc. of Symp. On Cavitation in Real Liquids*, GM Research, 1962. Davies. R, Ed., Elsevier. pp 80-101
- Taylor, R.I., 2004, "Simplifications to the short bearing approximation", *Proc. Instn Mech. Engrs Vol. 218 Part J*, 569-573.
- Tønder K., 2004, "Hydrodynamic effects of tailored inlet roughnesses: extended theory", *Tribology International* 37 pp. 137-142.
- Tonnesen J. and Hansen P.K., 1981, "Some Experiments on the Steady State Characteristics of a Cylindrical Fluid Film Bearing Considering Thermal Effects", *ASME Journal of Lubrication Technology*, 103, pp.107-114.
- Tucker P. G., and Keogh P. S., 1995, "A generalized computational fluid dynamics approach for journal bearing performance prediction" *Proc. IMechE*, Vol 209, Part J: *Journal of Engineering Tribology*, pp. 99-108.
- Van Doormaal J.P. and Raithby G.D., 1984, "Enhancement of the SIMPLE method for predicting incompressible fluid flows", *Numerical Heat Transfer*, 7, pp. 147-163.

- Versteeg H.K. and Malalasekera W, 1995, "An Introduction to the Computational Fluid Dynamics. The Finite Volume Method", Addison Wesley Longman Limited, Longman Group Ltd, Essex, England.
- Vijayaraghavan D. and Keith T.G., 1989, "Development and Evaluation of a Cavitation Algorithm" *STLE Tribol. Trans.*, 32, No. 2, pp. 225–233.
- Vijayaraghavan D. and Keith T.G., 1990a, "An Efficient, Robust, and Time Accurate Numerical Scheme Applied to a Cavitation Algorithm," *ASME JoT*, 112, pp. 44–51.
- Vijayaraghavan D. and Keith T.G., 1990b, "Grid Transformation and Adaption Techniques Applied to the Analysis of Cavitated Journal Bearings," *ASME JoT*, 112, pp. 52–59.
- Vijayaraghavan D. and Keith T.G., 1990c, "Analysis of a Finite Grooved Misaligned Journal Bearing Considering Cavitation and Starvation Effects", *ASME JoT*, 112, pp. 60-67.
- Vijayaraghavan D. and Keith T.G., 1992, "Effect of Type and Location of Oil Groove on the performance of Journal Bearings", *STLE Tribology Transactions*, 35, pp. 96-106
- Vijayaraghavan D., 1996, "An efficient numerical procedure for Thermohydrodynamic analysis of cavitating bearings". *ASME Journal of Tribology*, Vol. 118, 555-563.
- Vijayaraghavan, D., Keith Jr, T. G. and Brewe, D. E., 1996, "Effect of lubricant supply starvation on the thermohydrodynamic performance of a journal bearing", *Tribology Trans.*, 39, pp. 645-653.
- Wang D, Keith T.G., Yang Q and Vaidyanathan K, 2004, "Lubrication Analysis of a Connecting-Rod Bearing in a High-Speed Engine. Part I: Rod and Bearing Deformation', *Tribology Transactions*, 47:2, pp. 280-289.
- Wang J.K. and Khonsari M.M., 2006, "Influence of Inlet Oil Temperature on the Instability Threshold of Rotor-Bearing Systems", *ASME JoT*, 128, pp. 319-326.
- Wang J.K. and Khonsari M.M., 2008, "Effects of oil inlet pressure and inlet position of axially grooved infinitely long journal bearings. Part I: Analytical solutions and static performance", *Tribology International* 41, 119–131.
- Wang N, Ho C.L. and Cha K.C, 2000, "Engineering Optimum Design of Fluid-Film Lubricated Bearings", *Tribology Transactions*, 43:3, pp. 377-386.
- Wang N., Tsai C.-M., 2006, "Application of Thread-Level Parallel Programming to Thermohydrodynamic Lubrication Computation", *Tribology Transactions*, 49, pp. 473-481.
- Wang P., Keith JR. T.G. and Vaidyanathan K., 2001, "Non-Newtonian Effects on the Performance of Dynamically Loaded Elliptical Journal Bearings Using a Mass-Conserving Finite Element Cavitation Algorithm', *Tribology Transactions*, 44:4, pp. 533-542.
- Wang P., Keith JR. T.G. and Vaidyanathan K., 2001, "Non-Newtonian Effects on the Performance of Dynamically Loaded Elliptical Journal Bearings Using a Mass-Conserving Finite Element Cavitation Algorithm", *Tribology Transactions*, 44:4, pp. 533-542.
- Wang, P., Keith JR., T.G. and Vaidyanathan, K., 2002 "Combined Surface Roughness Pattern and Non-Newtonian Effects on the Performance of Dynamically Loaded Journal Bearings", *Tribology Transactions*, 45:1, pp. 1-10

- Wang Q., Shi F. and Lee S.C., 1998, "A Mixed-TEHD Model for Journal-Bearing Conformal Contact—Part II: Contact, Film Thickness, and Performance Analyses", *ASME JoT*, 120, pp. 206-213.
- Wang X.L. Zhu K.Q. and Wen S.Z., 2001, "Thermohydrodynamic analysis of journal bearings lubricated with couple stress fluids", *Tribology International* 34 pp. 335–343.
- Wang X.L. Zhu K.Q. and Wen S.Z., 2002, "On the performance of dynamically loaded journal bearings lubricated with couple stress fluids", *Tribology International* 35 pp. 185–191.
- Wang X.L. Zhu K.Q. and Gui C.L., 2002 "A study of a journal bearing lubricated by couple stress fluids considering thermal and cavitation effects", *Proc Instn Mech Engrs Vol 216 Part J: J Engineering Tribology*, pp. 293-305
- Wang X.L. and Zhu K.Q., 2006, "Numerical analysis of journal bearings lubricated with micropolar fluids including thermal and cavitating effects", *Tribology International* 39 pp. 227–237.
- Woods C.M. and Brewe D.E., 1989, "The Solution of the Elrod Algorithm for Dinamically Loaded Journal Bearings Using Multigrid Techniques", *ASME JoT*, 108, 627-637.
- Wu C.W., Ma G.J. and Zhou P., 2006, "Low Friction and High Load Support Capacity of Slider Bearing With a Mixed Slip Surface", *ASME JoT*, 128, pp. 904-907.
- Yang B.S., Lee Y.H., Choi B.K. and Kim H.J., 2001, "Optimum design of short journal bearings by artificial life algorithm", *Tribology International* 34 (2001) 427–435.
- Yu Q. And Keith Jr. T. G., 1994, "A boundary element cavitation algorithm", *STLE Tribology transactions*, Vol. 37, pp.217-226
- Yu T.H. and Sadeghi F., 2001, "Groove Effects on Thrust Washer Lubrication", *ASME JoT*, 123, pp. 295-304.
- Yu T.H. and Sadeghi F., 2002, "Thermal Effects in Thrust Washer Lubrication", *ASME JoT*, 124, pp.166-177.
- Zengeya M. and Gadala M., 2007, "Optimization of journal bearings using a hybrid scheme", *Proc. IMechE Vol. 221 Part J: J. Engineering Tribology*, pp. 591-607.
- Zengeya M., Gadala M. and Segal, G., 2007, "Hydrodynamic and Thermal Behavior of Journal Bearings using Upwind Petrov-Galerkin FEM", *Tribology Transactions*, 50:2, 227-247.
- Zhang C., Yi Z., and Zhang Z., 2000, "THD analysis of high speed heavily loaded journal bearings including thermal deformation, mass conserving cavitation, and turbulent effects" *ASME Journal of Tribology* Vol. 122, pp.597-602.
- Zhang C., 2002, "TEHD Behavior of Non-Newtonian Dynamically Loaded Journal Bearings in Mixed Lubrication for Direct Problem", *ASME JoT*, 124, pp. 178-185.
- Zhao, H., Choy, F.K. and Braun, M.J., 2002, "Modeling and Analysis of a Wavy Thrust Bearing", *Tribology Transactions*, 45:1, pp. 85-93.
- Zienkiewicz O.C., 1957, "Temperature distribution within lubricating films between parallel bearing surfaces and its effect on the pressures developed. In: *Proceedings of the Conference on Lubrication and Wear*, pp. 135–141 London, October 1–3.

APPENDIX I – CALCULATIONS OF THE TEMPERATURE PROFILE IN THE INLET SECTION (EXPONENTIAL TYPE)

(Detailing of Section III.11.5b)

a) Calculation of the coefficient C of the exponential curve

For an inlet temperature profile with the form:

$$\bar{T}_{\text{exp}}(\alpha_{le}, \eta) = \bar{T}_{bush_le} + (\bar{T}_{shaft} - \bar{T}_{bush_le}) \cdot \frac{e^{C\eta} - 1}{e^C - 1} \quad \text{for } \bar{T}_{bush_le} < \bar{T}_{is} < \bar{T}_{shaft} \quad \text{Eq. A1.1}$$

The value of the constant C should be so that the average temperature of this temperature profile coincides with \bar{T}_{is} , that is:

$$\frac{\int_0^1 \bar{u}_x(\alpha_{le}, \eta) \cdot \bar{T}(\alpha_{le}, \eta) \cdot d\eta}{\int_0^1 \bar{u}_x(\alpha_{le}, \eta) \cdot d\eta} = \bar{T}_{is} \quad \text{Eq. A1.2}$$

Approximating \bar{u}_x with a linear profile and carrying out an integration by parts, the following equality is obtained:

$$\bar{T}_{bush_le} + (\bar{T}_{shaft} - \bar{T}_{bush_le}) \cdot \frac{2e^C(C-1) + 2 - C^2}{C^2(e^C - 1)} - \bar{T}_{is} = 0 = f(C) \quad \text{Eq. A1.3}$$

This equality does not have an obvious analytical solution. Therefore, a numerical method must be used in order to find the root of $f(C)$, C_{root} . This is a delicate task since the function $f(C)$ possesses an undetermined form of the type $\frac{0}{0}$ for $C=0$. This could sometimes cause numerical instability which could ultimately abort the whole numerical process. It is therefore vital to deploy a robust algorithm based on some previous knowledge of the function.

By plotting $f(C)$ one arrives to the conclusion that if $\bar{T}_{bush_le} < \bar{T}_{is} < \bar{T}_{shaft}$ this function displays always a decreasing trend and possesses only one root, C_{root} . This means that it is possible to anticipate whether C_{root} is positive or negative by calculating the value of $f(C)$ at the origin, or, properly speaking, by calculating the limit of $f(C)$ when C tends to 0.

$$\begin{cases} \lim_{C \rightarrow 0} f(C) > 0 \Rightarrow C_{root} > 0 \\ \lim_{C \rightarrow 0} f(C) < 0 \Rightarrow C_{root} < 0 \end{cases} \quad \text{Eq. A1.4}$$

Although $f(C)$ possesses an undetermined form for $C=0$, the limit of the function when C tends to zero is finite and can be calculated with the help of *l'Hôpital's* rule (Ayres Jr., 1957), yielding:

$$\lim_{C \rightarrow 0} f(C) = \frac{1}{3}\bar{T}_{bush_le} + \frac{2}{3}\bar{T}_{shaft} - \bar{T}_{is} \quad \text{Eq. A1.5}$$

Therefore,

$$\begin{cases} \bar{T}_{is} < \frac{1}{3}\bar{T}_{bush_le} + \frac{2}{3}\bar{T}_{shaft} \Rightarrow C_{root} > 0 \\ \bar{T}_{is} > \frac{1}{3}\bar{T}_{bush_le} + \frac{2}{3}\bar{T}_{shaft} \Rightarrow C_{root} < 0 \end{cases} \quad \text{Eq. A1.6}$$

A suitable numerical method to find C_{root} should be chosen. In this case, the popular Newton method does not seem convenient since the “S” shape of $f(C)$ can cause the process to diverge. The False Position method, sketched in Figure VIII-1, seems especially suited for this task. Unlike, for instance, the secant method, which uses two moving points, the False Position method uses instead a fixed point $(C_0, f(C_0))$ and a movable one $(C_n, f(C_n))$.

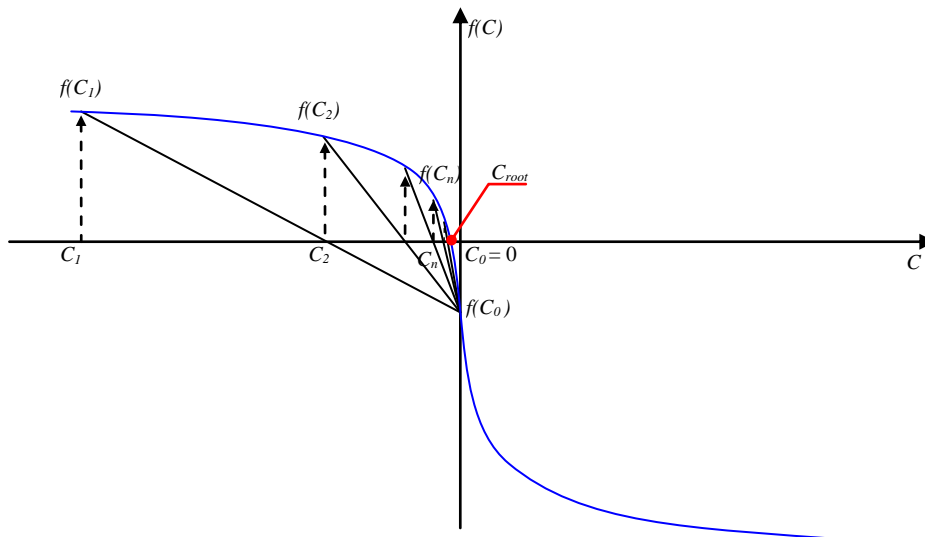


Figure VIII-1 – Outline of the application of the false position method in order to find the root of $f(C)$. The shape of the curve is similar to the one obtained in the real problem.

During the iterative process the straight line between the two points displays a zero which tends to approach the root of the function, C_{root} . This is made by sequentially choosing the new moving point to be located at the coordinate of the newly found zero:

$$C_n = C_0 - f(C_0) \frac{C_{n-1} - C_0}{f(C_{n-1}) - f(C_0)} \quad \text{Eq. A1.7}$$

The false position method can be fairly effective when there is some previous knowledge concerning the uniqueness and location of the root, as in the present case (it is possible to know in advance the signal of the root). This renders $C_0=0$ as the best choice for the fixed point. Additionally, this choice reduces the risk of the moving point passing close to this value, which contains an undetermined form of the function.

After choosing C_0 , the method can only start after a first moving point C_1 with $f(C_1)$ having an opposite signal to the fixed point is chosen. The process stops when $f(C_n)$ is closer to zero than a given convergence criterion.

Once C (C_{root}) has been found, the inlet section temperature profile (Eq. A1.1) is finally complete.

b) 2nd degree polynomial curve component deduction

(from discussion on page 107)

The values of \bar{T}_{is} which would correspond to the limit values of C ($\bar{T}_{is\lim}^+$ and $\bar{T}_{is\lim}^-$, respectively) are obtained by solving Eq. A1.3 in order to \bar{T}_{is} .

The polynomial curve is so that it complies with the following conditions:

$$\left\{ \begin{array}{l} \bar{T}_{Poly}(\alpha_{le}, \eta) = a\eta^2 + b\eta + c \\ \bar{T}_{Poly}(\alpha_{le}, 0) = 0 \\ \bar{T}_{Poly}(\alpha_{le}, 1) = 0 \\ \bar{T}_{is} = \bar{T}_{is\lim}^{-/+} + \bar{T}_{Poly_avg} \end{array} \right.$$

Where \bar{T}_{Poly_avg} is the average temperature of the polynomial curve, calculated through an analytical integration similar to the one of Eq. A1.2.

Applying these conditions, the following expression was found for the polynomial component of the inlet section temperature profile:

$$\bar{T}_{Poly}(\alpha_{le}, \eta) = 6(\bar{T}_{is\lim}^{-/+} - \bar{T}_{is}) \cdot (\eta^2 - \eta)$$

APPENDIX II – FINITE DIFFERENCE SOLUTION OF THE ENERGY EQUATION

(Detailing of section III.7)

The global algorithm used in the present work to solve the energy equation (Eq. III-62) was outlined in section III.7. It was originally proposed by Boncompain et al (1986) and later applied by Costa et al (2003). In this appendix, the semi-implicit numerical procedure used by the latter authors to solve the finite difference version of the energy equation is detailed.

The non-dimensional energy equation previously derived in section III.7 is the following:

$$Pe \left[\bar{u}_x \frac{\partial \bar{T}}{\partial \alpha} + \left(\frac{\bar{u}_y}{h} - \frac{\bar{u}_x \eta}{h} \frac{\partial h}{\partial \alpha} \right) \frac{\partial \bar{T}}{\partial \eta} \right] = \frac{1}{h^2} \frac{\partial^2 \bar{T}}{\partial \eta^2} + Br \frac{\bar{\mu}_{eq}}{h^2} \left(\frac{\partial \bar{u}_x}{\partial \eta} \right)^2 \quad \begin{array}{l} \text{Eq. A2.1} \\ \text{Eq. VIII-1} \end{array}$$

a) Transformation of the derivatives into finite differences

As seen before, in the circumferential direction the convective term of the energy equation (heat transport due to fluid motion) is normally dominant, while in the radial direction the diffusive term (heat transport due to conduction) is normally dominant. This dictates the use of backward and centered differences along each one of the directions, respectively. Therefore, the finite difference version of the derivatives is:

$$\left. \begin{array}{l} \frac{\partial \bar{T}}{\partial \alpha} \Big|_{j,k} = \frac{\bar{T}_{j,k} - \bar{T}_{j-1,k}}{\Delta \alpha_j} \quad (\Delta \alpha_j = \alpha_j - \alpha_{j-1}) \quad (\bar{u}_x > 0) \end{array} \right\} \text{Eq. A2.2}$$

$$\left. \begin{array}{l} \frac{\partial \bar{u}_x}{\partial \alpha} \Big|_{j,k} = \frac{\bar{u}_x|_{j,k} - \bar{u}_x|_{j-1,k}}{\Delta \alpha_j} \quad (\bar{u}_x > 0) \end{array} \right\} \text{Eq. A2.3}$$

$$\left. \begin{array}{l} \frac{\partial \bar{T}}{\partial \eta} \Big|_{j,k} = \frac{\bar{T}_{j,k+1} - \bar{T}_{j,k-1}}{2 \cdot \Delta \eta} \end{array} \right\} \text{Eq. A2.4}$$

$$\left. \begin{array}{l} \frac{\partial^2 \bar{T}}{\partial \eta^2} \Big|_{j,k} = \frac{\bar{T}_{j,k+1} - 2\bar{T}_{j,k} + \bar{T}_{j,k-1}}{2 \cdot \Delta \eta} \end{array} \right\} \text{Eq. A2.5}$$

The non-dimensional film thickness, h , may be analytically derived in order to the circumferential coordinate, α , by recalling the relationship between these parameters defined in Eq. III-6 (see page 63). Therefore:

$$\frac{\partial \bar{h}}{\partial \alpha} = -\varepsilon \sin(\gamma) \quad (\gamma = \alpha + \Gamma - \varphi) \quad \text{Eq. A2.6}$$

b) Grouping of variables for the explicitation of $\bar{T}_{j,k}$

The following groups of variables were defined:

$$\left\{ \begin{array}{l} EE_1 = \frac{Pe}{\Delta \alpha_j} \cdot \bar{u}_x|_{N_y, j, k} \\ EE_2 = \frac{Pe}{2\Delta \eta \cdot \bar{h}_j} \left[\bar{u}_y|_{N_y, j, k} + \bar{u}_x|_{N_y, j, k} \cdot \eta \cdot \varepsilon \cdot \sin \gamma \right] \\ EE_3 = \left(\frac{1}{\Delta \eta \cdot \bar{h}_j} \right)^2 \\ EE_4 = -Br \frac{\mu_{j,k}}{\bar{h}^2} \left[\frac{\bar{u}_x|_{N_y, j, k+1} - \bar{u}_x|_{N_y, j, k-1}}{2\Delta \eta} \right]^2 \end{array} \right.$$

Also

$$\left\{ \begin{array}{l} EE_5 = -(EE_1 + 2EE_3) \\ EE_6 = EE_2 - EE_3 \\ EE_7 = -(EE_2 + EE_3) \\ EE_8 = -EE_1 \end{array} \right. \quad \text{Eq. A2.7}$$

Therefore, the finite difference energy equation may be rewritten as:

$$-EE_5 \bar{T}_{j,k} + EE_6 \bar{T}_{j,k+1} + EE_7 \bar{T}_{j,k-1} + EE_8 \bar{T}_{j-1,k} + EE_4 = 0 \quad \text{Eq. A2.8}$$

Now, according to this equation, the calculation of $\bar{T}_{j,k}$ requires, in radial terms, the knowledge of the temperature at the contiguous nodes $\bar{T}_{j,k-1}$ $\bar{T}_{j,k+1}$. It would help if Eq. A2.8 could be manipulated in such a way that $\bar{T}_{j,k}$ would be calculated with the explicit knowledge of only one of the former temperatures (either $\bar{T}_{j,k-1}$ or $\bar{T}_{j,k+1}$). This would signify transforming the calculation of the radial temperature evolution from a boundary value problem into an initial value problem, much simpler to solve. The semi-implicit approach used is described in continuation.

A new variable $S_{j,k}$, standing as the temperature differential between node (j,k) and the inner bush surface, (j,1), is defined:

$$S_{j,k} = \bar{T}_{j,k} - \bar{T}_{j,1} \quad \text{Eq. A2.9}$$

Substituting into Eq. A2.8, the new version of the energy equation becomes:

$$-EE_5 S_{j,k} + EE_6 S_{j,k+1} + EE_7 S_{j,k-1} + EE_9 = 0 \quad \text{Eq. A2.10}$$

With

$$EE_9 = (-EE_5 + EE_6 + EE_7) \bar{T}_{j,1} + EE_8 \bar{T}_{j-1,k} + EE_4 \quad \text{Eq. A2.11}$$

c) Conversion into an initial value problem

Now, the problem under study would become an initial value problem if Eq. A2.10 could be rewritten under the following form:

$$S_{j,k} = A_{j,k} S_{j,k+1} + B_{j,k} \quad \text{Eq. A2.12}$$

The solution to the problem resides in finding the expressions for the two variables A and B which comply with Eq. A2.10.

This is easily made by, first, applying Eq. A2.12 to the previous radial node, $k-1$:

$$S_{j,k-1} = A_{j,k-1} S_{j,k} + B_{j,k-1} \quad \text{Eq. A2.13}$$

Next, $S_{j,k-1}$ is substituted in Eq. A2.10 by this expression:

$$S_{j,k} = \underbrace{\frac{EE_6}{EE_5 - EE_7 A_{j,k-1}}}_{A_{j,k}} S_{j,k+1} + \underbrace{\frac{EE_7 B_{j,k-1} + EE_9}{EE_5 - EE_7 A_{j,k-1}}}_{B_{j,k}} \quad \text{Eq. A2.14}$$

And so, the expressions for A and B have been found:

$$\left\{ \begin{array}{l} A_{j,k} = \frac{EE_6}{EE_5 - EE_7 A_{j,k-1}} \\ B_{j,k} = \frac{EE_7 B_{j,k-1} + EE_9}{EE_5 - EE_7 A_{j,k-1}} \end{array} \right. \quad \text{Eq. A2.15}$$

$$\text{Eq. A2.16}$$

It can be seen that $A_{j,k}$ and $B_{j,k}$ both depend on $A_{j,k-1}$ and $B_{j,k-1}$. Therefore, it is necessary to find initial values, $A_{j,1}$ and $B_{j,1}$ which comply with Eq. A2.12, solved for $k=1$. Therefore, taking into account the definition of $S_{j,k}$ (Eq. A2.9), it is obtained:

$$0 = A_{j,1}S_{j,2} + B_{j,1} \quad \text{Eq. A2.17}$$

One solution for this equation is:

$$\begin{cases} A_{j,1} = 0 \\ B_{j,1} = 0 \end{cases} \quad \text{Eq. A2.18}$$

d) Outline of the numerical algorithm

It is now possible to obtain the temperature field along the whole domain:

1. The calculations start in the first row of nodes downstream of the inlet section (leading edge of a groove), using the inlet temperature profile as initial condition;
2. For the same circumferential coordinate, j , calculate $A_{j,k}$ and $B_{j,k}$ sequentially for $k=2$ to N_y (Eq. A2.15 and Eq. A2.16).
3. For the same circumferential coordinate, j , calculate sequentially $S_{j,k}$ and $\bar{T}_{j,k}$ (Eq. A2.14 and Eq. A2.9, respectively) by the inverse order, for $k=N_y-1$ to 2. Note that S_{j,N_y} is an initial/boundary condition (for each iteration of the global thermal algorithm the shaft temperature and the inner bush surface temperature are fixed);
4. Go to the next circumferential position and repeat the previous steps. Do this until reaching the trailing edge of the next groove.

If a reverse flow / back flow region exists (a region with $\bar{u}_x < 0$), then the domain separation algorithm described in section III.7 must be applied. Namely, within the negative flow domain the derivatives $\frac{\partial \bar{T}}{\partial \alpha}$ and $\frac{\partial \bar{u}_x}{\partial \alpha}$ must be rewritten as backward differences. Despite the slight differences in the expressions obtained, the procedure is virtually identical to the one used for the positive velocity domain, which has just been described in this Appendix.

